Title

Advanced Modeling and Evaluation of the Response of Base-Isolated Nuclear Facility Structures to Vertical Earthquake Excitation

Author

Keldrauk, Eric Scott

Publication Date

2012

Peer reviewed|Thesis/dissertation

Advanced Modeling and Evaluation of the Response of Base-Isolated Nuclear Facility Structures to Vertical Earthquake Excitation

by

Eric Scott Keldrauk

A dissertation submitted in partial satisfaction of the
requirements for the degree of
Doctor of Philosophy

in

Engineering - Civil and Environmental Engineering

in the

Graduate Division

of the

University of California, Berkeley

Committee in charge:

Professor Božidar Stojadinović, Chair
Professor Per F. Peterson
Professor Emeritus James M. Kelly

Fall 2012

Advanced Modeling and Evaluation of the Response of Base-Isolated Nuclear Facility Structures to Vertical Earthquake Excitation

Abstract

Advanced Modeling and Evaluation of the Response of Base-Isolated Nuclear Facility Structures to Vertical Earthquake Excitation

by

Eric Scott Keldrauk

Doctor of Philosophy in Engineering - Civil and Environmental Engineering

University of California, Berkeley

Professor Božidar Stojadinović, Chair

The commissioning and construction of new nuclear power plants in the United States has dwindled over the past 30 years despite significant innovation in reactor technology. This is partially due to the ever-increasing seismic hazard estimates, which increases the demand on and risk to nuclear power plant structures.

Seismic base isolation is a mature technology which introduces a laterally-flexible and vertically-stiff layer between the foundation and superstructure to significantly reduce the seismic response of the structure, systems, and components therein. Such devices have also been noted to concentrate the displacement response in one plane, reduce higher-mode participation, and provide damping to protect against excessive displacements, all of which aid in increasing safety margins for seismically-isolated nuclear structures. Despite numerous studies analyzing the applicability of seismic base isolation to nuclear power plant structures, some of which are discussed herein, no seismically-isolated nuclear plant has been constructed in the United States.

This study presents a time-domain procedure for analyzing the performance of seismically-isolated nuclear structures in response to design-basis earthquake events using ALE3D. The simulations serve as a parametric study to assess the effects of soil column type, seismic isolation model, superstructure mesh, and ground motion selection on global displacements, rotations, and accelerations, as well as internal floor accelerations. Explicit modeling of the soil columns and superstructures enables detailed analysis of soil-structure interaction. The soil columns analyzed have constant properties over the height of the finite element soil mesh and include rock, soft rock, and stiff soil sites, as well as a "no soil" case for comparison. Four separate 3-dimensional seismic isolation bearing models were coded into ALE3D and validated. These include models for friction pendulum, triple friction pendulum, simplified lead rubber, and robust lead rubber bearings. Lastly, two superstructure finite element meshes were considered: a cylindrical plant design meant to represent a typical conceptual design for advanced reactors, and a rectangular plant design meant to represent an advanced boiling water reactor. The ground motions considered include 30 three-component time his-

tory records scaled to meet the seismic hazard for the Diablo Canyon nuclear plant. Every combination of soil column, isolator model, and superstructure were subjected to a subset of three of the harshest ground motions, termed the "basic motions", and the combinations which included the rectangular plant design atop the rock soil column were subjected to all 30 motions.

The results of the various simulations including accelerations in the soil columns and superstructures as well as displacements and rotations in the isolators and superstructures are presented. The results suggest three possible effects: an isolator-type effect, a soil-type effect, and a slenderness effect. The isolator-type effect refers to significant increases in vertical soil acceleration amplifications, isolator uplift/tension, and global rotations including torsion and overturning for friction bearings in comparison to elastomeric bearings. Additionally it is noted that inclusion of lead plug softening has the effect of increasing peak lateral isolator deformations, especially for the ground motions that naturally induce high-amplitude deformations in the bearings. These results suggest that uplift/tension may be troublesome in high-seismic areas and the use of restrainers should be analyzed as a possible solution. Furthermore, these results reinforce the lateral design displacement estimate procedures for seismically-isolated nuclear structures in ASCE4-11.

The results prove that explicit inclusion of the soil column is necessary for proper response characterization and the chosen soil properties greatly affect the efficacy of seismic isolation designs. The soil-type effect comes from observations of comparative simulations which show that, in general, peak isolator uplift/tension and deformation, as well as peak global displacements and rotations including torsion and overturning increase as the soil column becomes less-stiff, regardless of the isolator model or superstructure considered. These results suggest that although seismic isolation can be effective for structures atop a variety of soil columns, it is imperative that a single isolator design only be considered applicable to a corresponding soil column unless extensive analyses prove otherwise for a specific case.

Differences in peak response parameters between the two superstructures point to a possible slenderness effect. Specifically, the isolator deformations as well as the global displacements and rotations are observed to increase for the cylindrical superstructure in comparison to the rectangular superstructure cases utilizing the same ground motion, soil column, and isolator model. Should further research reaffirm this effect, a practical limit could be set for superstructure slenderness.

To the two most important women in my life: my mother, Clarinda, and my fiancé, Gemma.

Contents

Contents ii

List of Figures v

List of Tables xviii

1 Introduction 1

1.1 Objectives of Research 1
1.2 Organization of Thesis 2

2 Seismic Base Isolation 3

2.1 Concept 4
2.2 Elastomeric Bearings 7
2.2.1 Low-Damping Rubber Bearings 7
2.2.2 High-Damping Rubber Bearings 8
2.2.3 Lead-Rubber Bearings 8
2.3 Sliding Bearings 10
2.3.1 Friction Pendulum Bearings 11
2.3.2 Triple Friction Pendulum Beatings 12
2.4 Auxiliary Design Considerations 13
2.4.1 Supplemental Damping 14
2.4.2 Seismic Gap 16
2.4.3 Collision Restrainers and Bumpers 16
2.4.4 External Event Shield 16
2.4.5 Umbilicals 17
2.4.6 Isolation Level Location 18
2.5 Base Isolation Applications 19
2.5.1 Tall Buildings 19
2.5.2 Industrial Structures 20
2.5.3 Liquefied Natural Gas Tanks 20
2.5.4 Nuclear Power Facility Structures 21

3 Nuclear Power Plants **22**
3.1 Nuclear Facility Structural Design Codes 22
3.2 NPP Studies Utilizing SBI 24
3.2.1 PRISM 24
3.2.2 SAFR 24
3.2.3 EERC Bearing Tests 25
3.2.4 Recent Studies 26
3.3 The Kashiwazaki-Kariwa Nuclear Power Plant 27
3.3.1 2004 Chūetsu Earthquake 28
3.3.2 2007 Niigata Chūetsu-Oki Earthquake 28
3.3.3 Acceleration Amplification Data 29

4 Isolation Models **35**
4.1 Robust Friction Pendulum Model 35
4.1.1 Model Response 35
4.1.2 Validation 42
4.2 Simplified Friction Pendulum Bearing Model 53
4.2.1 Model Response 53
4.2.2 Validation 55
4.3 Simplified Lead-Rubber Bearing Model 63
4.3.1 Model Response 63
4.3.2 Validation 64
4.4 Robust Lead-Rubber Bearing Model 72
4.4.1 Model Response 72
4.4.2 Validation 75
4.5 Bearing Damage and Failure 85
4.5.1 Friction Bearings 85
4.5.2 Elastomeric Bearings 86
4.5.3 Progressive Failure 87
4.5.4 Property Variability 87

5 Superstructure Design **88**
5.1 Superstructural Models 88
5.1.1 Materials 89
5.1.2 Cylindrical Plant 89
5.1.3 Rectangular Box-Type Plant 90
5.2 Equipment 95
5.3 Foundation Model 98
5.4 Isolation System Models 98
5.4.1 FP Bearing Design 99
5.4.2 TFP Bearing Design 103
5.4.3 LR Bearing Design 103

5.4.4 Isolation System Layout . . . 105

6 Geotechnical Specifications **109**
6.1 Soil Strata Characterization . . . 109
6.2 Ground Motions . . . 110

7 Analysis **114**
7.1 Software . . . 114
7.2 Computing Facilities . . . 115
7.3 Analysis Cases . . . 115
7.4 Instrumentation . . . 116
7.5 Post-Processing . . . 117

8 Results and Conclusions **121**
8.1 Soil Column Response . . . 121
8.2 Isolator Deformation and Uplift Response . . . 122
8.3 Global Displacement, Torsion and Overturning . . . 124
8.4 Superstructure Response . . . 126
8.5 Summary of Conclusions . . . 127
8.6 Future Work . . . 128

Bibliography **129**

Appendices **137**

A Kashiwazaki-Kariwa Response Data **138**

B Ground Motion Records and Spectra **147**

C Soil Column Acceleration Data **211**

D Isolator Data **239**

E Global Torsion and Overturning Data **254**

F Superstructure Acceleration Data **319**

List of Figures

2.1 Response spectra for the Corralitos record of the 1989 Loma Prieta earthquake (6.9 M_W) with 5% damping demonstrating the effect of a period shift between non-isolated ($T \approx 0.25$ sec) and isolated ($T \approx 2.50$ sec) structures 6
2.2 Idealized unidirectional hysteresis for a LDR bearing 9
2.3 Section view of an HDR bearing for the Foothill Communities Law and Justice Center following tests at the UC Berkeley Richmond Field Station (photograph courtesy of James Kelly) 9
2.4 Schematic of an undeformed LR bearing 10
2.5 Schematic of an undeformed FP bearing 11
2.6 TFP bearing components used in tests at the UC Berkeley Richmond Field Station (Photographs courtesy of Tracy Becker) 13
2.7 Schematic of an undeformed TFP bearing 14
2.8 Schematic of the unidirectional displacement of FP and TFP bearings showing various stages of slider motion 14
2.9 Normalized monotonic load-displacement curve for a TFP bearing for the typical design case where $\mu_1 = \mu_2$ and $L_1 = L_2$ 15
2.10 Schematic of isolated structures showing the center-of-mass (CoM) and center-of-rigidity (CoR) for isolation planes at three levels: (a) base, (b) middle, and (c) top 19

3.1 Schematic of PRISM reactor module (Courtesy of Ian Aiken) 25
3.2 Schematic of SAFR reactor module (Courtesy of Ian Aiken) 26
3.3 Peak structural amplifications at the Kashiwazaki-Kariwa nuclear power plant in response to the main shock of the 2007 Niigata Chūetsu-Oki earthquake 31
3.4 Peak structural amplifications at the Kashiwazaki-Kariwa nuclear power plant in response to aftershock 1 of the 2007 Niigata Chūetsu-Oki earthquake 32
3.5 Peak structural amplifications at the Kashiwazaki-Kariwa nuclear power plant in response to aftershock 2 of the 2007 Niigata Chūetsu-Oki earthquake 32
3.6 Peak structural amplifications at the Kashiwazaki-Kariwa nuclear power plant in response to aftershock 3 of the 2007 Niigata Chūetsu-Oki earthquake 33
3.7 Peak structural amplifications at the Kashiwazaki-Kariwa nuclear power plant in response to aftershock 4 of the 2007 Niigata Chūetsu-Oki earthquake 33

3.8 Peak structural amplifications at the Kashiwazaki-Kariwa nuclear power plant in response to aftershock 5 of the 2007 Niigata Chūetsu-Oki earthquake 34
3.9 Peak structural amplifications at the Kashiwazaki-Kariwa nuclear power plant in response to aftershock 6 of the 2007 Niigata Chūetsu-Oki earthquake 34

4.1 Schematic of an undeformed TFP bearing depicting the physical input parameters for the model 36
4.2 Normalized uni-directional hysteresis for an individual slider 38
4.3 Schematic of a displaced TFP bearing showing the connection between lateral and vertical displacements 41
4.4 Displacement paths for the dispalcement-controlled test cases 43
4.5 Directional displacement time histories for the displacement-controlled test cases 44
4.6 2-dimensional input acceleration time histories (100% scale) for the Newhall record of the 1994 Northridge earthquake with a length scale of 2 45
4.7 3-dimensional input acceleration time histories (50% scale) for the 1978 Tabas earthquake record with a length scale of 2 45
4.8 Comparative directional hystereses of the TFP experiments and models for the uni-directional sine wave displacement orbit 46
4.9 Comparative directional hystereses and force path of the TFP experiments and models for the circular displacement orbit 47
4.10 Comparative directional hystereses and force path of the TFP experiments and models for the square displacement orbit 48
4.11 Comparative directional hystereses and force path of the TFP experiments and models for the figure-eight displacement orbit 49
4.12 Comparative directional hystereses and displacement path of the TFP experiments and models for the unrestrained response to the 1994 Northridge earthquake Newhall record 50
4.13 Comparative directional hystereses and displacement path of the TFP experiments and models for the unrestrained response to the 1978 Tabas record 51
4.14 Comparative vertical displacements of the TFP experiments and models for the displacement-controlled test cases 52
4.15 Comparative directional hystereses of the FP models for the uni-directional sine wave displacement orbit 56
4.16 Comparative directional hystereses and force path of the FP models for the circular displacement orbit 57
4.17 Comparative directional hystereses and force path of the FP models for the square displacement orbit 58
4.18 Comparative directional hystereses and force path of the FP models for the figure-eight displacement orbit 59
4.19 Comparative directional hystereses and displacement path of the FP models for the unrestrained response to the 1994 Northridge earthquake Newhall record . . 60

4.20 Comparative directional hystereses and displacement path of the FP models for the unrestrained response to the 1978 Tabas record 61
4.21 Comparative vertical displacement response of the FP models for the unrestrained response to the 1978 Tabas record 62
4.22 Idealized lateral hysteresis of an LR bearing depicting necessary inputs for the analytical model 64
4.23 Comparative directional hystereses of the simplified LR models for the uni-directional sine wave displacement orbit 65
4.24 Comparative directional hystereses and force path of the simplified LR models for the circular displacement orbit 66
4.25 Comparative directional hystereses and force path of the simplified LR models for the square displacement orbit 67
4.26 Comparative directional hystereses and force path of the simplified LR models for the figure-eight displacement orbit 68
4.27 Comparative directional hystereses and displacement path of the simplified LR models for the unrestrained response to the 1994 Northridge earthquake Newhall record 69
4.28 Comparative directional hystereses and displacement path of the simplified LR models for the unrestrained response to the 1978 Tabas record 70
4.29 Comparative vertical displacement response of the simplified LR models for the unrestrained response to the 1978 Tabas record 71
4.30 Schematic of an undeformed LR bearing depicting the physical input parameters for the model 72
4.31 Schematic of a deformed LR bearing showing change in vertical deformation with lateral displacement 74
4.32 Directional displacement time histories for the vertical LR validation test cases . 76
4.33 1-dimensional sine-wave displacement time history for the displacement-controlled test 77
4.34 1-dimensional input acceleration time history for the 1978 Tabas earthquake record 77
4.35 1-dimensional input acceleration time history for the 1994 Northridge earthquake record 78
4.36 1-dimensional input acceleration time history for the 1995 Kobe earthquake record 78
4.37 2-dimensional input acceleration time history for the 1999 Duzce earthquake record 79
4.38 2-dimensional input acceleration time history for the 1999 Chi-Chi earthquake record 79
4.39 Vertical validation test results 80
4.40 Comparative directional hysteresis of the robust LR models for the uni-directional sine wave displacement orbit 81
4.41 Comparative directional hysteresis of the robust LR models for the unrestrained response to the 1978 Tabas earthquake record 81
4.42 Comparative directional hysteresis of the robust LR models for the unrestrained response to the 1994 Northridge earthquake Rinaldi record 82

4.43 Comparative directional hysteresis of the robust LR models for the unrestrained response to the 1995 Kobe earthquake record 82
4.44 Comparative directional hystereses of the robust LR models for the unrestrained response to the 1999 Duzce earthquake Bolu record 83
4.45 Comparative directional hystereses of the robust LR models for the unrestrained response to the 1999 Chi-Chi earthquake TCU065 record 84
4.46 Comparative lead core temperature change time histories of the robust LR models for the unrestrained earthquake response tests 85

5.1 Plan and elevation view cross-section schematics of the cylindrical plant design . 91
5.2 Cross-section of the cylindrical plant finite element mesh 92
5.3 Plan and elevation view cross-section schematics of the rectangular, box-type plant design 93
5.4 Cross-section of the rectangular, box-type plant finite element mesh 94
5.5 Lumped-mass stick model composition 97
5.6 Displacement time histories for validation of stick model frequencies 100
5.7 Isolator layout for the cylindrical plant 107
5.8 Isolator layout for the rectangular plant 108

6.1 Soil shear wave velocity profiles 111
6.2 Full superstructure and soil model 3D mesh depicting boundary condition nodesets113

7.1 Legend for the analysis code 116
7.2 Schematic of tracer locations throughout the cylindrical superstructure 119
7.3 Schematic of tracer locations throughout the rectangular superstructure 120

A.1 Map of the Kashiwazaki-Kariwa nuclear power plant site (courtesy of TEPCO) . 139
A.2 Peak ground and superstructure acceleration data in response to the main shock of the 2007 Niigata Chūetsu-Oki (6.6 M_W) earthquake 140
A.3 Peak ground and superstructure acceleration data in response to aftershock 1 following the 2007 Niigata Chūetsu-Oki (6.6 M_W) earthquake 141
A.4 Peak ground and superstructure acceleration data in response to aftershock 2 following the 2007 Niigata Chūetsu-Oki (6.6 M_W) earthquake 142
A.5 Peak ground and superstructure acceleration data in response to aftershock 3 following the 2007 Niigata Chūetsu-Oki (6.6 M_W) earthquake 143
A.6 Peak ground and superstructure acceleration data in response to aftershock 4 following the 2007 Niigata Chūetsu-Oki (6.6 M_W) earthquake 144
A.7 Peak ground and superstructure acceleration data in response to aftershock 5 following the 2007 Niigata Chūetsu-Oki (6.6 M_W) earthquake 145
A.8 Peak ground and superstructure acceleration data in response to aftershock 6 following the 2007 Niigata Chūetsu-Oki (6.6 M_W) earthquake 146

B.1 Time history records for the Imperial Valley, USA (G-ELC) earthquake 151

B.2 Response spectra with 5% damping for the Imperial Valley, USA (G-ELC) earthquake . . . 152
B.3 Time history records for the Hollister, USA (C-HCH) earthquake . . . 153
B.4 Response spectra with 5% damping for the Hollister, USA (C-HCH) earthquake 154
B.5 Time history records for the Hollister, USA (D-HCH) earthquake . . . 155
B.6 Response spectra with 5% damping for the Hollister, USA (D-HCH) earthquake 156
B.7 Time history records for the Point Mugu, USA (PHN) earthquake . . . 157
B.8 Response spectra with 5% damping for the Point Mugu, USA (PHN) earthquake 158
B.9 Time history records for the Livermore, USA (A-ANT) earthquake . . . 159
B.10 Response spectra with 5% damping for the Livermore, USA (A-ANT) earthquake 160
B.11 Time history records for the Livermore, USA (A-KOD) earthquake . . . 161
B.12 Response spectra with 5% damping for the Livermore, USA (A-KOD) earthquake 162
B.13 Time history records for the Livermore, USA (A-SRM) earthquake . . . 163
B.14 Response spectra with 5% damping for the Livermore, USA (A-SRM) earthquake 164
B.15 Time history records for the Taiwan (05O07) earthquake . . . 165
B.16 Response spectra with 5% damping for the Taiwan (05O07) earthquake . . . 166
B.17 Time history records for the Westmorland, USA (PTS) earthquake . . . 167
B.18 Response spectra with 5% damping for the Westmorland, USA (PTS) earthquake 168
B.19 Time history records for the Double Springs, USA (WOO) earthquake . . . 169
B.20 Response spectra with 5% damping for the Double Springs, USA (WOO) earthquake 170
B.21 Time history records for the Friuli, Italy (B-BUI) earthquake . . . 171
B.22 Response spectra with 5% damping for the Friuli, Italy (B-BUI) earthquake . . 172
B.23 Time history records for the N Palm Springs, USA (MVH) earthquake . . . 173
B.24 Response spectra with 5% damping for the N Palm Springs, USA (MVH) earthquake 174
B.25 Time history records for the Irpinia, Italy (B-BIS) earthquake . . . 175
B.26 Response spectra with 5% damping for the Irpinia, Italy (B-BIS) earthquake . . 176
B.27 Time history records for the Chi-Chi, Taiwan (TCU116) earthquake . . . 177
B.28 Response spectra with 5% damping for the Chi-Chi, Taiwan (TCU116) earthquake 178
B.29 Time history records for the Chi-Chi, Taiwan (TCU120) earthquake . . . 179
B.30 Response spectra with 5% damping for the Chi-Chi, Taiwan (TCU120) earthquake 180
B.31 Time history records for the Chi-Chi, Taiwan (TCU138) earthquake . . . 181
B.32 Response spectra with 5% damping for the Chi-Chi, Taiwan (TCU138) earthquake 182
B.33 Time history records for the Chi-Chi, Taiwan (TCU067) earthquake . . . 183
B.34 Response spectra with 5% damping for the Chi-Chi, Taiwan (TCU067) earthquake 184
B.35 Time history records for the Victoria, Mexico (CHI) earthquake . . . 185
B.36 Response spectra with 5% damping for the Victoria, Mexico (CHI) earthquake . 186
B.37 Time history records for the Victoria, Mexico (HPB) earthquake . . . 187
B.38 Response spectra with 5% damping for the Victoria, Mexico (HPB) earthquake 188
B.39 Time history records for the Dinar, Turkey (DIN) earthquake . . . 189
B.40 Response spectra with 5% damping for the Dinar, Turkey (DIN) earthquake . . 190
B.41 Time history records for the Imperial Valley, USA (H-ECC) earthquake . . . 191

B.42 Response spectra with 5% damping for the Imperial Valley, USA (H-ECC) earthquake . . . 192
B.43 Time history records for the Superstition Hills, USA (B-ICC) earthquake 193
B.44 Response spectra with 5% damping for the Superstition Hills, USA (B-ICC) earthquake . . . 194
B.45 Time history records for the Superstition Hills, USA (B-WSM) earthquake . . . 195
B.46 Response spectra with 5% damping for the Superstition Hills, USA (B-WSM) earthquake . . . 196
B.47 Time history records for the Superstition Hills, USA (B-IVW) earthquake . . . 197
B.48 Response spectra with 5% damping for the Superstition Hills, USA (B-IVW) earthquake . . . 198
B.49 Time history records for the Corinth, Greece (COR) earthquake 199
B.50 Response spectra with 5% damping for the Corinth, Greece (COR) earthquake . 200
B.51 Time history records for the Northridge, USA (MUL) earthquake 201
B.52 Response spectra with 5% damping for the Northridge, USA (MUL) earthquake 202
B.53 Time history records for the Northridge, USA (LDM) earthquake 203
B.54 Response spectra with 5% damping for the Northridge, USA (LDM) earthquake 204
B.55 Time history records for the Northridge, USA (GLE) earthquake 205
B.56 Response spectra with 5% damping for the Northridge, USA (GLE) earthquake 206
B.57 Time history records for the Kobe, Japan (SHI) earthquake 207
B.58 Response spectra with 5% damping for the Kobe, Japan (SHI) earthquake . . . 208
B.59 Time history records for the Loma Prieta, USA (LGP) earthquake 209
B.60 Response spectra with 5% damping for the Loma Prieta, USA (LGP) earthquake 210

C.1 Peak soil column acceleration data from the simulations with the cylindrical superstructure and FP bearings subjected to ground motion 08 218
C.2 Peak soil column acceleration data from the simulations with the rectangular superstructure and FP bearings subjected to ground motion 08 219
C.3 Peak soil column acceleration data from the simulations with the cylindrical superstructure and FP bearings subjected to ground motion 09 220
C.4 Peak soil column acceleration data from the simulations with the rectangular superstructure and FP bearings subjected to ground motion 09 221
C.5 Peak soil column acceleration data from the simulations with the cylindrical superstructure and FP bearings subjected to ground motion 22 222
C.6 Peak soil column acceleration data from the simulations with the rectangular superstructure and FP bearings subjected to ground motion 22 223
C.7 Peak soil column acceleration data from the simulations with the cylindrical superstructure and simplified LR bearings subjected to ground motion 08 224
C.8 Peak soil column acceleration data from the simulations with the rectangular superstructure and simplified LR bearings subjected to ground motion 08 225
C.9 Peak soil column acceleration data from the simulations with the cylindrical superstructure and simplified LR bearings subjected to ground motion 09 226

C.10 Peak soil column acceleration data from the simulations with the rectangular superstructure and simplified LR bearings subjected to ground motion 09 227
C.11 Peak soil column acceleration data from the simulations with the cylindrical superstructure and simplified LR bearings subjected to ground motion 22 228
C.12 Peak soil column acceleration data from the simulations with the rectangular superstructure and simplified LR bearings subjected to ground motion 22 229
C.13 Peak soil column acceleration data from the simulations with the cylindrical superstructure and robust LR bearings subjected to ground motion 08 230
C.14 Peak soil column acceleration data from the simulations with the rectangular superstructure and robust LR bearings subjected to ground motion 08 231
C.15 Peak soil column acceleration data from the simulations with the cylindrical superstructure and robust LR bearings subjected to ground motion 09 232
C.16 Peak soil column acceleration data from the simulations with the rectangular superstructure and robust LR bearings subjected to ground motion 09 233
C.17 Peak soil column acceleration data from the simulations with the cylindrical superstructure and robust LR bearings subjected to ground motion 22 234
C.18 Peak soil column acceleration data from the simulations with the rectangular superstructure and robust LR bearings subjected to ground motion 22 235
C.19 Median and standard deviation soil data from the simulations with the rectangular superstructure and FP bearings subjected to all ground motions 236
C.20 Median and standard deviation soil data from the simulations with the rectangular superstructure and simplified LR bearings subjected to all ground motions 237
C.21 Median and standard deviation soil data from the simulations with the rectangular superstructure and robust LR bearings subjected to all ground motions . . 238

D.1 Peak isolator data from the simulations with the cylindrical superstructure subjected to ground motion 08 245
D.2 Peak isolator data from the simulations with the rectangular superstructure subjected to ground motion 08 246
D.3 Peak isolator data from the simulations with the cylindrical superstructure subjected to ground motion 09 247
D.4 Peak isolator data from the simulations with the rectangular superstructure subjected to ground motion 09 248
D.5 Peak isolator data from the simulations with the cylindrical superstructure subjected to ground motion 22 249
D.6 Peak isolator data from the simulations with the rectangular superstructure subjected to ground motion 22 250
D.7 Peak isolator compression displacement data from the simulations with the rectangular superstructure subjected to all ground motions 251
D.8 Peak isolator uplift/tension displacement data from the simulations with the rectangular superstructure subjected to all ground motions 252

D.9 Peak isolator lateral displacement data from the simulations with the rectangular superstructure subjected to all ground motions 253

E.1 Peak displacement data from the simulations with the cylindrical superstructure and FP isolators subjected to ground motion 08 265
E.2 Peak displacement data from the simulations with the rectangular superstructure and FP isolators subjected to ground motion 08 266
E.3 Peak rotation data from the simulations with the cylindrical superstructure and FP isolators subjected to ground motion 08 267
E.4 Peak rotation data from the simulations with the rectangular superstructure and FP isolators subjected to ground motion 08 268
E.5 Peak displacement data from the simulations with the cylindrical superstructure and FP isolators subjected to ground motion 09 269
E.6 Peak displacement data from the simulations with the rectangular superstructure and FP isolators subjected to ground motion 09 270
E.7 Peak rotation data from the simulations with the cylindrical superstructure and FP isolators subjected to ground motion 09 271
E.8 Peak rotation data from the simulations with the rectangular superstructure and FP isolators subjected to ground motion 09 272
E.9 Peak displacement data from the simulations with the cylindrical superstructure and FP isolators subjected to ground motion 22 273
E.10 Peak displacement data from the simulations with the rectangular superstructure and FP isolators subjected to ground motion 22 274
E.11 Peak rotation data from the simulations with the cylindrical superstructure and FP isolators subjected to ground motion 22 275
E.12 Peak rotation data from the simulations with the rectangular superstructure and FP isolators subjected to ground motion 22 276
E.13 Peak displacement data from the simulations with the cylindrical superstructure and simple LR isolators subjected to ground motion 08 277
E.14 Peak displacement data from the simulations with the rectangular superstructure and simple LR isolators subjected to ground motion 08 278
E.15 Peak rotation data from the simulations with the cylindrical superstructure and simple LR isolators subjected to ground motion 08 279
E.16 Peak rotation data from the simulations with the rectangular superstructure and simple LR isolators subjected to ground motion 08 280
E.17 Peak displacement data from the simulations with the cylindrical superstructure and simple LR isolators subjected to ground motion 09 281
E.18 Peak displacement data from the simulations with the rectangular superstructure and simple LR isolators subjected to ground motion 09 282
E.19 Peak rotation data from the simulations with the cylindrical superstructure and simple LR isolators subjected to ground motion 09 283

E.20 Peak rotation data from the simulations with the rectangular superstructure and simple LR isolators subjected to ground motion 09 284
E.21 Peak displacement data from the simulations with the cylindrical superstructure and simple LR isolators subjected to ground motion 22 285
E.22 Peak displacement data from the simulations with the rectangular superstructure and simple LR isolators subjected to ground motion 22 286
E.23 Peak rotation data from the simulations with the cylindrical superstructure and simple LR isolators subjected to ground motion 22 287
E.24 Peak rotation data from the simulations with the rectangular superstructure and simple LR isolators subjected to ground motion 22 288
E.25 Peak displacement data from the simulations with the cylindrical superstructure and robust LR isolators subjected to ground motion 08 289
E.26 Peak displacement data from the simulations with the rectangular superstructure and robust LR isolators subjected to ground motion 08 290
E.27 Peak rotation data from the simulations with the cylindrical superstructure and robust LR isolators subjected to ground motion 08 291
E.28 Peak rotation data from the simulations with the rectangular superstructure and robust LR isolators subjected to ground motion 08 292
E.29 Peak displacement data from the simulations with the cylindrical superstructure and robust LR isolators subjected to ground motion 09 293
E.30 Peak displacement data from the simulations with the rectangular superstructure and robust LR isolators subjected to ground motion 09 294
E.31 Peak rotation data from the simulations with the cylindrical superstructure and robust LR isolators subjected to ground motion 09 295
E.32 Peak rotation data from the simulations with the rectangular superstructure and robust LR isolators subjected to ground motion 09 296
E.33 Peak displacement data from the simulations with the cylindrical superstructure and robust LR isolators subjected to ground motion 22 297
E.34 Peak displacement data from the simulations with the rectangular superstructure and robust LR isolators subjected to ground motion 22 298
E.35 Peak rotation data from the simulations with the cylindrical superstructure and robust LR isolators subjected to ground motion 22 299
E.36 Peak rotation data from the simulations with the rectangular superstructure and robust LR isolators subjected to ground motion 22 300
E.37 Peak foundation, isolated slab, and roof x displacement data from the simulations with the rectangular superstructure and FP bearings subjected to all ground motions 301
E.38 Peak foundation, isolated slab, and roof x displacement data from the simulations with the rectangular superstructure and simplified LR bearings subjected to all ground motions 302

E.39 Peak foundation, isolated slab, and roof x displacement data from the simulations with the rectangular superstructure and robust LR bearings subjected to all ground motions . . . 303
E.40 Peak foundation, isolated slab, and roof y displacement data from the simulations with the rectangular superstructure and FP bearings subjected to all ground motions . . . 304
E.41 Peak foundation, isolated slab, and roof y displacement data from the simulations with the rectangular superstructure and simplified LR bearings subjected to all ground motions . . . 305
E.42 Peak foundation, isolated slab, and roof y displacement data from the simulations with the rectangular superstructure and robust LR bearings subjected to all ground motions . . . 306
E.43 Peak foundation, isolated slab, and roof z displacement data from the simulations with the rectangular superstructure and FP bearings subjected to all ground motions . . . 307
E.44 Peak foundation, isolated slab, and roof z displacement data from the simulations with the rectangular superstructure and simplified LR bearings subjected to all ground motions . . . 308
E.45 Peak foundation, isolated slab, and roof z displacement data from the simulations with the rectangular superstructure and robust LR bearings subjected to all ground motions . . . 309
E.46 Peak foundation, isolated slab, and roof torsion data from the simulations with the rectangular superstructure and FP bearings subjected to all ground motions 310
E.47 Peak foundation, isolated slab, and roof torsion data from the simulations with the rectangular superstructure and simplified LR bearings subjected to all ground motions . . . 311
E.48 Peak foundation, isolated slab, and roof torsion data from the simulations with the rectangular superstructure and robust LR bearings subjected to all ground motions . . . 312
E.49 Peak foundation, isolated slab, and roof x overturning rotation data from the simulations with the rectangular superstructure and FP bearings subjected to all ground motions . . . 313
E.50 Peak foundation, isolated slab, and roof x overturning rotation data from the simulations with the rectangular superstructure and simplified LR bearings subjected to all ground motions . . . 314
E.51 Peak foundation, isolated slab, and roof x overturning rotation data from the simulations with the rectangular superstructure and robust LR bearings subjected to all ground motions . . . 315
E.52 Peak foundation, isolated slab, and roof y overturning rotation data from the simulations with the rectangular superstructure and FP bearings subjected to all ground motions . . . 316

E.53 Peak foundation, isolated slab, and roof y overturning rotation data from the simulations with the rectangular superstructure and simplified LR bearings subjected to all ground motions . . . 317
E.54 Peak foundation, isolated slab, and roof y overturning rotation data from the simulations with the rectangular superstructure and robust LR bearings subjected to all ground motions . . . 318

F.1 Peak superstructure acceleration amplification data from the simulations with the cylindrical superstructure, no soil, and FP bearings subjected to the basic motions . . . 320
F.2 Peak superstructure acceleration amplification data from the simulations with the cylindrical superstructure, no soil, and simplified LR bearings subjected to the basic motions . . . 321
F.3 Peak superstructure acceleration amplification data from the simulations with the cylindrical superstructure, no soil, and robust LR bearings subjected to the basic motions . . . 322
F.4 Peak superstructure acceleration amplification data from the simulations with the rectangular superstructure, no soil, and FP bearings subjected to the basic motions . . . 323
F.5 Peak superstructure acceleration amplification data from the simulations with the rectangular superstructure, no soil, and simplified LR bearings subjected to the basic motions . . . 324
F.6 Peak superstructure acceleration amplification data from the simulations with the rectangular superstructure, no soil, and robust LR bearings subjected to the basic motions . . . 325
F.7 Peak superstructure acceleration amplification data from the simulations with the cylindrical superstructure, soil column B, and FP bearings subjected to the basic motions . . . 326
F.8 Peak superstructure acceleration amplification data from the simulations with the cylindrical superstructure, soil column B, and simplified LR bearings subjected to the basic motions . . . 327
F.9 Peak superstructure acceleration amplification data from the simulations with the cylindrical superstructure, soil column B, and robust LR bearings subjected to the basic motions . . . 328
F.10 Peak superstructure acceleration amplification data from the simulations with the rectangular superstructure, soil column B, and FP bearings subjected to the basic motions . . . 329
F.11 Peak superstructure acceleration amplification data from the simulations with the rectangular superstructure, soil column B, and simplified LR bearings subjected to the basic motions . . . 330

F.12 Peak superstructure acceleration amplification data from the simulations with the rectangular superstructure, soil column B, and robust LR bearings subjected to the basic motions . . . 331
F.13 Peak superstructure acceleration amplification data from the simulations with the cylindrical superstructure, soil column C, and FP bearings subjected to the basic motions . . . 332
F.14 Peak superstructure acceleration amplification data from the simulations with the cylindrical superstructure, soil column C, and simplified LR bearings subjected to the basic motions . . . 333
F.15 Peak superstructure acceleration amplification data from the simulations with the cylindrical superstructure, soil column C, and robust LR bearings subjected to the basic motions . . . 334
F.16 Peak superstructure acceleration amplification data from the simulations with the rectangular superstructure, soil column C, and FP bearings subjected to the basic motions . . . 335
F.17 Peak superstructure acceleration amplification data from the simulations with the rectangular superstructure, soil column C, and simplified LR bearings subjected to the basic motions . . . 336
F.18 Peak superstructure acceleration amplification data from the simulations with the rectangular superstructure, soil column C, and robust LR bearings subjected to the basic motions . . . 337
F.19 Peak superstructure acceleration amplification data from the simulations with the cylindrical superstructure, soil column D, and FP bearings subjected to the basic motions . . . 338
F.20 Peak superstructure acceleration amplification data from the simulations with the cylindrical superstructure, soil column D, and simplified LR bearings subjected to the basic motions . . . 339
F.21 Peak superstructure acceleration amplification data from the simulations with the cylindrical superstructure, soil column D, and robust LR bearings subjected to the basic motions . . . 340
F.22 Peak superstructure acceleration amplification data from the simulations with the rectangular superstructure, soil column D, and FP bearings subjected to the basic motions . . . 341
F.23 Peak superstructure acceleration amplification data from the simulations with the rectangular superstructure, soil column D, and simplified LR bearings subjected to the basic motions . . . 342
F.24 Peak superstructure acceleration amplification data from the simulations with the rectangular superstructure, soil column D, and robust LR bearings subjected to the basic motions . . . 343
F.25 Median superstructure acceleration amplification peaks from the simulations with the rectangular superstructure, soil column B, and FP bearings subjected to all ground motions . . . 344

F.26 Median superstructure acceleration amplification peaks from the simulations with the rectangular superstructure, soil column B, and simplified LR bearings subjected to all ground motions . . . 345
F.27 Median superstructure acceleration amplification peaks from the simulations with the rectangular superstructure, soil column B, and robust LR bearings subjected to all ground motions . . . 346

List of Tables

3.1 Target Performance Goals from ASCE 43-05 23
3.2 Date and time for the 2007 Niigata Chūetsu-Oki (6.6 M_W) earthquake and aftershocks 28
3.3 Free field seismometer information at Kashiwazaki-Kariwa NPP 29
3.4 In-structure accelerometer information at Kashiwazaki-Kariwa NPP 30

4.1 Input parameters of TFP bearings used in validation tests 46
4.2 Values of evolution constants in existing base isolation software 54
4.3 Input parameters of the FP bearings used in validation tests 55
4.4 Input parameters of FP bearings used in validation tests 64
4.5 Material properties governing the evolution of lead core temperature of LR bearings 75
4.6 Ground motions used for robust LR validation 76
4.7 Input parameters of LR bearings used in validation tests 80

5.1 Material properties for the structural reinforced-concrete used in the analyses presented herein 95
5.2 Volume and weight takeoff for the cylindrical structure 95
5.3 Volume and weight takeoff for the rectangular structure 95
5.4 Ideal dynamic properties for the lumped-mass stick models 96
5.5 Lumped-massl stick model masses and geometry 98
5.6 Spectral displacements and accelerations at $T = 3$ sec with 5% damping for the scaled input ground motions 101
5.7 Input parameters for the FP analyses in ALE3D ("spring2") 103
5.8 Input parameters for the TFP analyses in ALE3D ("spring3") 104
5.9 Input parameters for the simple LR analyses in ALE3D ("spring4") 105
5.10 Input parameters for the robust LR analyses in ALE3D ("spring5") 105

6.1 Geotechnical properties for soil layers 110
6.2 Earthquake records used in seismic analyses 112

7.1 Number of analysis cases for each combination of soil column, superstructure type, and isolator model 117

8.1 Mean foundation acceleration peak amplification factors of each soil type for the analyses subjected to the basic motions . . . 122
8.2 Mean isolation displacement peak data for the analyses subjected to the basic motions . . . 124
8.3 Mean superstructure peak displacement amplification ratios for the simulations subjected to the basic motions . . . 125
8.4 Mean roof peak rotations for the simulations subjected to the basic motions . . 125
8.5 Median (standard deviation) superstructure peak torsion for the rectangular superstructure atop soil column B . . . 126
8.6 Median (standard deviation) superstructure peak overturning rotation amplifications for the rectangular superstructure atop soil column B . . . 126

B.1 Peak ground accelerations in each direction for the scaled input ground motions 148
B.2 Peak ground velocities in each direction for the scaled input ground motions . . 149
B.3 Peak ground displacements in each direction for the scaled input ground motions 150

C.1 Peak soil column acceleration data for the soil B cases in response to the basic motions . . . 212
C.2 Peak soil column acceleration data for the soil C cases in response to the basic motions . . . 213
C.3 Peak soil column acceleration data for the soil D cases in response to the basic motions . . . 214
C.4 Peak soil column acceleration data for the soil B cases with a rectangular superstructure and FP bearings in response to all motions . . . 215
C.5 Peak soil column acceleration data for the soil B cases with a rectangular superstructure and simplified LR bearings in response to all motions . . . 216
C.6 Peak soil column acceleration data for the soil B cases with a rectangular superstructure and robust LR bearings in response to all motions . . . 217

D.1 Isolator data for the soil N and B cases in response to the basic motions 240
D.2 Isolator data for the soil C and D cases in response to the basc motions 241
D.3 Isolator data for the soil B cases with a rectangular superstructure and isolator model 2 in response to all motions . . . 242
D.4 Isolator data for the soil B cases with a rectangular superstructure and isolator model 4 in response to all motions . . . 243
D.5 Isolator data for the soil B cases with a rectangular superstructure and isolator model 5 in response to all motions . . . 244

E.1 Displacement data for the soil N and B cases in response to the basic motions . 255
E.2 Displacement data for the soil C and D cases in response to the basic motions . 256
E.3 Displacement data for the soil B cases with a rectangular superstructure and FP bearings in response to all motions . . . 257

E.4 Displacement data for the soil B cases with a rectangular superstructure and simplified LR bearings in response to all motions 258
E.5 Displacement data for the soil B cases with a rectangular superstructure and robust LR bearings in response to all motions 259
E.6 Rotation data for the soil N and B cases in response to the basic motions 260
E.7 Rotation data for the soil C and D cases in response to the basic motions 261
E.8 Rotation data for the soil B cases with a rectangular superstructure and FP bearings in response to all motions 262
E.9 Rotation data for the soil B cases with a rectangular superstructure and simplified LR bearings in response to all motions 263
E.10 Rotation data for the soil B cases with a rectangular superstructure and robust LR bearings in response to all motions 264

Acknowledgments

I want to express my deepest gratitude to my research advisor, Božidar Stojadinović. His support, patiance, and guidance throughout the last four years have been instrumental in the completion of my studies and research.

I would also like to thank the other members of my disseration committee. Professor James Kelly, with his unparalleled expertise in the field of seismic base isolation, has been vital in shaping and directing my research with respect to isolation bearings, their properties, and applicable modeling techniques. Professor Per Peterson's guidance concerning the design and regulations pertaining to nuclear power structures and reactors has been truly invaluable.

Much of my professional developement came as a graduate student instructor, where I had the privilege of working for and learning from extraordinary faculty members. In this capacity, professors Filip Filippou, Abolhassan Astaneh-Asl, Anil Chopra, and Troy Morgan all served as personal mentors. I would also like to thank Professors Douglas Greger and Per-Olof Perrson who served as members of my qualifying examination committee.

The computational analyses presented herein were completed using the high-performance computing capabilities at Lawrence Livermore National Laboratory. Therefore, I would be remiss if I did not acknowledge Rose and Dave McCallen for bringing me to LLNL as well as Tarabay Antoun, Lara Leininger, and Randolph Settgast for helping with the transition to the lab. Specifically, I would like to express my gratitude towards Randy who helped teach and advise on nearly all analytical aspects of my research from finite element meshing to isolator modeling. The knowledge gained under his tutelage was essential to the completion of my research. Additional assistance with modeling and analysis issues was provided by Quazi Hossain, Ed Kokko, and Sarah Minkoff.

During my collegiate career, I have had the good fortune of knowing many great friends and collegues who have had a profound impact on my growth both personally and professionally. I thank Mike Mieler and Tracy Becker, with whom I have worked very closely on various projects during graduate school. Their advice has been invaluable and I sincerely appreciate sharing the Ph.D process with them both. I would also like to express my appreciation for my fellow classmates Finley Wise, Jamie Beard, Nate Van Etten, Timmy Siauw, Dan Tran, Eugene Gordin, Luke Ruggeri, and Joe Weber, who were among the many that made studying at UC Berkeley truly enjoyable.

Finally, I would like to thank my family, whose love and support have helped me through this arduous process.

Chapter 1

Introduction

Despite recent advancements in reactor technologies, construction of new nuclear power plants in the US has been scarce over the past 30 years. This has been partially due to the public backlash following major events at Three Mile Island, USA (1979), Chernobyl, Ukraine (1986), and Fukishima, Japan (2011), as well as the ever-increasing seismic hazard risk as determined by geotechnical scientists, engineers, and policy makers.

Seismic base isolation is a mature technology used around the world to reduce the lateral acceleration response in structures located in areas of high-seismicity. Isolation offers a means of mitigating seismic effects on nuclear power structures, significantly increasing safety margins, and facilitating equipment qualification.

1.1 Objectives of Research

This study presents explicit, time-domain numerical simulations of seismically-isolated nuclear power structures subjected to high-amplitude seismic excitation, which contrast the frequency-domain approach typically employed. The models are comprised of finite element formulations for the soil column, foundation, isolation bearings, and superstructure which simultaneously achieve a variety of research objectives.

Of primary importance is the 3D coupled performance of base isolation systems under design-basis earthquake events. The analysis of multiple isolation models, superstructures, ground motions, and earthquake motions will illuminate the characteristics which promote potentially-hazardous global performance including structural uplift, overturning, and torsion. The consideration of two different superstructures will serve as a basis to determine which types of future nuclear plants may be best suited for isolation. The analysis of a variety of soil columns highlights the effect of soil properties on response parameters of interest, and may suggest any possibly limitations of isolation implementation. Finally, the analysis of multiple ground motions aids in determining which seismic parameters (i.e. displacements, velocities, accelerations, and frequency content) in which directions induce deleterious effects.

The dimensions of proposed bearings, as well as the magnitude of prospective loads and input accelerations preclude the use of existing experimental facilities, even for scaled specimens. Thus, numerical simulations, such as those presented, are the primary means of evaluating the applicability of seismic base isolation to nuclear structures. Because of the size and aspect ratio of the analyzed superstructures, this study also serves to evaluate the response of tall base-isolated structures to large amplitude seismicity.

1.2 Organization of Thesis

This thesis is organized into eight chapters. Relevant background information is covered in Chapters 2 and 3. Chapter 2 summarizes the current state of seismic base isolation including its conceptual and historical basis, various existing isolation devices accompanied by respective advantages and disadvantages, necessary special design considerations, and noteworthy applications. Chapter 3 details the practice of nuclear power plant design including applicable standards for fixed-base and isolated plant designs. Past and current studies regarding seismic base isolation for nuclear application are also presented. Finally, this chapter includes a case history of the Kashiwazaki-Kariwa nuclear power plant, a fixed-base Japanese plant which recorded extensive data in response to a large earthquake, in order to demonstrate the response magnitude when base isolation is not utilized.

The numerical models and inputs for the seismic analysis presented are described in Chapters 4 through 6. Chapter 4 presents four seismic base isolation models which have been implemented into ALE3D. For each model, the numerical formulae which serve as the model basis are given, as well as descriptions of and results from associative validation cases used to demonstrate proper functioning. This chapter also discusses the concepts of damage and failure in seismic base isolation devices. Chapter 5 describes the superstructural meshes and materials implemented in the analyses. Additionally, it presents designs for isolation systems, internal plant equipment, and foundation mats. Chapter 6 presents all geotechnical information including meshes and materials used for soil columns, as well as descriptions of ground motions and boundary conditions applied to the models.

Chapter 7 enumerates the different analyses run and describes the ALE3D software and computing facilities used to complete them. Results and conclusions of these simulations are presented in Chapter 8. A bibliography containing references used as well as Appendices A through F immediately follow Chapter 8.

Chapter 2

Seismic Base Isolation

The expensive and deadly consequences of large earthquakes have become more alarming in recent decades, exemplified by the 1989 Loma Prieta (6.9 M_W), 1994 Northridge (6.7 M_W), and 1995 Kobe (6.8 M_W) earthquakes. As a result of the extensive damage and large death tolls induced by powerful events in urban areas previously thought to be well-designed for seismicity, structural engineering has evolved to include new standards of practice and technologies such as seismic base isolation (SBI). SBI is a means of reducing structural accelerations and forces from seismic events by introducing a laterally flexible layer between the foundation and superstructure. Over the past two decades, SBI has become increasingly prevalent in the design of commercial, industrial, and essential structures, most notably in Japan.

The 2011 Tōhuku (9.0 M_W) and 2007 Niigata Chūetsu-Oki (6.6 M_W) earthquakes, as well as subsequent geologic events (i.e. tsunami and aftershocks), greatly impacted the Fukushima Daiichi and Kashiwazaki-Kariwa nuclear power plants respectively, exemplifying the potential risk associated with high-amplitude seismicity near nuclear power structures. In the former case, tsunami impact induced failure of backup power generators, inducing meltdowns in multiple reactor units. In the latter, the earthquake and following aftershocks caused significant damage to non-safety related structures, systems, and components, leading to a lengthy plant shutdown. Other plants in Japan were also affected by these events, including the Onagawa nuclear power station, which was closest to the Tōhuku epicenter. This plant was safely shut down when basement accelerations of 0.58 g were measured, and damage to oil tanks and heat exchangers occured when the tsunami hit (Obonai and Watanabe, 2012). Beyond design-basis seismic excitation provides sufficient reason to consider SBI for nuclear applications. As seismic response modification devices, isolators can significantly reduce the damaging effects of earthquakes on nuclear power structures, thereby increasing safety margins and promoting efficient design, review, and construction processes through the use of universal designs and modularized manufacturing.

This chapter reviews the science and practice of SBI. Section 2.1 presents the dynamic concept behind SBI. Sections 2.2 and 2.3 illustrate the many common types of elastomeric and sliding bearings, respectively, as well as the material composition, response characteristics, advantages, and drawbacks of each bearing design. Section 2.4 enumerates some structural engineering design options and issues which must be solved prior to SBI implementation. Finally, Section 2.5 presents various applications of SBI, both nuclear and non-nuclear.

2.1 Concept

Documented proof of SBI as an engineering concept dates back to the early 20th Century (Kelly, 1986), although it has been suggested that the use of sliding planes below structures may have been used centuries earlier. In 1909, following the devastating Messina earthquake (7.2 M_W) the previous year, an Italian commission of engineers and professors suggested introducing a sliding layer of sand or rollers underneath structures as one method of creating structures with increased seismic-resistance (Accademia dei Lincei, 1909). Around the same time, an English medical practitioner, Dr. Calantarients (1909), applied for a patent which suggested the use of a sand or talc layer under structures, specifically for earthquake engineering application. In the century since its conceptual infancy, the practice of SBI has developed to include a variety of complex devises which have been implemented world-wide.

In classical structural engineering (i.e. non-isolated or fixed-base design), two paradigms exist for designing structures to avoid seismically-induced damage. In the first, the structure is made with stiff, bulky members, which are strong enough to accept the large accelerations and forces imparted by the ground motion. The high cost of the resulting structure due to the member size, as well as the high accelerations transferred to the non-structural components, can be prohibitive for design. The second concept utilizes flexible members which reduce the accelerations and forces in the structure. The flexible response of the system may include large interstory drifts which can cause member failure, cracking in non-structural facades and glass, as well as serviceability issues. Thus, each concept has inherent disadvantages.

SBI is a structural technology which has the ability to simultaneously reduce superstructural accelerations while limiting interstory drifts. Various types of SBI devices, sometimes called bearings, have been invented and are described in Sections 2.2 and 2.3, however, all share the property of being laterally-flexible relative to the superstructure. By putting isolators between the foundation and superstructure, a laterally flexible layer is created, essentially decoupling the structure from the ground. For a single-degree-of-freedom (SDOF) system in which mass, m, is held constant, the horizontal dynamic vibration period, T, is inversely proportional to the square root of the lateral stiffness, k, as shown in Equation 2.1. Consequently, even for multiple-degree-of-freedom (MDOF) systems, a large reduction in stiffness will result in a significant lengthening of the fundamental horizontal period. The dynamic implications of this are depicted in the acceleration, velocity, and displacement response spectra for the Corralitos record of the 1989 Loma Prieta (6.9 M_W) earthquake in Figure 2.1. By lengthening the fundamental period, the response moves away from the acceleration-sensitive region, effectively reducing the accelerations transferred to the superstructure from the primary mode. The period shift from 0.25 seconds to 2.50 seconds depicted in Figure 2.1 results in a 92% spectral acceleration reduction in both lateral directions.

$$T = \frac{2\pi}{\omega} = 2\pi\sqrt{\frac{m}{k}} \tag{2.1}$$

A seemingly disadvantageous result of the period shift is the increase in spectral displacements as the response is shifted into the velocity or displacement-sensitive region. However, the increased displacement is concentrated in the flexible isolation layer, and the interstory drifts in the comparatively stiff superstructure are negligible in comparison. By lengthening the fundamental period, the acceleration response due to the primary dynamic mode is greatly decreased, without any adverse superstructural deformation effects. Thus, the major drawbacks of both classical structural engineering paradigms are averted.

The higher-mode response is also diminished in base-isolated structures, although this is done differently by elastomeric and sliding bearings as a result of dynamic variations between the two. For elastomeric bearings, the fundamental mode shape, ϕ_f, is approximated by a vector of ones, representing deformation of the isolation layer and negligible additional superstructural drift. The force influence vector, ι, representing the nodal-mass-normalized force at each DOF, is by definition, the ones vector, since an earthquake at the base can be viewed equivalently as nodal-mass-proportional forces in the opposite direction at each node. Because the primary mode shape is nearly identical to that of the force influence vector, and dynamic modes are orthogonal by definition, the principal of modal orthogonality results in near-zero modal participation factors for higher-order modes. Thus, elastomeric bearings are said to "filter-out" higher-mode response.

The dynamics of sliding bearings are slightly different because the friction force always opposes the direction of velocity, leading to a slightly different dynamic mode shape which does not filter higher-order modes as effectively. Instead, sliding bearings limit the force transmitted to the superstructure by reducing the friction coefficient on the sliding surface. Thus, the sliding surface acts as a "fuse" to limit the forces capable of inducing higher-order response. The "filter" and "fuse" concepts are imperative to minimizing high-frequency response in structures utilizing SBI.

The efficacy of SBI is founded in the ability to significantly shift the fundamental period of the structure. However, care must be taken by the engineer to avoid a design in which the isolation system resonates with either the soil column below, or superstructure above (Ariga et al. 2006). If the structure is flexible, with a long non-isolated period, the base isolation system will naturally excite the fundamental mode of the structure, and the system will be ineffective or possibly detrimental to the response. Similarly, if the soil is very soft, the resulting seismic motions will have long predominant periods which resonate with the bearings, and the natural response of the system will be greatly increased, exacerbating the probability of bearing failure as resonance is approached (Chopra, 2007). Consequently, SBI is most useful at stiff soil or rock sites underlying stiff structures with short fundamental periods, such as nuclear power structures.

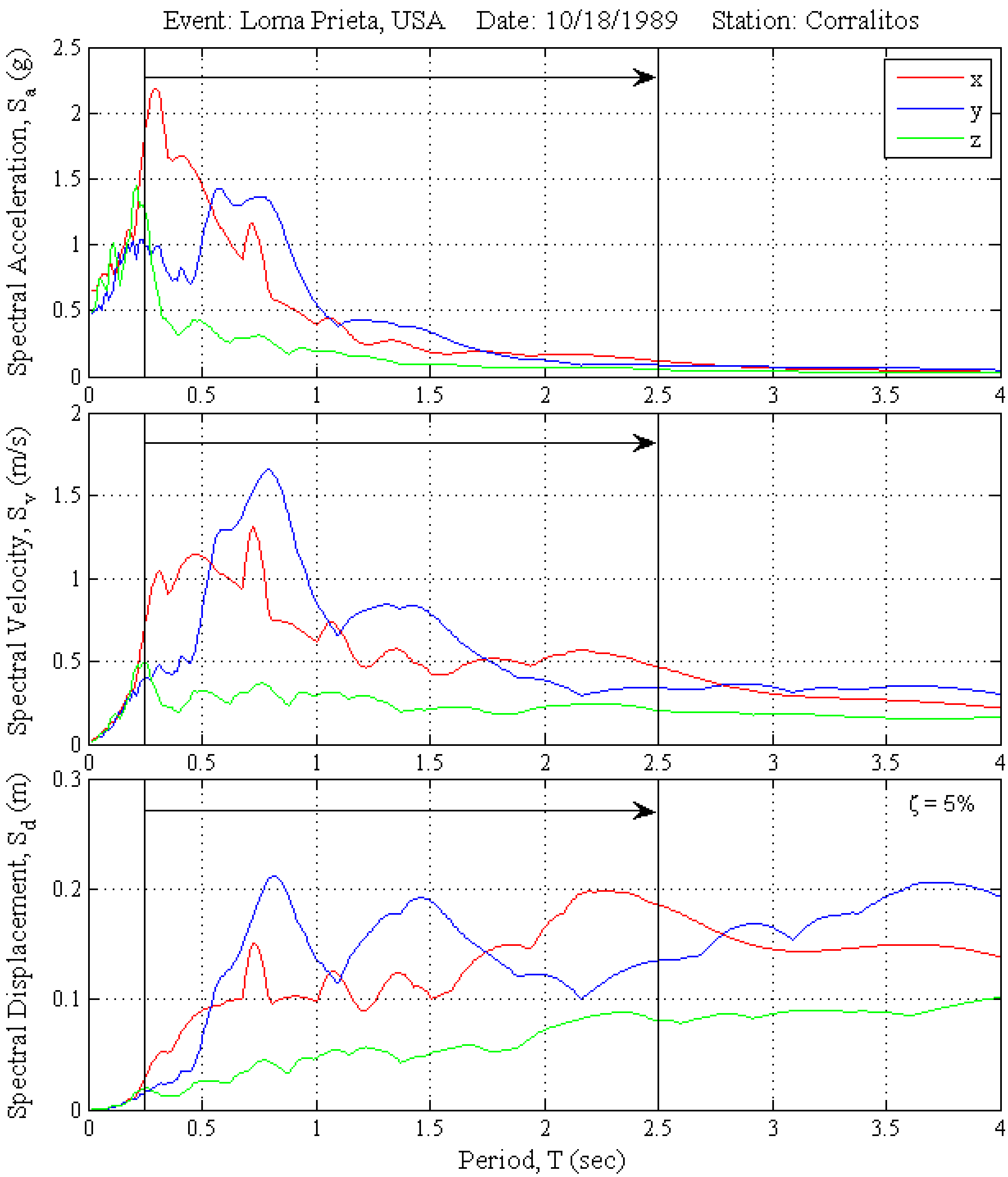

Figure 2.1: Response spectra for the Corralitos record of the 1989 Loma Prieta earthquake (6.9 M_W) with 5% damping demonstrating the effect of a period shift between non-isolated ($T \approx 0.25$ sec) and isolated ($T \approx 2.50$ sec) structures

2.2 Elastomeric Bearings

The French engineer Eugène Freyssinet is credited with the first patent for elastomeric bearings in 1954 (Kelly and Konstantinidis, 2011). Technological improvement of elastomeric bearings towards their modern form commenced in the 1970s with studies in the United States and New Zealand (Skinner et al., 1975). Rubber-based bearings have since become widely used for vibration isolation in high acoustic environments, thermal expansion of highway bridges, and seismic isolation of structures in earthquake-prone regions. Elastomeric bearings consist of alternating bonded steel and elastomer laminates, which provide lateral flexibility while remaining vertically stiff and stable. The thickness of the rubber layers controls both the vertical and horizontal stiffness and displacement capacity. The bonding of layers enables the bearings to have tension capacity and a more predictable response. Steel plates are used to limit the thickness of individual rubber layers, thereby reducing bulging, and to assure the bearing deforms in shear as opposed to bending. Distinctive rubber bearing variations differ primarily in the type of elastomer used and the method of energy dissipation. This section will enumerate the various existing elastomeric bearing designs, focusing on their histories, physical characteristics, advantages, and drawbacks.

2.2.1 Low-Damping Rubber Bearings

Low-damping natural or synthetic rubber (hereafter LDR) bearings were first used in 1966 to isolate a London apartment complex from the vibrations of the London Underground. Subsequent projects maintained LDR bearing use for vibration control in hospitals and concert halls. The first seismic application for base isolation was in 1969 for the Pestalozzi school building in Skopje, Macedonia. The rubber isolators, designed by Staudacher et al. (1970) were unreinforced, leading to bulging under gravity loading and rocking during excitation. Since then, bearings have become more refined to reduce or eliminate such undesirable characteristics.

Using natural or synthetic rubber, LDR bearings are noted for having low critical damping values in the range of 2-3% (Kelly and Konstantinidis, 2011). The low shear modulus reduces the horizontal stiffness of the structure and increases the isolated period. The bearing stiffness remains linear at strains exceeding 100%. The bearings are often supplemented with damping devices, such as viscous dampers, to achieve desired damping ranges.

Because of the low damping in the rubber, the bearing behavior is nearly linear, enabling an easily-predictable response. The low level of inherent damping and linear response are apparent in the thin force-displacement loop presented in Figure 2.2. Known for their longevity, the LDR bearings have the additional advantage that the response is independent of loading rate, loading history, or temperature. Unfortunately, because they often require intricate supplemental damping systems which are more susceptible to fatigue, the complexity and cost of LDR isolation systems can be prohibitive. LDR systems are not analyzed herein, nonetheless, they are frequently used in Japan to isolate structures.

2.2.2 High-Damping Rubber Bearings

In 1985, the Foothill Communities Law and Justice Center in Cucamonga, California became the first base-isolated structure in the United States when it was constructed with high-damping natural rubber (hereafter HDR) bearings. HDR bearings use rubber vulcanized with fillers (e.g. resins or carbon black) which has an equivalent linear viscous damping of 10-20% (Naeim and Kelly, 1999) and is capable of producing an advantageous nonlinear response. At low shear strains, the tangled elastomer molecule chains are twisted around each other and extension requires considerable energy to pull chains past other chains and filler materials, leading to a high initial stiffness. At larger shear strains, the stiffness significantly decreases as fewer obstacles exist to impede molecular extension. Finally, at shear strains greater than 100%-150%, the molecular chains approach their deformation capacity and begin resist extension. Rubber molecules may also experience strain crystallization, a restructuring of rubber molecules in the direction of principle tension to form crystallites, in response to large shear strains. As a result the bearing experiences increases in stiffness and damping as it nears its displacement capacity. The movement of chains past filler material also serves to dissipate energy during load reversals. The total response is beneficial as it reduces motion in response to small excitations (e.g. wind, ambient vibration, and low amplitude seismicity), allows for considerable deformation capacity and acceleration reduction under moderate seismicity, and limits maximum deformation under extreme seismicity while offering considerable damping. Because damping is inherent in HDR bearings, depicted in Figure 2.3, no internal plugs or external supplemental energy dissipating device is required.

Recent studies prove HDR bearing properties vary significantly as a function of time, temperature, load-history, strain-rate, velocity, and curing conditions, among others (Thompson et al., 2000). Together, these issues can cause sizeable changes in material properties during the service life of the bearing. Significant strength deterioration, or scragging, over the inital loading cycles is typical in HDR bearings. Subsequently, the proposed AASHTO property modification factors for aging and scragging, λ, are significantly greater than 1.0 for HDR bearings in stark contrast to those for LDR and LR bearings (Thompson et al., 2000). This is prohibitive to the creation of accurate predictive analytical models for HDR bearings. Grant et al. (2004) created the most-accurate model of HDR bearings, which can be calibrated to model scragging following laboratory testing, but has not been proven reliable to accurately predict bearing behavior. Analyis of HDR bearing systems is not included in this report.

2.2.3 Lead-Rubber Bearings

Lead-rubber (hereafter LR) or lead-plug bearings were developed in the 1970s by Bill Robinson (Robinson and Tucker, 1977). One of the earliest implementations of LR bearings in the United States was for the University of Southern California Teaching Hospital, which was constructed in 1991 and experienced ground accelerations of 0.49g during the 1994 Northridge (6.7 M_W) earthquake. Instrumentation showed the isolation system reduced roof accelerations to nearly 40% of the PGA, whereas other nearby hospitals saw significant acceleration

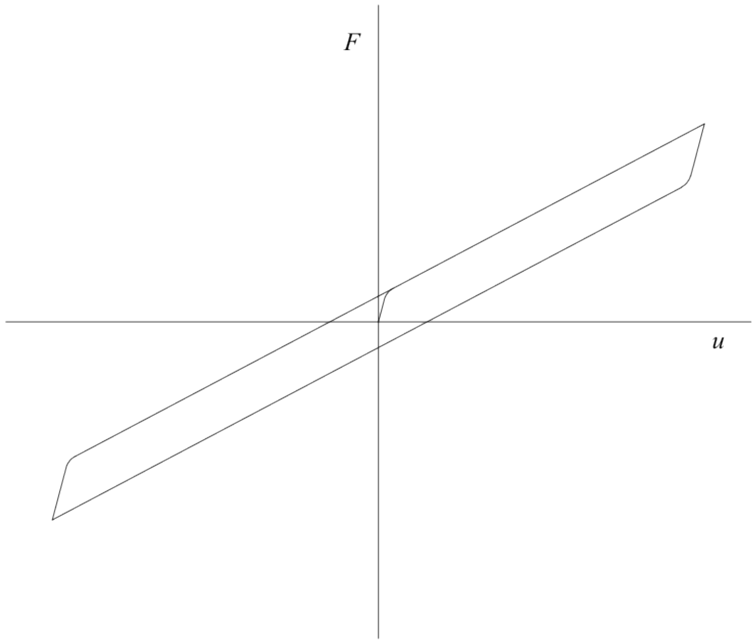

Figure 2.2: Idealized unidirectional hysteresis for a LDR bearing

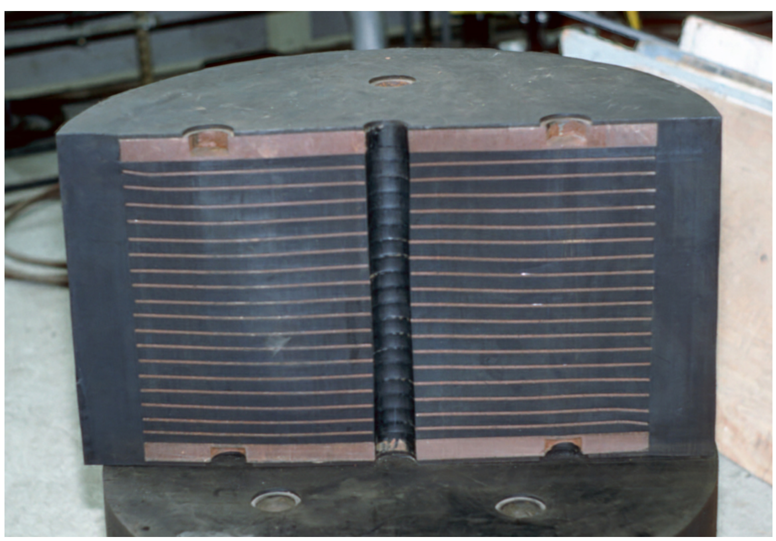

Figure 2.3: Section view of an HDR bearing for the Foothill Communities Law and Justice Center following tests at the UC Berkeley Richmond Field Station (photograph courtesy of James Kelly)

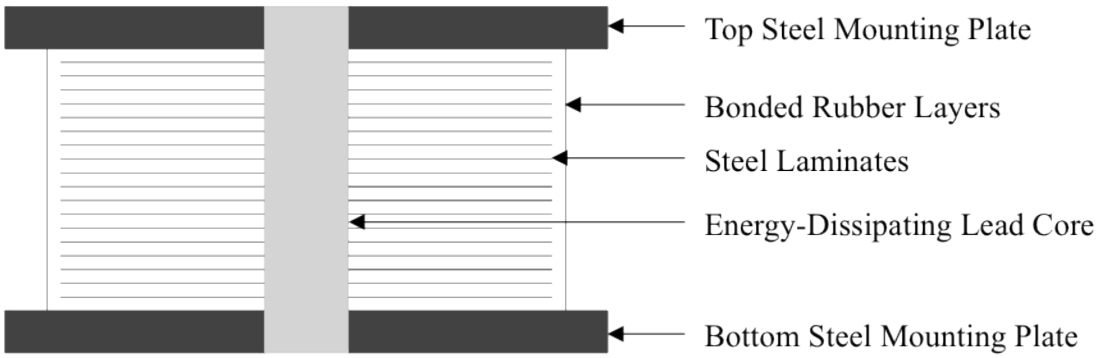

Figure 2.4: Schematic of an undeformed LR bearing

amplifications. Similar reductions were observed in Japan during the Kobe earthquake of 1995, proving the efficacy of LR bearing designs.

The bearings utilize low-damping natural rubber, and dissipate energy through the yielding of one or more lead plugs embedded vertically inside the bearing, depicted in Figure 2.4, which also aid in providing restoring action. Thus, no supplemental damping is required. LR bearings are typically designed for shear strains of up to 200%, and damping ratios as high as 35%. Laboratory tests have shown that elastomeric bearings can reach shear strains exceeding 400% prior to failure (Konstantinidis et al., 2008).

The main disadvantage of LR bearings is the temperature dependence of the bearing, and specifically the lead core (Kalpakidis et al., 2010). During repeated cyclic loading, energy dissipation tends to heat the core, leading to a softening of the lead plug. The deteriorated yeild strength results in a bearing that dissipates less energy per cycle. Reductions of yield strength exceeding 25% were noted after only a few large-amplitude cycles.

Many numerical models exist for the characterization of LR bearings both laterally and vertically. Perhaps the most well-known three-dimensional model was originally proposed by Kikuchi and Aiken (1997), and has since been updated (Yamamoto et al., 2008)(Kikuchi et al., 2010). This model requires numerous calibration factors which diminish its appeal for predictive analyses. Consequently, the model by Kalpakidis et al. (2010), which is based on bearing geometry, and includes the effects of lead-core heating, is used for the lateral response in analyses presented herein. The interaction of lateral and vertical responses is achieved using the Warn et al. (2007) model which utilizes a pre-existing two-spring, P-Δ-like approach (Koh and Kelly, 1987)(Kelly, 1996).

2.3 Sliding Bearings

Sliding bearings introduce a low-friction interface between the foundation and superstructure which limits the transmittable force. Unlike elastomeric bearings which have chemical

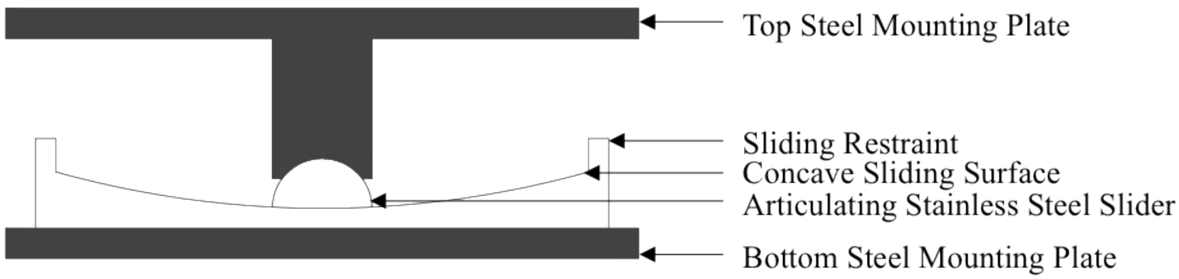

Figure 2.5: Schematic of an undeformed FP bearing

bonds between various elements, most sliding bearings require gravity to maintain the contact between surfaces. Sliding bearings capable of transferring tension do exist, however, they are less common and are not presented here. This section will discuss some existing sliding bearing designs, focusing on their histories, physical characteristic, advantages and disadvantages.

2.3.1 Friction Pendulum Bearings

Victor Zayas invented the original friction pendulum (hereafter FP) bearing, and founded Earthquake Protective Systems (EPS), Inc. in 1985 to manufacture bearings and further develop the technology (Zayas et al., 1987)(Zayas et al., 1989). One of its earliest implementations is evidenced in the US Court of Appeals building in San Francisco, California in 1994, which at the time was the largest seismically-isolated structure in the world. The bearings were heralded for enabling a design with more open space (i.e. smaller structural elements) at a lower cost (Amin and Mokha, 1995).

The significant components of the bearing are the stainless steel concave surface and self-lubricating articulating slider shown in Figure 2.5. The surfaces are generally coated in Teflon, which provides a low friction coefficient and thereby decreases the effective lateral stiffness, achieving the required period shift. The outer edge of the sliding surface has a steel lip which restrains slider displacements to a specific range.

The lateral force on a bearing, f_l, with a given radius, R, friction coefficient, μ, and overbearing force, P, is given Equation 2.2 for a specificed lateral displcement, u, and velocity, $\dot{u}$ (Morgan, 2008). From Equation 2.3, it naturally follows that the period of the FP-isolated structure depends solely on isolator geometry, and not on the overbearing mass, unlike with elastomeric isolators. The threshold force, Q, and hysteresis loop thickness of FP bearings are specified by the friction coefficient of the sliding surface. Since the stiffness of bearings scales with the overbearing force, the excitation of torsional modes is greatly reduced, as incidental eccentricities cause the center-of-mass and center-of-rigidity to move almost in unison (Becker et al., 2012). These measures make the dynamic response of the structure more predictable and practical for nuclear implementation.

$$f_l = \mu P \text{sign}(\dot{u}) + \frac{P}{R}u \tag{2.2}$$

$$T = 2\pi\sqrt{\frac{m}{k}} = 2\pi\sqrt{\frac{P}{g}\frac{R}{P}} = 2\pi\sqrt{\frac{R}{g}} \tag{2.3}$$

All materials in FP bearings are metallic, and as such, the vertical compression stiffness of bearings are 7-10 times greater than high-shape-factor elastomeric bearings (EPS, 2003). Thus, vertical amplification factors are less for FP bearings than for their elastomeric counterparts. Unlike with elastomeric bearings, FP bearings are capable of maintaining their vertical stiffness at full design displacement due to the high rigidity of the sliding surfaces.

The usage of single FP bearing does have a few drawbacks. Primarily, the coupled vertical and horizontal displacements effectively means that any differential horizontal displacement between isolators, possibly from torsion, can result in differential vertical displacement. These could induce large forces in the base slab or induce uplift in selective bearings. Although torsion is expected to be minimialized in response to lateral loading, uplift and overturning can reduce or eliminate the horizontal response in friction bearings, significantly shifting the center-of-rigidity away from the center-of-mass and inducing torsion (Almazán and de la Llera, 2003). Additionally, horizontal displacement is limited by the width of the isolator. For example, if the required displacement at the isolation level was 60.0 cm and the inner slider had a diameter of 20.0 cm, the lubricated surface would have to be 140.0 cm in diameter. Exceeding the displacement limit may induce impact against the restraint, transmitting large accelerations into the superstructure. By adding additional sliding surfaces, the triple pendulum bearings can help to avoid the use of excessively wide bearings. Yet another disadvantage is that full recentering is not assured after seismic loading, because the friction force always opposes the direction of impending motion. Finally, numerous tests have shown that cycling of bearings can lead to wear and heating of the bearings surfaces, which can produce dynamic effects that are still not completely understood or predictable.

2.3.2 Triple Friction Pendulum Beatings

Triple friction pendulum (hereafter TFP) bearings are a progression of the FP concept consisting of five components: an inner slider, two outer sliders, and two outer concaves. The inner slider has convex outer surfaces which slide along the concave inner surfaces of the outer sliders. The two outer sliders have convex outer surfaces which slide along the outer concaves. The complete bearing, shown in Figure 2.6, features four self-lubricating sliding surfaces which enable three separate pendulum mechanisms of motion. A schematic of the TFP bearing components is shown in Figure 2.7. Careful selection of the individual slider widths, radii, and friction coefficients allows the designer to tailor the isolation system so as to offer optimum performance in response to myriad seismic hazard levels (Morgan, 2008)(Morgan and Mahin, 2008). High initial stiffness assures minimal deformations in

Figure 2.6: TFP bearing components used in tests at the UC Berkeley Richmond Field Station (Photographs courtesy of Tracy Becker)

response to wind excitation, low-amplitude seismic motions, and ambient vibrations. Low stiffness at moderate displacements allows a response free from high-amplitude acceleration under moderate to large seismic loading. Finally, a restiffening at large displacements as the individual sliders approach their displacement limit, induces increased energy dissipation under extreme loading. This can be seen in the idealized monotonic weight-normalized loading curve in Figure 2.9.

TFP bearings also exhibit coupled horizontal and vertical motion, complicated by the fact that sliding exists on four separate surfaces. A schematic comparing the various stages of motion of FP and TFP bearings resulting from unidirectional displacement is depicted in Figure 2.8. The figure also demonstrates how TFP bearings require smaller bearings to achieve the same displacements as FP bearings. The TFP bearing is modeled using the Becker and Mahin model (2011) which tracks individual slider locations in order to accurately distinguish various phases of lateral and vertical motion.

2.4 Auxiliary Design Considerations

The application of seismic isolation systems to any structure introduces a multitude of auxiliary design considerations stemming from the sizeable differential displacement capacity between the superstructure and foundation. Due to the safety-critical nature of nuclear power structures, the additional risk posed by these design issues is exacerbated. Consequently, designers must carefully consider the design of the isolation gap, supplemental damping system, collision restrainers and bumpers, umbilicals, and external event shield to maintain adequate safety margins for design-basis events (DBE) as well as beyond-design-basis events (BDBE or MCE). Blandford et al. (2009) considered some of these design issues conceptu-

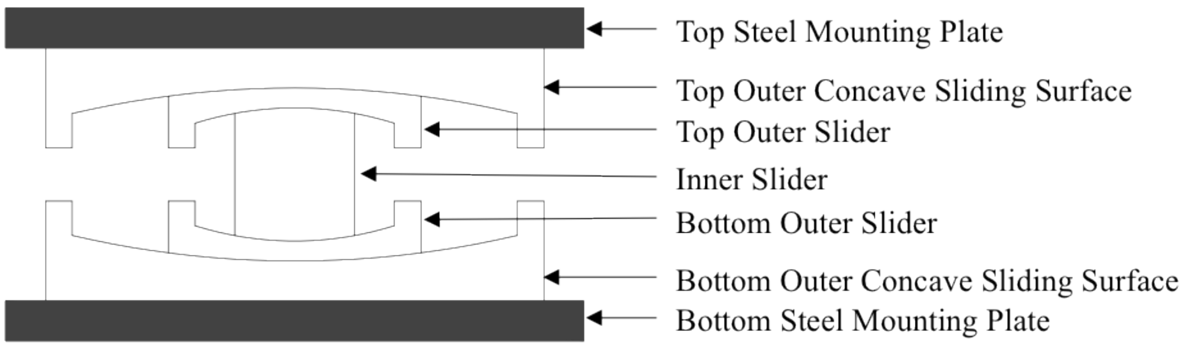

Figure 2.7: Schematic of an undeformed TFP bearing

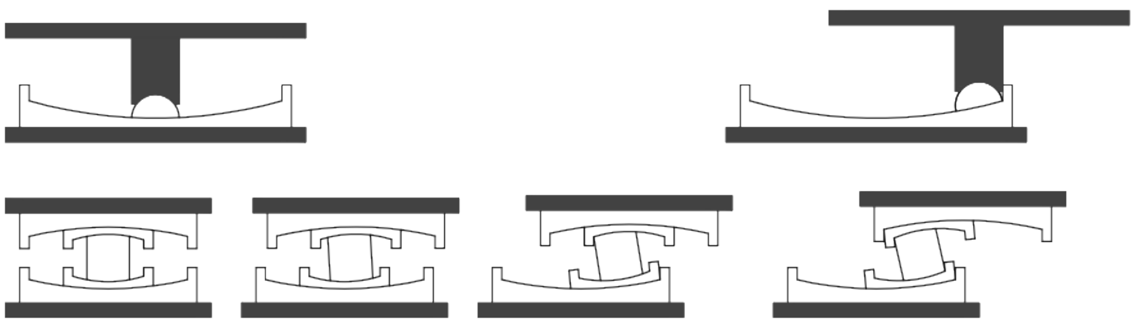

Figure 2.8: Schematic of the unidrectional displacement of FP and TFP bearings showing various stages of slider motion

ally and numerically. The following sections illuminate the design challenges induced by the application of seismic isolation devices.

2.4.1 Supplemental Damping

Increased seismic demands from building codes, as well as the opinion of some that seismically-isolated structures are vulnerable to large pulse-like motions, have significantly affected the design of isolation systems with respect to damping. In cases where the damping imparted by the bearings is deemed insufficient, supplemental dampers may become necessary. Supplemental dampers are devices that are independent of the isolation bearings, which dissipate energy in order to reduce the displacement response of the system. Supplemental damping devices can impart considerable energy dissipation (exceeding 40%) in order to diminish the effect of large pulse-like ground motions on structures (Hall, 1999). However, many argue that immoderate damping levels caused by supplemental dampers or overly-damped isolators (i.e. LR bearings with large lead cores or FP/TFP bearings with high friction coef-

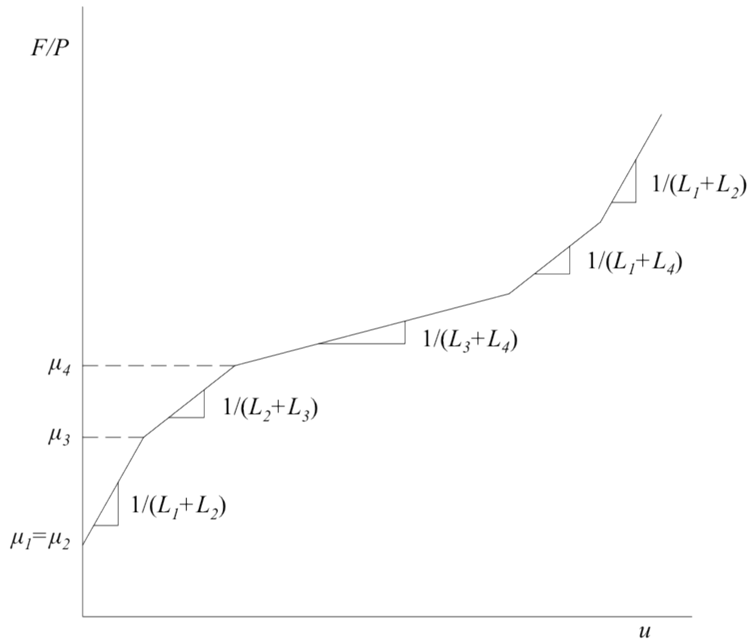

Figure 2.9: Normalized monotonic load-displacement curve for a TFP bearing for the typical design case where $\mu_1 = \mu_2$ and $L_1 = L_2$

ficients) effectively stiffen the isolation system and increase the superstructural accelerations the system was initially designed to mitigate (Kelly, 1999)(Providakis, 2008). Thus, it is recommended that the use of these systems be minimized when not absolutely necessary, and that nuclear power structures not be constructed at sites where near-field effects are expected.

Common dampers include viscous fluid dampers and friction dampers. Viscous fluid dampers dissipate energy by forcing silicon oil through apertures, thus creating heat which is radiated to the surrounding air. The instantaneous damping level is directly related to the velocity of the damped body, and therefore, extreme veolcities can induce high temperatures capable of damaging damper linings. Friction dampers utilize a slotted slip joint with friction surfaces that rub against one another during excitation, thereby damping energy (Symans et al., 2008). Supplemental damping systems can be rather complex to design. Besides having responses that may be both displacement and velocity dependent (sometimes to fractional powers), it is necessary to place dampers symmetrically to avoid inducing any torsional response. Additionally, the dampers can be sizeable, blocking access to isolators which can hinder in-field inspection.

2.4.2 Seismic Gap

When the seismically-isolated structure is embedded to any extent and/or enclosed by an external event shield, a seismic gap must be designed to assure that displacements resulting from design-level excitation will not cause impact with the non-isolated retaining wall or shield on the other side of the gap. Such an impact could induce high-frequency motion in the isolated superstructure as well as cause structural damage, and therefore should be avoided. Along those lines, conservative guidelines have been set in ASCE4-11 (2011) to size the gap at 3 times the maximum displacement.

As the size of the isolation gap increases, subsequent design issues ensue. Primarily, a larger gap will cause the retaining walls or event shield to be larger, which may significantly increase the cost of the project. Similarly, a larger gap results in a larger volume of soil which must be excavated for embedded structures, again increasing costs. Sizing of the isolation gap has a profound effect on the subsequent design of collision restrainers and bumpers, external event shield, and umbilicals, which are discussed in Sections 2.4.3 through 2.4.5.

2.4.3 Collision Restrainers and Bumpers

A conservative isolation design should include a contingency plan for BDBE or MCE loading that may induce impact as the structure traverses the isolation gap. This may include collision restrainers and/or bumpers. Collision restrainers have been proposed in multiple forms, one of which employs a lead bar enclosed in a cylindrical bearing with a radius shorter than the seismic gap. Once the imposed displacement exceeds the radius, the bar contacts the cylinder and the stiffness is significantly increased. Collision bumpers are flexible devices present on either the isolated superstructure or non-isolated containing structure. They are activated during impending pounding, and provide energy dissipation and an inhibiting force, which lessen the severity of the collision. A Hertzian impact model was used by Komodromos (2007) to demonstrate the efficacy of collision restrainers and bumpers to gradually increase the system stiffness and reduce the impact-induced accelerations.

Because the use of collision restrainers and bumpers has the ability to impart high frequency excitation on the superstructure, it is necessary that they are designed to be activated only after MCE-level excitation has been exceeded.

2.4.4 External Event Shield

In response to the September 11, 2001 attacks on the World Trade Center, the USNRC issued a rule that all new reactor applicants must assess the ability of a proposed plant design to mitigate the effects of intentional impact from a large commercial aircraft (USNRC, 2007) (USNRC, 2009). Analysis from Blandford et al. (2009) suggests that the next generation of nuclear power plants will have trouble accepting the loads from commercial aircraft impact without significant inelasticity or large accelerations as a result of increasingly smaller and lighter plant designs.

Two methods are presented to accommodate loads from aircraft impact and to assure safe decommissioning: a decoupled external event shield, and below-grade construction, often referred to as embedding or undergrounding. The former uses a perimeter wall or other barrier to block potential projectiles from reaching the superstructure. The additional mass of the external event shield was considered a possible advantage to locating it atop the seismically-isolated slab, allowing for larger elastomeric bearings, the size of which depends on the overbearing load, with larger displacement capacities. However, the induced shock loads from impact lead to the conclusion that decoupling was more advantageous (Blandford et al., 2009). The major disadvantage of an external event shield, either coupled or decoupled, is the additional construction cost as plant size grows.

The risk associated with airplane collision is nearly eliminated by situating plants below-grade or undergrounding. However, the excavation and construction costs increase with both plant area and height. Each design alternative would require careful consideration of the seismic gap size as previously noted. The effect of embedment in response to seismic loading was analyzed in Xu, et al. (2006).

2.4.5 Umbilicals

Umbilicals are conduits through which materials are transferred to and from nuclear structures. During DBE and MCE-level excitation, the superstructure is expected to displace considerably relative to the foundation, yet the integrity of utility cables and conduits carrying electricity, communication lines, high-pressure steam, and coolant must be maintained for the plant to safely function or, if necessary, perform shutdown sequences. Thus, flexible umbilicals capable of maintaining functionality during and after DBE and MCE shaking are required of all designs.

The failure of umbilicals in response to seismic activity is a concern for isolated and non-isolated structures alike. Much of the damage from the 1906 San Francisco earthquake (7.9 M_W) was caused by fires which ignited when gas lines broke, and were increasingly difficult to extinguish due to failed water lines. The tsunami-induced partial meltdown of the Fukushima Daiichi nuclear plant in 2011 was caused by failed power generators which were unable to cool the reactors when primary power was lost. Thus, umbilicals must be a primary safety concern for nuclear power structures.

Large-diameter umbilicals used to carry high-temperature and/or high-pressure fluids pose the biggest challenge to design engineers (Blandford et al., 2009). Consequently, plants utilizing closed-cycle gas power conversion, capable of being configured on the isolation platform with the reactor are preferred, as they eliminate the need for these large, high-stress umbilicals.

The design of flexible umbilicals for nuclear application was completed for the International Thermonuclear Experimental Reactor (ITER), which was intended to be partially-isolated in order to mitigate large seismic forces (Hashimoto et al., 1998). Some of the proposed designs include the use of a rubber duct system able to stretch and bend, as well as pipe configurations utilizing multiple U-bends, flexible joints, spring supports, and oil dampers that can accommodate motion in any direction.

2.4.6 Isolation Level Location

Most seismically-isolated structures have bearings below the superstructure, hence the name "base isolation". However, isolators do not necessarily have to be placed at the base of the superstructure, and in fact, the location of the isolators has a profound effect on the dynamic response of the structure. Because an effective base isolation system is significantly more-flexible than the superstructure, the center-of-rigidity (CoR) for the fundamental dynamic mode is found in the isolation plane. The vertical location of this plane relative to the structures center-of-mass (CoM) affects the manner in which the horizontal response is coupled with the vertical and/or rotational response.

Consider the three seismically-isolated structures presented in Figure 2.10. Structures a, b, and c are isolated at the base, mid-height, and roof, respectively. The dynamic properties (i.e. modal shapes, ϕ, and frequencies, ω) of these three structures were solved by Kelly (1997) when the vertical and rotation frequencies are equal (i.e. $\omega_z = \omega_\theta$) and are presented in Equation 2.4 for a value of vertical eccentricity, $e_z = h_{CoM} - h_{CoR}$.

$$\phi = \begin{bmatrix}\phi_x \\ \phi_\theta \\ \phi_z\end{bmatrix}, \phi_1 = \begin{bmatrix}1 \\ -e_z\alpha \\ 0\end{bmatrix}, \phi_2 = \begin{bmatrix}0 \\ 1 \\ 1\end{bmatrix}, \phi_3 = \begin{bmatrix}0 \\ 1 \\ -1\end{bmatrix} \tag{2.4}$$

In this equation, α is based on the lateral frequency, ω_x, vertical frequency, ω_z, and radius of gyration, r, for the structure. Based on these mode shapes, it is clear that vertical excitation induces rotation regardless of eccentricity. Horizontal excitation also induces rotation when the vertical eccentricity is non-zero. Thus, there is an advantage to placing the isolation system at or near the elevation of the CoM to minimize coupling. Also from the first mode shape, it is evident that when e_z is negative (i.e. CoR above CoM), the rotational term acts to restore the structure back to the original location. Conversely, in the base-isolated system the mass acts to exacerbate the displacement and rotation during excitation (akin to P-Δ forces). Hence, placing isolators at the base of the structure is not ideal in terms of dynamics. However, two design advantages result when isolators are placed at the base. First, this configuration does not require additional exterior members or diaphragms to act as an isolation platform and to transfer forces, since there is already ample room under the structure to place bearings. Second, this configuration minimizes tension in gravity-load-carrying members, and does not require members to span long distances between isolators, and thereby being preferable for reinforced concrete structures.

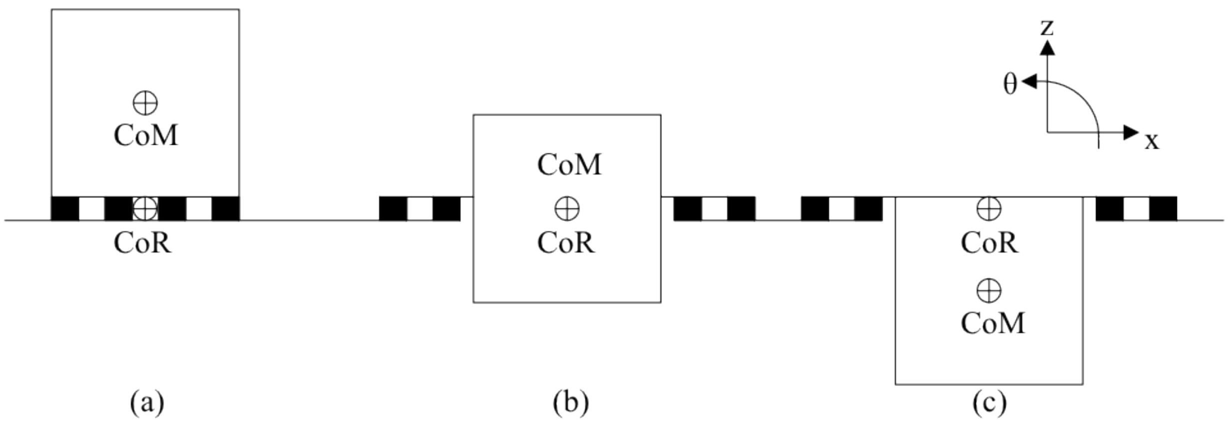

Figure 2.10: Schematic of isolated structures showing the center-of-mass (CoM) and center-of-rigidity (CoR) for isolation planes at three levels: (a) base, (b) middle, and (c) top

2.5 Base Isolation Applications

The ability of base isolation systems to reduce the harmful effects of seismic activity have made them appealing for a variety of structures. Early isolation implementations were in essential structures (e.g. hospitals, fire stations, etc.) and buildings of historical or civic importance (e.g. city halls, courtrooms, etc.). Recently, however, isolation systems have been used or considered for tall buildings and safety-critical facilities such as industrial structures, chemical storage tanks, and nuclear power structures. These additional applications are described in Sections 2.5.1 through 2.5.4.

2.5.1 Tall Buildings

The 2001 completion of the Los Angeles City Hall retrofit resulted in the tallest base-isolated structure in the world. The isolation system was comprised mainly of HDR bearings of various sizes, and also includes flat sliders. Despite its overall height of 138 m, the footprint is rather stout, and the slender tower only exists over half the full height (Yousef and Hata, 2005). Thus, overturning was not an issue. Isolated structures with larger aspect ratios have been constructed in Japan including the Sendai MT building (completed in 1997 in Sendai City, Miyagi Prefecture) and Thousand Tower (completed in 2001 in Kawasaki City, Kanagawa Prefecture) which had heights of 84.9 m and 135 m, respectively.

Although base isolation is not ideal for tall, slender (i.e. long period) structures, a study by Komuro et al. (2005) was undertaken to determine the efficacy of bearing systems for such buildings. The analysis found displacement response reductions up to 60% for seismically-isolated structures with fixed-based superstructural periods up to 4.0 seconds. Additionally, the study collected response data from the isolation level as well as the 1st, 10th, and 18th floors of the 18-story, base-isolated Sendai MT Building following the 2003 Off-Miyagi (7.0 M_W) earthquake. This study confirmed that the isolators performed effectively in reducing interstory drifts and in limiting PGA amplification to a 17% increase in the lateral directions. Therefore, base isolation is a realistic design consideration for tall structures in seismically-active regions.

2.5.2 Industrial Structures

Base isolation has become increasing popular for industrial and manufacturing structures which may contain heavy, acceleration-sensitive equipment. Sliding bearings have been used for offshore oil platforms including the Chirag 1 off Azerbaijan in the Caspian Sea (Medeot and Infanti, 1997) and Sakhalin II off Russia in the Sea of Okhotsk (EPS, 2006), the latter of which uses the largest load-carrying seismic isolation bearings ever manufactured. In addition to providing seismic isolation, the bearings are useful for isolation of wave, ice, and thermal expansion loading.

Applications in high-tech manufacturing and laboratories containing sensitive equipment have increased in the last decade. Hughes Satellite operations facility, Conexant Semiconductor plants, Immunex research facility, and the Stanford linear particle accelerator are just a few examples of base-isolated high-tech facilities on the West Coast (DIS, 2011). In most cases, the isolators are necessary to reduce damage from earthquakes, as well as to eliminate small acceleration spikes from ambient vibrations which could ruin precision parts or experiments.

2.5.3 Liquefied Natural Gas Tanks

Liquefied natural gas (LNG) is stored in aboveground tanks consisting of an inner cylindrical, steel vessel encased in an outer protective concrete layer. The capacity of LNG tanks can exceed 180,000 m^3 of liquefied gas cooled to -165°C, and therefore represents a considerable quantity of stored chemical energy (Rötzer et al., 2005)(Summers et al. 2004). Gas leaks could cause explosions, fires, and environmental disasters, all of which endanger human life, and therefore, the seismic requirements for LNG tanks are quite stringent (Tarjirian, 1998). These tanks have resonant frequencies which overlap with the predominant frequencies of severe seismic events. Historically, fixed-base tanks have performed poorly in response to seismic excitation, due to the combination of hydrostatic and hydrodynamic pressures (Tarjirian, 1998). Thus, base isolation is an effective design option for reducing structural demands, and in turn, increasing safety margins. Thus far, LRB and FP bearings have been installed in LNG and other chemical tanks in many countries around the world (EPS, 2004)(EPS, 2008).

2.5.4 Nuclear Power Facility Structures

Nuclear power facilities are typically constructed of thick, reinforced-concrete (RC) walls in order to provide temperature, pressure, and radiation shielding; and as a result, the structures are very heavy and stiff. These characteristics make nuclear power structures ideal for base isolation implementation, as the short fundamental period can be readily increased and the stiff walls will nearly eliminate superstructure deformations in the isolated configuration. Additionally, in order to maintain desired bearing pressures, heavy structures require the use of wider-diameter bearings, which can be designed to reach larger displacements, and do so while remaining stable.

One of the earliest applications of base isolation was in foreign nuclear power facilities. The four-unit Cruas nuclear power plant in France, completed in 1984, is a pressurized water reactor (PWR) isolated by 1800 rudimentary, square neoprene bearings (Postollec, 1982), measuring 50.0 cm $\times$ 50.0 cm $\times$ 6.6 cm. Completed in 1985, the two-unit Koeberg power plant in South Africa is isolated with 3600 neoprene bearings, measuring 70.0 cm $\times$ 70.0 cm $\times$ 13.0 cm, which have a limited deformation capability, and are topped by steel and lead-bronze-alloy slip-plates capable of sliding once the rubber has reached its deformation capacity (Plichon et al., 1980). The design SSE peak ground acceleration for the plants was 0.3 g and 0.2 g, respectively. The elastomeric bearings used in both projects are considered unrefined by today's isolation standards, and are not considered for future applications. Similar designs were developed but never completed in western Iran, Mexico, and Western France (Tarjirian, 1998). The Cadarache Nuclear Centre, expected to be completed by 2014 in southern France, contains the Jules Horowitz reactor (RJH), which utilizes 195 square, neoprene bearings measuring 90.0 cm $\times$ 90.0 cm $\times$ 18.1 cm (DeGrandis et al., 2011). This construction represents the first NPP application of SBI since Cruas and Koeberg.

Since 1984, isolation systems have been studied and considered for nuclear application in the US, UK, New Zealand, and Japan, yet no base-isolated plants have been commissioned (Buckle, 1984)(Derham, 1985)(Kato et al., 1991). Despite the lack of approved base-isolated nuclear power plant designs in Japan and the United states, regulations exist in both countries which could eventually make them a reality. Large-amplitude seismicity and the expectation of high-frequency ground motions have led to harsh design guidelines which retard the approval of plant designs in the United States. US Nuclear Regulatory Commission Regulatory Guide 1.165 (USNRC, 1997) imposes the strict requirement that the seismic design of new plants be based on a probabilistic seismic hazard assessment (PSHA) for a 100,000-year return period. Although many contend that base isolation is a cost-effective way to achieve adequate response under such extreme loading events, the relative infancy of the technology and limited in-field data of its response hinder its implementation in new plant designs. Additionally, the requirement that seismically-isolated superstructures must remain elastic forces overdesign of superstructural members, thereby reducing or eliminating the potential cost benefit of base isolation.

Chapter 3

Nuclear Power Plants

20% of the total power currently generated in the United States comes from the 104 commercial reactors, consisting of 69 pressurized water reactors (PWRs) and 35 boiling water reactors (BWRs), that operate at 65 nuclear power plants (NPPs) (USEIA, 2011). All of the 132 NPPs constructed in the US, 28 of which have been permanently shut down, were begun between 1958 and 1974. The partial meltdown of the Three Mile Island NPP in 1979 aided in the cancellation of most of the remaining orders for NPPs. As a result, only a few studies analyzing the use of SBI for NPPs were undertaken. Suggestions of a "nuclear renaissance" beginning in the 21st Century, spurred by the formulation of Generation III, III+, and IV reactors, have reintroduced the possibility of NPPs utilizing SBI.

This chapter presents applicable design codes, as well as relevant past and current studies pertaining to NPPs. Section 3.1 details the current engineering codes which govern the design of NPP structures. Section 3.2 presents analyses of isolated NPP designs, including SAFR, PRISM, and a conventional sample plant used by Huang et al. (2007)(2009). Section 3.3 presents data from numerous recording devices inside the fixed-base Kashiwazaki-Kariwa NPP during the 2007 Chūetsu offshore (6.6 M_W) earthquake.

3.1 Nuclear Facility Structural Design Codes

The design basis for all components of NPPs, which includes the superstructure, foundation, and isolation system for seismically-isolated designs, is controlled by ASCE 4-11 (2011) and ASCE 43-05 (2005). ASCE 43-05 defines the following design objectives for NPPs:

1. 1% probability of unacceptable performance in response to 100% DBE excitation
2. 10% probability of unacceptable performance in response to 150% DBE excitation

These two goals are simultaneously satisfied using the probabilistic design method in ASCE 43-05, which sets a performance goal comprising a quantative assessment of the seismic risk and a qualitative consideration of the response objective. The seismic risk is quantified

Seismic Design Category	SDC-3	SDC-4	SDC-5
Target Performance Goal, P_F	10×10^{-5}	4×10^{-5}	1×10^{-5}
Hazard Exceedence Probability, H_D	40×10^{-5}	40×10^{-5}	10×10^{-5}
Probability Ratio, $R_P = H_D/P_F$	4	10	10

Table 3.1: Target Performance Goals from ASCE 43-05

by probabilistically determining the mean annual hazard exceedence frequency, H_D, and target performance goal (the annual probability that the acceptable performance limit is exceeded), P_F, which define the Design Basis Earthquake (DBE). The precise (H_D, P_F) pair, or target probabilistic performance goal, is determined by the Seismic Design Category (SDC) as set in ASCE 43-05. SDCs range from 1 to 5 depending on the type of structure, with nuclear facilitiy structures, systems, and components (SSCs) falling under SDC-3, 4 and 5, through ANSI/ANS 2.26. The higher the SDC, the larger potential risk, necessitating a rarer performance goal. The target probabilistic performance goals for those SDCs are listed in Table 3.1. A description of how these probability goals are used to determine associative DBEs is presented in Chapter 6.

Unacceptable performance is defined in terms of particular Limit States in ASCE 43-05. These Limit States describe the amount of acceptable damage which can be incurred in a particular SSC and include:

A. Large permanent displacement short of collapse

B. Moderate permanent distortion

C. Limited permanent distortion

D. Essentially elastic or operational behavior

Together, the SDC and Limit State form a Seismic Design Basis (SDB), which for NPP structures requires minimal inelastic behavior in response to the rarest considered events (SDB-5D). Thus, SDBs are used to assure that the structures which pose the greatest risk to public safety have the most stringent definitions of unacceptable behavior, and have the lowest probability of exceeding said limits even in response to the strongest considered events.

The consideration of SBI devices with respect to SDBs is of some debate, since all devices, by design, incur significant inelastic deformation during high-amplitude seismic excitations. The extension of the SDB concept to SBI devices will be discussed further in Section 3.2.4. Nevertheless, the superstructure and foundation shall conform to SBD-5D, and must not incur any significant inelastic deformation which may threaten operation or safe shutdown.

3.2 NPP Studies Utilizing SBI

Studies applying SBI to NPPs began as the technology approached maturation (Skinner et al., 1976). Domestic interest in applying SBI to NPPs peaked in the mid-1980s following the construction of isolated French NPP designs in Koeberg, South Africa and Cruas, France at sites with safe shutdown earthquake (SSE) acceleration limits of 0.3 g and 0.2 g, respectively. What followed were two US DOE-supported conceptual designs for seismically-isolated compact advanced liquid metal reactor (ALMR) NPPs. The PRISM and SAFR designs, described in Sections 3.2.1 and 3.2.2 respectively, incorporated SBI, "to support plant standardization, enhance plant safety margins, permit siting in zones with higher seismicity, and to potentially reduce plant cost" (Tajirian et al., 1990). Both plants had design SSEs with peak vertical and horizontal accelerations of 0.3 g which was considered to envelope the NRC Regulatory Guide 1.60 spectra, and cover 80% of potential US nuclear sites outside California. The studies did confirm that SBI systems could be successfully engineered for sites with peak design earthquake accelerations exceeding 0.5 g.

3.2.1 PRISM

The Power Reactor Inherently Safe Module (PRISM) plant is a 155 MWe compact standardized LMR designed by General Electric (Tajirian et al., 1989). The conceptual plant, shown in Figure 3.1, has a design weight of 40,000 kN supported on 20 HDR bearings which laterally isolate the structure and do not require supplemental damping. The bearings are 132 cm in diameter and 58.8 cm tall with a shape factor of 23, providing the structure with fundamental lateral and vertical periods of 1.33 sec and 0.05 sec, respectively.

Comparative dynamic tests show significant decreases in the lateral acceleration response spectra of reactor components as a result of SBI implementation. Consequently, it is believed that SBI may enable significant cost and design savings for superstructure design keys. The peak lateral displacement of bearings during SSE-level dynamic testing, including torsional effects, was measured as 19 cm (127% shear strain).

3.2.2 SAFR

The Sodium Advanced Fast Reactor (SAFR) plant is a 450 MWe pool-type LMR designed by Rockwell International (Tajirian et al., 1990). The conceptual plant, shown in Figure 3.2, is significantly heavier than the PRISM design with a design weight of 280,000 kN that is supported on 100 low shape factor (LSF) HDR bearings which isolate the structure laterally and vertically. The bearings are 107 cm in diameter and 41.3 cm tall with a shape factor of 2.4, providing the structure with fundamental lateral and vertical periods of 2.00 sec and 0.33 sec, respectively.

Comparative dynamic analyses were run on the isolated and fixed-base SAFR plants (Tajirian et al., 1990). The resulting response spectra showed significant horizontal reductions at frequencies over 1.0 Hz, and vertical reductions at frequencies over 4.0 Hz, enveloping

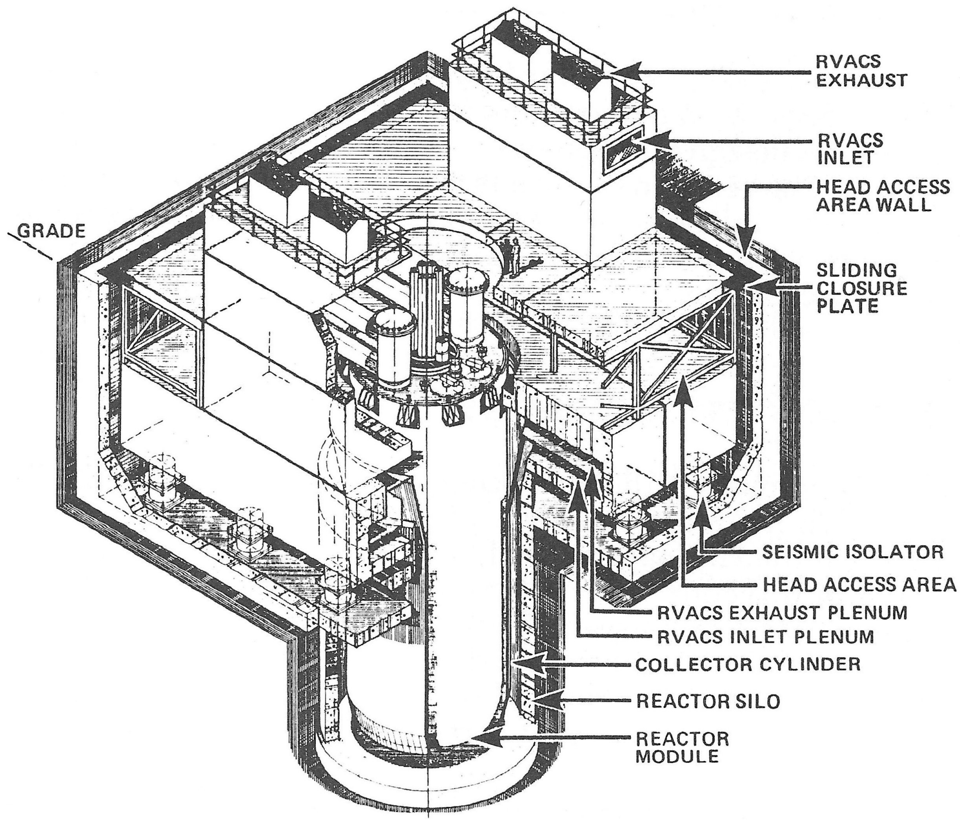

Figure 3.1: Schematic of PRISM reactor module (Courtesy of Ian Aiken)

the typical frequency ranges of standard NPP equipment. Although these simulations observed only a small amount of rocking-induced uplift, the authors note that rocking is a significant concern for NPPs utilizing LSF bearings. The peak lateral displacement of bearings during SSE-level dynamic testing, including torsional effects, was measured as 23 cm (191% shear strain).

3.2.3 EERC Bearing Tests

Testing of HDR bearings for the PRISM project, as well as HDR and LDR LSF bearings for the SAFR project, were completed at EERC (Aiken et al., 1989)(Tajirian et al., 1990) in order to properly characterize the horizontal and vertical mechanics of each. These tests included standard and offset shear tests, vertical and buckling tests, failure mode tests, and combined loading tests for bolted and dowelled bearings.

The report concluded that both bearings can be effectively used as lateral SBI, and that LSF bearings can also providee vertical SBI. Regardless of connection type, the bearings were capable of reaching 400% of the SSE displacements. Additionally, mechanical properties of

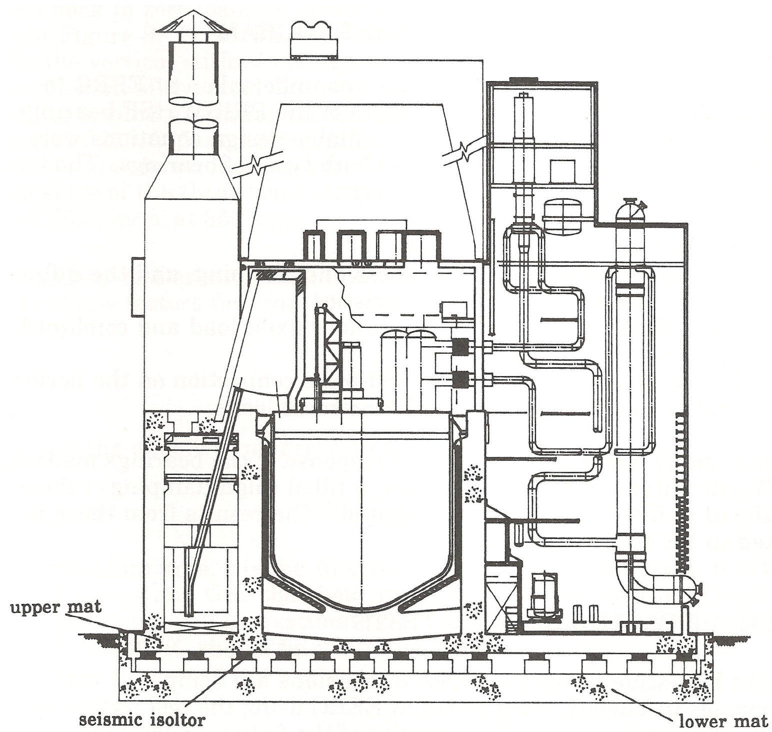

Figure 3.2: Schematic of SAFR reactor module (Courtesy of Ian Aiken)

the bearings were found to have no property degradation following extreme loading and severe distortions. The report noted the difficulty in modeling LSF bearings due to stiffness non-linearity, as well as a need for further dynamic testing.

Following testing, the PRISM design was approved by the USNRC. The PRISM design would later be updated by GE-Hitachi as part of the Gen III+ program. Although that design does not use SBI, its implementation has been recommended by many. The SAFR design was not approved by the USNRC.

3.2.4 Recent Studies

Huang et al. (2007)(2009) analyzed the response of SBI systems for application with NPPs utilizing SAP2000. The former report employed SBI systems, composed of either FP, LR, LDR, or HDR bearings, supporting a lumped-mass stick model designed to represent a conventional NPP reactor building. Isolated and fixed-base models were subject to horizonatal seismic motion representative of East and West Coast sites at SSE and DBE levels, in order to monitor the effect of SBI on secondary systems in NPPs. The study showed that seismic demands on secondary systems were significantly reduced for NPPs utilizing SBI of all types. These reductions were largest for the low-amplitude seismicity characteristic of East Coast sites. For such excitation, choice of the characteristic strength, Q (based on F_y, μ, or level of rubber damping), has a much larger impact on the response in comparison to bearings subjected to West Coast motions at the same hazard level.

The second study analyzed a rigid superstructure atop either LR, LDR, or FP SBI systems. The models were subjected to three-component DBE and BDBE motions from the Central and Eastern United States (CEUS) and Western United States (WUS). Additionally, the analysis cases that were studied considered the variability of bearing mechanical properties as a result of aleatoric uncertainty in manufacturing, as well as differences in deterioration over time due to various factors. Based on the results, the authors recommended extending the ASCE 43-05 provisions to NPPs with SBI as follows:

1. Individual isolators shall suffer no damage in response to DBE excitation
2. 1% probability of the isolated nuclear structure impacting the surrounding structure (moat) in response to 100% DBE excitation
3. 10% probability of the isolated nuclear structure impacting the surrounding structure (moat) in response to 150% DBE excitation
4. Individual isolators sustain gravity and earthquake-induced axial loads at 90th percentile lateral displacements consistent with 150% DBE excitation

These guidelines help to extend the ASCE43-05 SDB-5D requirement for NPPs to SBI devices that are inherently plastic in nature. Although the definition of damage as it pertains to SBI devices is specific to the bearing type, the recommended prescriptions establish a protocol for unacceptable group response (i.e. impact), as well as for testing requirements of bearing designs. The concept of bearing damage and failure will be discussed in Section 4.5.

3.3 The Kashiwazaki-Kariwa Nuclear Power Plant

In 1980, construction began on the Kashiwazaki-Kariwa NPP in Niigata Prefecture, on the west coast of Honshu, Japan. The resulting seven-unit facility - a map of which is shown in Appendix A - houses five boiling water reactors (BWRs) and the worlds first two advanced boiling water reactors (ABWRs), all of which were completed and commissioned by 1997. The design specification acceleration limits for safe shutdown and rapid restart were 0.46 g and 0.28 g, respectively, corresponding to an expected 6.5 M_L (Richter magnitude) event (WNN, 2007).

During it's service life, the plant has been subjected to various large earthquakes and aftershocks. The seismic events and the NPP response are presented in Sections 3.3.1 through 3.3.3. The case study serves to demonstrate the potential risk involved with fixed-base NPPs subjected to BDBE events.

Event	Date	Time
Main Shock	07/16/2007	10:13
Aftershock 1	07/16/2007	11:00
Aftershock 2	07/16/2007	15:37
Aftershock 3	07/16/2007	17:42
Aftershock 4	07/16/2007	21:08
Aftershock 5	07/25/2007	06:52
Aftershock 6	08/04/2007	00:16

Table 3.2: Date and time for the 2007 Niigata Chūetsu-Oki (6.6 M_W) earthquake and aftershocks

3.3.1 2004 Chūetsu Earthquake

At 17:56 local time on October 23, 2004, the 6.8 M_W Chūetsu earthquake struck the west coast of Japan. Seismological measurements at the plant suggest the intensity at the site was significantly lower than at other nearby locations. Consequently, only minor operational interruptions were incurred, as Unit 7 was briefly shut down during an aftershock (note that at the time of the main shock, Unit 4 was shut down for maintenance).

3.3.2 2007 Niigata Chūetsu-Oki Earthquake

At 10:13 local time on July 16, 2007, the 6.6 M_W Niigata Chūetsu-Oki earthquake (also referred to as the Chūetsu Offshore earthquake) struck 13 km from the Kashiwazaki-Kariwa NPP. Over the following 20 days, six more major aftershocks occurred, as well as a 6.8 M_W event in the Sea of Japan which was deemed to be caused by a different geologic mechanism. The date and time of the main shock and subsequent aftershocks are presented in Table 3.2.

At the time of the initial earthquake, Units 1, 5, and 6 were shut down for maintenance. The remaining units automatically shut down in response to the event, and resuming power production was halted until structural and nuclear safety inspections could be completed by the Tokyo Electric Power Company (TEPCO) and the International Atomic Energy Agency (IAEA). These inspections confirmed no significant damage to nuclear equipment or safety related components, however significant damage to non-safety related structures, systems, and components was observed. Additionally, four radioactive material leaks were found in the ABWR units. The investigators recommended a re-evaluation of the seismic hazard as well as detailed geophysical studies of the site.

Following a nearly two year period of inspections, repairs, upgrades, tests, and government approvals, full power was restored to Unit 7. Power generation was restored to Units 1, 5, and 6 by December of 2010. TEPCO's total financial losses have been estimated at \$10 billion due to fuel costs, restoration expenses, and the drop in company stock (WNN, 2008)(Bloomberg, 2007).

Location	Name	Depth, z (m)	P-Wave Velocity, V_P (km/s)	S-Wave Velocity, V_S (km/s)
Service Hall	SG1	65.1	0.65	0.31
Service Hall	SG2	16.7	1.59	0.35
Service Hall	SG3	-31.9	1.67	0.50
Service Hall	SG4	-182.3	1.78	0.64
Unit 1	G7	5.0	1.53	0.30
Unit 1	G8	-40.0	1.60	0.50
Unit 1	G9	-122	1.75	0.54
Unit 1	G10	-250	1.85	0.70
Unit 5	G51	9.3	1.38	0.16
Unit 5	G52	-24.0	1.73	0.50
Unit 5	G53	-100.0	1.93	0.66
Unit 5	G54	-180.0	2.02	0.84
Unit 5	G55	-300.0	2.29	0.87

Table 3.3: Free field seismometer information at Kashiwazaki-Kariwa NPP

3.3.3 Acceleration Amplification Data

The Kashiwazaki-Kariwa NPP was constructed on an approximately 5 km^2 plot of land, and is highly instrumented with two iterations of seismometers. Acceleration data was provided by TEPCO (2011) for free field and structural response to each of the seven distinct ground motions of the 2007 Niigata Chūetsu-Oki Earthquake.

Free field acceleration data was recorded at as many as three locations for each event: adjacent to the service hall (SH) approximately 1.3 km east of the nearest unit, adjacent to Unit 1, and adjacent to Unit 5. Seismometer name and elevation/depth, z, relative to Tokyo Bay mean sea level (TMSL) for each free field instrument, as well as the P-wave velocity, V_P, and S-wave velocity, V_S, of the surrounding soil material at the instrument locations are presented in Table 3.3.

Structural acceleration data was recorded using accelerometers at multiple locations, including at least two instruments in each unit. Every unit consists of two buildings, a Reactor building and a Turbine building, each with numerous floors including multiple below-grade or basement levels (B1 through B5) and above-grade levels (L1 through L3), which include the turbine pedestal (p). Additionally, Units 1 and 5 have seismic acceleration data from observation (o) sheds located outside the main structures. For each unit, accelerometer location, name, and elevation/depth, z, relative to Tokyo Bay mean sea level (TMSL) are presented in Table 3.4.

Plots for all seven ground motions displaying peak acceleration, a, of free field and superstructure sensors with depth, z, are presented in Appendix A. These plots demonstrate the large-magnitude ground motions, which neared or exceeded the design basis for the main

Location	Building	Name	Depth, z (m)
Unit 1	Observation Shed	1-G1	18.3
Unit 1	Reactor (L2)	1-R1	12.8
Unit 1	Turbine (L1p)	1-T2	5.3
Unit 1	Reactor (B5)	1-R2	-32.5
Unit 2	Reactor (L2)	2-R1	12.8
Unit 2	Turbine (L1p)	2-T2	5.3
Unit 2	Turbine (L1)	2-T1	5.3
Unit 2	Turbine (B3)	2-T3	-16.3
Unit 2	Reactor (B5)	2-R2	-32.5
Unit 3	Reactor (L2)	12.8	12.8
Unit 3	Turbine (L1p)	5.3	5.3
Unit 3	Turbine (B3)	2-T3	-16.3
Unit 3	Reactor (B5)	2-R2	-32.5
Unit 4	Reactor (L2)	4-R1	12.8
Unit 4	Turbine (L1p)	4-T2	5.3
Unit 4	Turbine (L1)	4-T1	5.3
Unit 4	Turbine (B3)	4-T3	-16.3
Unit 4	Reactor (B5)	4-R2	-32.5
Unit 5	Reactor (L3)	5-R1	27.8
Unit 5	Observation Shed	5-G1	24.3
Unit 5	Turbine (L2p)	5-T2	22.1
Unit 5	Reactor (B4)	5-R2	-17.5
Unit 6	Reactor (L3)	6-R1	23.5
Unit 6	Reactor (B3)	6-R2	-8.2
Unit 7	Reactor (L3)	7-R1	23.5
Unit 7	Turbine (L2p)	7-T2	20.4
Unit 7	Turbine (L2)	7-T1	20.4
Unit 7	Reactor (B3)	7-R2	-8.2
Unit 7	Turbine (B2)	7-T3	-10.0

Table 3.4: In-structure accelerometer information at Kashiwazaki-Kariwa NPP

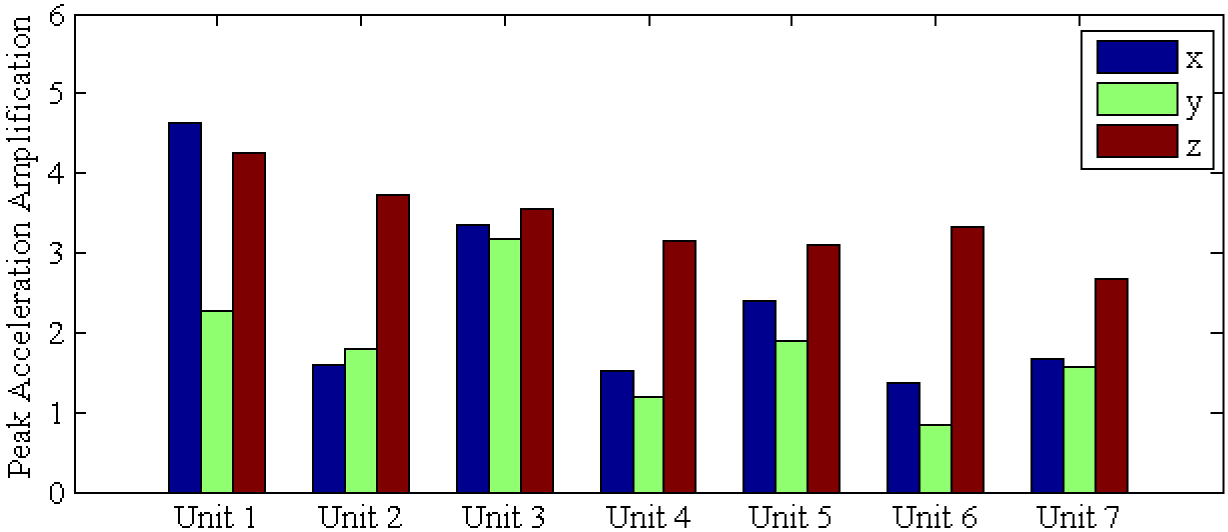

Figure 3.3: Peak structural amplifications at the Kashiwazaki-Kariwa nuclear power plant in response to the main shock of the 2007 Niigata Chūetsu-Oki earthquake

shock, and exceeded the rapid restart levels for two of the aftershocks. These plots also show a general increase in peak acceleration with increasing elevation (i.e. decreasing depth) in both the soil and superstructure. The maximum superstructure responses were generally found at the pedestal and observation shed locations in each unit.

Figures 3.3 through 3.9 plot the peak structural accelerations at all units in each direction normalized by the maximum directional reading from the nearest free field sensor to the bottom of each unit. For units 1 through 4, the nearest sensor is G8, from the unit 1 free field location at a depth of 40.0 m below TMSL. For units 5 through 7, the nearest sensor is G52, from the Unit 5 free field location at a depth of 24.0 m below TMSL. When data from either of the aforementioned locations was not recorded or presented, sensor SG3 from the Service Hall free field location at a depth of 31.9 m below TMSL was used for normalization purposes. Acceleration amplification data from the seven events shows amplification ratios exceeding 4.0 in at least one unit for a majority of the events. Furthermore, these plots show that the vertical amplification is often as large as or greater than the lateral amplification. This data suggests that fixed base structures in response to earthquakes of all sizes are likely to amplify the ground motion significantly. As the structurral accelerations increase, the demands on equipment and SSCs also increase. The result is a higher threshold for which structural components must be designed and for which equipment must be qualified. SBI presents an effective way of reducing such accelerations, increasing safety factors, and expediting equipment qualification.

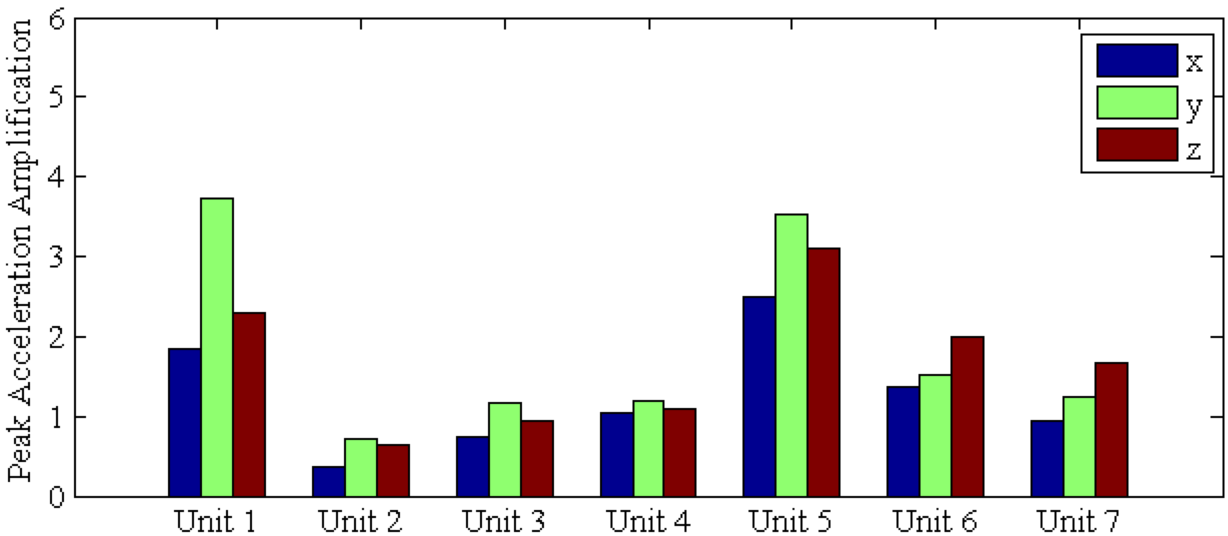

Figure 3.4: Peak structural amplifications at the Kashiwazaki-Kariwa nuclear power plant in response to aftershock 1 of the 2007 Niigata Chūetsu-Oki earthquake

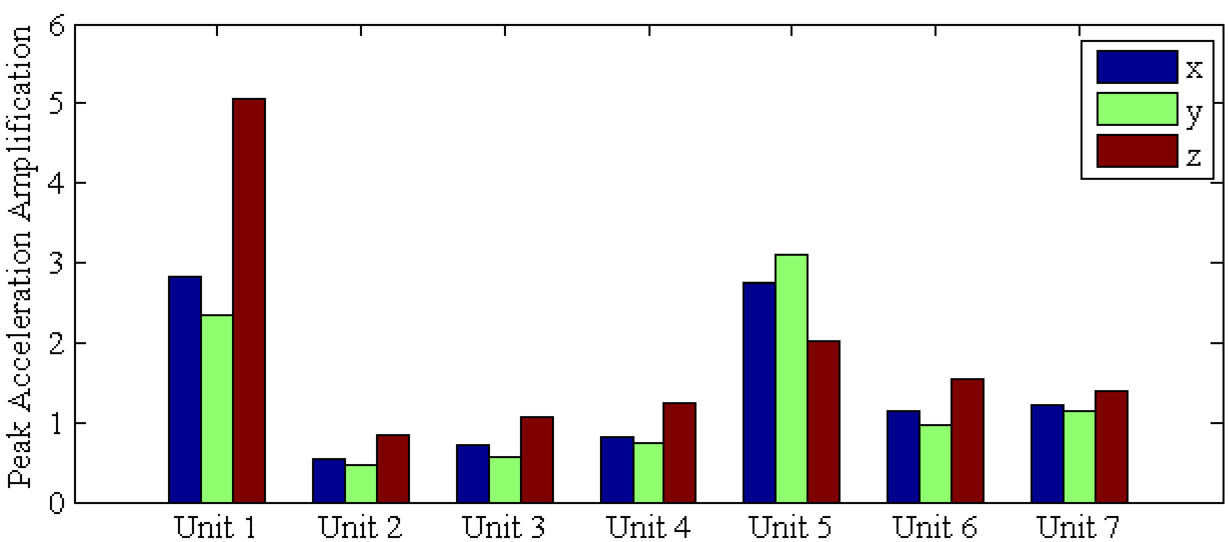

Figure 3.5: Peak structural amplifications at the Kashiwazaki-Kariwa nuclear power plant in response to aftershock 2 of the 2007 Niigata Chūetsu-Oki earthquake

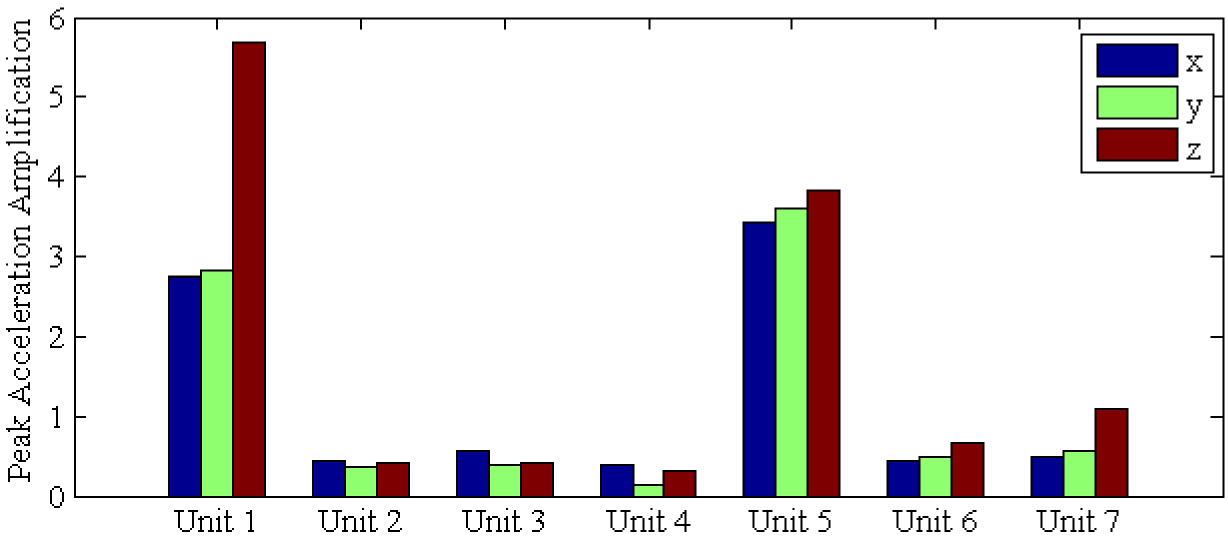

Figure 3.6: Peak structural amplifications at the Kashiwazaki-Kariwa nuclear power plant in response to aftershock 3 of the 2007 Niigata Chūetsu-Oki earthquake

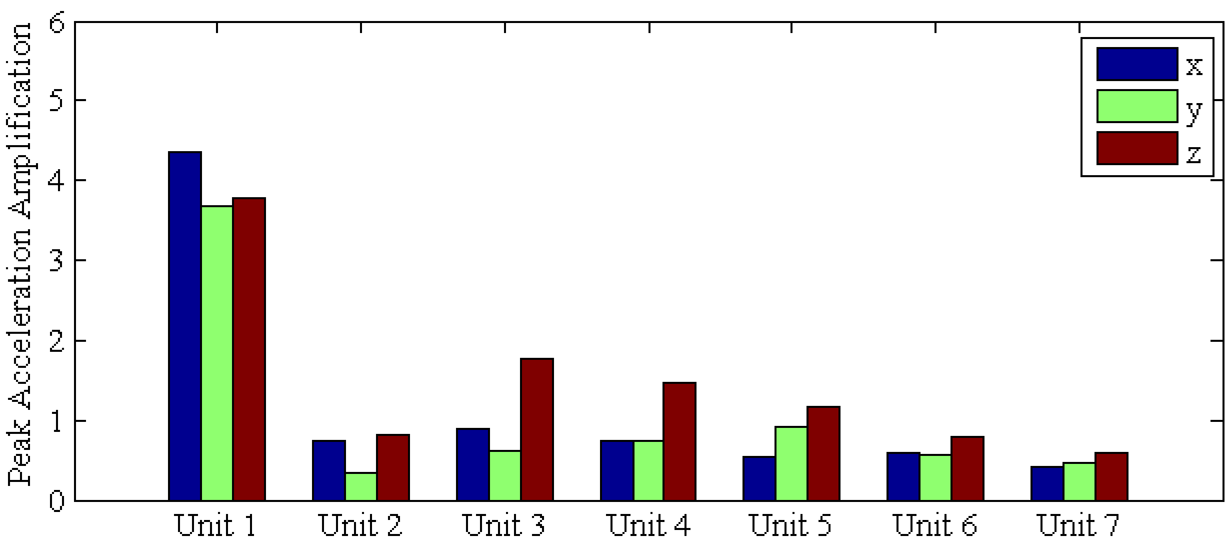

Figure 3.7: Peak structural amplifications at the Kashiwazaki-Kariwa nuclear power plant in response to aftershock 4 of the 2007 Niigata Chūetsu-Oki earthquake

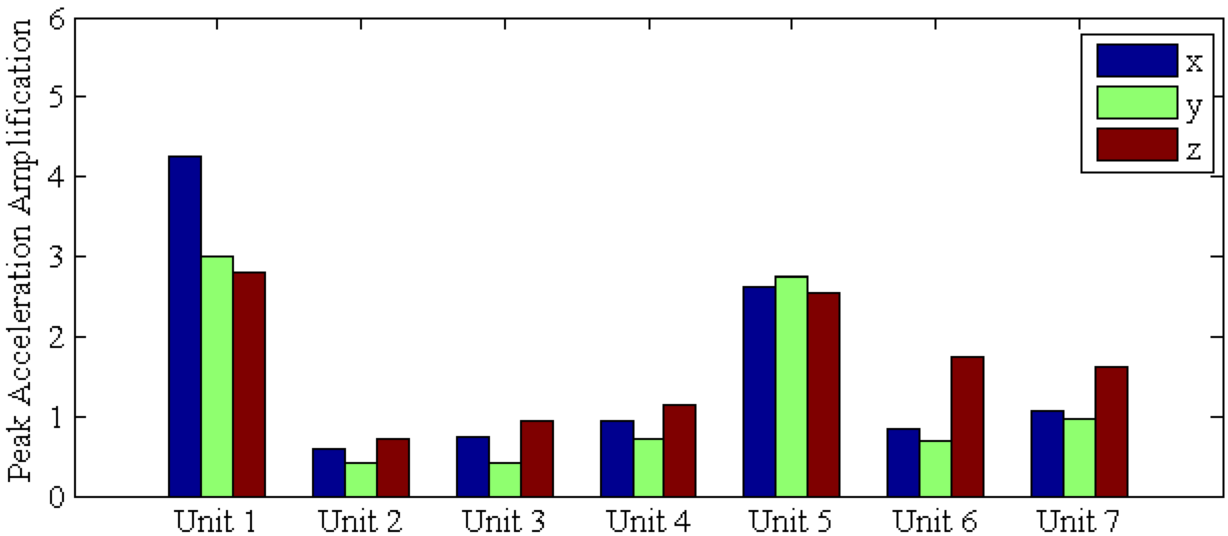

Figure 3.8: Peak structural amplifications at the Kashiwazaki-Kariwa nuclear power plant in response to aftershock 5 of the 2007 Niigata Chūetsu-Oki earthquake

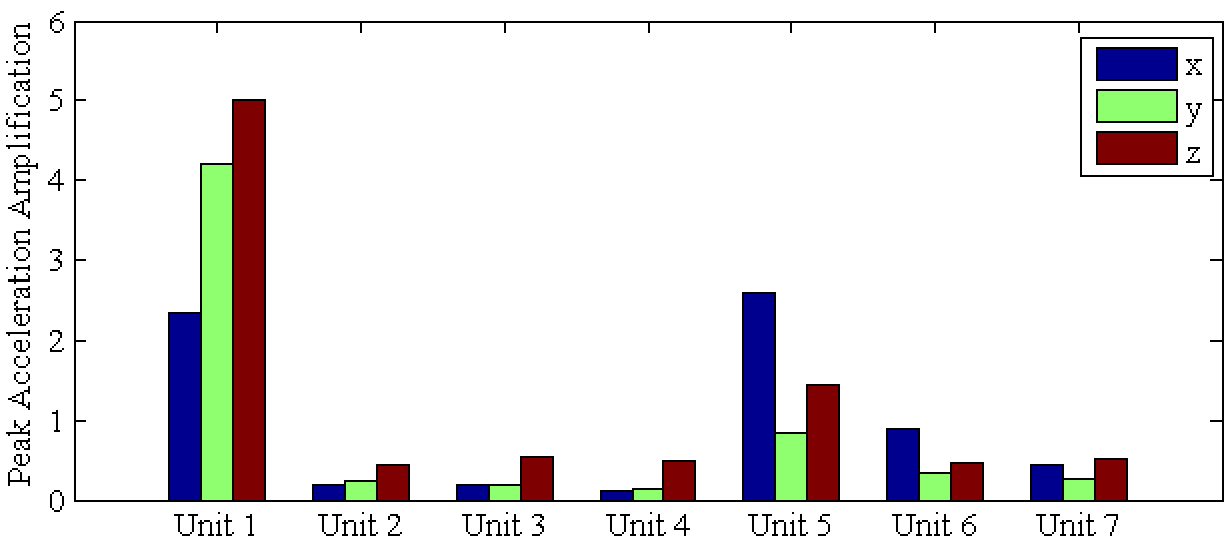

Figure 3.9: Peak structural amplifications at the Kashiwazaki-Kariwa nuclear power plant in response to aftershock 6 of the 2007 Niigata Chūetsu-Oki earthquake

Chapter 4

Isolation Models

The 3-dimensional, non-linear analyses proposed herein utilize a variety of numerical element models intended to approximate the dynamic response of isolation bearings. For both isolator types (i.e. friction pendulum bearings and elastomeric bearings), multiple response models are implemented and compared, including a simplified model typical of existing commercial software, as well as a more robust model representing the cutting edge of academic pursuits in the field.

This chapter describes the numerical models used including relevant theoretical bases, input parameters, and algorithms. Relevant changes are explicitly stated and the accuracy of each model is validated using comparative tests with the original models. The robust TFP and simplified FP models are described in Sections 4.1 and 4.2, respectively. The simplified and robust LR models are presented in Sections 4.3 and 4.4, respectively. Finally, the concept of damage and failure in SBI bearings is discussed in Section 4.5.

4.1 Robust Friction Pendulum Model

The Becker and Mahin (2011) model is a two-dimensional, non-linear, kinematic model that tracks the location of each slider of a TFP bearing on its respective sliding surface. A bi-directional plasticity model proposed by Mosqueda et al. (2004) is implemented to account for the hysteretic behavior of each slider. This research extends the model to explicitly consider three dimensions by imposing a vertical geometric constraint described by Becker (2011). The resulting model is used to complete robust analyses of triple friction pendulum bearings in ALE3D, where it is referred to as “spring3”.

4.1.1 Model Response

A schematic of an undeformed TFP bearing is shown in Figure 4.1. The important parameters for each of the four sliding surfaces are displayed and include the sliding surface radius,

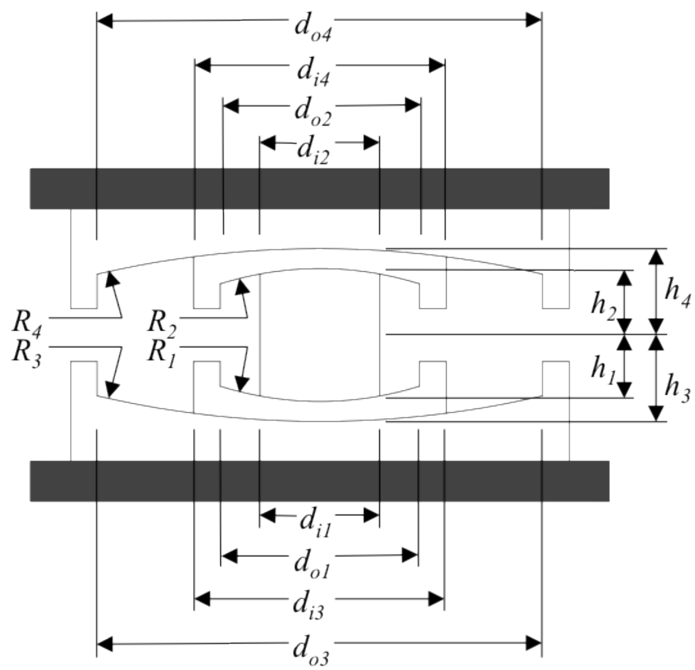

Figure 4.1: Schematic of an undeformed TFP bearing depicting the physical input parameters for the model

R_n, outer restraint diameter of the surface, d_{on}, inner slider diameter, d_{in}, and undisplaced surface-to-mid-height distance, h_n.

The model tracks the lateral displacements of each slider, u_n, which sum to the total lateral displacement, u, as shown in Equation 4.1. The lateral displacements on each surface can be found from the directional displacements on the surface, u_{nx} and u_{ny}, using Equation 4.2. The sliding surfaces are spherical, and therefore u_n can be found as the product of the surface radius, R_n, and the sine of the angle with respect to the slider normal, θ_n. Since u_n is measured at the mid-height of the bearing and not at the surface level, its relationship with the directional angle, θ_n, is altered as depicted in Equation 4.3.

$$u = \sum_{n=1}^{4} u_n \tag{4.1}$$

$$u_n = \sqrt{u_{nx}^2 + u_{ny}^2} \tag{4.2}$$

$$u_n = (R_n - h_n)\sin\theta_n = L_n \sin\theta_n \approx L_n\theta_n \tag{4.3}$$

L_n in the previous expression is referred to as the effective pendulum length of the sliding surface. Once displacement occurs in one direction the effective pendulum length is reduced in the perpendicular direction. The directional effective pendulum lengths, L_{nx} and L_{ny}, reflect this reduction, and are found using Equation 4.4 at each time step.

$$\begin{aligned} L_{nx} &= \sqrt{L_n^2 - u_{ny}^2} \\ L_{ny} &= \sqrt{L_n^2 - u_{nx}^2} \end{aligned} \tag{4.4}$$

The local displacement vector, $\mathbf{u}$, is written as $[u_{1x}, u_{2x}, u_{3x}, u_{4x}, u_{1y}, u_{2y}, u_{3y}, u_{4y}]^T$. The model assumes the outer concaves remain parallel and do not rotate, leaving a 6x1 vector of independent global displacement variables, $\mathbf{U}$, written as $[u_x, u_y, \theta_{1x}, \theta_{2x}, \theta_{1y}, \theta_{2y}]$. Utilizing Equation 4.1 in both directions, and the rotational constraint, the transformation matrix, $\mathbf{T}$, relating $\mathbf{U}$ to $\mathbf{u}$, is formed as shown in Equation 4.5.

$$\mathbf{T} = \begin{bmatrix} 0 & 0 & L_{1x} & 0 & 0 & 0 \\ 0 & 0 & 0 & L_{2x} & 0 & 0 \\ \frac{L_{3x}}{L_{3x}+L_{4x}} & 0 & \frac{-L_{3x}(L_{1x}+L_{4x})}{L_{3x}+L_{4x}} & \frac{L_{3x}(-L_{2x}+L_{4x})}{L_{3x}+L_{4x}} & 0 & 0 \\ \frac{L_{4x}}{L_{3x}+L_{4x}} & 0 & \frac{L_{4x}(-L_{1x}+L_{3x})}{L_{3x}+L_{4x}} & \frac{-L_{4x}(L_{2x}+L_{3x})}{L_{3x}+L_{4x}} & 0 & 0 \\ 0 & 0 & 0 & 0 & L_{1y} & 0 \\ 0 & 0 & 0 & 0 & 0 & L_{2y} \\ 0 & \frac{L_{3y}}{L_{3y}+L_{4y}} & 0 & 0 & \frac{-L_{3y}(L_{1y}+L_{4y})}{L_{3y}+L_{4y}} & \frac{L_{3y}(-L_{2y}+L_{4y})}{L_{3y}+L_{4y}} \\ 0 & \frac{L_{4y}}{L_{3y}+L_{4y}} & 0 & 0 & \frac{L_{4y}(-L_{1y}+L_{3y})}{L_{3y}+L_{4y}} & \frac{-L_{4y}(L_{2y}+L_{3y})}{L_{3y}+L_{4y}} \end{bmatrix} \tag{4.5}$$

The local stiffness matrix at any point in time is found as the summation of a local hysteretic stiffness matrix, $\mathbf{k_s}$, a local geometric stiffness matrix, $\mathbf{k_g}$, and a contact stiffness matric, $\mathbf{k_c}$. Each matrix is 8×8 representing the assemblage of indivdual 2×2 local displacements from each of the four sliding surfaces.

Typical hysteretic behavior of a single sliding surface on a TFP bearing is shown in Figure 4.2 and accounted for in the local hysteretic matrix, $\mathbf{k_s}$. The response is bilinear with the elastic portion resulting from the friction yield force, $q_{n,yield} = P\mu_n$, being exceeded over an idealized yield displacement, u_{yield}, taken as 0.0254 cm in this study. Thus, the resulting elastic stiffness, k_{no}, is found using Equation 4.6.

$$k_{no} = \frac{q_{n,yield}}{u_{yield}} = \frac{P\mu_n}{u_{yield}} \tag{4.6}$$

At any point in time, the directional total slider displacements, u_n, intial offsets, u_{ns}, and plastic displacments, u_{np} are used to calculate the trial force, $q_{n,trial}$, as shown in Equations 4.7 and 4.8. Comparison of $q_{n,trial}$ with the yield force, $q_{n,yield}$, produces the yield condition, Y_n, in Equation 4.9.

$$\begin{aligned} q_{n,trial,x} &= k_{no}(u_{nx} - u_{nsx} - u_{npx}) \\ q_{n,trial,y} &= k_{no}(u_{ny} - u_{nsy} - u_{npy}) \end{aligned} \tag{4.7}$$

$$q_{n,trial} = \sqrt{q_{n,trial,x}^2 + q_{n,trial,y}^2} \tag{4.8}$$

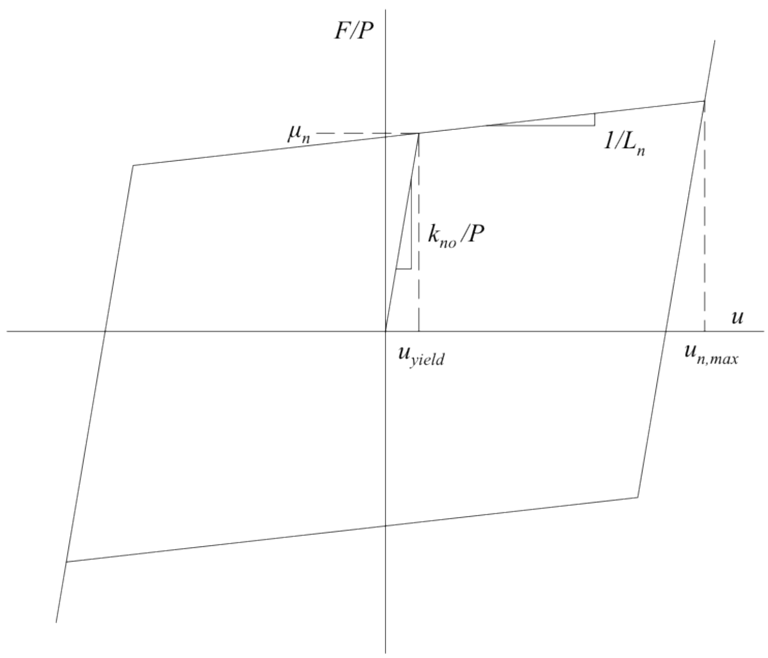

Figure 4.2: Normalized uni-directional hysteresis for an individual slider

$$Y_n = q_{n,trial} - q_{n,yield} \tag{4.9}$$

When $Y_n \leq 0$, the surface behaves elastically, and the slider hysteretic matrix, $\mathbf{k_{ns}}$, is written as shown in Equation 4.10.

$$\mathbf{k_{ns}} = \begin{bmatrix} k_{no} + \frac{P}{L_{nx}} & 0 \\ 0 & k_{no} + \frac{P}{L_{ny}} \end{bmatrix} \tag{4.10}$$

When $Y_n > 0$, yield occurs and plastic flow is induced. The slip rate of the plastic flow, γ_n, calculated in Equation 4.11, is used to find the change in plastic displacements, Δu_{npx} and Δu_{npy}, which are subsequently calculated in Equation 4.12. Equation 4.13 represents the softening of the hysteretic stiffness matrix, $\mathbf{k_{ns}}$.

$$\gamma_n = \frac{Y_n}{k_{no}} \tag{4.11}$$

$$\begin{aligned} \Delta u_{npx} &= \tfrac{q_{n,trial,x}}{q_{n,trial}} \gamma_n \\ \Delta u_{npy} &= \tfrac{q_{n,trial,y}}{q_{n,trial}} \gamma_n \end{aligned} \tag{4.12}$$

$$\mathbf{k_{ns}} = \begin{bmatrix} \frac{q_{n,yield} q^2_{n,trial,y}}{q^3_{n,trial}} k_{no} + \frac{P}{L_{nx}} & -\frac{q_{n,yield} q_{n,trial,x} q_{n,trial,y}}{q^3_{n,trial}} k_{no} \\ -\frac{q_{n,yield} q_{n,trial,x} q_{n,trial,y}}{q^3_{n,trial}} k_{no} & \frac{q_{n,yield} q^2_{n,trial,x}}{q^3_{n,trial}} k_{no} + \frac{P}{L_{ny}} \end{bmatrix} \tag{4.13}$$

The model assumes the outer sliding concaves remain horizontal and do not rotate, however as the inner sliders move along the outer sliding surfaces, they rotate relative to the outer concaves, inducing force changes on the inner sliding surfaces (Becker, 2011). The force changes are accounted for in the local geometric stiffness matrix, $\mathbf{k_g}$, shown in Equation 4.14.

$$\mathbf{k_g} = \begin{bmatrix} 0 & 0 & \frac{P}{L_{3x}} & 0 & 0 & 0 & 0 & 0 \\ 0 & 0 & 0 & \frac{P}{L_{4x}} & 0 & 0 & 0 & 0 \\ 0 & 0 & 0 & 0 & 0 & 0 & 0 & 0 \\ 0 & 0 & 0 & 0 & 0 & 0 & 0 & 0 \\ 0 & 0 & 0 & 0 & 0 & 0 & \frac{P}{L_{3y}} & 0 \\ 0 & 0 & 0 & 0 & 0 & 0 & 0 & \frac{P}{L_{4y}} \\ 0 & 0 & 0 & 0 & 0 & 0 & 0 & 0 \\ 0 & 0 & 0 & 0 & 0 & 0 & 0 & 0 \end{bmatrix} \tag{4.14}$$

The bilinear hysteretic response continues on each sliding surface until contact with the restraining surface occurs. The displacement capacity of the sliding surface is $(d_{on} - d_{in})/2$, however the model displacements are measured at the bearing center. Thus, the maximum displacement prior to contact, $u_{n,\max}$, or stroke for a particular slider, is found using Equation 4.15.

$$u_{n,\max} = \frac{(d_{on} - d_{in})}{2} \frac{L_n}{R_n} \tag{4.15}$$

Once contact occurs, the contact force, $\mathbf{F_{nc}}$, is perpendicular to the contact plane, and therefore parallel to the displcement direction. Numerically, this is demonstrated in Equation 4.16. The complete contact stiffness matrix is shown in Equation 4.17, where the rotation stiffness matrix, $\mathbf{k_{nr}}$, is found by finite difference on Equation 4.16. Clearly, if contact on a surface has not occurred, then $\mathbf{F_{nc}}$, $\mathbf{k_{nc}}$, and $\mathbf{k_{nr}}$ are all $\mathbf{0}$.

$$\mathbf{F_{nc}} = \begin{bmatrix} F_{ncx} \\ F_{ncy} \end{bmatrix} = \begin{bmatrix} \frac{u_{nx}}{\sqrt{u_{nx}^2 + u_{ny}^2}} \\ \frac{u_{ny}}{\sqrt{u_{nx}^2 + u_{ny}^2}} \end{bmatrix} \|\mathbf{F_{nc}}\| \tag{4.16}$$

$$\mathbf{k_{nc}} = k_{no} \begin{bmatrix} \frac{u_{nx}^2}{\sqrt{u_{nx}^2 + u_{ny}^2}} & \frac{u_{nx} u_{ny}}{\sqrt{u_{nx}^2 + u_{ny}^2}} \\ \frac{u_{nx} u_{ny}}{\sqrt{u_{nx}^2 + u_{ny}^2}} & \frac{u_{ny}^2}{\sqrt{u_{nx}^2 + u_{ny}^2}} \end{bmatrix} + \mathbf{k_{nr}} \tag{4.17}$$

Following the assemblage of local stiffness matrices from the individual slider stiffness components, the 6×6 global stiffness matrix for the isolator, $\mathbf{k_t}$, is calculated using Equation 4.18. Because the internal rotations are not specifically needed, the resulting global stiffness matrix in Equation 4.19 is statically condensed as shown in Equation 4.20, forming the global isolator stiffness matrix, $\mathbf{K}$.

$$\mathbf{k_t} = \mathbf{T}^T (\mathbf{k_s} + \mathbf{k_g} + \mathbf{k_c}) \mathbf{T} \tag{4.18}$$

$$\mathbf{k_t} = \begin{bmatrix} \mathbf{k_{tt}} & \mathbf{k_{to}} \\ \mathbf{k_{ot}} & \mathbf{k_{oo}} \end{bmatrix} \tag{4.19}$$

$$\mathbf{K} = \mathbf{k_{tt}} - \mathbf{k_{to}}\mathbf{k_{oo}^{-1}}\mathbf{k_{ot}} \tag{4.20}$$

Once the global stiffness matrix has been found, the change in local and global displacements from time t_{i-1} to time t_i can be found using Equations 4.21 through 4.23. From these, the contact force increment, $\mathbf{\Delta F_c}$, and global force increment, $\mathbf{\Delta F}$, can be found using Equations 4.24 and 4.25, respectively.

$$\mathbf{\Delta U_{ex}} = \begin{bmatrix} \Delta u_x \\ \Delta u_y \end{bmatrix} = \begin{bmatrix} u_x(t_i) - u_x(t_{i-1}) \\ u_y(t_i) - u_y(t_{i-1}) \end{bmatrix} \tag{4.21}$$

$$\mathbf{\Delta U} = \begin{bmatrix} \mathbf{\Delta U_{ex}} \\ -\mathbf{k_{oo}}^{-1}\mathbf{k_{ot}}\mathbf{\Delta U_{ex}} \end{bmatrix} \tag{4.22}$$

$$\mathbf{\Delta u} = \mathbf{T}\mathbf{\Delta U} \tag{4.23}$$

$$\mathbf{\Delta F_c} = \mathbf{k_c}\mathbf{\Delta u} \tag{4.24}$$

$$\mathbf{\Delta F} = \begin{bmatrix} \Delta f_x \\ \Delta f_y \end{bmatrix} = \mathbf{K}\mathbf{\Delta U_{ex}} \tag{4.25}$$

The local displacements and global forces are then incremented, as shown in Equations 4.26 and 4.27.

$$\mathbf{u}(t_i) = \mathbf{u}(t_{i-1}) + \mathbf{\Delta u} \tag{4.26}$$

$$\begin{aligned} f_x(t_i) &= f_x(t_{i-1}) + \Delta f_x \\ f_y(t_i) &= f_y(t_{i-1}) + \Delta f_y \end{aligned} \tag{4.27}$$

Figure 4.3 depicts a displaced TFP bearing, demonstrating the dependence of the vertical displacement on the lateral displacement. Once the local slider displacements have been determined, the theoretical vertical location is calculated by imposing a geometric constraint that forces movement of each slider along a spherical surface. First, the slider displacements, which are measured at the bearing mid-height, must be scaled as in Equation 4.28 to determine the the true lateral displacements at the slider surface, u'_n. Based on the the geometry of the indivdual displaced slider, the compatible vertical displacement, u_{vn}, is calculated using Equation 4.29.

$$u'_n = \sqrt{u_{nx}^2 + u_{ny}^2}\frac{R_n}{L_n} \tag{4.28}$$

$$u_{vn} = R_n\left(1 - \cos(\theta_n)\right) = R_n - \sqrt{R_n^2 - u_n'^2} \tag{4.29}$$

The ideal total verticle displacement, u_v is the sum of five terms shown in Equations 4.30 through 4.34, representiing the five separate components of the FTP bearing. Each term shows the change in bearing height due to horizontal motion, as well as component rotation.

$$u_{v1} = R_3 - \sqrt{R_3^2 - (u'_3 + u'_1\tan\theta_3)^2} \tag{4.30}$$

$$u_{v2} = \left(h_3 - h_1 + R_1 - \sqrt{R_1^2 - u_1'^2} - R_3 + \sqrt{R_3^2 - u_1'^2}\right)\cos\theta_3 - h_3 + h_1 \tag{4.31}$$

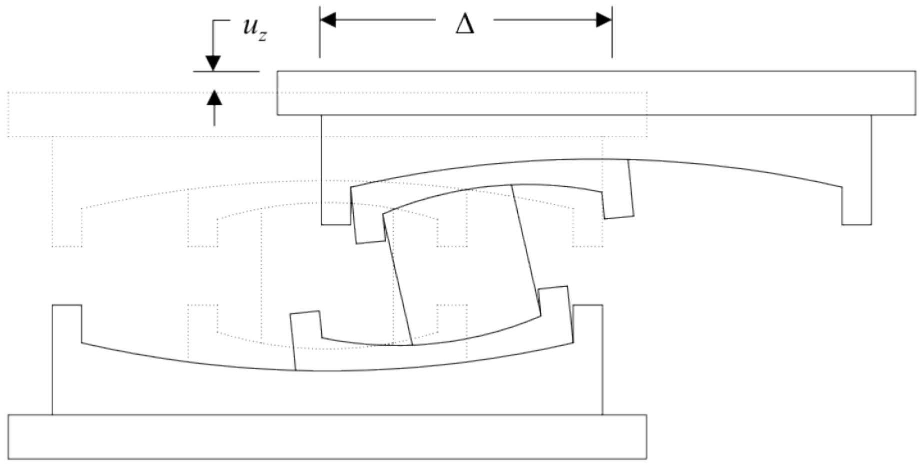

Figure 4.3: Schematic of a displaced TFP bearing showing the connection between lateral and vertical displacements

$$u_{v3} = (h_1 + h_2)\left(\cos(\theta_1 + \theta_2) - 1\right) \tag{4.32}$$

$$u_{v4} = \left(h_4 - h_2 + R_2 - \sqrt{R_2^2 - u_2'^2} - R_4 + \sqrt{R_4^2 - u_2'^2}\right)\cos\theta_4 - h_4 + h_2 \tag{4.33}$$

$$u_{v5} = R_4 - \sqrt{R_4^2 - (u_4' + u_2' \tan\theta_4)^2} \tag{4.34}$$

$$u_v = \sum_{i=1}^{5} u_{vi} \tag{4.35}$$

The overbearing force, P, which scales all lateral forces, will generally be different from the vertical isolator force, f_z, which also includes a component to induce the desired vertical displacement, u_v. The axial stiffness of the bearing, k_z, is idealized as that of a round steel column with diameter, d_{i1}, and height, $h_3 + h_4$ (i.e. the overal height of the moving components of a TFP bearing), as demonstrated in Equation 4.36. The elastic modulus of steel, E_s, used for this calculation is 200 GPa. The overbearing force, calculated in Equation 4.37, is a function of the difference between the actual vertical displacement, u_z, and the idealized vertical displacement, u_v, as calculated with Equations 4.30 through 4.35. It should be noted that the bearing has no tension capacity as reflected in Equation 4.37.

$$k_z = \frac{E_s A_s}{L_s} = \frac{E_s \pi d_{i1}^2}{4(h_3 + h_4)} \tag{4.36}$$

$$P = \begin{cases} -k_z(u_z(t_i) - u_v(t_{i-1})) & \text{if} \quad u_z(t_i) - u_v(t_{i-1}) < 0 \\ 0 & \text{if} \quad u_z(t_i) - u_v(t_{i-1}) \geq 0 \end{cases} \tag{4.37}$$

Ideally, P stays constant in the absence of vertical excitation, even though the isolator displaces vetically in response to horizontal excitation. The total vertical force output by the isolator, f_z, is the force required to move the top surface to the ideal vertical position, u_v, and is calculated in Equation 4.38. Because the horizontal location of each slider must be determined prior to imposing the vertical constraint, the vertical position lags by one time step.

$$f_z(t_i) = -\frac{m}{\Delta t_i}\left[\frac{1}{\Delta t_i}\left(u_v(t_i) - u_v(t_{i-1})\right) - \frac{1}{\Delta t_{i-1}}\left(u_v(t_{i-1}) - u_v(t_{i-2})\right)\right] - P \tag{4.38}$$

Where m in Equation 4.38 is the mass of the connected node, and the second term in the brackets represents the vertical velocity of the slider at the beginning of the current time step.

4.1.2 Validation

Validation of the ALE3D implementation of the Becker and Mahin model was achieved using some of the test cases presented in Becker and Mahin (2011) and Becker (2011). These include four displacement-controlled tests and two unrestrained earthquake-response tests. The models used in the analyses utilize a single bearing element connecting two lumped-mass nodes. When subjected to the displacement-controlled motions, the bottom node is fixed at a single location, and the top node is given the predetermined lateral motion. Gravity is introduced, and the top node is able to move freely in the vertical direction in response to the motion. When subjected to earthquake motions, the bottom node is given a two or three-dimensional ground motion input record. The top node is free to respond to the excitation, and includes the effect of gravity.

The displacement-controlled motions have oscillatory paths which increase in magnitude over the duration of the record. The various path shapes include 1D sine waves (imposed in the y-direction), 2D concentric circles, 2D concentric squares, and 2D concentric figure-eights. The input orbits and displacement time histories are depicted in Figures 4.4 and 4.5, respectively. The earthquake records used for unrestrained response validation are the Newhall record from the 1994 Northridge earthquake and the 1978 Tabas earthquake record. The acceleration time histories for these two records are plotted in Figures 4.6 and 4.7.

The TFP bearing parameters used in the validation analyses for each sliding surface are listed in Table 4.1, and match the test bearings in Becker and Mahin (2011). The value of the mass concentrated at each node is 7708 kg, corresponding to an average overbearing weight of 75.6 kN, which was measured during the physical experiments.

The results of the displacement-controlled validation and urestrained earthquake tests are shown in Figures 4.8 through 4.14, along with the data from both the physical experiments and the original Becker (2011) analyses for comparative purposes. From these cases it is evident that the ALE3D model very accurately replicates the Becker results for both the displacement-controlled and unrestrained earthquake-response tests, and is a good approximation of the experimental data for the same cases.

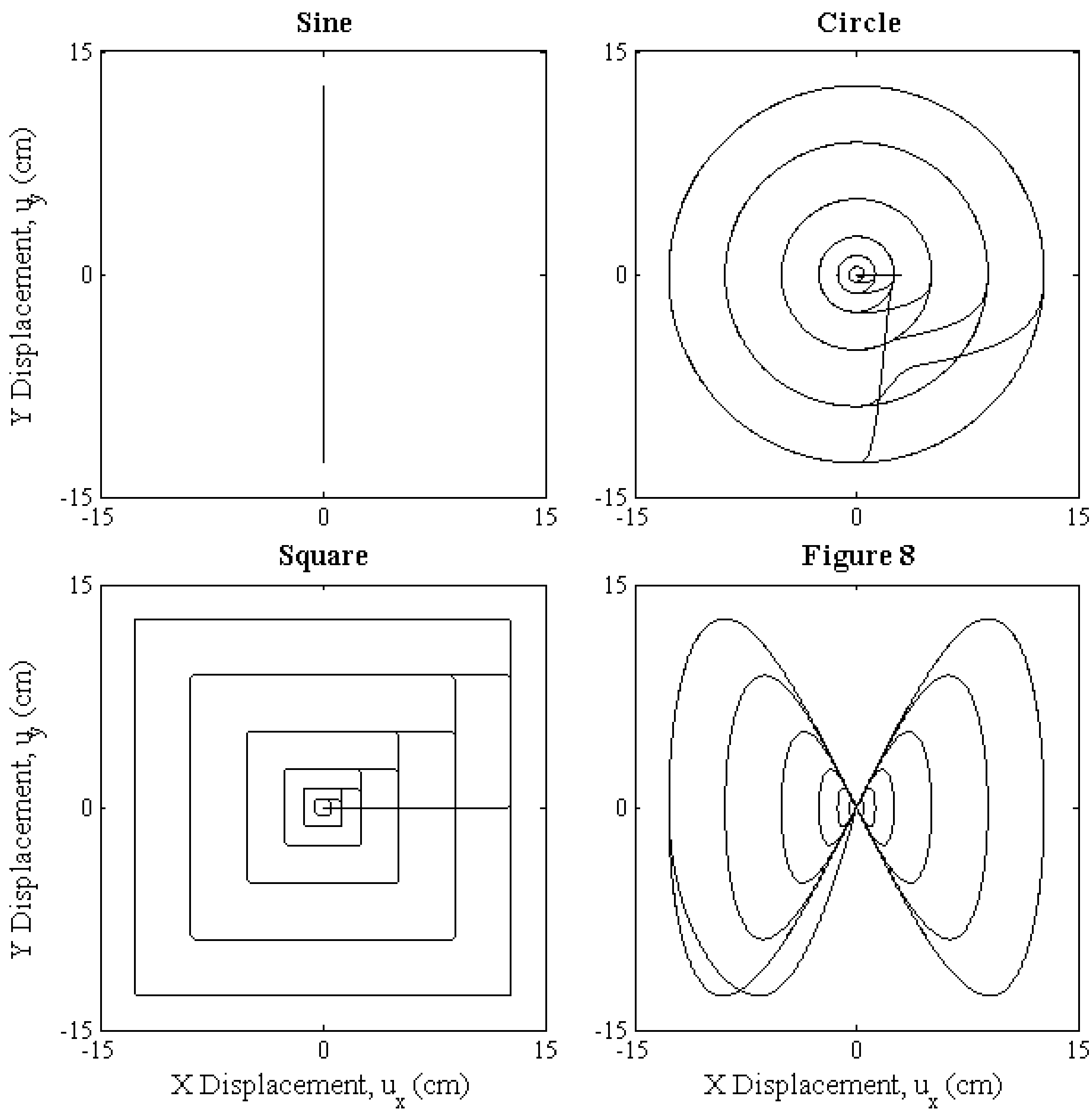

Figure 4.4: Displacement paths for the dispalcement-controlled test cases

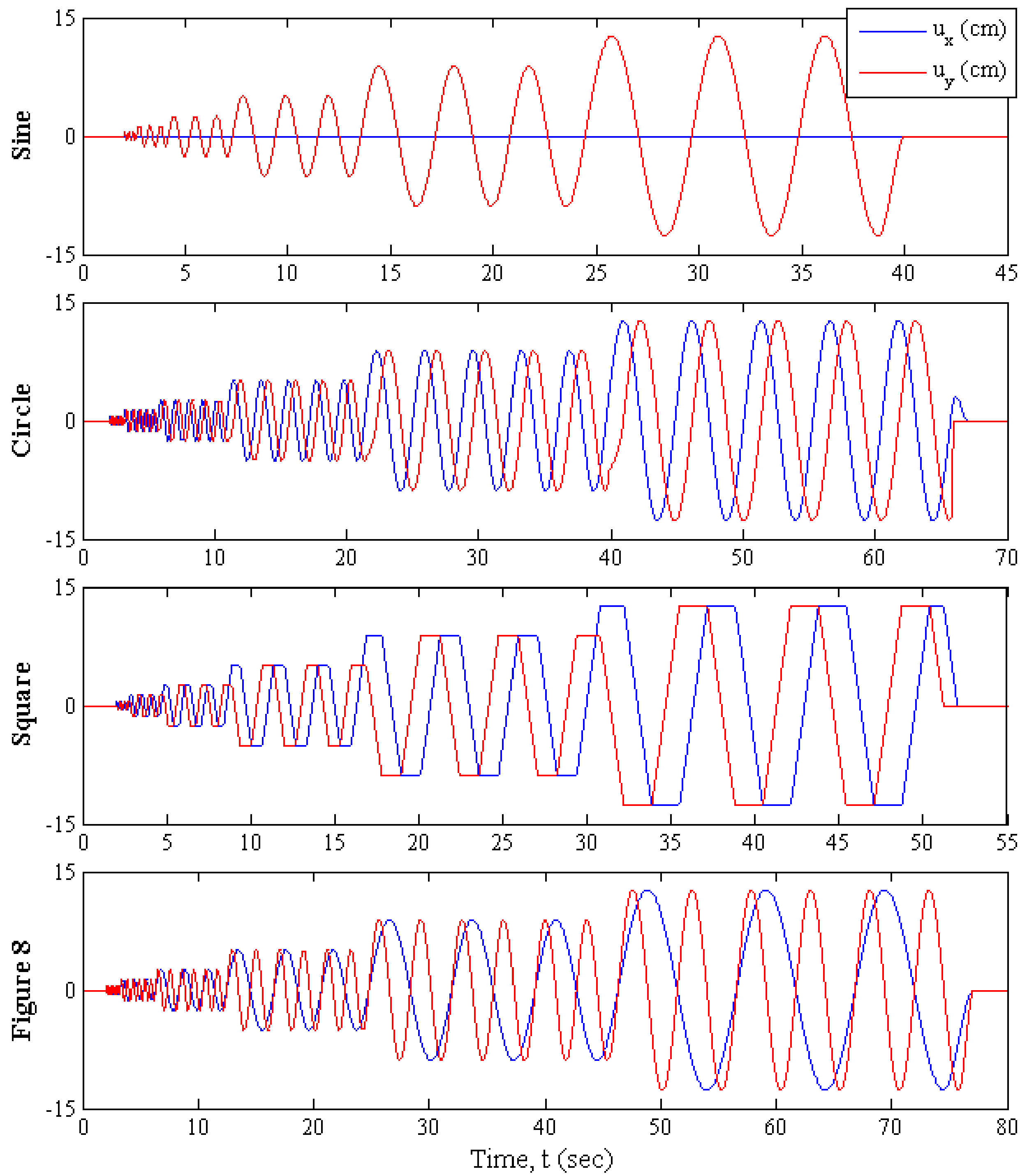

Figure 4.5: Directional displacement time histories for the displacement-controlled test cases

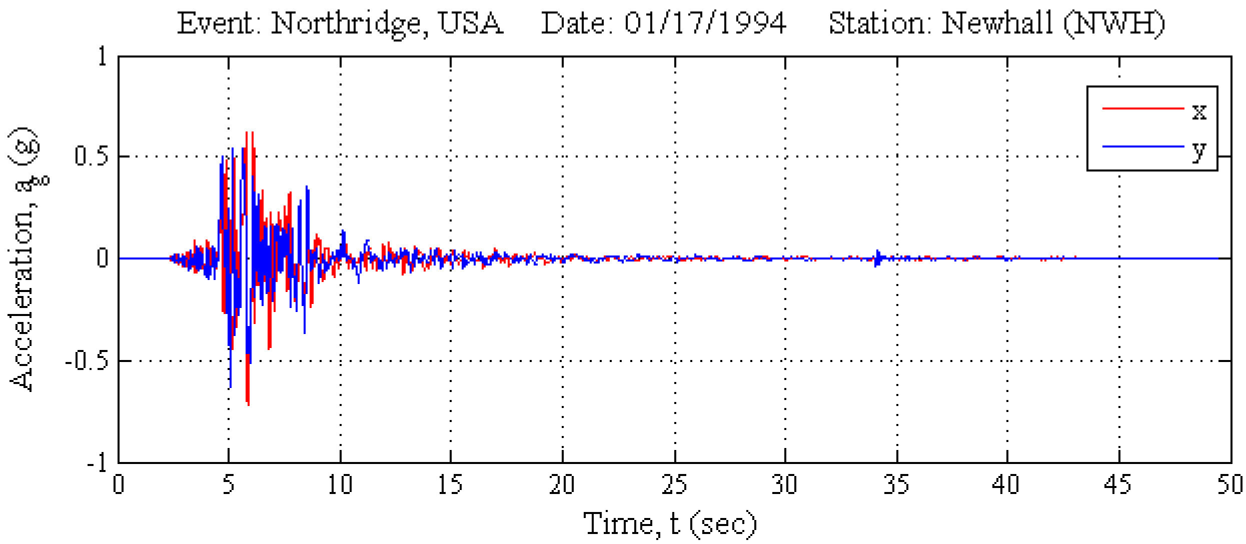

Figure 4.6: 2-dimensional input acceleration time histories (100% scale) for the Newhall record of the 1994 Northridge earthquake with a length scale of 2

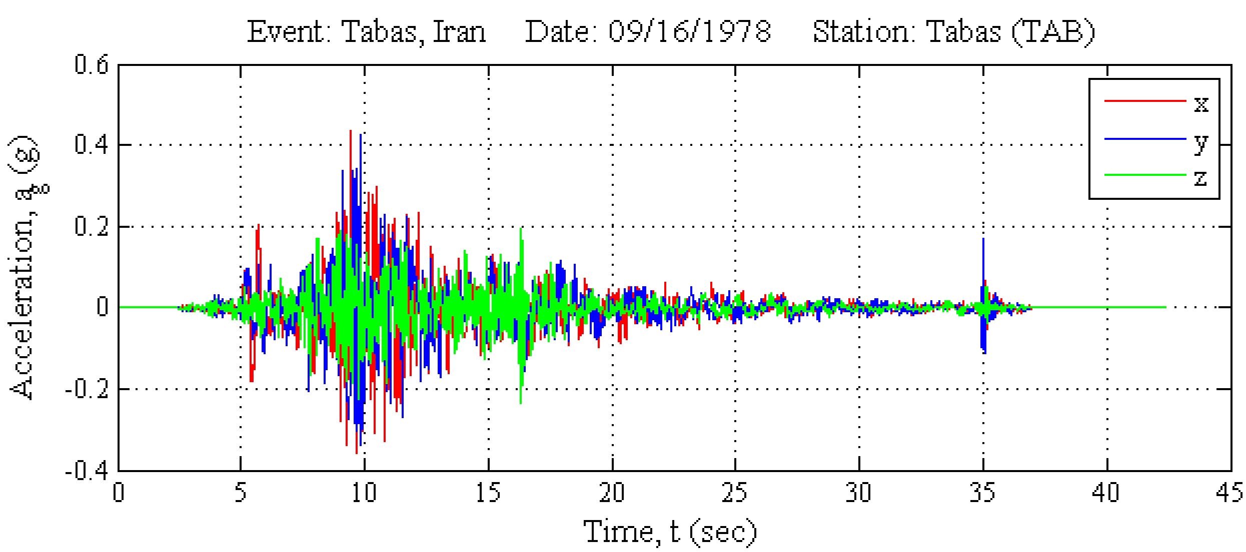

Figure 4.7: 3-dimensional input acceleration time histories (50% scale) for the 1978 Tabas earthquake record with a length scale of 2

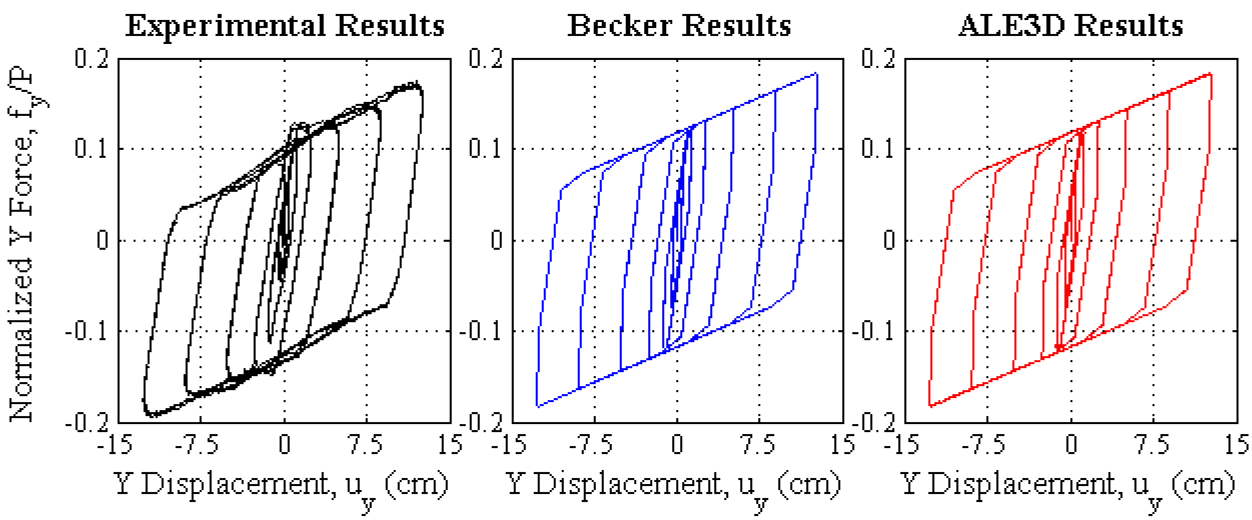

Figure 4.8: Comparative directional hystereses of the TFP experiments and models for the uni-directional sine wave displacement orbit

Parameter	Surfaces 1 and 2	Surface 3	Surface 4
Radius, R_n	7.62 cm	99.06 cm	99.06 cm
Outer Diameter, d_{on}	6.35 cm	25.90 cm	25.90 cm
Inner Diameter, d_{in}	3.81 cm	7.62 cm	7.62 cm
Surface-to-Mid-Height Distance, h_n	1.27 cm	2.54 cm	2.54 cm
Friction Coefficient, μ_n	0.036	0.118	0.128

Table 4.1: Input parameters of TFP bearings used in validation tests

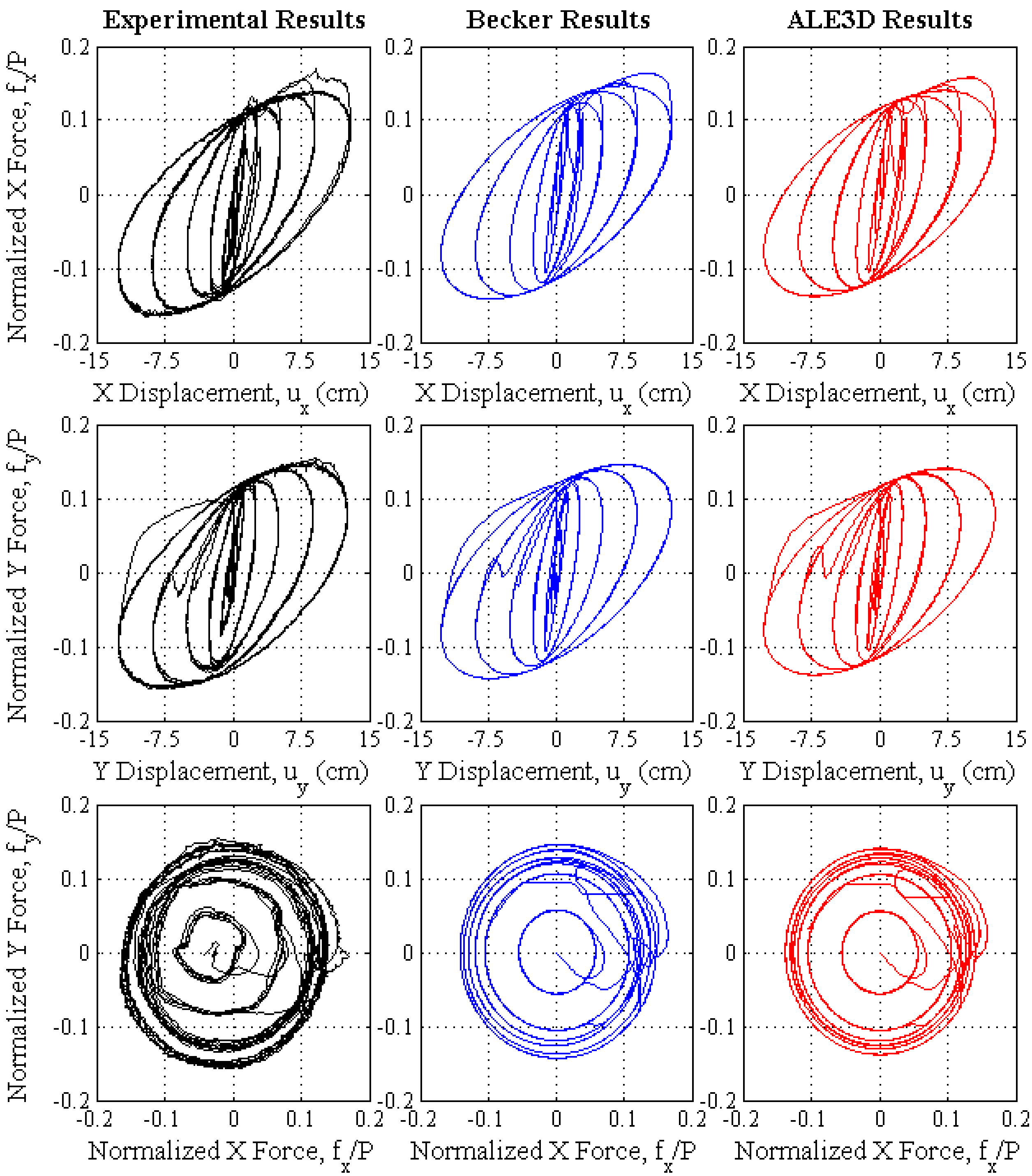

Figure 4.9: Comparative directional hystereses and force path of the TFP experiments and models for the circular displacement orbit

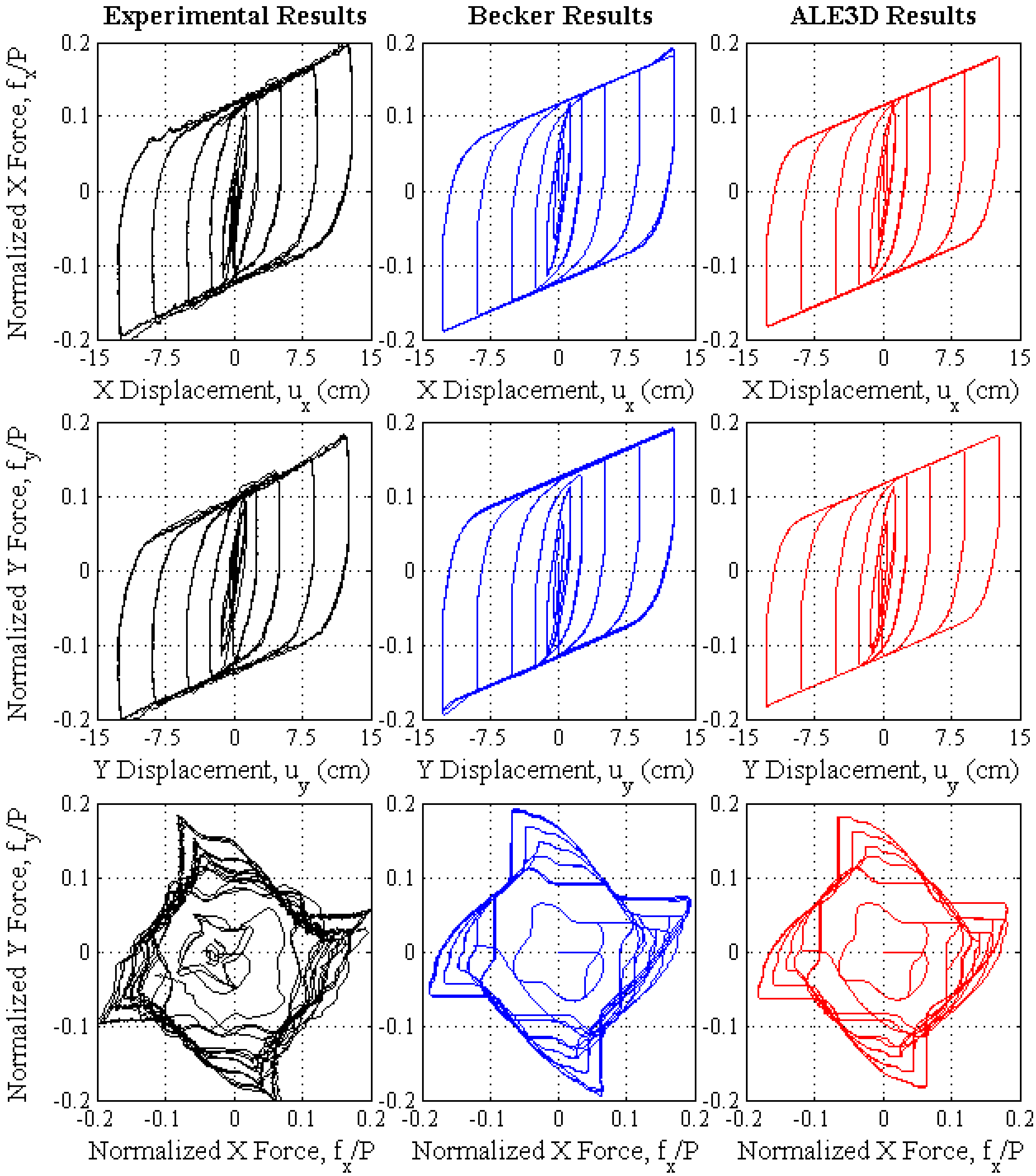

Figure 4.10: Comparative directional hystereses and force path of the TFP experiments and models for the square displacement orbit

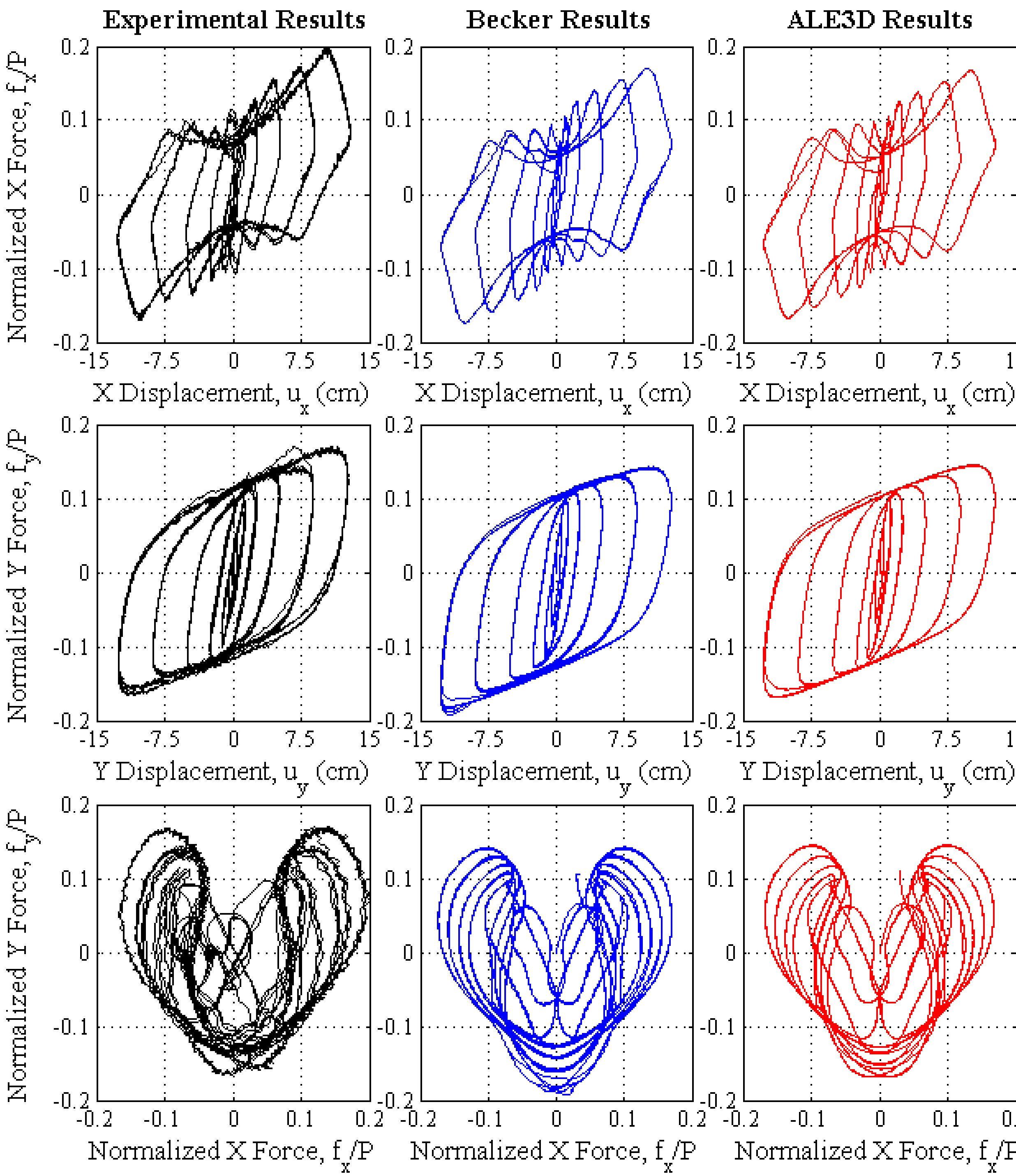

Figure 4.11: Comparative directional hystereses and force path of the TFP experiments and models for the figure-eight displacement orbit

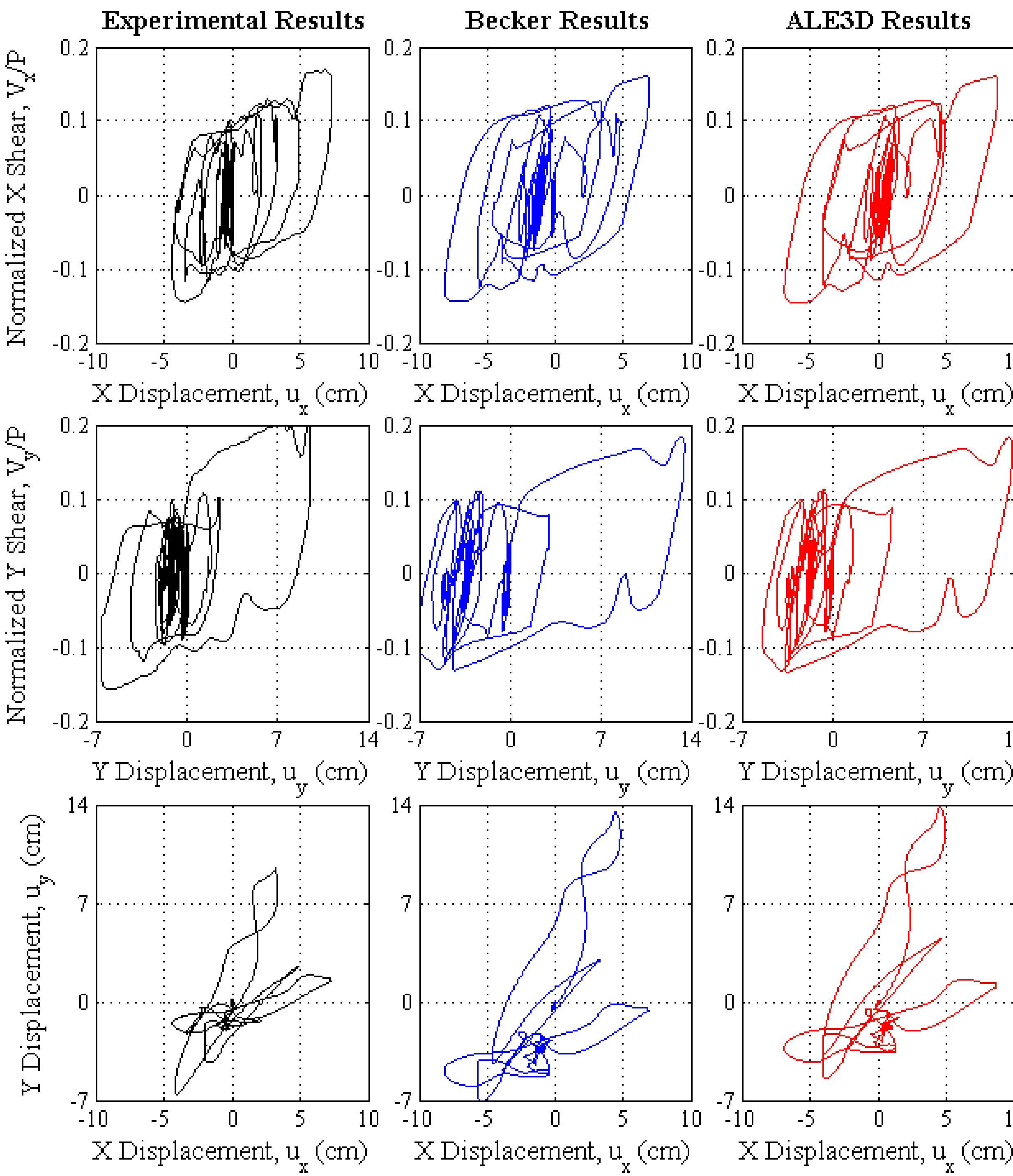

Figure 4.12: Comparative directional hystereses and displacement path of the TFP experiments and models for the unrestrained response to the 1994 Northridge earthquake Newhall record

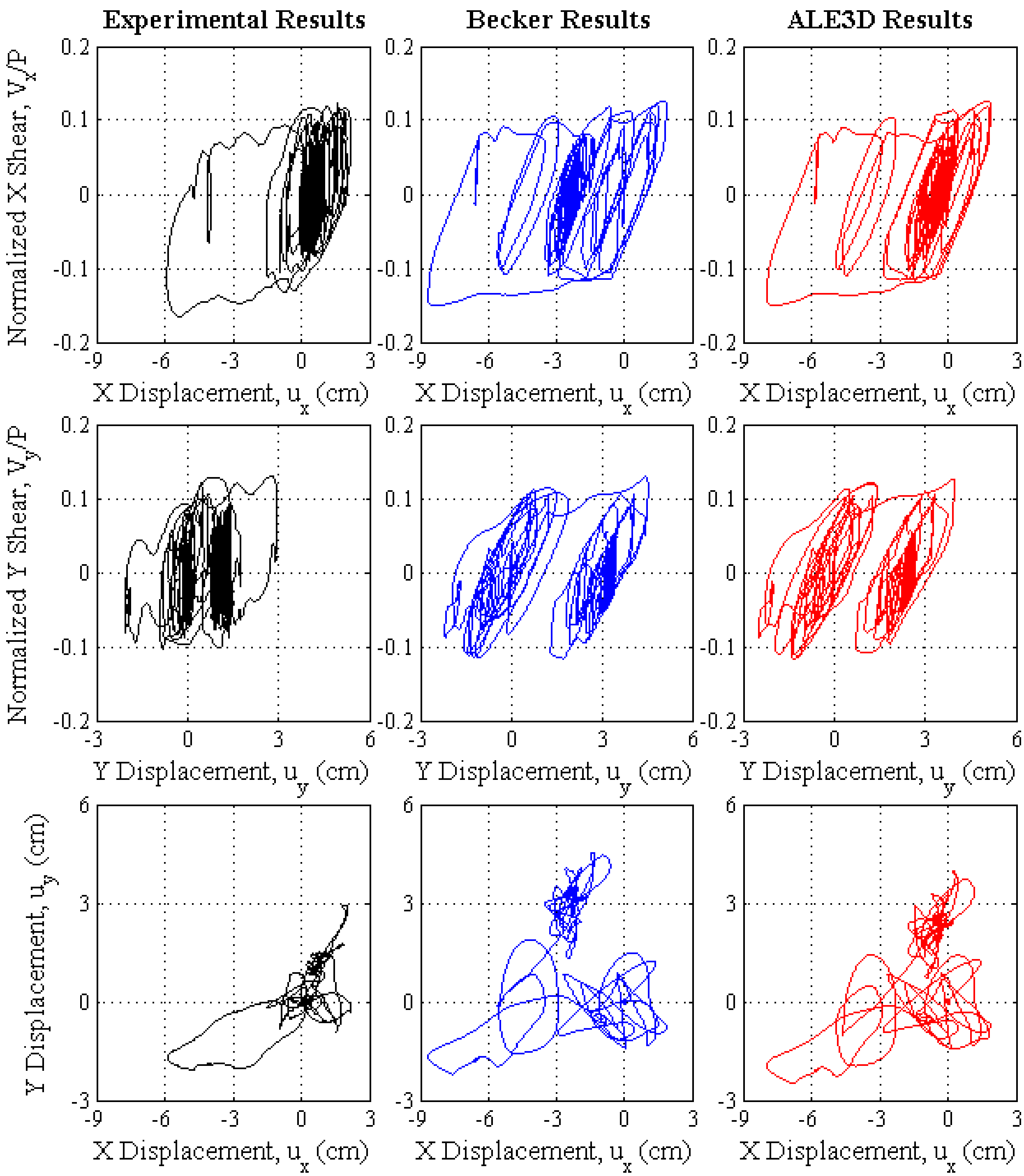

Figure 4.13: Comparative directional hystereses and displacement path of the TFP experiments and models for the unrestrained response to the 1978 Tabas record

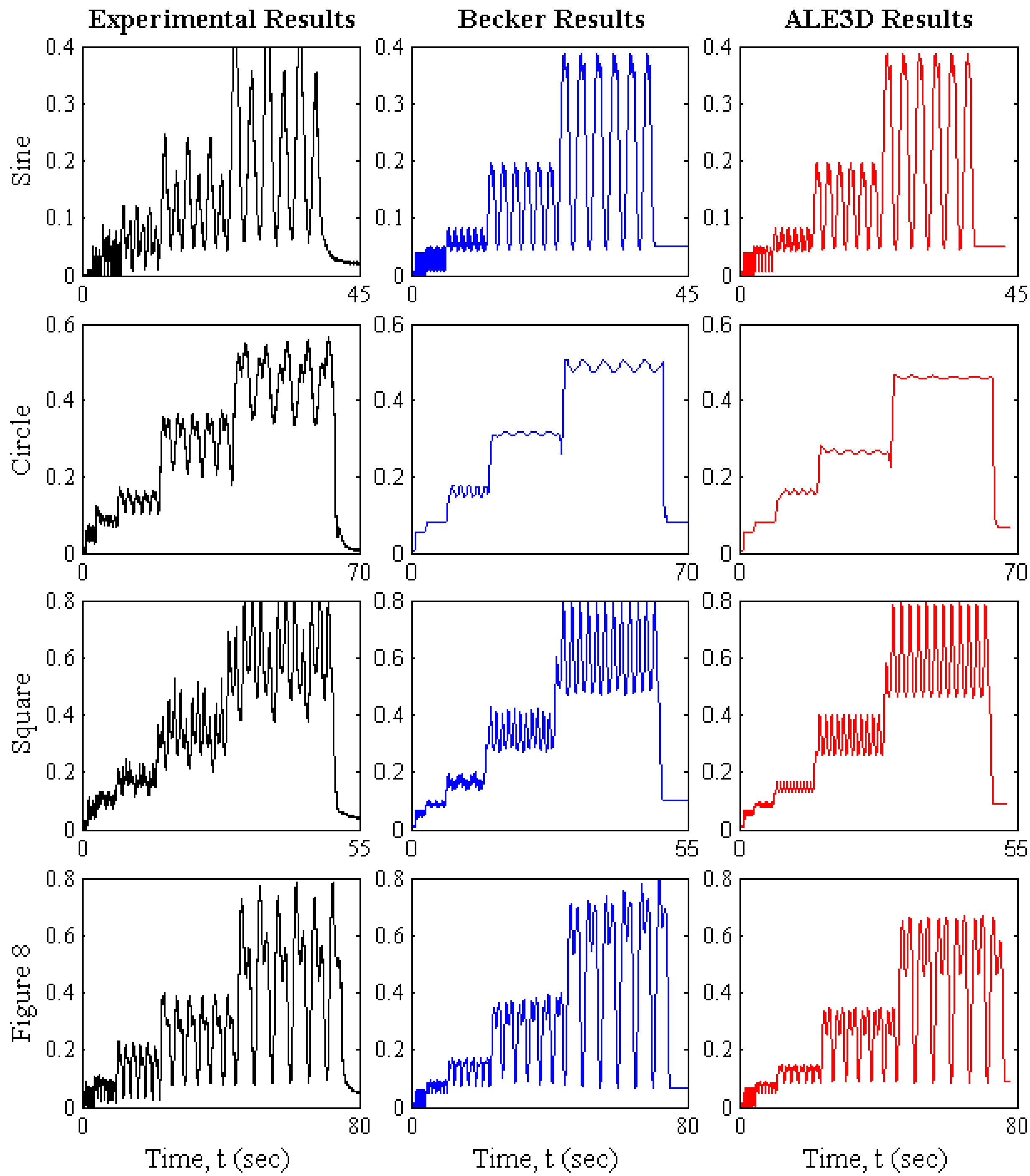

Figure 4.14: Comparative vertical displacements of the TFP experiments and models for the displacement-controlled test cases

4.2 Simplified Friction Pendulum Bearing Model

The Nagarajaiah et al. (1991) model serves as the numerical basis for sliding friction bearings in various commercial structural engineering software, including SAP2000, ETABS, and 3D-BASIS (Reinhorn et al., 1994). It utilizes a hysteretic model component proposed by Wen (1976) and Park et al. (1986), and is used in conjunction with a pendulum component recommended in Zayas et al. (1990) for frictional sliding on spherical surfaces, as with single FP bearings. This model is used for the simplified analysis of friction pendulum bearings in ALE3D, where it is referred to as “spring2”.

4.2.1 Model Response

The vertical component of the model response force, f_z, is non-linear under compressive loading with no tension capacity, as is indicative of most FP bearings. The compressive response, depicted in Equations 4.39 and 4.40, is a function of vertical stiffness, k_z, and damping, c_z, yet only the response from the stiffness term is used to calculate the overbearing load, P, which scales all lateral response terms. Equation 4.41 shows the relationship between k_z and c_z for a given mass, m, and desired damping ratio, ζ_z.

$$f_z = P + \begin{cases} c_z \dot{u}_z & \text{if} \quad u_z < 0 \\ 0 & \text{if} \quad u_z \geq 0 \end{cases} \tag{4.39}$$

$$P = \begin{cases} k_z u_z & \text{if} \quad u_z < 0 \\ 0 & \text{if} \quad u_z \geq 0 \end{cases} \tag{4.40}$$

$$\zeta_z = \frac{c_z}{2\sqrt{k_z m}} \tag{4.41}$$

It is important to note that unlike the TFP model in Section 4.1.1, the vertical response of the FP model does not include the effect of the curved sliding surface which constrains vertical motion depending on the lateral displacement. The vertical component in this model is decoupled from the lateral response, except for the aforementioned scaling by the overbearing load. Thus, this model is inherently limited in the accuracy of its vertical displacements.

The lateral responses, f_x and f_y, from Equation 4.42 are the summation of a pendulum term representing elastic deformation and a friction term acting as the hysteretic component. The elastic terms, f_{xe} and f_{ye}, are proportional to the overbearing load, P, and the sine of the directional angles of the displaced slider from the undeformed state, θ_x and θ_y, which are equivalent to the ratio of the lateral displacements, u_x and u_y, to the dish radii, R_x and R_y, in each direction as presented in Equation 4.43. The hysteretic friction forces, f_{xh} and f_{yh}, shown in Equation 4.44, are the product of the overbearing load, P, hysteretic variables, z_x and z_y, as well as the friction coefficients, μ_x and μ_y, which are usually considered equal in analyses. The friction coefficients are velocity-dependent terms which evolve from the minimum or slow-velocity friction coefficients, $\mu_{x\,\mathrm{min}}$ and $\mu_{y\,\mathrm{min}}$, to the maximum

Software	A	B	γ
CSI	1.0	0.5	0.5
3D-BASIS	1.0	0.1	0.9

Table 4.2: Values of evolution constants in existing base isolation software

or fast-velocity friction coefficient, $\mu_{x\max}$ and $\mu_{y\max}$, with Equation 4.45 (Constantinou et al., 1990)(Nagarajaiah et al., 1991). During multi-directional loading cycles, the friction coefficient may change from maximum to minimum and back many times, with the transitions being predicated by the velocity, $\dot{u}$, and the effective inverse velocity, r, which is a function of rate parameters, α_x and α_y, as shown in Equation 4.46. In 3D-BASIS, these rate parameters are set to 0.9, whereas they are input variables in the other software programs mentioned.

$$\begin{aligned} f_x &= f_{xe} + f_{xh} \\ f_y &= f_{ye} + f_{yh} \end{aligned} \tag{4.42}$$

$$\begin{aligned} f_{xe} &= -P \sin\theta_x = -P\left(\frac{u_x}{R_x}\right) \\ f_{ye} &= -P \sin\theta_y = -P\left(\frac{u_y}{R_y}\right) \end{aligned} \tag{4.43}$$

$$\begin{aligned} f_{xh} &= -P\mu_x z_x \\ f_{yh} &= -P\mu_y z_y \end{aligned} \tag{4.44}$$

$$\begin{aligned} \mu_x &= \mu_{x\max} - (\mu_{x\max} - \mu_{x\min})e^{-r\dot{u}} \\ \mu_y &= \mu_{y\max} - (\mu_{y\max} - \mu_{y\min})e^{-r\dot{u}} \end{aligned} \tag{4.45}$$

$$r = \frac{\alpha_x \dot{u}_x^2 + \alpha_y \dot{u}_y^2}{\dot{u}^2} \tag{4.46}$$

$$\dot{u} = \sqrt{\dot{u}_x^2 + \dot{u}_y^2} \tag{4.47}$$

Initially, the dimensionless hysteretic variables, z_x and z_y, are both zero, and evolve based on Equation 4.48, initially proposed by Park et al. (1986). These variables are constrained to have a range $\sqrt{z_x^2 + z_y^2} \leq 1$, where $\sqrt{z_x^2 + z_y^2} = 1$ represents the yield surface of the bearing. The values of the evolution constants A, B, and γ control the shape of the hysteretic loop and vary between existing commercial codes. The values used herein are 1, 0.5, and 0.5, respectively, as adopted in SAP2000 and ETABS. Table 4.2 presents these values for Computers & Structures Inc. (CSI) codes (e.g. SAP2000 and ETABS) as well as 3D-BASIS. The differential equation is evolved using the forward Euler approach in Equation 4.49 for a given time step, Δt_i.

$$\begin{aligned} \dot{z}_x u_{yield} &= A\dot{u}_x - z_x^2\left(\gamma \text{sign}(\dot{u}_x z_x) + B\right)\dot{u}_x - z_x z_y\left(\gamma \text{sign}(\dot{u}_y z_y) + B\right)\dot{u}_y \\ \dot{z}_y u_{yield} &= A\dot{u}_y - z_x z_y\left(\gamma \text{sign}(\dot{u}_x z_x) + B\right)\dot{u}_x - z_y^2\left(\gamma \text{sign}(\dot{u}_y z_y) + B\right)\dot{u}_y \end{aligned} \tag{4.48}$$

$$\begin{aligned} z_{x,i+1} &= z_{x,i} + \dot{z}_{x,i}\Delta t_i \\ z_{y,i+1} &= z_{y,i} + \dot{z}_{y,i}\Delta t_i \end{aligned} \tag{4.49}$$

Parameter	Value
Mass, m	54.41 Mg
Vertical Stiffness, k_v	716000 kN/cm
Vertical Damping, c_v	62.4 kN-s/cm (5%)
Radius, R	111.2 cm
Maximum X Friction Coefficient, $\mu_{x\,\max}$	0.0465
Maximum Y Friction Coefficient, $\mu_{y\,\max}$	0.0465
Minimum X Friction Coefficient, $\mu_{x\,\min}$	0.0465
Minimum Y Friction Coefficient, $\mu_{y\,\min}$	0.0465
X Rate Parameter, α_x	0.55
Y Rate Parameter, α_y	0.55
Yield Displacement, u_{yield}	0.941 cm

Table 4.3: Input parameters of the FP bearings used in validation tests

4.2.2 Validation

The simplified FP bearing response model in AEL3D was verified using the displacement-controlled and unrestrained earthquake test cases presented in Section 4.1.2. Comparative analyses were run using SAP2000. Because force data was not able to be extracted from the FP model in SAP during validation tests, the results of the LR SAP analysis are used and an equivalent FP bearing was tested in ALE3D. The equivalent properties were obtained by equating u_{yield} in the two models, then solving for R and μ by equating Equation 4.43 with Equation 4.54 and Equation 4.44 with Equation 4.55. The resulting formulae are shown in Equations 4.50 and 4.51, leading to the input parameters shown in Table 4.3. It should be noted that by equating all the friction coefficients, this model does not include the effect of velocity on frictional sliding. However, this feature was not intended to be used for analysis, so its validation is not required. Additionally, the LR model results do not display vertical force-dependance, which should only have a small effect on the unrestrained response to the Tabas event.

$$R = \frac{u_{yield}}{\alpha}\left(\frac{P}{f_{yield}}\right) \tag{4.50}$$

$$\mu = (1-\alpha)\frac{f_{yield}}{P} \tag{4.51}$$

The results of the validation tests are shown in Figures 4.15 through 4.21. All tests show the AL3D model very accurately captures the SAP model response. Slight discrepancies in the Tabas results are attributed to the dependence of the lateral response on the normal force, which is not a factor in the LR model used for validation.

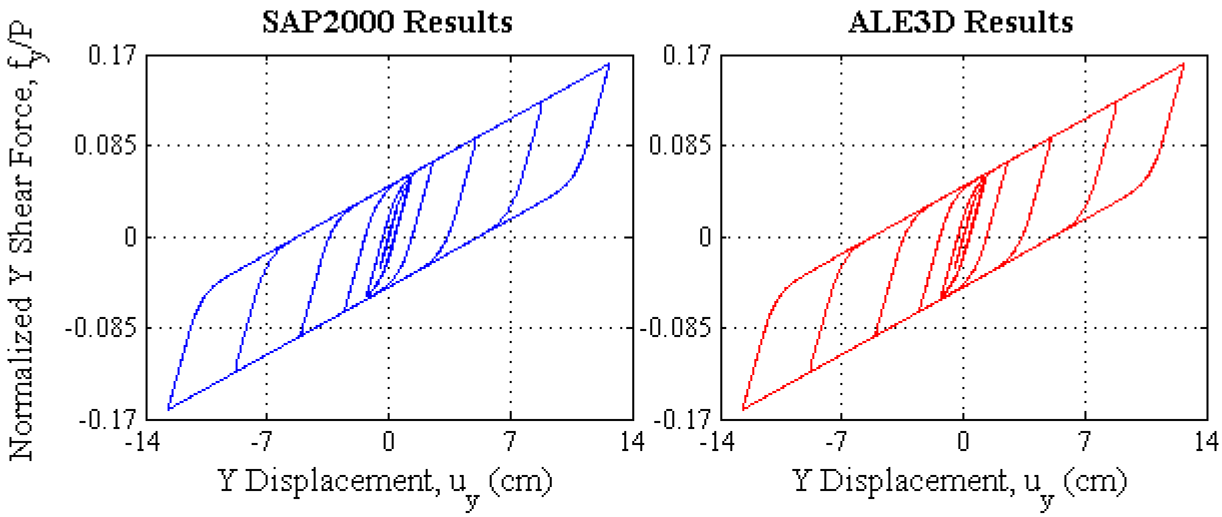

Figure 4.15: Comparative directional hystereses of the FP models for the uni-directional sine wave displacement orbit

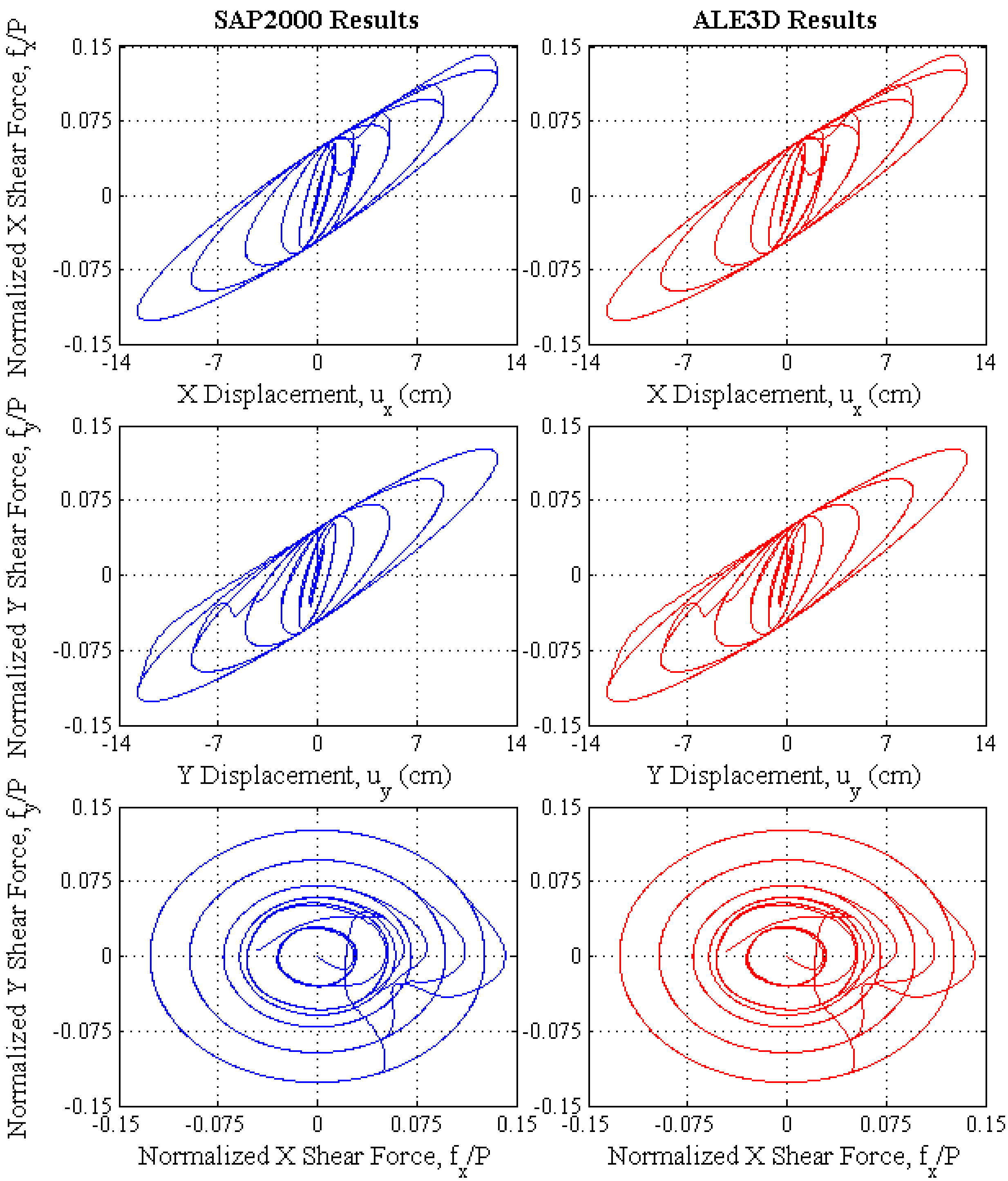

Figure 4.16: Comparative directional hystereses and force path of the FP models for the circular displacement orbit

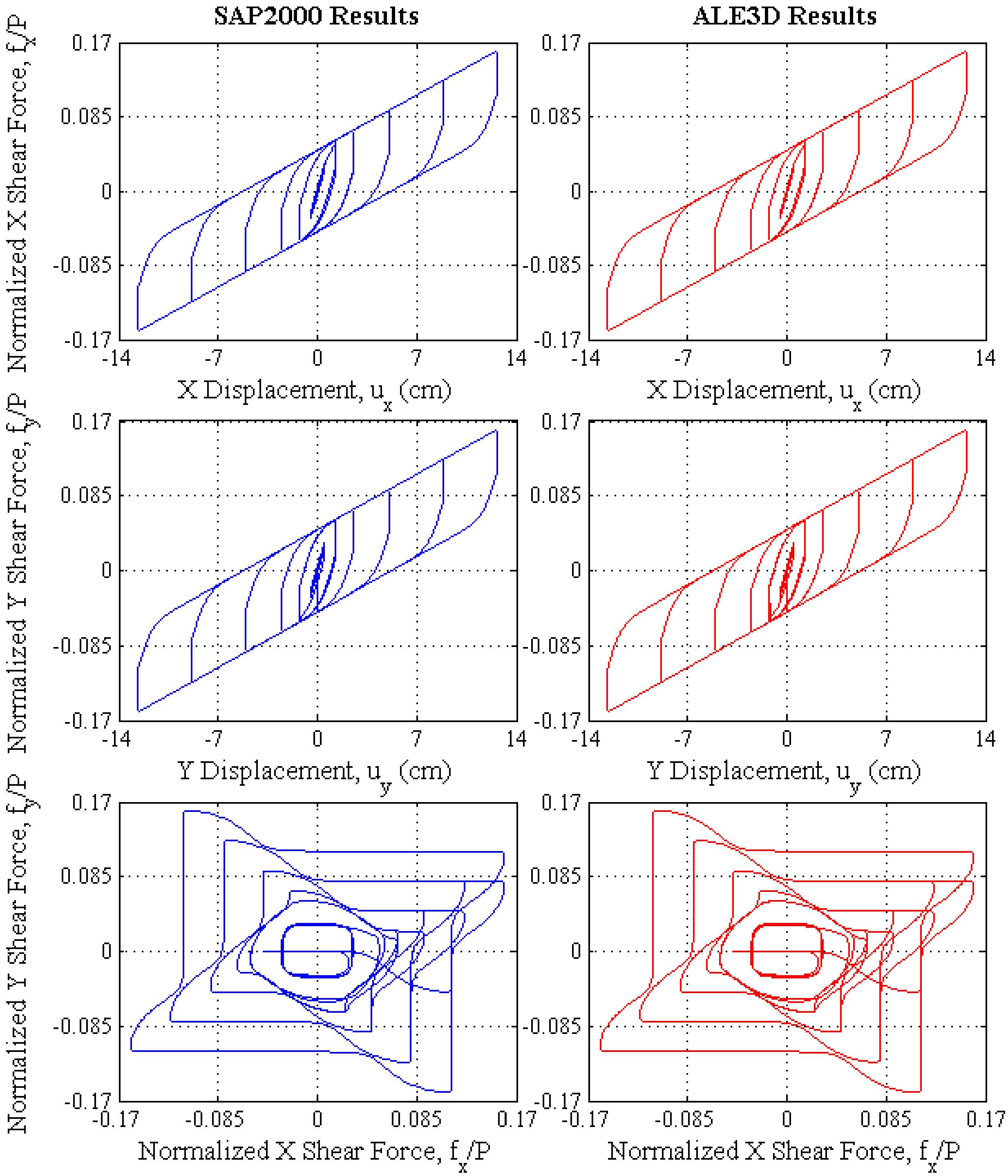

Figure 4.17: Comparative directional hystereses and force path of the FP models for the square displacement orbit

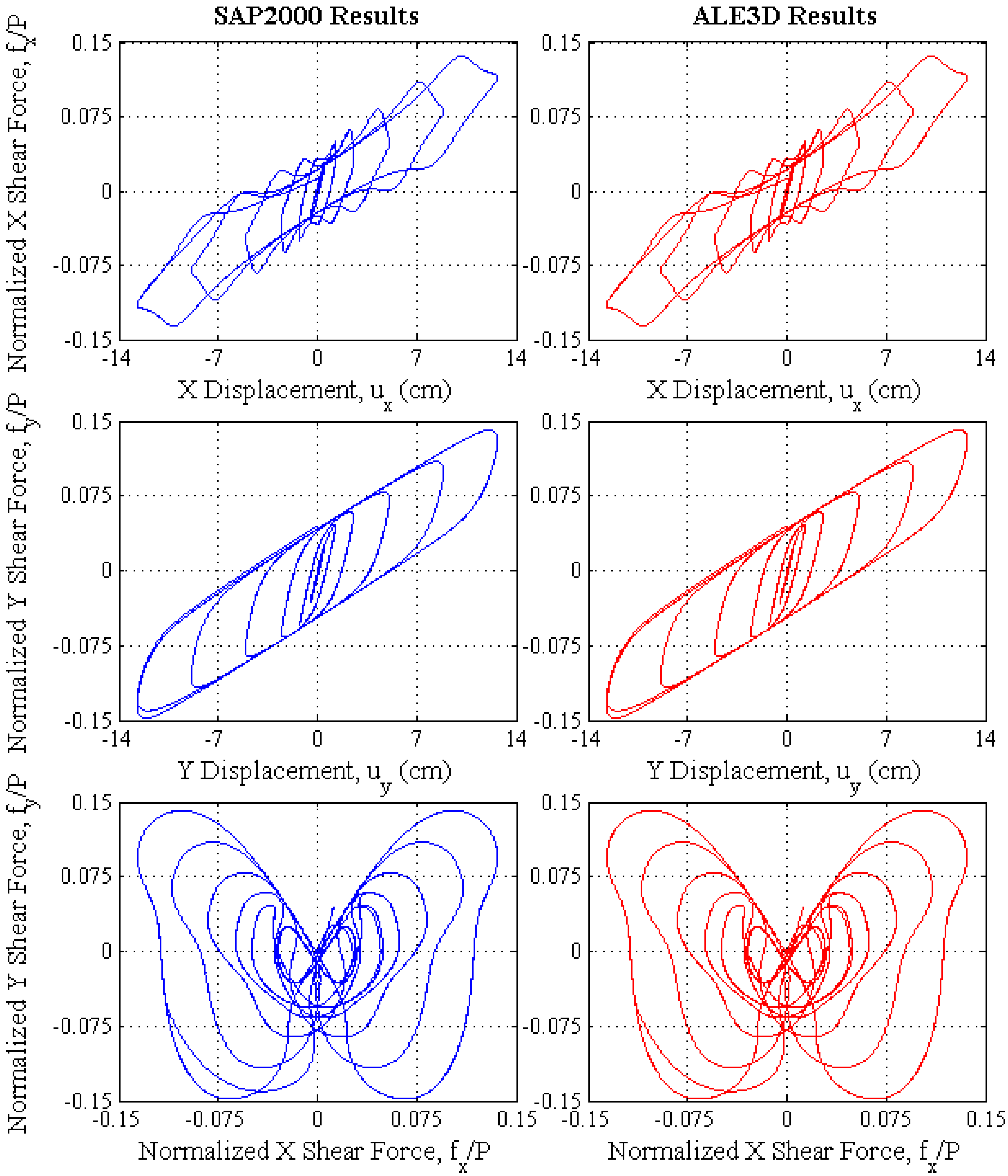

Figure 4.18: Comparative directional hystereses and force path of the FP models for the figure-eight displacement orbit

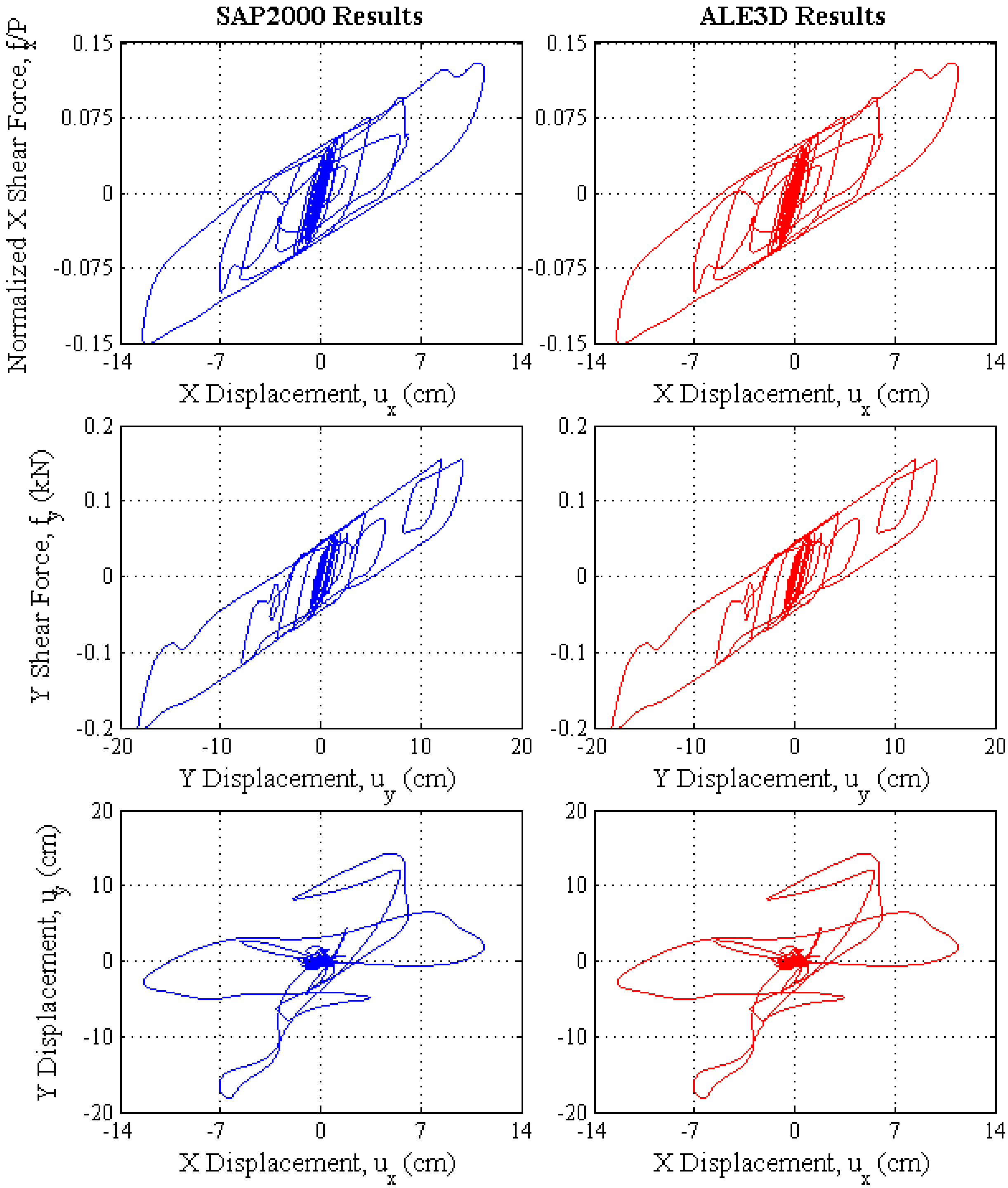

Figure 4.19: Comparative directional hystereses and displacement path of the FP models for the unrestrained response to the 1994 Northridge earthquake Newhall record

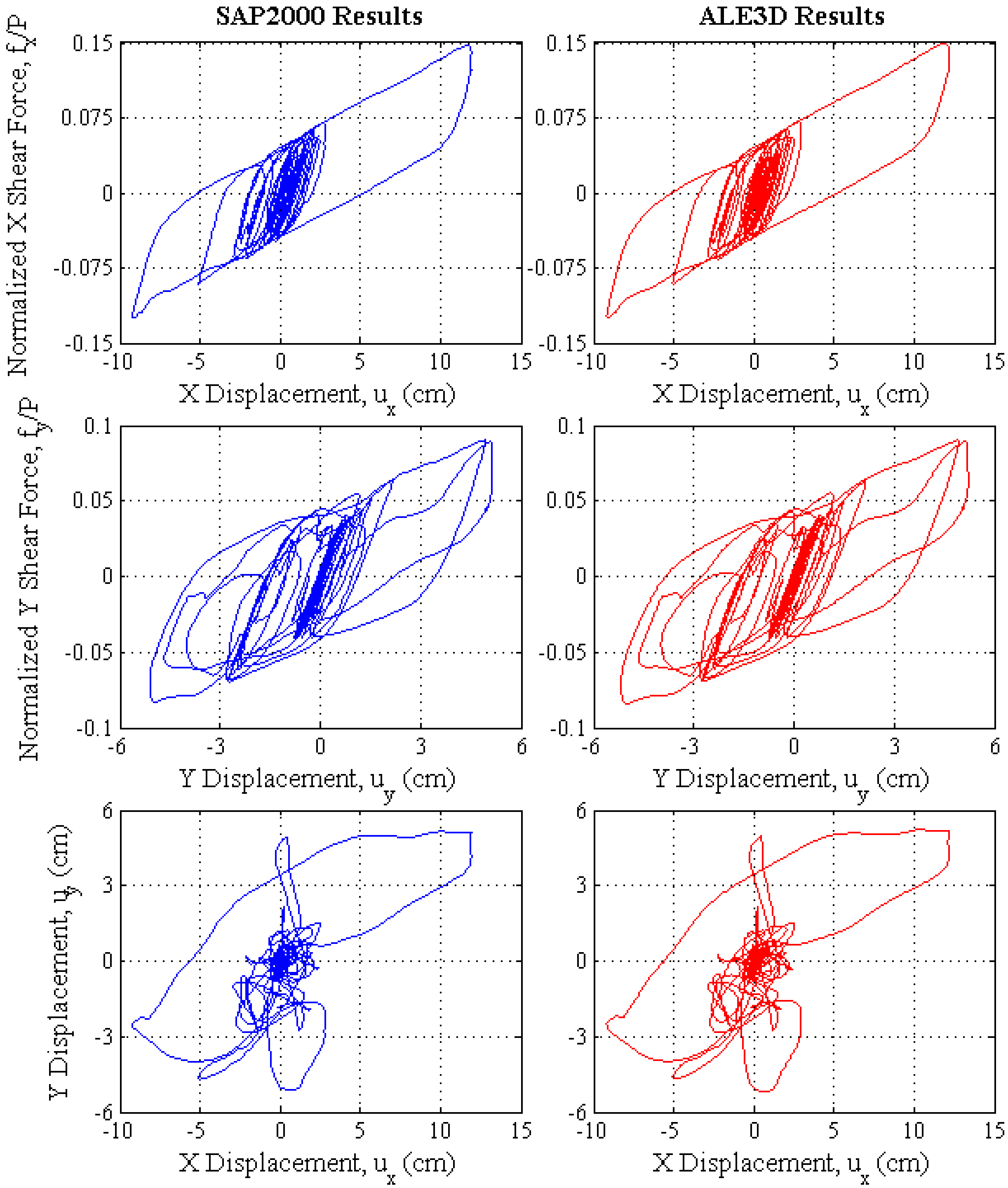

Figure 4.20: Comparative directional hystereses and displacement path of the FP models for the unrestrained response to the 1978 Tabas record

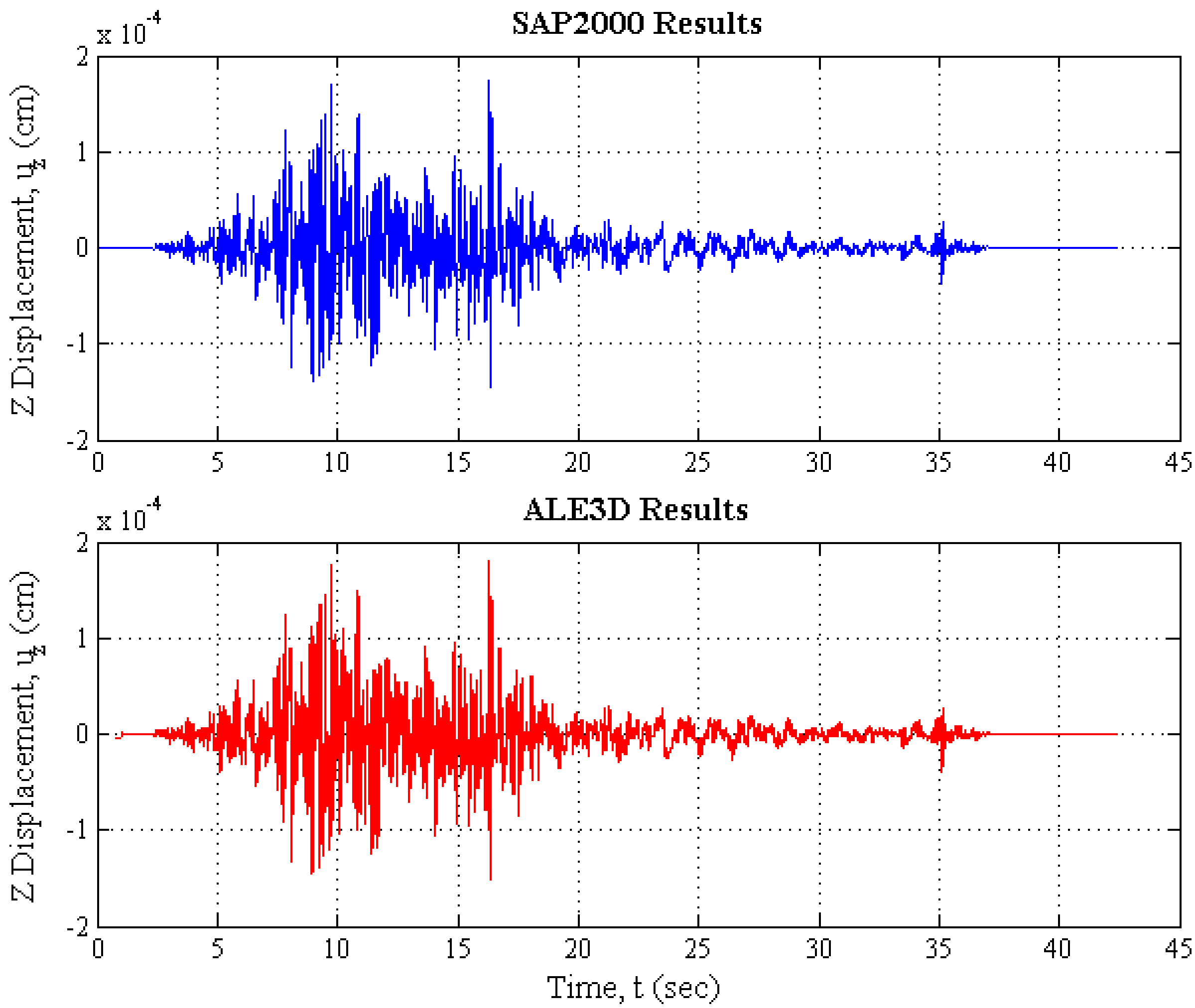

Figure 4.21: Comparative vertical displacement response of the FP models for the unrestrained response to the 1978 Tabas record

4.3 Simplified Lead-Rubber Bearing Model

The Nagarajaiah et al. (1991) model also serves as the numerical basis for elastomeric bearings in various commercial structural engineering software, including SAP2000, ETABS, and 3D-BASIS. It utilizes the same hysteretic model described in Section 4.2, originally proposed by Wen (1976) and Park et al. (1986). The resulting model has the idealized lateral hysteresis shown in Figure 4.22, which presents the necessary inputs for the lateral model including the yield force, f_{yield}, the yield displacement, u_{yield}, and the ratio of post-yield to pre-yield stiffness, α. This model is used for the simplified analysis of lead-rubber bearings in ALE3D, where it is referred to as "spring4".

4.3.1 Model Response

The vertical component of the model response force, f_z, is non-linear under compressive loading as well as tension loading, unlike the FP model. The response, depicted in Equation 4.52, is a function of vertical stiffness, k_z, and damping, c_z. Equation 4.41 shows the relationship between k_z and c_z for a given mass, m, and desired damping ratio, ζ_z.

$$f_z = c_z \dot{u}_z + k_z u_z \tag{4.52}$$

The vertical component of this model is completely decoupled from the lateral response. Thus, this model is limited in the accuracy of its vertical displacements and does not include the interaction of vertical and horizontal response. The SAP2000 model for LR bearings does not include vertical damping, which has been added in ALE3D to better approximate realistic response.

The lateral responses, f_x and f_y, from Equation 4.53 are the summation of a linear term representing elastic deformation of the elastomer and a non-linear hysteretic component, accounting for the plasticity of the lead plug. The linear terms, f_{xe} and f_{ye}, are the directional components of the post-yield stiffness of the bearing, k_e, which is based on the stiffness of the rubber layers. These terms are found by determining the pre-yield stiffness as the ratio of f_{yield} to u_{yield}, and modifying it by α, as shown in Equation 4.54. The hysteretic forces, f_{xh} and f_{yh}, shown in Equation 4.55, are the product of hysteretic variables, z_x and z_y, and the characteristic strength of the lead core, $Q_d = (1-\alpha)f_{yield}$, which represents the fraction of f_{yield} attributed to the yielding of the lead core (a small fraction of f_{yield} is due to the elastic deformation of the rubber over the distance u_{yield}).

$$\begin{aligned} f_x &= f_{xe} + f_{xh} \\ f_y &= f_{ye} + f_{yh} \end{aligned} \tag{4.53}$$

$$\begin{aligned} f_{xe} &= k_e u_x = \alpha \left(\frac{f_{yield}}{u_{yield}}\right) u_x \\ f_{ye} &= k_e u_y = \alpha \left(\frac{f_{yield}}{u_{yield}}\right) u_y \end{aligned} \tag{4.54}$$

$$\begin{aligned} f_{xh} &= (1-\alpha) f_{yield} z_x = Q_d z_x \\ f_{yh} &= (1-\alpha) f_{yield} z_y = Q_d z_y \end{aligned} \tag{4.55}$$

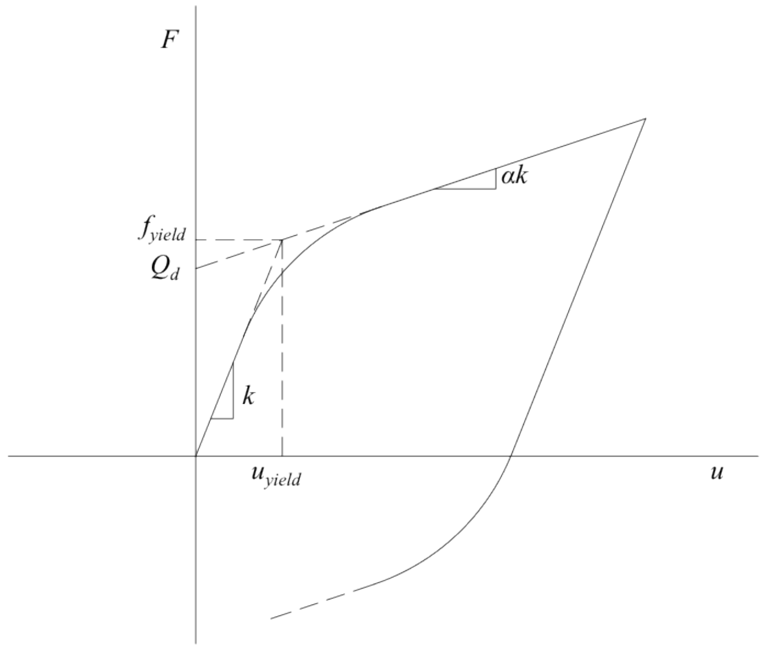

Figure 4.22: Idealized lateral hysteresis of an LR bearing depicting necessary inputs for the analytical model

Parameter	Value
Mass, m	54.41 Mg
Vertical Stiffness, k_z	716000 kN/cm
Vertical Damping, c_z	62.4 kN-s/cm (5%)
Yield Force, f_{yield}	29.4 kN
Yield Displacement, u_{yield}	0.941 cm

Table 4.4: Input parameters of FP bearings used in validation tests

As with the FP model, the hysteretic variables of the LR model evolve based on Equations 4.48 and 4.49.

4.3.2 Validation

The simplified LR bearing response model in ALE3D was verified using the displacement-controlled and unrestrained earthquake test cases presented in Section 4.1.2. Comparative analyses were run using SAP2000. The input parameters for the LR model are shown in Table 4.4.

The results of the validation tests are shown in Figures 4.23 through 4.29. All tests show

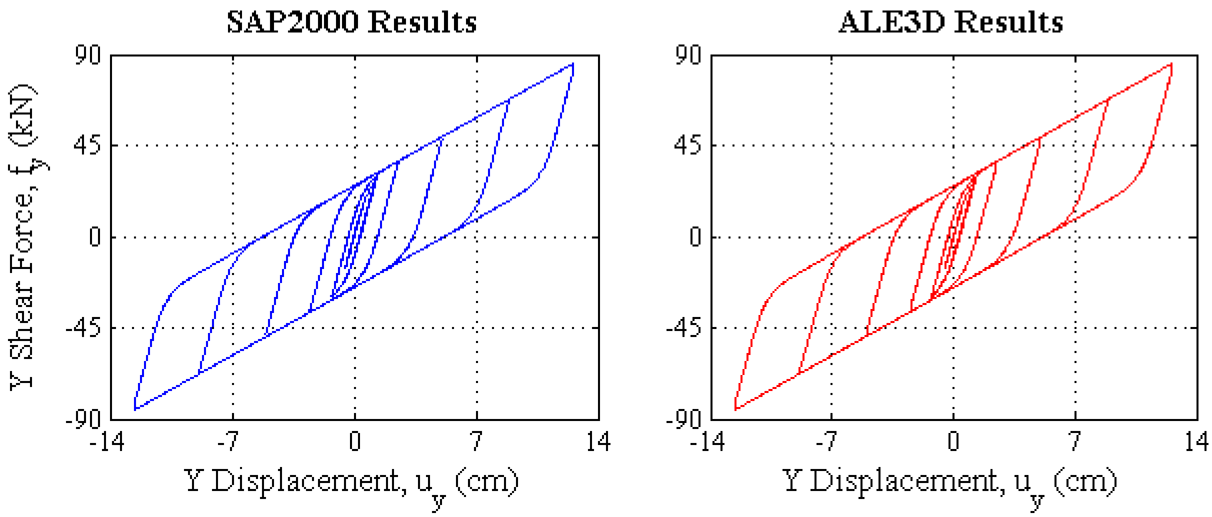

Figure 4.23: Comparative directional hystereses of the simplified LR models for the unidirectional sine wave displacement orbit

the ALE3D model very accurately captures the SAP model response.

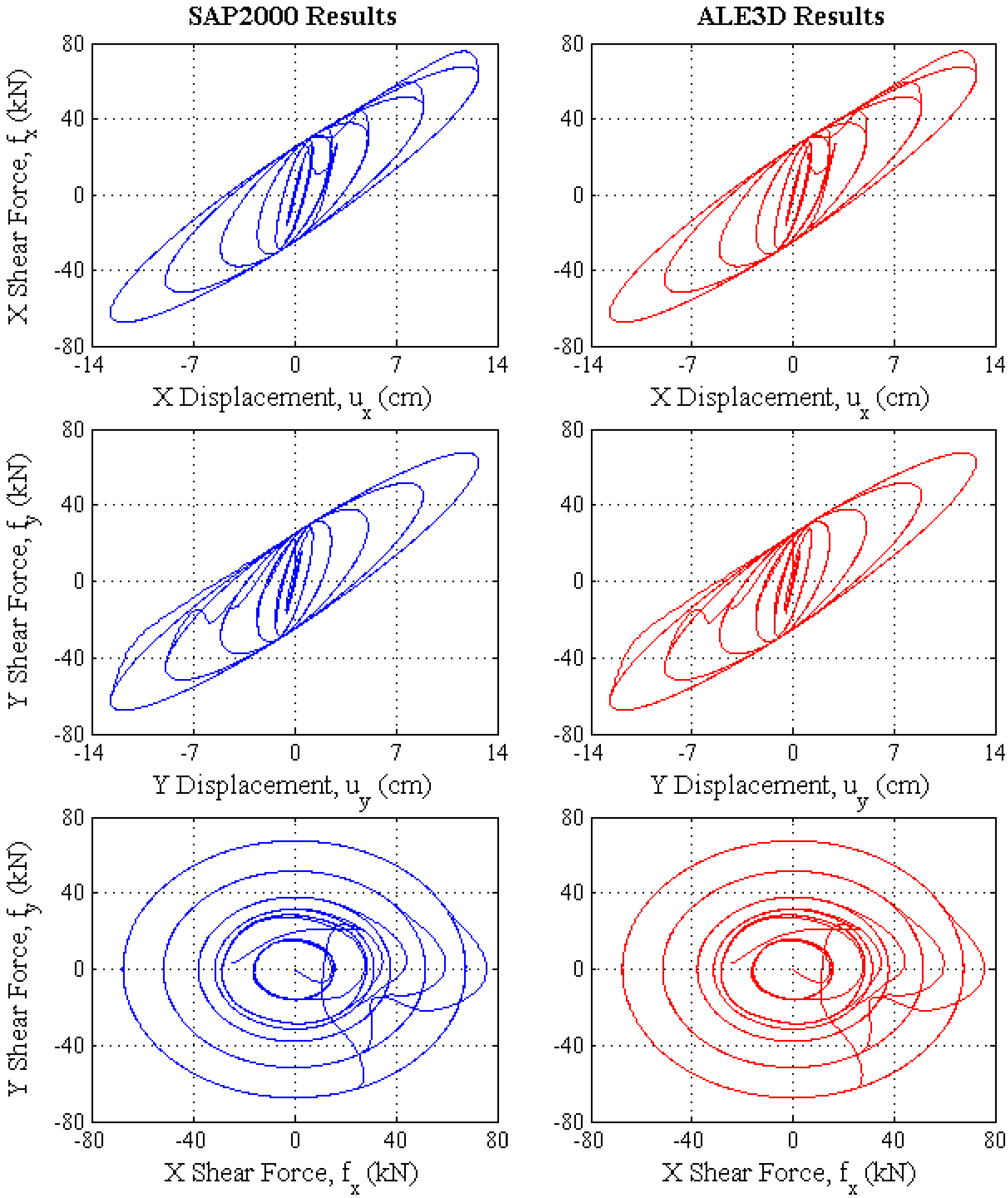

Figure 4.24: Comparative directional hystereses and force path of the simplified LR models for the circular displacement orbit

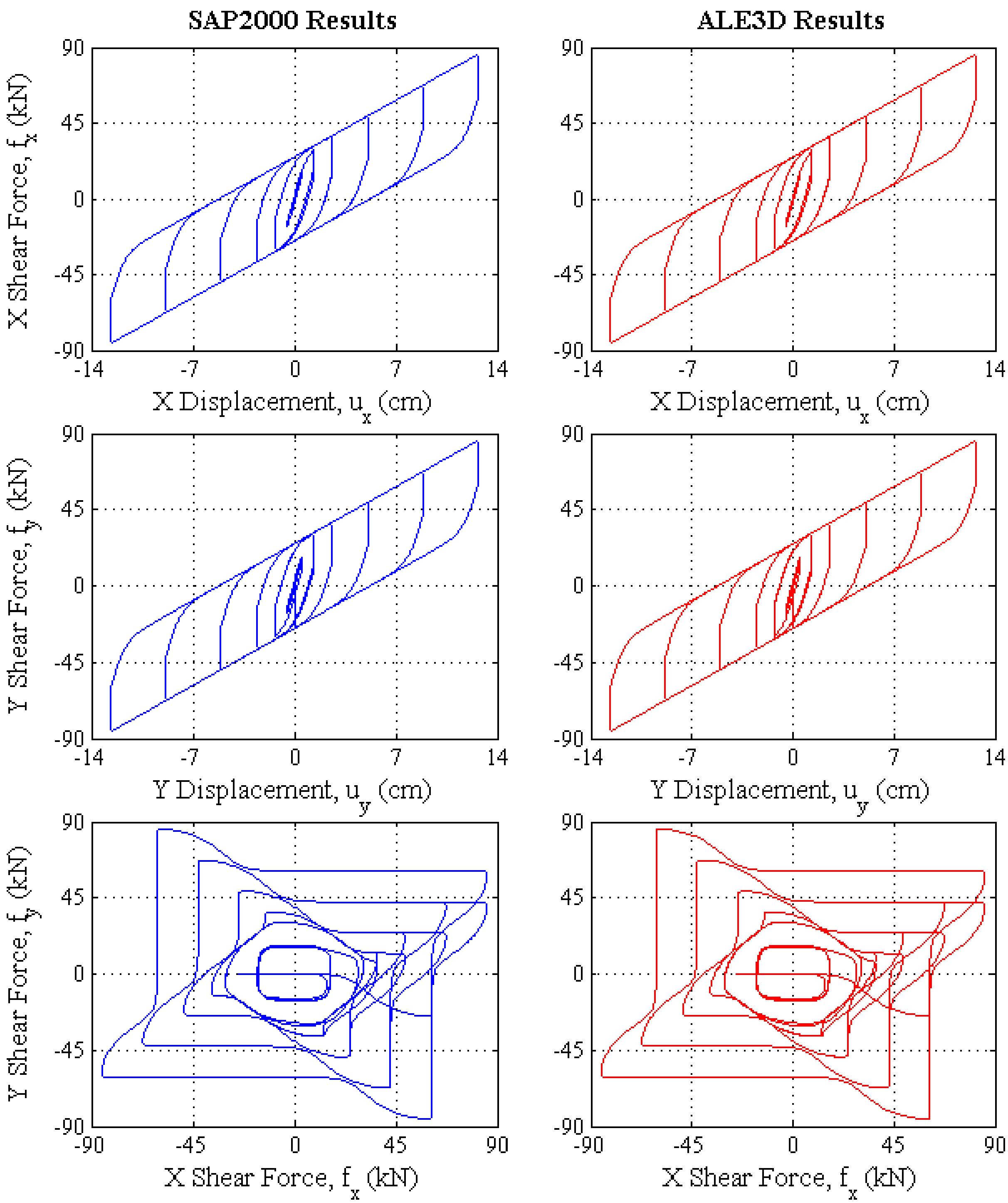

Figure 4.25: Comparative directional hystereses and force path of the simplified LR models for the square displacement orbit

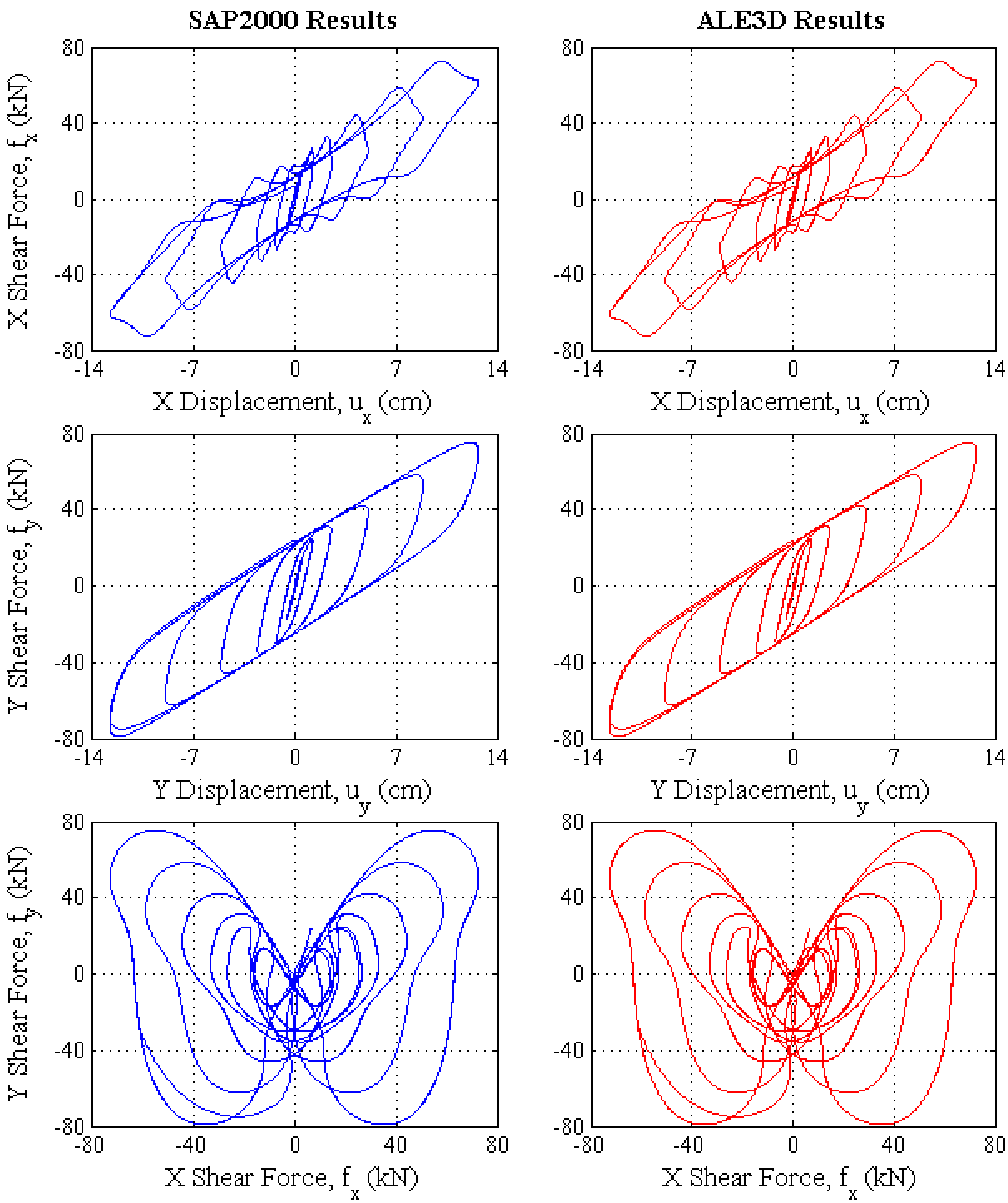

Figure 4.26: Comparative directional hystereses and force path of the simplified LR models for the figure-eight displacement orbit

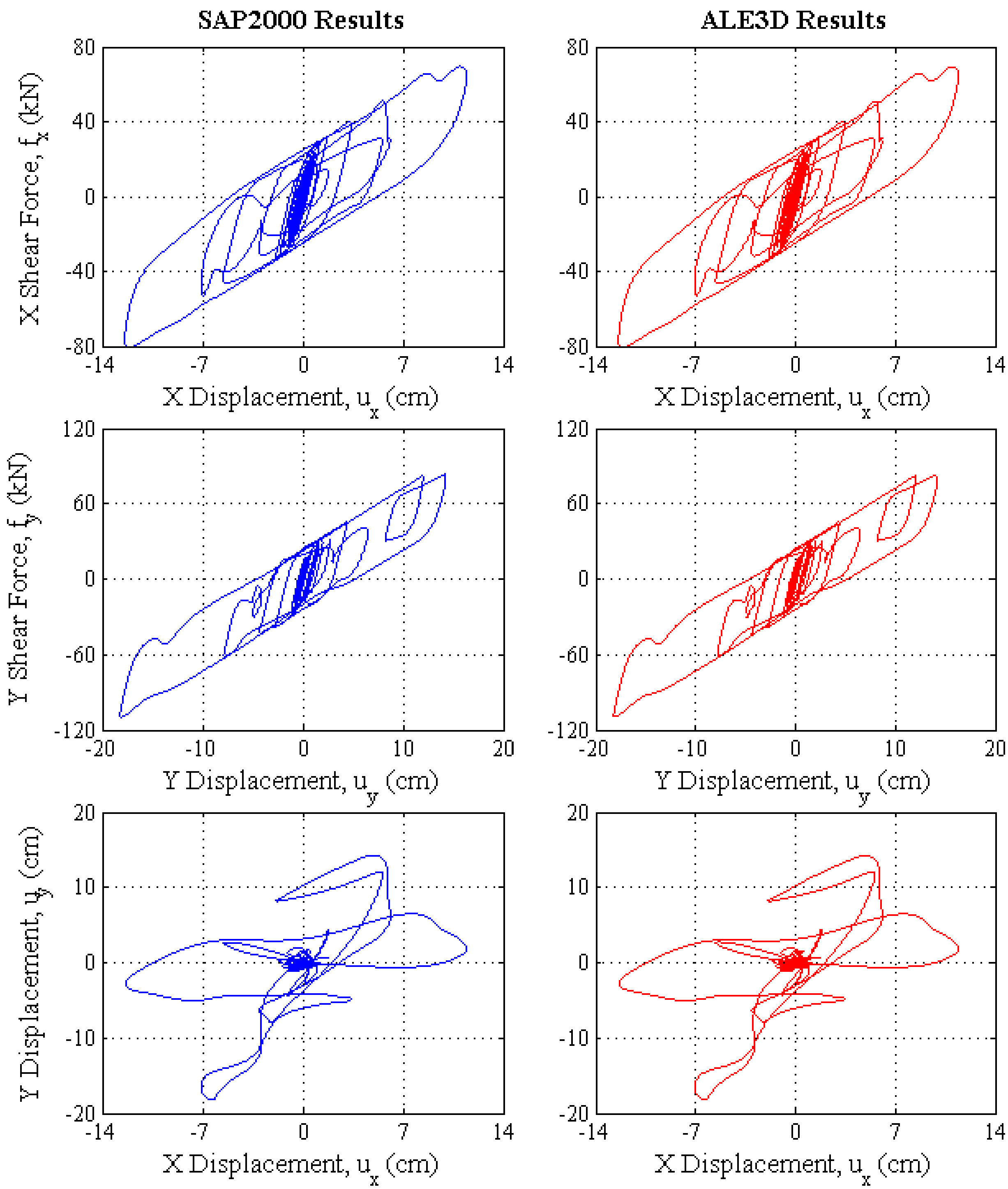

Figure 4.27: Comparative directional hystereses and displacement path of the simplified LR models for the unrestrained response to the 1994 Northridge earthquake Newhall record

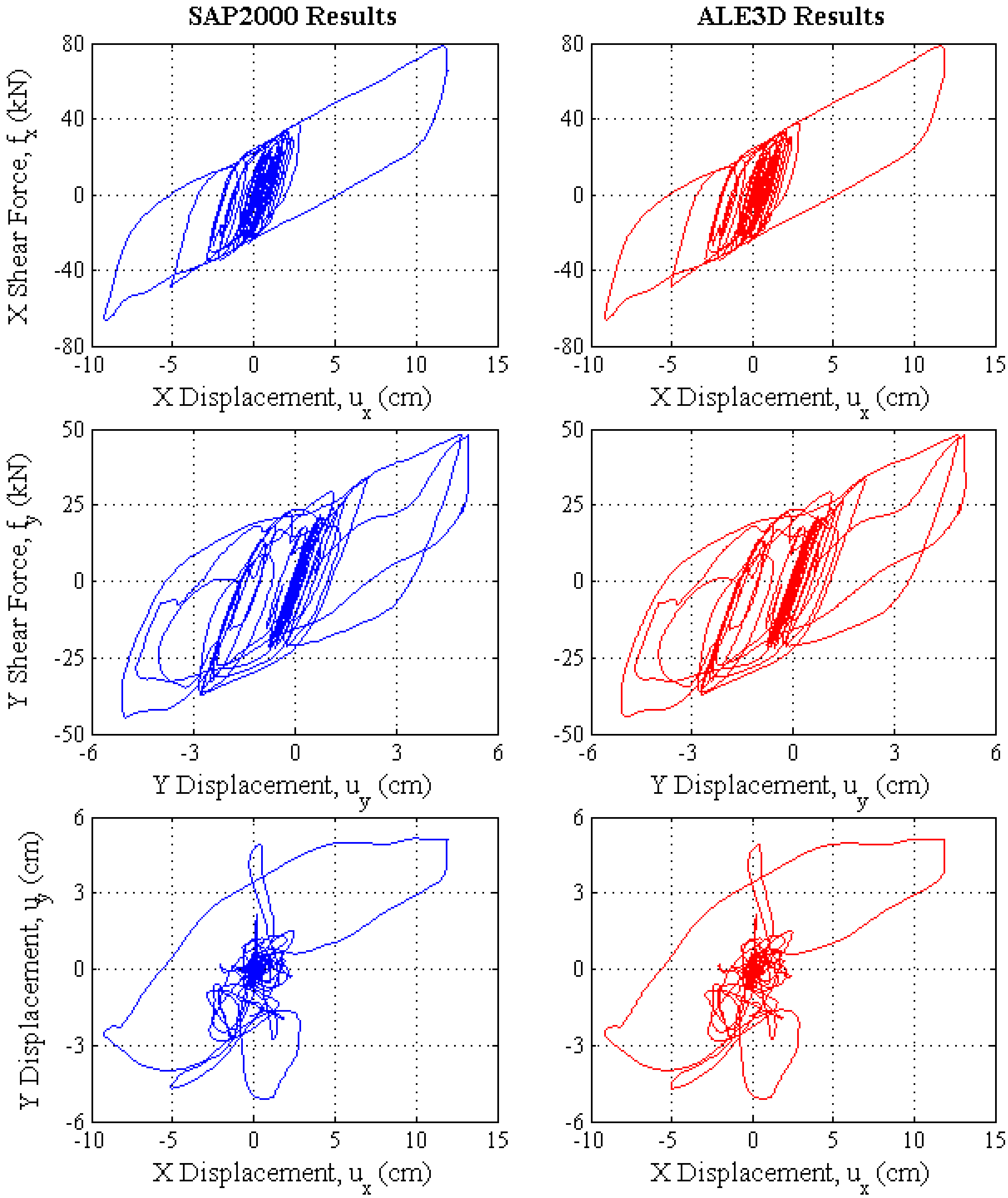

Figure 4.28: Comparative directional hystereses and displacement path of the simplified LR models for the unrestrained response to the 1978 Tabas record

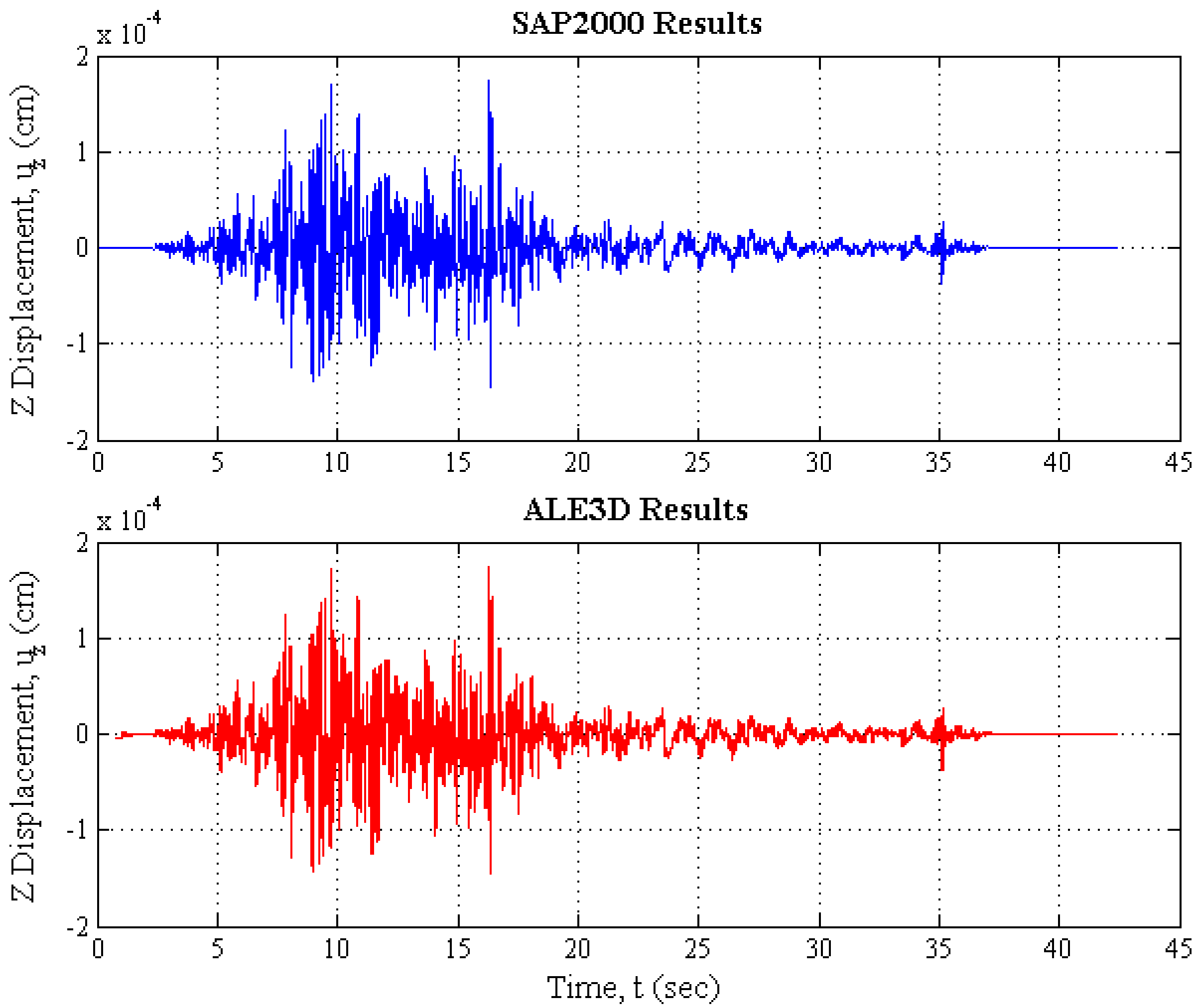

Figure 4.29: Comparative vertical displacement response of the simplified LR models for the unrestrained response to the 1978 Tabas record

4.4 Robust Lead-Rubber Bearing Model

The Kalpakidis et al. (2010) model serves as the numerical basis for the lateral response of the robust LR bearing model in ALE3D, where it is referred to as "spring5". It utilizes the same hysteretic model described in Section 4.2, originally proposed by Wen (1976) and Park et al. (1986), a viscous damping term representing inherent rubber damping, as well as a strength degredation term which accounts for the effect of lead core heating under repeated load cycling (Kalpakidis and Constantinou, 2008). The model is extended to three dimensions by introducing a two-spring, P-Δ-like model presented in Warn et al. (2007) and Warn and Whittaker (2006), which analyzed and simplified the model originally proposed by Koh and Kelly (1987).

4.4.1 Model Response

A schematic of an undeformed LR bearing is shown in Figure 4.30. The important parameters for the bearing are displayed, and include the outer radius of steel laminates, R, lead core radius, a, lead core height between mounting plates, h_L, and individual rubber layer thickness, t_r, which is taken as the average of the n rubber layers if the thickness is not constant. The lead plug height can be solved for using Equation 4.56 for a given constant steel reinforcing plate thickness, t_s.

$$h_L = nt_r + (n-1)t_s \tag{4.56}$$

The vertical component of the model response force, f_z, is non-linear under compression and tension loading, unlike the FP model. The response, depicted in Equation 4.57, is a

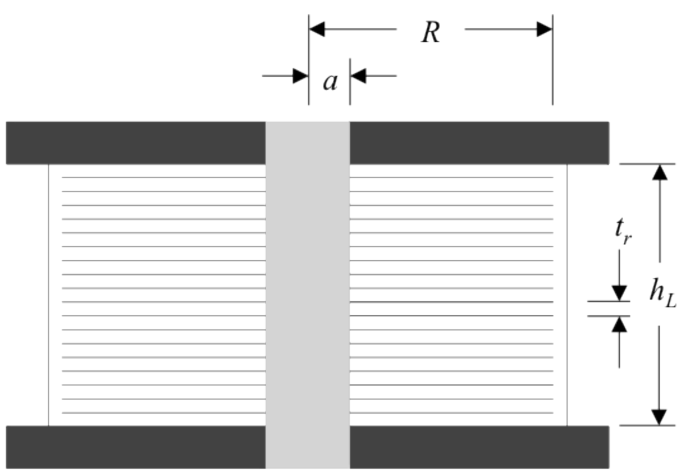

Figure 4.30: Schematic of an undeformed LR bearing depicting the physical input parameters for the model

function of vertical stiffness, k_z, and damping, c_z. Equation 4.41 shows the relationship between k_z and c_z for a given mass, m, and desired damping ratio, ζ_z.

$$f_z = c_z \dot{u}_z + k_z u_z \tag{4.57}$$

When subjected to constant compression loading, a horizontally-displaced LR bearing will reduce in height as shown in Figure 4.31. This is numerically modeled as a decrease in vertical stiffness, k_z, when displaced. The vertical stiffness of an undeformed LR bearings, k_{zo}, is a function of the rubber elastic compression modulus, E_c, the bonded rubber area, $A_b = \pi(R^2 - a^2)$, and the total rubber thickness, $T_r = nt_r$, as shown in Equation 4.58. E_c is solved for using Equation 4.59.

$$k_{zo} = \frac{E_c A_b}{T_r} \tag{4.58}$$

$$\frac{1}{E_c} = \frac{1}{6GS^2F} + \frac{4}{3K} \tag{4.59}$$

In the previous expression, G is the effective shear modulus, F is a constant based on bearing geometry calculated in Equation 4.60, K is the bulk modulus of rubber, and S is the shape factor for the given bearing, calculated in Equation 4.61.

$$F = \frac{\left(\frac{R}{a}\right)^2 + 1}{\left(\frac{R}{a} - 1\right)^2} + \frac{\frac{R}{a} + 1}{\left(1 - \frac{R}{a}\right)\ln\left(\frac{R}{a}\right)} \tag{4.60}$$

$$S = \frac{\text{Loaded Area}}{\text{Area Free to Bulge}} = \frac{R^2 - a^2}{2Rt_r} \tag{4.61}$$

Kelly and Koh (1997) used a two-spring approximation to relate the vertical stiffness, k_z, to the total lateral displacement, $u = \sqrt{u_x^2 + u_y^2}$, as shown in Equation 4.62. Studies by Warn et al. (2007) have shown that empirical data is more closely matched using a simple piecewise-linear relation depicted in Equation 4.63. The latter expression is used for the robust LR model in ALE3D.

$$k_z = \frac{k_{zo}}{1 + \frac{12}{\pi^2}\left(\frac{u}{R}\right)^2} \tag{4.62}$$

$$k_z = \begin{cases} \left[1 - 0.4\left(\frac{u}{R}\right)\right] k_{zo} & \text{if } \frac{u}{R} \leq 2 \\ 0.2k_{zo} & \text{if } \frac{u}{R} > 2 \end{cases} \tag{4.63}$$

The lateral responses, f_x and f_y, from Equation 4.64 are the summation of a linear term representing elastic deformation of the elastomer, a viscous term representing the small amount of damping inherent to the rubber compound, and a non-linear hysteretic component accounting for the plasticity of the lead plug. The linear terms, f_{xe} and f_{ye}, are the directional components of the post-yield stiffness of the bearing, k_e, which is based on the stiffness of the rubber layers. These terms are found by determining the pre-yield stiffness as the ratio of the yield force, f_{yield}, to the yield displacement, u_{yield}, and modifying them by a ratio of the post-yield to pre-yield stiffness, α, as shown in Equation 4.54. The viscous forces, f_{xv} and

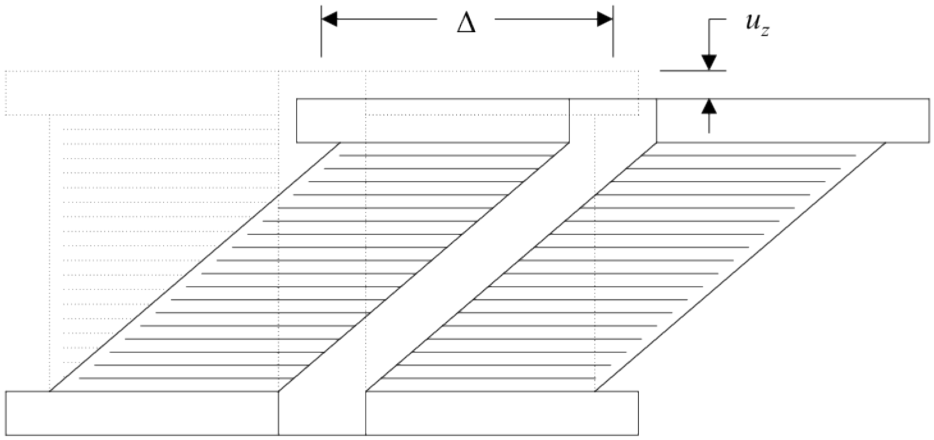

Figure 4.31: Schematic of a deformed LR bearing showing change in vertical deformation with lateral displacement

f_{yv}, shown in Equation 4.66, are velocity-proportional terms scaled by c_d, the small amount of damping attributed to the rubber compound during excitation. The hysteretic forces, f_{xh} and f_{yh}, shown in Equation 4.67, are the product of the temperature-dependent yield stress of the lead core, σ_L, the area of the lead core, $A_L = \pi a^2$, and the hysteretic variables z_x and z_y. σ_L accounts for softening of the lead core, a phenomenon which occurs in LR bearings responding to high-amplitude, multi-cycle excitation.

$$\begin{aligned} f_x &= f_{xe} + f_{xv} + f_{xh} \\ f_y &= f_{ye} + f_{yv} + f_{yh} \end{aligned} \tag{4.64}$$

$$\begin{aligned} f_{xe} &= f_e u_x = \alpha \left(\frac{f_{yield}}{u_{yield}} \right) u_x \\ f_{ye} &= f_e u_y = \alpha \left(\frac{f_{yield}}{u_{yield}} \right) u_y \end{aligned} \tag{4.65}$$

$$\begin{aligned} f_{xv} &= c_d \dot{u}_x \\ f_{yv} &= c_d \dot{u}_y \end{aligned} \tag{4.66}$$

$$\begin{aligned} f_{xh} &= \sigma_L A_L z_x = \sigma_L (\pi a^2) z_x \\ f_{yh} &= \sigma_L A_L z_y = \sigma_L (\pi a^2) z_y \end{aligned} \tag{4.67}$$

As with the previous models, the hysteretic variables of the LR model evolve based on Equations 4.48 and 4.49.

The evolution of the lead core temperature, T_L, follows Equation 4.68. The change in core temperature per unit time, $\dot{T}_L$, calculated in Equation 4.69, is based on material properties of the various bearing components including the density of lead, ρ_L, the specific heat of lead,

Property	Value
Bulk Modulus of Rubber, K	2000 MPa
Density of Lead, ρ_L	11200 kg/m^3
Specific Heat of Lead, c_L	130J/(kg°C)
Thermal Conductivity of Steel, k_s	50 W/(m°C)
Thermal Diffusivity of Steel, α_s	1.41×10^{-5}m^2/s
Inverse Temeprature, E_2	0.0069/°C

Table 4.5: Material properties governing the evolution of lead core temperature of LR bearings

c_L, thermal conductivity of steel, k_s, thermal diffusivity of steel, α_s, and inverse temperature, E_2. Material paramters used for this model in simulations are presented in Table 4.5.

$$T_{Li} = T_{L(i-1)} + \dot{T}_{L(i-1)}\Delta t \tag{4.68}$$

$$\dot{T}_L = \frac{\sigma_L\sqrt{z_x^2+z_y^2}\sqrt{\dot{u}_x^2+\dot{u}_y^2}}{\rho_L c_L h_L} - \frac{k_s T_L}{a\rho_L c_L h_L}\left(\frac{1}{F_L} + \frac{1.274t_s}{a}(\tau)^{-1/3}\right) \tag{4.69}$$

$$\tau = \frac{\alpha_s t}{a^2} \tag{4.70}$$

$$F_L = \begin{cases} 2(\frac{\tau}{\pi})^{1/2} - \frac{\tau}{\pi}\left(2 - (\frac{\tau}{4}) - (\frac{\tau}{4})^2 - \frac{15}{4}(\frac{\tau}{3})^3\right) & \text{if} \quad \tau < 0.6 \\ \frac{8}{3\pi} - \frac{1}{2\sqrt{\pi\tau}}\left(1 - \frac{1}{3(4\tau)} + \frac{1}{6(4\tau)^2} - \frac{1}{12(4\tau)^3}\right) & \text{if} \quad \tau \geq 0.6 \end{cases} \tag{4.71}$$

$$\sigma_L = \sigma_{Lo}e^{-E_2 T_L} \tag{4.72}$$

4.4.2 Validation

The vertical and horizontal responses from the robust LR bearing models in ALE3D were verified independently using the validation cases presented in Warn et al. (2007) and Kalpakidis et al. (2010), respectively. The vertical response validation involved subjecting the bearings to a series of lateral displacements, u, between $0R$ and $2.5R$, and determining the vertical stiffness, k_z, via vertical sine-wave displacement-controlled excitation at each lateral displacement. The applied displacement-controlled time histories are presented in Figure 4.32.

The horizontal response was validated using displacement-controlled and earthquake response analysis cases. The displacement-controlled sine-wave time history is presented in Figure 4.33. The five lateral 1D and 2D ground motion records are listed in Table 4.6 and associated acceleration time histories are shown in Figures 4.34 through 4.38. The first three motions are all from the SAC Steel Project (1997) near-fault site suite.

The three validation tests from Warn et al. (2007) and Kalpakidis et al. (2010) utilize three different LR bearings, the properties of which are presented in Table 4.7. The response from the ALE3D models demonstrate close agreement with the test cases presented.

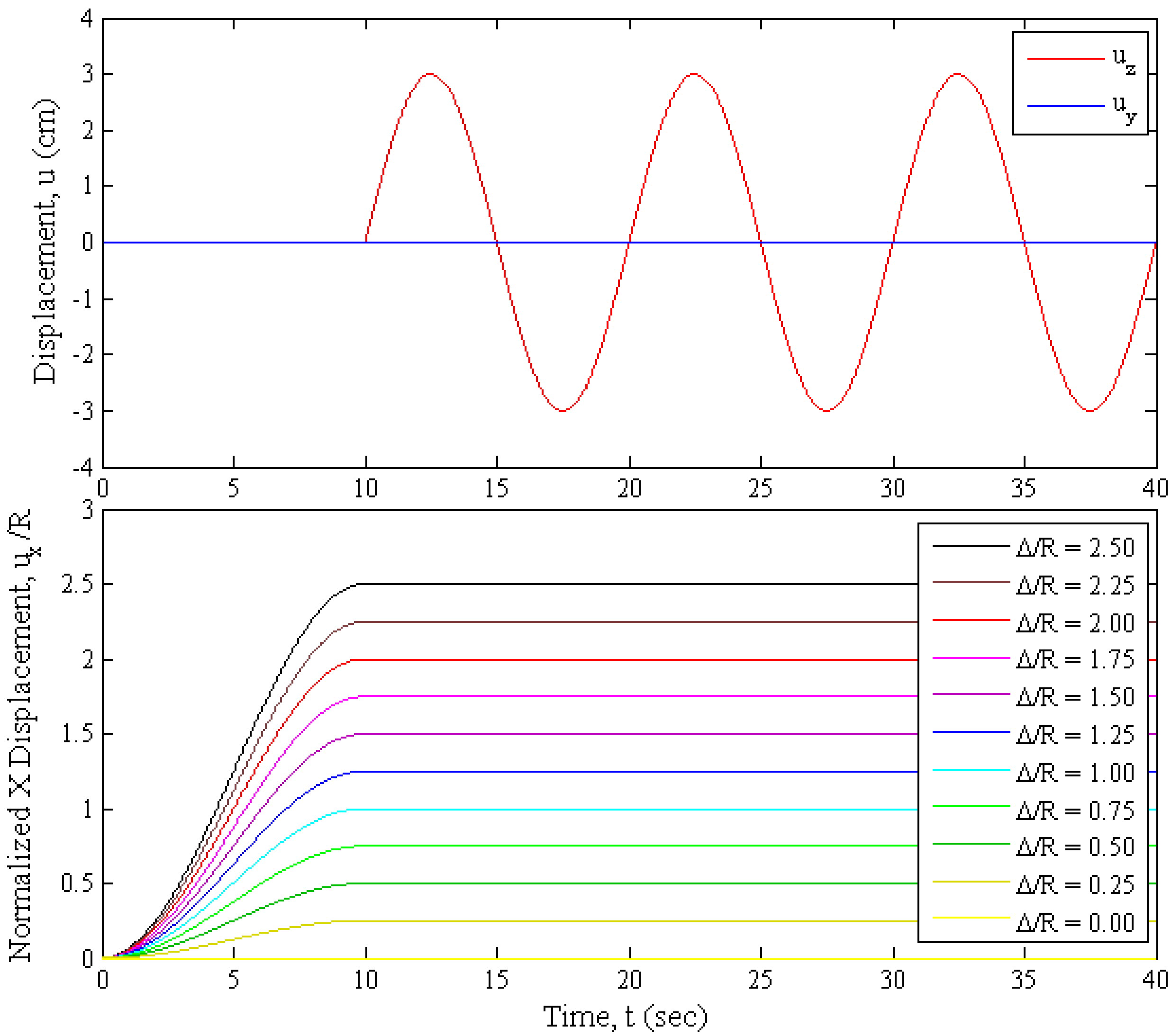

Figure 4.32: Directional displacement time histories for the vertical LR validation test cases

No	Event	Record	Date
1	Tabas, Iran	Tabas (NF02)	09/16/1978
2	Northridge, USA	Rinaldi (NF13)	01/17/1994
3	Kobe, Japan	Kobe (NF17)	01/16/1995
4	Duzce, Turkey	Bolu (BOL)	11/12/1999
5	Chi-Chi, Taiwan	TCU065	09/20/1999

Table 4.6: Ground motions used for robust LR validation

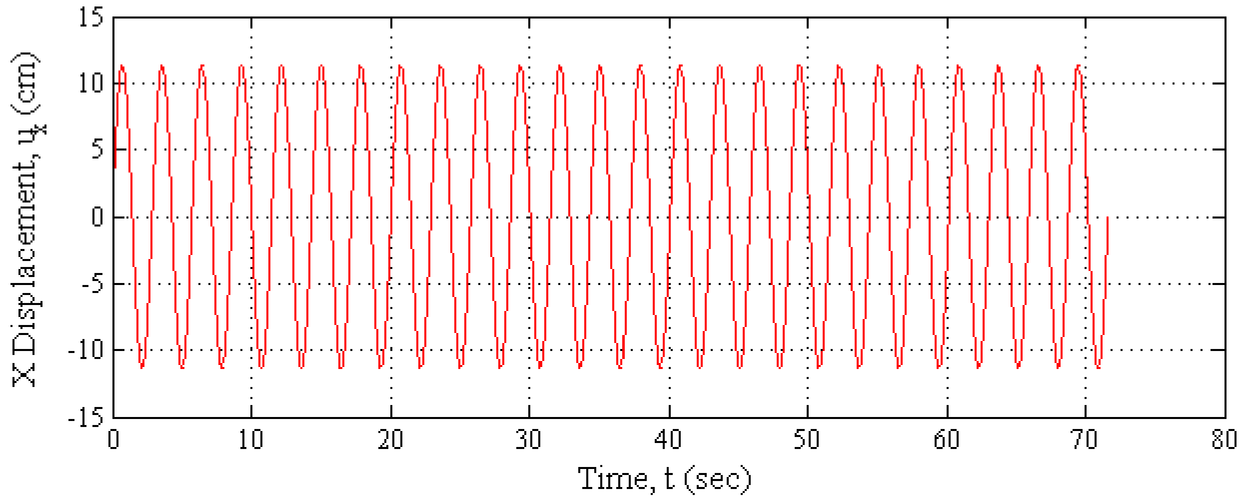

Figure 4.33: 1-dimensional sine-wave displacement time history for the displacement-controlled test

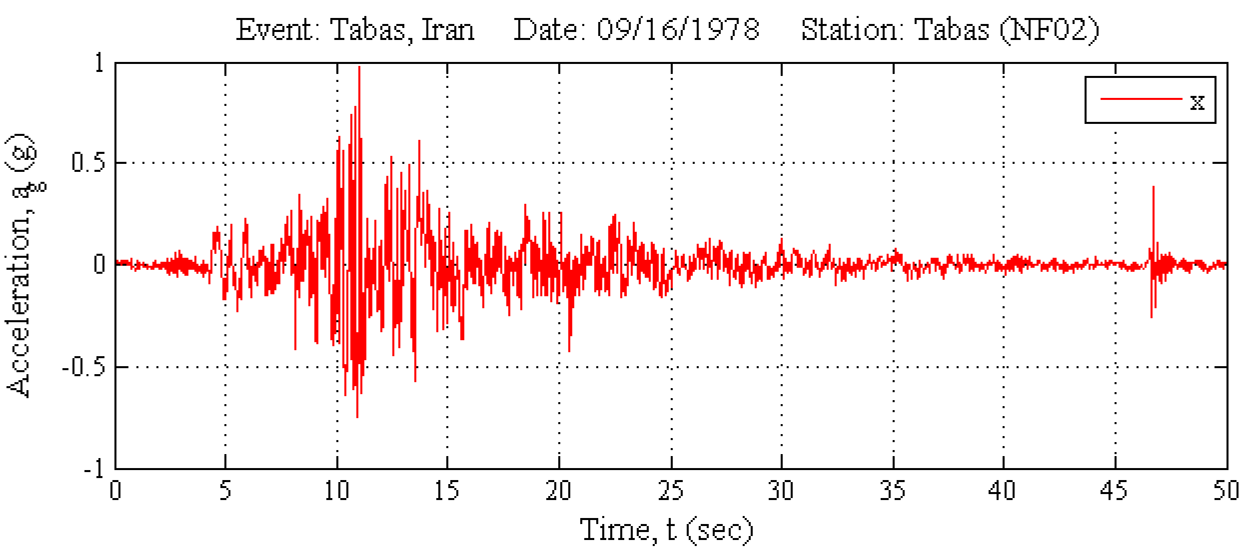

Figure 4.34: 1-dimensional input acceleration time history for the 1978 Tabas earthquake record

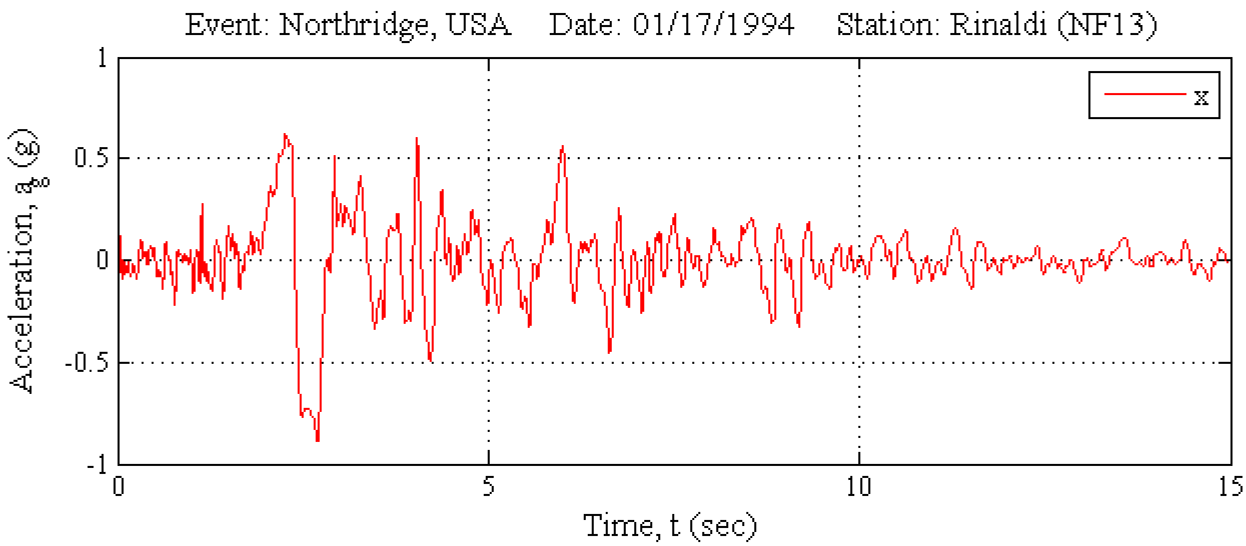

Figure 4.35: 1-dimensional input acceleration time history for the 1994 Northridge earthquake record

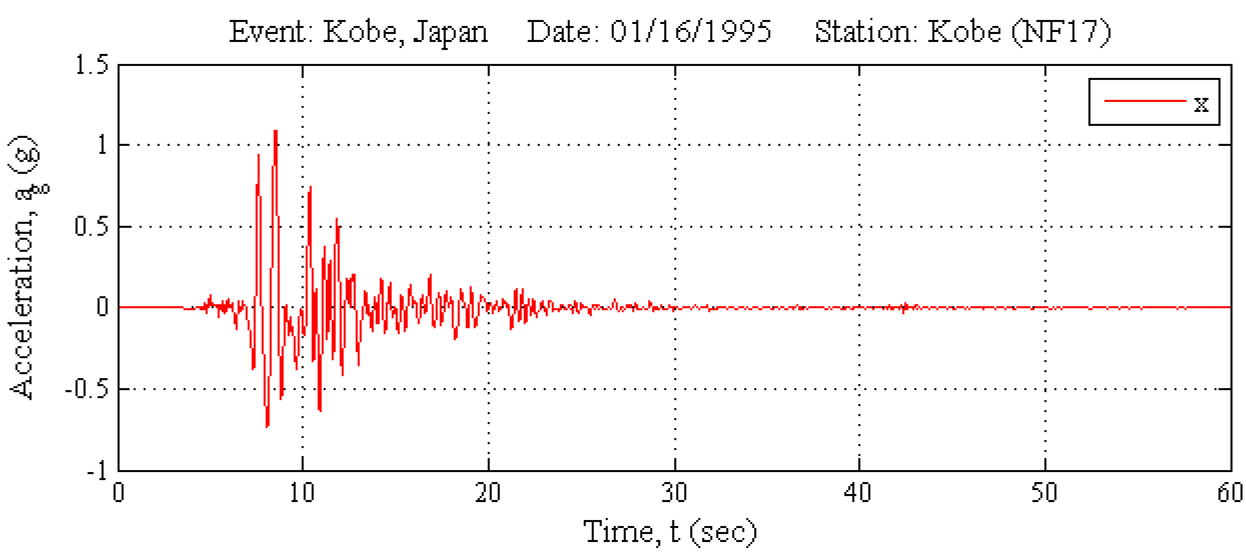

Figure 4.36: 1-dimensional input acceleration time history for the 1995 Kobe earthquake record

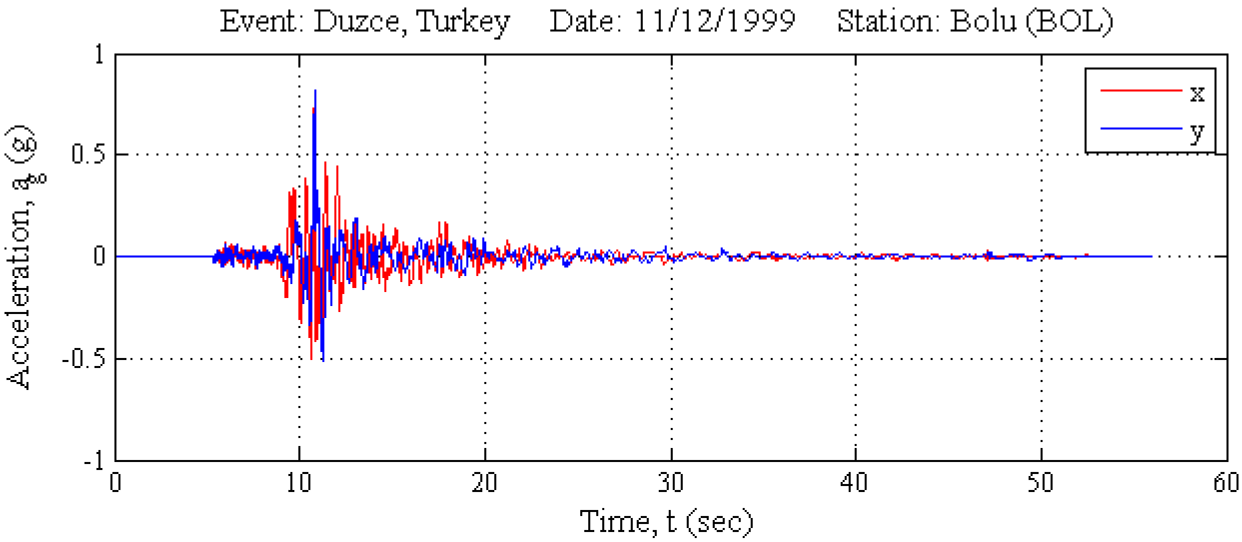

Figure 4.37: 2-dimensional input acceleration time history for the 1999 Duzce earthquake record

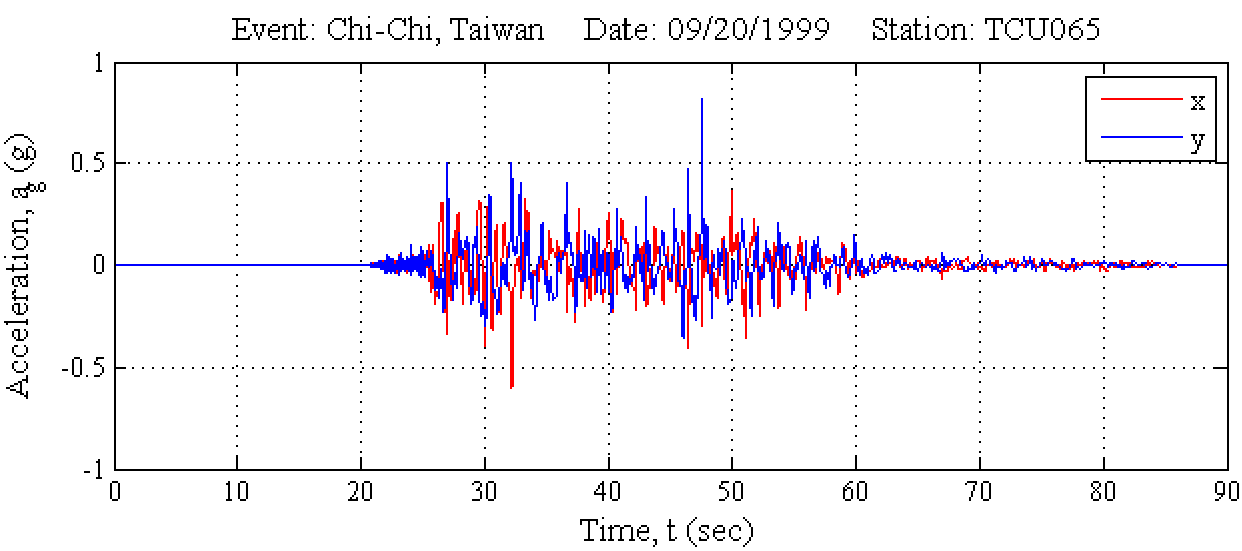

Figure 4.38: 2-dimensional input acceleration time history for the 1999 Chi-Chi earthquake record

Parameter	Vertical Test	Controlled-Displacement Test	Earthquake Response Test
Mass, m	6.12 Mg	146.9 Mg	1046 Mg
Reinforced Rubber Radius, R	7.6 cm	24.1 cm	55.9 cm
Lead Core Radius, a	1.5 cm	7.0 cm	15.3 cm
Lead Core Height, h_L	11.7 cm	22.4 cm	33.3 cm
Rubber Layer Thickness, t_r	0.30 cm	0.95 cm	0.80 cm
Number of Rubber Layers, n	20	16	26
Yield Force, f_{yield}	9.85 kN	208 kN	1303 kN
Yield Displacement, u_{yield}	0.32 cm	0.7 cm	3.0 cm
Yield Stiffness Ratio, α	0.067	0.036	0.046
Damping Coefficient, c_d	N/A	1280 Ns/cm	890 Ns/cm
Initial Lead Yield Stress, σ_{Lo}	N/A	13.0 MPa	16.9 MPa

Table 4.7: Input parameters of LR bearings used in validation tests

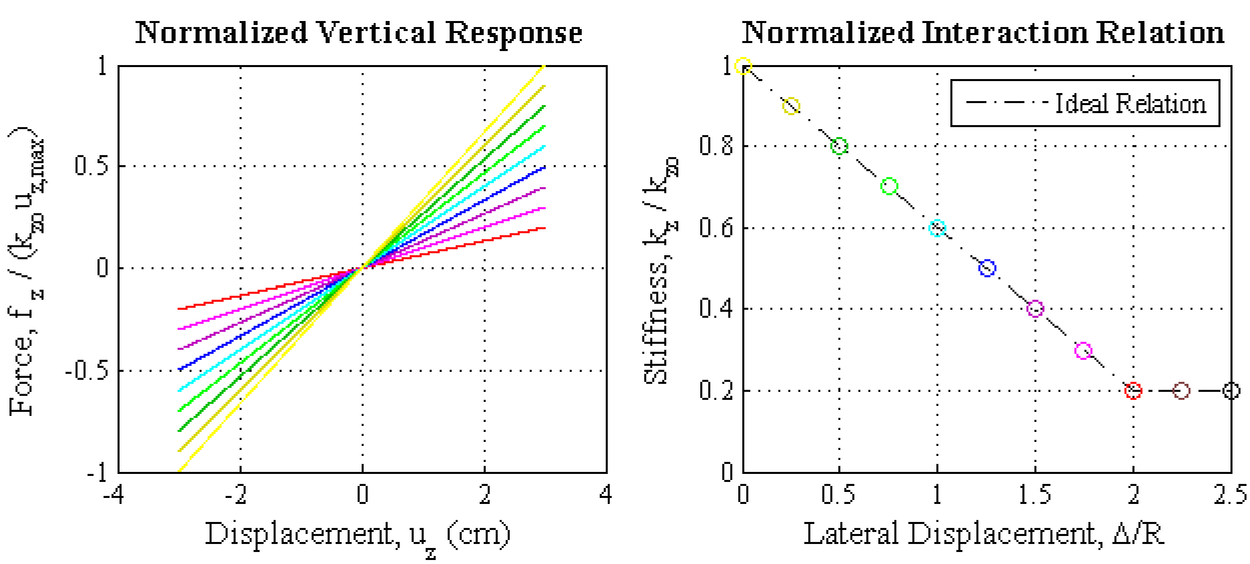

Figure 4.39: Vertical validation test results

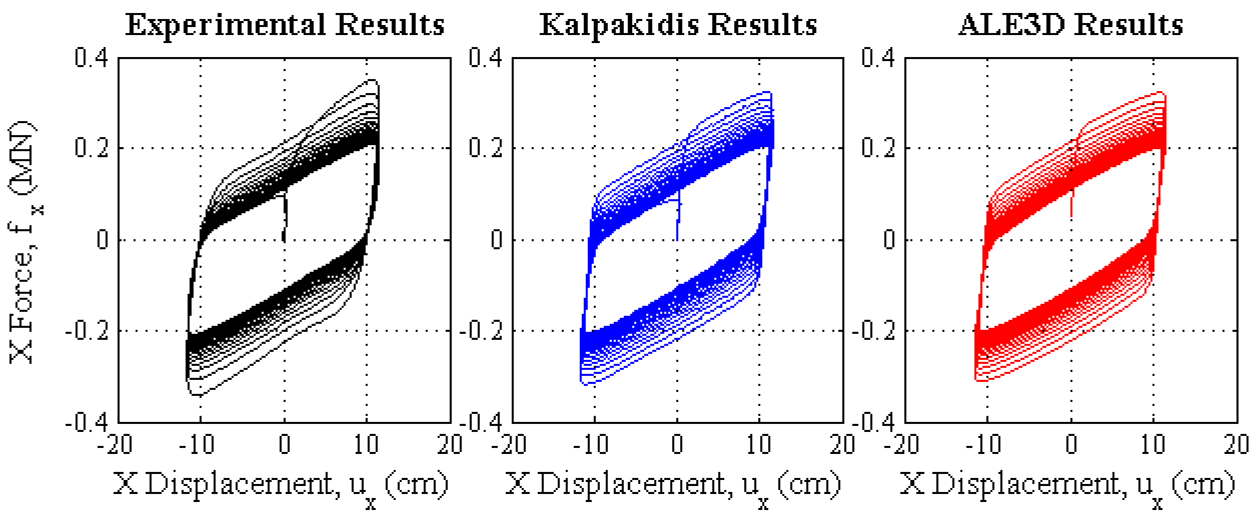

Figure 4.40: Comparative directional hysteresis of the robust LR models for the uni-directional sine wave displacement orbit

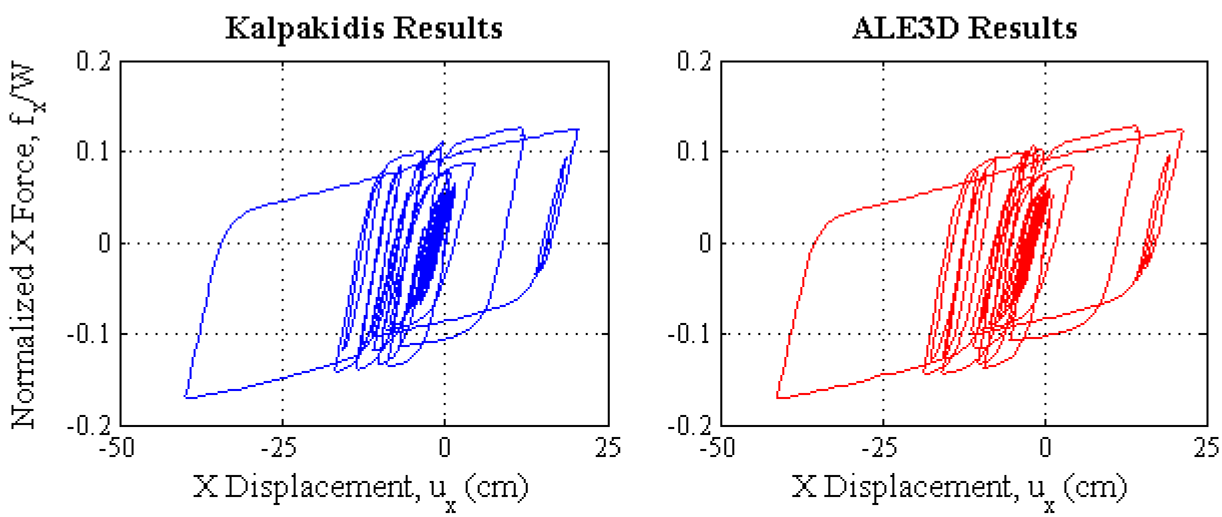

Figure 4.41: Comparative directional hysteresis of the robust LR models for the unrestrained response to the 1978 Tabas earthquake record

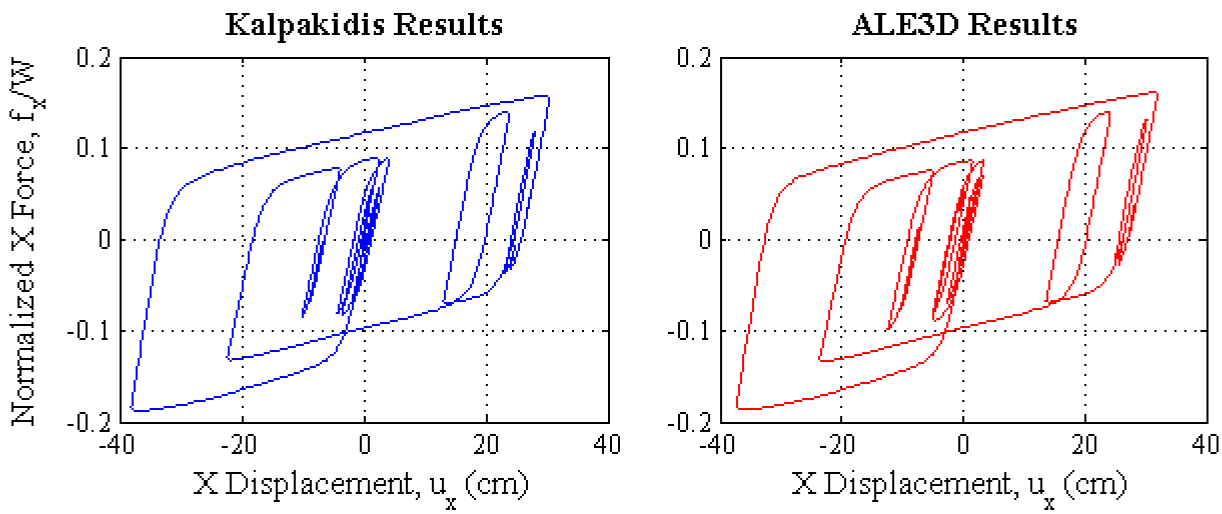

Figure 4.42: Comparative directional hysteresis of the robust LR models for the unrestrained response to the 1994 Northridge earthquake Rinaldi record

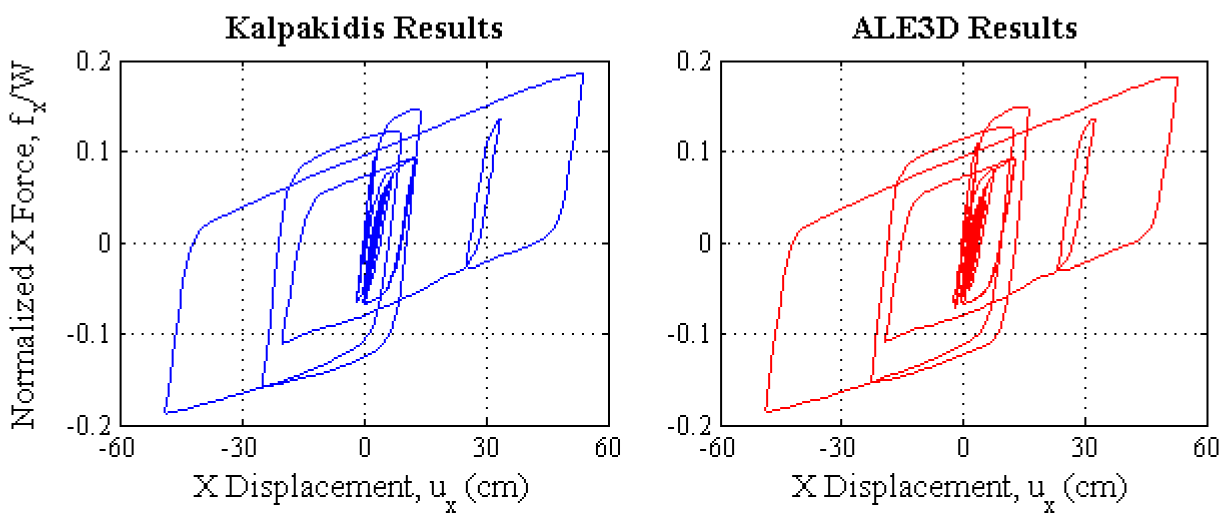

Figure 4.43: Comparative directional hysteresis of the robust LR models for the unrestrained response to the 1995 Kobe earthquake record

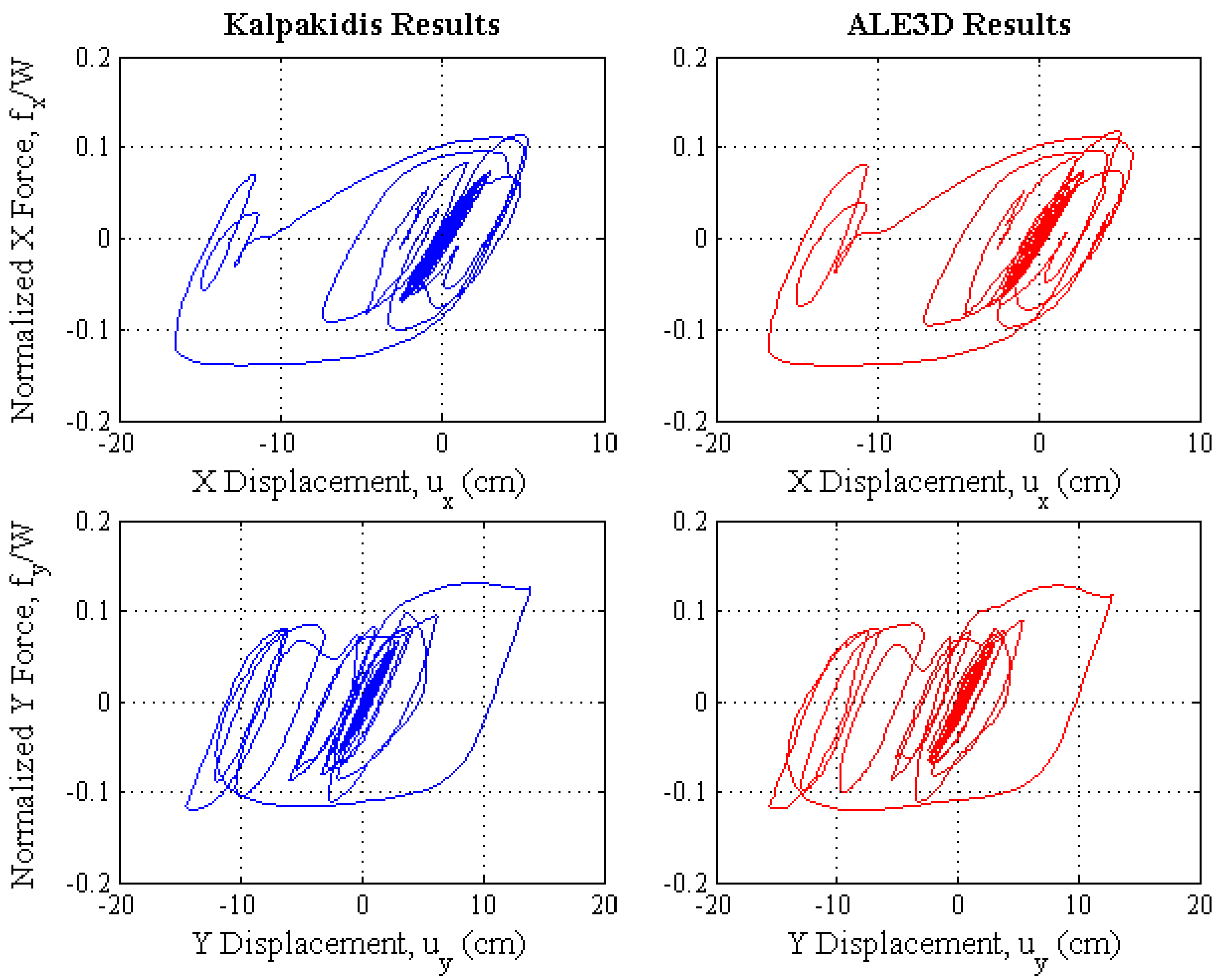

Figure 4.44: Comparative directional hystereses of the robust LR models for the unrestrained response to the 1999 Duzce earthquake Bolu record

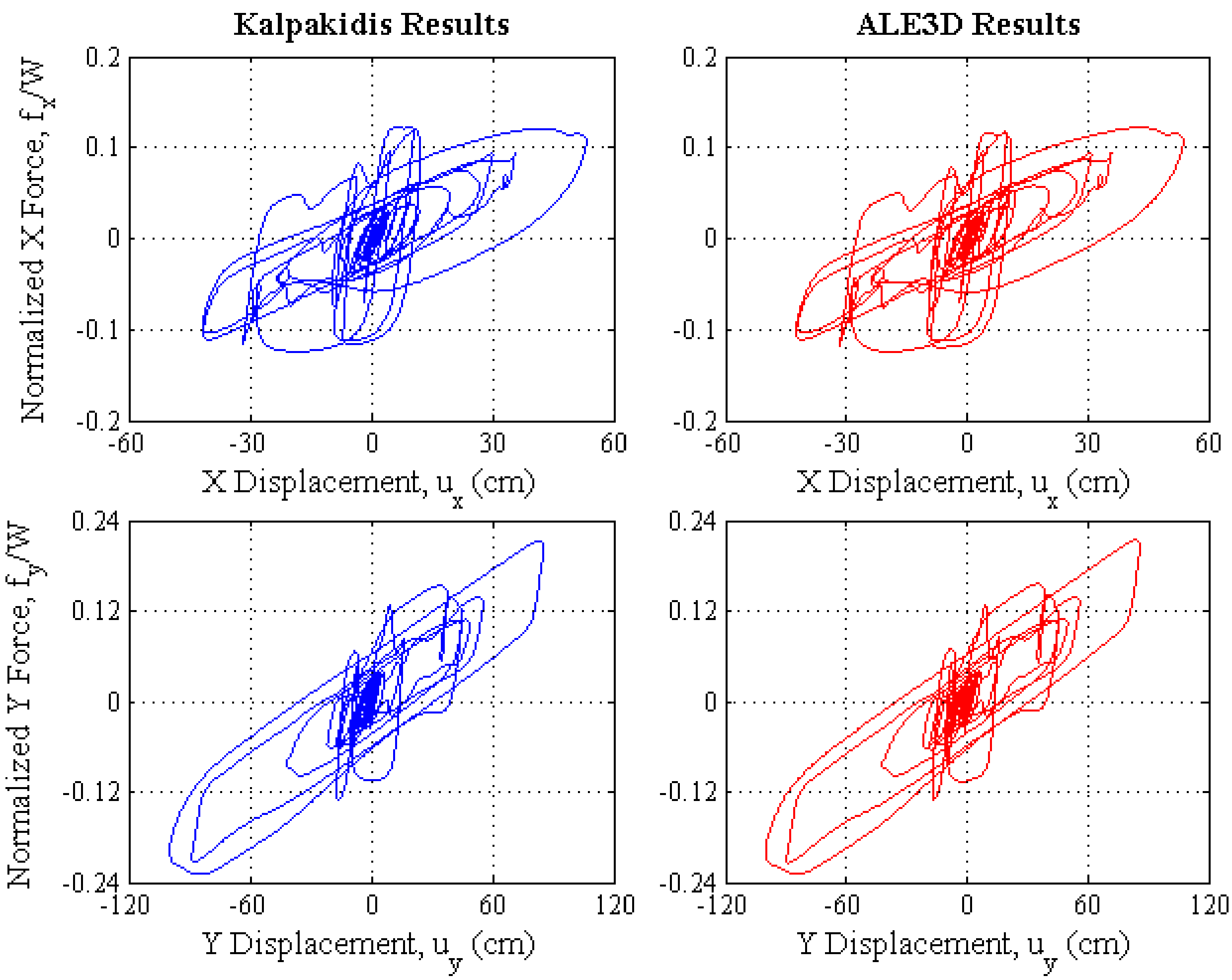

Figure 4.45: Comparative directional hystereses of the robust LR models for the unrestrained response to the 1999 Chi-Chi earthquake TCU065 record

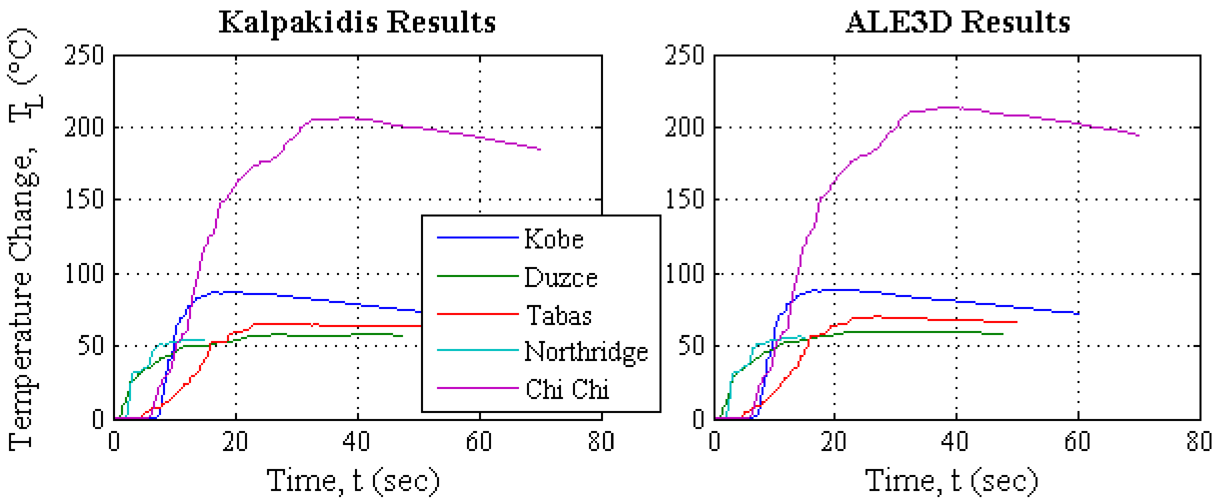

Figure 4.46: Comparative lead core temperature change time histories of the robust LR models for the unrestrained earthquake response tests

4.5 Bearing Damage and Failure

Much of the apprehension preventing full US NRC support of an NPP design utilizing SBI centers around the concepts of damage and failure of bearings, particularly as they pertain to reliability and redundancy under BDBE excitation. Bearing damage and failure in SBI bearings have not been analyzed as extensively as service-level mechanical and dynamic properties, and as such, specific limit states, as well as the dynamic response near the capacity limits, are based on theoretical analysis and a limited number of experimental tests where such limits were observed.

The distinction between damage and failure is not always clear, and can lead to confusion. SBI damage is any deterioration of a material component or response property, generally caused by a physical change, which cannot be recovered. SBI failure refers to any response which inhibits adequate functioning of the bearing device. It should be noted that damge can occur without failure and failure without damage, although excessive amounts of damage can eventually lead to failure. The different types of bearing damage and failure for friction and elastmeric SBI bearings are described in Sections 4.5.1 and 4.5.2, respectively. Finally, Sections 4.5.3 and 4.5.4 discuss the concepts of progressive failure and property variability.

4.5.1 Friction Bearings

Observations of experimental tests utilizing FP and TFP bearings have shown damage and undesirable performance are possible, but specific limit states of bearings have not been widely analyzed (Troy Morgan, personal communication, October 4, 2012). High pressure and temperature can cause shedding of the bearing liner, and deterioration of the rubber casing due to contact with the restrainer has been noted, but the effects of these on performance are still unknown.

The main concern regarding friction bearings is the possibility of uplift, which could lead to overturning or cause the top concave to displace past the restrainer liimits. Experiments were performed that mechanically displaced the bearing, lifted the top concave, displaced the top concave in a separate direction, and subsequently lowered the top concave (Troy Morgan, personal communication, October 4, 2012). Recontact occurred cleanly as the inner slider was able to quickly move and deform to the new positioning of the top concave. Thus, uplift should not necessarily be considered a failure mode although future testing should focus on the stability of the inner slider during motions that may naturally induce uplift. In any location where the probability of uplift is considered prohibitive, FP bearings with tension-carrying capabilities may be used.

When a friction bearing reaches its displacement capacity and contacts the restrainer, the bearing generally does not fail, and conversely, restrainers have been witnessed to deform in response to contact (Troy Morgan, personal communication, October 4, 2012). Nevertheless, contact with restrainer may transmit deleterious accelerations and forces to the superstructure, rendering the bearing ineffective at that moment. Thus, contact with the restrainer under DBE excitation is considered a practical limit state. Future research should attempt to qualitatively assess the resulting effects of contact with the restrainer for BDBE. In cases where this risk is too large, resizing the restrainer diameter should be considered part of the design basis.

4.5.2 Elastomeric Bearings

The study of elastomeric bearing failure is mainly concerned with limit states relating to shear and axial loading. A number of studies have observed stable, undamaged bearing behavior at shear strains in excess of 400% (Feng et al., 2000). However, at larger strains, tearing of the rubber material and delamination of the rubber and steel shim layers have been observed. Experiments by Kasalanati and Constantinou (1999) noted that post-test inspection revealed delamination in one HDR bearing (likely due to improper curing), despite having little change in bearing response and no occurrence of catastrophic failure. LR tests by Tyler and Robinson (1984) also showed fracturing of the lead core, discovered during post test inspections. Thus, although individual material within an LR bearing may fail, these should only be considered damage since they do not necessarily induce failure.

Numerous publications have analyzed the mechanics governing the compression and tension buckling of elastomeric bearings. Kelly (1997) used a two-spring model to solve for the critical compression buckling load, $P_{cr} \approx \pm\sqrt{P_S P_E}$, where the shear rigidity, P_S, is given in Equation 4.73 and the Euler buckling load, P_E, is presented in Equation 4.74. Combined bending and compression can also cause bursting of the steel shims (Kelly and Konstantinidis, 2011).

$$P_S = GA_s = GA_b \frac{h}{T_r} = \pi G(R^2 - a^2)\frac{h}{T_r} \tag{4.73}$$

$$P_E = \frac{\pi^2 EI_s}{h^2} = \frac{\pi^2 EI}{hT_r} \tag{4.74}$$

Tension buckling is more complex. Under pure tension where the bearing is locked without any shear deformation, the rubber undergoes cavitation. However, in real conditons when the bearing is also undergoing laterally deformation, the tensile load is handled by means of shear in the bearing (Kelly and Konstantinidis, 2011).

4.5.3 Progressive Failure

Progressive failure refers to the possibility of a single bearing failure inducing additional failure in other bearings under the same structure, in a cascading fashion. Although this behavior has never been observed in experiments or actual structures utilizing SBI, engineering measures should be taken to reduce this specific risk. Similar to the protocol in structures with multiple columns, a procedure for reducing risk of progressive failure in structures utilizing SBI should be to assure the structure can support the superstructure gravity load after the loss of any single isolator. Regular inspection and testing should be required to identify and replace any failed bearings. In the situation where a bearing fails as a result of earthquake excitation, the proper design of the seismic gap as well as collision restrainers and bumpers can ensure progressive failure is avoided.

4.5.4 Property Variability

As with any engineering material, a certain amount of property variability is expected. Consequently, the rubber stiffness and damping in LR bearings, as well as the friction coefficients in FP and TFP bearings, may differ significantly from the ideal value. This variability was analyzed in Huang et al. (2009) and experimental tests run by Kasalanati and Constantinou (1999) attributed incurred damage in one of the bearings to improper curing. Although there will always be variability between individual isolators, testing of all isolators prior to installation is sure to be a requirement for NPP structures to assure adequate strength and damping exists. Additionally, the periodic testing of spare or temporarily-removed isolators should be required to diagnose any detrimental aging or creep effects.

Chapter 5

Superstructure Design

The structural design of an NPP must provide two main functions. Primarily it must house and protect equipment and safety-related systems, structures, and components (SSCs) against a myriad of internal mechanical demands, as well as external loading from environmental and man-made threats, such that emergency shutdown capabilities are preserved. To satisfy this function, all sources of sources of risk including extreme seismicity, weather effects, high temperatures and pressure, adverse chemical conditions, interaction with auxiliary structures, and human attack should be considered and designed for. Secondarily, but of equal importance, the structure must provide a physical barrier, or shield, to block radiation as well as any accidental radioactive material leak from affecting the outsied environment. Thus the structural design dually serves to protect the nuclear processes from the external environment, and protect the environment from the nuclear processes. To this end, accurate portrayal of structural members, densities, and material properties is essential.

This chapter describes the various aspects of the analyzed superstructures. Section 5.1 describes the FEM models considered as well as the materials that comprise them. Section 5.2 discusses the inclusion of equipment in the superstructure models. Sections 5.3 and 5.4 describe the foundation and isolation systems, respectively, which connect the superstructure to the soil column.

5.1 Superstructural Models

Numerical analyses of NPP structures often employ lumped-mass stick (LMS) models to aproximate the response of the containment structure, internal structures, and major equipment (Huang, 2008). However, such a characterization neglects to model proper mass and stiffness distribution in the structure, hindering accurate portrayal of soil-structure interaction, and interaction between various structures and equipment (Hossain, 2004). Thus, this study utilizes finite element method (FEM) models similar to those presented in Xu et al. (2006) to overcome the shortcomings of other superstructure characterizations.

5.1.1 Materials

Nuclear power structures are generally designed with large reinforced-concrete (RC) shells, which provide structural strengh as well as significant radiation shielding. Additionally, some designs utilize structural steel members at locations with high demand or anticipiated tension. Steel plates may be utilized as cast-in-place forms or as containment vessels for individual equipment. The simplified FEM meshes presented herein utilize a single RC material for a majority of the superstructure. The material properties of the 27.58 MPa (4000 psi) concrete used in Xu et al. (2006) are presented in Table 5.1. It should be noted that ALE3D is only capable of setting a single mass-proportional damping over all regions or materials, and therefore no damping besides the hysteretic damping in the isolators is present in the model. Steel reinforcement with yield strength, f_y = 413.7 MPa (60 ksi), is added in all three dimensions of all concrete members at a constant volume ratio, ρ_s, of 1.0%. These concrete and rebar specifications fall within the guidelines of ASCE43-05.

Design guidelines for NPP structures utilizing SBI require linear-elastic behavior of the supported superstructure subjected to DBE loading (ASCE43-05, 2005). Although base isolation has the ability to reduce the demand on structural members, SBI implementation is not likely to result in significant member size reductions since radiation shielding is still required.

In the ALE3D analyses described, the superstructure concrete is characterized using a non-linear, inelastic DTRA concrete model which is meant to reproduce Model 45 in DYNA3D (ALE3D, 2011b). This is one of two models which allows for consideration of steel reinforcement. Although this model conservatively overestimates inelasticity resulting from cyclic loading, it does not require complex calibration, and therefore is used here. The model is comprised of elasticity parameters, entered in ALE3D model "elasmodel 7", a yield surface model, "ysmodel 107", a failure surface model, "hardmodel 207", and a compaction model, "eosmodel 307". The only elasticity parameter for this model is Poisson's ratio, ν, and a table is used to define the yield parameters in the yield surface model. The failure surface model includes strain hardening and softening phenomena, which characterize the effect of a strain parameter, η, and strain rate enhancement factor, β, on the damage level, λ. Additionally, it stores the accumulated inelastic strain, ε_{in}, and material flow strength, $\bar{\sigma}$, for determination of failure. The compaction model simulates the effect of changes in volumetric strain, ε_v, on the pressure, p, and elastic bulk modulus achieved during unloading, K. The inelastic DTRA model was utilized in ALE3D for two purposes: to detect if inelasticity occurs in the superstructure, and to gauge whether or not any induced inelasticity has a significant effect on the structural response.

5.1.2 Cylindrical Plant

The cylindrical plant design was based on the model used in Xu et al. (2006), which was meant to represent a typical conceptual design for advanced reactors with a lateral period of 0.19 sec when partially embedded. The design, shown in Figure 5.1, is 46.0 m tall with an outer footprint diameter of 26.0 m, resulting in an aspect ratio of 1.77. The cylindrical exterior walls are 1.0 m thick, and the main three interior walls, consisting of a central wall and two perpendicular walls separated by 13.6 m, are 2.0 m thick. These naturally form two large cavities intended for the reactor and power conversion vessels. The basemat, roof, and reactor vessel floor are 3.0 m, 1.0 m, and 2.0 m thick, respectively. Because this structure was designed to be fixed-based and partially-embedded, the aspect ratio is large when isolated, suggesting it may be susceptible to overturning.

The plant design was meshed using Cubit, a mesh generation software developed at Sandia National Laboratory. The resulting mesh, displayed in Figure 5.2, consists of 21 merged volumes with 164,520 hex elements totalling 10,167 m^3. The mesh size was chosen to have side length of at most 0.5 m with an aspect ratio of no more than 2 in any direction. All walls and floors were designed to have at least 4 elements across the smallest dimension (i.e. thickness). The total weight of the structural members is 350.5 MN. A breakdown of structural member volumes and weights, related by the RC weight density, w_c, is shown in Table 5.2. The fundamental fixed-base period of this superstructure was approximated from time history records as 0.26 sec. This is slightly longer than the period presented in Xu et al. (2008), which is expected since that was for a partially embedded structure.

5.1.3 Rectangular Box-Type Plant

The rectangular plant design was based on the model used in Xu et al. (2006), which was meant to represent an Advanced Boiling Water Reactor (ABWR) with a fundamental lateral period of 0.14 sec. The design, shown in Figure 5.3 is 78.0 m tall with a square footprint of side length 60.0 m, resulting in an aspect ratio of 1.30. The exterior walls are 2.75 m thick, reduced form the original thickness of 2.80 m for ease of modeling, and the interior walls are 2.0 m thick. The isolation slab is 5.0 m thick, which was altered from the original design which had a 10.0 m thick slab. This reduction was due to the fact that the original base was meant to serve as the foundation, and therefore was overdesigned for the purposes of a rigid isolation slab. The first floor, second floor and roof have thicknesses of 2.75 m, 1.75 m, and 1.75 m, respectively. In comparison to the cylindrical plant, this design is far more heavy and stout, putting it at a lesser risk for overturning.

The resulting mesh, displayed in Figure 5.4, consists of 92 merged volumes with 384,489 hex elements totalling 93,216 m^3. The mesh size was chosen to be at most 1 m^3 with an aspect ratio of no more than 2 in any direction. The total weight of the structural members is 2308 MN, significantly higher than the weight used in Xu et al. (2008). A takeoff of structural member volumes and weights, related by the RC weight density, w_c, is shown in Table 5.3 to defend the choice fo the structural weight used. The fundamental fixed-base period of this superstructure was approximated from time history records as 0.31 sec, which is longer than the design period as a result of the larger weight considered. Nonetheless, the structure is quite stiff and ideal for SBI implementation.

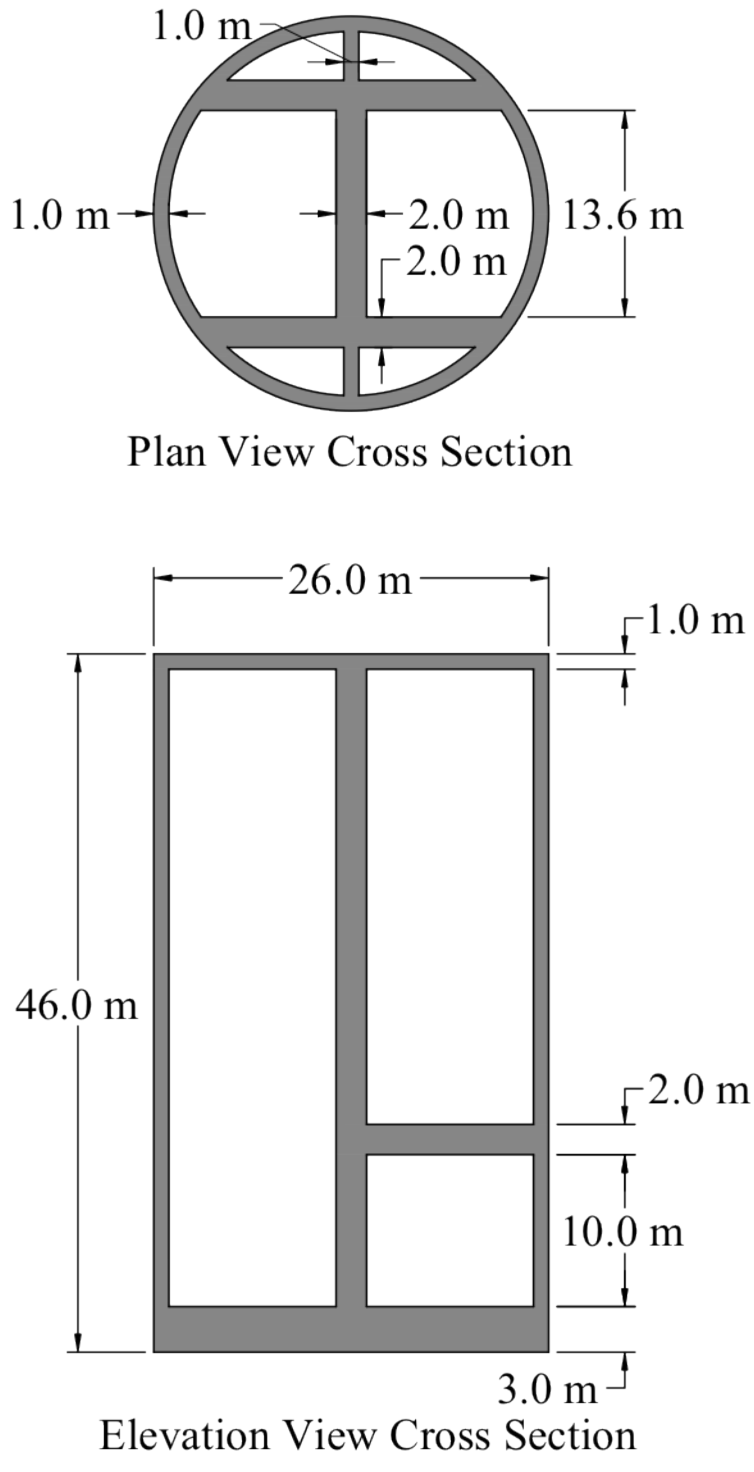

Figure 5.1: Plan and elevation view cross-section schematics of the cylindrical plant design

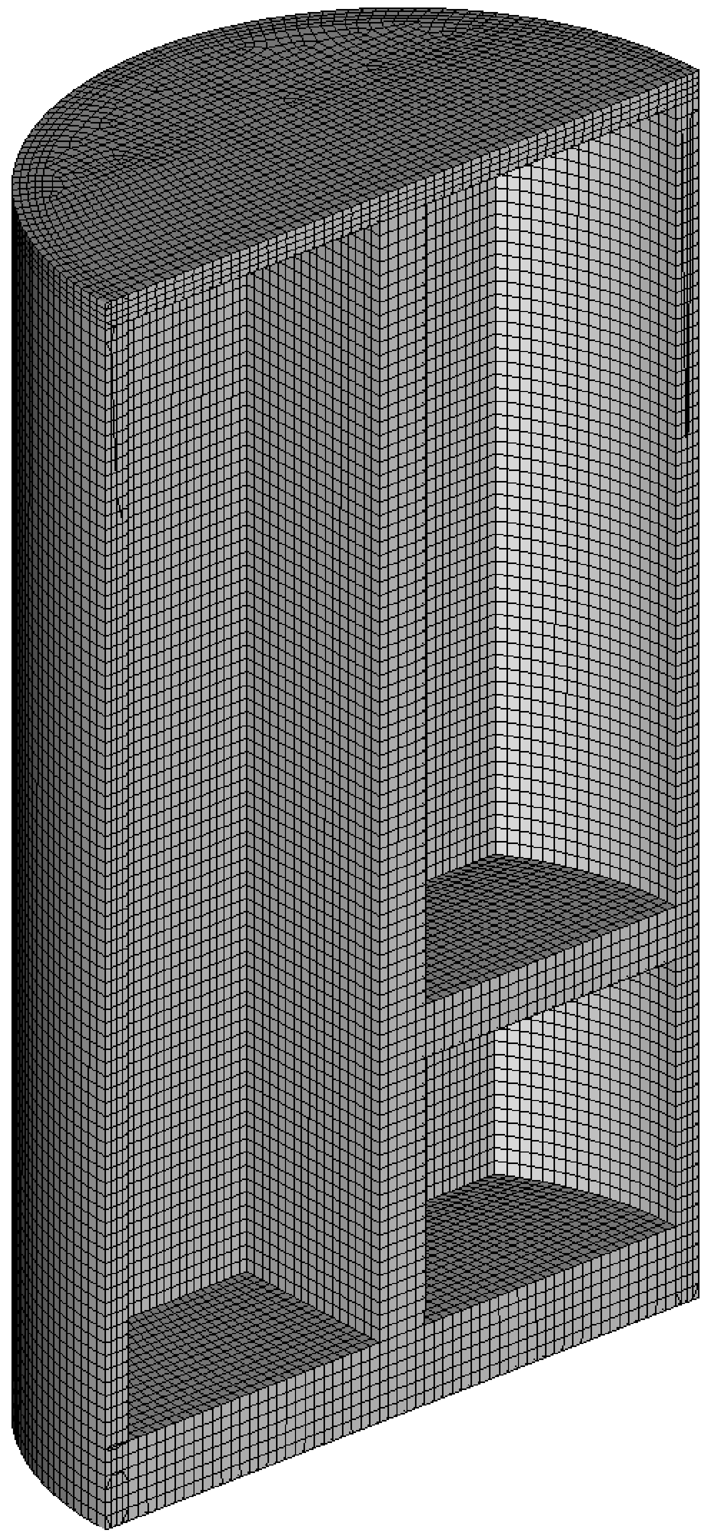

Figure 5.2: Cross-section of the cylindrical plant finite element mesh

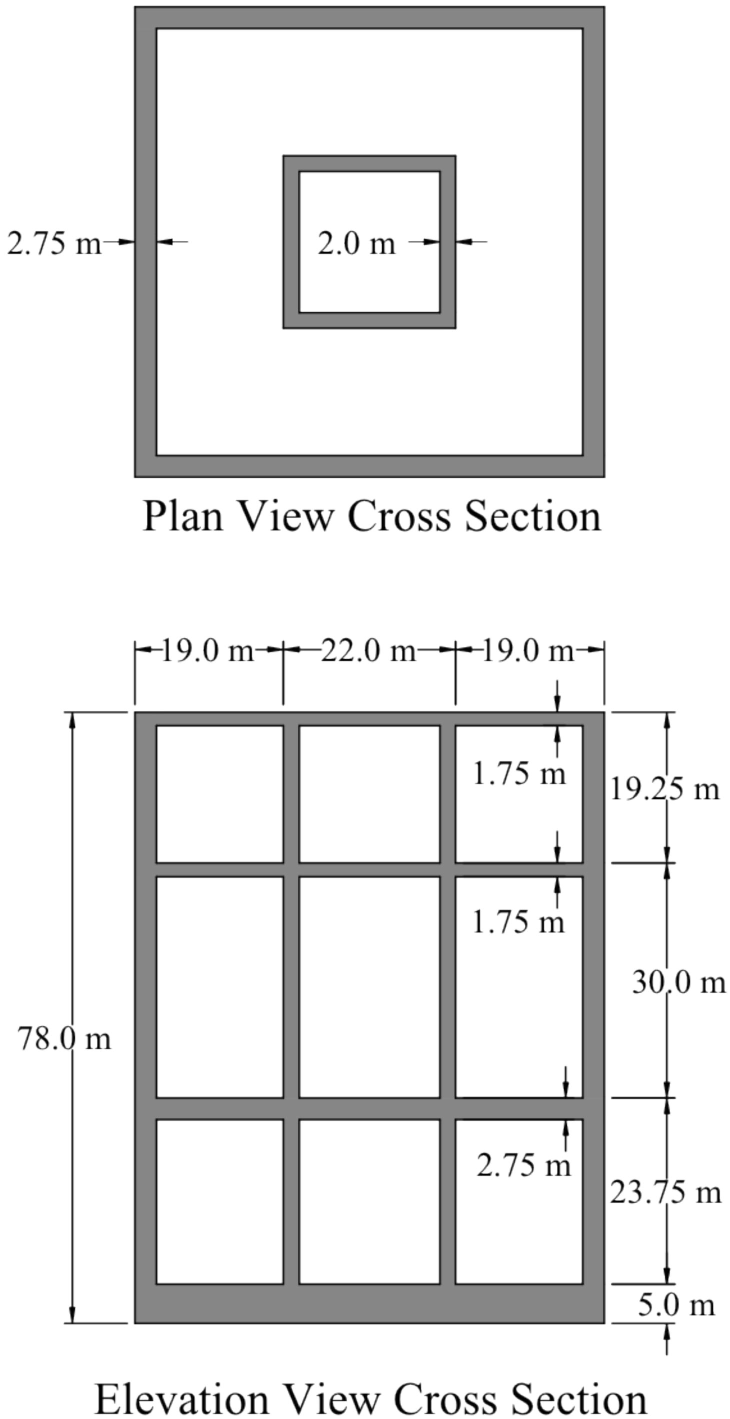

Figure 5.3: Plan and elevation view cross-section schematics of the rectangular, box-type plant design

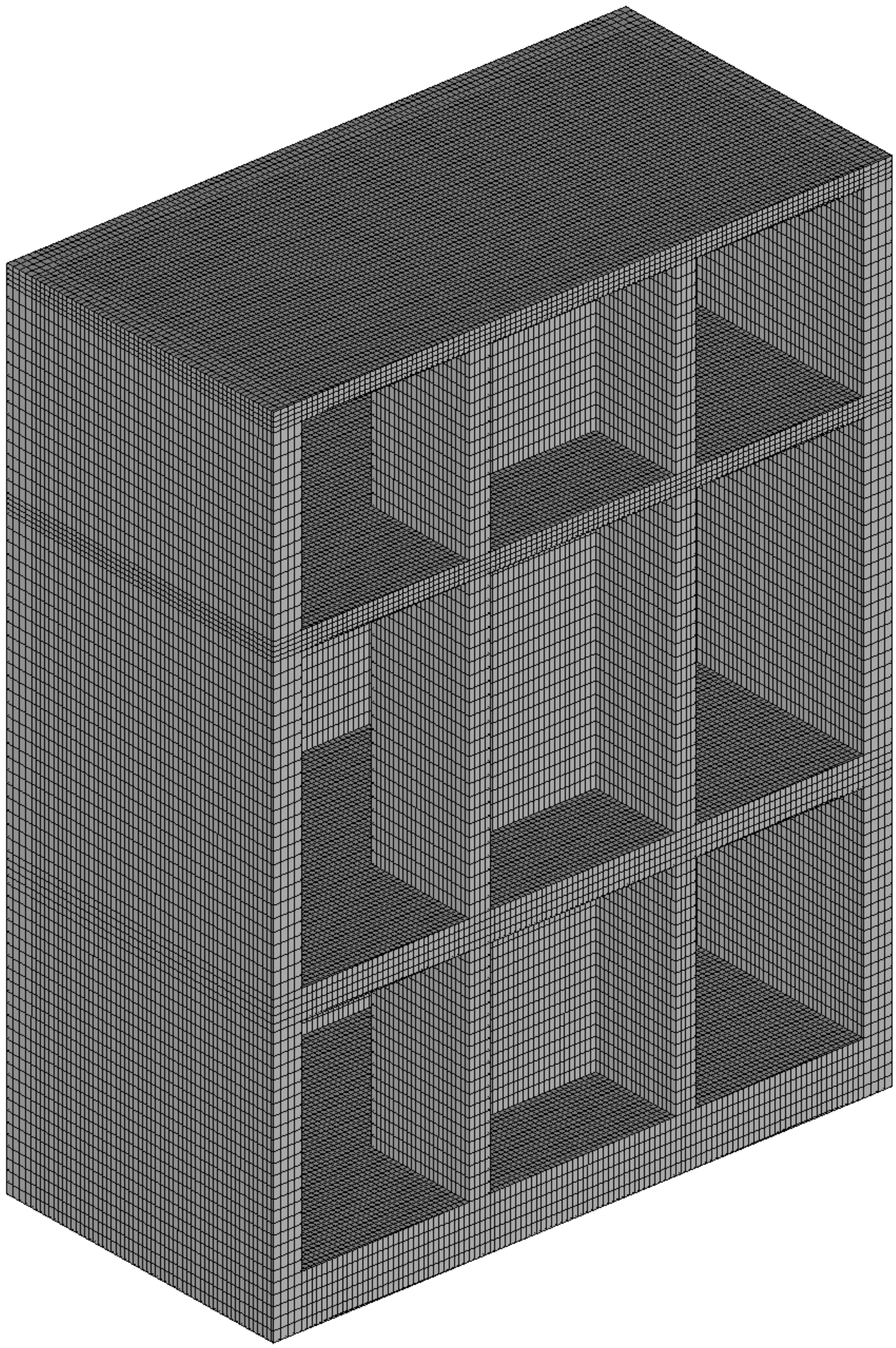

Figure 5.4: Cross-section of the rectangular, box-type plant finite element mesh

Property	Value
Compressive Strength, f'_c	27.58 MPa
Weight Density, w_c	23.57 kN/m^3
Young's Modulus, E_c	26.44 GPa
Poisson's Ratio, ν	0.20

Table 5.1: Material properties for the structural reinforced-concrete used in the analyses presented herein

Component	Volume, V (m^3)	Weight, W (MN)
Roof	531	12.5
Walls	7763	183.0
Basemat	1593	37.5
Interior Floors	281	6.6
Equipment	0	110.9
Total	10167	350.5

Table 5.2: Volume and weight takeoff for the cylindrical structure

Component	Volume, V (m^3)	Weight, W (MN)
Roof	6300	148
Walls	52716	1243
Basemat	18000	424
Interior Floors	16200	382
Equipment	0	111
Total	93216	2308

Table 5.3: Volume and weight takeoff for the rectangular structure

5.2 Equipment

The characterization of complex equipment and substructure response within NPP structures (e.g. reactors, generators, mechanical cranes, containment vessels, etc.) is typically accomplished by implementing one or more LMS models within the finite element mesh. The LMS model frequencies and masses are chosen to match those of the equiment they are characterizing such that proper lateral dynamic response and structure-equipment interaction is modelled. In Xu et al. (2006), two LMS models were implemented to approximate the response of reactor and power conversion vessels weighing 8229 kN and 13520 kN, respectively. All other equipment weight, summing to 88960 kN, was distributed over the structural volume for those studies.

In lieu of these LMS models, a series of eight LMS models was designed by Quazi Hossain

No	Frequency, f (Hz)	Legnth, L (m)	Distributed Mass, m_L (kg/m)	Moment of Inertia, I (m^4)	Nodes, n
1	1	2	1.130×10^6	2.884×10^{-4}	3
2	21	2	5.650×10^5	6.360×10^{-2}	3
3	7	8	1.130×10^5	3.618×10^{-1}	5
4	14	4	5.650×10^5	4.523×10^{-1}	3
5	14	4	1.130×10^5	9.045×10^{-2}	3
6	5	8	2.825×10^5	4.615×10^{-1}	5
7	7	2	5.650×10^5	7.066×10^{-3}	3
8	21	4	2.260×10^5	4.070×10^{-1}	3

Table 5.4: Ideal dynamic properties for the lumped-mass stick models

(2012) to model a range of expected equipment frequencies, f, in small modular reactors (SMRs). The design mass per unit length, m_d, was scaled from the original formulation, such that the net weight matched the total equipment weight specified in Xu et al. (2006). The moment of inertia, I, was then calculated by using Equation 5.1, which is derived from the formula for the natural period of a rod with uniformly-distributed mass. In doing so, the frequencies, and lengths, L, were left unchanged. The material is assumed to be steel with an elastic modulus, $E_c = 200$ GPa.

$$I = 3.1906\frac{m_d L^4}{E_c} f^2 \tag{5.1}$$

The resulting design properties of the eight LMS models are listed in Table 5.4. Note that each stick model comprises either 3 or 5 nodes, n, connected by beams. 25% of the total equipement weight is used in the LMS models, such that the resulting models are of similar weight to the original reactor and containment vessel LMSs. The rest of the mass is distributed evenly over the superstructure volume, such that the concrete weight density, w_c, becomes 31.74 kN/m^3 and 24.32 kN/m^3 for the cyclidrical and rectangular plants, respectively. The distributed mass, m_L, is set at 11.5% of the total LMS mass, or $0.0288 m_d$. The density of each beam material, ρ, is altered such that this distributed mass is achieved, significantly increasing the analysis timestep, Δt. The remaining mass, $m_{LMS} = 0.221 m_d L$, is divided among the lumped-mass nodes based on tributary area (thus outer nodes have mass, $\frac{1}{2(n-1)} m_{LMS}$, and inner nodes have mass, $\frac{1}{n-1} m_{LMS}$). The nodes are evenly spaced over the length of the stick as shown in Figure 5.5.

Individual stick models were input into ALE3D as cylindrical beams with the prescribed lengths, connecting nodes with the prescribed lumped-mass. Validation tests were run by inputing initial velocities in the approximate shape of the first mode on the nodes of the stick models, and altering the moment of inertia for each until the ideal frequency was approximated. The results of these tests are shown in Figure 5.6. The final total stick masses, m_{LMS}, as well as the beam density, ρ_b, inner diameter, d_{in}, and outer diameter, d_{out},

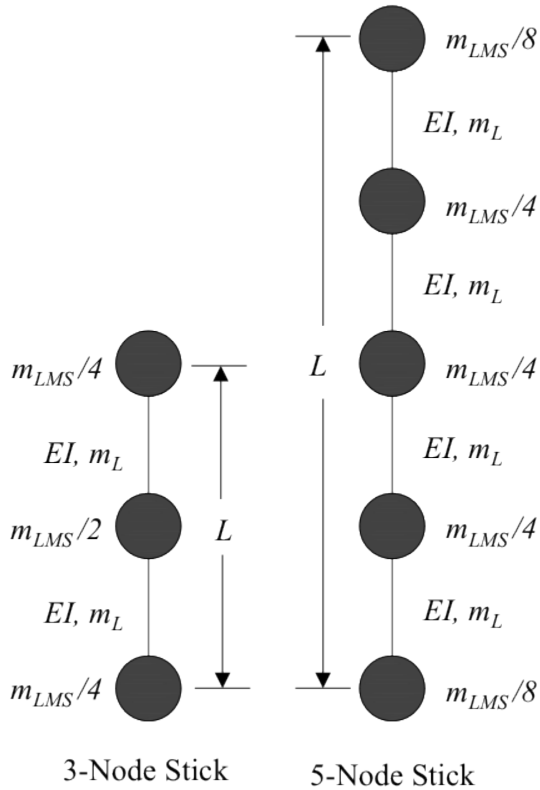

Figure 5.5: Lumped-mass stick model composition

are listed in Table 5.5. It should be noted that beams in ALE3D are treated as infinitesimally-thin, one-dimensional objects connecting two points. Associated dimensions are only used to calculate masses and stiffnesses.

The stick models were designed to be placed in a variety of locations along the height of the structure. Sticks 1 and 2 are to be located on the first floor (i.e. isolated slab), 3 and 4 on the second floor, 5 and 6 on the third floor, and 7 and 8 on the roof. For the rectangular structure with 3 floors and a roof, the stick layout matched exactly. For the cylindrical structure, only 2 floors and a roof exist, so sticks 1 through 4 are all located on the isolated slab, and the rest are distributed in pairs on the other levels. For each floor, the sticks with the lower frequencies are placed in the center of the floor where the diaphragm is most-flexible. Contrarily, the sticks with the larger frequencies are placed 1.5 m from interior corners in both directions where the diaphragm is stiffest. These locations are chosen to excite the fundamental modes of the individual sticks. Steel reinforcing beams are added across two nodes in each direction in order to prevent piercing, and to distribute the dynamic response of the sticks over a wider area.

No	Mass, m_{LMS} (Mg)	Density, ρ (g/cm^3)	Inner Diameter, d_{in} (cm)	Outer Diameter, d_{out} (cm)
1	565	500	14.7	32.3
2	282.5	10	55.6	154
3	226	2	89.0	169
4	565	2	80.0	331
5	113	2	60.0	156
6	565	10	106	147
7	282.5	10	25.6	146
8	226	2	90.4	223

Table 5.5: Lumped-massl stick model masses and geometry

5.3 Foundation Model

For simulations involving underlying soil, rectangular foundation models are presented to transfer soil excitations to the isolation units, and to distribute structural forces to the soil column. The foundation is modeled using an RC concrete slab with thicknesses of 5 m and 8 m for the cylindrical and rectangular plants, respectively. The width of the slab is chosen as the width of the superstructure plus 5 m on each side in order to account for distribution of the bearing force. The same material model and reinforcement parameters used for the superstructure are employed for the foundation model. Steel plates were used in the top two mesh layers of each foundation in order to spread the isolation bearing forces without inducing concrete crushing. Note that this is the same procedure used at the bottom of the superstructures.

5.4 Isolation System Models

Separate isolation system designs were completed for FP, TFP, and LR bearings. For each, design targets were set for an effective period, $T_{eff} = 3$ sec, and equivalent viscous damping, $\zeta_{eq} = 15\%$, at the DBE-level excitation. The same bearing designs are used for each superstructure, with the only change being the quantity and spacing of isolators such that the average bearing pressure is approximately equal.

The design basis is characterized by the 30 scaled ground motion records described in Chapter 6. The scaled response spectra for DBE excitation at 5% damping are displayed in Appendix B. The displacement and acceleration response parameters, S_d and S_a, are evaluated at the design period in both lateral directions for 5% damping and are listed in Table 5.6. The directional quantities are combined using an SRSS approximation, which conservatively assumes simultaneous occurence of peak directional responses. The mean of the combined properties were calculated as 85 cm and 0.38 g for the displacement and acceleration, respectively. These are considered the design basis for the system damped at 5%. Conversion to target damping ratios other than 5% is achieved through the use of a spectral reduction factor, H. Equations for H exist in many publications, including ASCE7. For this study, H is calculated using Equation 5.2 proposed by Kawashima and Aizawa (1986).

$$H(\zeta) = \frac{1}{40\zeta + 1} + 0.5 \tag{5.2}$$

After using Equation 5.2, the design displacement, u_m, and acceleration become 61 cm and 0.27 g, respectively. The resulting design shear, V_m, is then found as $0.27P$. The MCE-level event is generally found by scaling the DBE parameters. It has been suggested that the scaling term should be as high as 3 (Huang et al., 2009), but for this study it will be set as 2, making the MCE displacement 120 cm. Note that this scaling term is very important for designing the maximum displacement capacity of an isolation bearing as the bearing must be able to sustain gravity load under 90% of the peak MCE displacement (Huang et al., 2009).

The dead load weight calculated in Section 5.1 only accounts for structural members and internal equipment. These weights are increased by 20% to include live loads on the structures. The resulting total vertical overbearing force for the cylindrical and rectangular structures then becomes 420.6 MN and 2769 MN, respectively.

5.4.1 FP Bearing Design

Single FP bearings are designed for a given design displacement, u_m, and overbearing force, P, using the iterative approach described below. An FP isolation system is designed by specifying the sliding surface radius, R, displacement restraint diameter, d_o, slider diameter, d_i, friction coefficient, μ, and bearing height, h, as well as the quantity, N, and layout of isolators.

The characteristic strength, Q, and post-yield stiffness, k_d, can be related to the bearing properties through Equations 5.3 and 5.4. From these, the peak force, attained at u_m, can be calculated as shown in Equation 5.5 and compared to V_m.

$$Q = \frac{P\mu}{N} \tag{5.3}$$

$$k_d = \frac{P}{NR} \tag{5.4}$$

$$F_{max} = Q + u_m k_d \tag{5.5}$$

After a trial solution is determined, the effective stiffness, k_{eff}, effective period, T_{eff}, and equivalent damping, ζ_{eq} can be determined as shown in Equations 5.6 through 5.8 and compared to the target parameters. Note that the latter equation is based on the ratio of

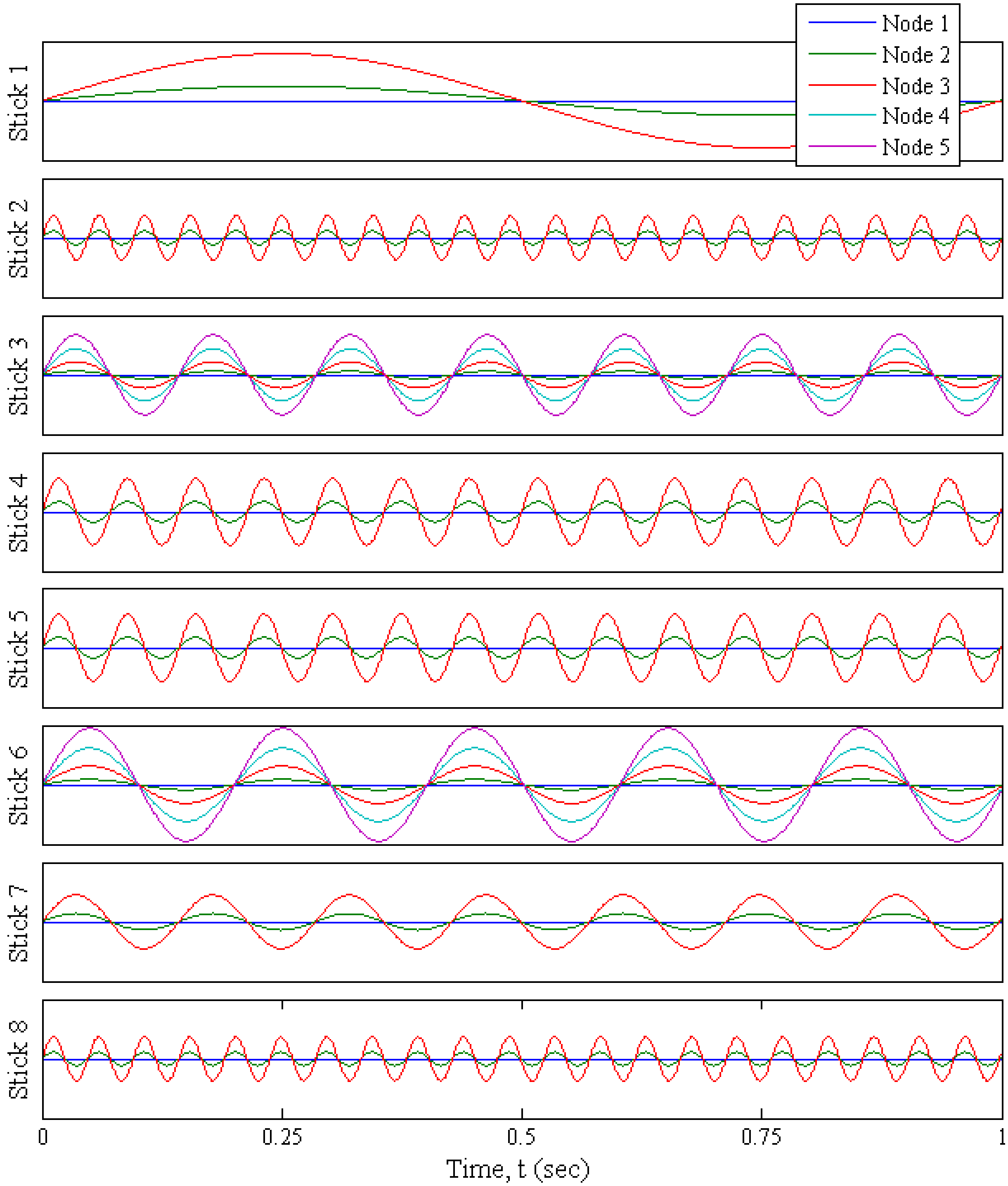

Figure 5.6: Displacement time histories for validation of stick model frequencies

No	Event Name (Record)	S_{dx} (m)	S_{dy} (m)	S_d (m)	S_{ax} (g)	S_{ay} (g)	S_a (g)
1	Imperial Valley (G-ELC)	0.19	0.26	0.32	0.08	0.12	0.14
2	Hollister (C-HCH)	0.16	0.24	0.29	0.07	0.11	0.13
3	Hollister (B-HCH)	0.45	0.32	0.55	0.20	0.14	0.24
4	Point Mugu (PHN)	0.46	0.20	0.50	0.21	0.09	0.23
5	Livermore (A-ANT)	0.31	0.81	0.86	0.14	0.36	0.39
6	Livermore (A-KOD)	0.69	0.53	0.87	0.31	0.24	0.39
7	Livermore (A-SRM)	0.29	0.75	0.81	0.13	0.34	0.36
8	Taiwan (05O07)	0.22	0.41	0.46	0.10	0.18	0.21
9	Westmorland (PTS)	1.17	1.03	1.56	0.52	0.46	0.69
10	Double Springs (WOO)	0.48	0.19	0.51	0.21	0.08	0.22
11	Friuli (B-BUI)	0.44	0.61	0.76	0.20	0.27	0.34
12	N Palm Springs (MVH)	0.81	0.95	1.25	0.36	0.42	0.55
13	Irpinia (B-BIS)	0.37	0.31	0.48	0.17	0.14	0.22
14	Chi-Chi (TCU116)	0.82	0.69	1.07	0.37	0.31	0.48
15	Chi-Chi (TCU120)	1.04	0.85	1.34	0.46	0.38	0.60
16	Chi-Chi (TCU138)	0.40	0.52	0.66	0.18	0.23	0.29
17	Chi-Chi (TCU067)	0.59	0.68	0.90	0.26	0.30	0.40
18	Victoria (CHI)	0.53	1.00	1.14	0.24	0.45	0.51
19	Victoria (HPB)	0.61	0.63	0.87	0.27	0.28	0.39
20	Dinar (DIN)	0.69	0.52	0.87	0.31	0.23	0.39
21	Imperial Valley (H-ECC)	0.71	0.99	1.22	0.32	0.44	0.54
22	Superstition Hills (B-ICC)	0.47	0.63	0.78	0.21	0.28	0.35
23	Superstition Hills (B-WSM)	0.70	1.21	1.40	0.31	0.54	0.62
24	Superstition Hills (B-IVW)	0.89	0.97	1.32	0.40	0.43	0.59
25	Corinth (COR)	0.65	0.49	0.81	0.29	0.22	0.36
26	Northridge (MUL)	0.49	0.30	0.58	0.22	0.14	0.26
27	Northridge (LDM)	0.35	0.88	0.94	0.16	0.39	0.42
28	Northridge (GLE)	0.60	0.39	0.72	0.27	0.18	0.32
29	Kobe (SHI)	0.69	0.43	0.81	0.31	0.19	0.36
30	Loma Prieta (LGP)	0.89	0.47	1.01	0.40	0.21	0.45

Table 5.6: Spectral displacements and accelerations at $T = 3$ sec with 5% damping for the scaled input ground motions

the total area of the hysteretic loop, A_h, to the area under the line for the equivalent linear system, A_l.

$$k_{eff} = \frac{F_{max}}{u_m} \tag{5.6}$$

$$T_{eff} = 2\pi\sqrt{\frac{P}{Ngk_{eff}}} \tag{5.7}$$

$$\zeta_{eq} = \frac{A_h}{4\pi A_l} = \frac{2Q}{\pi F_{max}} \tag{5.8}$$

Once an acceptable combination of R, N, and μ are found, the other properties are found by imposing pressure and displacement limits. μ values vary with the normal pressure on the sliding surface, p (Constantinou et al., 1990). Therefore, it is standard practice to design the bearing with a p of approximately 55 MPa, and d_i is sized using Equations 5.9.

$$d_i = \sqrt{\frac{4P}{\pi Np}} \tag{5.9}$$

d_o is determined by assuring the required displacement for MCE motion, 120 cm, can be achieved prior to slider contact with the restraining surface. The available stroke for a given bearing is $\frac{1}{2}(d_o - d_i)$, which can be rearranged as shown in Equation 5.10 to solve for d_o.

$$d_o = 2u_m + d_i \tag{5.10}$$

The final FP design utilized a sliding surface with a radius of 3.05 m and a friction coefficient of 0.07. The bearing radius was chosen to match one of the standard radii for large bearings offered by Earthquake Protection Systems, Inc (EPS). The outer diameter of the surface is 3.00 m and the slider diameter is 0.55 m, giving the bearing a 1.23 m displacement capacity. These properties result in a bearing with an effective period of 3.01 seconds and equivalent damping ratio of 16.5% at the design displacement. These are within acceptable error of the ideal design properties at the design displacement. The height of the bearing is chosen to be 0.50 m.

The vertical stiffness of the bearing, k_z, is found by approximating the bearing as a column of height, h, and diameter, d_i, and using Equation 5.11, with E_c = 200 GPa. The vertical damping constant, c_z, is then found by utilizing Equation 4.41, with the mass determined from the average normal force per bearing. The full set of resulting isolator inputs for the ALE3D FP isolator function are displayed in Table 5.7.

$$k_z = \frac{E_c \pi d_i^2}{4h} \tag{5.11}$$

Parameter	Value
Verical Stiffness, k_z	950.3 MN/cm
Vertical Damping, c_z	356.8 kN-s/cm
Radius, R	304.8 cm
Friction Coefficients, μ	0.07
Rate Parameters, α	1.0
Yield Displacement, u_{yield}	0.0127 cm

Table 5.7: Input parameters for the FP analyses in ALE3D ("spring2")

5.4.2 TFP Bearing Design

Although the Becker model is set up for the possibility of different properties on all four surfaces, TFP bearings are typically designed with equal properties for the inner sliders (i.e. $\mu_1 = \mu_2$ and $R_1 = R_2$), as well as for the outer sliders (i.e. $\mu_3 = \mu_4$ and $R_3 = R_4$). The resulting force-displacement curve will be trilinear with an initial rigid segment, a stiff segment representing motion on the inner surfaces, and a flexible segment representing motion on the outer surfaces.

Special care should be taken to assure that of sliding on the outer surfaces is initiated prior to inner slider contact with the inner sliding surface restraints, a condition that would induce acceleration spikes in the response and eliminate the hardening segment prior to reaching the maximum bearing displacement. From Becker (2011), this is achieved by satisfying the design condition in Equation 5.12.

$$\mu_3 \leq \mu_1 + \frac{d_{o1} - d_{i1}}{2L_1} \tag{5.12}$$

The design proceedure of Section 5.4.1 is used for TFP bearings with slight variations to account for multiple sliding surfaces. The full set of resulting isolator inputs for the ALE3D TFP isolator function are displayed in Table 5.8. As with the FP bearing, the individual slider properties were chosen to match common sizes utilized by EPS. The final design results in an effective period of 3.44 seconds and an equivalent damping ratio of 16.7%. The longer natural period was necessitated by the modeling of the slider restrainer, which had to be made large enough to avoid contact during all motions. Subsequently, the outer dish radii had to be increased such that the surface slope at the restrainer edge was not too steep to prohibit application of small angle approximations.

5.4.3 LR Bearing Design

LR bearings are designed for a given design displacement, u_m, and overbearing force, P, using the iterative approach described below. An LR isolation system is designed by specifying the radius of steel-reinforced rubber (not counting cover), R, lead core radius, a, individual rubber layer thickness, t_r, individual steel reinforcing plate thickness, t_s, and number of

Parameter	Surfaces 1 and 2	Surfaces 3 and 4
Radius, R_n	50 cm	224 cm
Outer Diameter, d_{on}	60 cm	250 cm
Inner Diameter, d_{in}	50 cm	65 cm
Surface-to-Mid-Height Distance, h_n	15 cm	25 cm
Friction Coefficient, μ_n	0.03	0.06

Table 5.8: Input parameters for the TFP analyses in ALE3D ("spring3")

rubber layers, n, as well as the quantity and layout of isolators, N. Typical rubber and lead properties used for design are shown in Table 4.5.

The characteristic strength, Q, and post-yield stiffness, k_d, can be related to the bearing properties through Equations 5.13 and 5.14. Note that for the robust LR model, the inital yield stress of the lead core, σ_{Lo}, is taken as 13.0 MPa, since models with this value were validated in the displacement-controlled tests presented in Section 4.4.2. For the purposes of Q, the deteriorated yield stress during the third cycle, σ_{L_3}, is used and taken as 10.0 MPa, the lower bound for said parameter as suggested by Kalpakidis et al. (2010). The same report also suggests that $\sigma_{Lo} = 1.35\sigma_{L_3}$, which is nearly true for the chosen parameters. From these, the peak force, attained at u_m, can be calculated as shown in Equation 5.5 and compared to V_m.

$$Q = A_L\sigma_L = \pi a^2\sigma_L \tag{5.13}$$

$$k_d = \frac{GA_r}{T_r} = \frac{G\pi(R^2 - a^2)}{nt_r} \tag{5.14}$$

The ratio of post-yield stiffness to pre-yield stiffness, α, generally varies between $\frac{1}{20}$ and $\frac{1}{10}$. Here, α is set to $\frac{1}{15}$, and the yield force, f_{yield}, and yield displacement, u_{yield}, are found using Equations 5.15 and 5.16.

$$f_{yield} = \frac{Q}{1-\alpha} \tag{5.15}$$

$$u_{yield} = f_{yield}\frac{\alpha}{k_d} \tag{5.16}$$

After a trial solution is determined, the effective stiffness, k_{eff}, effective period, T_{eff}, and equivalent damping, ζ_{eq} can be determined as shown in Equations 5.6, 5.7, and 5.17, respectively, and compared to the target parameters. Note that the latter equation does not match Equation 5.8 because the unloading and reloading portions of the hysteretic loop are not approximately vertical, due to some portion of the lead core displacement being elastic.

$$\zeta_{eq} = \frac{A_h}{4\pi A_l} = \frac{2Q(u_m - u_{yield})}{\pi F_{max}u_m} \tag{5.17}$$

The vertical stiffness, k_z, is a function of only the rubber material, and can be found using Equations 4.58 through 4.63 at any lateral displacement, u.

Parameter	Value
Vertical Stiffness, k_z	68.60 MN/cm
Yield Force, f_{yield}	972.8 kN
Yield Displacement, u_{yield}	1.50 cm
Yield Stiffness Ratio, α	0.0667

Table 5.9: Input parameters for the simple LR analyses in ALE3D ("spring4")

Parameter	Value
Reinforced Rubber Radius, R	80 cm
Lead Core Radius, a	17 cm
Lead Core Height, h_L	40 cm
Rubber Layer Thickness, t_r	1.0 cm
Number of Rubber Layers, n	31
Yield Force, f_{yield}	972.8 kN
Yield Displacement, u_{yield}	1.50 cm
Yield Stiffness Ratio, α	0.0667
Rubber Damping Coefficient, c_d	964 N-s/cm

Table 5.10: Input parameters for the robust LR analyses in ALE3D ("spring5")

The final isolator parameters used for the LR models are presented in Tables 5.9 and 5.10. Note that the design for the two is the same, yet the two models have different input parameters, which must be specified. The design has an effective period of 3.01 seconds and an equivalent damping ratio of 16.3%. These are within acceptable error of the ideal design properties at the design displacement.

5.4.4 Isolation System Layout

The quantity of isolators is generally predicated on the overbearing force. The layout of said isolators is made to fulfill 3 criteria. First, it is desirable to have roughly equal bearing pressures on all isolators. Second, sufficient spacing must exist such that isolator inspection and replacement is facilitated. Third, the isolators must be organized such that the loss of any one isolator does not result in superstructure inelasticity or induce additional isolator failures.

The layout of isolators is different for the cylindrical and rectangular superstructures, due to the vastly different structural weights. The former utilizes 32 isolators arranged in a polar array around the center of the structural footprint. The latter utilizes 220 isolators arranged in a grid. Each of the three isolator types were designed such that they could utilize the same two layouts decribed below.

The isolation system layout for the cylindrical plant consists of 3 concentric rings of isolators. The outer ring contains 16 isolators evenly distributed at a radius of 10.875 m. The middle ring contains 12 isolators evenly distributed at a radius of 6.625 m. The inner ring contains 4 isolators evenly distributed at a radius of 2.375 m. This configuration is depicted in Figure 5.7.

The isolation system layout for the rectangular plant consists of two overlapping 11×10 grids of isolators. The spacing of isolators within a grid is 5.50 m in both directions. Opposing grids are offset by 2.75 m in both directions, such that the resulting arrangement has diagonal isolator spacings of 3.89 m. This configuration is depicted in Figure 5.8.

Because of grid spacing in the FEM models, some of the isolators are unable to be placed at the exact locations specified above. In such cases, the isolators are placed at the nearest FEM grid node to the ideal location. The maximum discrepancy between ideal and actual isolator locations was found to be 25.5 cm (1.0% of the side lenght) and 25.0 cm (0.4% of the side length) for the cylindrical and rectangular structures, respectively.

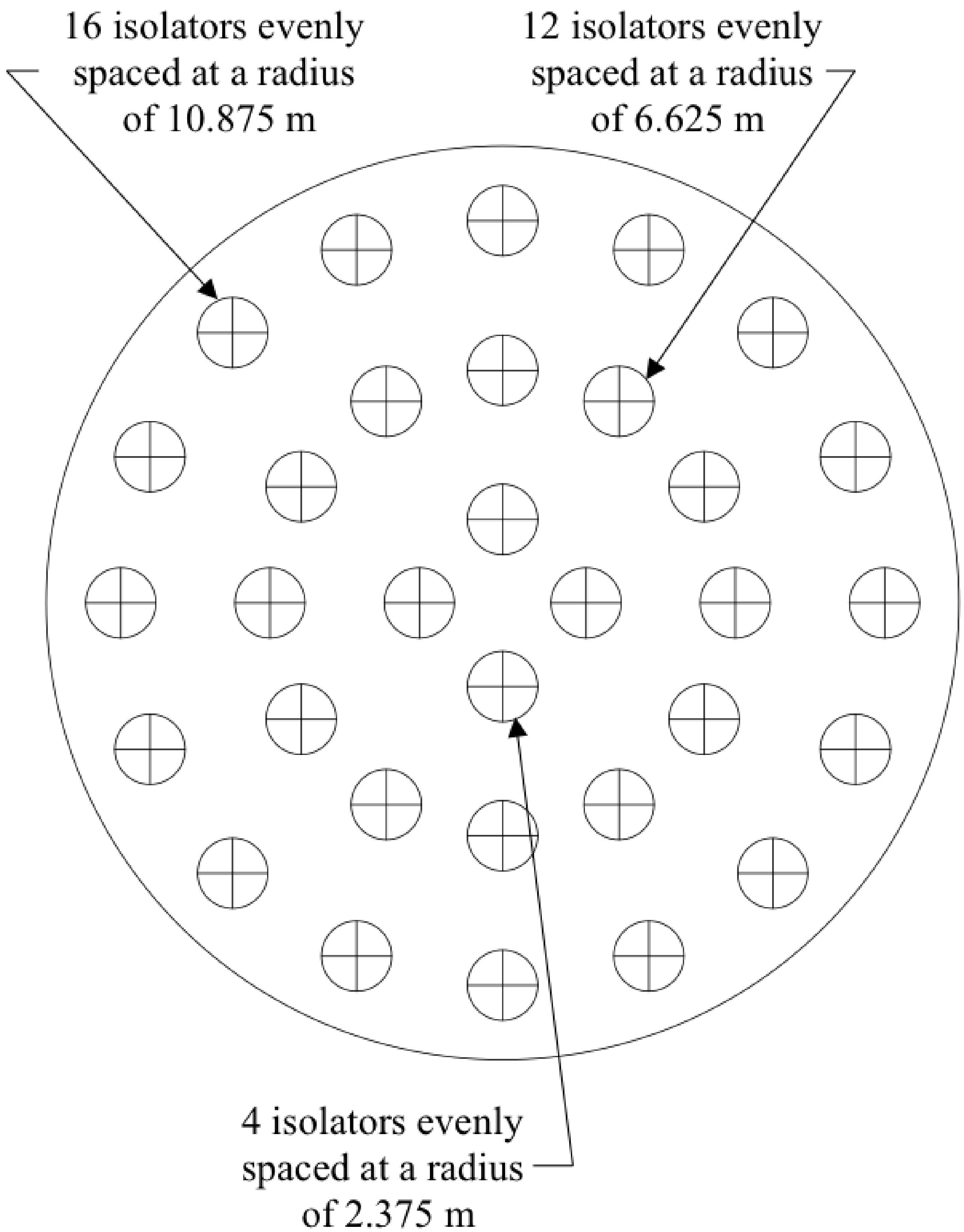

Figure 5.7: Isolator layout for the cylindrical plant

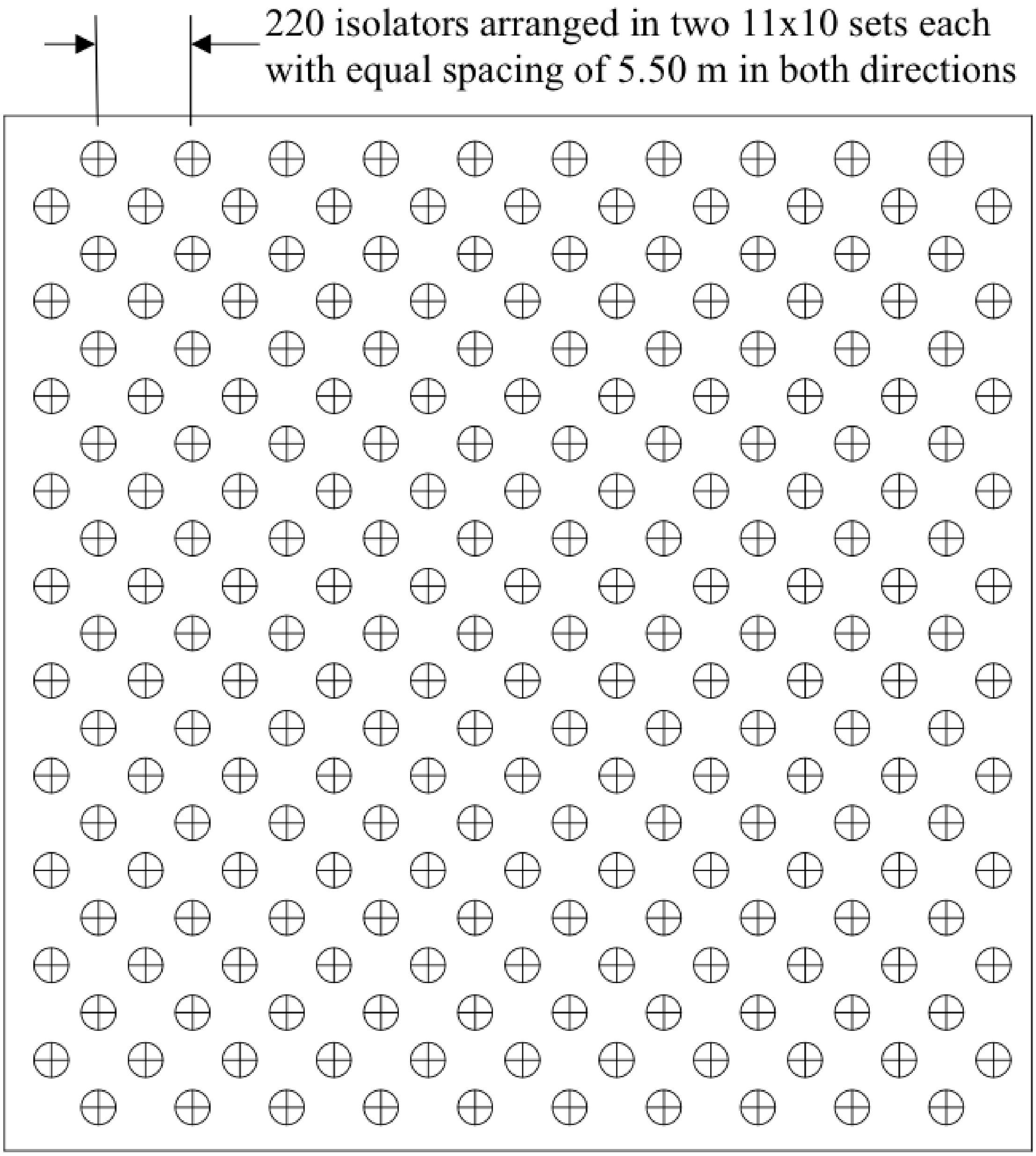

Figure 5.8: Isolator layout for the rectangular plant

Chapter 6

Geotechnical Specifications

Due to the large size and weight of NPP structures, soil structure interaction (SSI) analyses are required for design approval. Thus, a crucial aspect of NPP design is the detailed modeling of the underlying soil strata and consideration of the appropriate seismic risk. This chapter discusses the necessary geotechnical modeling aspects for the given structural analyses. Section 6.1 describes the geotechnical soil properties, and outlines the profiles used. Section 6.2 presents the procedure used for selection and scaling of the ground motions applied to the bottom of the soil columns.

6.1 Soil Strata Characterization

Soil layer properties were chosen to match those presented in Xu, et al. (2006), which in part assessed the effect of various soil columns on the seismic response of deeply embedded nuclear structures. That study analyzed three distinct soil columns: a uniform rock site (herein referred to as Soil Column B), a uniform stiff soil site (Soil Column D), as well as a layered soil column not considered in this study. Instead, a uniform soft rock or very dense soil site (Soil Column C) is considered in this report. Finally, a "no soil" case is considered (Soil Column N), where the ground motions are applied directly to the bottom of the isolation devises. This final case is used to gauge how accurately a solution without soil can approximate an SSI solution.

Each soil column is 80 m tall, representing overbearing soil and rock above the bedrock. The pertinent properties, including shear wave velocity, β, weight density, γ, and Poisson's ratio, ν, for the soil profiles are presented in Tables 6.1. Figure 6.1 depicts the shear wave velocity profiles for each of the three soil columns considered. Notice that the soil columns were specifically chosen to represent a variety of soil classifications as defined in the International Building Code (IBC, 2006).

A linear-elastic soil material is chosen such that soil results could be verified by alternate software if desired. Thus, the damping ratios assumed in Xu et al. (2006) are not utilized in the analyses. The desired shear wave velocities are converted to shear moduli, G, and

Property	Soil Column B	Soil Column C	Soil Column D
Shear Wave Velocity, β	1000 m/s	625 m/s	250 m/s
Weight Density, γ	17.28 kN/m^3	17.28 kN/m^3	17.28 kN/m^3
Poisson Ratio, ν	0.30	0.30	0.30
IBC Soil Classification	B	C	D

Table 6.1: Geotechnical properties for soil layers

subsequently elastic moduli, E, using Equations 6.1 and 6.2.

$$G = \frac{\gamma\beta^2}{g} \tag{6.1}$$

$$E = 2G(1+\nu) \tag{6.2}$$

The soil column footprint is square with side lengths equal to twice the width of the superstructure used. These lengths are 52 m and 120 m for the cylindrical and rectangular plants, respectively. The resulting soil column meshes, including foundation elements, are composed of 216,320 and 207,360 hex elements, respectively.

A non-reflecting boundary condition is imposed at each of the side faces of the soil column along the entire height. This boundary condition, "simulate[s] a non-reflecting boundary for cases where a finite computational domain is used on a problem where a region is effectively infinite in extent. The accelerations normal to the external boundary are modified to match the solution of the one dimensional wave equation. This boundary condition cancels the elastic portion of a propagating wave hitting the boundary, but will give some reflection if the region is deforming plastically" (ALE3D, 2011a). In order to reduce hourglassing at the edges of the soil column, the boundary condition was not applied to the nodes on the edges of the soil column. The nodesets to which the non-reflecting boundary condition is applied is shown in Figure 6.2

6.2 Ground Motions

Safety-critical facilities such as nuclear power plants pose a higher risk to the environment, as well as to the general public due to the dangerous materials they house. Consequently, ASCE 43-05 (2005) requires that nuclear structures (SDC-5) shall consider Design-Basis Earthquake (DBE) ground motions which closely approximate the Uniform Hazard Response Spectrum (UHRS) specified at a mean hazard annual frequency of exceedence, H_D, of 1×10^{-4} (10,000 year return period). This hazard is significantly larger than that for typical commercial or industrial construction. Since accurate measurement of seismological processes has been limited to only the most recent centuries, proper characterization of such rare events is difficult and is a subject of much academic contention.

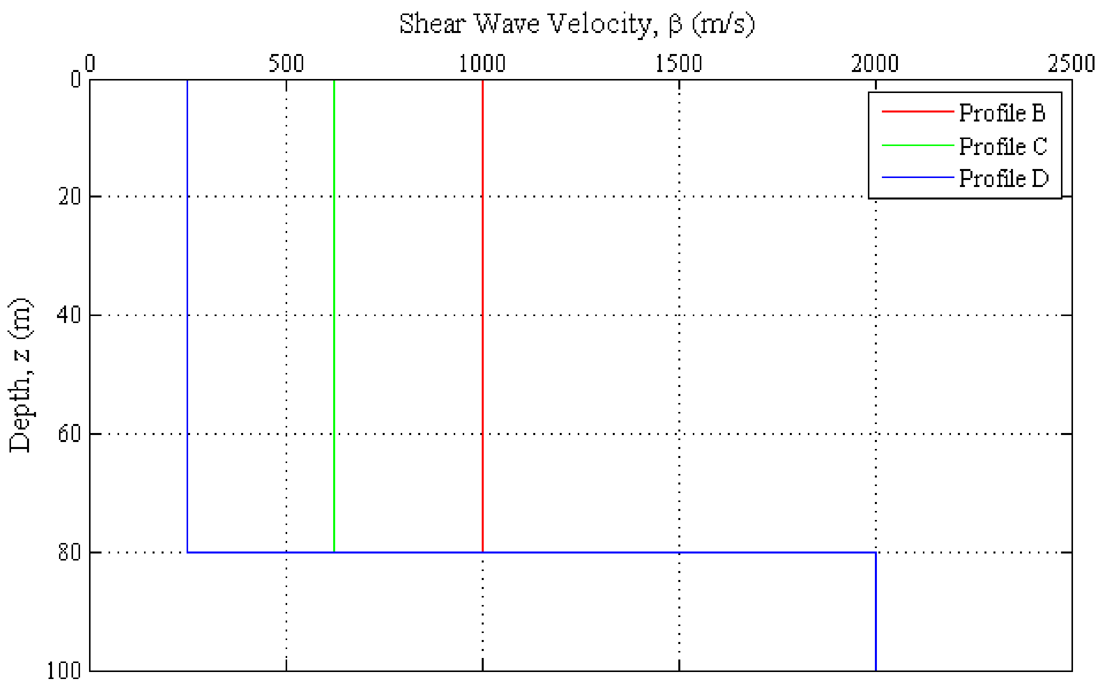

Figure 6.1: Soil shear wave velocity profiles

A probabilistic seismic hazard analysis (PSHA) was completed by Abrahamson and Gregor (2012) for the Diablo Canyon NPP in Avila Beach, California at the required annual frequency of exceedence, resulting in horizontal and vertical design spectra. Deaggregation of the PSHA highlighted the controlling geologic mechanisms, events, and distances for the hazard level, which served as the basis for the 30 candidate, 3-component ground motions chosen from the NGA database for the site. Additionally, similarity of the natural spectral shape of prospective motions to the target spectra was considered during selection. Table 6.2 lists the event name (epicenter location), record (measuring station), moment magnitude, M_W, number of data points, n, and time step, dt, for the 30 unscaled or "seed" earthquake motions chosen.

The "seed" motion time histories were scaled using a time-domain-based spectral matching procedure (Abrahamson, 1992), which alters the motion such that the resulting spectra match the given target spectra. This procedure emphasizes maintaing the non-stationary phase characteristics of the original time histories. Plots of the scaled time histories and resulting response spectra with 5% damping can be found in Appendix B along with data of the peak scaled ground motion parameters (i.e. accelerations, velocities, and displacements). The lateral spectral parameters at the design period with 5% damping are used as design inputs for the isolation system and presented in Table 5.6.

The ground motions are applied as velocity time histories to the bottom-most layer of

No	Event Name	Record	Date	M_W	R_{rup} (km)	n	dt (sec)
1	Imperial Valley, USA	G-ELC	06/14/53	5.50	15.64	4000	0.0050
2	Hollister, USA	C-HCH	04/09/61	5.50	18.09	8000	0.0050
3	Hollister, USA	B-HCH	04/09/61	5.60	19.56	8000	0.0050
4	Point Mugu, USA	PHN	02/21/73	5.65	17.72	4637	0.0050
5	Livermore, USA	A-ANT	01/24/80	5.80	15.13	7999	0.0050
6	Livermore, USA	A-KOD	01/24/80	5.80	17.24	4196	0.0050
7	Livermore, USA	A-SRM	01/24/80	5.80	17.93	7998	0.0050
8	Taiwan	05O07	01/29/81	5.90	24.93	2500	0.0100
9	Westmorland, USA	PTS	04/26/81	5.90	16.66	8000	0.0050
10	Double Springs, USA	WOO	09/12/94	5.90	12.84	1399	0.0100
11	Friuli, Italy	B-BUI	09/15/76	5.91	11.03	5278	0.0050
12	N Palm Springs, USA	MVH	07/08/86	6.06	12.07	4032	0.0050
13	Irpinia, Italy	B-BIS	11/23/80	6.20	14.74	12997	0.0029
14	Chi-Chi, Taiwan	TCU116	09/20/99	6.20	22.13	20000	0.0050
15	Chi-Chi, Taiwan	TCU120	09/20/99	6.20	23.85	19800	0.0050
16	Chi-Chi, Taiwan	TCU138	09/20/99	6.20	22.15	8751	0.0040
17	Chi-Chi, Taiwan	TCU067	09/25/99	6.30	24.67	12199	0.0050
18	Victoria, Mexico	CHI	06/09/80	6.33	18.96	2692	0.0100
19	Victoria, Mexico	HPB	06/09/80	6.33	7.27	1834	0.0100
20	Dinar, Turkey	DIN	10/01/95	6.40	3.36	5595	0.0050
21	Imperial Valley, USA	H-ECC	10/15/79	6.53	7.31	7997	0.0050
22	Superstition Hills, USA	B-ICC	11/24/87	6.54	18.20	8000	0.0050
23	Superstition Hills, USA	B-WSM	11/24/87	6.54	13.03	8000	0.0050
24	Superstition Hills, USA	B-IVW	11/24/87	6.54	23.85	8800	0.0050
25	Corinth, Greece	COR	02/24/81	6.60	10.27	4132	0.0100
26	Northridge, USA	MUL	01/17/94	6.69	17.15	2999	0.0100
27	Northridge, USA	LDM	01/17/94	6.69	5.92	5315	0.0050
28	Northridge, USA	GLE	01/17/94	6.69	13.35	2999	0.0100
29	Kobe, Japan	SHI	01/16/95	6.90	19.15	4096	0.0100
30	Loma Prieta, USA	LGP	10/18/89	6.93	3.88	5001	0.0050

Table 6.2: Earthquake records used in seismic analyses

the finite element model (i.e. bottom of the deepest soil layer for the soil cases, or directly to the bottom of the isolators for the no soil case). For the soil cases, this nodeset is depicted in Figure 6.2. Velocity time histories are created by numerically integrating the input acceleration time histories using a trapezoidal approximation, and applied equally to the bottom surface with no directionality.

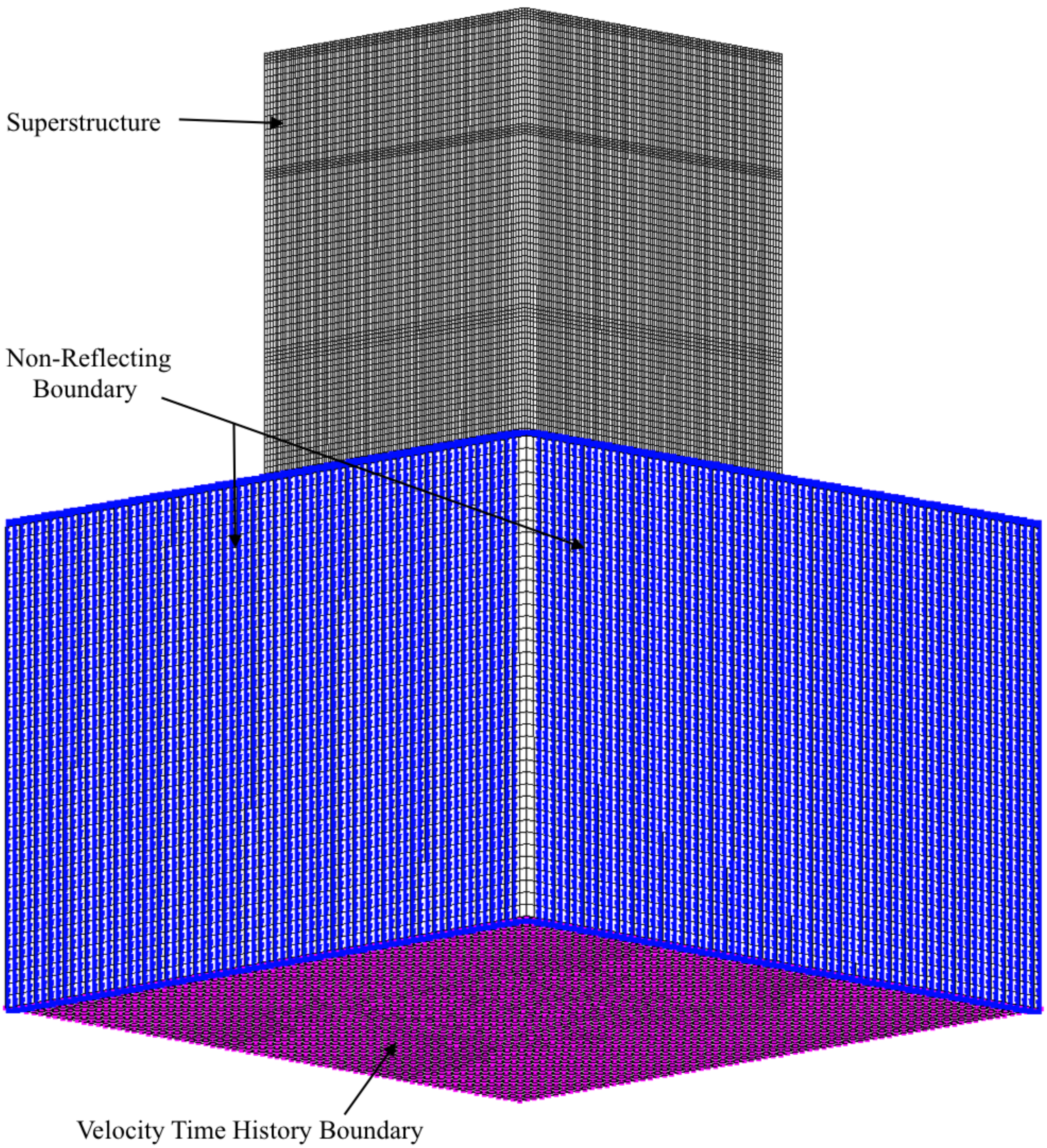

Figure 6.2: Full superstructure and soil model 3D mesh depicting boundary condition nodesets

Chapter 7

Analysis

This chapter describes the computational characteristics of the numerical analyses undertaken. Sections 7.1 and 7.2 describe the software and hardware, respectively, used to run the simulations. Section 7.3 enumerates the different combinations of superstructure, isolator model, soil profile, and earthquake record analyzed. Section 7.4 describes the different sensors positioned throughout the analyzed models, as well as the type of data collected by each.

7.1 Software

The analyses presented in this report were completed using ALE3D, a high-performance, multi-physics simulation software developed at LLNL, which utilizes arbitrary Lagrangian-Eulerian (ALE) techniques to solve a variety of physics and engineering problems in 2D and 3D. The hybrid finite element and finite volume formulation enables modeling of all states of matter, including elastic and inelastic materials on unstructured grids. The resulting software is able to achieve accurate and efficient results using implicit and explicit techniques to solve problems with long and short time-scales respectively (WCI, 2010).

ALE3D is a single code capable of modeling a wide array of physical processes including explicit and implicit hydrodynamics, fracture and fragmentation, heat transfer, incompressible flow, Lagrangian particulate modeling, magneto-hydrodynamics (MHD), chemical kinetics and species diffusion, multi-phase processes, structural response to various excitation, void collapse in solids, as well as detonation, deflagration, and convective burn of explosive events (WCI, 2010). Furthermore, the code has a wide range of material models available to the user, including four new SBI spring elements added by the writer.

ALE3D accepts mesh designs, comprising hexahedral, spring (e.g. isolator), shell, and beam elements from a variety of meshing software. The current analyses utilized Cubit (Sandia, 2012), a meshing software created at Sandia National Laboratory, to produce structural meshes that were then regenerated for ALE3D analysis using GEN3D.

ALE3D was designed with the requirement that it be operational on massively parallel machines. This is achieved by decomposing the mesh into computational subdomains which primarily communicate through message passing. Such a design enables parallel computations on multi-core processors within a single workstation, as well as on a network of workstations.

7.2 Computing Facilities

The large model size and lengthy analysis run times necessitate high-performance computing facilities provided by Livermore Computing Center (LC). LC provides myriad clusters with parallel capabilities specifically intended for the computing needs of laboratory projects.

Analaysis runs were completed using 32 processors over two nodes on the LC unclassified Restricted Zone (RZ) system RZMerl. Individual analysis run times were limited to 12 hours, with some simulations requiring multiple runs. Note, that in consideration of overall computational run time, some analyses were not run to the completion of the ground motion record. In such cases, analyses were affirmed to have included the peak input parameters as well as sufficient time post-peak to attain the peak response. The typical timestep, Δt, for the analyses varied between 10 and 70 μsec, depending on the superstructure mesh used, as well as the grid deformation, element stiffness, and ground motion intensity at a given moment.

7.3 Analysis Cases

153 different numerical analysis cases comprised of 397 simulations requiring a total of 108,884 processor-hours were run using ALE3D. The various simulations are identified using a five-character, alpha-numeric code exemplified in Figure 7.1. The first character in the code is a letter signifying the superstructure type, and will be either “C” for the cylindrical plant, or “R” for the rectangular box-type plant. The second character is a number corresponding to the spring model designation of the isolator model type used in ALE3D: “2” for the simplified FP bearing model, “3” for the robust TFP model, “4” for the simplified LR model, or “5” for the robust LR model. The third character is a letter used to differentiate between the four soil column types, with “B”, “C”, and “D” referring to the soil columns of the same letter, and “N” signifying the no-soil case. The final characters are a two-digit number between 01 and 30 corresponding to the earthquake numbers in Table 6.2.

In consideration of time, brevity, and computational cost, not all possible combinations of superstructure, isolator, soil column, and ground motion were analyzed. Instead, all 30 motions were only applied to the simulations involving the rectangular superstructure atop soil column B. For the other combinations, only three motions, called the basic motions, were applied such that comparisons can be made. The three ground motions were Taiwan (08), which has the highest vertical acceleration response at short periods, Westmorland (09), which has the largest lateral response displacement at long periods, and Superstrition

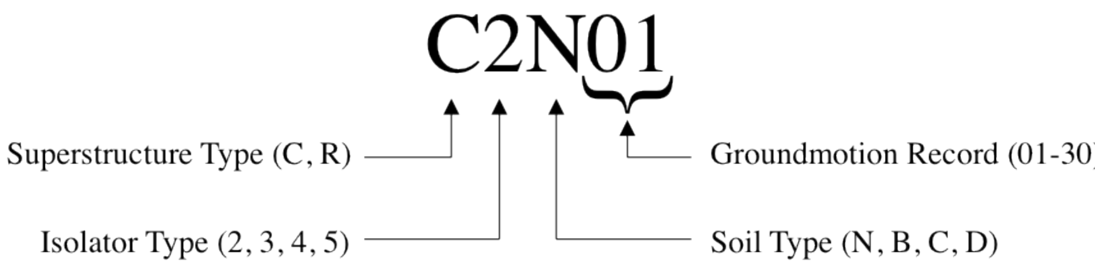

Figure 7.1: Legend for the analysis code

Hills (22), which has the largest lateral PGA. These three motions will help illuminate which ground motion characteristics induce undesireable behavior in isolated structures. A summary of the number of simulations involving each combination of soil column, superstructure type, and isolator model is shown in Table **??**.

7.4 Instrumentation

Time history data in ALE3D is recorded by using sensors at desired locations, or by requesting specific element data. The sensors, called "tracers" in the software, can be placed anywhere within a problem and will record the desired response data at that point, even as it displaces throughout the simulation.

For the models at hand, numerous tracers were used to record the response of the soil and superstructure. The cylindrical superstructure has 8 three-component velocity tracers along the height of the structure in the middle of the major walls including the center wall, and the Northern, Southern, Eastern, and Western-most portions of the outer cylindrical wall. Additionally, each section of floor and roof has four vertical velocity tracers spaning East-to-West. This layout is depicted in Figure 7.2.

The rectangular superstructure is much larger and therefore, the tracers are more spread out. This superstructure mesh has 10 three-component velocity tracers along the height of the structure in the center of the four outer walls, as well as in the center of the Northwern and Western inner walls. Additionally, each section of floor and roof has 8 vertical velocity tracers beginning at the center of each level and extending Northward and Westward to the outer walls. This layout is depicted in Figure 7.3.

The soil columns are instrumented with three-component velocity tracers in the center of the column every 5 m along the height. Note, the uppermost tracers in the soil column will be in the structure foundation. Three-dimensional displacement tracers are also used at the bottom corners of the foundation slab in order to measure torsion and overturning below the isolation layer.

Superstructure	Cylindrical (C)			Rectangular (R)		
Isolator Model	FP (2)	Simplified LR (4)	Robust LR (5)	FP (2)	Simplified LR (4)	Robust LR (5)
No Soil (N)	3 (08,09,22)	3 (08,09,22)	3 (08,09,22)	3 (08,09,22)	3 (08,09,22)	3 (08,09,22)
Soil Column B	3 (08,09,22)	3 (08,09,22)	3 (08,09,22)	30 (01-30)	30 (01-30)	30 (01-30)
Soil Column C	3 (08,09,22)	3 (08,09,22)	3 (08,09,22)	3 (08,09,22)	3 (08,09,22)	3 (08,09,22)
Soil Column D	3 (08,09,22)	3 (08,09,22)	3 (08,09,22)	3 (08,09,22)	3 (08,09,22)	3 (08,09,22)

Table 7.1: Number of analysis cases for each combination of soil column, superstructure type, and isolator model

Finally, isolator data including directional displacements and forces are collected for desired bearings. For the cylindrical structure, data from the four outer bearings in each cardinal direction is collected. For the rectangular structure, the four corner bearings are chosen for data collection. This data is used to identify the severity of uplift in bearings, as well as the peak displacmeent, which is used to predict damage and failure in the bearings.

7.5 Post-Processing

The output data from the ALE3D simulations is collected at time steps predicated by mesh size, deformation, and material stiffness. For the cylindrical and rectangular superstructures, the intial timestep is 22 μsec and 66 μsec respectively, and varies thereafter. Total runtime is a function of the groundmotion record time, the individual time step size over the run, and the number of FEM elements. Most simulations have a total number of time steps on the order of millions.

A majority of the output is velocity data which must be converted to acceleration or displacement data. This post-processing is achieved using MATLAB and consists of three parts: resampling, filtering, and calculation. First the data is resampled, by means of linear interpolation using MATLAB function “interp1”, to an even timestep of 0.001 sec. This reduces the quantity of data, thereby significantly decreasing post processing time, and normalizes the time step, reducing the likelihood of acceleration spikes resulting from momentary drops in time step. Next, the resampled data is filtered to remove high-frequency content enabled by the small time step. A fifth-order Butterworth filter is implemented at a cutoff frequency of 25 Hz using the MATLAB functions “butter” and “filter”. Note that the latter function assumes equally-sampled data, necessitating the previous resampling step.

Finaly, the filtered velocity data is converted to either displacement or acceleration data using trapezoidal numerical integration or secant numerical differentiation, respectively.

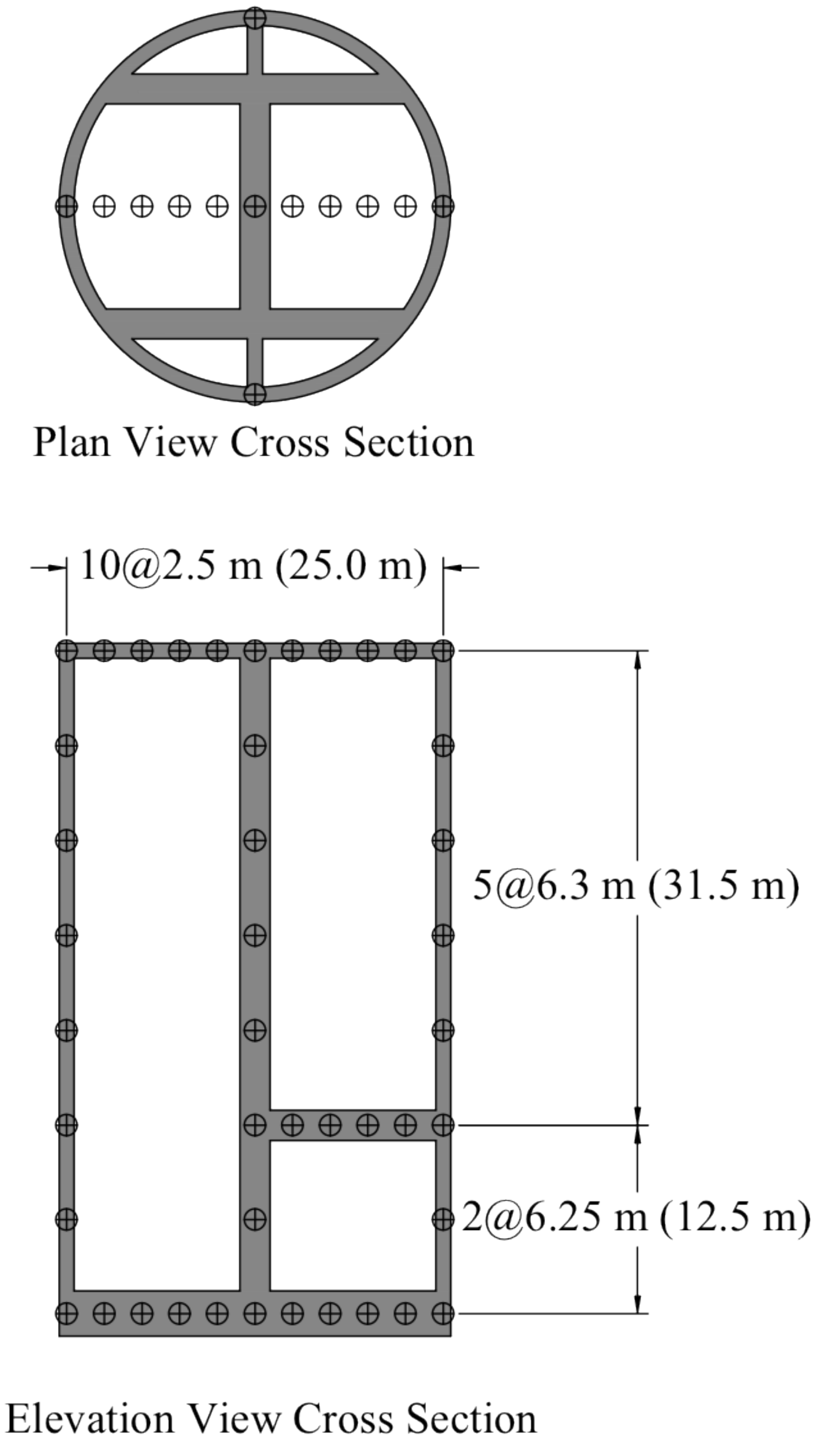

Figure 7.2: Schematic of tracer locations throughout the cylindrical superstructure

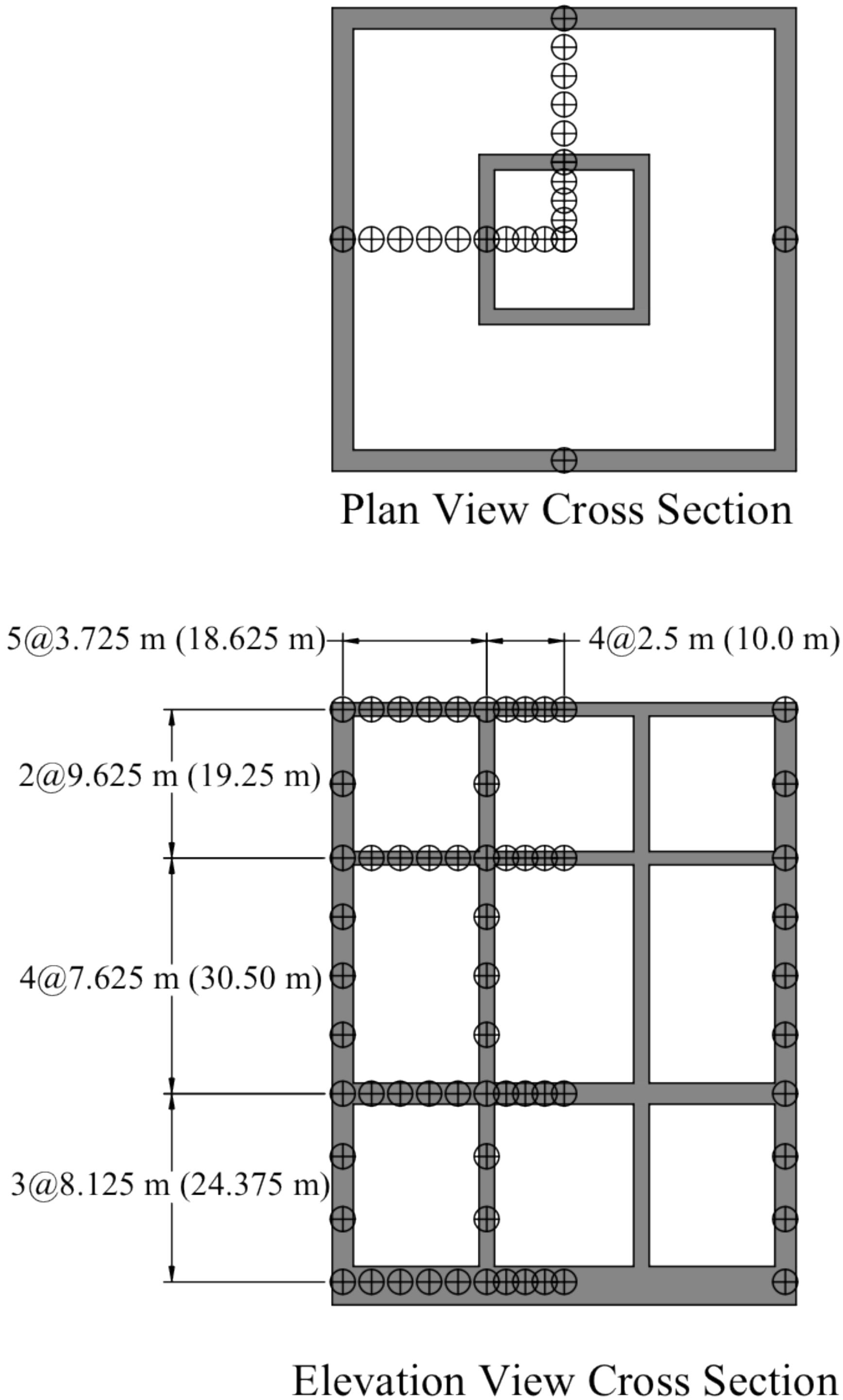

Figure 7.3: Schematic of tracer locations throughout the rectangular superstructure

Chapter 8

Results and Conclusions

This chapter presents the results of the aforementioned analyses. In each section, the numerical output is shown, explained, and used to draw conclusions regarding the applicability of SBI for NPPs. Section 8.1 describes the acceleration response of the various soil columns analyzed. Section 8.2 displays peak directional deformations of corner isolation bearings, indicating the lateral demand on isolation bearings, as well as the magnitude of uplift or tension. Section 8.3 shows peak global displacement, torsion, and directional overturning values at the foundation, isolated slab, and roof levels. Section 8.4 exhibits peak acceleration data throughout each superstructure. A summary of design conclusions is presented in Section 8.5. Finally, Section 8.6 describes the future work planned on the subject.

8.1 Soil Column Response

The peak directional soil acceleration response, a_{max}, along the soil column height is presented for all analysis runs in Appendix C. Figures C.1 through C.18 show the peak directional soil amplification factors, a_{max}/PGA, along the height for all combinations of soil column, isolator type, and superstructure mesh subjected to the basic motions. Figures C.19 through C.21 show the median of the peak amplification values with standard deviation bars for the collection of cases involving the rectangular superstructure atop soil column B subjected to the entire suite of ground motions. Together, this data is used to characterize the effect of soil conditions on the accelerations at the foundation surface, as well as SSI effects for the simulations involving all superstructures and isolation models considered. This data was obtained using a time-domain analysis. A comparison with results from frequency-domain analyses for the same motions and soil columns was not done and is indicated as a topic for future research.

The full set of ground motions was run on the simulations involving a rectangular superstructure atop soil column B. The FP bearing cases experienced median (standard deviation) acceleration amplification peaks at the foundation surface, a^f_{max}/PGA, of 1.32 (0.16), 1.25 (0.14), and 4.54 (0.89) in the x, y, and z directions respectively. For the LR cases, the same

Soil Type	$a^f_{x,max}/PGA_x$	$a^f_{y,max}/PGA_y$	$a^f_{z,max}/PGA_z$
B	1.29	1.25	3.88
C	1.08	1.09	3.85
D	0.63	0.60	1.94

Table 8.1: Mean foundation acceleration peak amplification factors of each soil type for the analyses subjected to the basic motions

median (standard deviation) amplification peaks were measured as 1.27 (0.13), 1.23 (0.13), and 3.28 (0.83). From these results, it can be inferred that SSI acceleration effects regarding seismically-isolated structures are much greater in the vertical direction than in the lateral directions. Furthermore, the standard deviations in the vertical direction are significantly higher than the lateral standard deviations, suggesting a greater uncertainty in the vertical acceleration response. Similar trends can be noted for all soil types as shown in Table 8.1. The data also shows that the median vertical acceleration peak in the foundation underlying FP-isolated structures is 38% larger than in the foundation underlying LR-isolated structures. This is an SSI effect resulting from FP bearings being stiffer vertically and lacking uplift restraint, such that impact occurs.

For the comparative tests of both cylindrical and rectangular superstructures in response to the basic motions, the mean directional acceleration amplification factors at the surface are summarized in Table 8.1. The data points to an increase in foundation surface accelerations amplification with increasing soil stiffness. Although this suggests that a softer soil column imparts less-severe accelerations on the superstructures, it fails to fully characterize the displacements and frequencies going through the soil columns. These issues will be discussed in the following sections. Finaly, it should be noted that the vertical amplification factors are rather large as a result of linear elastic soil material and lack of additional damping. These suggest that the resulting surface motions may be representative of a higher seismic risk than the given input motions.

8.2 Isolator Deformation and Uplift Response

Peak isolator data including compression deformation, dz^c_{max}, uplift/tension deformation, dz^t_{max}, and lateral deformation, $\Delta_{max} = [\sqrt{dx^2 + dy^2}]_{max}$, was compiled from the analysis runs and is presented in Appendix D. Tables D.1 and D.2 as well as Figures D.1 through D.6 present peak isolator deformation data for the comparative tests which utilize all combinations of superstructure, soil, and isolator type to the basic motions. Peak values for the cases involving the rectangular superstructure atop soil column B subjected to all ground motions are shown in Tables D.3 through D.5 and Figures D.7 through D.9. Using Figures D.1 through D.9 the peak isolation bearing response is characterized, and the competence of the original designs under various conditions is analyzed.

Because the metallic sliding components of friction bearings provide increased compression stiffness that is approximately one order-of-magnitude greater than elastomeric bearings, but offer no tension resistance, the vertical deformation exrema are notably different for the two bearing types. For the B soil cases, the median dz^c_{max} value for the sliding bearings was an average of 90% less that that for the elastomeric bearings. The other soil cases showed only a minor variation from this percentage, but with no set pattern. The median peak uplift for the rectangular superstructure cases with friction pendulum bearings atop soil column B in response to all ground motions was 6.5 times greater than the median tension deformation of the elastomeric bearings for the same cases. The standard deviation of the uplift/tension deformation data for the FP and LR simulations was 1.89 cm and 0.19 cm respectively. This data shows that FP bearings lacking uplift restraint exhibit significantly greater vertical motion than LR bearings.

For the comparative cases with both superstructures using the basic motions, the ratio of FP uplift to LR tension deformation under the same motions is shown to be 0.80 for the N soil cases, but grows to 11, 16, and 18 for the B, C, and D soil column cases respectively. This suggests that softer soil columns increase the tension response of SBI bearings; an effect which is more-pronounced for FP bearings lacking tension restraint. Furthermore, the mean tension/uplift peaks increase by 12% in the cases utilizing the more-slender cylindrical superstructure in comparison to the rectangular superstructure.

The soil type also has a considerable effect on the peak lateral displacement response of bearings. The peak lateral deformation, Δ_{max}, of each simulation was compared to the practical failure limit, Δ_{lim}, for the bearing type considered, which was determined to be the displacement that causes contact with the sliding restraint for FP bearings or the displacement that causes 400% rubber shear strain for the LR bearings. These limits were discussed in Section 4.5, and are found to be 123 cm and 124 cm respectively. The mean values of the deformation peaks from the comparative tests which utilized all superstructure, soil, and isolator combinations in response to the base motions are summarized in Table 8.2. Notice from Tables D.1 thorugh D.5 that the number of test runs that exceeded Δ_{lim} for soil columns N, B, C, and D are 0, 0, 1, and 6 respectively out of a total of 18 simulations for each. Thus, softer soils induce larger displacement demands on SBI bearings. Although bearings act as filters for ground motions, extreme caution should be applied when considering the same bearing design for sites with considerably different soil conditions.

The data from the rectangular superstructure simulations atop soil column B in response to the full set of motions showed median (standard deviation) $\Delta_{max}/\Delta_{lim}$ ratios of 34% (20%), 32% (16%), and 32% (20%) and maximum ratios of 81%, 73%, and 90% for the FP, simplified LR, and robust LR runs respectively. For these simulations, the maximum ratios are 2.35, 2.56, and 2.90 standard deviations above the respective median ratios, and the failure level is 3.30, 4.25, and 3.40 standard deviations above the median ratios. This data matches well with the suggested procedure for displacement design presented in Huang et al. (2009) and adopted in ASCE4-11 (2011) for time-history SSI analyses. These numbers also present the largest discrepancy beween the simplified and robust LR model responses, implying that consideration of lead core heating is very important for properly characterizing

Soil Type	dz^c_{max} (cm)	dz^t_{max} (cm)	Δ_{max} (cm)	$\Delta_{max}/\Delta_{lim}$
N	0.97	0.57	57.0	46%
B	1.59	3.73	59.5	48%
C	1.91	6.17	69.1	56%
D	2.04	8.04	107.9	88%

Table 8.2: Mean isolation displacement peak data for the analyses subjected to the basic motions

peak lateral displacements and predicting possible strain-based limit states. Considerable softening of the lead core under high-amplitude seismicity is also the likely cause of the increase in $\Delta_{max}/\Delta_{lim}$ ratio standard deviations from simpified to robust LR simulations.

Finally, comparison of Δ_{max} data from the rectangular and cylindrical test cases suggests that tall, slender structures may respond less-favorably to earthquake excitation, expecially for the soil cases. For said cases, the mean lateral deformation peaks are shown to be 1%, 16%, 55%, and 81% greater for the cylindrical superstructure analyses utilizing the soil N, B, C, and D columns respectively. This points to a possible confluence of soil column and slenderness effects. Although too few comparative simulations were run to make any sweeping conclusions, this issue should be analyzed more-extensively when discussing base isolation applicability.

8.3 Global Displacement, Torsion and Overturning

Peak data for global displacements, u_x, u_y, and u_z, as well as for global rotations including torsion about the building vertical axis, θ, and directional overturning, ϕ_x and ϕ_y, at the foundation (f), isolated slab (i), and roof (r) levels is shown in Appendix E. Figures E.1 through E.36 depict results from the comparative cases utilizing all combinations of soil column, isolator model, and superstructure mesh subjected to the basic motions. Figures E.37 through E.54 show results from the full set of 30 ground motions applied to the cases with a rectangular superstructure atop soil column B.

Tables E.1 through E.5 show global peak directional displacement values. Average directional displacement amplification factors for the comparative cases with all combinations of soil column, isolator type, and superstructure mesh subjected to the basic motions are given in Table 8.3. These values show minimal amplification of vertical displacements, but significant amplification of lateral displacements from the foundation to the superstructure levels. Furthermore, the lateral amplification at the roof is shown to be considerably higher than the lateral amplification at the isolated-slab level, suggesting that overturning rotations can exacerbate peak lateral displacements at the roof level. Finally, the peak displacements appear to increase as soil columns become more flexible. Because of this, implementation of SBI designs should be limited to soil columns of similar stiffnesses, as softer columns

Soil Type	$\frac{u^i_{x,max}}{u^f_{x,max}}$	$\frac{u^i_{y,max}}{u^f_{y,max}}$	$\frac{u^i_{z,max}}{u^f_{z,max}}$	$\frac{u^r_{x,max}}{u^f_{x,max}}$	$\frac{u^r_{y,max}}{u^f_{y,max}}$	$\frac{u^r_{z,max}}{u^f_{z,max}}$
N	1.56	1.42	1.01	1.62	1.48	1.03
B	1.46	1.22	1.12	1.80	1.66	1.17
C	1.60	1.26	1.12	2.03	1.89	1.17
D	2.18	2.28	1.13	2.84	2.89	1.14

Table 8.3: Mean superstructure peak displacement amplification ratios for the simulations subjected to the basic motions

Soil Type	Superstructure Type	$\theta^r_{max}(^\circ)$	$\phi^r_{x,max}(^\circ)$	$\phi^r_{y,max}(^\circ)$
N	Cylindrical (C)	0.081	0.021	0.025
B	Cylindrical (C)	0.30	0.31	0.35
C	Cylindrical (C)	0.60	0.45	0.47
D	Cylindrical (C)	0.75	0.66	0.62
N	Rectangular (R)	0.0079	0.013	0.0097
B	Rectangular (R)	0.035	0.063	0.057
C	Rectangular (R)	0.059	0.12	0.086
D	Rectangular (R)	0.13	0.30	0.25

Table 8.4: Mean roof peak rotations for the simulations subjected to the basic motions

may necessitate isolators with larger deformation capacities and isolation gaps with larger displacement and rotation capacities.

Comparison of superstructural displacement values shows that for the comparative cases where all combinations of soil column, isolator type, and superstructure mesh are analyzed, the simulations utilizing the cylindrical superstructure experienced a 36% increase in peak X displacements, and a 26% increase in peak Y displacements over the rectangular superstructure. Although there was no noticeable change in Z displacements between the two, this data suggests a slenderness effect.

Peak torsion and overturning rotation values are presented in Tables E.6 through E.10. Although some of the angles seem small, remember that a rotation of 1.0° results in over 0.50 m of differential displacement across a 30 m distance. The mean of the peak values from the comparative tests are shown in Table 8.4 for the various combinations of soil type and superstructure type subjected to the basic motions. Although there arent enough cases to make definitive conclusions, the values show a clear trend that both torsion and overturning increase as the soil columns become softer.

The bearing type has a considerable effect on peak rotation values, which is likely attributable to the lack of uplift restraint. For the simulations utilizing the rectangular superstructure atop soil column B in response to all ground motions, the median (standard deviation) of the peak isolated-slab and roof torsion are shown in Table 8.5. At both loca-

Bearing Type	$\theta^i_{max}(^\circ)$	$\theta^r_{max}(^\circ)$
2	0.045 (0.019)	0.048 (0.020)
4	0.021 (0.0086)	0.023 (0.013)
5	0.021 (0.0087)	0.025 (0.012)

Table 8.5: Median (standard deviation) superstructure peak torsion for the rectangular superstructure atop soil column B

Bearing Type	$\phi^i_{x,max}/\phi^f_{x,max}$	$\phi^i_{y,max}/\phi^f_{y,max}$	$\phi^r_{x,max}/\phi^f_{x,max}$	$\phi^r_{y,max}/\phi^f_{y,max}$
2	1.40 (0.38)	1.62 (0.50)	1.71 (0.41)	1.76 (0.54)
4	1.21 (0.080)	1.23 (0.10)	1.49 (0.18)	1.54 (0.18)
5	1.23 (0.14)	1.24 (0.11)	1.52 (0.20)	1.53 (0.18)

Table 8.6: Median (standard deviation) superstructure peak overturning rotation amplifications for the rectangular superstructure atop soil column B

tions, the peak torsion median is at least twice as large for the FP-isolated cases than for the LR-isolated cases. Note that neither structure was specifically designed to minimize torsion and FP bearings are lauded for their ability to mitigate rotation due to structural eccentricity, yet LR bearings were more effective in reducing torsional effects. Analysis of time history records showed that significant torsion in FP structures initiated around the same time as primary uplift in any the outer bearings. Table 8.6 presents the median (standard deviation) amplification factors for peak directional overturning rotation of the isolated slab and roof above those of the foundation slab. These values are 13% to 32% larger for the FP cases, suggesting that the FP bearings induce larger overturning in the isolated superstructure than LR bearings.

Finally, the slenderness effect is reinforced by the values of torsion and overturning for the comparative cases utilizing all combinations of soil column, isolator type, and superstructure mesh. The simulations involving the cylindrical superstructure experience peak torsion and overturning values that are, on average, 4.17 times and 6.73 times larger than the same values for the rectangular superstructure cases respectively.

8.4 Superstructure Response

Peak directional superstructure acceleration amplification data, a_{max}/a^f_{max}, was collected for each simulation. Figures F.1 through F.27 presented in Appendix F show the average acceleration amplification peaks in the walls, isolated slab floor, and roof. Some vertical data, generally in the roofs, experienced large acceleration amplifications near some equipment LMS models. These models were not designed for vertical response, but their weight and stiffness enabled them to drive the local response unrealistically. For the cylindrical superstructure, this data was omitted and only the east roof is considered, wheras that data is present for the rectangular superstructure since both sets of roof data include these LMS models.

It should also be noted that the amplification data presents only the maximum acceleration response which is generally short duration data that is significantly larger than the rest of the response. These peaks are at times quite large for a few reasons including abrupt stiffness changes in the bearing models, lack of damping in the non-isolation elements, and heavy stiff equipment models which concentrate response. All these approximations induce unrealistically high, short-duration acceleration peaks which are presented in the aforementioned figures. Although, some of these peak values are high, they can still be useful for comparative purposes.

Observation of the structural acceleration amplification data shows a few meaningful academic conclusions. The lateral data suggests that more-flexible, unbraced wall portions experience higher accelerations within the superstructure, suggesting that these sections are likely excited by short duration acceleration pulses formed when the bearings undergo load reversal. Note that the stiffened portions of these structures (e.g. wall-to-wall connections and wall-to-floor connections) experience much smaller peak amplifications.

Vertical amplifications in the superstructure, without exception, increase with the height of the structure. The median data suggests that the amplification of vertical accelerations is smaller in FP isolated structures, consistent with expectations since FP bearings approximate vertical rigidity. However, it should be remembered that FP bearing analyses exhibited larger magnitude vertical accelerations in the soil and foundation due to SSI effects. Thus, the vertical stiffness of FP bearings simultaneously increases soil and foundation amplifications relative to the input motion, and decreases superstructure amplifications relative to the foundation.

8.5 Summary of Conclusions

This study presented explicit, time-domain numerical simulations of seismically-isolated nuclear power structures subjected to high-amplitude seismic excitation. The models were comprised of finite element formulations for the soil column, foundation, isolation bearings, and superstructure which simultaneously achieved a variety of research objectives.

Although not exhaustive of all parameter combinations, the analytical simulations employed were used to make general design recommendations for implementing SBI in new NPP structures. In these studies, potentially-harmful levels of uplift/tension, torsion, and overturning were observed in the isolated superstructures and were larger in magnitude for the cases where friction bearings were utilized. Therefore, the use of SBI should include means to prevent or limit excessive uplift/tension. Such prevention devices would reduce overturning and possibly limit torsion as well. Additionally, these would prevent impact upon recontact which is believed to be one major cause of high superstructure accelerations observed.

These analyses suggest that isolation can be effective for a range of soil types, however, softer soil sites will likely induce longer period motion, requiring a bearing design with a larger displacement capacity. Thus, although the use of SBI may enable modularization of plant designs, a separate SBI design is required at each site to assure adequate performance objectives and safety margins are maintained. SBI can be considered an effective filter under various soil classes, but a single SBI design is only valid for a narrow range of soil conditions.

Although only two superstructures were examined, peak displacement and rotation response quantities were larger for the cylindrical structure. This suggests that a slenderness effect may exist for base-isolated superstructures. Additionally, all these effects appear to exacerbate one another when certain combinations of soil type, superstructure type, isolator type, and ground motion are analyzed.

8.6 Future Work

Future research regarding the use of FEM models to fully characterize the seismic response NPPs utilizing SBI will focus on model refinement in three areas: isolation algorithms, soil column variability, and superstructural materials. This section describes the intended future work.

Currently, the TFP model exhibits extreme torsion, as much as an order of magnitude larger than the FP model, in resposne to the DBE-level events analyzed. During shake table tests (Becker et al., 2012) under lower-amplitude excitation, such torsion was not observed, leading to the conclusion that the TFP model used is currently unfit for analyses including extreme vertical excitations which may cause uplift. Future work will focus on adjusting this model to reflect a more-accurate portrayal of the torsional response under high-amplitude excitations, possibly using existing or future physical tests to validate the torsional response.

The FP model will be refined to include the spherically-constrained motions which induce compatible vertical motion when displaced laterally. Such alterations will enable the analyses to highlight possible bearing uplift as a consequence of differential lateral displacement.

Subsequent analyses will include soil profiles with more realistic characteristics. Profiles with a variety of soil types, layer thicknesses and slopes, shear wave velocities, and water table depths will be considered to determine the effects of said properties on the overall response. Additionally, soil models utilizing damping and inelasticity may be implemented. Future simulations should also be compared with frequency-domain SSI analyses to determine the accuracy of such methods.

Superstructure inelasticity throughout the simulations was minimal and only appeared at the connection between structural elements and equipment LMS models where massive forces are unrealistically concentrated at single nodes. Therefore, new equipment models and connection means will be considered to reduce the unfavorable local response.

Finally, future work will involve analyzing each combination of soil column, superstructure type, and SBI bearing type to the full collection of ground motions such that definitive statistical conclusions can be made.

Bibliography

Abrahamson, N.A. (1992). Non-stationary spectral matching. *Seismological research letters*, 63(1):30

Abrahamson, N.A. and Gregor, N.J. (2012). Scaled Ground Motions for Diablo Canyon Nuclear Power Plant. Unpublished raw data

Accademia dei Lincei (1909), Relazione della Commissione Reale Incaricata di Designare le Zone piu Adatte per la Reconstruzione degli Abitati Colpiti dal Terremoto del 28 Decembre 1908 o da Altri Precedenti, Roma, Italia

Aiken I.D., Kelly J.M., and Tajiran F.F. (1989). "Mechanics of Low Shape Factor Elastomeric Seismic Isolation Bearings." *Report No. UCB/EERC-89/13*, University of California, Berkeley, CA

ALE3D (2011a). *ALE3D: An Arbitrary Lagrange/Eulerian 2D and 3D Code System. Volume 1: General Information, Version 4.14.x*, LLNL-SM-531811. Lawrence Livermore National Laboratory, Livermore, CA

ALE3D (2011b). *ALE3D: An Arbitrary Lagrange/Eulerian 2D and 3D Code System. Volume 2: Material and Chemical Models, Version 4.14.x*, LLNL-SM-531811. Lawrence Livermore National Laboratory, Livermore, CA

Almazán, J.L., and de la Llera, J.C. (2003). Accidental torsion due to overturning in nominally symmetric structures isolated with the FPS. *Earthquake Engineering and Structural Dynamics*, 32:919-948

Amin, N. and Mokha, A. (1995). Base Isolation Gets Its Day in Court. *Civil Engineering*, 65(2):44-47

Ariga, T., Kanno, Y., and Takewaki, I., (2006). Resonant behavior of base-isolated high-rise buildings under long-period ground motions. *The Structural Design of Tall and Special Buildings*, 15(3):325-338

ASCE 43-05 (2005). "Seismic design criteria for structures, systems, and components in nuclear facilities." American Society of Civil Engineers, ASCE, Reston, VA

ASCE 4-11 (2011). "Seismic analysis of safety-related nuclear structures and commentary." American Society of Civil Engineers, ASCE, Reston, VA

Becker, T.C. and Mahin, S.A. (2011). Experimental and analytical study of the bi-directional behavior of the triple friction pendulum isolator. *Earthquake Engineering and Structural Dynamics*

Becker, T.C. (2011). *Advanced Modeling of the Performance of Structures Supported on Triple Friction Pendulum Bearings* (Doctoral Dissertation). University of California, Berkeley, CA

Becker, T.C., Keldrauk, E.S., Mieler, M.W., Stojadinović, B., and Mahin, S.A. (2012). "Effects of Mass Offset on the Torsional Response in Friction Pendulum Isolated Structures," *Proceedings*, 15th World Conference on Earthquake Engineering, 15WCEE, Lisbon, Portugal

Blandford, E., Keldrauk, E., Laufer, M., Mieler, M., Wei, J., Stojadinović, B., and Peterson, P.F. (2009). Advanced Seismic Base Isolation Methods for Modular Reactors. University of California, Berkeley, CA

Bloomberg (2007). "Tokyo Electric Shares Drop Most in 7 Years on Quake (Update 1)." *bloomberg.com*, Bloomberg News, July 2007. Web. Jan. 2012

Buckle, I.G. (1984). New Zealand Seismic Base Isolation Concepts and their Application to Nuclear Engineering. *Nuclear Engineering and Design*. 313-326

Calantarients, J.A. (1909). "Improvements in and Connected with Building and Other Works and Appurtenances to Resist the Action of Earthquakes and the Like." Paper No. 325371, Engineering Library, Stanford University. Stanford, CA

Chopra, A.K. (2007). Dynamics of Structures: Theory and Applications to Earthquake Engineering, 3rd Edition, Pearson/Prentice Hall. Upper Saddle River, NJ

Constantinou, M.C., Mokha, A., and Reinhorn, A.M. (1990). Teflon bearings in base isolation II: Modeling. *Journal of Structural Engineering*, ASCE, 116(2):455-474

Dao, N. D., Ryan, K. L., Sato, E., Okazaki, T., Mahin, S. A., Zaghi, A. E., Kajiwara, K., Matsumori, T. (2011). "Experimental Evaluation of an Innovative Isolation System for a Lightweight Steel Moment Frame Building at E-Defense," Structures Congress, ASCE, Las Vegas, NV

De Grandis, S., Forni, M., De Bruyn, D., and Cardini, S. (2011). "Seismic Isolation of Gen IV Lead-Cooled Reactors," *Proceedings*, 21st International Conference on Structural Mechanics in Reactor Technology, SMiRT 21, New Delhi, India

Derham, C., Kelly, J., and Thomas, A. (1985). Nonlinear natural rubber bearings for seismic isolation. *Nuclear Engineering and Design*, 84(3)

DIS (2011) "Applications." *dis-inc.com.* Dynamic Isolation Systems, Inc., 2011. Web. Jan. 2012

EPS (2003) "Technical Characteristics of Friction Pendulum Bearings." *environmentalprotection.com.* Earthquake Protection Systems, Inc., Sept. 2003. Web. Jan. 2012

EPS (2004) "Seismic Isolation of LNG Tanks (Revithoussa, Greece)- The largest seismically isolated tanks in the world use Friction Pendulum bearings." *environmentalprotection.com.* Earthquake Protection Systems, Inc., Jan. 2004. Web. Jan. 2012

EPS (2006) "Sakhalin II Offshore Platforms." *environmentalprotection.com.* Earthquake Protection Systems, Inc., Aug. 2006. Web. Jan. 2012

EPS (2008) "Peru LNG (Melchorita, Peru) - Triple Pendulum bearings protect critical storage tanks." *environmentalprotection.com.* Earthquake Protection Systems, Inc., Dec. 2008. Web. Jan. 2012

Feng, D., Miyami, T., Masuda, K., Liu, W., Zhou, F., Zheng, B., and Li, Z. (2000). "A Detailed Experimental Study on Chinese Lead Rubber Bearing," *Proceedings*, 12th World Conference on Earthquake Engineering, WCEE12, Auckland, New Zealand

Grant, D., Fenves, G.L., and Whittaker, A.S. (2004). Bidirectional modeling of high-damping rubber bearings. *Journal of Earthquake Engineering*, ASCE, 8(1):161-185

Hall, J.F. (1999). Discussion of 'The Roll of Damping in Seismic Isolation'. *Earthquake Engineeering and Structural Dynamics*, 28:1717-1720

Hashimoto, M., Tsunematsu, T., Ohkaw, Y., Fukatsu, S., Naruse, H., Yamada, H., Sasamoto, T., Kobayashi, H., Shibukuwa, K., Murano, Y., Itoh, I., Funabashi, K., Kawahara, S., Yoshida, T., and Kikunaga, H. (1998). Pipe support across isolated and seismic structure in ITER. *Fusion Engineering and Design*, 41(1):407-414

Hossain, Q.A. (2004). "Critical Soil-Structure Interaction Analysis Considerations for Seismic Qualification of Safety Equipment," *Proceedings*, ASME Pressure Vessel and Piping Conference, San Diego, CA

Huang, Y.-N., Whittaker, A.S., Constantinou, M.C., and Malhushte, S. (2007). Seismic demands on secondary systems in base-isolated nuclear power plants. *Earthquake Engineering and Structural Dynamics*, 36:1741-1761

Huang, Y.-N., Whittaker, A.S., Kennedy, R.P., and Mayes, R.L. (2009). "Assessment of Base-Isolated Nuclear Structures for Design and Beyond-Design Basis Earthquake Shaking." *MCEER-09-0008*, State University of New York, Buffalo, NY

IBC (2006). *International Building Code*, International Code Council, Inc., Country Club Hills, IL

Kalpakidis, I.V. and Constantinou, M.C. (2008). "Effects of Heating and Load History on the Behavior of Lead-Rubber Bearings." *MCEER-08-0027*, State University of New York, Buffalo, NY

Kalpakidis, I.V., Constantinou, M.C., and Whittaker, A.S. (2010). Modeling strength degredation in lead-rubber bearings under earthquake shaking. *Earthquake Engineering and Structural Dynamics*, 39:1533-1549

Kasalanati, A. and Constantinou, M.C. (1999). "Experimental Study of Bridge Elastomeric and Other Isolation and Energy Dissipation Systems with Emphasis on Uplift Prevention and High Velocity Near-Source Seismic Excitation." *MCEER-99-0004*, State University of New York, Buffalo, NY

Kato, M., Sato, S., and Shimomura, I. (1991). Utilities/industries joint study on seismic isolation systems for LWRs - Part I. Experimental and analytical studies on seismic isolation systems. *Nuclear Engineering and Design*, 127:303-312

Kawashima K. and Aizawa, K. (1986). "Modification of earthquake response spectra with respect to damping ratio," *Proceedings*, 3rd US National Conference on Earthquake Engineering, vol. II, Charleston, SC

Kelly, J. M. (1986). Aseismic base isolation: review and bibliography. *Soil Dynamics and Earthquake Engineering*, 5(4):202-217

Kelly, J.M. (1996). *Earthquake-Resistant Design with Rubber*, 2nd Ed., Springer, New York, NY

Kelly, J.M. (1999). Role of Damping in Seismic Isolation. *Earthquake Engineering and Structural Dynamics*, 28:3-20

Kelly, J.M. and Konstantinidis, D.A. (2011). *Mechanics of Rubber Bearings for Seismic and Vibration Isolation*. John Wiley & Sons, Ltd, Chichester, UK

Kikuchi, M., and Aiken, I.D. (1997). An Analytical Hysteresis Model for Elastomeric Seismic Isolation Bearings. *Earthquake Engineering and Structural Dynamics*, 26(2)

Kikuchi, M., Nakamura, T., and Aiken, I.D. (2010). Three-dimensional analysis for square seismic isolation bearings under large shear deformations and high axial loads. *Earthquake Engineering and Structural Dynamics*, 39:1513-1531

Koh, G.C. and Kelly, J.M. (1987). "Effects of axial load on elastomeric isolation bearings." *Report No. UCB/EERC-86/12*, University of California, Berkeley, CA

Komodromos, P. (2007). Simulation of the earthquake-induced pounding of seismically isolated buildings. *Computers and Structures*, 86:618-626

Komuro, T., Nishikawa, Y., Kimura, Y., and Isshiki, Y. (2005). Development and Realization of Base Isolation System for High-Rise Buildings. *Journal of Advanced Concrete Technology*, 3(2):233-239

Konstantinidis, D.A., Kelly, J.M., and Makris, N. (2008). "Experimental Investigation on the Seismic Response of Bridge Bearings." *Report No. UCB/EERC-2008/02*, University of California, Berkeley, CA

Medeot, R., and Infanti, S. (1997). "Seismic retrofit of Chirag 1 offshore platform," *Proceedings*, Int. Post-SMiRT Conference Seminar on Seismic Isolation, Passive Energy Dissipation and Active Control of Seismic Vibrations of Structures, Taormina, Italy

Morgan, T.A., and Mahin, S.A. (2008). "The Optimization of Multi-Stage Friction Pendulum Isolators for Loss Mitigation Considering a Range of Seismic Hazard," *Proceedings*, 14th World Conference on Earthquake Engineering, WCEE14, Beijing, China

Morgan, T.A. (2008). *The Use of Innovative Base Isolation Systems to achieve Complex Seismic Performance Objectives* (Doctoral Dissertation). University of California, Berkeley, CA

Mosqueda, G., Whittaker, A.S., and Fenves, G.L. (2004). Characterization and modeling of friction pendulum bearings subjected to multiple components of excitation. *ASCE Journal of Structural Engineering*, 130(3):423-432

Naeim, F., and Kelly, J.M. (1999). *Design of Seismic Isolated Structures - From Theory to Practice*, John Wiley & Sons Ltd., New York, NY

Nagarajaiah, S., Reinhorn, A.M., and Constantinou, M.C. (1991). Nonlinear Dynamic Analysis of 3-D-Base-Isolated Structures. *Journal of Structural Engineering*, ASCE, 117(7):2035-2054

Obonai, A. and Watanabe, T. (2012). "Successful Cold Shut Down of Onagawa: The Closest NPS to the 3/11/'11 Epicenter," *Proceedings*, International Meeting on Severe Accident Assessment and Management: Lessons Learned from Fukushima Dai-ichi, ANS Winter Meeting, San Diego, CA

Orr, R.S., Tunon-Sanjur, L., and Tinic, S.(2005). "Finite Element Modeling of the AP1000 Nuclear Island for Seismic Analyses at Generic Soil and Rock Sites," *Proceedings*, 18th International Conference on Structural Mechanics in Reactor Technology, SMiRT18, Beijing, China

Park, Y.J., Wen, Y.K., and Ang, A.H.-S. (1986). Random vibration of hysteretic systems under bi-directional ground motions. *Earthquake Engineering and Structural Dynamics*, 14(4):543-557

Plichon, C., Gueraud, R., Richli, M.H., and Casagrande, J.F. (1980). Protection of Nuclear Power Plants against Seism. *Nuclear Technology*,49(2):295-306

Postollec, J.C. (1982). Les Fondations Antisismiques de la Centrale Nucléaire de Cruas-Meysse. *Travaux*, 569:75-83

Providakis, C.P. (2008). Effect of LRB isolators and supplemental viscous dampers on seismic isolated buildings under near-fault excitations. *Engineering Structures*, 30:1187-1198

Reinhorn, A.M., Nagarajaiah, S., Constantinou, M.C., Tsopelas, P., and Li, R. (1994). "3D-BASIS-TABS: Version 2.0. Computer Program for Nonlinear Dynamic Analysis of Three Dimensional Base Isolated Structures." *NCEER-94-0018*, State University of New York, Buffalo, NY

Robinson, W.H. and Tucker, A.G. (1977). A lead-rubber shear damper. *Bulletin of the New Zealand Society for Earthquake Engineering*, 10(3):151-153

Rötzer, J., Douglas, H. and Maurer, H. (2005). Hazard and Safety Investigations for LNG Tanks. Part 1: Earthquakes. *LNG Journal*, 23-24

SAC (1997). "Develope Suites of Time Histories, Task: 5.4.1," SAC Joint Venture Steel Project Phase 2, Woodward-Clyde Federal Services, Pasadena, CA

Sandia (2012). *Cubit 13.2 User Documentation*, 13.2. Sandia National Laboratory, Livermore, CA

Skinner, R.I., Beck, J.L., and Bycroft, G.N. (1975). A Practcal System for Isolating Structures from Earthquake Attack. *Earthquake Engineering and Structural Dynamics*, 3:297-309

Skinner, R.I., Tyler, R.G., and Hodder, S.B. (1976). Isolation of Nuclear Power Plants from Earthquake Attack. *Bulletin of the New Zealand National Society for Earthquake Engineering*, 9(4):199-204

Staudacher, E., Habacher, C., and Siegenthaler, R. (1970). "Erdbebensicherung in Baum, Neue Zurcher Zeitung, Technikbeilage." Zurich, Switzerland

Summers, P., Jacobs, P., Marti, J., Bergamo, G., Dorfmann, L., Castellano, G., Poggianti, A., Karabalis, A., Silbe, H., and Triantafillou, S. (2004). "Developement of new base isolation devices for application at refineries and petrochemical facilities," *Proceedings*, 13th World Conference on Earthquake Enginerering, WCEE13, Vancouver, BC

Symans, M.D., Charney, F.A., Whittaker, A.S., Constantinou, M.C., Kircher, C.A., Johnson, M.W., and McNamara, R.J. (2008). Energy Dissipation Systems for Seismic Applications: Current Practice and Recent Developments. *Journal of Structural Engineering*, ASCE, 134(1):3-21

Tajirian, F.F., Kelly, J.M., and Gluekler, E.L. (1989). "Testing of Seismic Isolation for the PRISM Advanced Liquid Metal Reactor Under Extreme Loads," *Proceedings*, 10th International Conference on Structural Mechanics in Reactor Technology, SMiRT10, San Francisco, CA

Tajirian, F.F., Kelly, J.M., and Aiken, I.D. (1990). Seismic Isolation for Advanced Nuclear Power Stations, *Earthquake Spectra*, 6(2):371-401

Tajirian, F.F. (1998). "Base isolation design for civil components and civil structures," *Proceedings*, Structural Engineers World Congress, San Francisco, CA

TEPCO (2011). "Acceleration-Time History Waveforms of Niigata-Chūetsu-Oki Earthquake Collected at Kashiwazaki-Kariwa Nuclear Power Station (Mainshock and 6 Aftershocks)," Compact Disc, Tokyo Electric Power Company Inc., Distributed by the Association for Earthquake Disaster Prevention, No. 1027

Thompson, A.C.T., Whittaker, A.S., Fenves, G.L., and Mahin, S.A. (2000). "Property Modification Factors for Elastomeric Seismic Isolation Bearings," *Proceedings*, 12th World Conference on Earthquake Engineering, WCEE12, Aukland, New Zealand

Tyler, R.G. and Robinson, W.H. (1984). High-Strain Tests on Lead-Rubber Bearings for Earthquake Loading. *Bulletin of the New Zealand National Society for Earthquake Engineering*, 17(2)

USEIA (2011). "Annual Energy Review 2010," U.S. Energy Information Administration, DOE/EIA-0384

USNRC (1997). "Identification and Characterization of Seismic Sources and Determination of Safe Shutdown Earthquake Ground Motion," U.S. Nuclear Regulatory Commission, Regulatory Guide 1.165

USNRC (2007). "Proposal to Include Aircraft Impact Design Requirements For New Reactors," U.S. Nuclear Regulatory Commission, NRC COMGBJ-07-001

USNRC (2009). "NRC Issues Final Rule on New Reactor Aircraft Impact Assessments," U.S. Nuclear Regulatory Commission, NRC News, 09-030

Warn, G.P. and Whittaker, A.S. (2006). "A Study of the Coupled Horizontal-Vertical Behavior of Elastomeric and Lead-Rubber Seismic Isolation Bearings." *MCEER-06-0011*, State University of New York, Buffalo, NY

Warn, G.P., Whittaker, A.S., and Constantinou, M.C. (2007). Vertical Stiffness of Elastomeric and Lead-Rubber Seismic Isolation Bearings. *Journal of Structural Engineering*, ASCE, 133(9):1227-1236

WCI (2010). "About ALE3D." *wci.llnl.gov.* Weapons and Complex Integration, Lawrence Livermore National Laboratory, Livermore, CA. Web. Jan. 2012

Wen, Y. K. (1976). "Method for random vibration of hysteretic systems." *Journal of Engineering Mechanics.* Div., 102(2):249263

WNN (2007). "Profits shaken at Tepco." *world-nuclear-news.org.* World Nuclear News. Web. Jan. 2012

WNN (2008). "No aftershock in Tepco year-end loss." *world-nuclear-news.org.* World Nuclear News. Web. Jan. 2012

Xu, J., Miller, C., Costantino, C., Hofmayer, C., and Graves, H.L. (2006). "Assessment of Seismic Analysis Methodologies for Deeply Embedded Nuclear Power Plant Structures." *NUREG/CR–6896, BNL–NUREG–75410–2006*, Brookhaven National Laboratory, Brookhaven, NY

Yamamoto, S., Kikuchi, M., Ueda, M., and Aiken, I.D. (2008). "Analytical Modeling of Elastomeric Isolation Bearings Under Severe Axial Load and Shear Deformation," *Proceedings*, 14th World Conference on Earthquake Engineering, WCEE14, Beijing, China

Yousef, N., and Hata, O. (2005). "Seismic Retrofit and Instrumentation of Los Angeles City Hall," *Proceedings*, California Strong Motion Instrumentation Program, SMIP05, Seminar on Utilization of Strong-Motion Data, Los Angeles, CA

Victor A. Zayas, V.A., Low, S.S., and Mahin, S.A. (1987). "The FPS Earthquake Resisting System." *Report No. UCB/EERC-87/01*, University of California, Berkeley, CA

Victor A. Zayas, V.A., Low, S.S., and Mahin, S.A. (1989). "Feasibility and Performance Studies on Improving the Earthquake Resistance of New and Existing Buildings Using the Friction Pendulum System." *Report No. UCB/EERC-89/09*, University of California, Berkeley, CA

Victor A. Zayas, V.A., Low, S.S., and Mahin, S.A. (1990). A Simple Pendulum Technique For Achieving Seismic Isolation. *Earthquake Spectra*, 6(2):317-333

Appendices

Appendix A

Kashiwazaki-Kariwa Response Data

The following data was recorded at the Kashiwazaki-Kariwa power plant during the 2007 Niigata Chūetsu-Oki Earthquake (6.6 M_W) and six of the subsequent aftershocks. The data was provided by TEPCO (2011). Figure A.1 shows a map of the site location, and Figures A.2 through A.8 display acceleration data from the recording devices throughout the soil columns and structures.

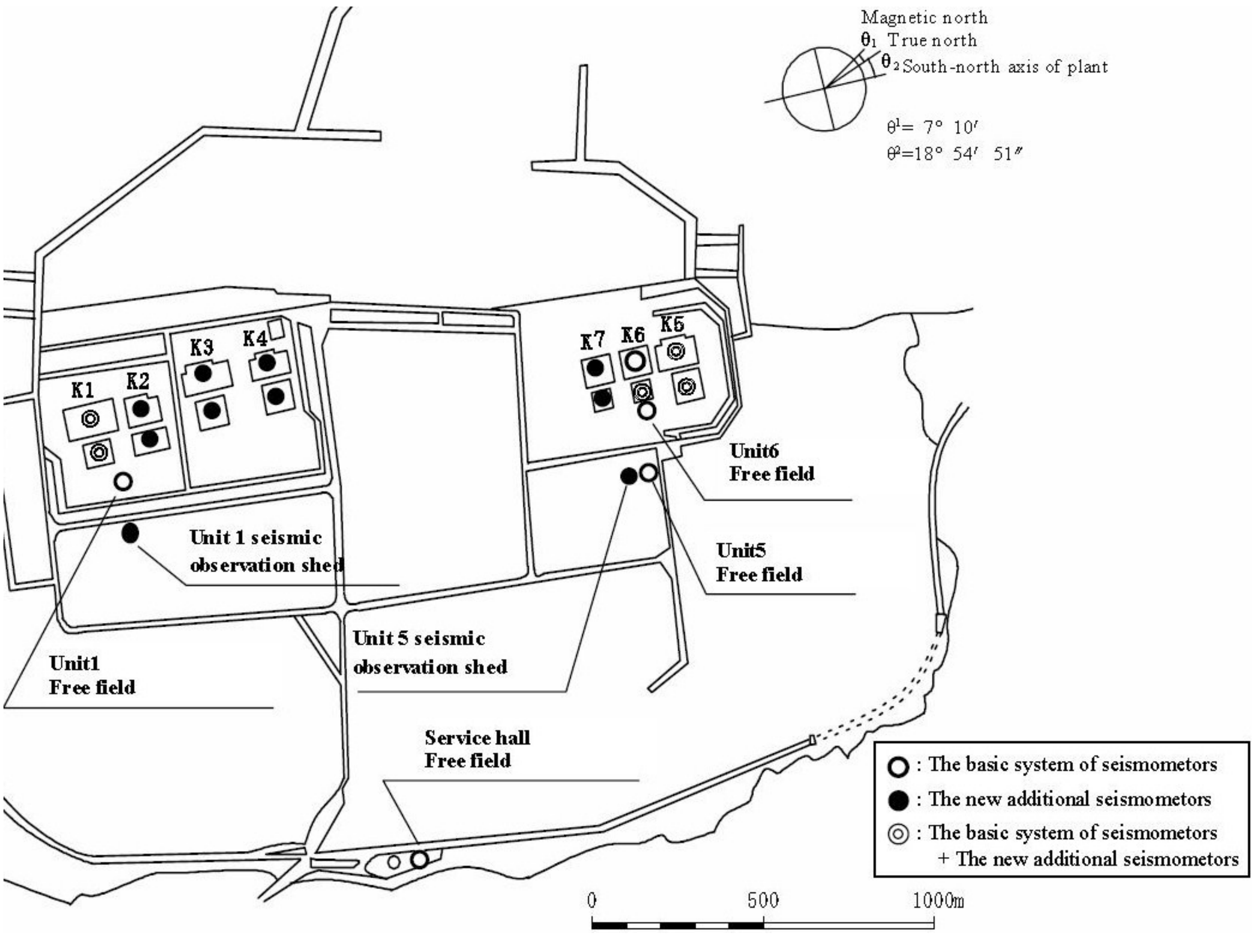

Figure A.1: Map of the Kashiwazaki-Kariwa nuclear power plant site (courtesy of TEPCO)

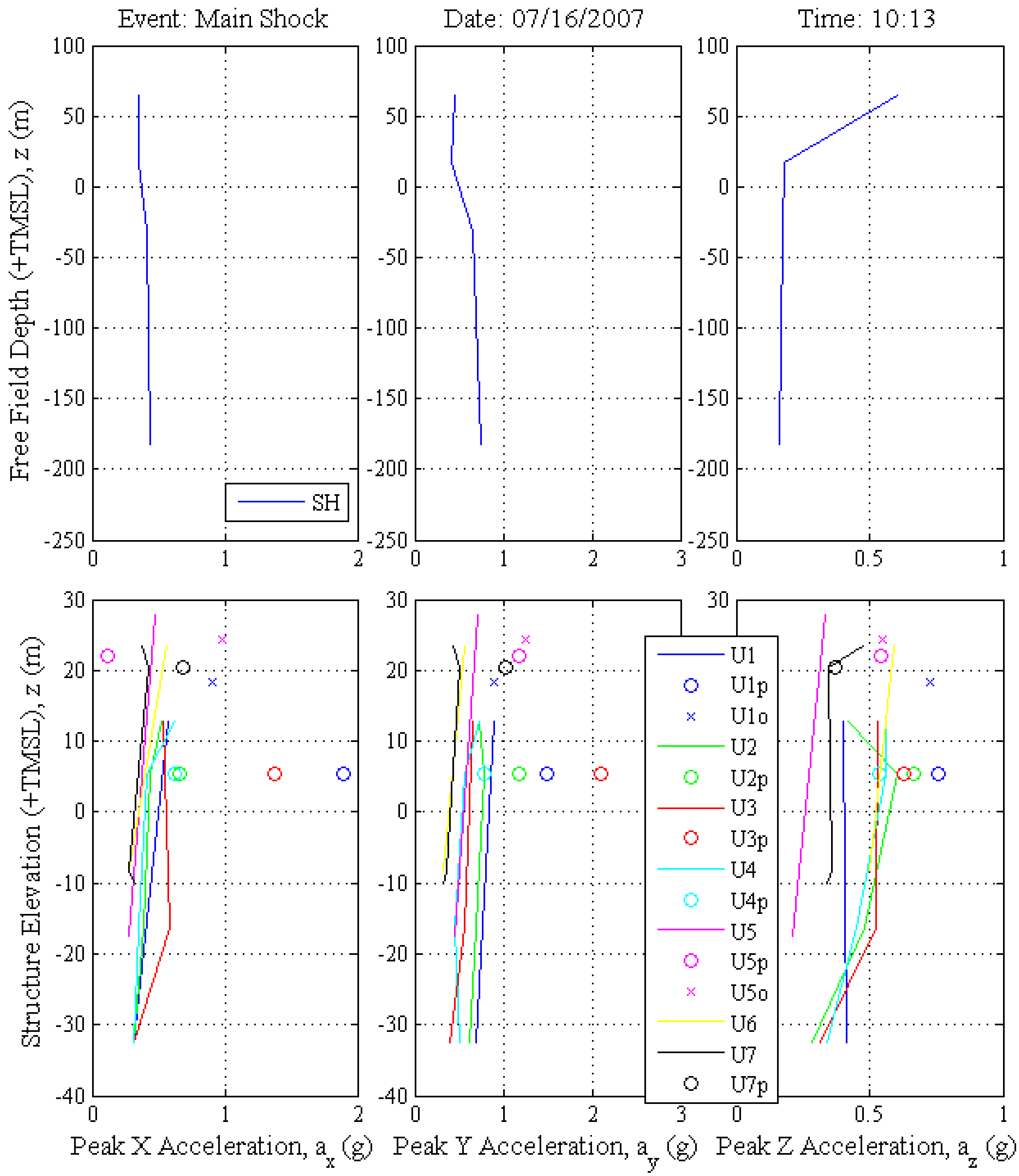

Figure A.2: Peak ground and superstructure acceleration data in response to the main shock of the 2007 Niigata Chūetsu-Oki (6.6 M_W) earthquake

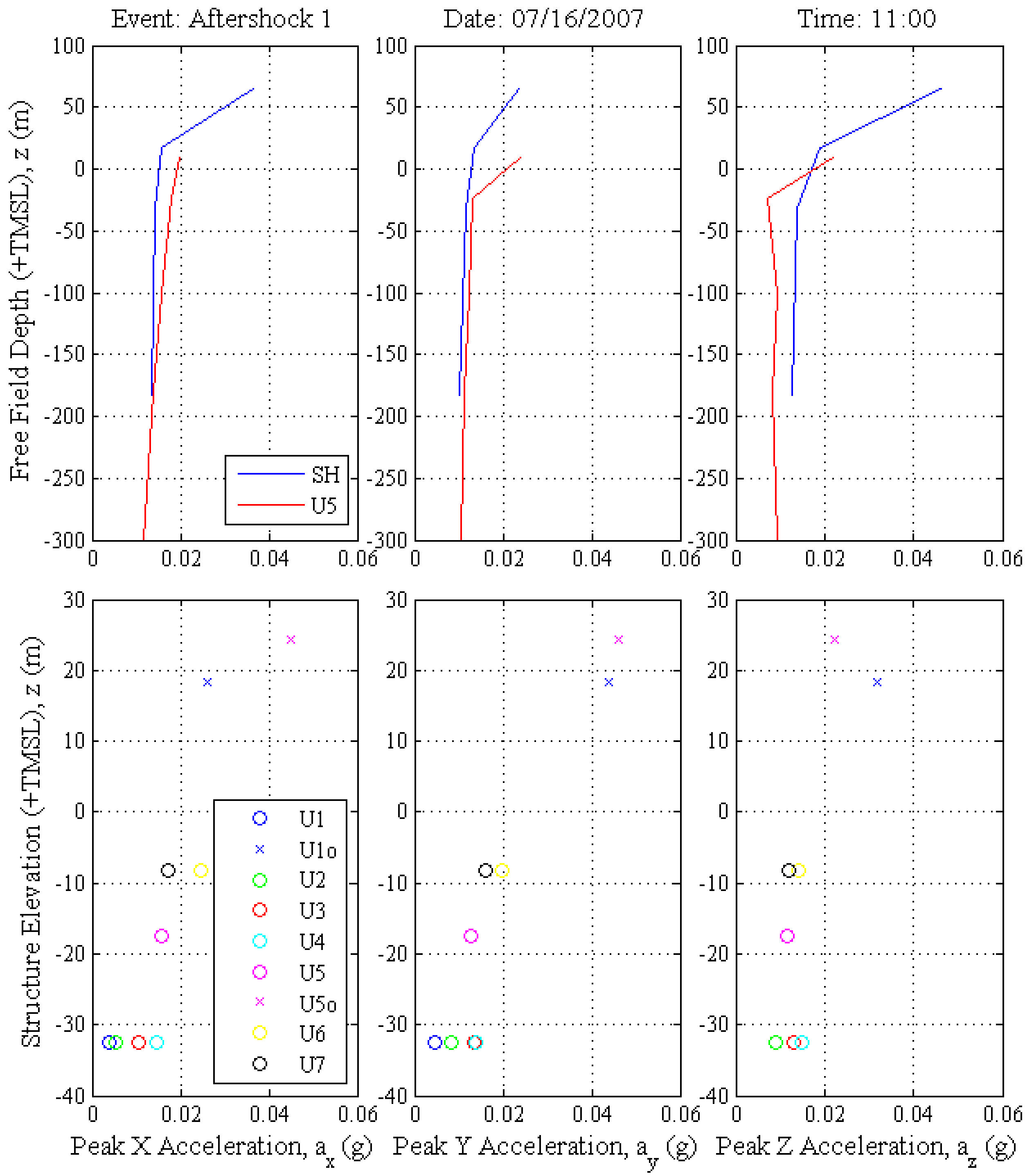

Figure A.3: Peak ground and superstructure acceleration data in response to aftershock 1 following the 2007 Niigata Chūetsu-Oki (6.6 M_W) earthquake

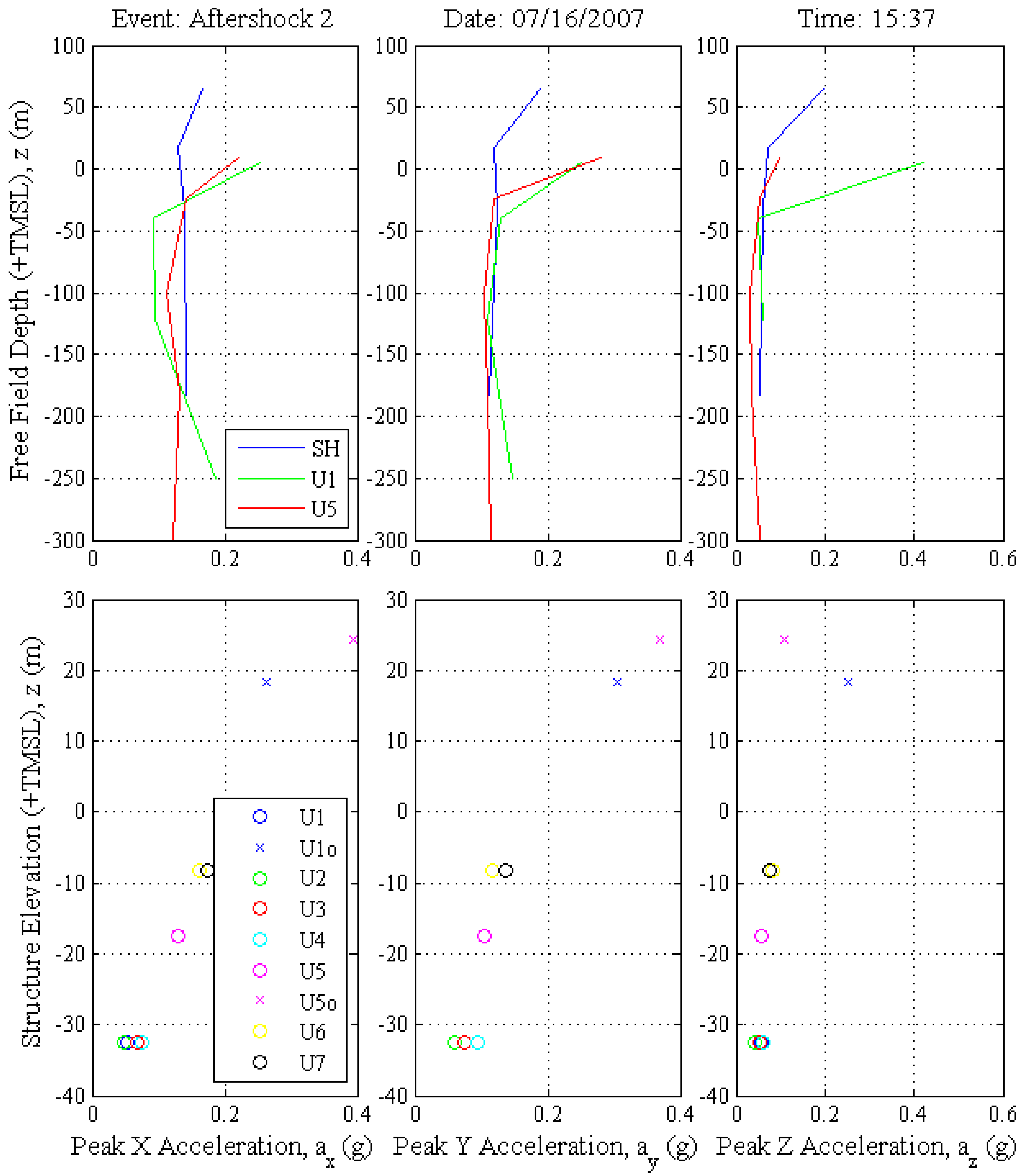

Figure A.4: Peak ground and superstructure acceleration data in response to aftershock 2 following the 2007 Niigata Chūetsu-Oki (6.6 M_W) earthquake

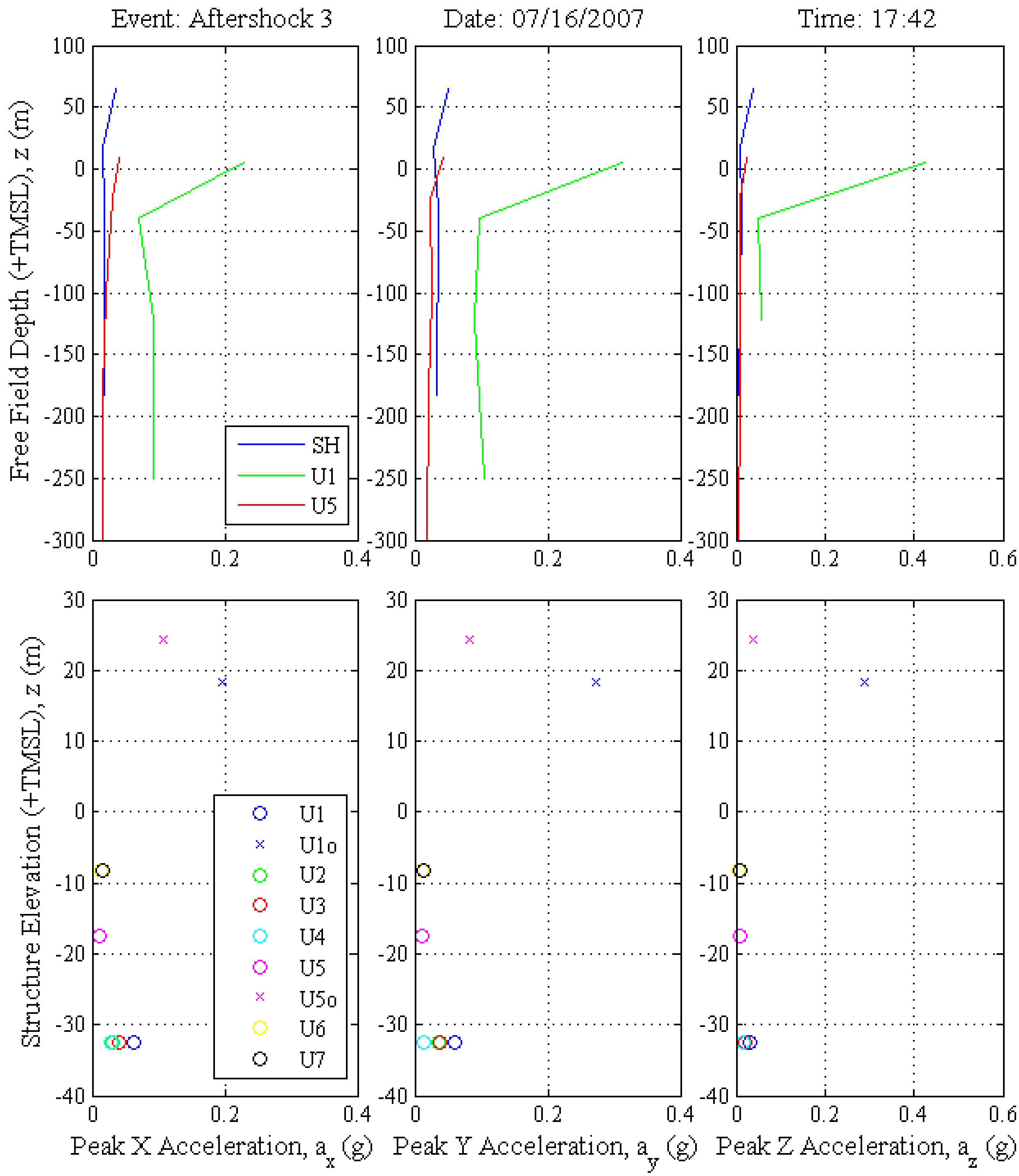

Figure A.5: Peak ground and superstructure acceleration data in response to aftershock 3 following the 2007 Niigata Chūetsu-Oki (6.6 M_W) earthquake

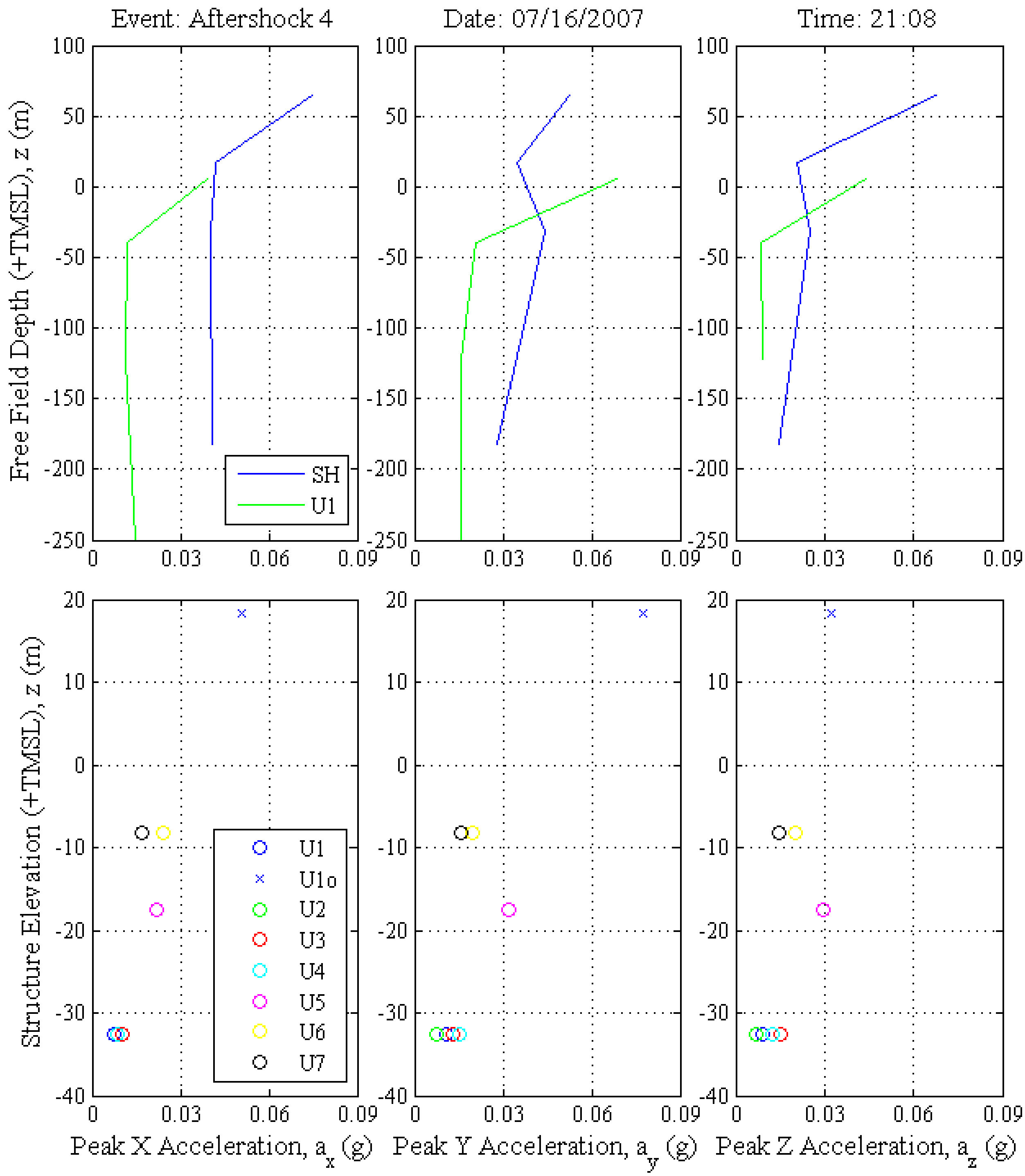

Figure A.6: Peak ground and superstructure acceleration data in response to aftershock 4 following the 2007 Niigata Chūetsu-Oki (6.6 M_W) earthquake

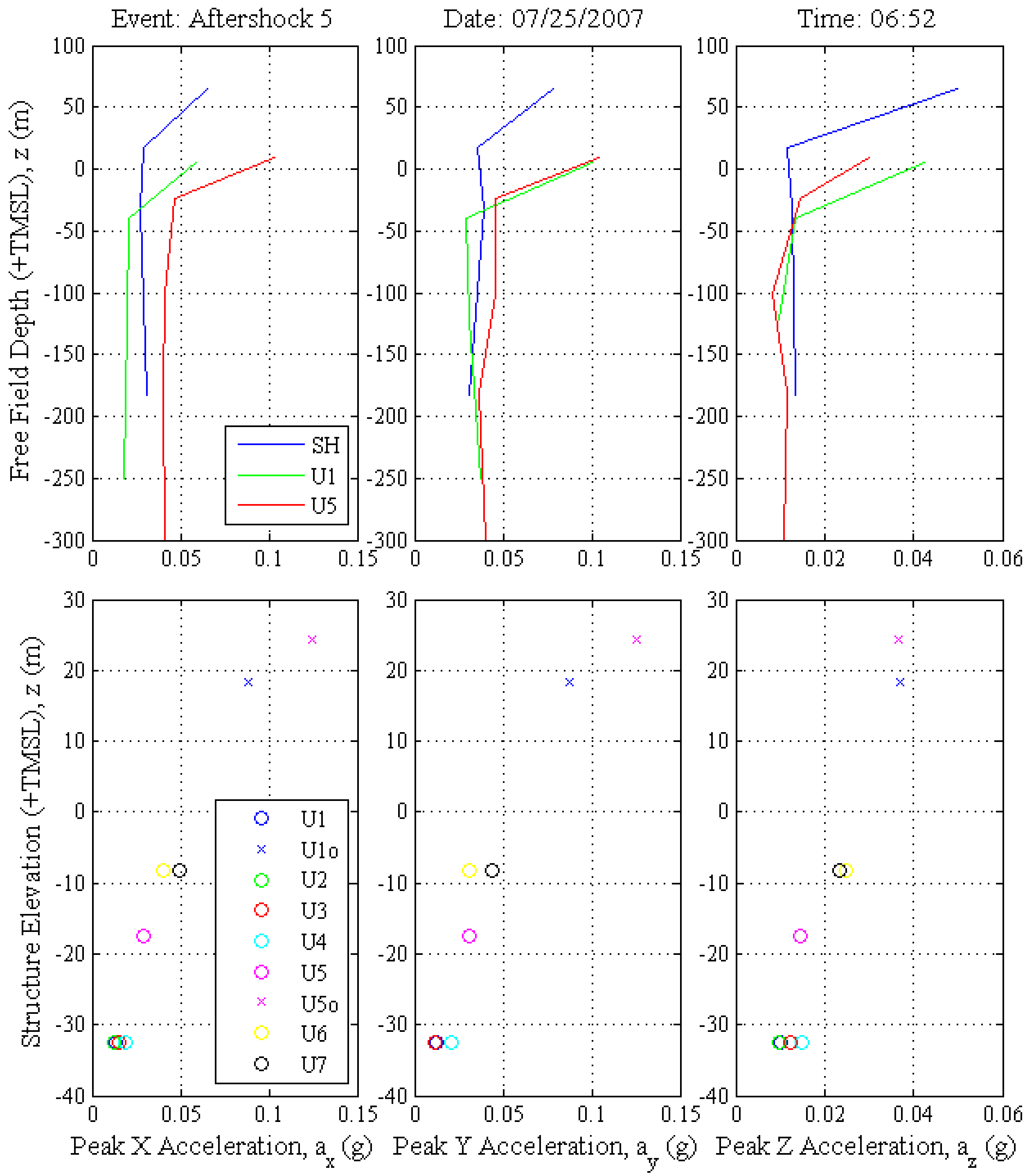

Figure A.7: Peak ground and superstructure acceleration data in response to aftershock 5 following the 2007 Niigata Chūetsu-Oki (6.6 M_W) earthquake

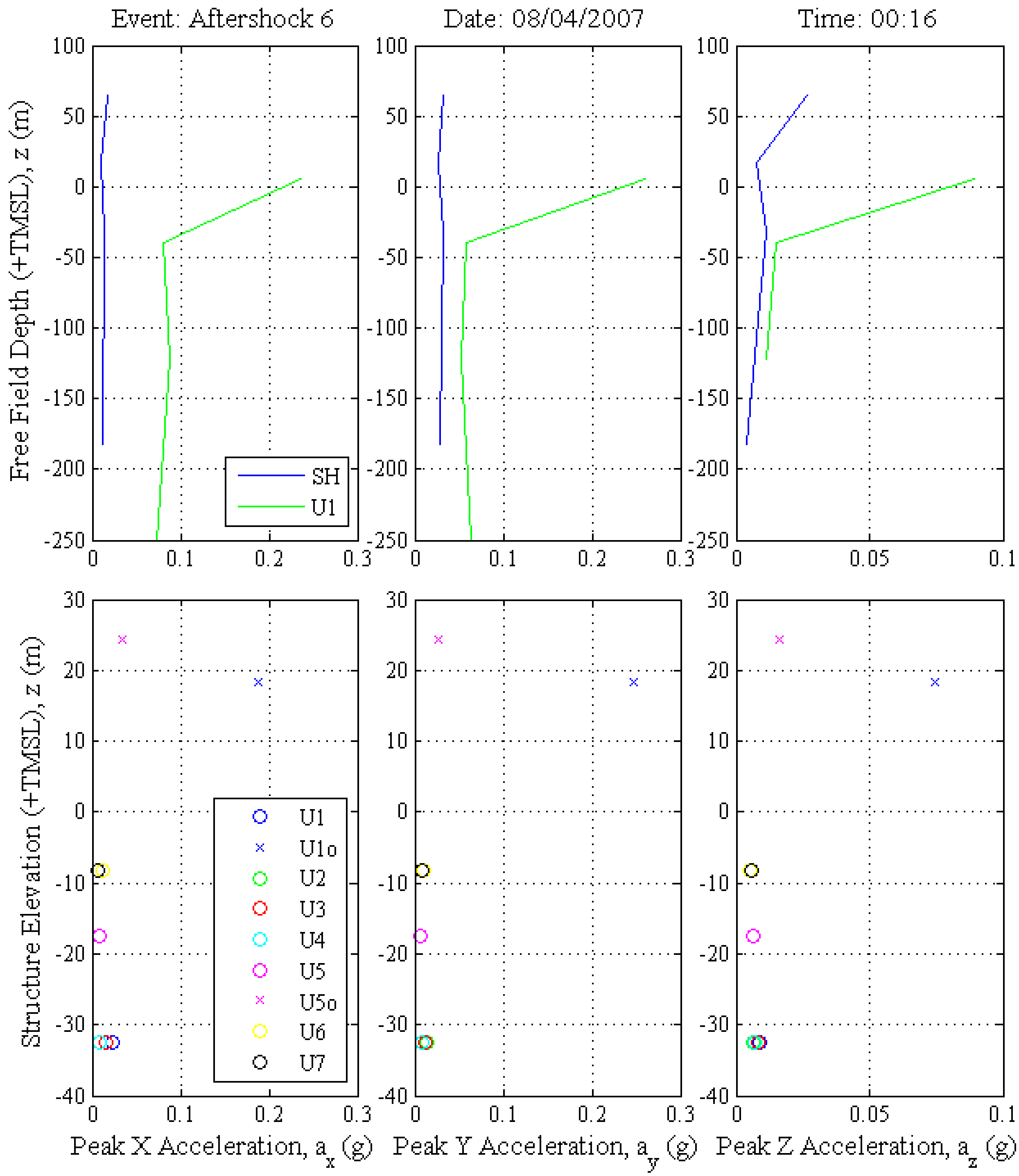

Figure A.8: Peak ground and superstructure acceleration data in response to aftershock 6 following the 2007 Niigata Chūetsu-Oki (6.6 M_W) earthquake

Appendix B

Ground Motion Records and Spectra

This appendix presents the scaled input ground motions as determined by Abrahamson et al (2012) to match the UHRS at an annual frequency of exceedence, f, of 1×10^{-4}, the hazard required for nuclear power structure design. These motions were used as the input motions for the seismic analyses presented. Tables B.1 through B.3 list the peak ground accelerations (PGA), velocities (PGV), and displacements (PGD) for each component of the scaled ground motions. For each of the 30 scaled groundmotions, two plots are presented to characterize the earthquake. The first plot is a time history depicting the variation of ground acceleration, velocity, and displacement in each direction. The second plot shows the acceleration, velocity, and displacement response spectra in each direction. These spectra show the peak dynamic response of SDOF systems subjected to the given ground motions over the period range of 0 to 4 seconds, which should contain the fundamental period in all directions.

No	Event Name (Record)	PGA$_x$ (g)	PGA$_y$ (g)	PGA$_z$ (g)
1	Imperial Valley (G-ELC)	0.84	0.88	0.79
2	Hollister (C-HCH)	0.83	0.84	0.89
3	Hollister (B-HCH)	0.83	0.85	0.82
4	Point Mugu (PHN)	0.88	0.85	0.78
5	Livermore (A-ANT)	0.85	0.83	0.82
6	Livermore (A-KOD)	0.94	0.84	0.83
7	Livermore (A-SRM)	0.83	0.82	0.84
8	Taiwan (05O07)	0.77	0.80	0.85
9	Westmorland (PTS)	0.85	0.83	0.82
10	Double Springs (WOO)	0.86	0.75	0.81
11	Friuli (B-BUI)	0.84	0.83	0.79
12	N Palm Springs (MVH)	0.82	0.80	0.81
13	Irpinia (B-BIS)	0.84	0.87	0.82
14	Chi-Chi (TCU116)	0.86	0.80	0.78
15	Chi-Chi (TCU120)	0.82	0.85	0.82
16	Chi-Chi (TCU138)	0.84	0.85	0.78
17	Chi-Chi (TCU067)	0.80	0.84	0.80
18	Victoria (CHI)	0.84	0.84	0.84
19	Victoria (HPB)	0.85	0.90	0.84
20	Dinar (DIN)	0.92	0.84	0.81
21	Imperial Valley (H-ECC)	0.84	0.82	0.82
22	Superstition Hills (B-ICC)	0.85	1.04	0.81
23	Superstition Hills (B-WSM)	0.84	0.83	0.79
24	Superstition Hills (B-IVW)	0.83	0.85	0.82
25	Corinth (COR)	0.83	0.90	0.82
26	Northridge (MUL)	0.82	0.83	0.88
27	Northridge (LDM)	0.89	0.84	0.82
28	Northridge (GLE)	0.85	0.78	0.89
29	Kobe (SHI)	0.87	0.85	0.82
30	Loma Prieta (LGP)	0.80	0.83	0.79

Table B.1: Peak ground accelerations in each direction for the scaled input ground motions

No	Event Name (Record)	PGV$_x$ (m/s)	PGV$_y$ (m/s)	PGV$_z$ (m/s)
1	Imperial Valley (G-ELC)	0.60	0.87	0.23
2	Hollister (C-HCH)	0.52	0.73	0.35
3	Hollister (B-HCH)	0.56	0.75	0.54
4	Point Mugu (PHN)	1.19	0.59	0.29
5	Livermore (A-ANT)	0.73	0.73	0.62
6	Livermore (A-KOD)	0.82	0.72	0.31
7	Livermore (A-SRM)	0.56	0.75	0.46
8	Taiwan (05O07)	0.62	0.83	0.36
9	Westmorland (PTS)	1.06	0.94	0.33
10	Double Springs (WOO)	0.93	0.67	0.23
11	Friuli (B-BUI)	0.72	0.79	0.45
12	N Palm Springs (MVH)	0.72	1.00	0.31
13	Irpinia (B-BIS)	0.76	0.94	0.73
14	Chi-Chi (TCU116)	0.99	0.73	1.50
15	Chi-Chi (TCU120)	1.21	1.24	0.74
16	Chi-Chi (TCU138)	0.81	0.88	0.85
17	Chi-Chi (TCU067)	0.86	0.86	0.85
18	Victoria (CHI)	0.94	0.91	0.36
19	Victoria (HPB)	0.78	0.99	0.28
20	Dinar (DIN)	0.81	0.66	0.37
21	Imperial Valley (H-ECC)	0.84	1.29	0.36
22	Superstition Hills (B-ICC)	0.91	1.17	0.36
23	Superstition Hills (B-WSM)	0.72	0.85	0.29
24	Superstition Hills (B-IVW)	0.81	0.67	0.25
25	Corinth (COR)	0.82	0.89	0.50
26	Northridge (MUL)	0.74	0.86	0.25
27	Northridge (LDM)	1.13	1.18	0.37
28	Northridge (GLE)	0.93	0.64	0.28
29	Kobe (SHI)	1.01	0.79	0.61
30	Loma Prieta (LGP)	0.79	0.85	0.46

Table B.2: Peak ground velocities in each direction for the scaled input ground motions

No	Event Name (Record)	PGD$_x$ (m)	PGD$_y$ (m)	PGD$_z$ (m)
1	Imperial Valley (G-ELC)	0.11	0.16	0.033
2	Hollister (C-HCH)	0.088	0.13	0.065
3	Hollister (B-HCH)	0.13	0.16	0.19
4	Point Mugu (PHN)	0.16	0.11	0.071
5	Livermore (A-ANT)	0.15	0.24	0.23
6	Livermore (A-KOD)	0.26	0.15	0.055
7	Livermore (A-SRM)	0.14	0.23	0.12
8	Taiwan (05O07)	0.090	0.19	0.091
9	Westmorland (PTS)	0.36	0.38	0.061
10	Double Springs (WOO)	0.22	0.10	0.032
11	Friuli (B-BUI)	0.17	0.14	0.084
12	N Palm Springs (MVH)	0.19	0.19	0.045
13	Irpinia (B-BIS)	0.28	0.35	0.35
14	Chi-Chi (TCU116)	0.32	0.25	0.69
15	Chi-Chi (TCU120)	0.36	0.29	0.28
16	Chi-Chi (TCU138)	0.17	0.18	0.28
17	Chi-Chi (TCU067)	0.17	0.19	0.23
18	Victoria (CHI)	0.25	0.43	0.13
19	Victoria (HPB)	0.21	0.22	0.065
20	Dinar (DIN)	0.17	0.16	0.096
21	Imperial Valley (H-ECC)	0.33	0.39	0.11
22	Superstition Hills (B-ICC)	0.21	0.26	0.20
23	Superstition Hills (B-WSM)	0.28	0.29	0.099
24	Superstition Hills (B-IVW)	0.38	0.34	0.028
25	Corinth (COR)	0.17	0.18	0.098
26	Northridge (MUL)	0.18	0.15	0.052
27	Northridge (LDM)	0.20	0.24	0.082
28	Northridge (GLE)	0.23	0.16	0.061
29	Kobe (SHI)	0.23	0.14	0.14
30	Loma Prieta (LGP)	0.30	0.18	0.12

Table B.3: Peak ground displacements in each direction for the scaled input ground motions

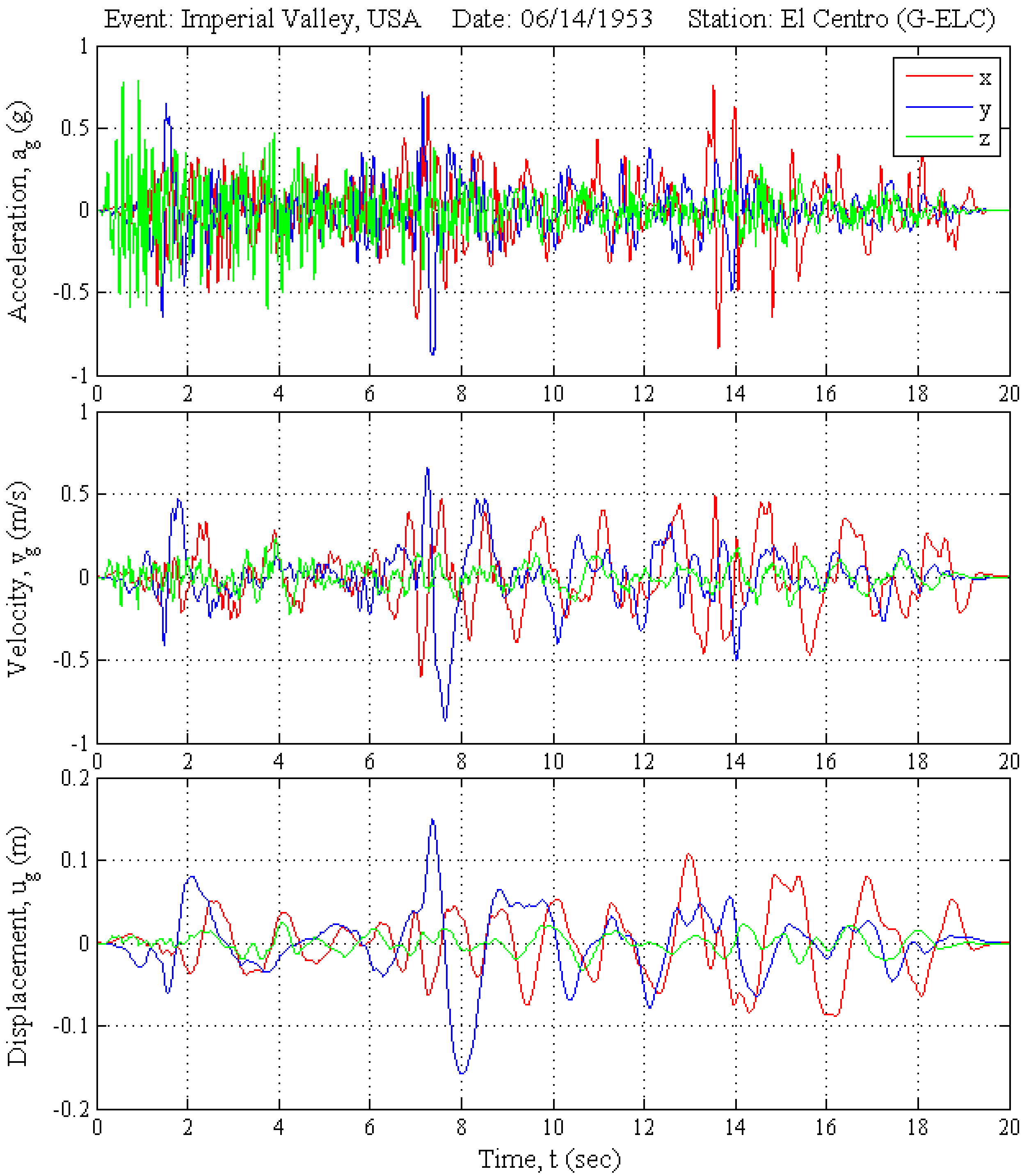

Figure B.1: Time history records for the Imperial Valley, USA (G-ELC) earthquake

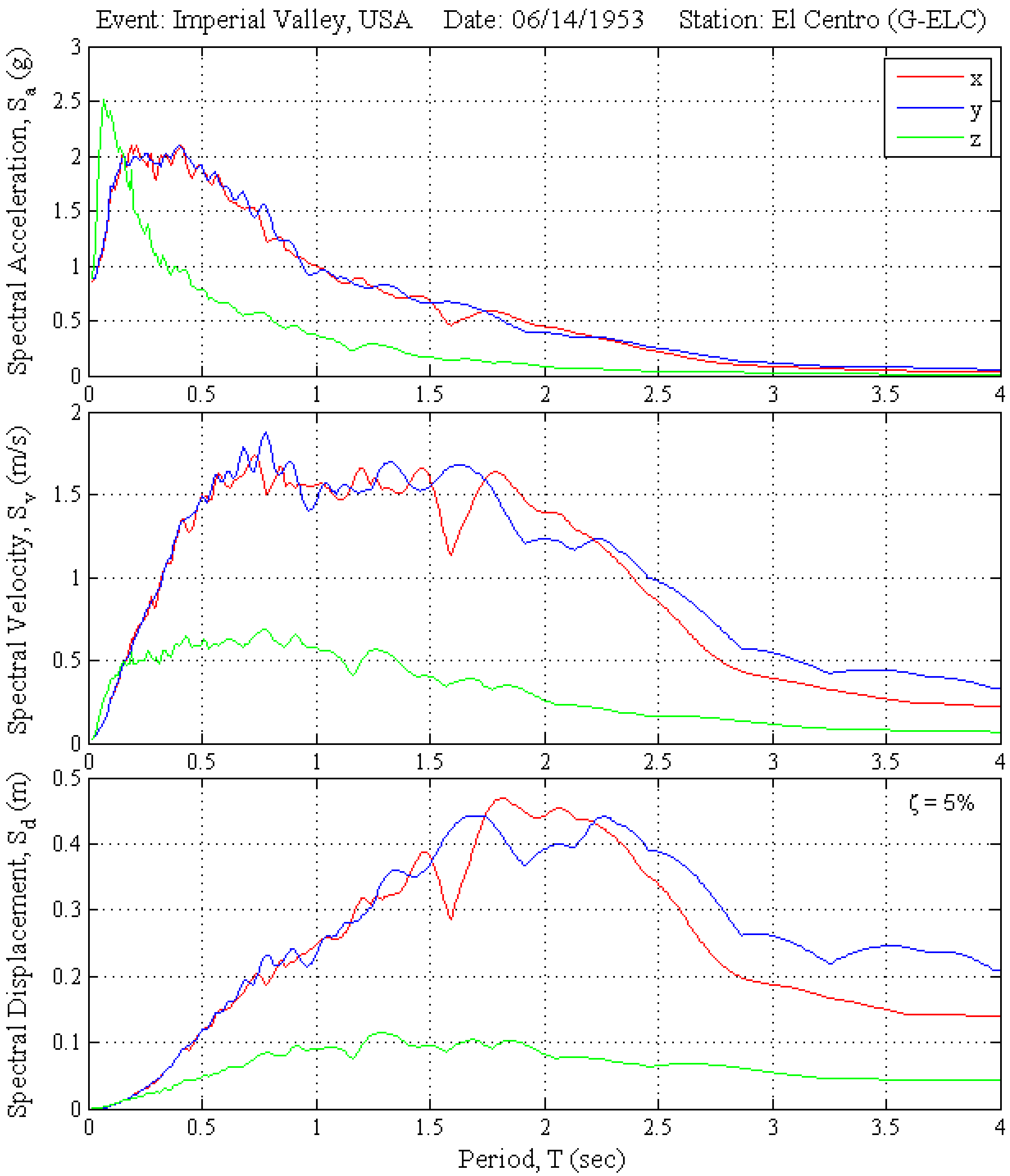

Figure B.2: Response spectra with 5% damping for the Imperial Valley, USA (G-ELC) earthquake

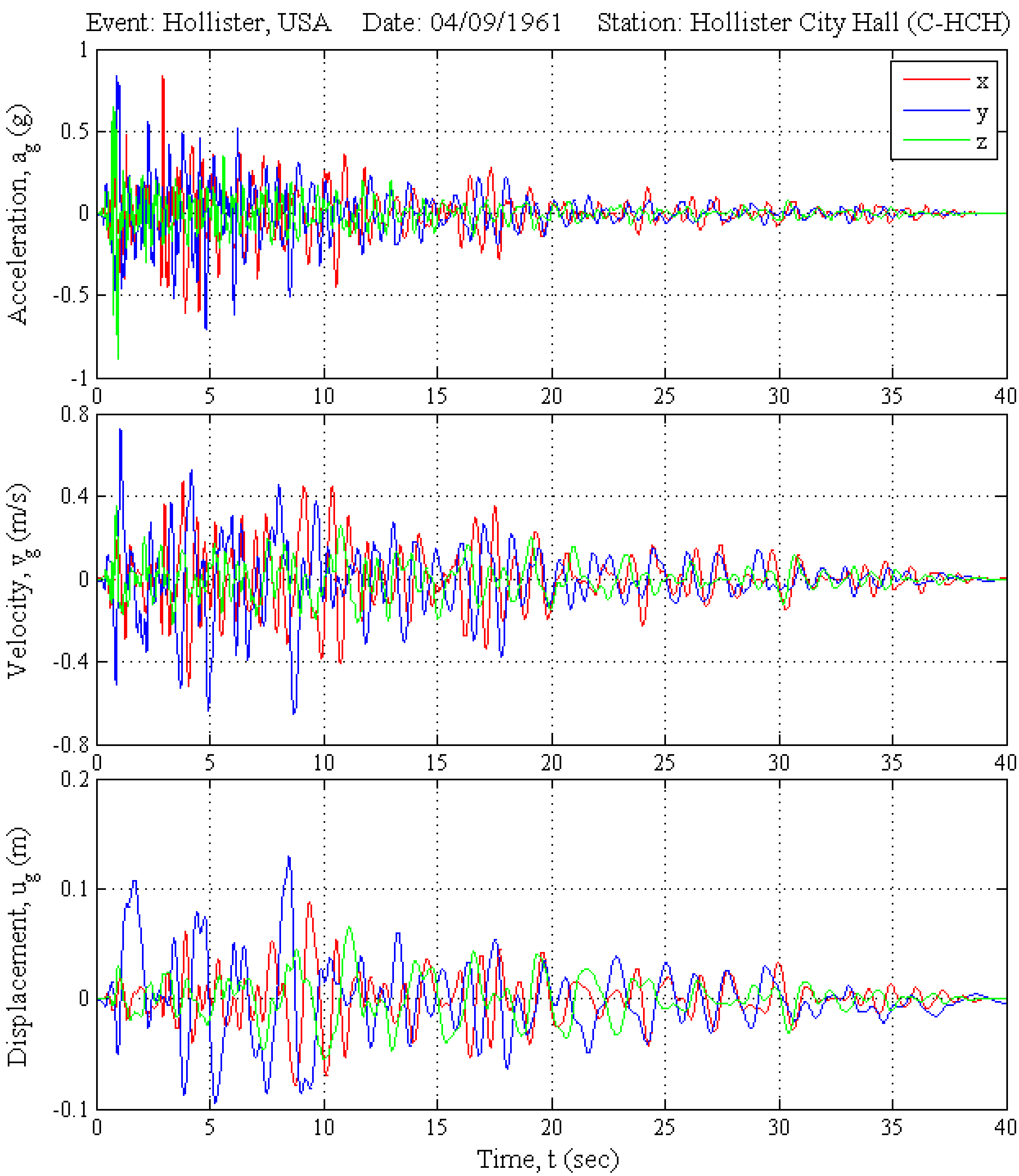

Figure B.3: Time history records for the Hollister, USA (C-HCH) earthquake

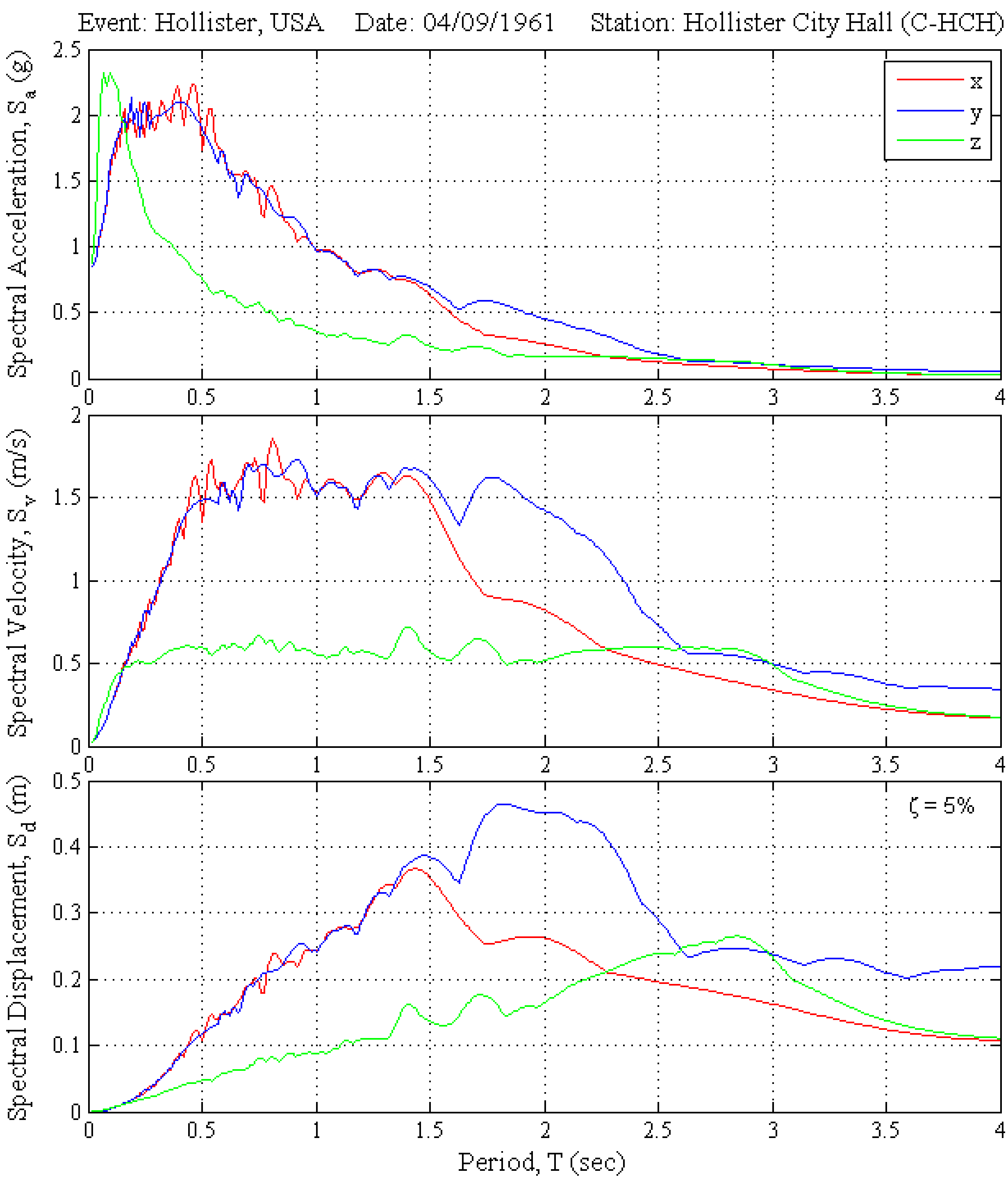

Figure B.4: Response spectra with 5% damping for the Hollister, USA (C-HCH) earthquake

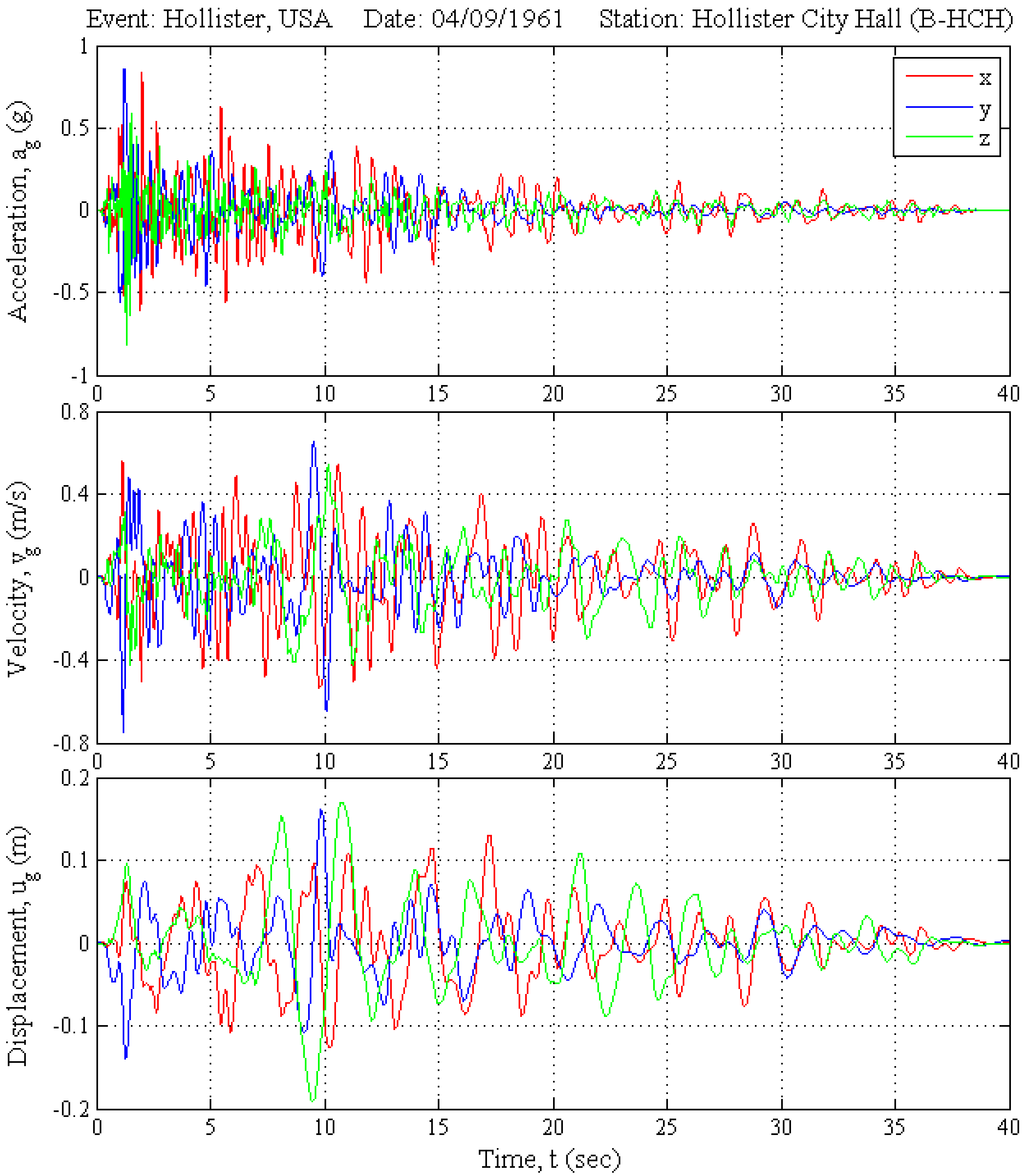

Figure B.5: Time history records for the Hollister, USA (D-HCH) earthquake

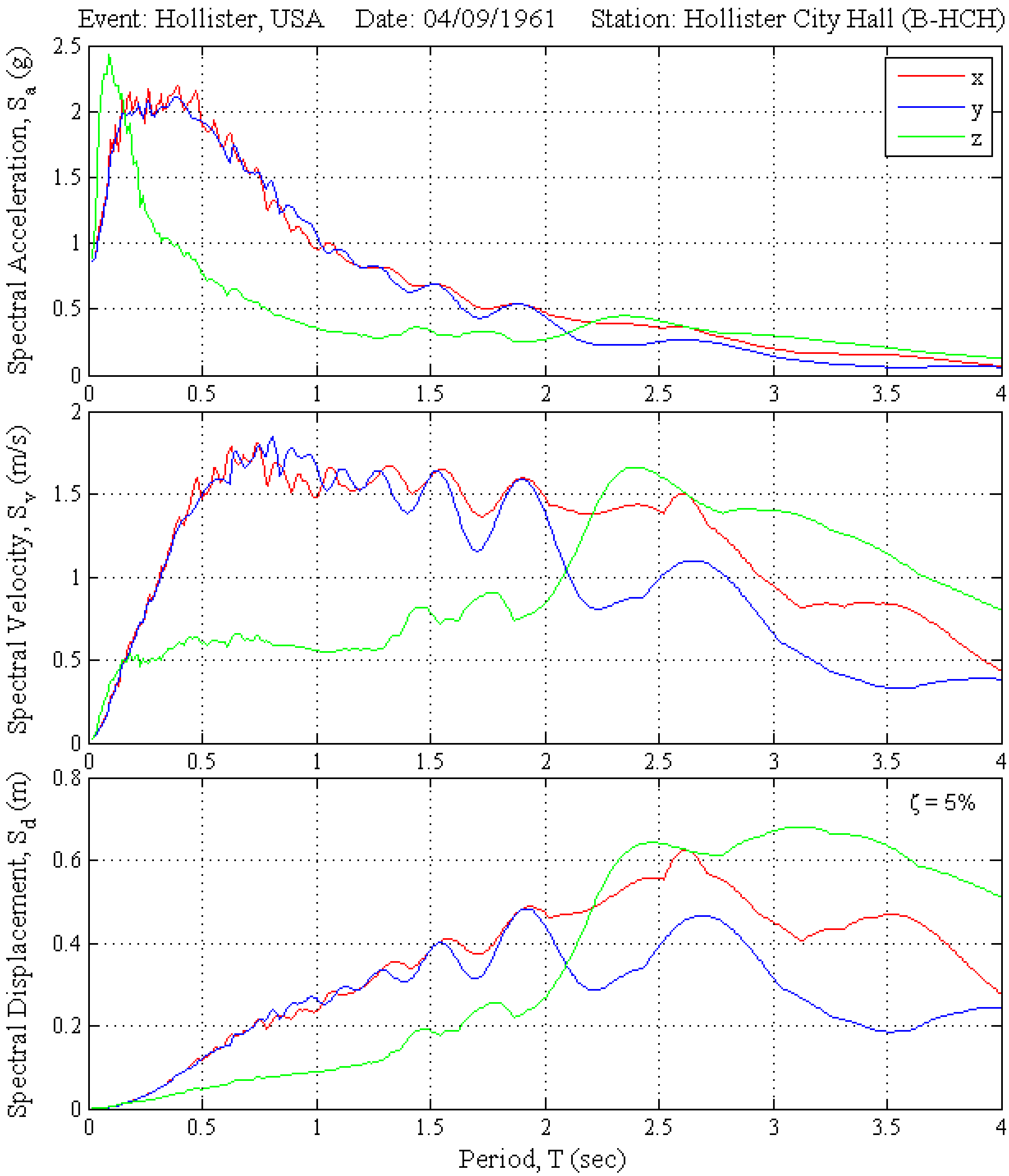

Figure B.6: Response spectra with 5% damping for the Hollister, USA (D-HCH) earthquake

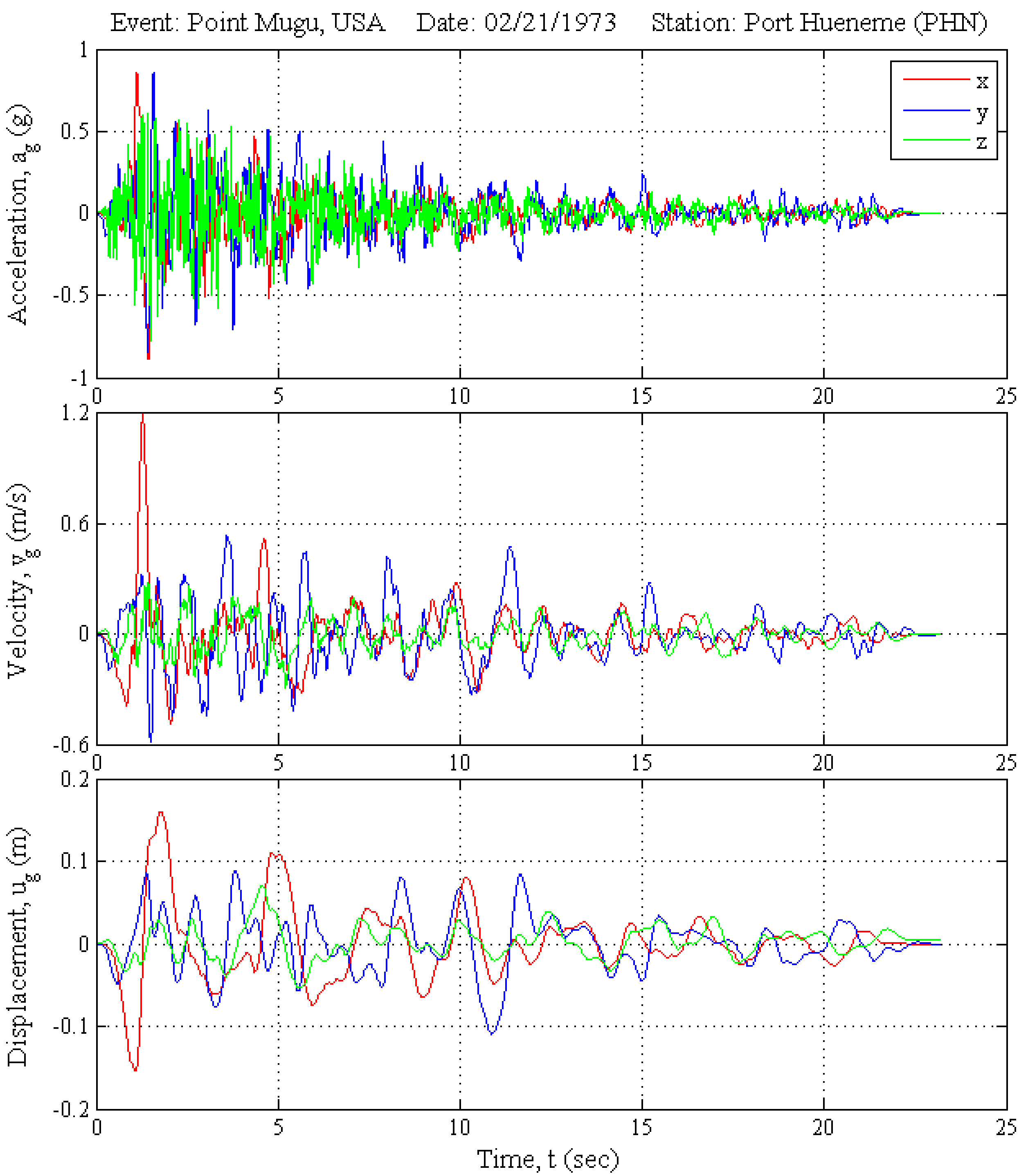

Figure B.7: Time history records for the Point Mugu, USA (PHN) earthquake

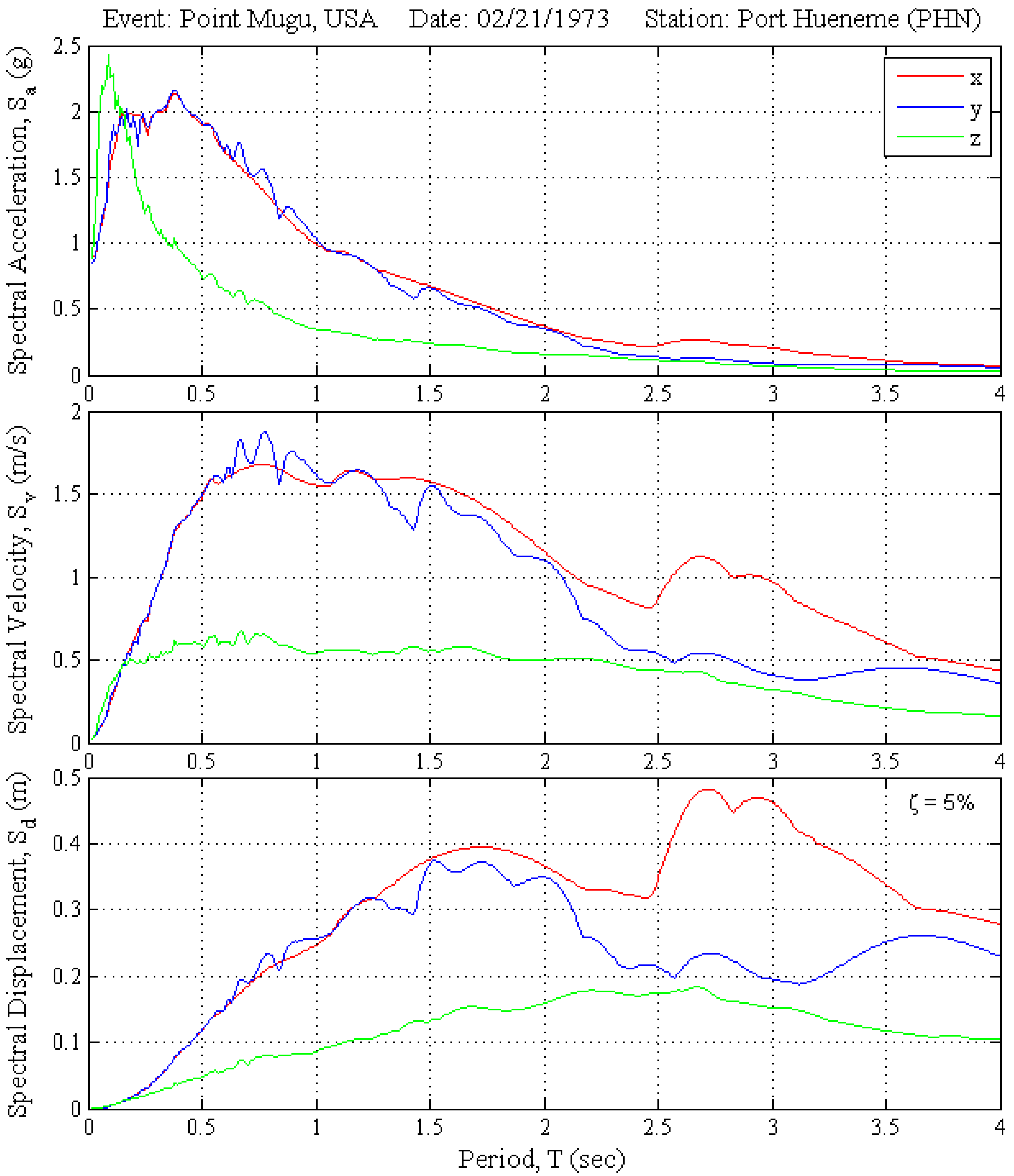

Figure B.8: Response spectra with 5% damping for the Point Mugu, USA (PHN) earthquake

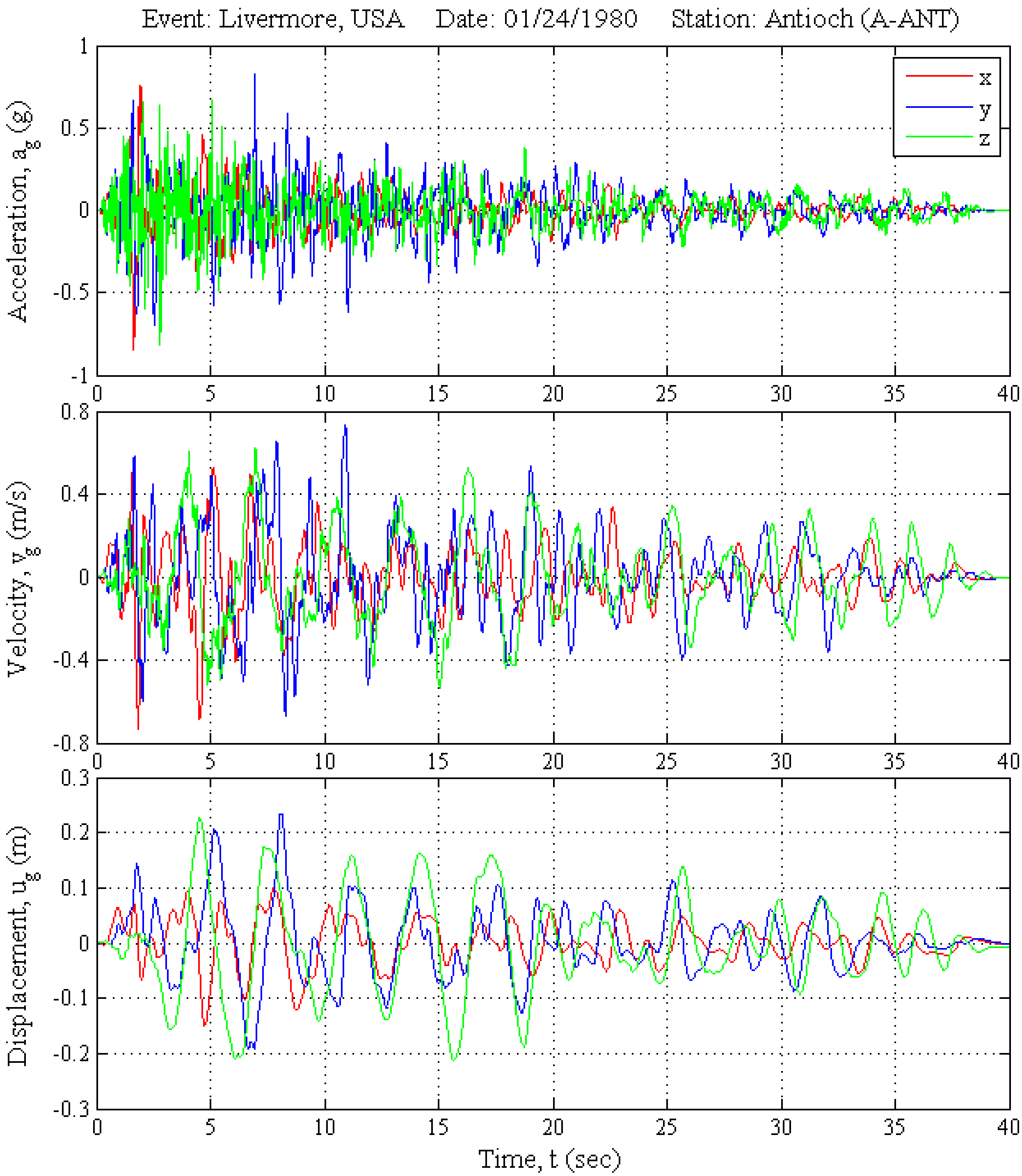

Figure B.9: Time history records for the Livermore, USA (A-ANT) earthquake

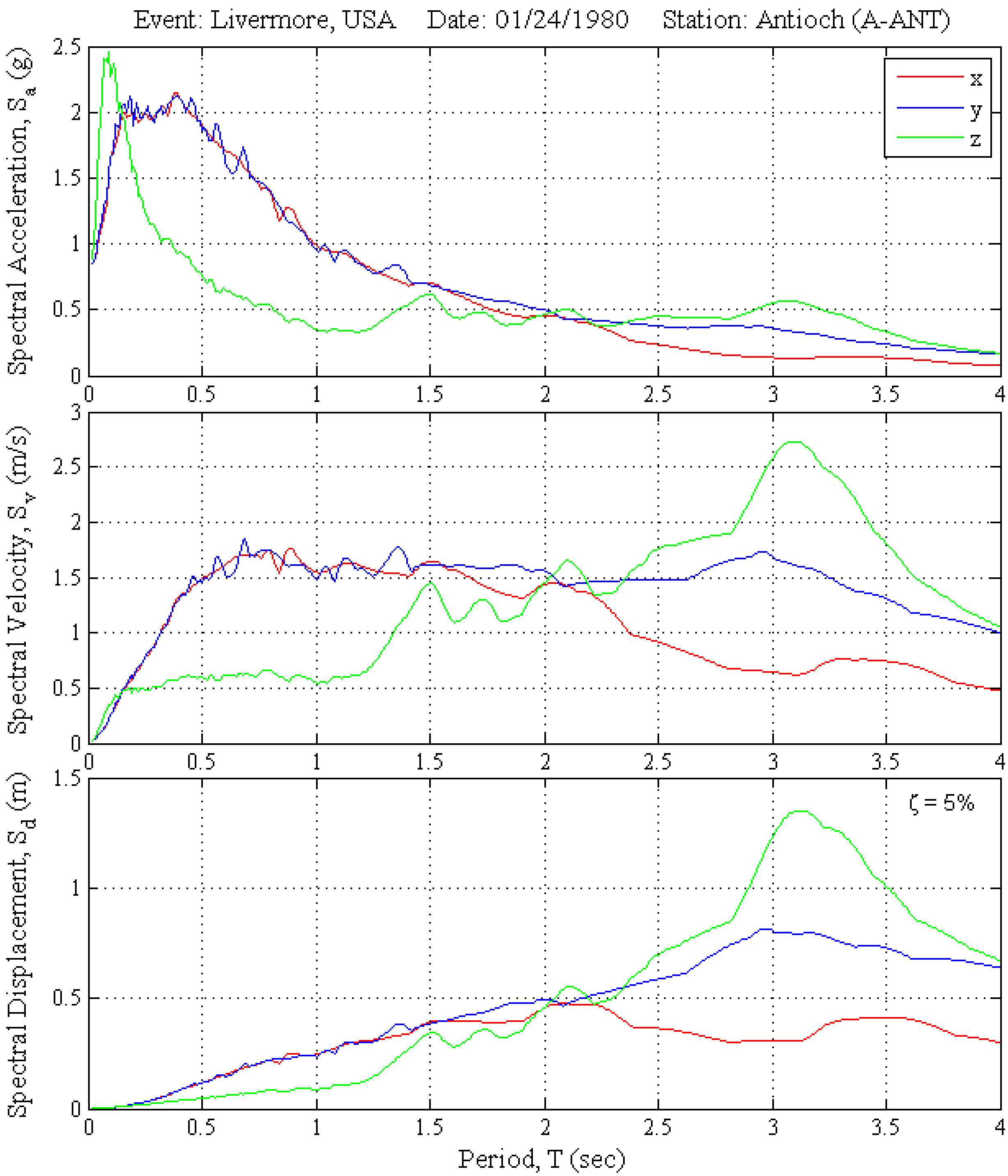

Figure B.10: Response spectra with 5% damping for the Livermore, USA (A-ANT) earthquake

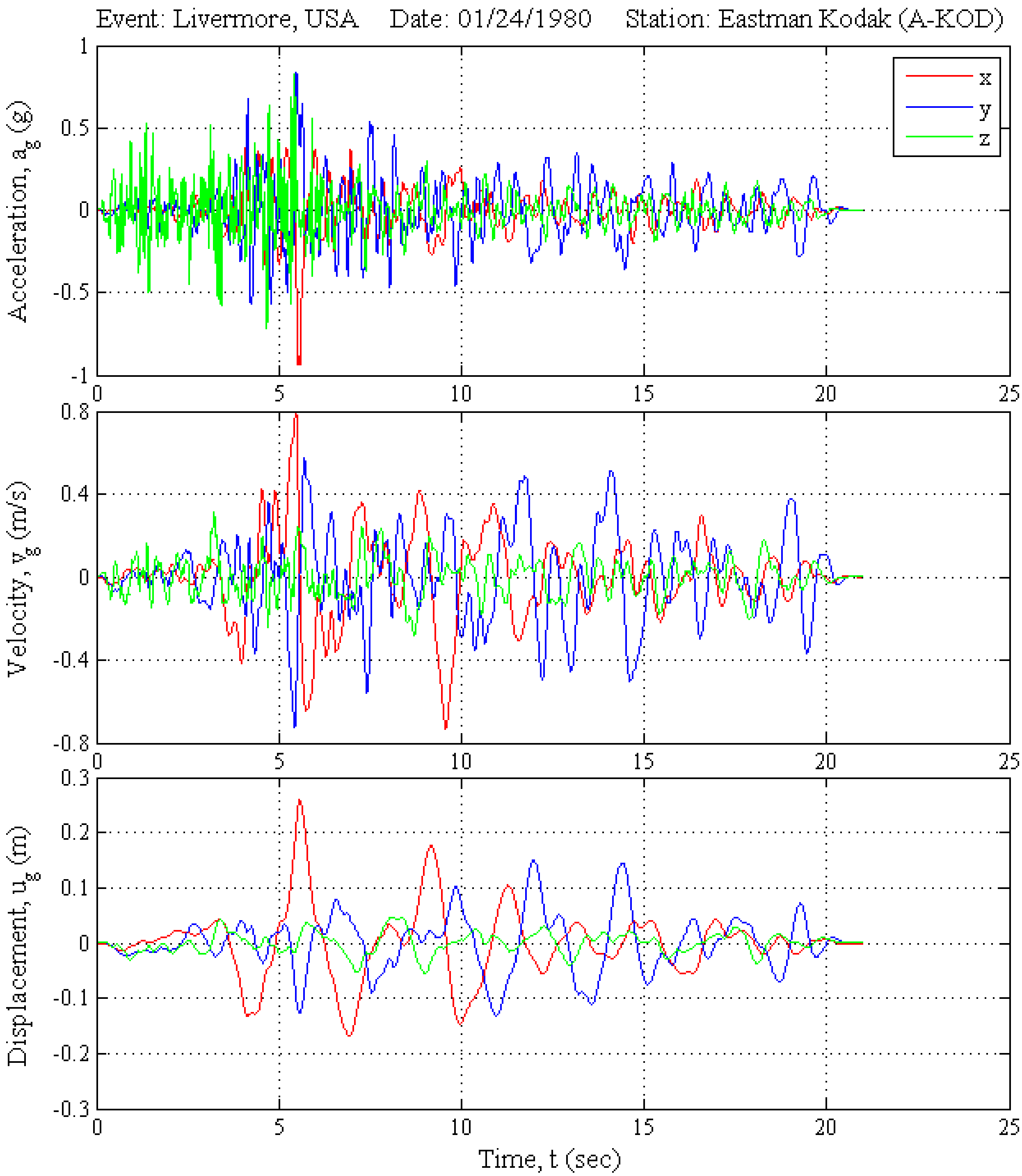

Figure B.11: Time history records for the Livermore, USA (A-KOD) earthquake

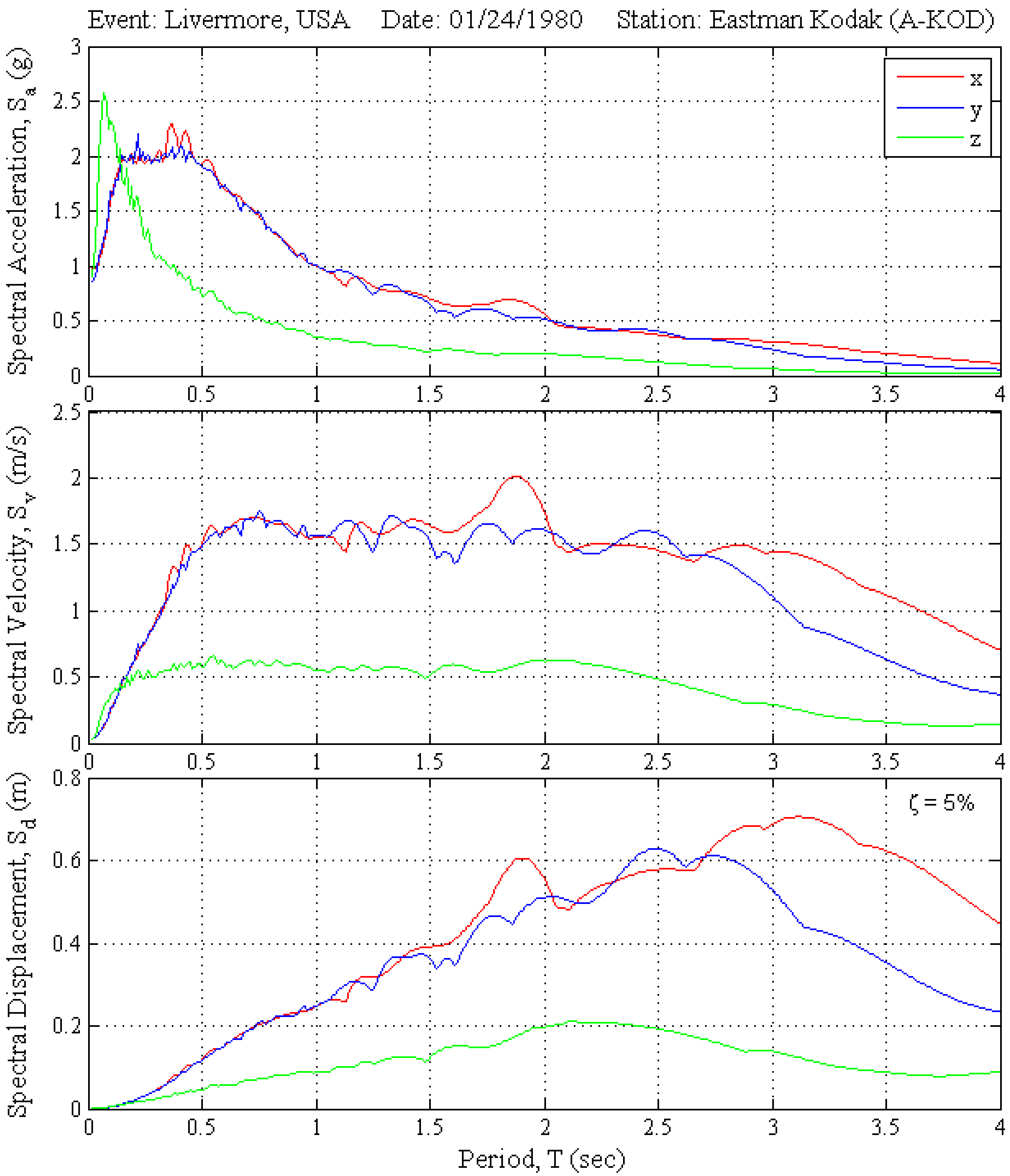

Figure B.12: Response spectra with 5% damping for the Livermore, USA (A-KOD) earthquake

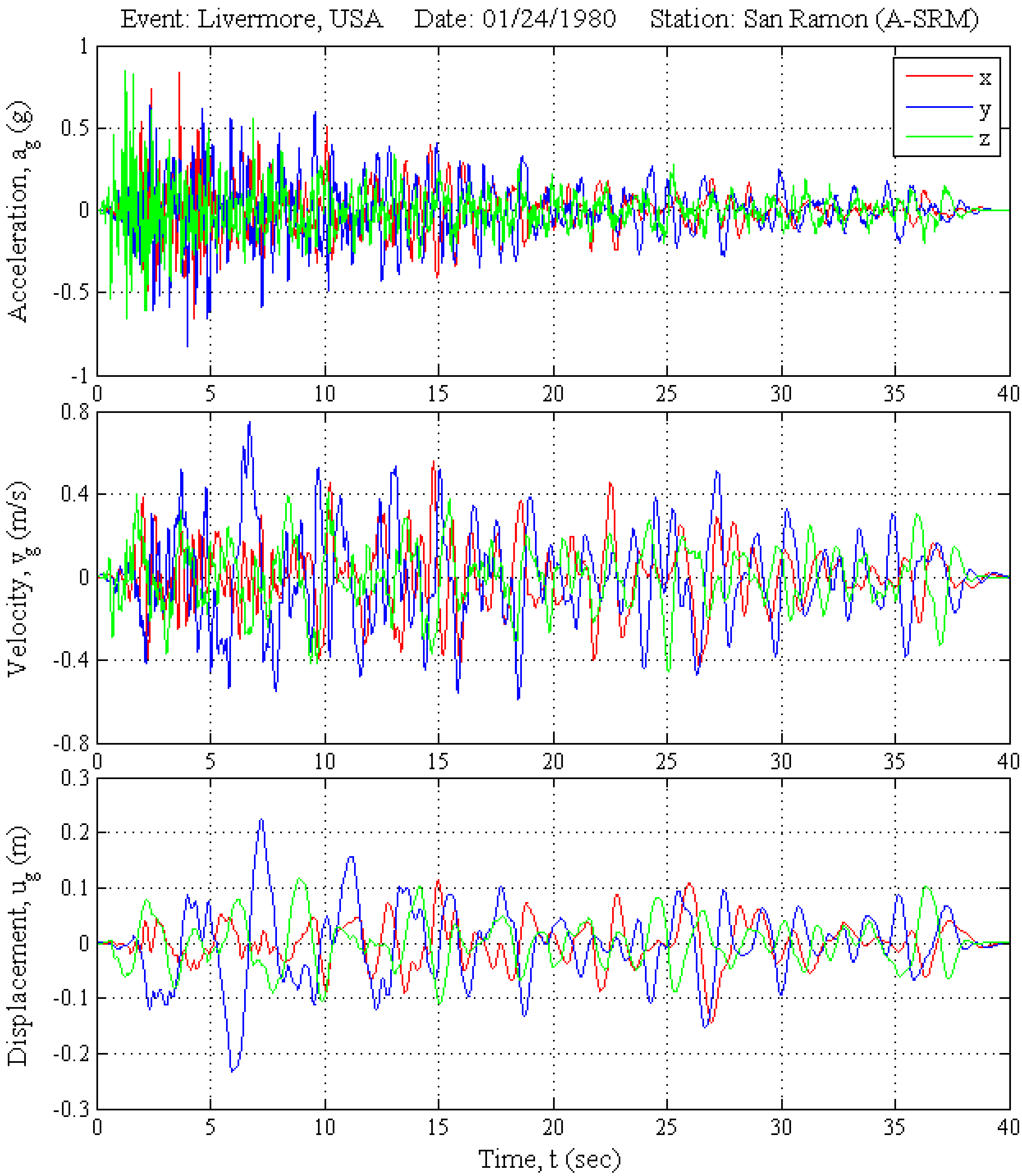

Figure B.13: Time history records for the Livermore, USA (A-SRM) earthquake

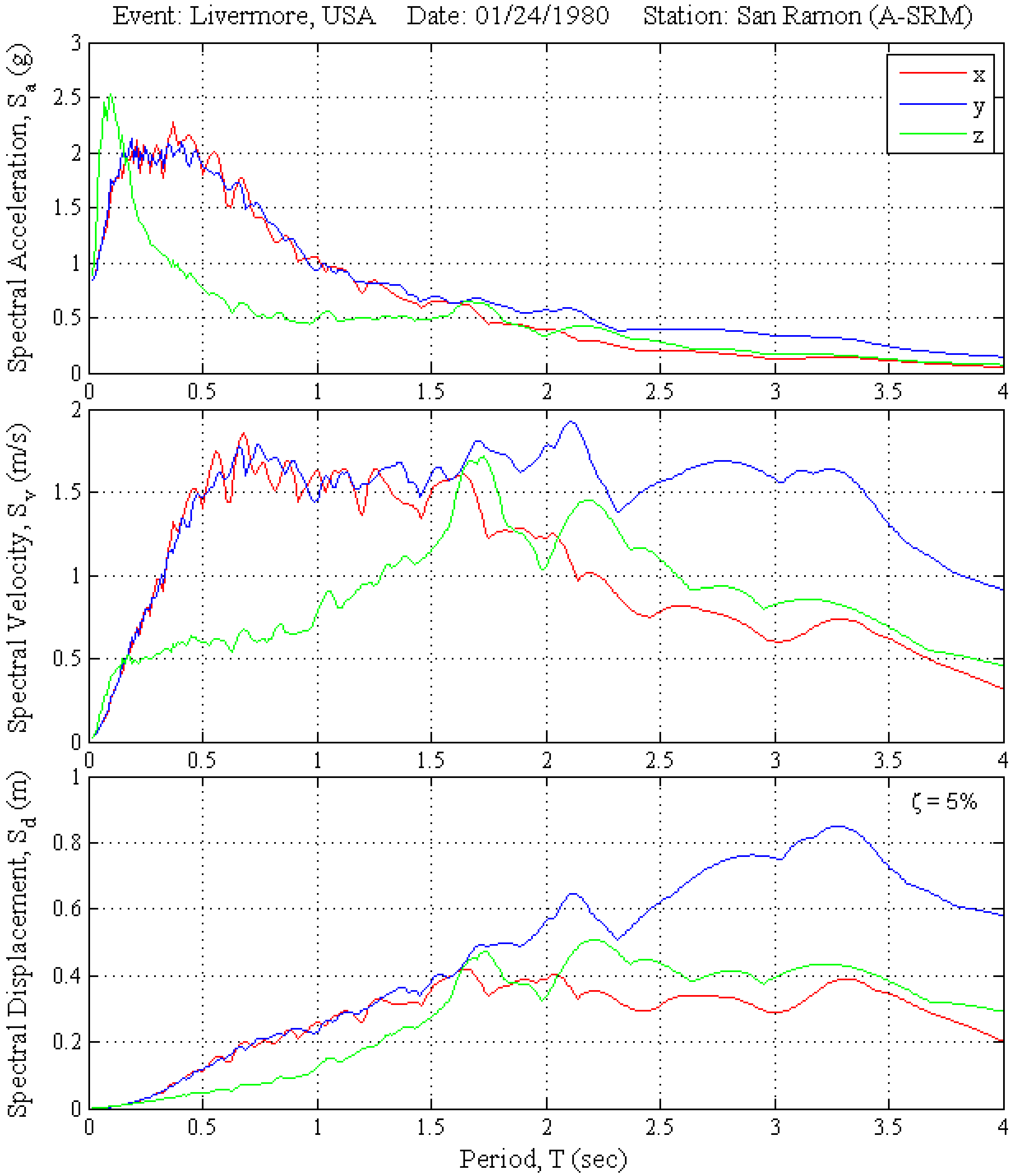

Figure B.14: Response spectra with 5% damping for the Livermore, USA (A-SRM) earthquake

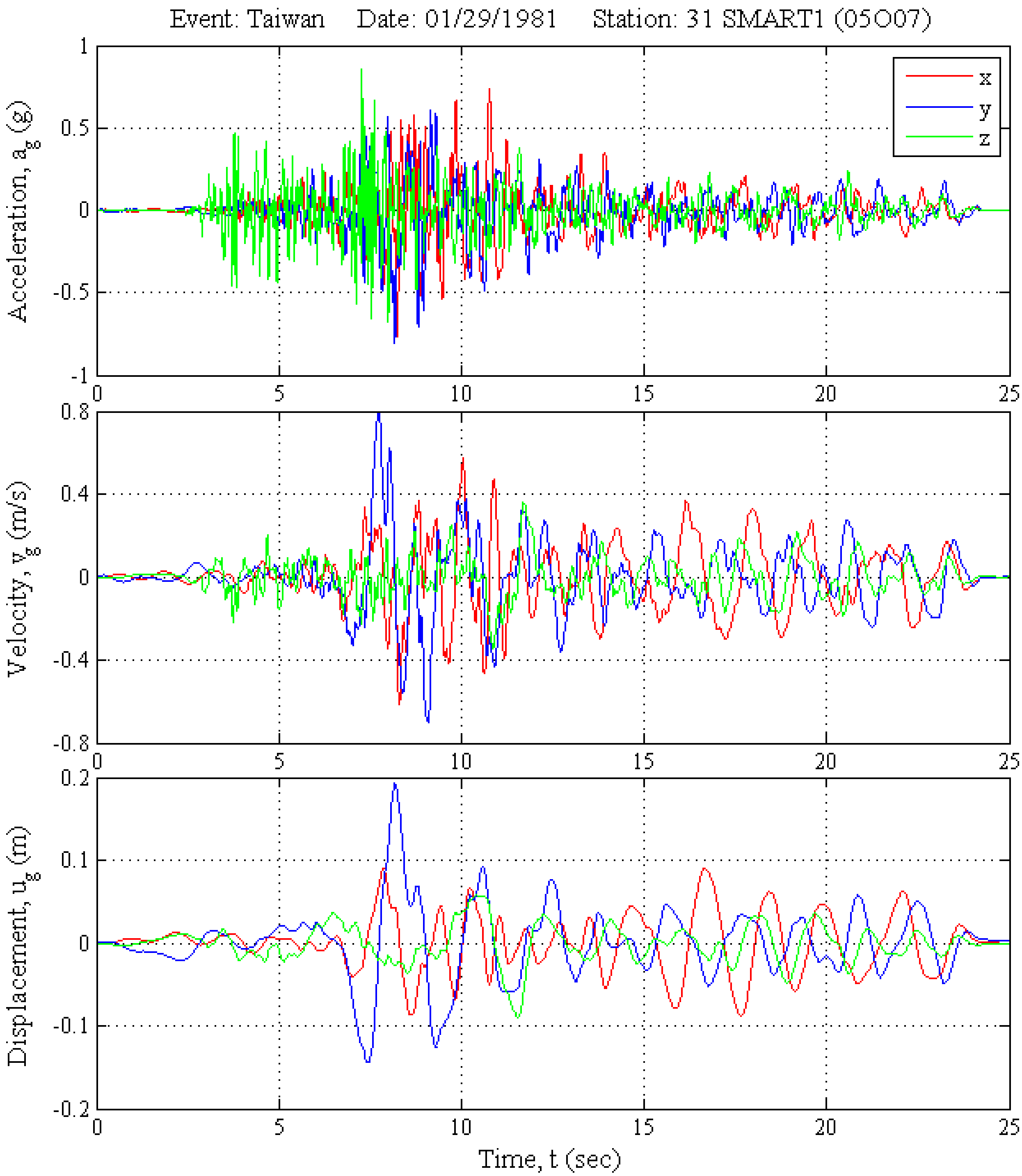

Figure B.15: Time history records for the Taiwan (05O07) earthquake

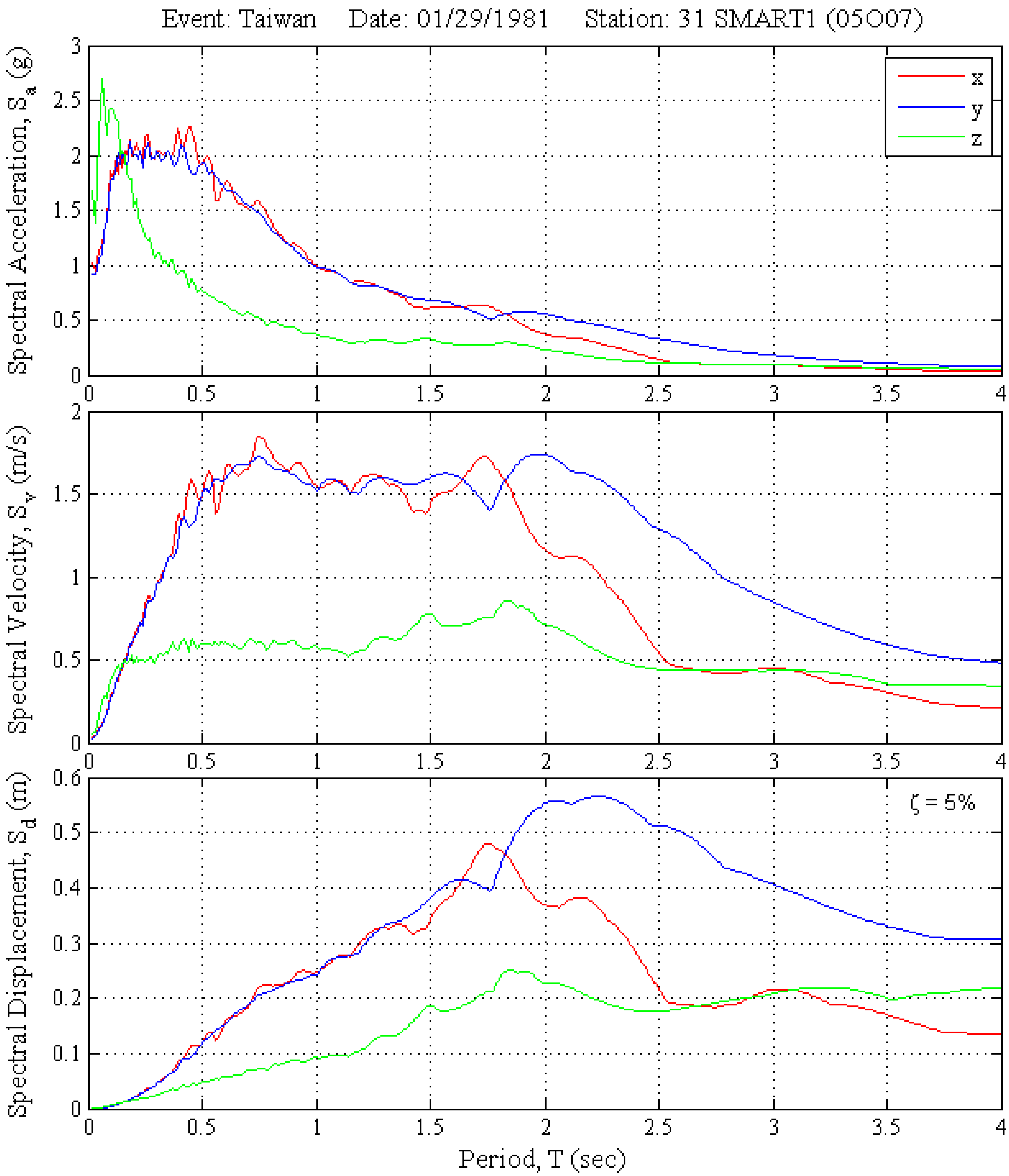

Figure B.16: Response spectra with 5% damping for the Taiwan (05O07) earthquake

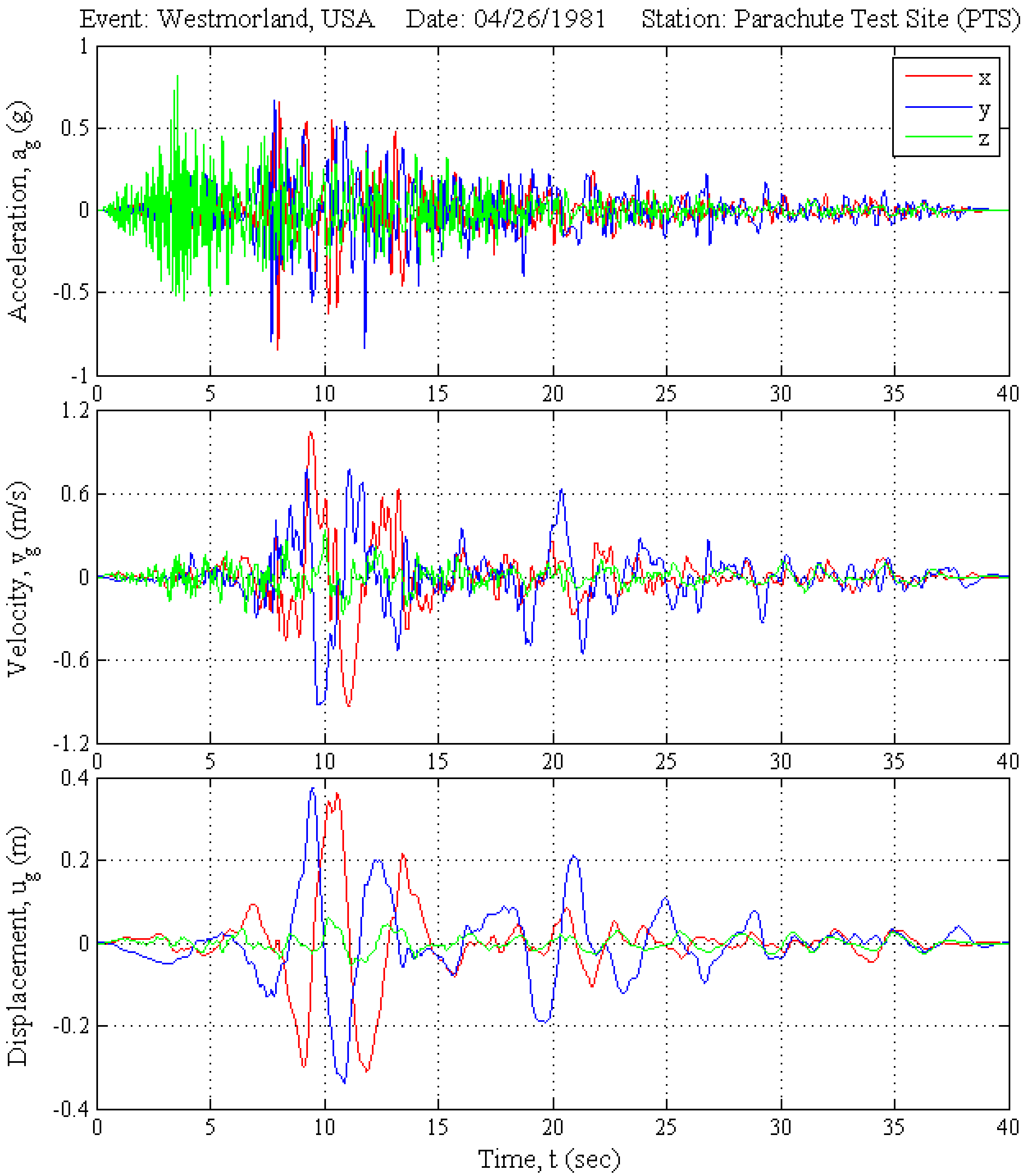

Figure B.17: Time history records for the Westmorland, USA (PTS) earthquake

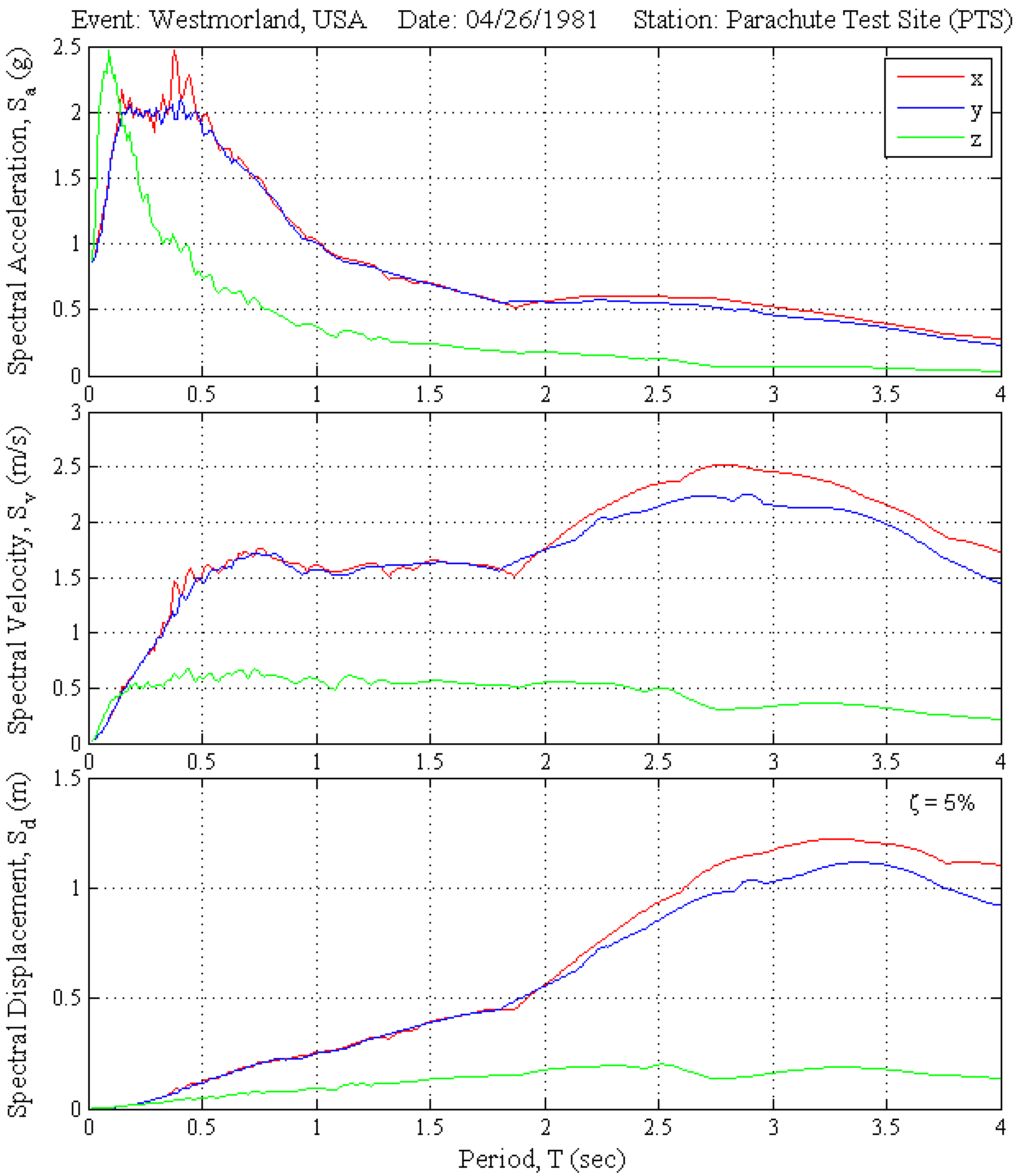

Figure B.18: Response spectra with 5% damping for the Westmorland, USA (PTS) earthquake

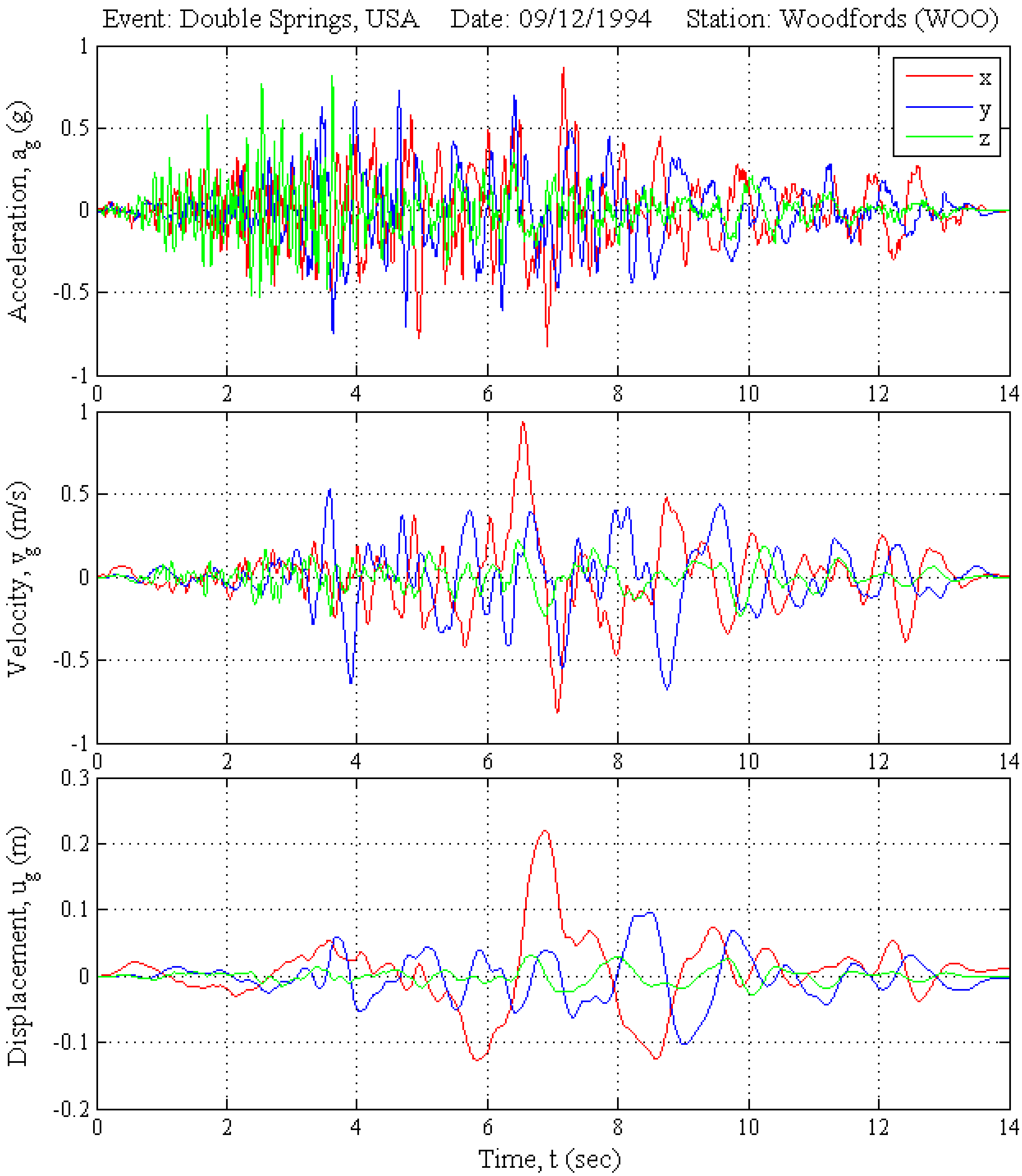

Figure B.19: Time history records for the Double Springs, USA (WOO) earthquake

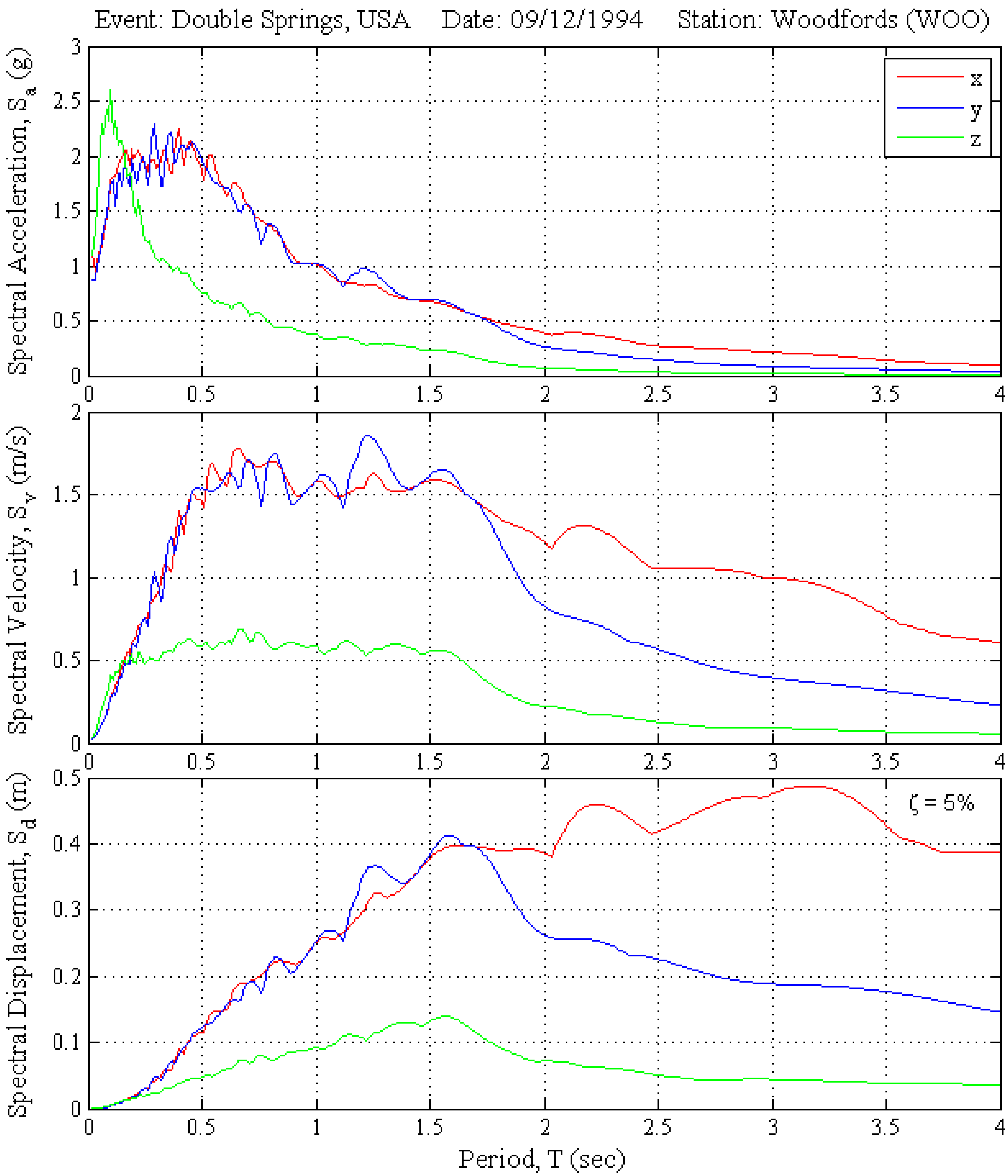

Figure B.20: Response spectra with 5% damping for the Double Springs, USA (WOO) earthquake

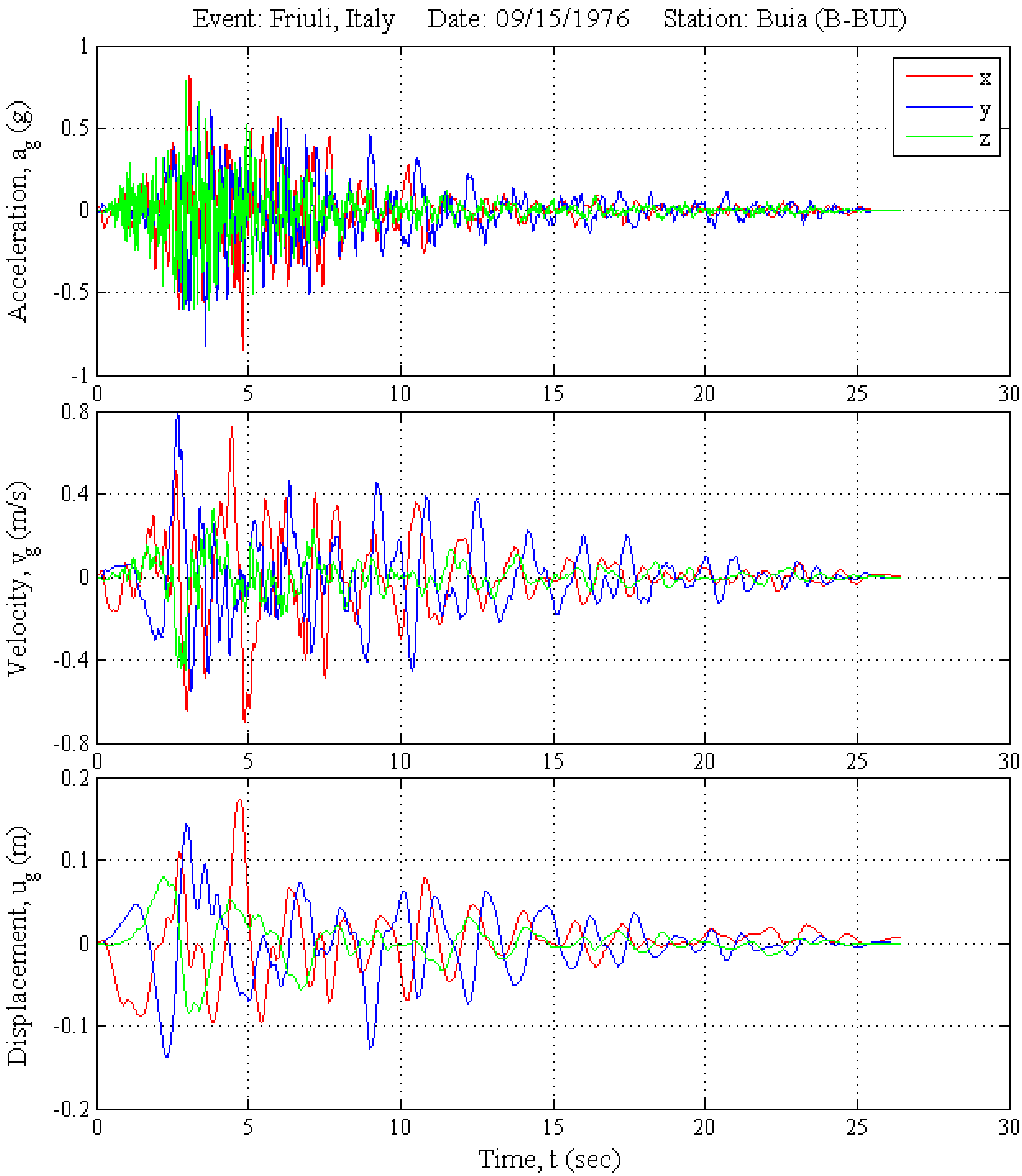

Figure B.21: Time history records for the Friuli, Italy (B-BUI) earthquake

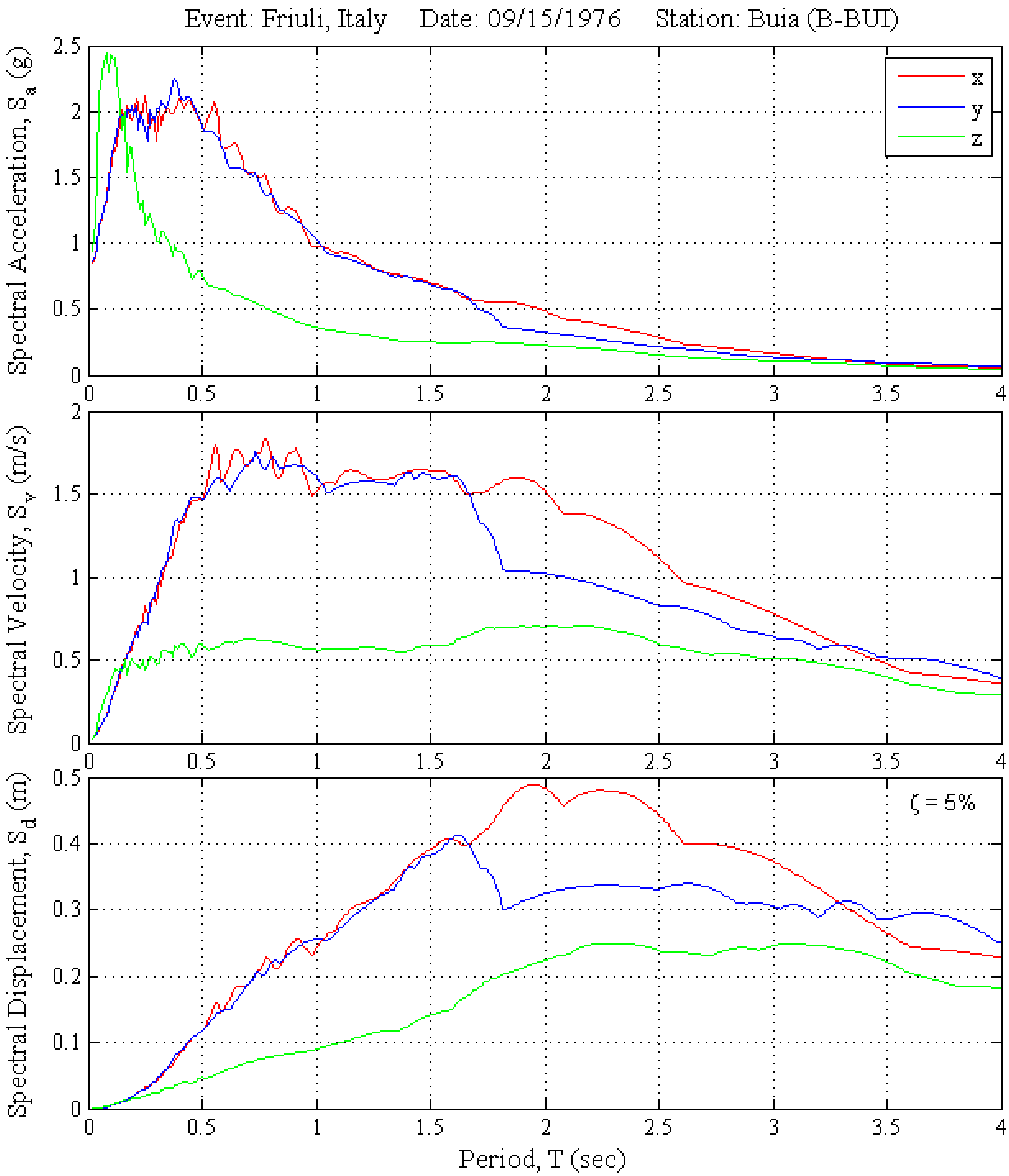

Figure B.22: Response spectra with 5% damping for the Friuli, Italy (B-BUI) earthquake

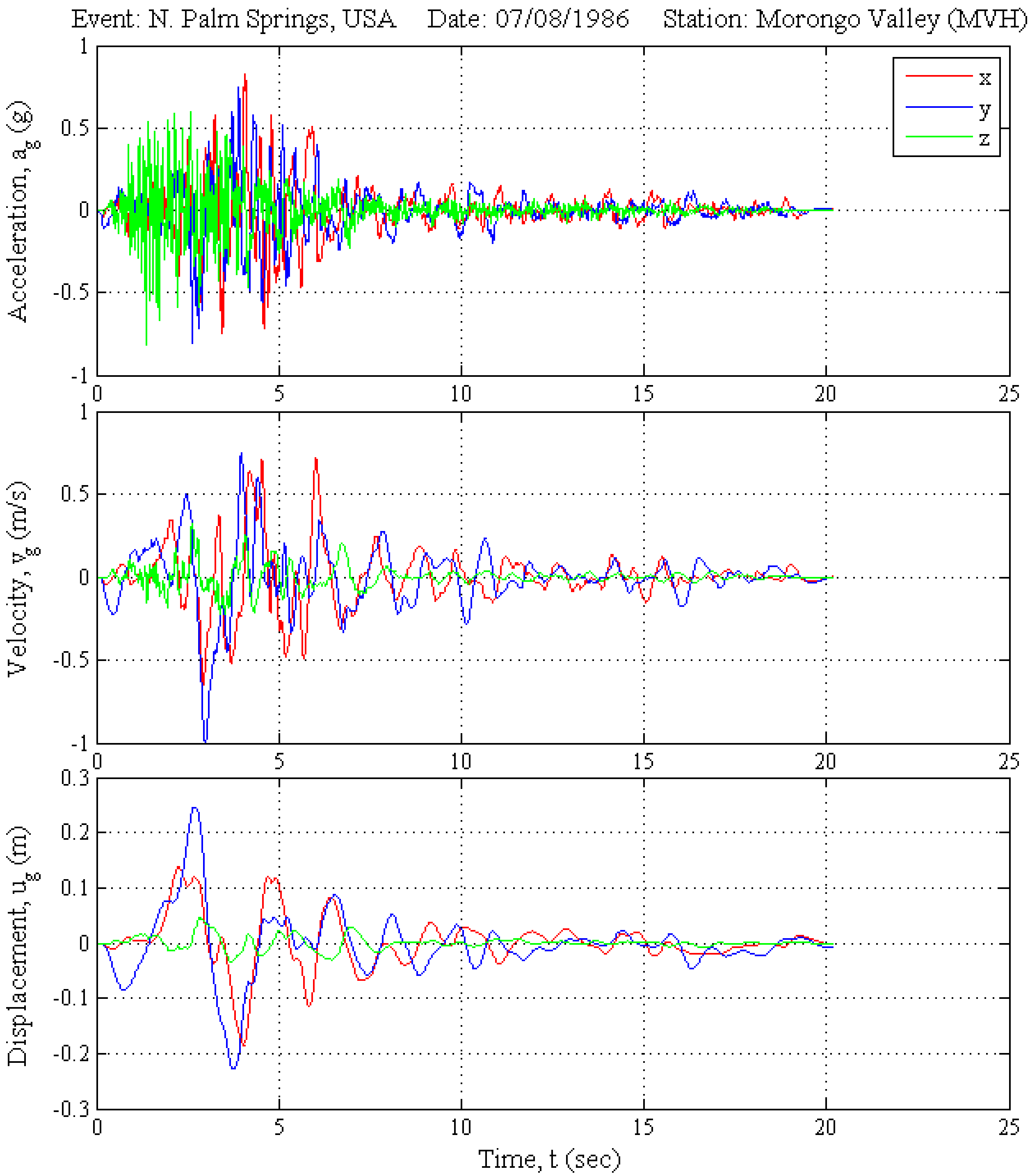

Figure B.23: Time history records for the N Palm Springs, USA (MVH) earthquake

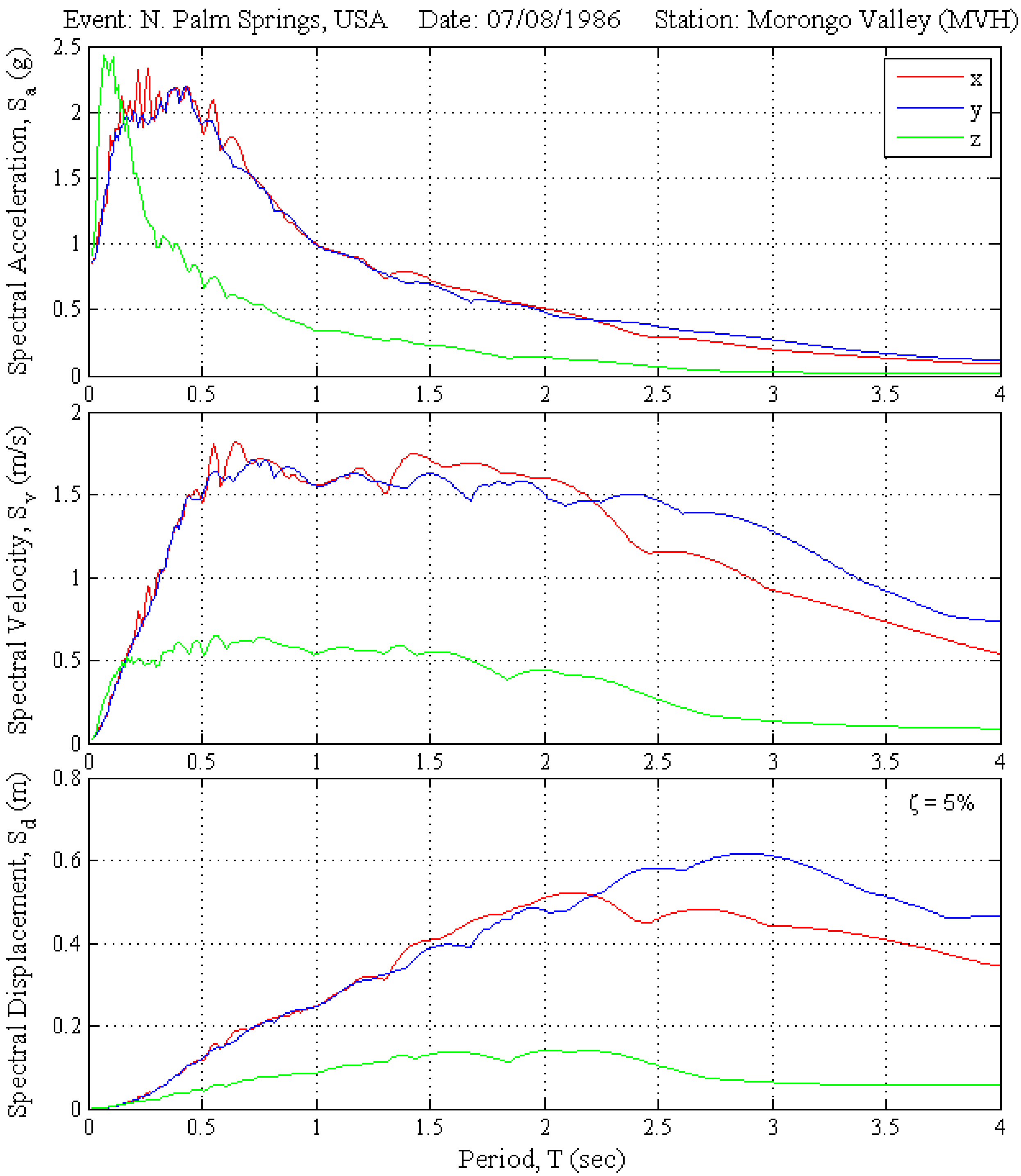

Figure B.24: Response spectra with 5% damping for the N Palm Springs, USA (MVH) earthquake

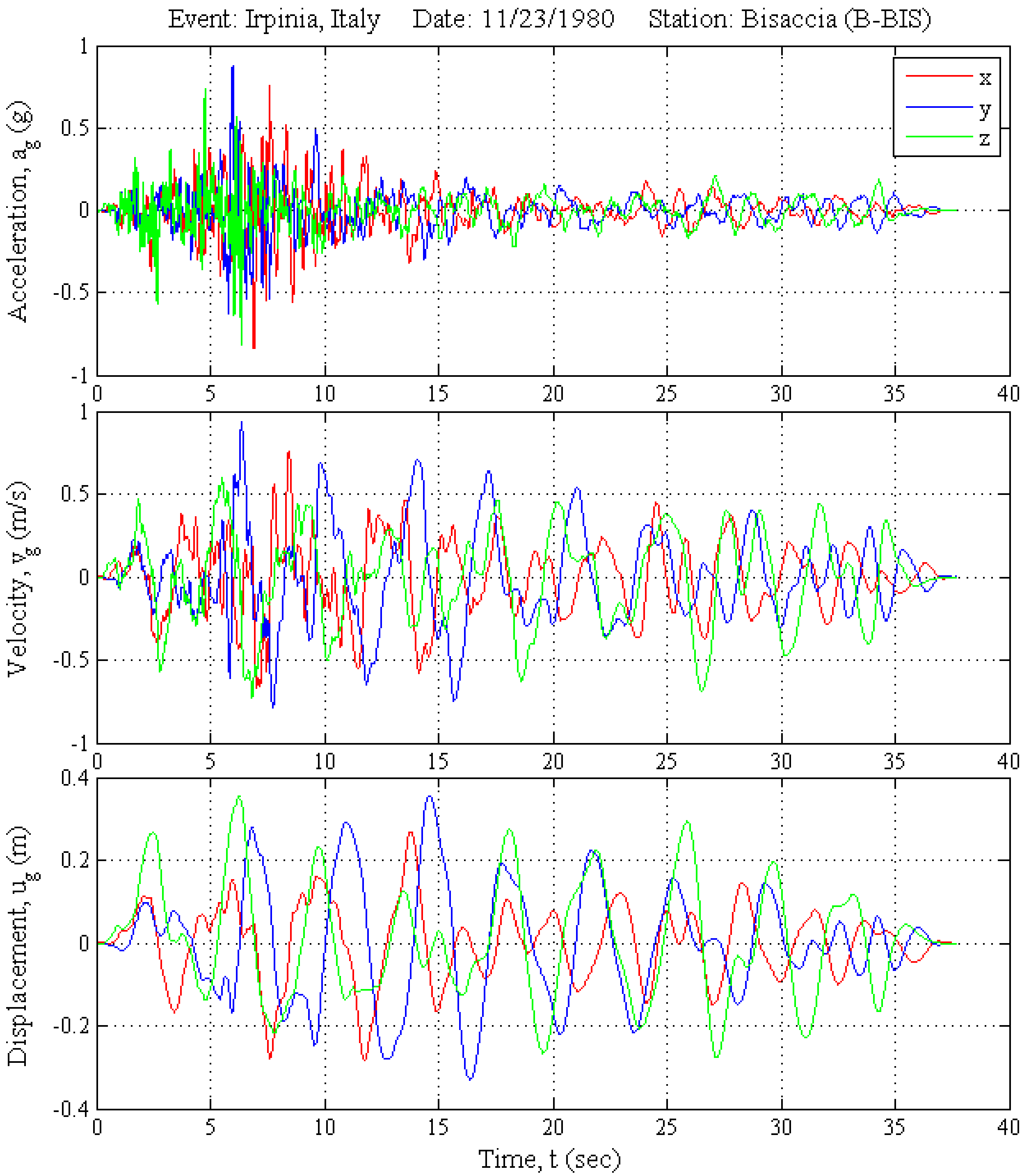

Figure B.25: Time history records for the Irpinia, Italy (B-BIS) earthquake

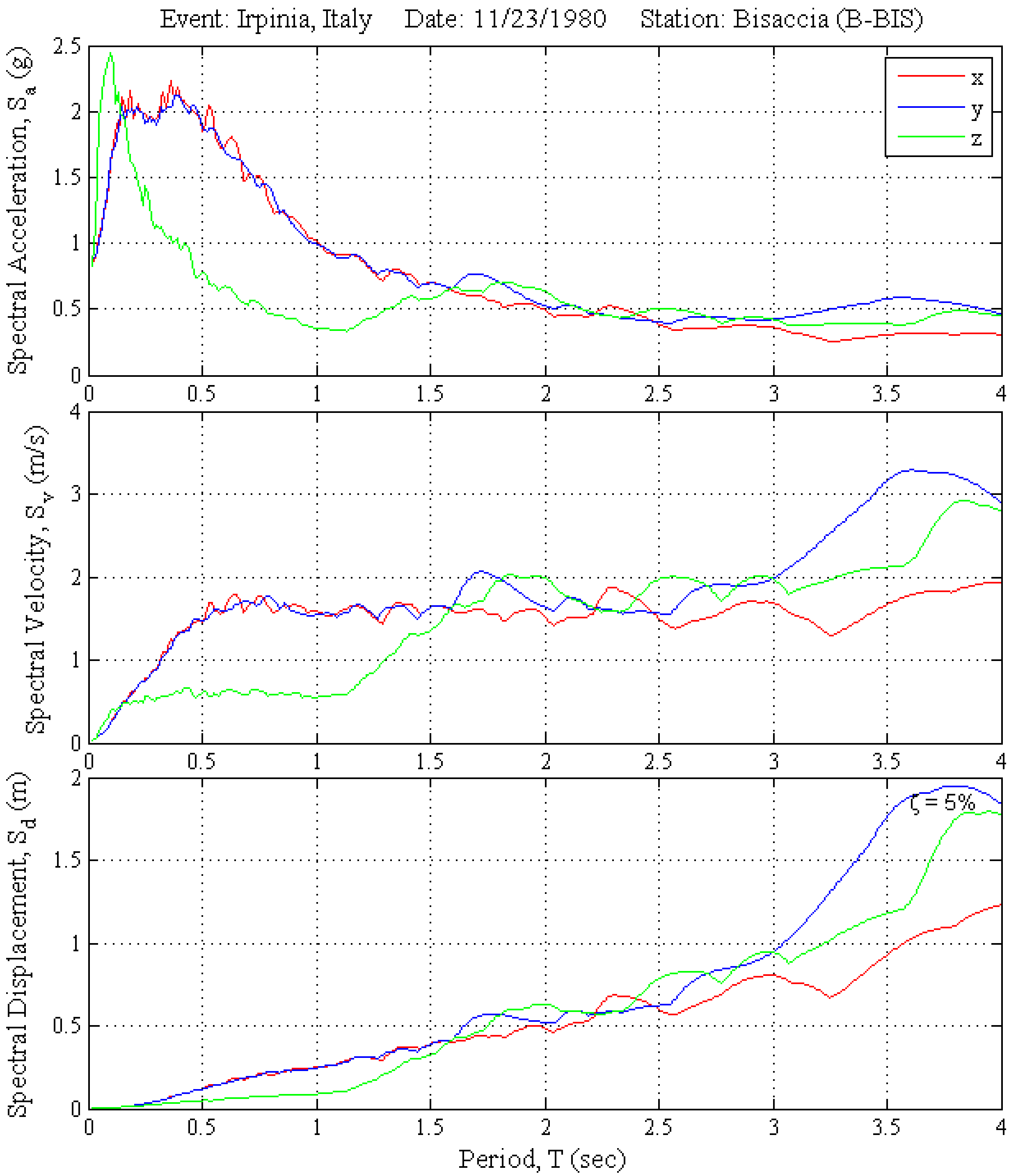

Figure B.26: Response spectra with 5% damping for the Irpinia, Italy (B-BIS) earthquake

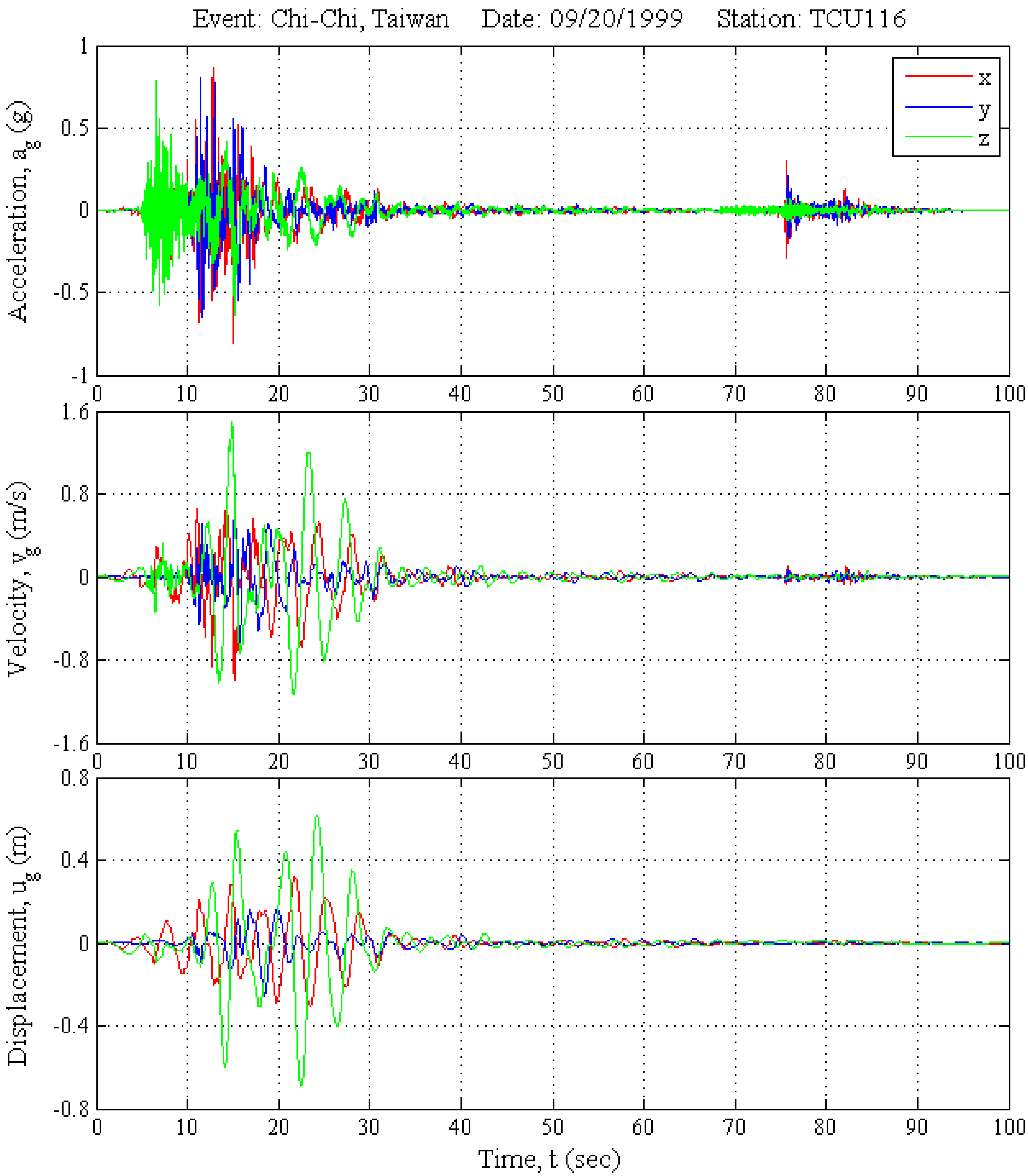

Figure B.27: Time history records for the Chi-Chi, Taiwan (TCU116) earthquake

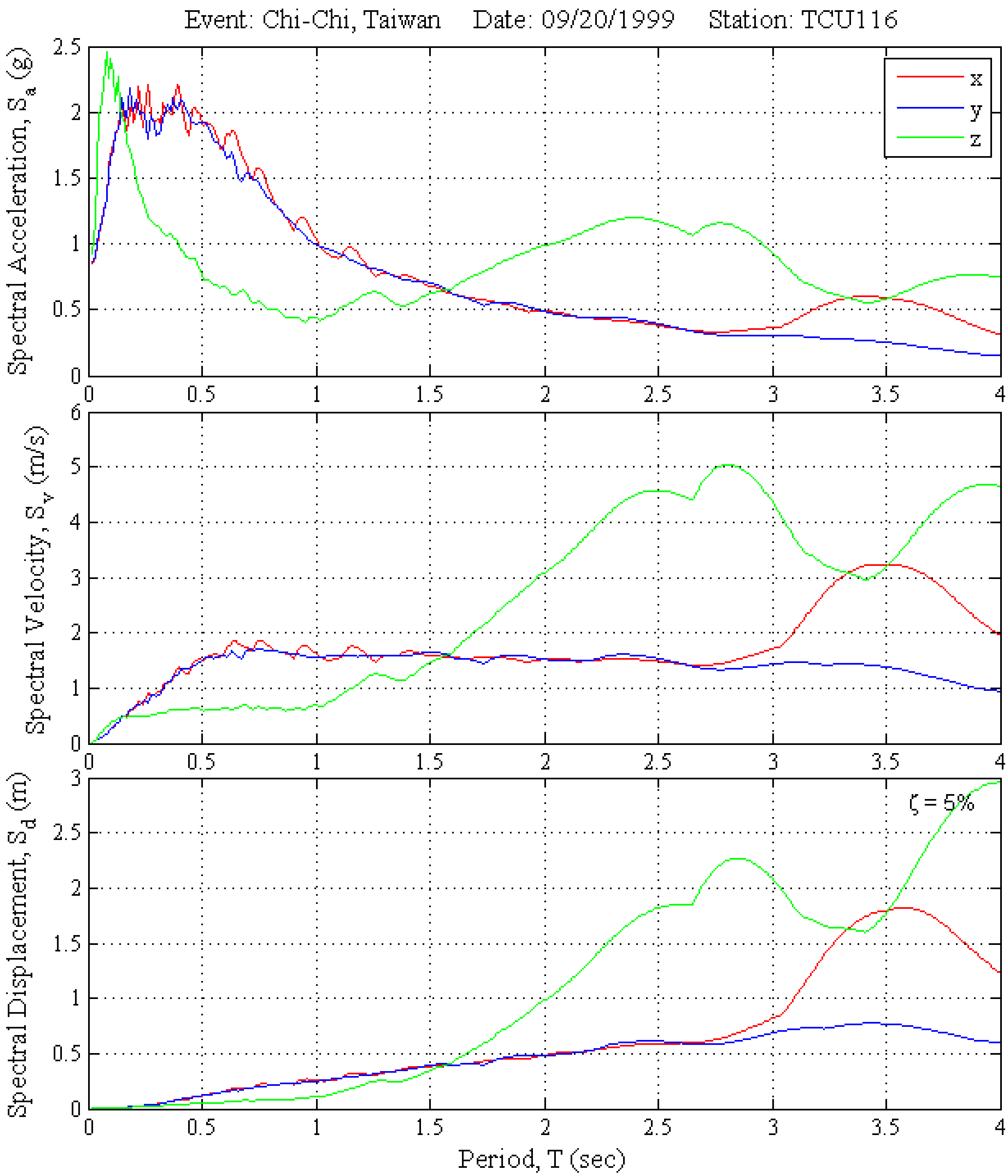

Figure B.28: Response spectra with 5% damping for the Chi-Chi, Taiwan (TCU116) earthquake

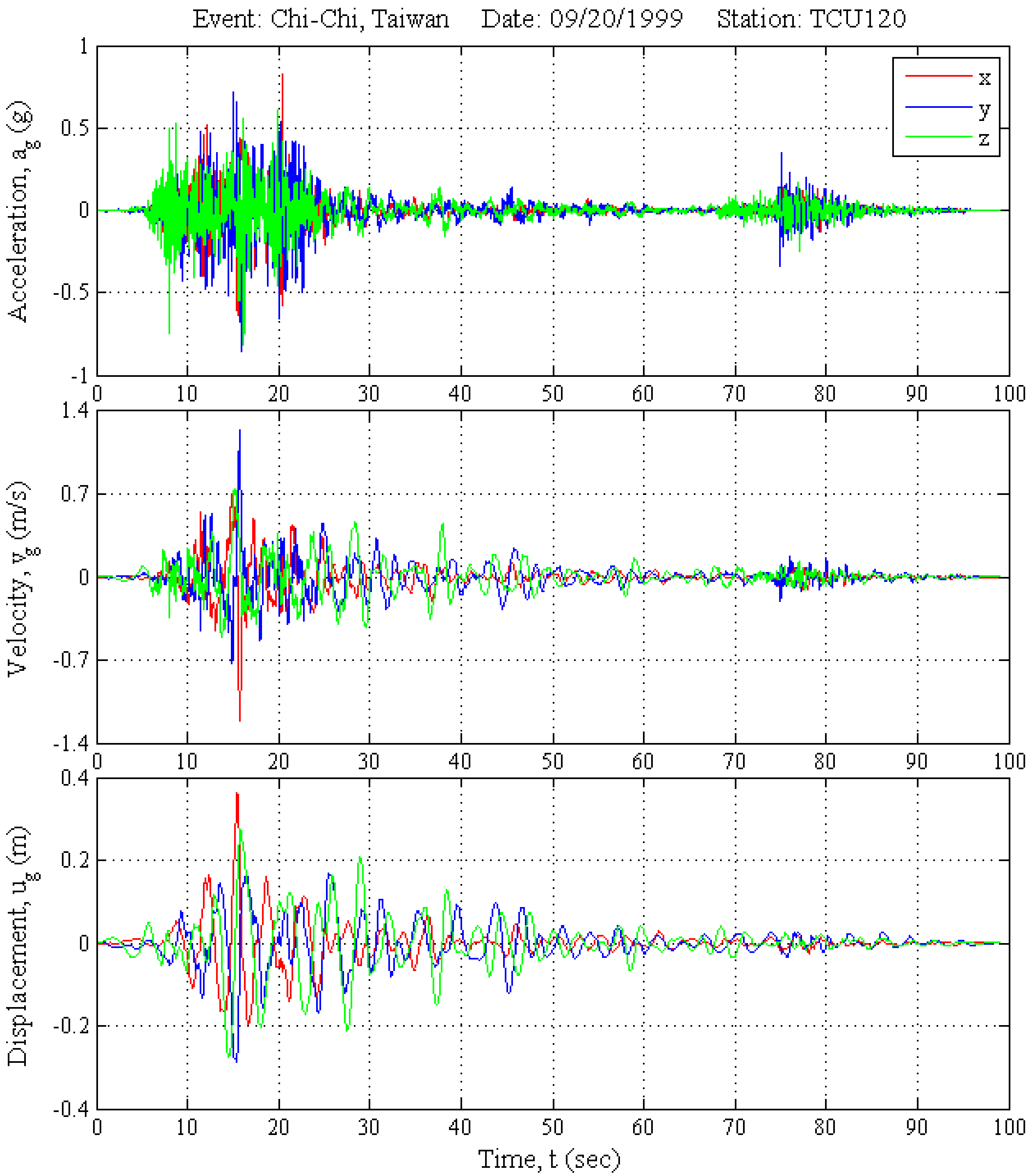

Figure B.29: Time history records for the Chi-Chi, Taiwan (TCU120) earthquake

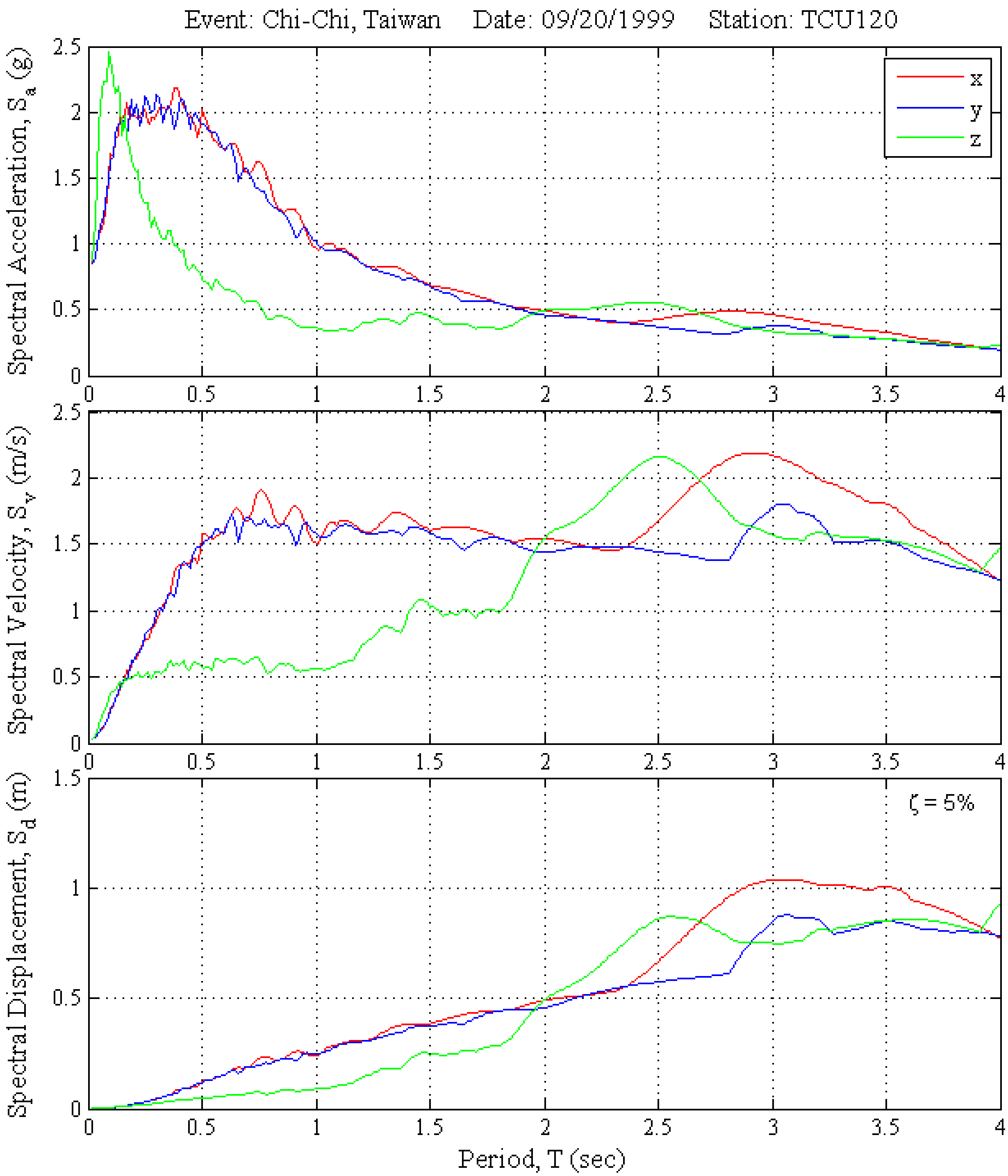

Figure B.30: Response spectra with 5% damping for the Chi-Chi, Taiwan (TCU120) earthquake

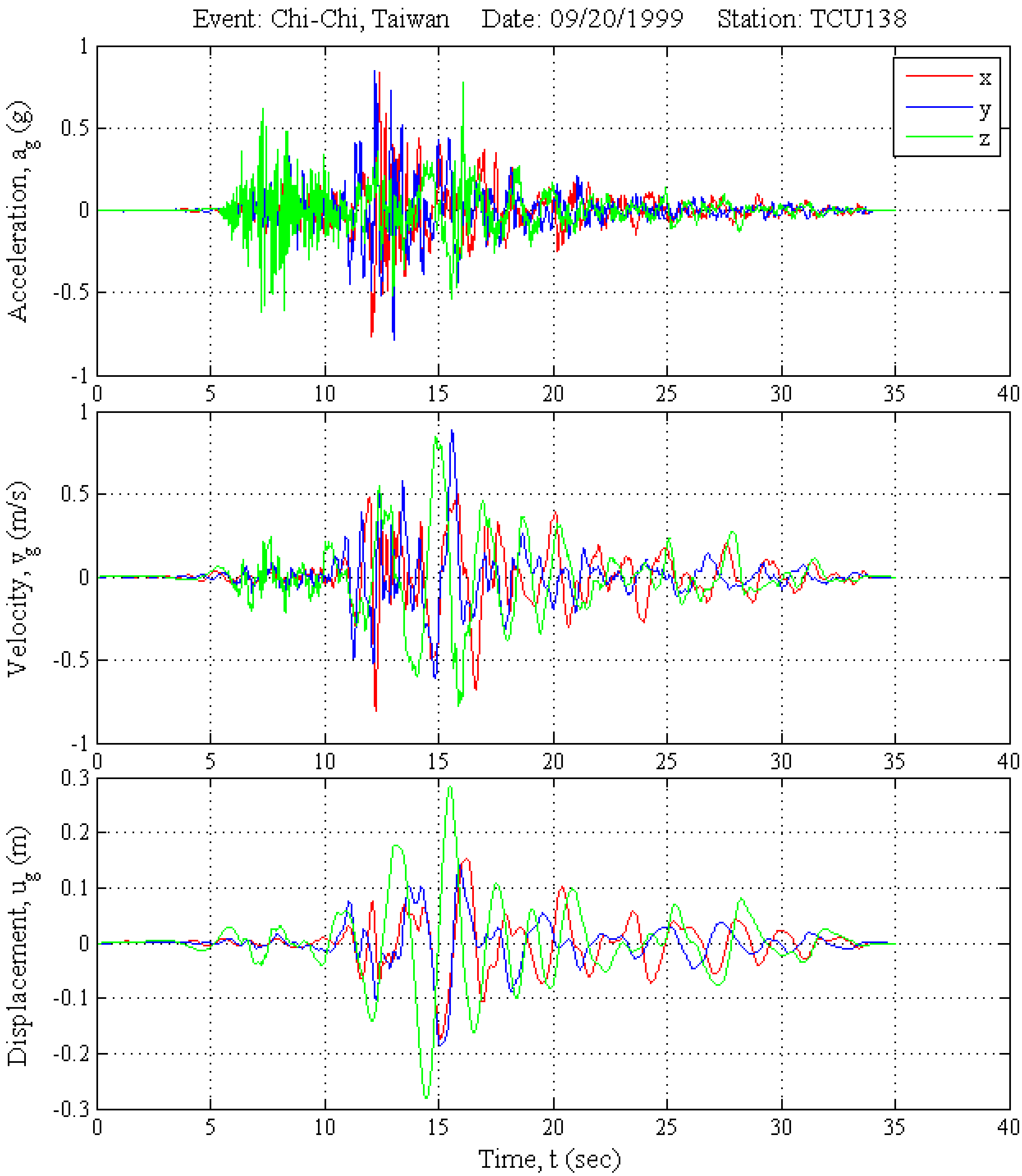

Figure B.31: Time history records for the Chi-Chi, Taiwan (TCU138) earthquake

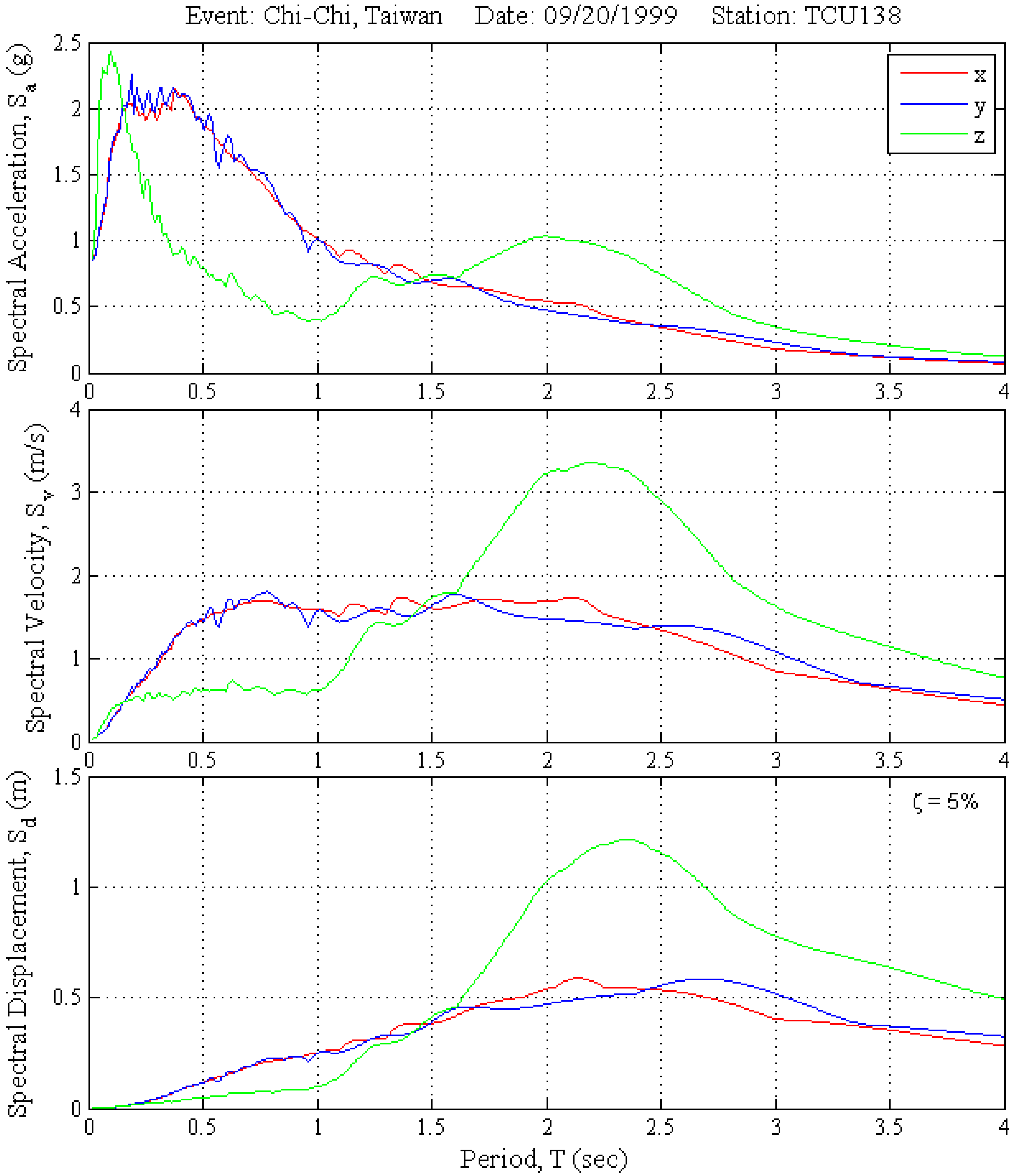

Figure B.32: Response spectra with 5% damping for the Chi-Chi, Taiwan (TCU138) earthquake

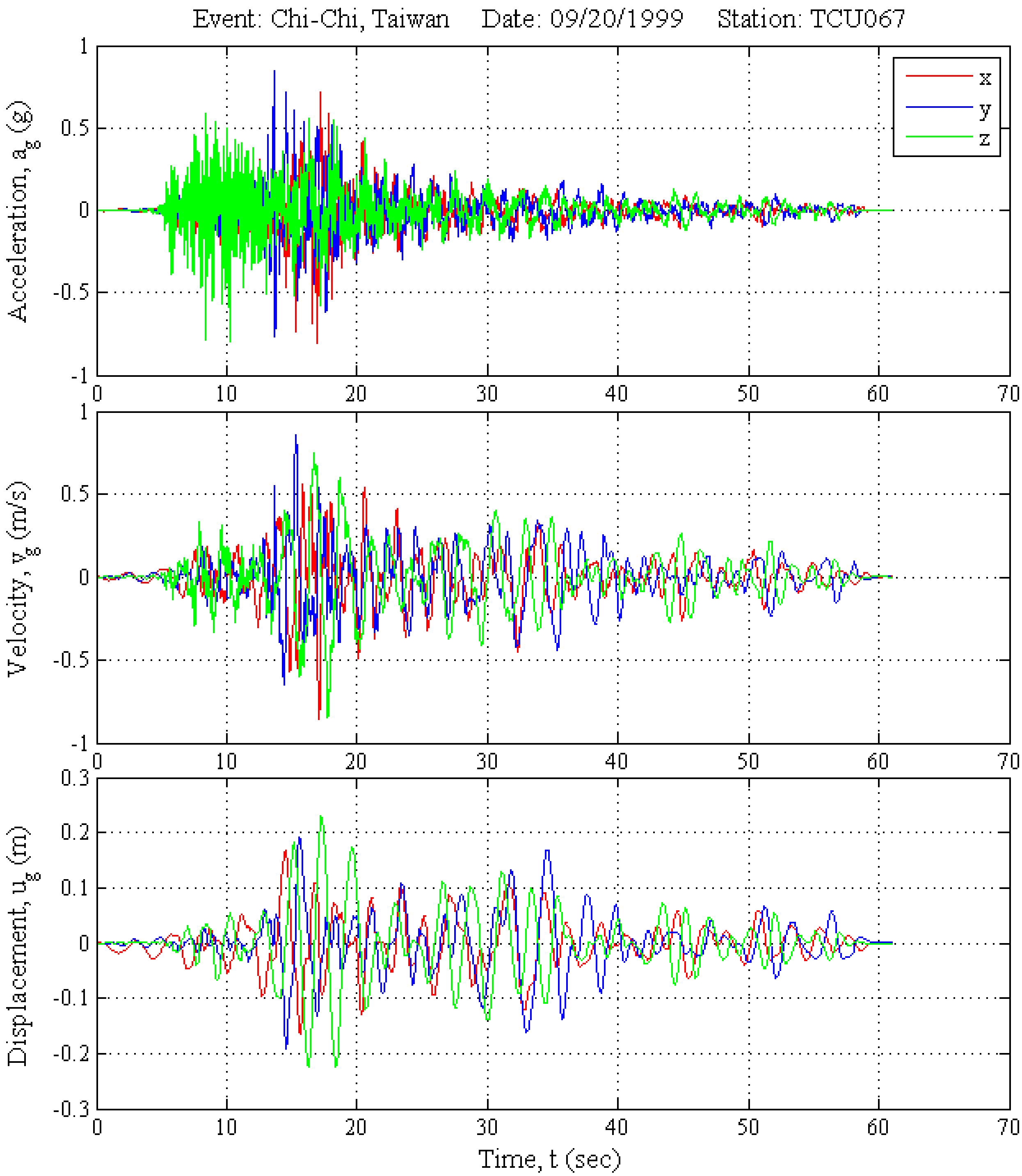

Figure B.33: Time history records for the Chi-Chi, Taiwan (TCU067) earthquake

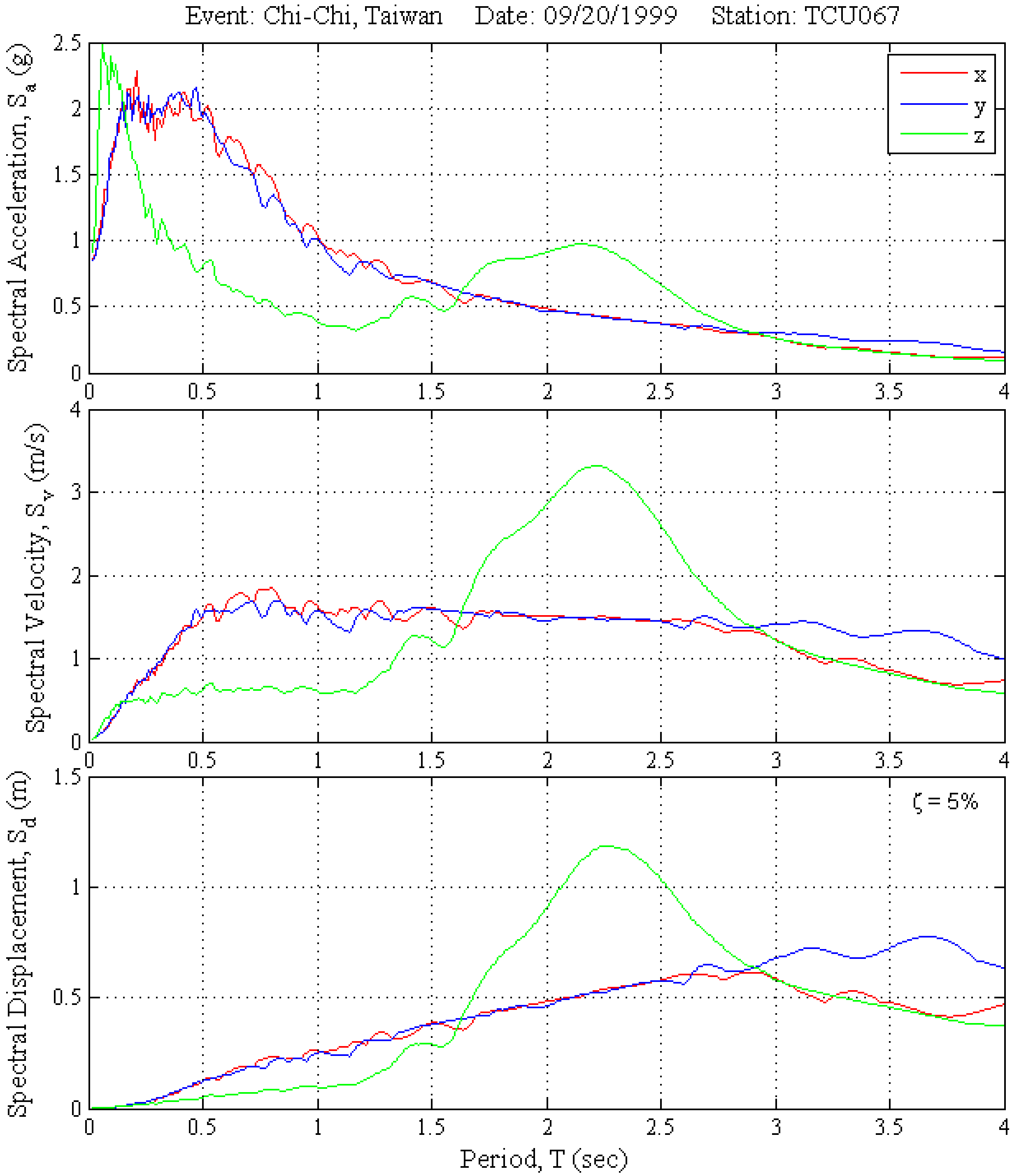

Figure B.34: Response spectra with 5% damping for the Chi-Chi, Taiwan (TCU067) earthquake

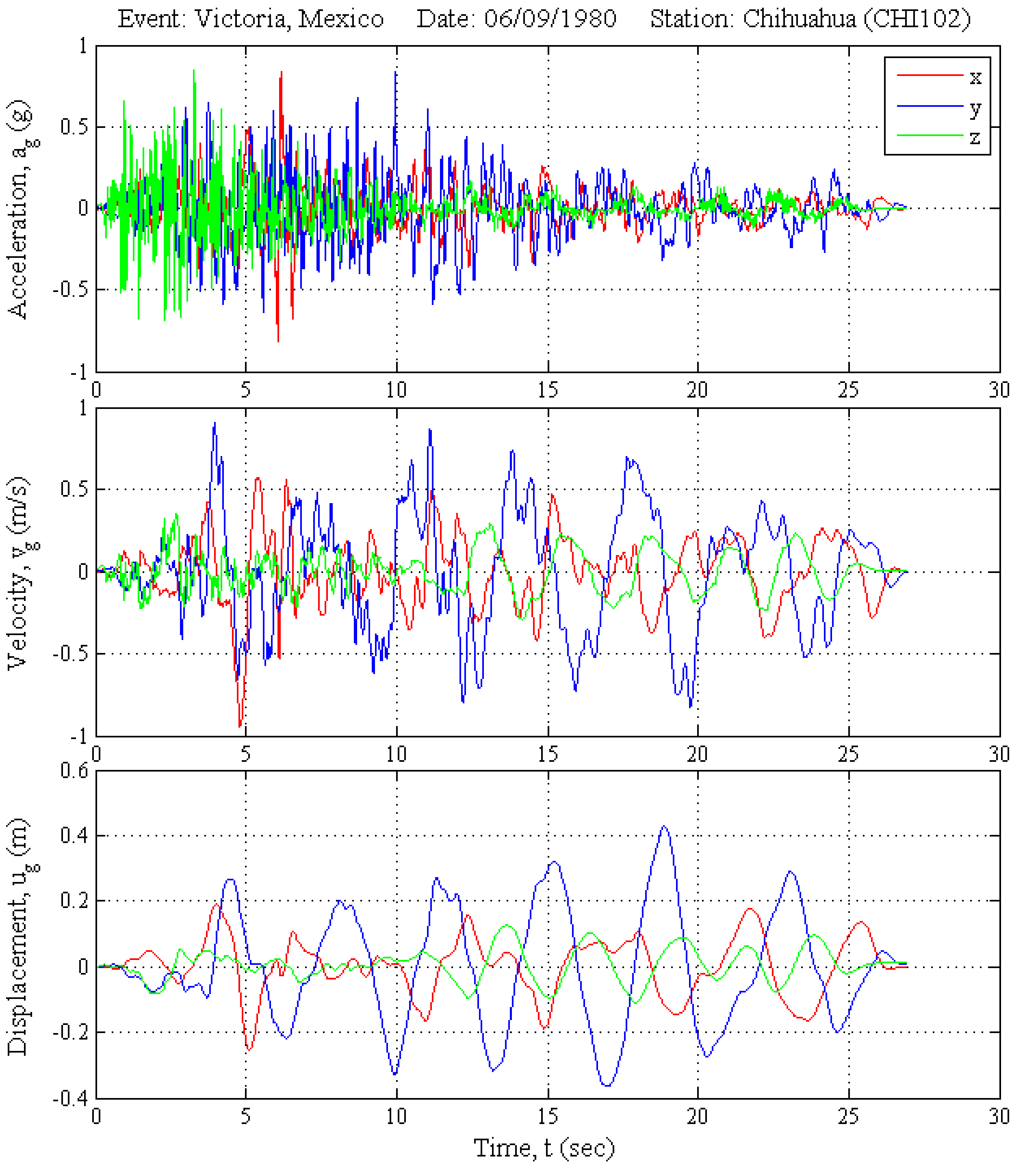

Figure B.35: Time history records for the Victoria, Mexico (CHI) earthquake

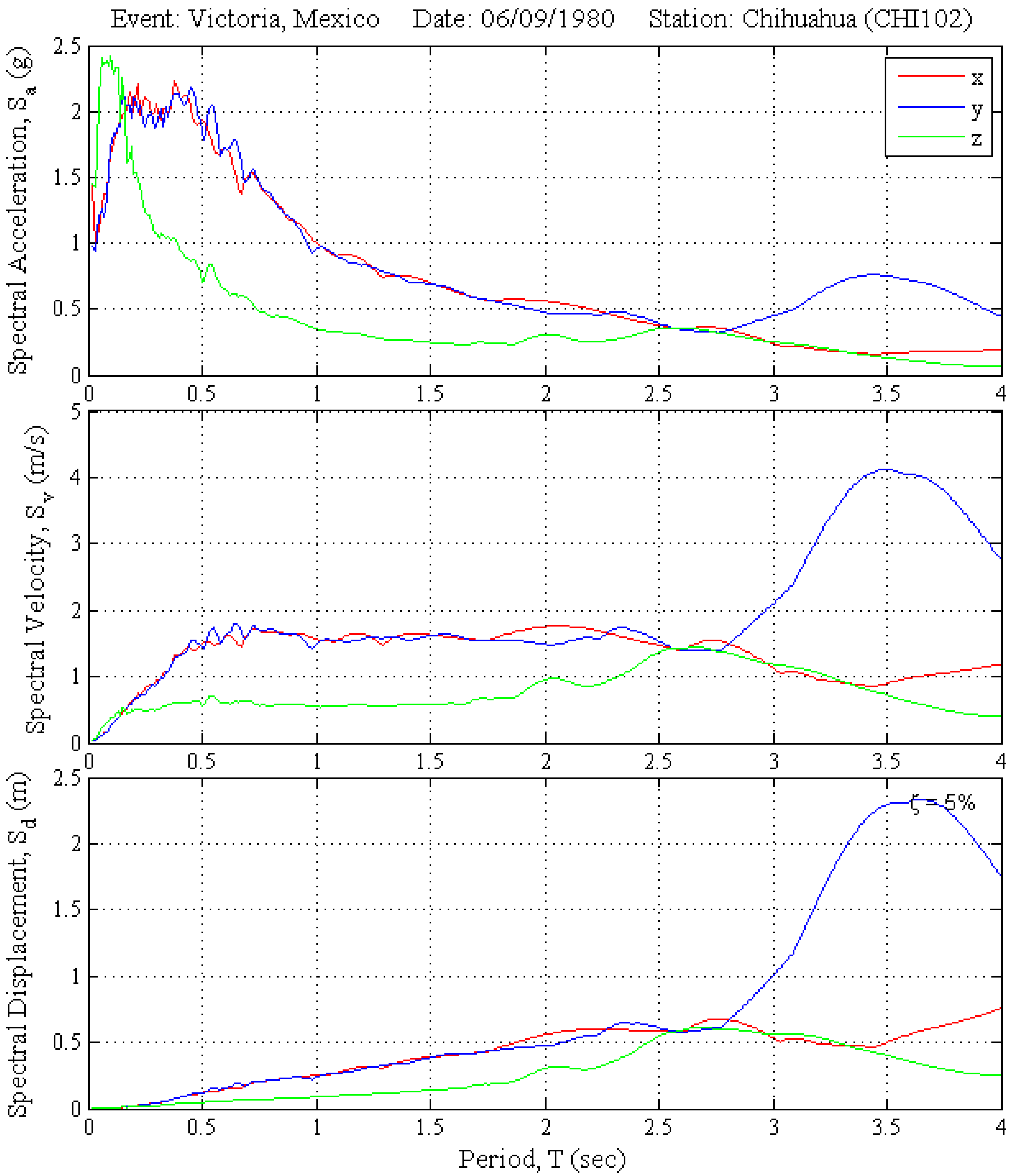

Figure B.36: Response spectra with 5% damping for the Victoria, Mexico (CHI) earthquake

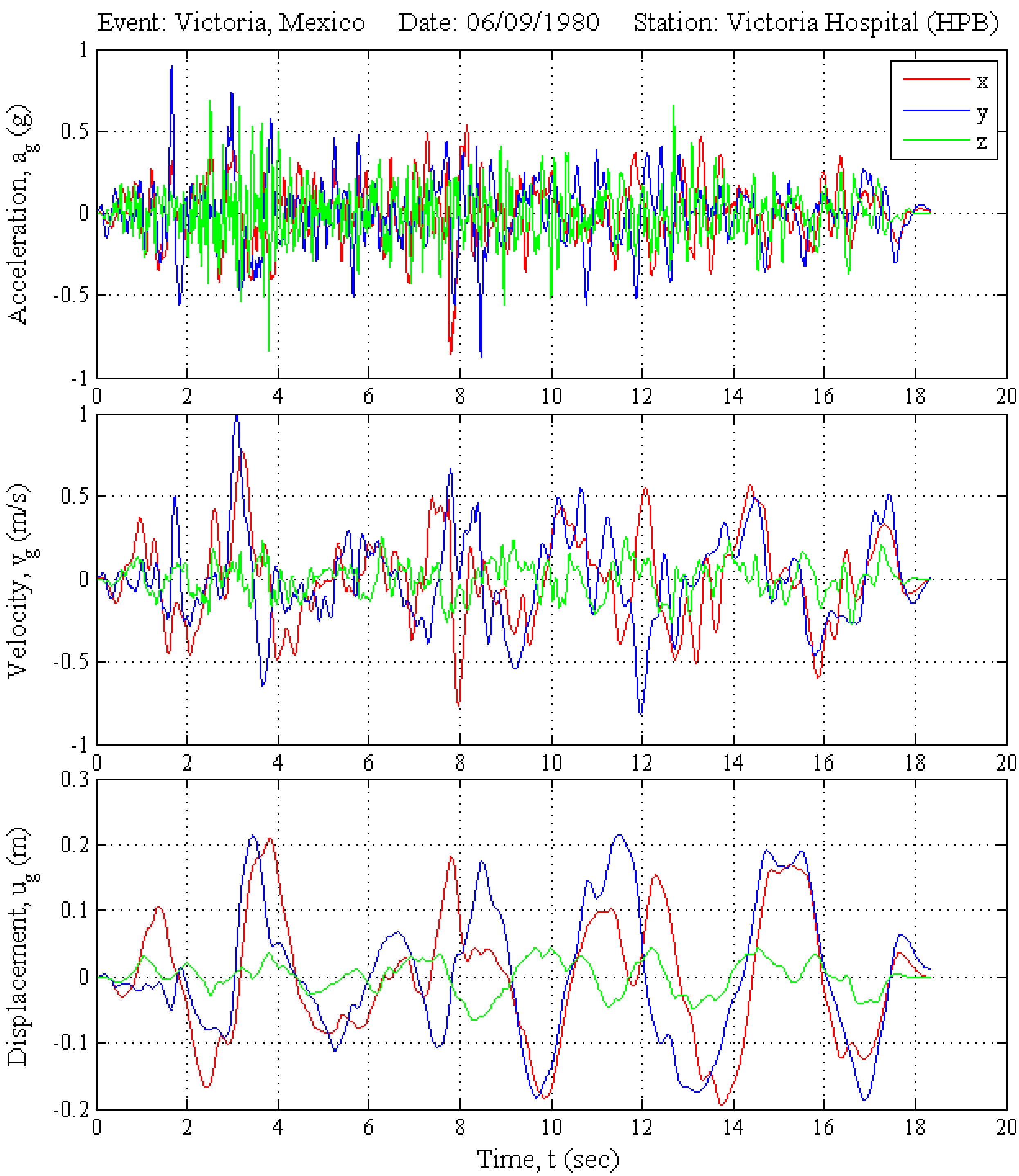

Figure B.37: Time history records for the Victoria, Mexico (HPB) earthquake

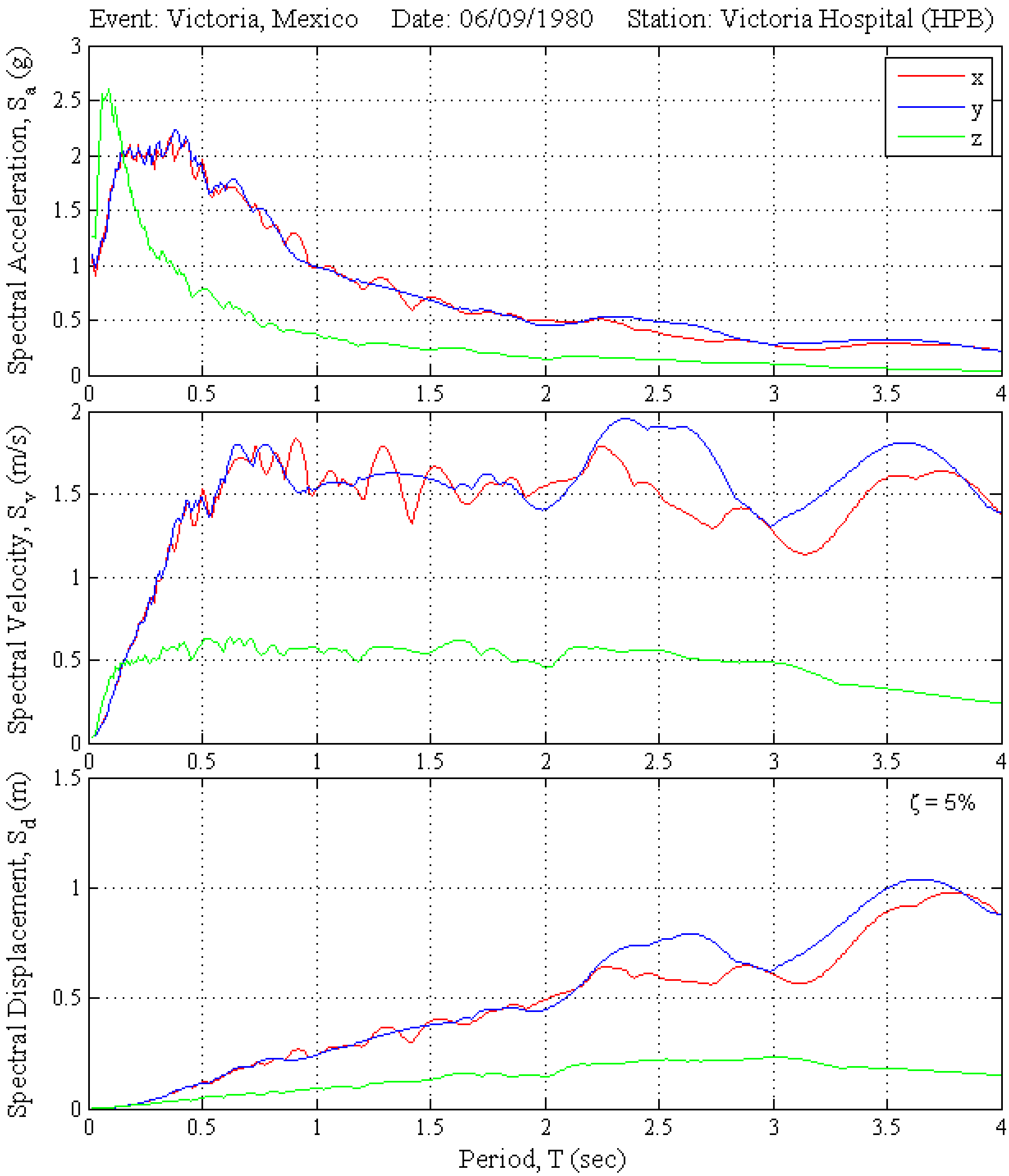

Figure B.38: Response spectra with 5% damping for the Victoria, Mexico (HPB) earthquake

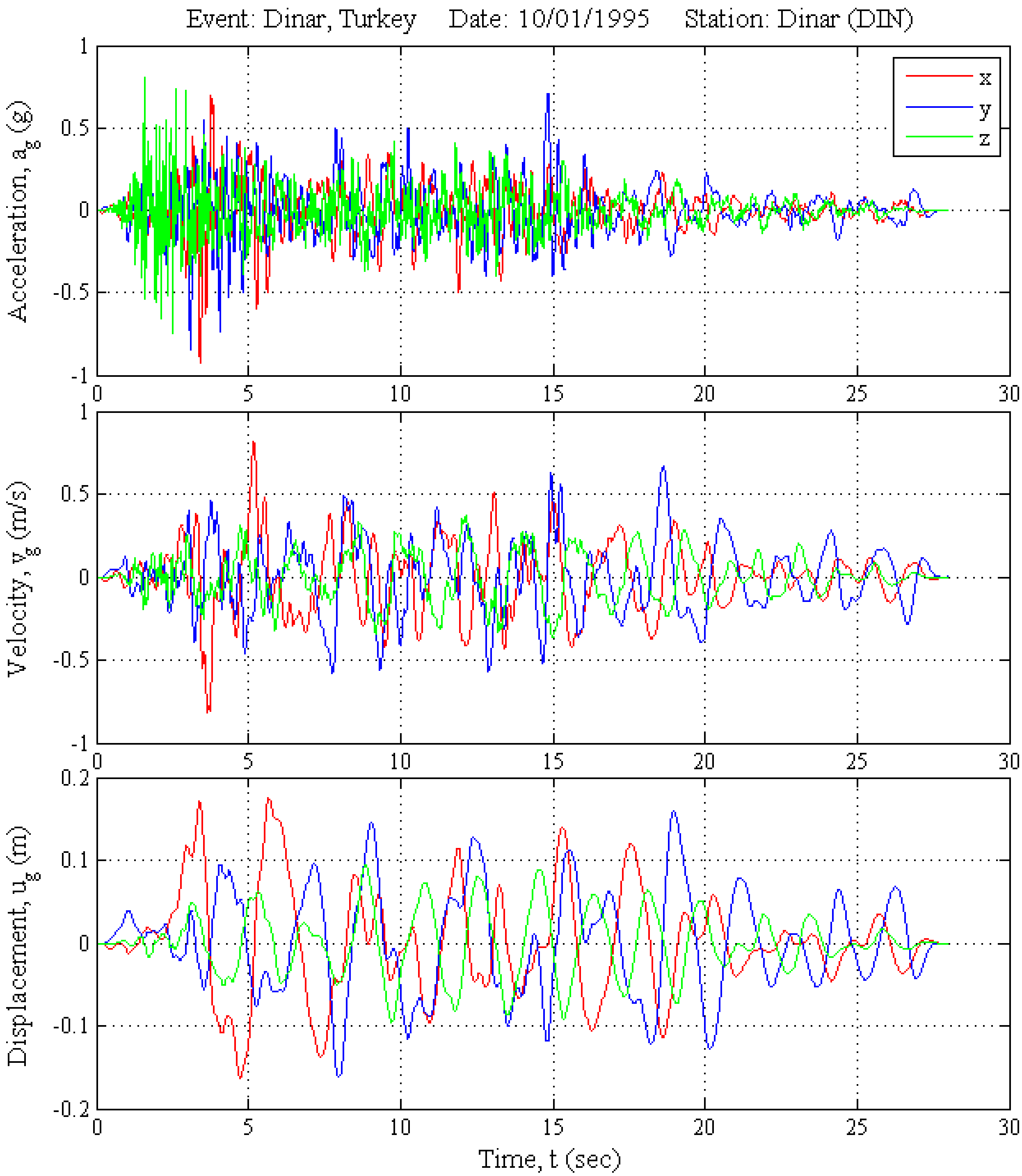

Figure B.39: Time history records for the Dinar, Turkey (DIN) earthquake

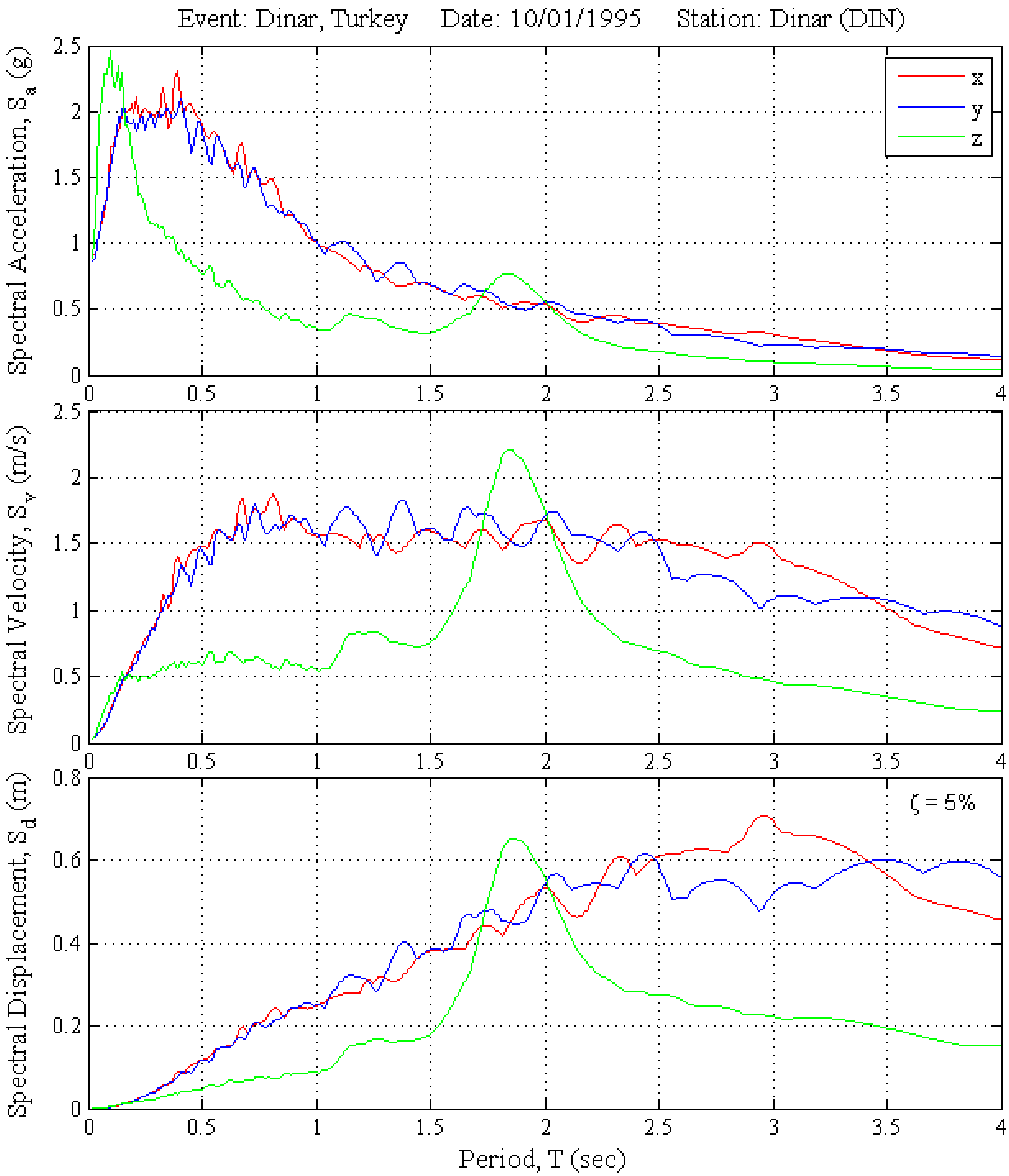

Figure B.40: Response spectra with 5% damping for the Dinar, Turkey (DIN) earthquake

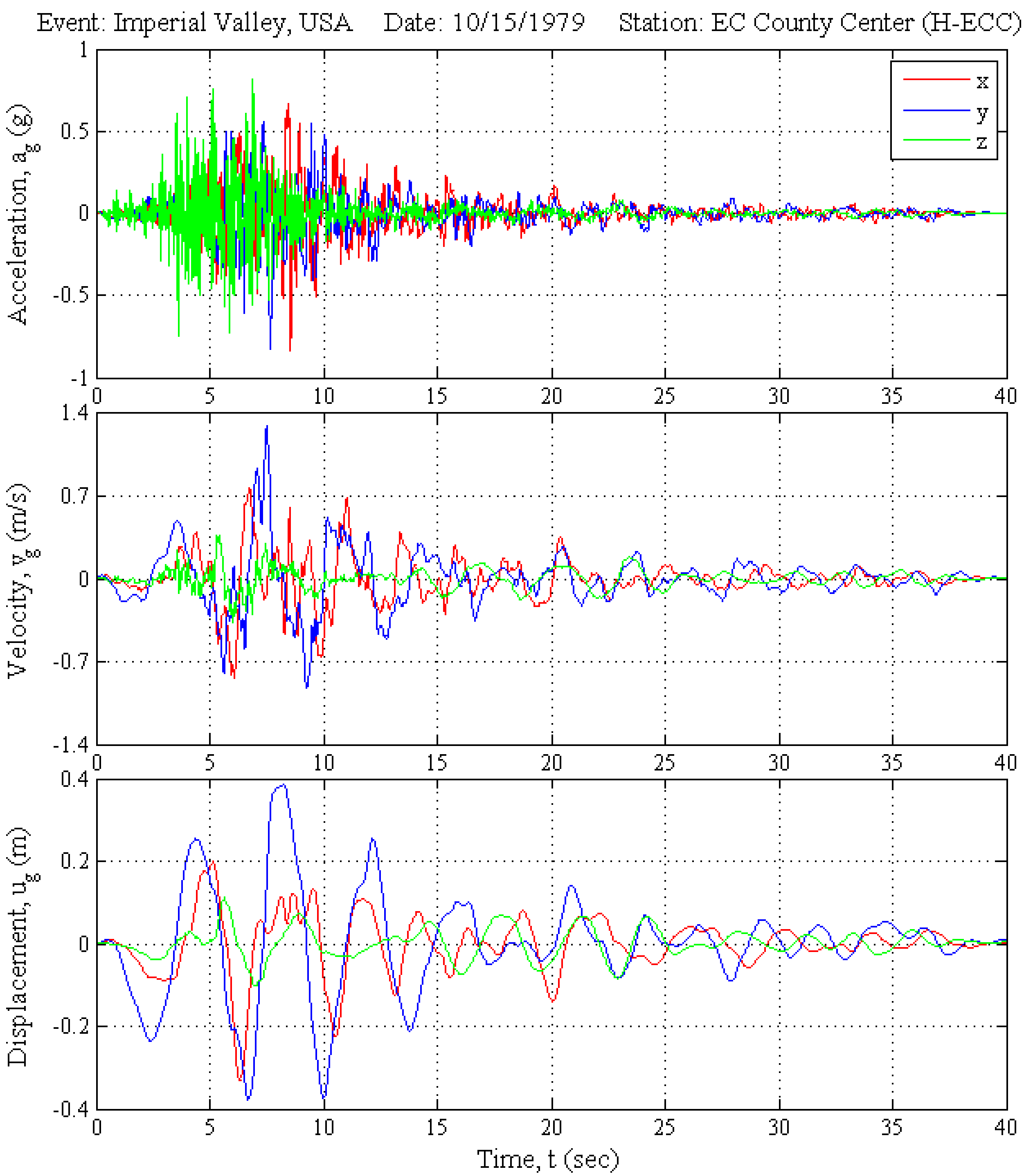

Figure B.41: Time history records for the Imperial Valley, USA (H-ECC) earthquake

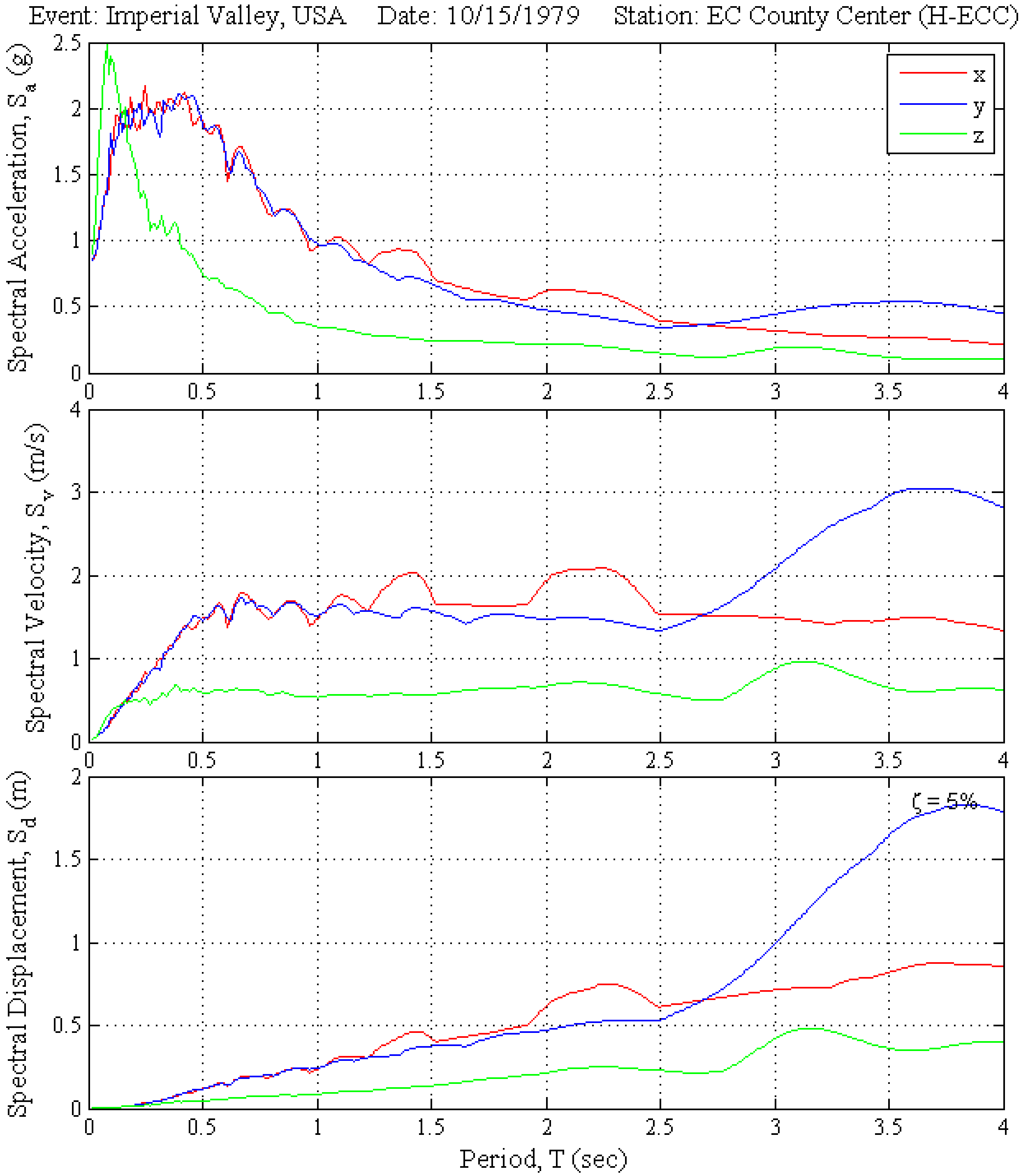

Figure B.42: Response spectra with 5% damping for the Imperial Valley, USA (H-ECC) earthquake

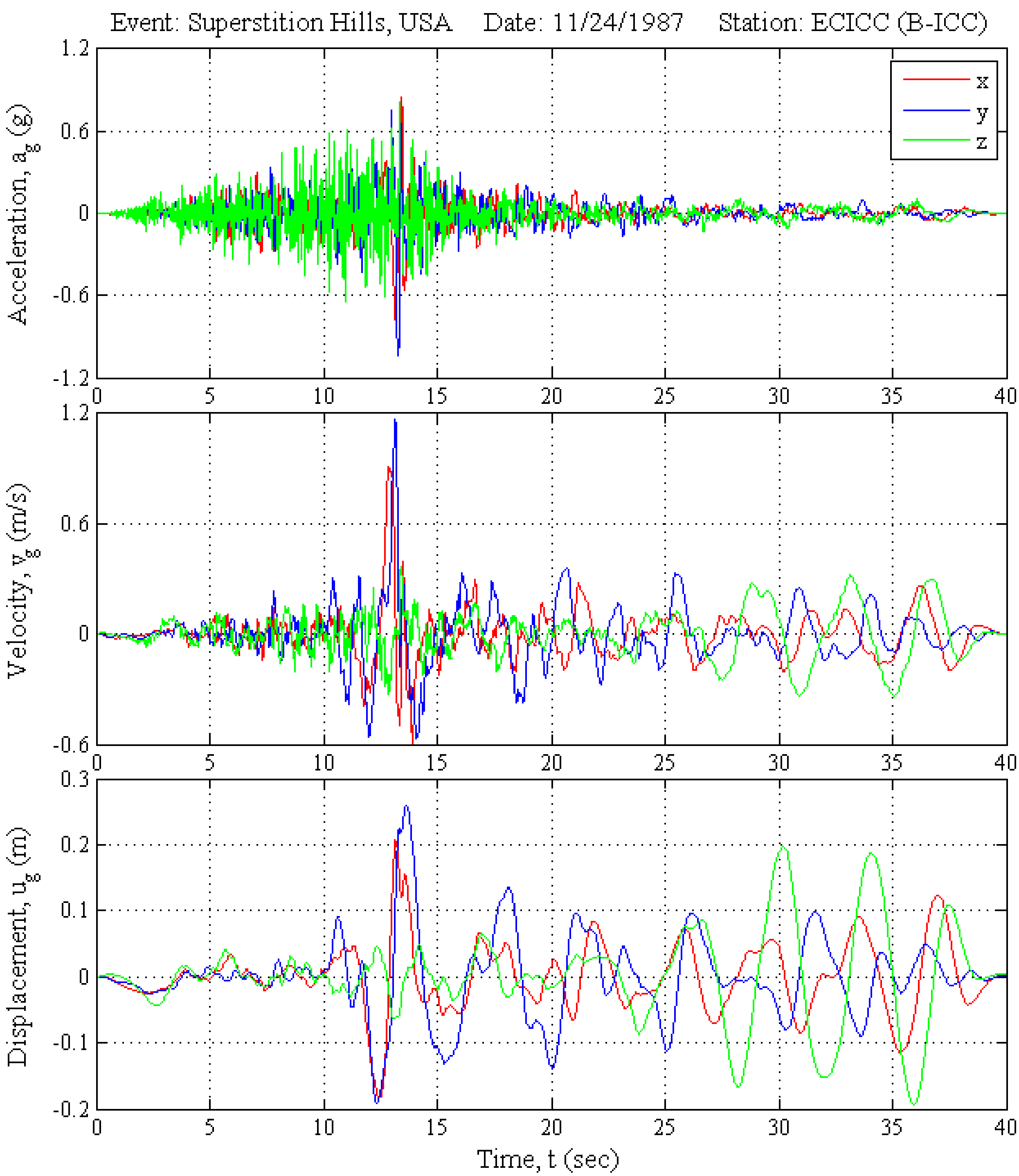

Figure B.43: Time history records for the Superstition Hills, USA (B-ICC) earthquake

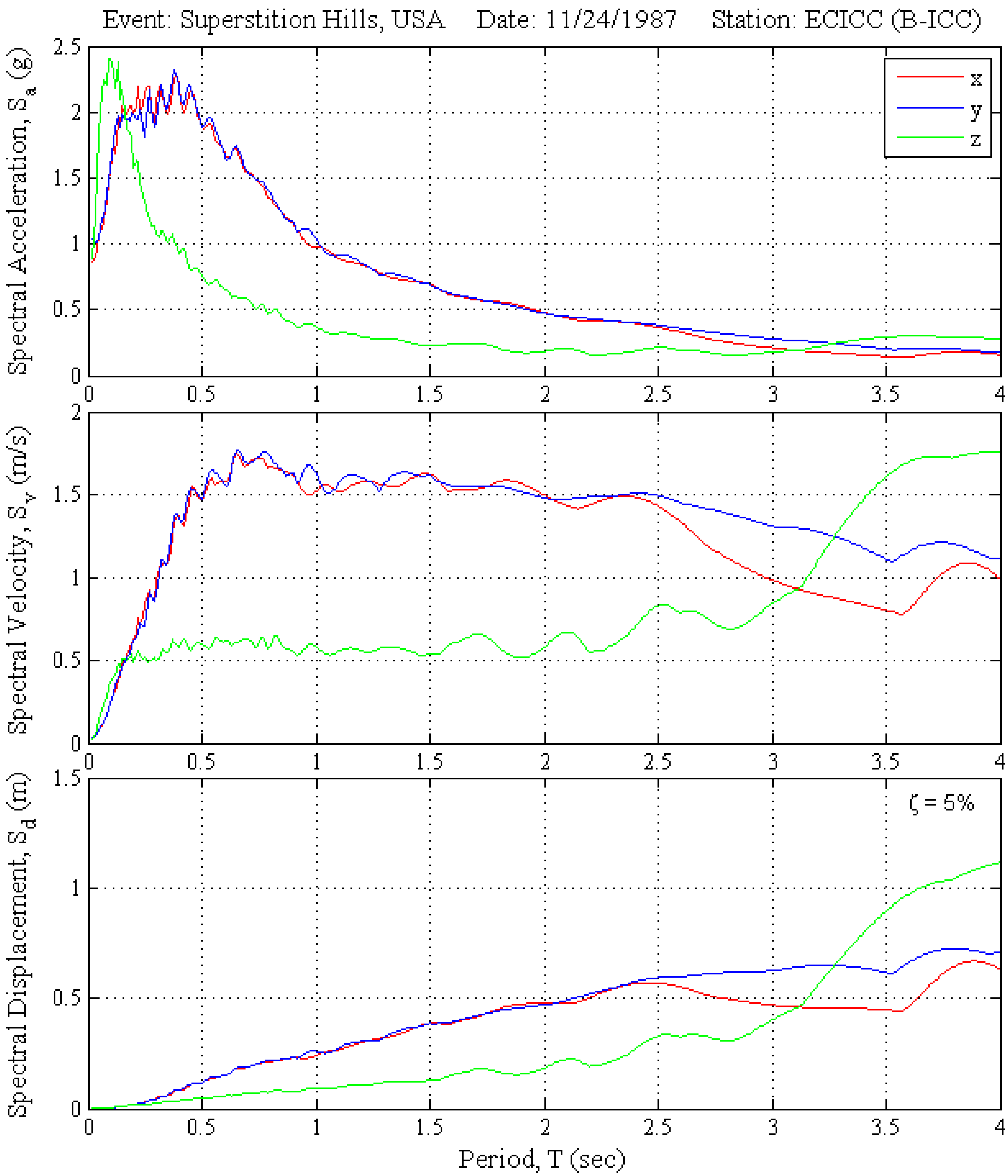

Figure B.44: Response spectra with 5% damping for the Superstition Hills, USA (B-ICC) earthquake

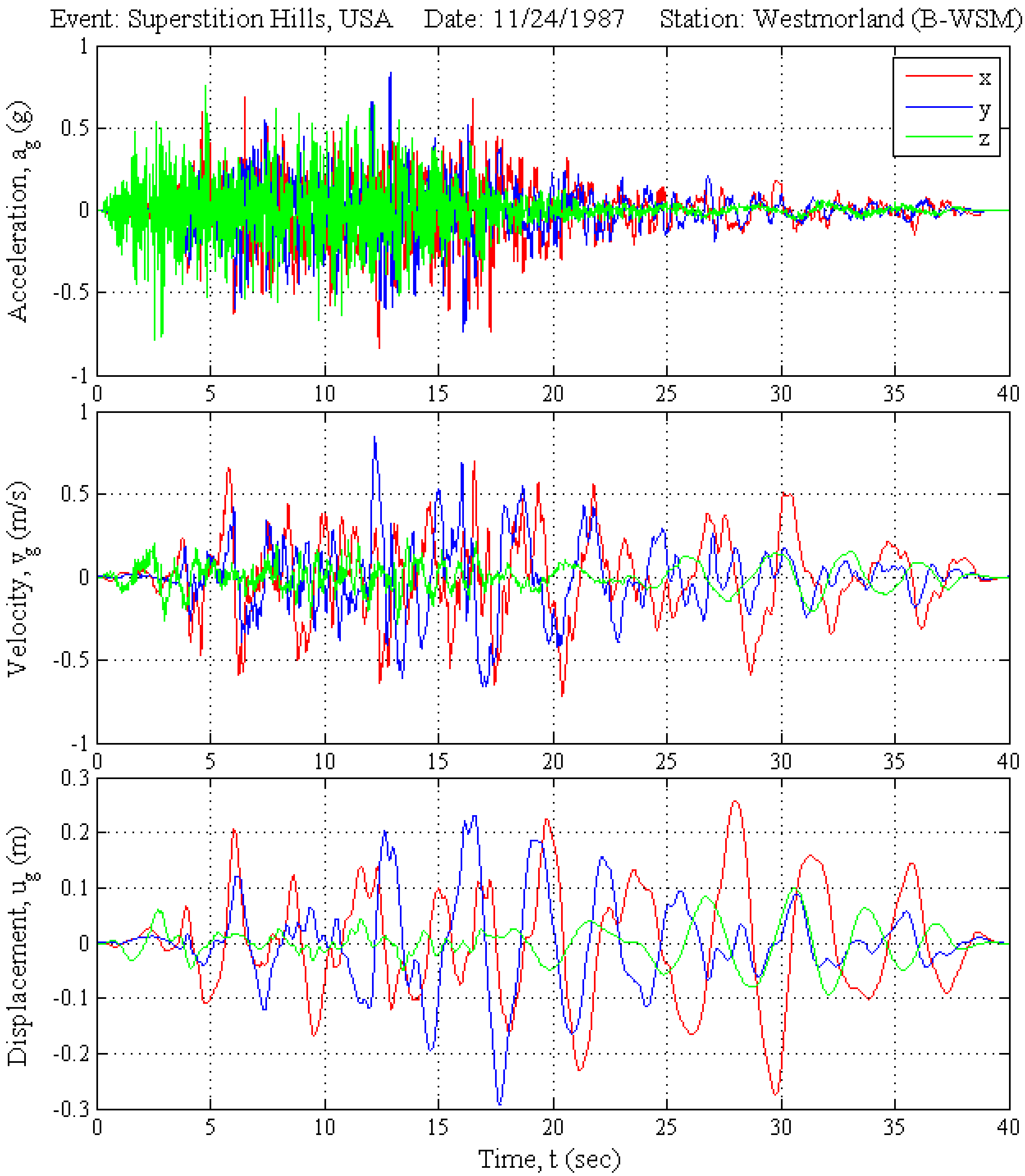

Figure B.45: Time history records for the Superstition Hills, USA (B-WSM) earthquake

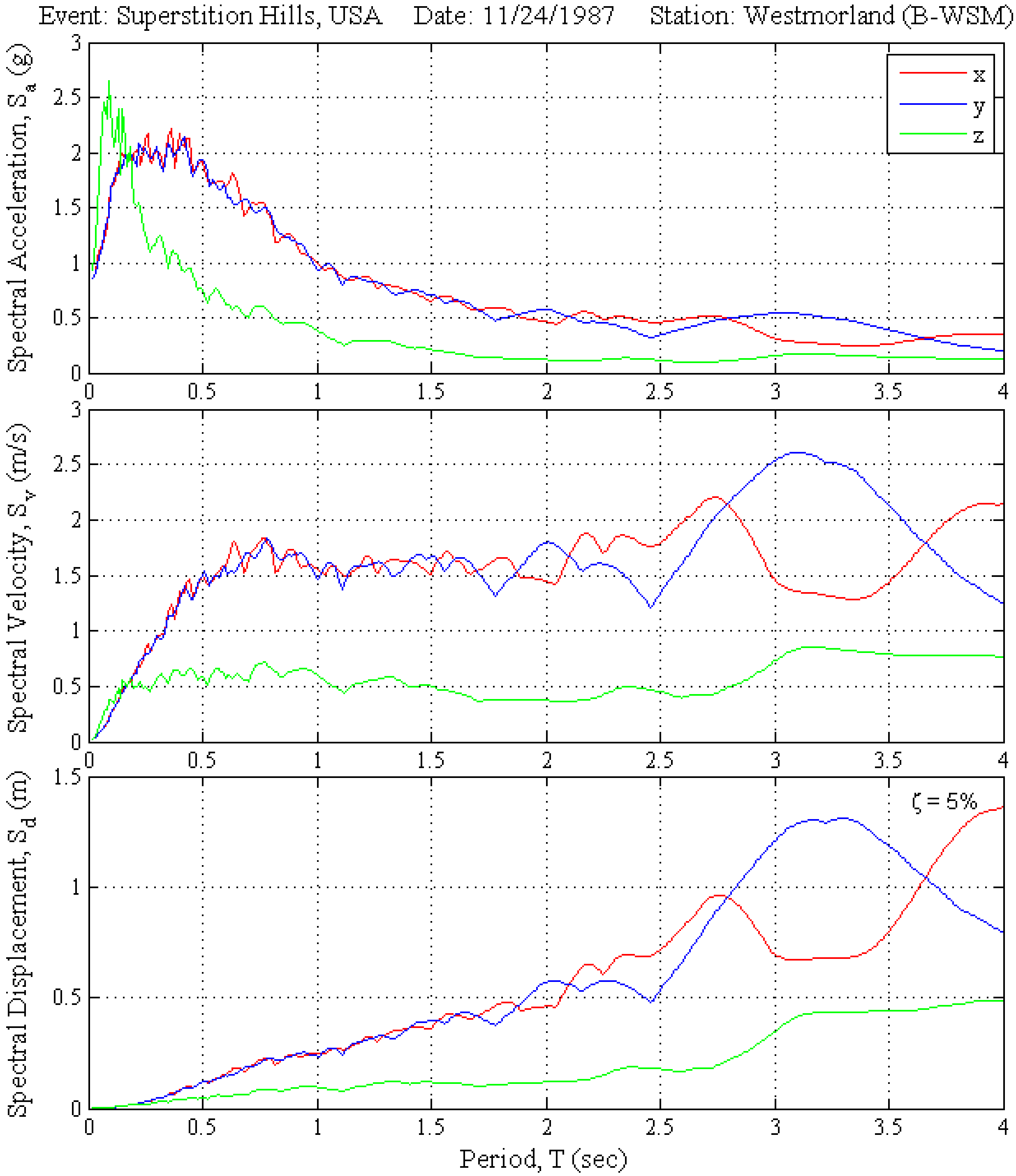

Figure B.46: Response spectra with 5% damping for the Superstition Hills, USA (B-WSM) earthquake

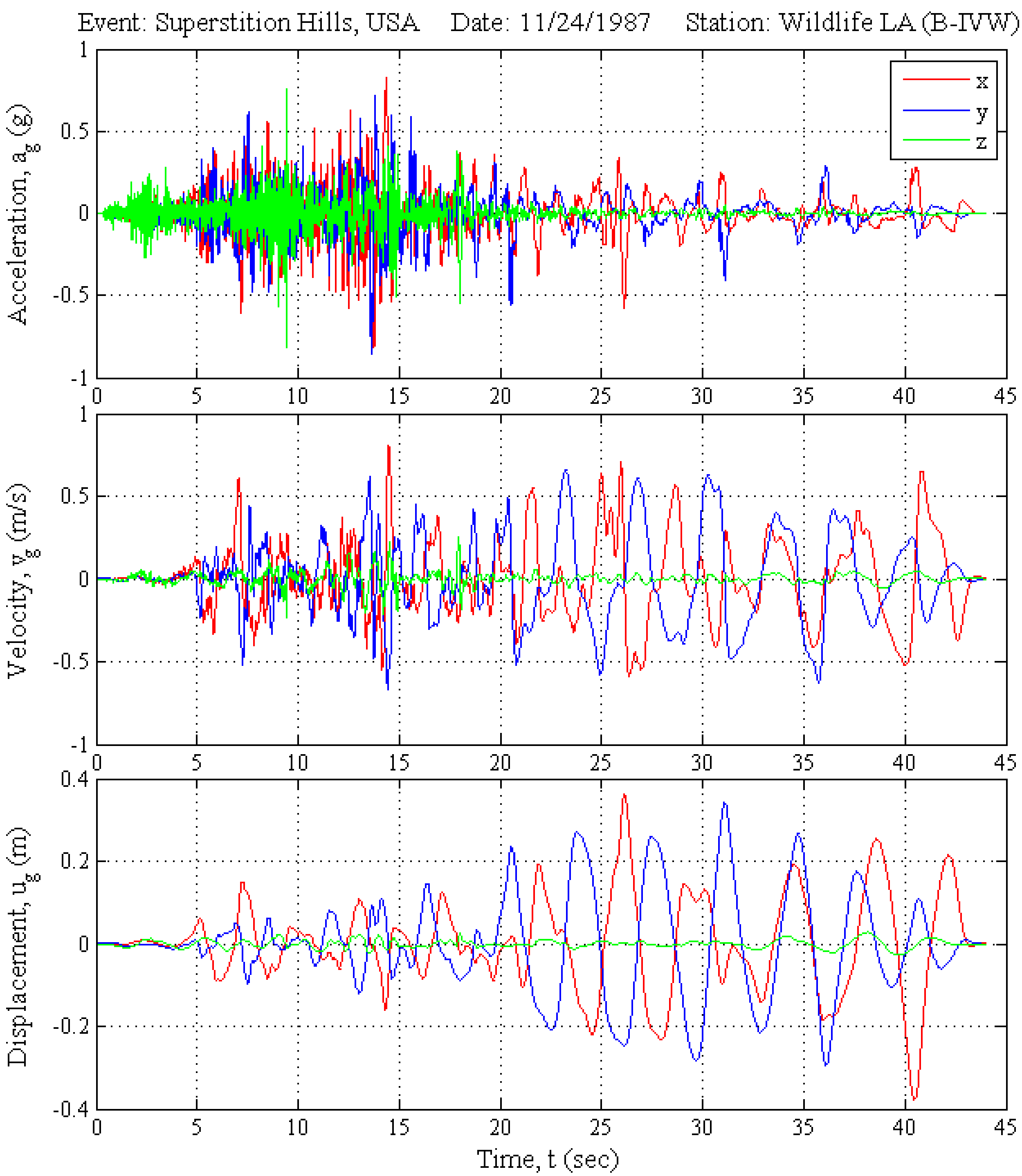

Figure B.47: Time history records for the Superstition Hills, USA (B-IVW) earthquake

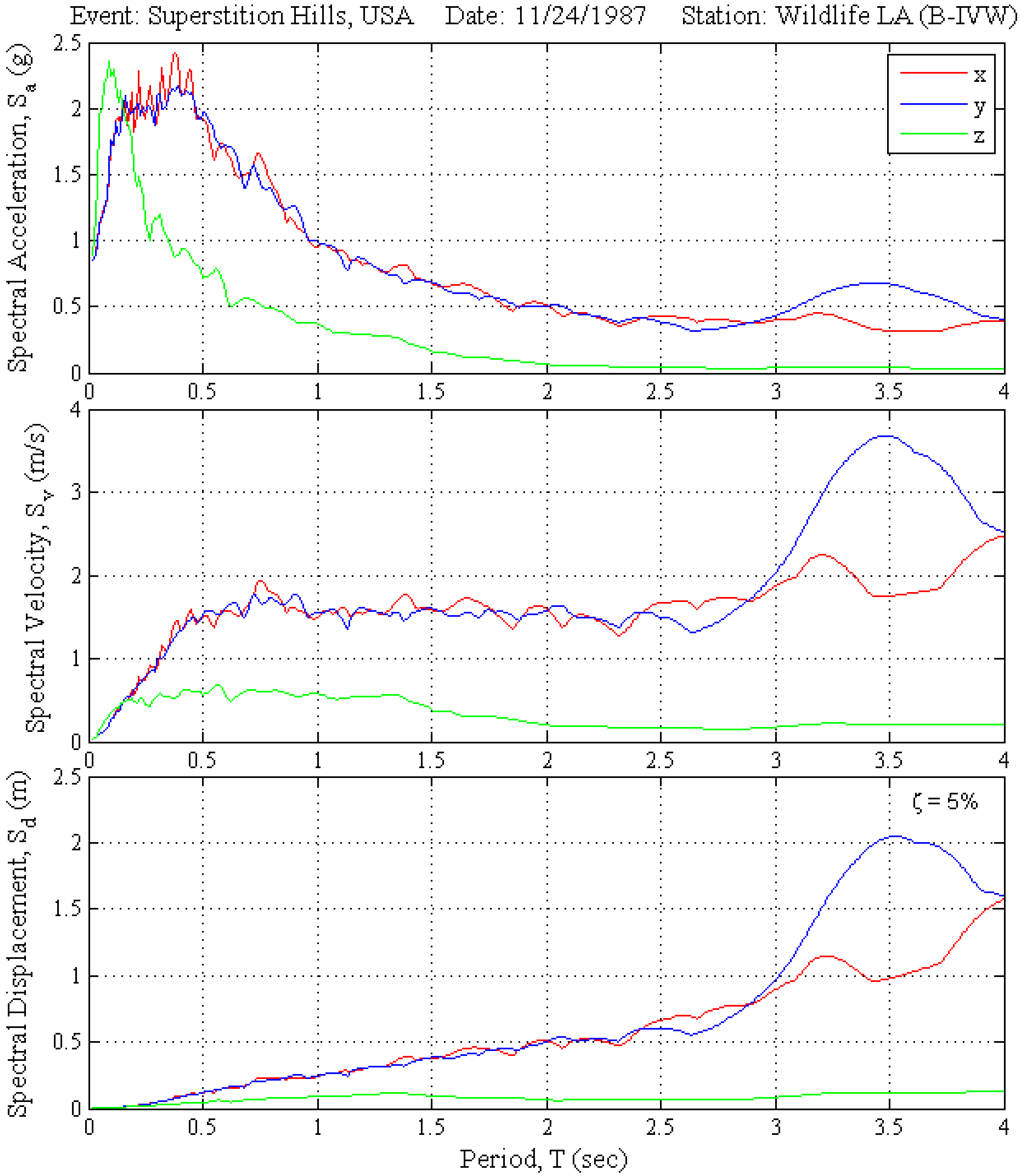

Figure B.48: Response spectra with 5% damping for the Superstition Hills, USA (B-IVW) earthquake

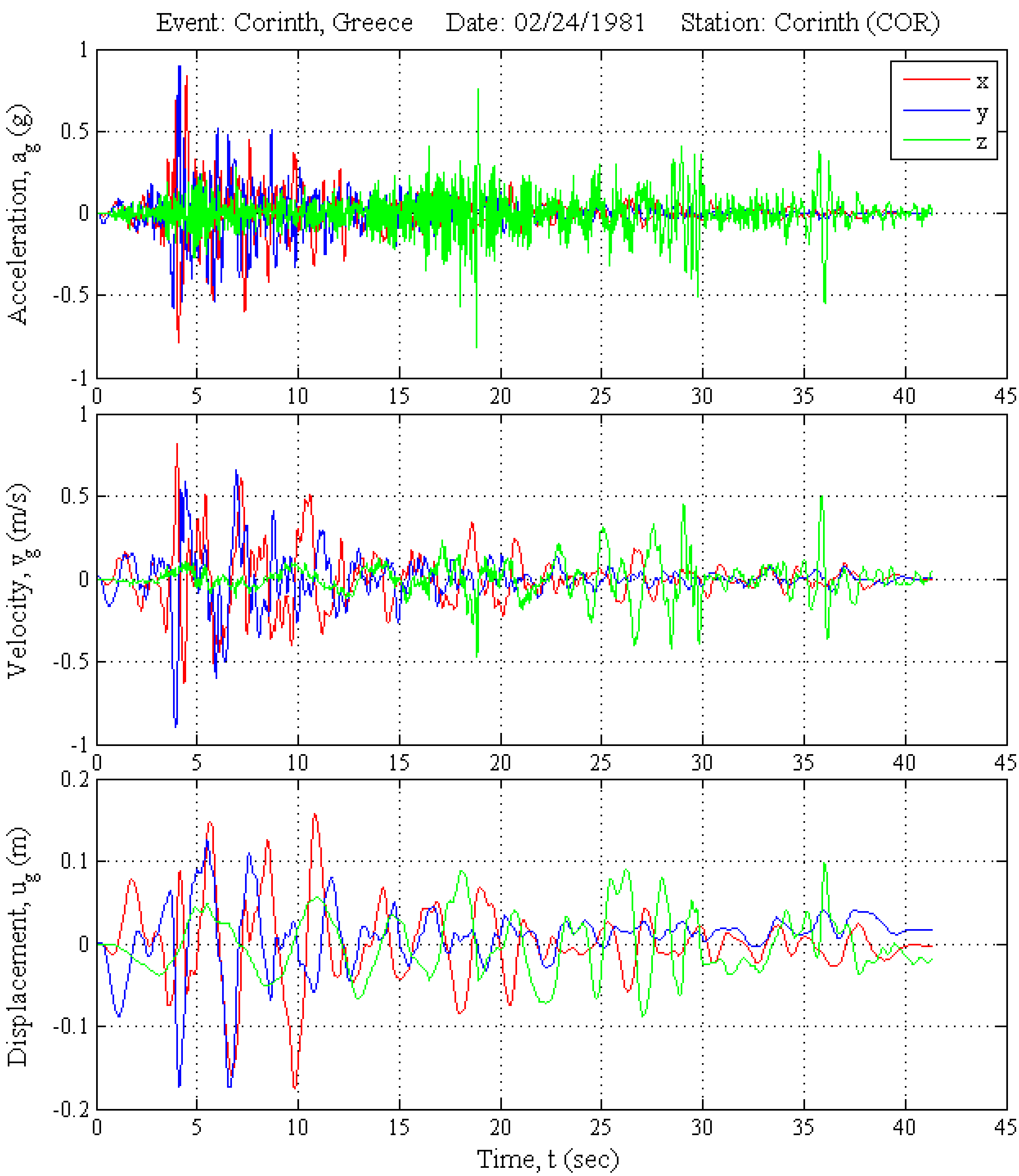

Figure B.49: Time history records for the Corinth, Greece (COR) earthquake

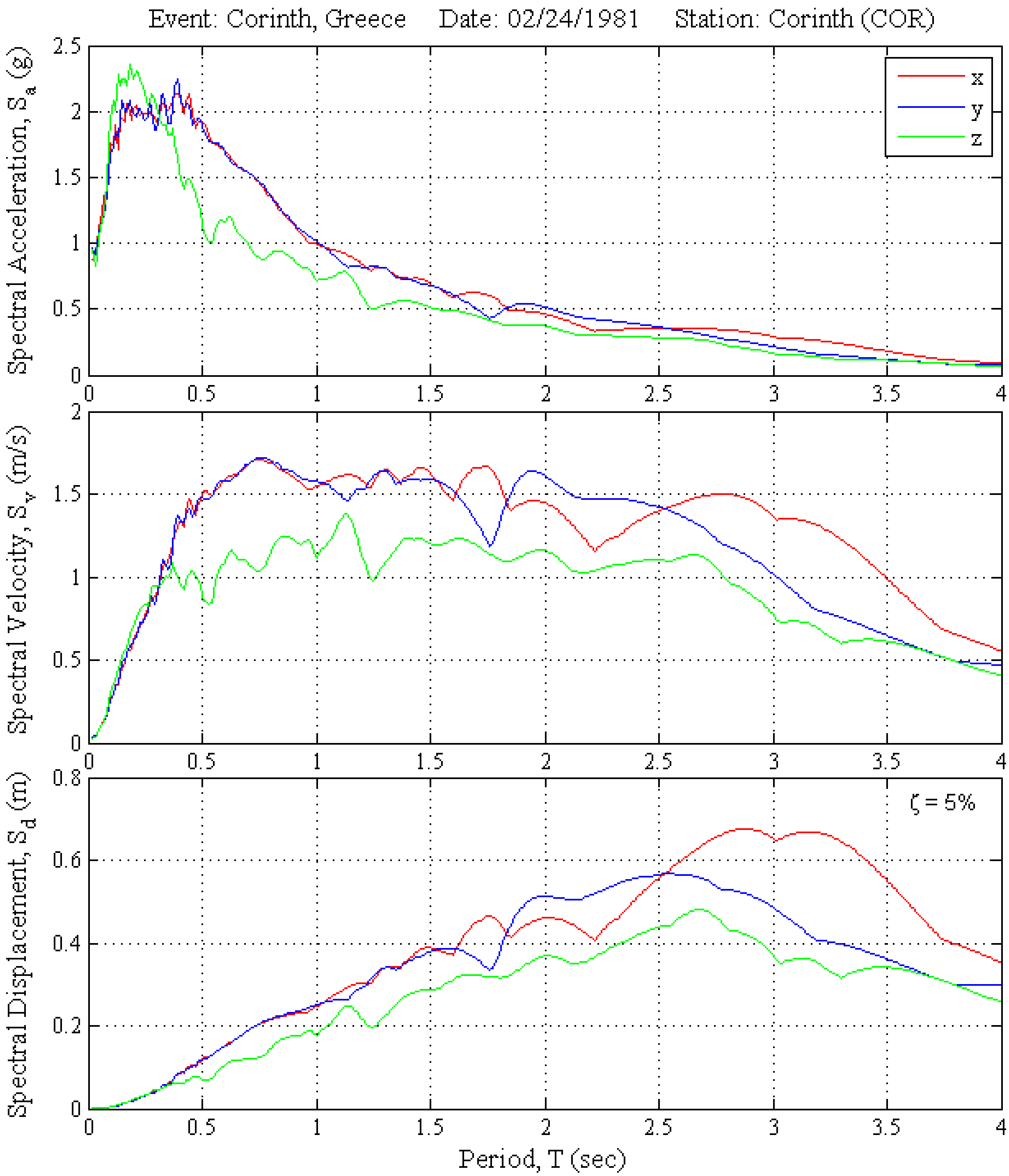

Figure B.50: Response spectra with 5% damping for the Corinth, Greece (COR) earthquake

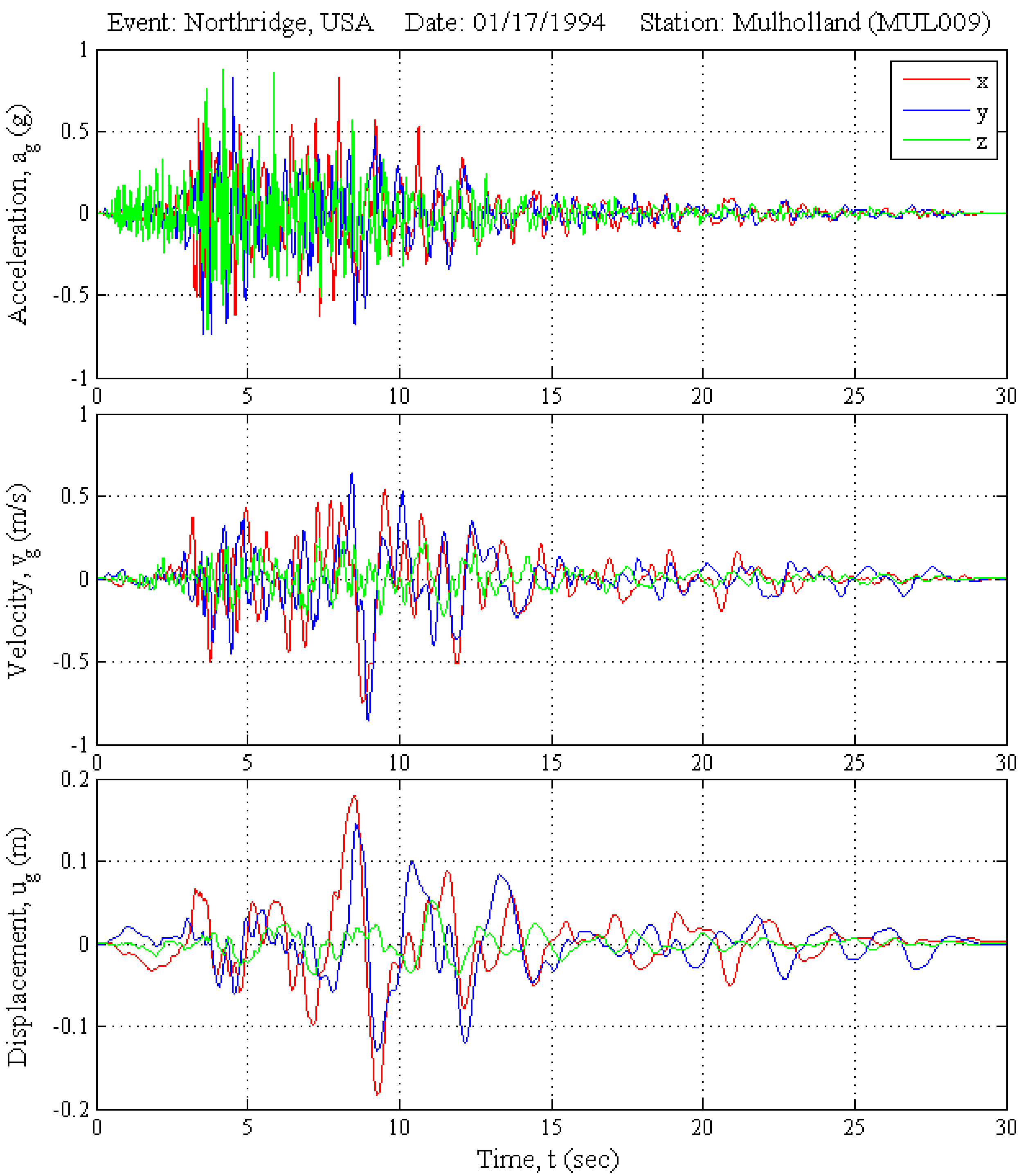

Figure B.51: Time history records for the Northridge, USA (MUL) earthquake

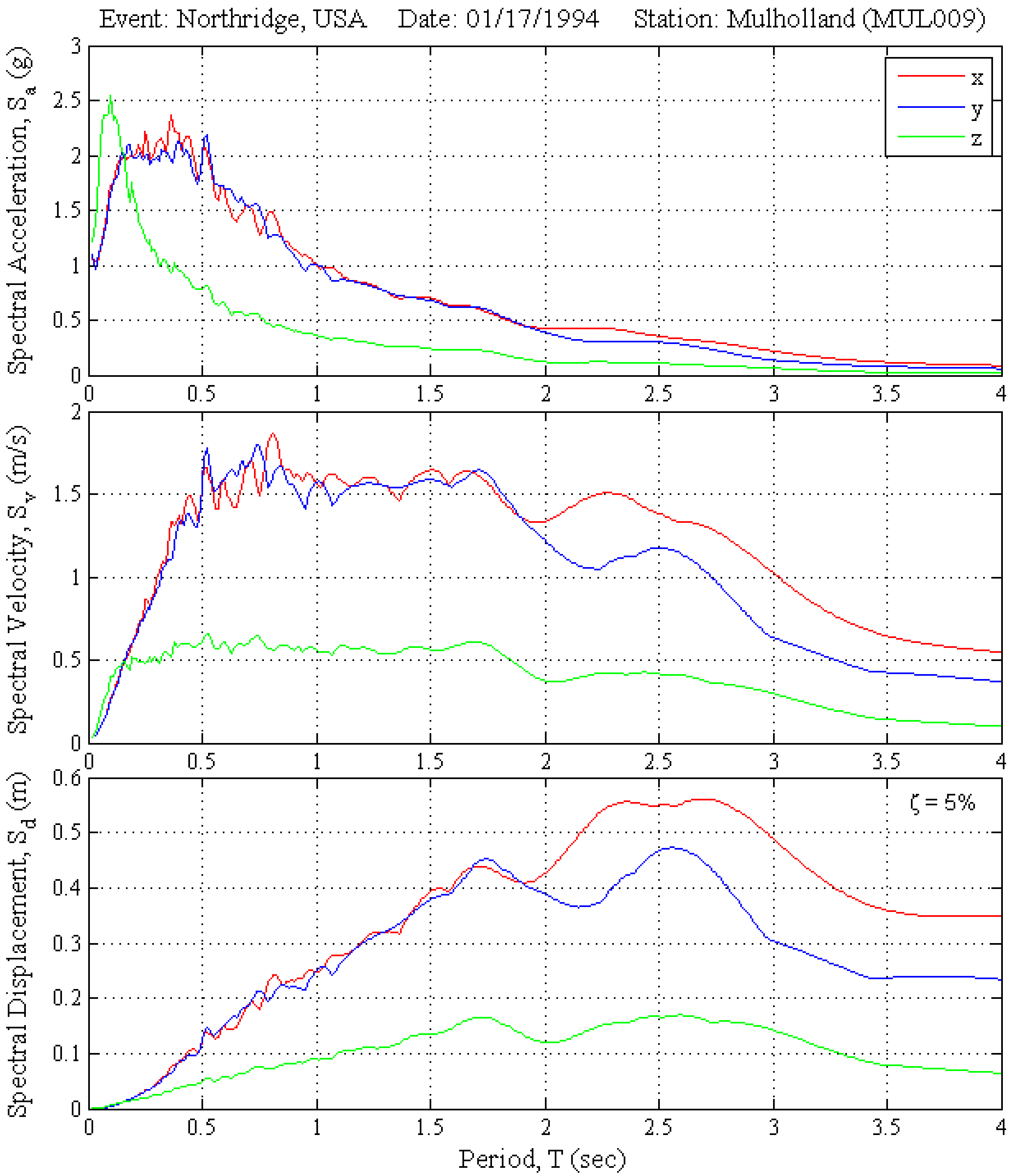

Figure B.52: Response spectra with 5% damping for the Northridge, USA (MUL) earthquake

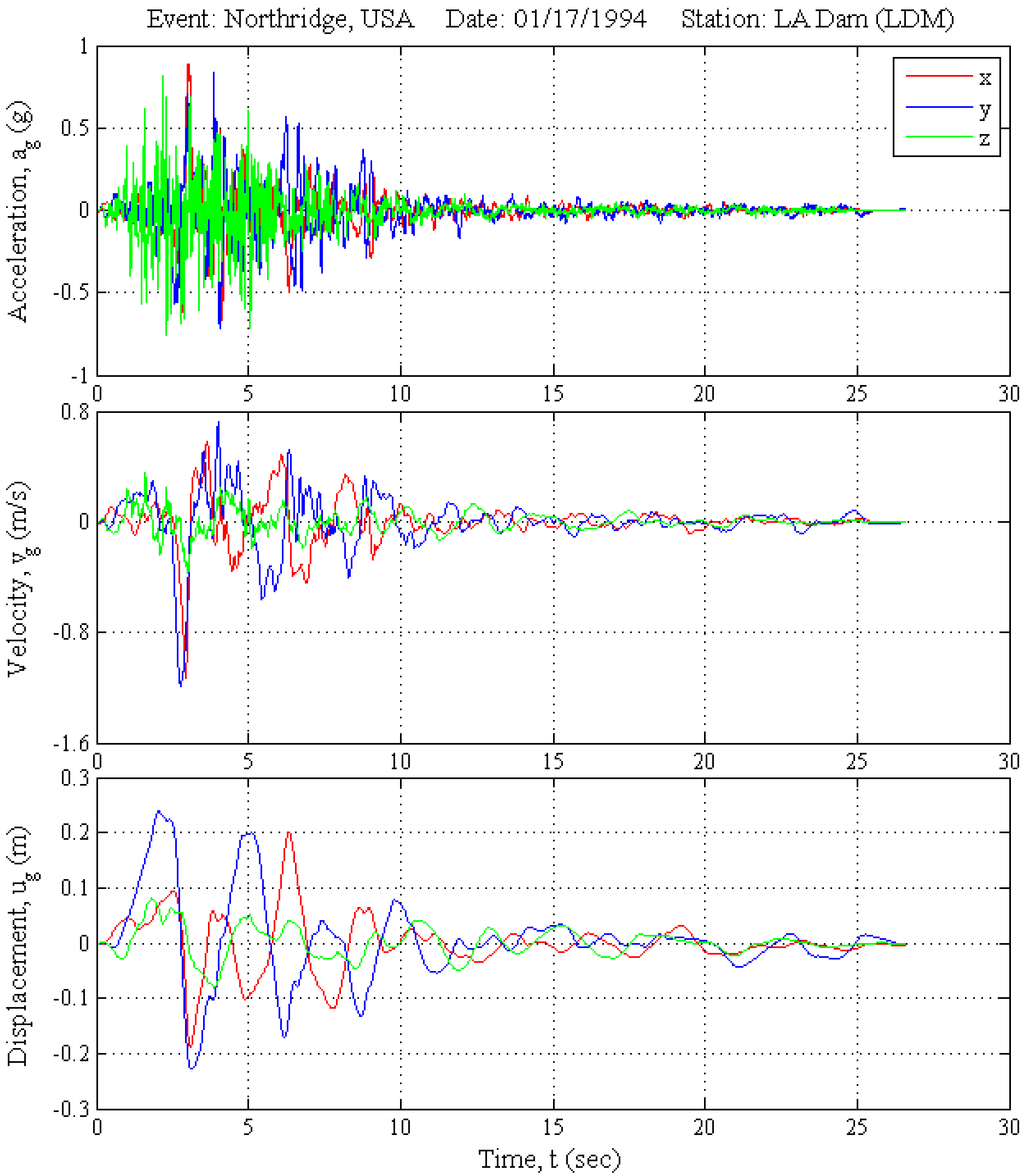

Figure B.53: Time history records for the Northridge, USA (LDM) earthquake

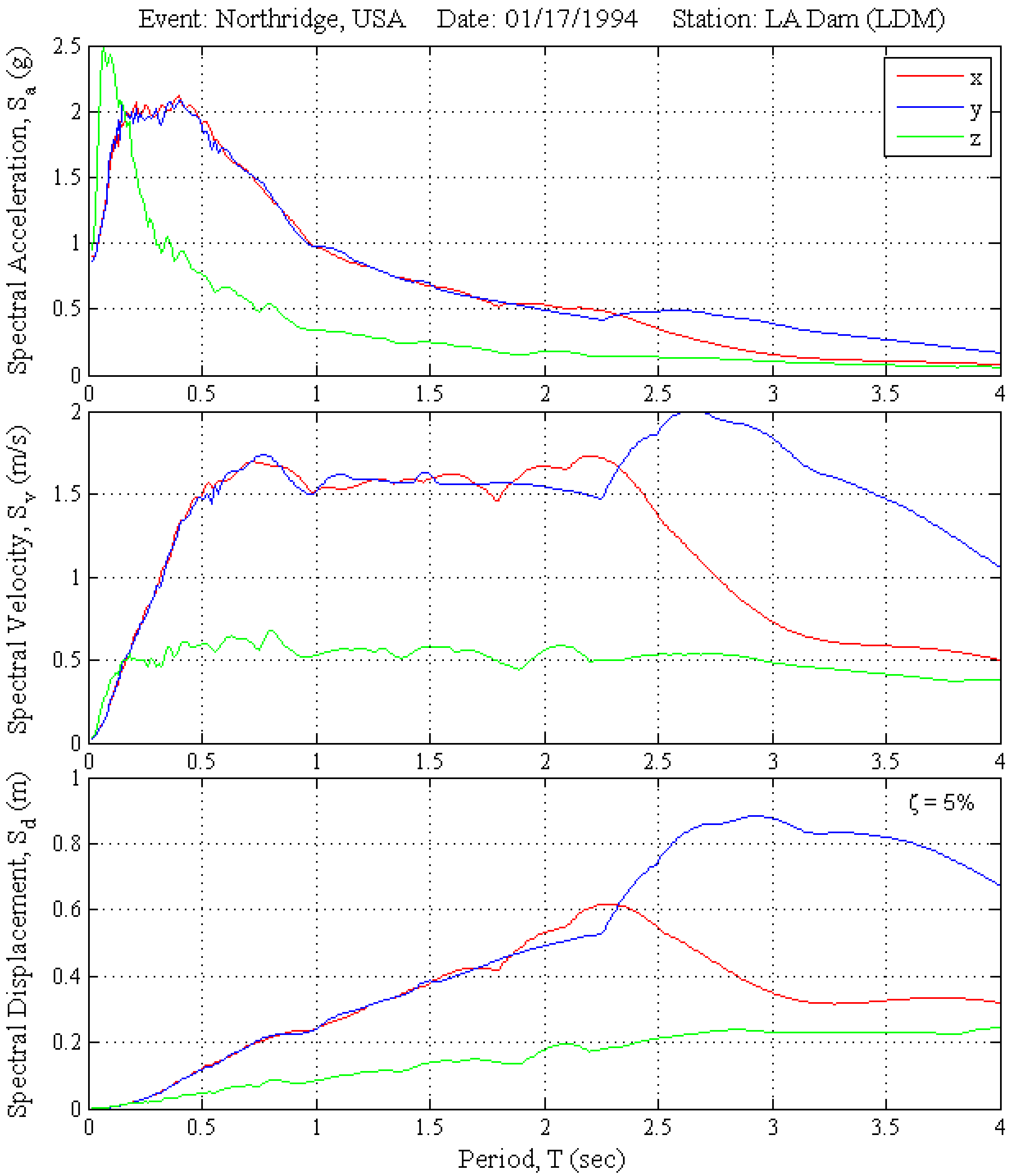

Figure B.54: Response spectra with 5% damping for the Northridge, USA (LDM) earthquake

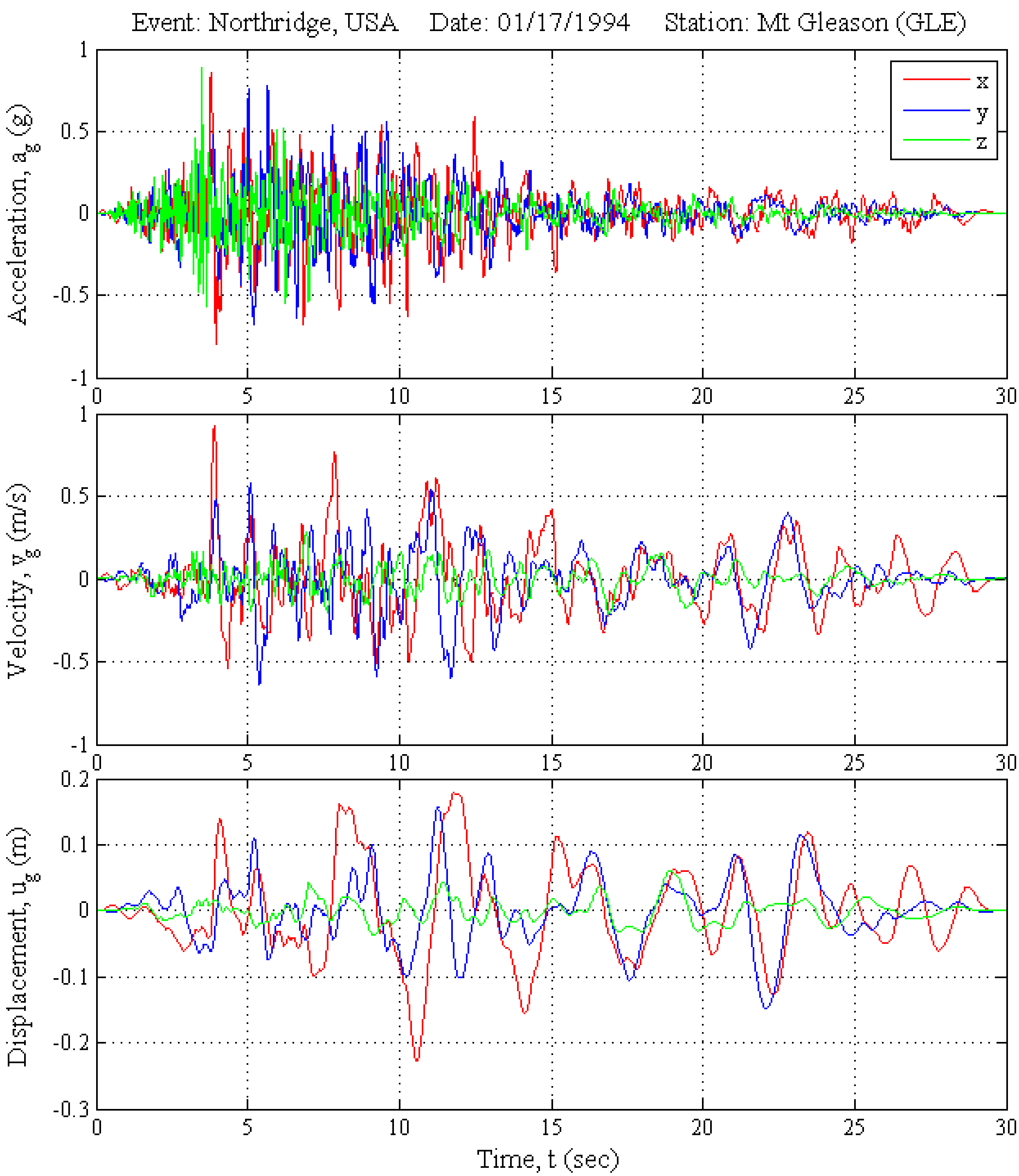

Figure B.55: Time history records for the Northridge, USA (GLE) earthquake

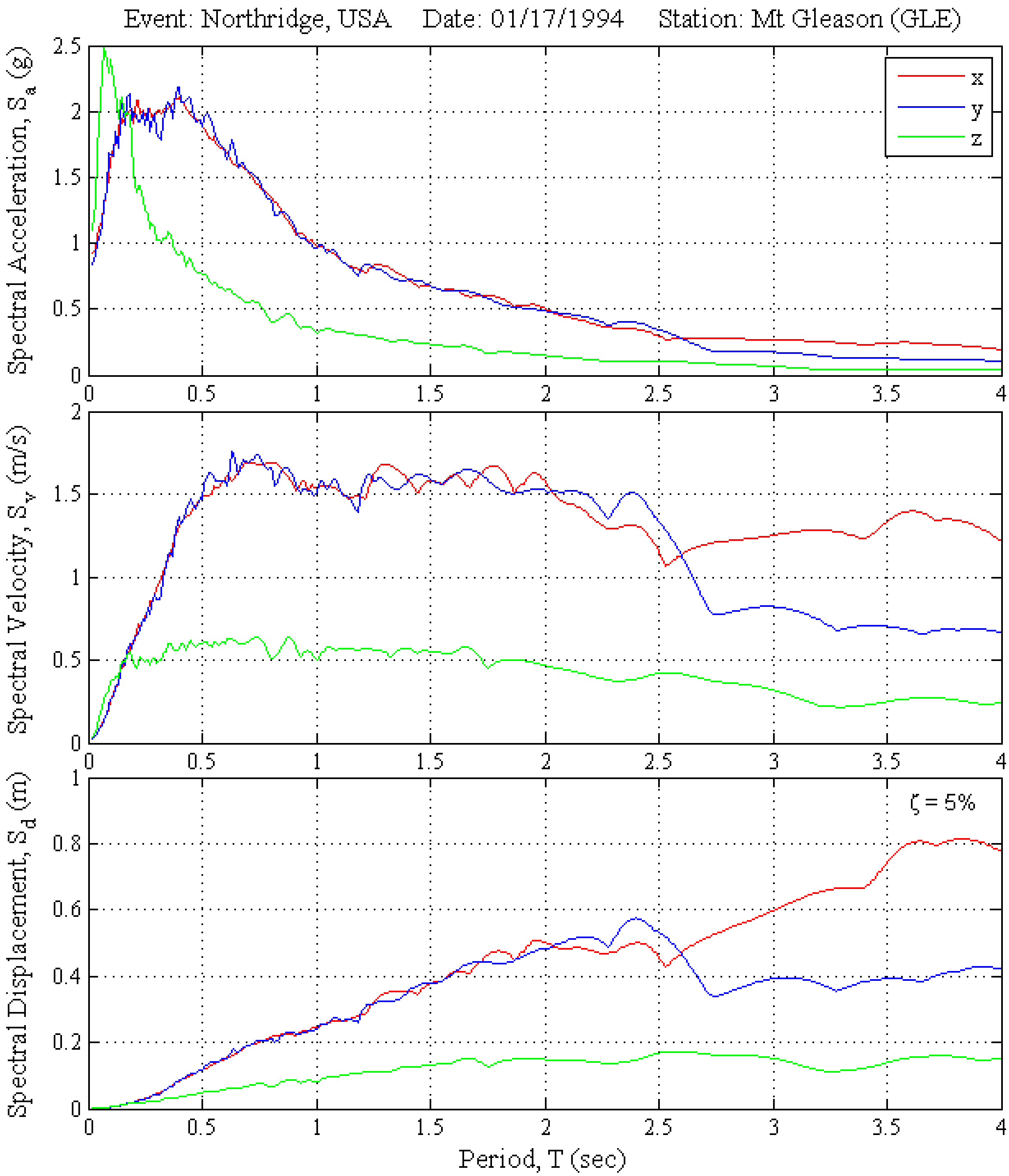

Figure B.56: Response spectra with 5% damping for the Northridge, USA (GLE) earthquake

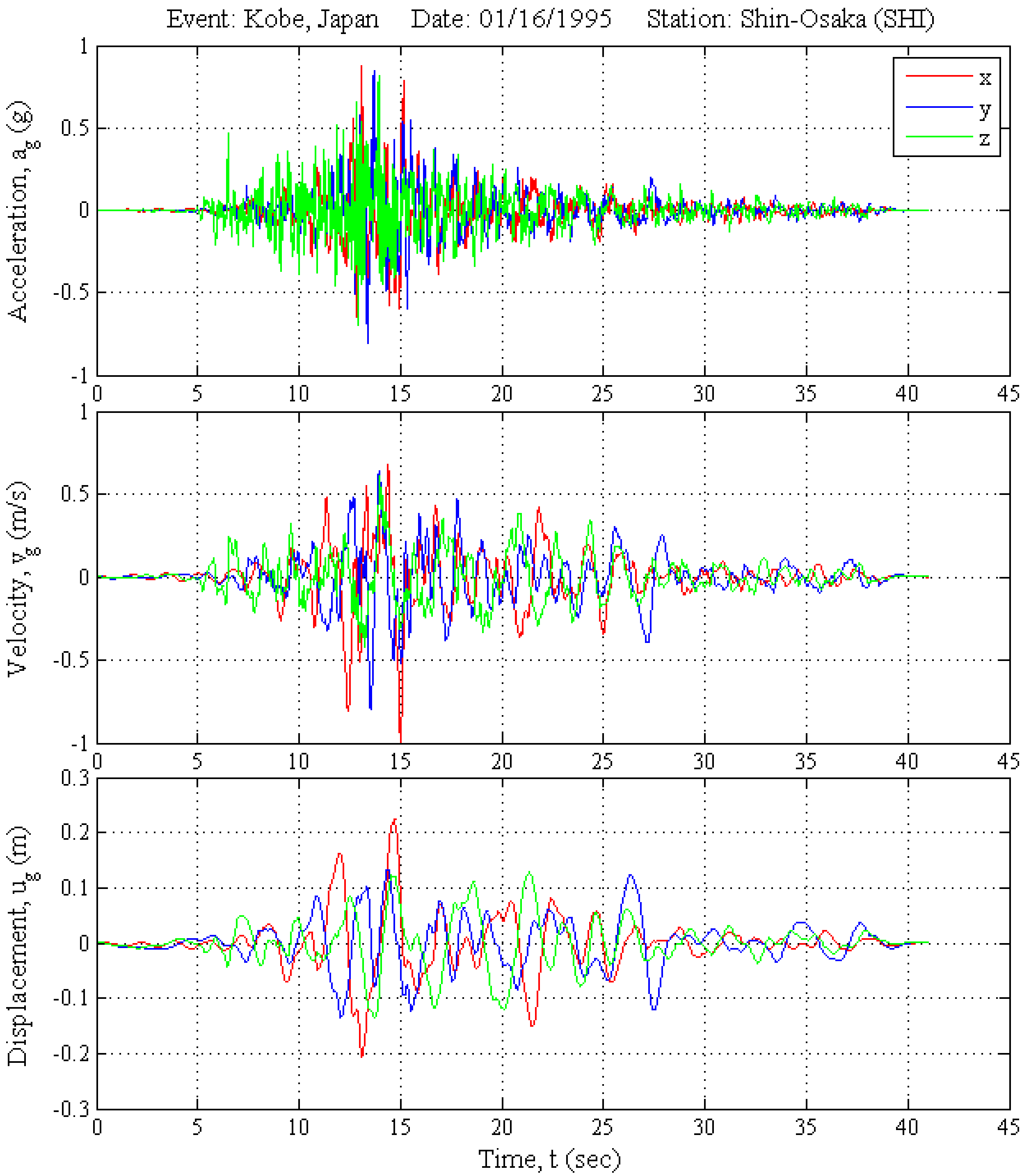

Figure B.57: Time history records for the Kobe, Japan (SHI) earthquake

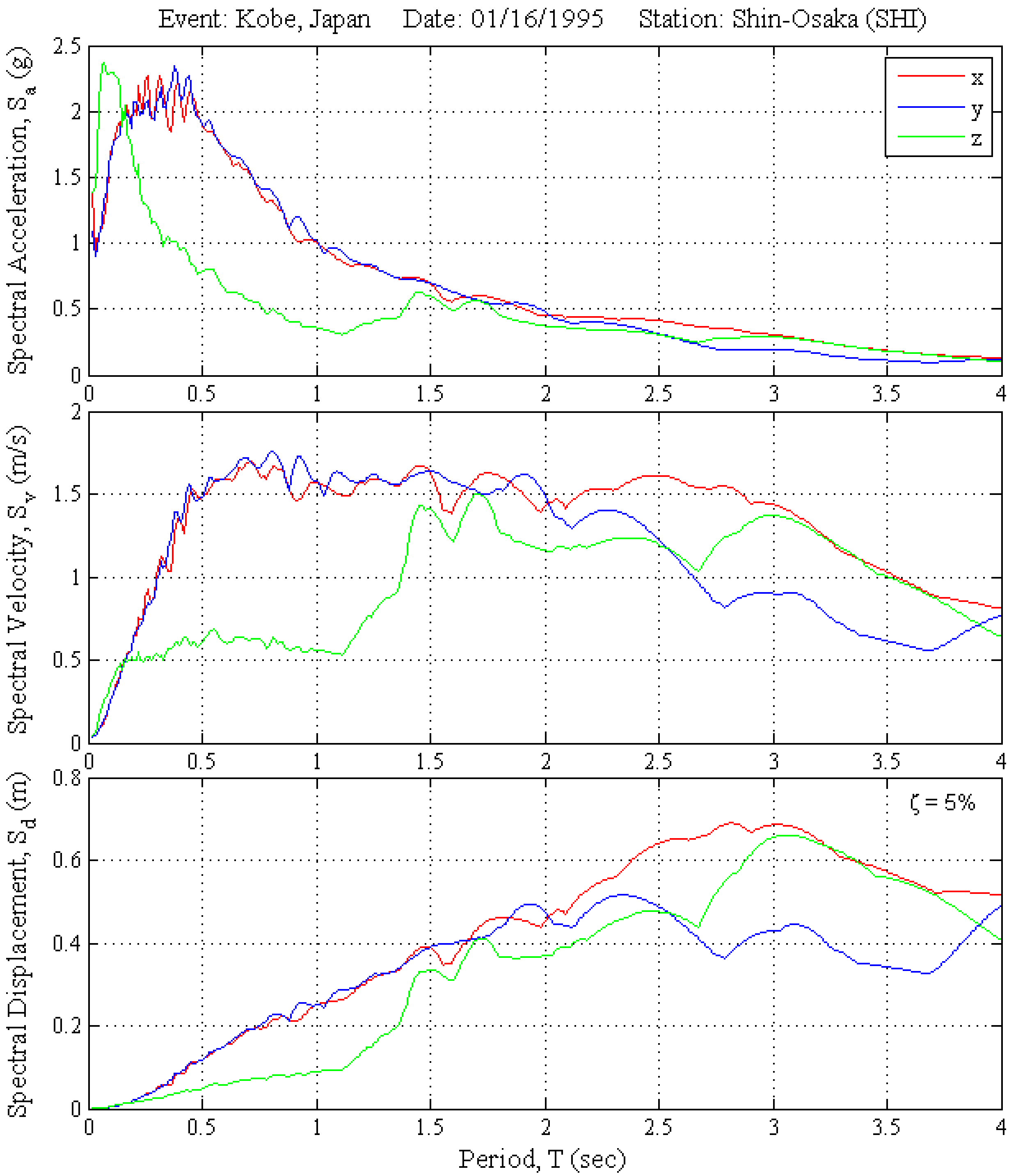

Figure B.58: Response spectra with 5% damping for the Kobe, Japan (SHI) earthquake

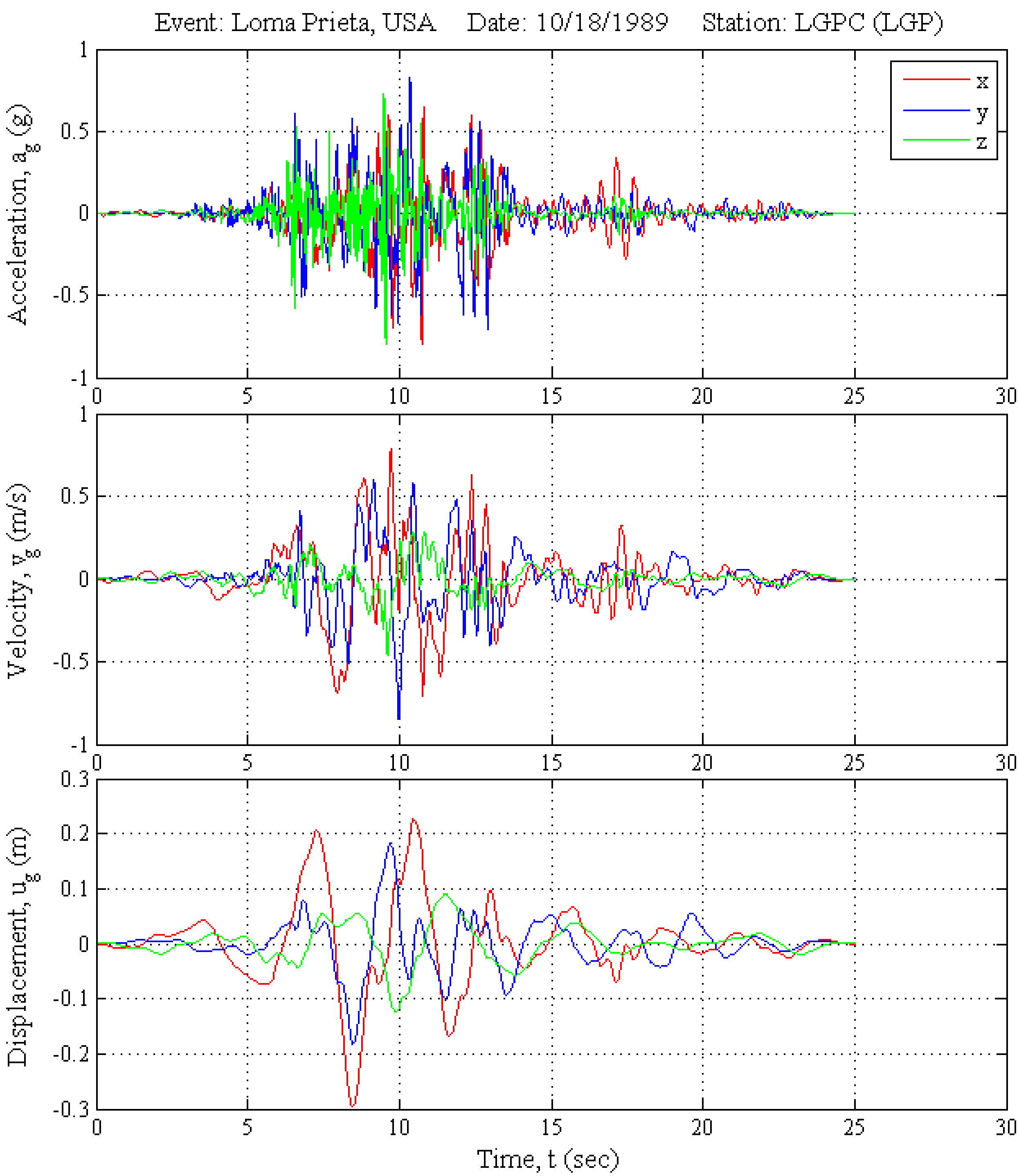

Figure B.59: Time history records for the Loma Prieta, USA (LGP) earthquake

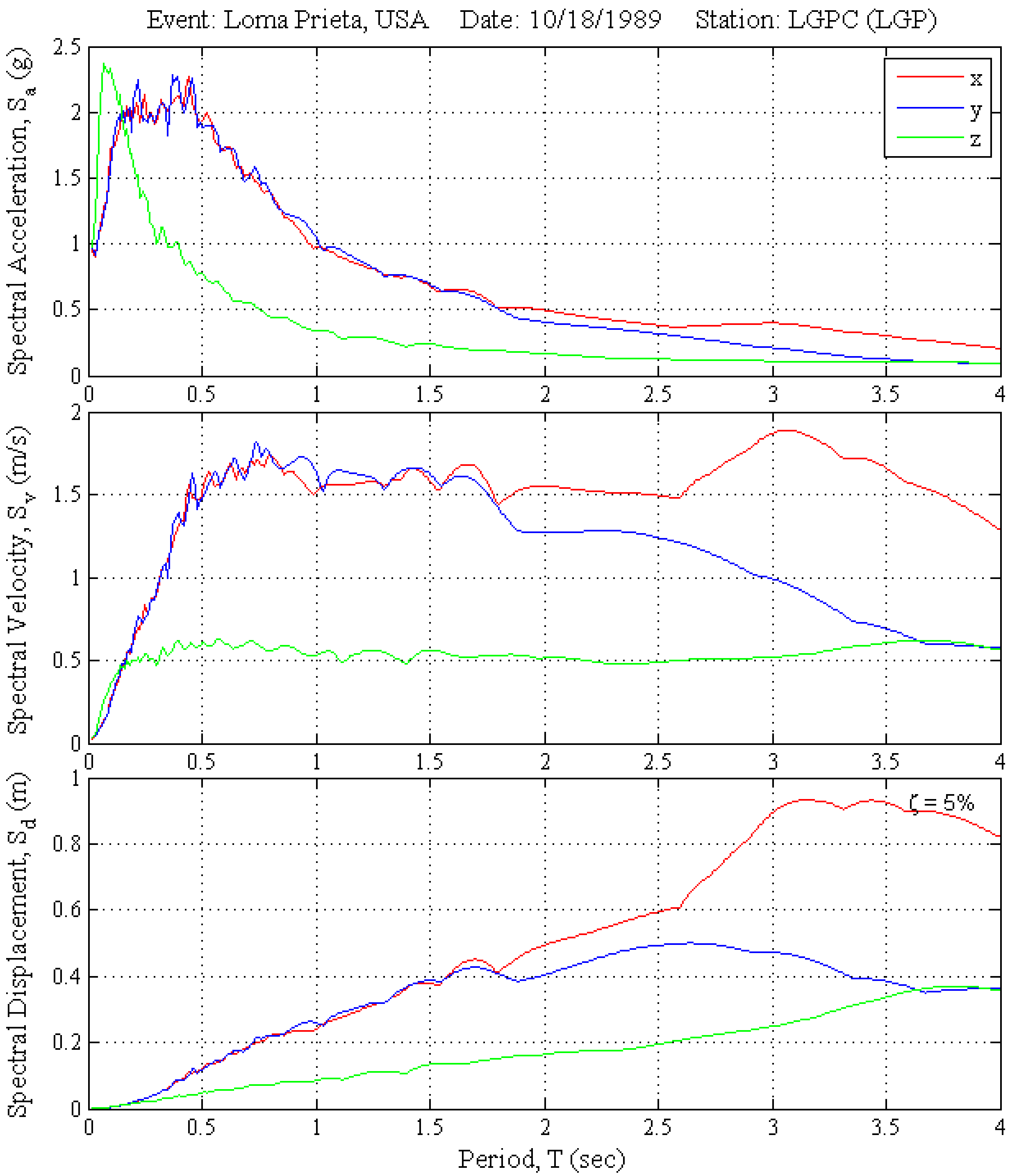

Figure B.60: Response spectra with 5% damping for the Loma Prieta, USA (LGP) earthquake

Appendix C

Soil Column Acceleration Data

This appendix presents the acceleration data recorded by tracers at the center of the soil column along the height. Tables C.1 through C.6 present peak directional acceleration amplification factors at the foundation surface, a_{max}/PGA. Figures C.1 through C.18 depict peak soil acceleration values recorded along the height of the column in all three orthogonal directions, normalized by the directional PGAs for the individual analysis cases undertaken. Figures C.19 through C.21 present median, M, amplification factors as well as standard deviation bars, $M \pm \sigma$, for the cases with a rectangular superstructure and soil column B subjected to all 30 ground motions.

Case	$a^f_{x,max}$ (g)	$a^f_{y,max}$ (g)	$a^f_{z,max}$ (g)	$\frac{a^f_{x,max}}{PGA_x}$	$\frac{a^f_{y,max}}{PGA_y}$	$\frac{a^f_{z,max}}{PGA_z}$
C2B08	0.96	0.86	6.19	1.25	1.07	7.28
C2B09	1.07	0.81	3.24	1.26	0.98	3.96
C2B22	1.19	1.25	4.84	1.40	1.20	5.98
C4B08	0.90	0.85	2.74	1.16	1.06	3.23
C4B09	1.00	0.86	3.01	1.18	1.04	3.68
C4B22	1.18	1.40	2.65	1.39	1.35	3.27
C5B08	0.90	0.86	2.74	1.16	1.07	3.22
C5B09	1.01	0.86	3.05	1.18	1.03	3.72
C5B22	1.18	1.40	2.75	1.38	1.35	3.39
R2B08	0.96	0.92	3.97	1.25	1.15	4.67
R2B09	1.07	1.15	3.05	1.25	1.38	3.72
R2B22	1.36	1.58	3.29	1.60	1.52	4.06
R4B08	0.88	1.04	2.44	1.15	1.30	2.88
R4B09	1.11	1.25	2.92	1.30	1.51	3.57
R4B22	1.17	1.43	2.78	1.38	1.38	3.43
R5B08	0.88	1.04	2.48	1.15	1.30	2.92
R5B09	1.11	1.24	2.80	1.31	1.50	3.41
R5B22	1.17	1.43	2.81	1.37	1.38	3.46

Table C.1: Peak soil column acceleration data for the soil B cases in response to the basic motions

Case	$a^f_{x,max}$ (g)	$a^f_{y,max}$ (g)	$a^f_{z,max}$ (g)	$\frac{a^f_{x,max}}{PGA_x}$	$\frac{a^f_{y,max}}{PGA_y}$	$\frac{a^f_{z,max}}{PGA_z}$
C2C08	0.76	0.95	4.31	0.99	1.18	5.07
C2C09	0.78	0.80	4.20	0.92	0.97	5.12
C2C22	1.03	0.96	3.32	1.21	0.92	4.10
C4C08	0.71	0.78	4.65	0.92	0.98	5.47
C4C09	0.81	0.80	3.57	0.95	0.97	4.36
C4C22	1.17	1.00	3.73	1.38	0.96	4.60
C5C08	0.65	0.77	4.56	0.84	0.96	5.36
C5C09	0.80	0.80	3.69	0.94	0.96	4.50
C5C22	1.16	0.99	4.05	1.36	0.96	5.00
R2C08	0.89	1.18	2.51	1.15	1.48	2.95
R2C09	0.85	0.80	3.91	0.99	0.96	4.79
R2C22	1.12	1.33	2.24	1.32	1.28	2.77
R4C08	0.87	0.98	2.18	1.13	1.23	2.56
R4C09	0.85	0.77	1.84	0.99	0.92	2.25
R4C22	0.95	1.38	2.19	1.12	1.33	2.70
R5C08	0.87	0.99	2.13	1.13	1.24	2.51
R5C09	0.85	0.76	2.18	1.01	0.92	2.66
R5C22	0.95	1.41	2.12	1.12	1.35	2.62

Table C.2: Peak soil column acceleration data for the soil C cases in response to the basic motions

Case	$a^f_{x,max}$ (g)	$a^f_{y,max}$ (g)	$a^f_{z,max}$ (g)	$\frac{a^f_{x,max}}{PGA_x}$	$\frac{a^f_{y,max}}{PGA_y}$	$\frac{a^f_{z,max}}{PGA_z}$
C2D08	0.34	0.39	1.65	0.44	0.49	1.94
C2D09	0.44	0.49	1.96	0.52	0.59	2.39
C2D22	0.55	0.53	2.50	0.64	0.51	3.09
C4D08	0.33	0.40	1.47	0.43	0.50	1.73
C4D09	0.40	0.46	1.40	0.47	0.55	1.71
C4D22	0.56	0.52	2.04	0.66	0.50	2.51
C5D08	0.32	0.39	1.47	0.42	0.49	1.73
C5D09	0.40	0.46	1.63	0.47	0.55	1.98
C5D22	0.56	0.52	2.16	0.65	0.50	2.67
R2D08	0.60	0.62	1.23	0.77	0.78	1.45
R2D09	0.67	0.56	3.14	0.79	0.68	3.82
R2D22	0.64	0.78	2.82	0.75	0.75	3.48
R4D08	0.56	0.64	0.86	0.73	0.80	1.01
R4D09	0.59	0.53	0.85	0.69	0.64	1.04
R4D22	0.67	0.51	0.97	0.79	0.49	1.19
R5D08	0.56	0.64	0.86	0.73	0.81	1.01
R5D09	0.57	0.54	0.83	0.68	0.65	1.02
R5D22	0.67	0.50	0.96	0.78	0.48	1.19

Table C.3: Peak soil column acceleration data for the soil D cases in response to the basic motions

Case	$a^f_{x,max}$ (g)	$a^f_{y,max}$ (g)	$a^f_{z,max}$ (g)	$\frac{a^f_{x,max}}{PGA_x}$	$\frac{a^f_{y,max}}{PGA_y}$	$\frac{a^f_{z,max}}{PGA_z}$
R2B01	1.08	1.12	3.46	1.29	1.27	4.38
R2B02	1.11	1.24	4.15	1.33	1.48	4.66
R2B03	1.01	1.21	4.08	1.22	1.43	4.98
R2B04	1.18	1.25	3.79	1.34	1.47	4.86
R2B05	1.49	1.03	3.63	1.75	1.24	4.43
R2B06	1.40	1.05	2.61	1.49	1.25	3.14
R2B07	0.88	1.04	5.15	1.06	1.26	6.13
R2B08	0.96	0.92	3.97	1.25	1.15	4.67
R2B09	1.07	1.15	3.05	1.25	1.38	3.72
R2B10	1.04	1.03	4.06	1.21	1.38	5.01
R2B11	1.13	1.10	4.08	1.34	1.32	5.17
R2B12	1.06	0.90	4.33	1.30	1.12	5.34
R2B13	1.19	1.07	2.96	1.42	1.23	3.61
R2B14	1.11	1.01	4.37	1.29	1.26	5.60
R2B15	0.93	1.18	3.92	1.13	1.39	4.78
R2B16	0.92	1.15	4.56	1.10	1.35	5.84
R2B17	1.09	1.03	4.25	1.36	1.22	5.31
R2B18	1.15	0.89	3.34	1.37	1.06	3.98
R2B19	1.21	1.07	2.72	1.42	1.18	3.23
R2B20	1.31	0.90	3.26	1.42	1.07	4.03
R2B21	0.95	0.95	4.36	1.13	1.16	5.32
R2B22	1.36	1.58	3.29	1.60	1.52	4.06
R2B23	1.06	0.94	3.47	1.26	1.13	4.40
R2B24	1.20	1.06	2.09	1.44	1.25	2.55
R2B25	1.13	1.05	3.83	1.36	1.17	4.68
R2B26	0.93	0.96	2.83	1.14	1.15	3.22
R2B27	1.36	1.02	4.84	1.53	1.22	5.90
R2B28	1.21	1.11	3.45	1.42	1.42	3.88
R2B29	1.05	0.89	3.29	1.21	1.05	4.01
R2B30	0.93	1.30	3.06	1.16	1.57	3.87
M	1.10	1.05	3.71	1.32	1.25	4.54
σ	0.15	0.15	0.70	0.16	0.1403	0.89

Table C.4: Peak soil column acceleration data for the soil B cases with a rectangular superstructure and FP bearings in response to all motions

Case	$a^f_{x,max}$ (g)	$a^f_{y,max}$ (g)	$a^f_{z,max}$ (g)	$\frac{a^f_{x,max}}{PGA_x}$	$\frac{a^f_{y,max}}{PGA_y}$	$\frac{a^f_{z,max}}{PGA_z}$
R4B01	1.10	1.08	2.31	1.31	1.23	2.92
R4B02	1.00	1.13	2.21	1.20	1.35	2.49
R4B03	1.03	1.17	2.81	1.24	1.38	3.42
R4B04	1.20	1.04	3.28	1.36	1.22	4.21
R4B05	1.18	1.06	1.64	1.39	1.28	1.99
R4B06	1.39	1.04	1.79	1.48	1.23	2.15
R4B07	0.86	0.94	2.98	1.03	1.15	3.55
R4B08	0.88	1.04	2.44	1.15	1.30	2.88
R4B09	1.11	1.25	2.92	1.30	1.51	3.57
R4B10	1.00	0.97	2.65	1.16	1.29	3.27
R4B11	1.00	0.92	2.57	1.19	1.11	3.26
R4B12	0.96	0.98	2.64	1.17	1.23	3.27
R4B13	1.24	1.03	2.12	1.48	1.18	2.58
R4B14	1.11	0.95	2.50	1.29	1.19	3.21
R4B15	0.96	0.82	4.67	1.17	0.96	5.70
R4B16	0.95	1.03	3.39	1.13	1.22	4.34
R4B17	1.06	1.07	2.77	1.32	1.27	3.46
R4B18	1.19	0.91	3.75	1.42	1.08	4.46
R4B19	1.20	1.11	2.35	1.41	1.23	2.79
R4B20	1.21	0.88	3.00	1.32	1.05	3.70
R4B21	1.03	1.02	2.88	1.22	1.25	3.51
R4B22	1.17	1.43	2.78	1.38	1.38	3.43
R4B23	1.07	0.90	3.69	1.27	1.08	4.68
R4B24	0.99	1.14	2.11	1.19	1.35	2.58
R4B25	1.17	1.05	4.07	1.41	1.16	4.96
R4B26	0.84	0.95	2.71	1.03	1.14	3.08
R4B27	1.30	0.99	2.65	1.46	1.18	3.23
R4B28	1.08	1.20	2.25	1.27	1.54	2.53
R4B29	0.94	0.80	2.26	1.08	0.94	2.76
R4B30	1.01	1.06	2.81	1.27	1.28	3.56
M	1.06	1.04	2.68	1.27	1.23	3.27
σ	0.13	0.13	0.66	0.13	0.13	0.83

Table C.5: Peak soil column acceleration data for the soil B cases with a rectangular superstructure and simplified LR bearings in response to all motions

Case	$a^f_{x,max}$ (g)	$a^f_{y,max}$ (g)	$a^f_{z,max}$ (g)	$\frac{a^f_{x,max}}{PGA_x}$	$\frac{a^f_{y,max}}{PGA_y}$	$\frac{a^f_{z,max}}{PGA_z}$
R5B01	1.10	1.09	2.24	1.31	1.24	2.83
R5B02	1.01	1.14	2.21	1.22	1.36	2.49
R5B03	1.05	1.17	2.90	1.26	1.37	3.53
R5B04	1.20	1.03	3.58	1.37	1.21	4.59
R5B05	1.19	1.05	1.64	1.41	1.27	2.01
R5B06	1.39	1.04	1.81	1.48	1.24	2.19
R5B07	0.86	0.93	3.03	1.04	1.13	3.61
R5B08	0.88	1.04	2.48	1.15	1.30	2.92
R5B09	1.11	1.24	2.80	1.31	1.50	3.41
R5B10	1.00	0.97	2.59	1.16	1.29	3.20
R5B11	0.99	0.92	2.44	1.18	1.11	3.09
R5B12	0.96	1.01	2.68	1.18	1.26	3.31
R5B13	1.26	1.04	2.13	1.50	1.20	2.59
R5B14	1.12	0.94	2.56	1.30	1.17	3.29
R5B15	0.97	0.82	4.62	1.18	0.97	5.63
R5B16	0.95	1.02	3.28	1.13	1.20	4.20
R5B17	1.03	1.06	3.15	1.29	1.27	3.94
R5B18	1.19	0.91	3.74	1.42	1.09	4.45
R5B19	1.20	1.11	2.42	1.41	1.23	2.88
R5B20	1.20	0.86	2.99	1.30	1.02	3.69
R5B21	1.04	1.03	2.83	1.23	1.26	3.45
R5B22	1.17	1.43	2.81	1.37	1.38	3.46
R5B23	1.08	0.89	3.65	1.28	1.07	4.62
R5B24	1.00	1.14	2.01	1.20	1.34	2.46
R5B25	1.18	1.05	3.82	1.42	1.17	4.66
R5B26	0.84	0.95	2.63	1.02	1.14	2.99
R5B27	1.30	0.99	2.41	1.46	1.17	2.94
R5B28	1.07	1.19	2.17	1.26	1.53	2.43
R5B29	0.93	0.80	2.19	1.07	0.94	2.67
R5B30	0.99	1.05	2.63	1.24	1.27	3.33
M	1.06	1.03	2.63	1.27	1.23	3.30
σ	0.13	0.13	0.65	0.13	0.13	0.83

Table C.6: Peak soil column acceleration data for the soil B cases with a rectangular superstructure and robust LR bearings in response to all motions

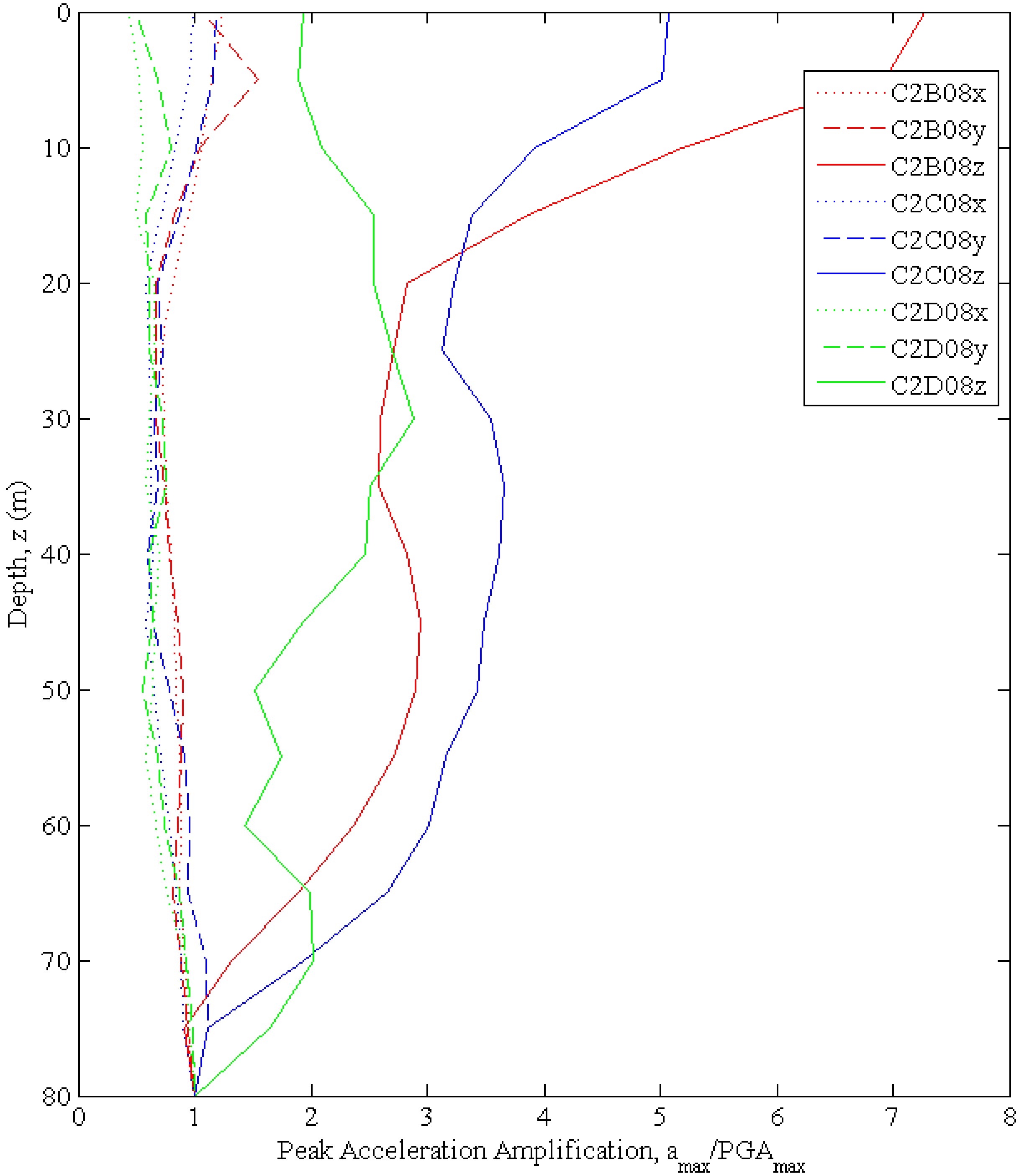

Figure C.1: Peak soil column acceleration data from the simulations with the cylindrical superstructure and FP bearings subjected to ground motion 08

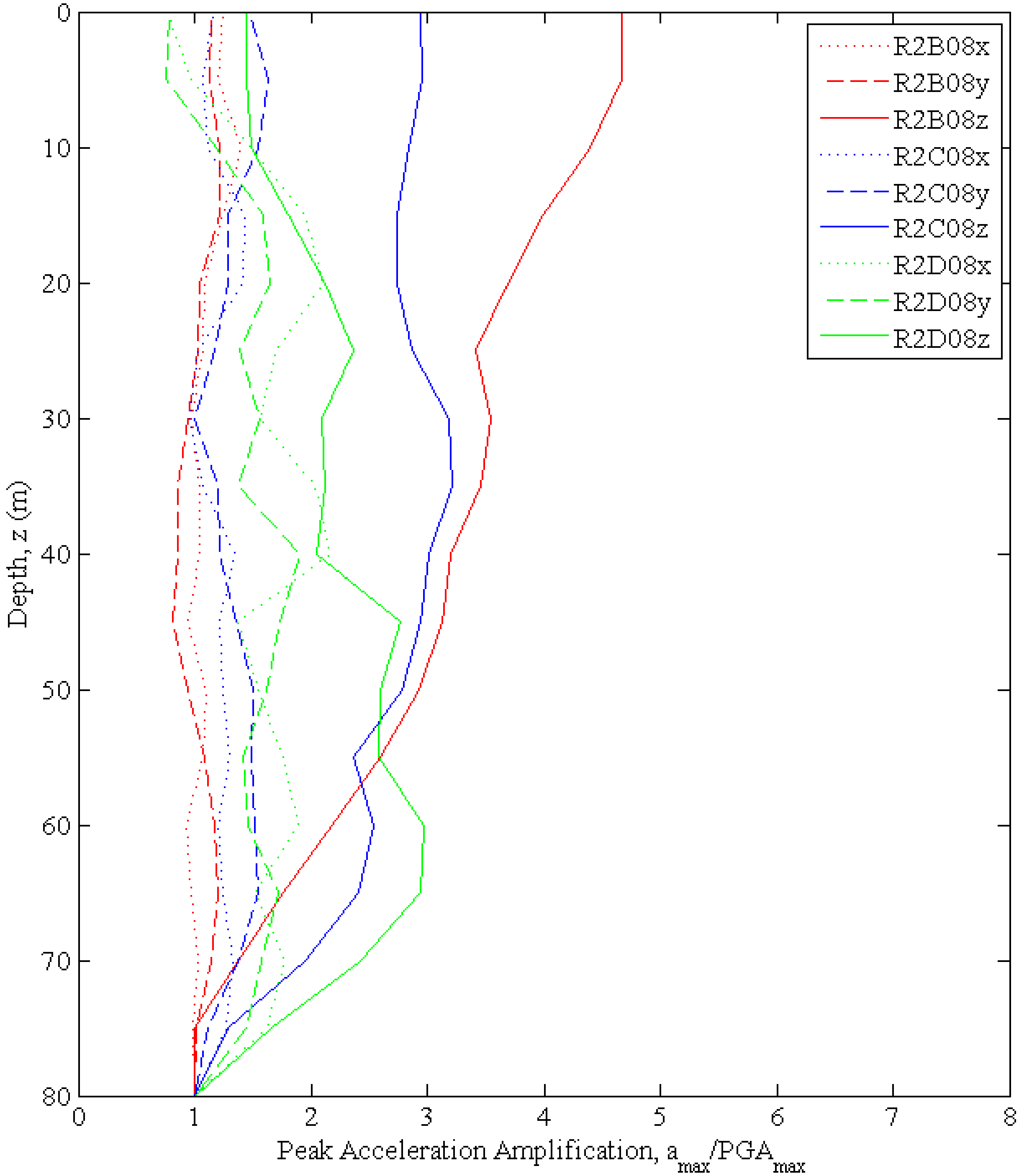

Figure C.2: Peak soil column acceleration data from the simulations with the rectangular superstructure and FP bearings subjected to ground motion 08

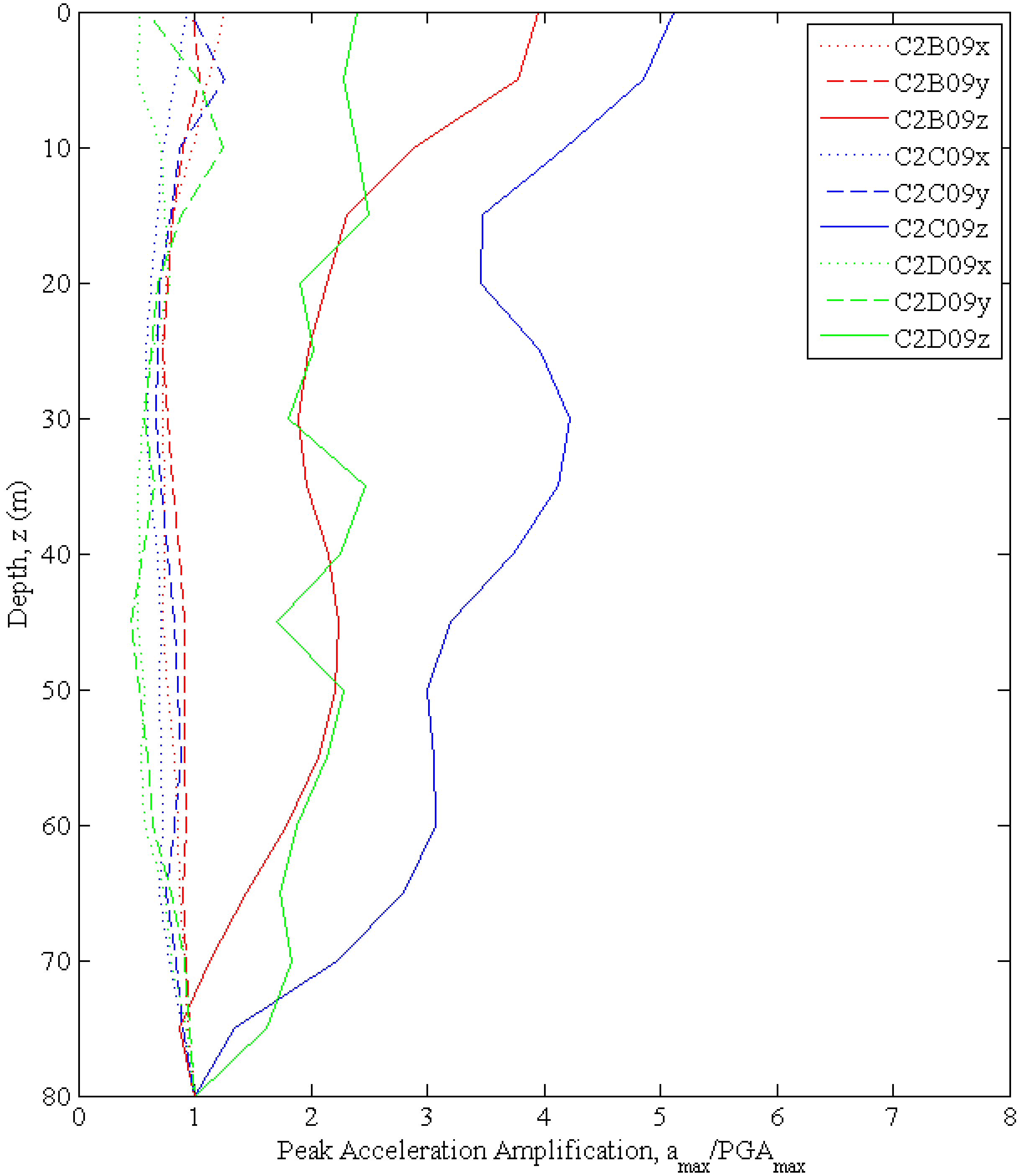

Figure C.3: Peak soil column acceleration data from the simulations with the cylindrical superstructure and FP bearings subjected to ground motion 09

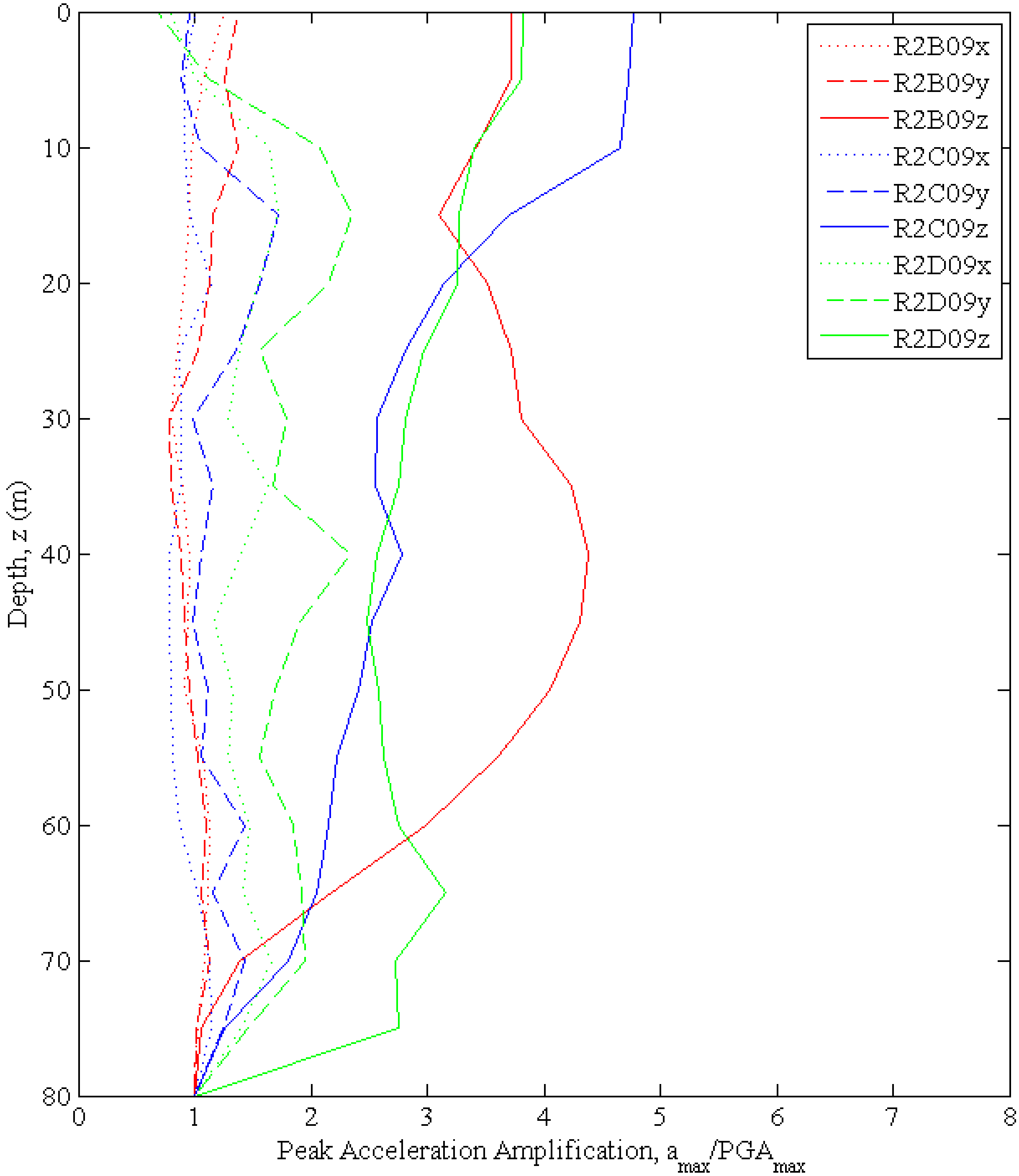

Figure C.4: Peak soil column acceleration data from the simulations with the rectangular superstructure and FP bearings subjected to ground motion 09

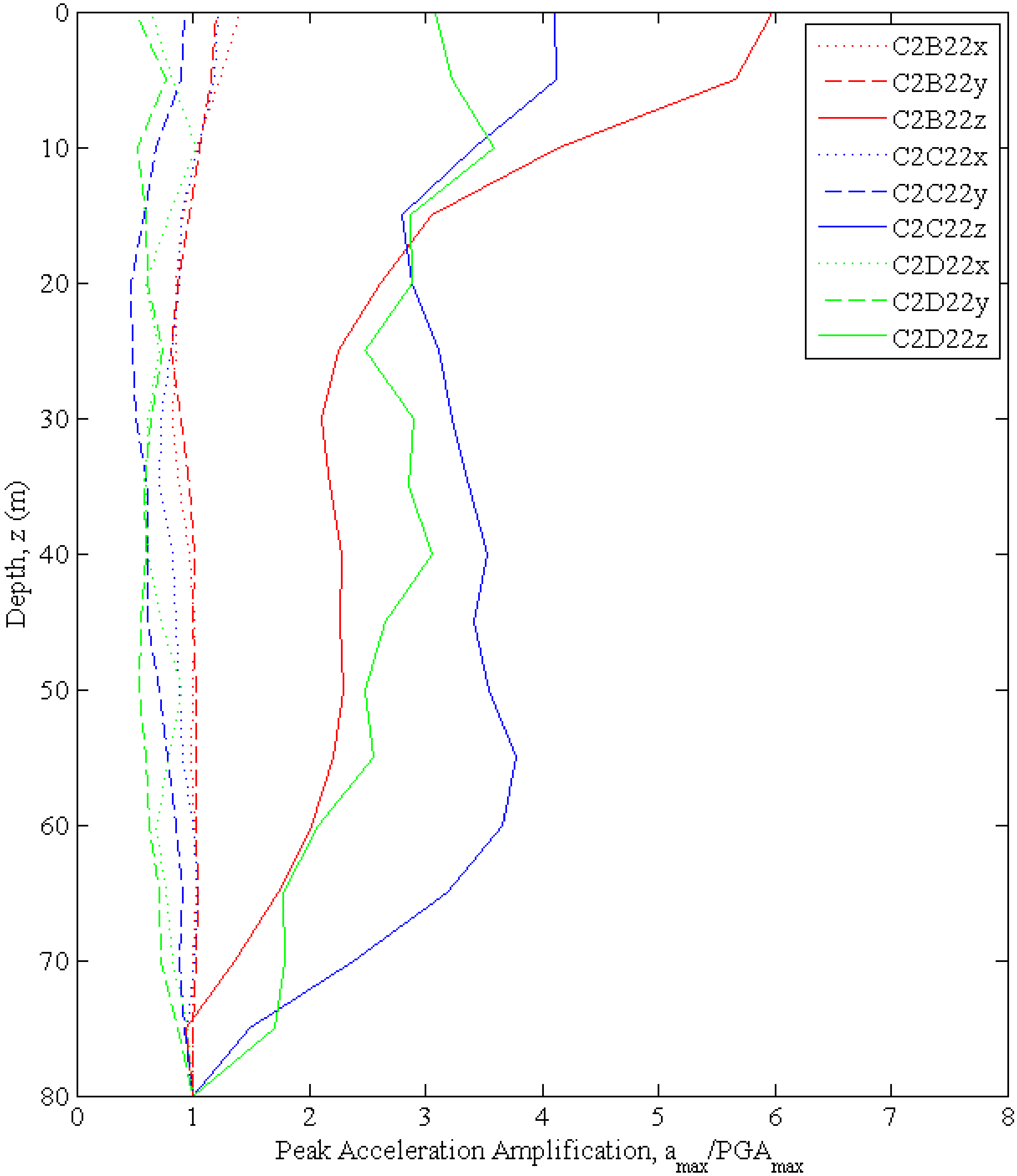

Figure C.5: Peak soil column acceleration data from the simulations with the cylindrical superstructure and FP bearings subjected to ground motion 22

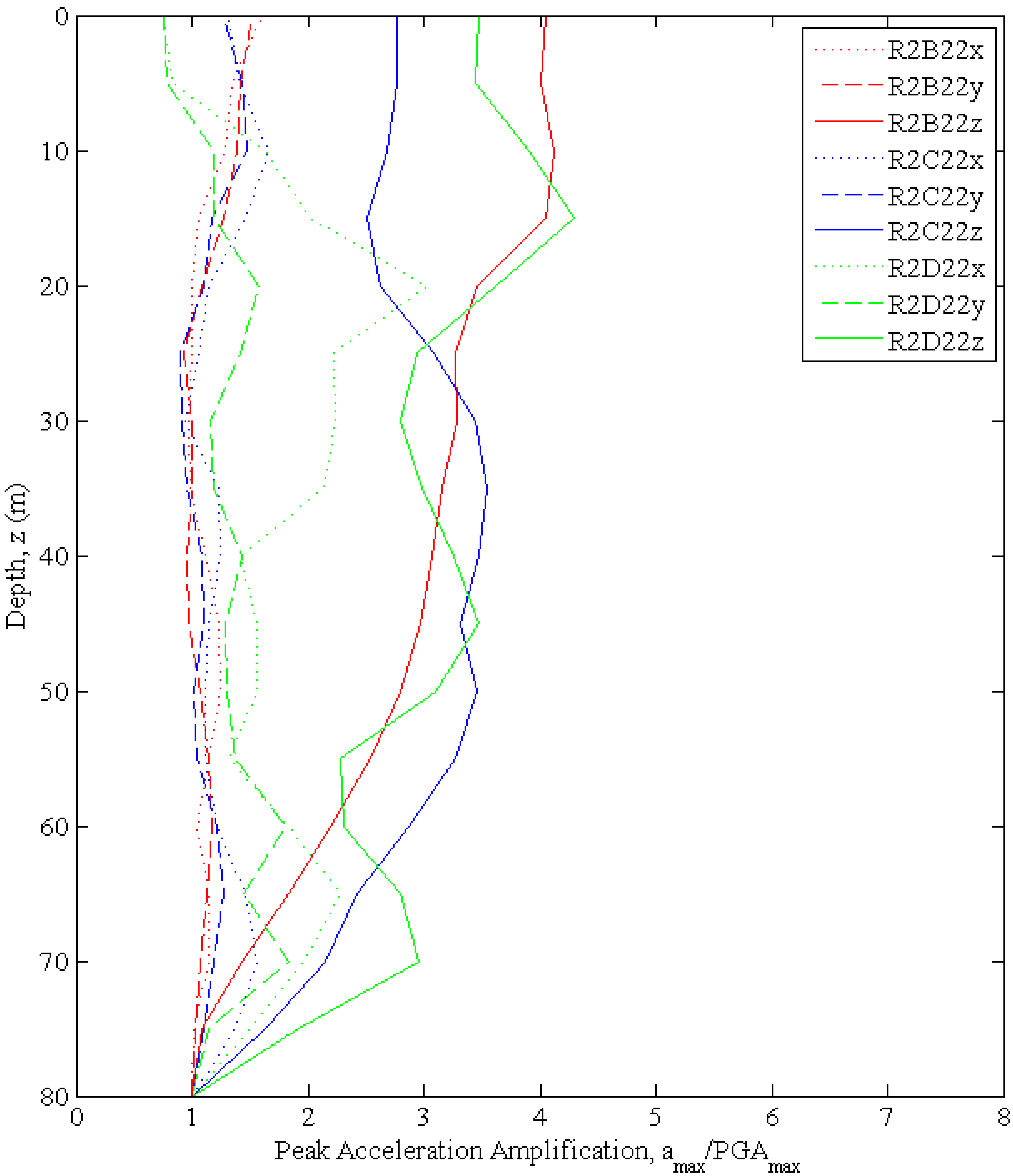

Figure C.6: Peak soil column acceleration data from the simulations with the rectangular superstructure and FP bearings subjected to ground motion 22

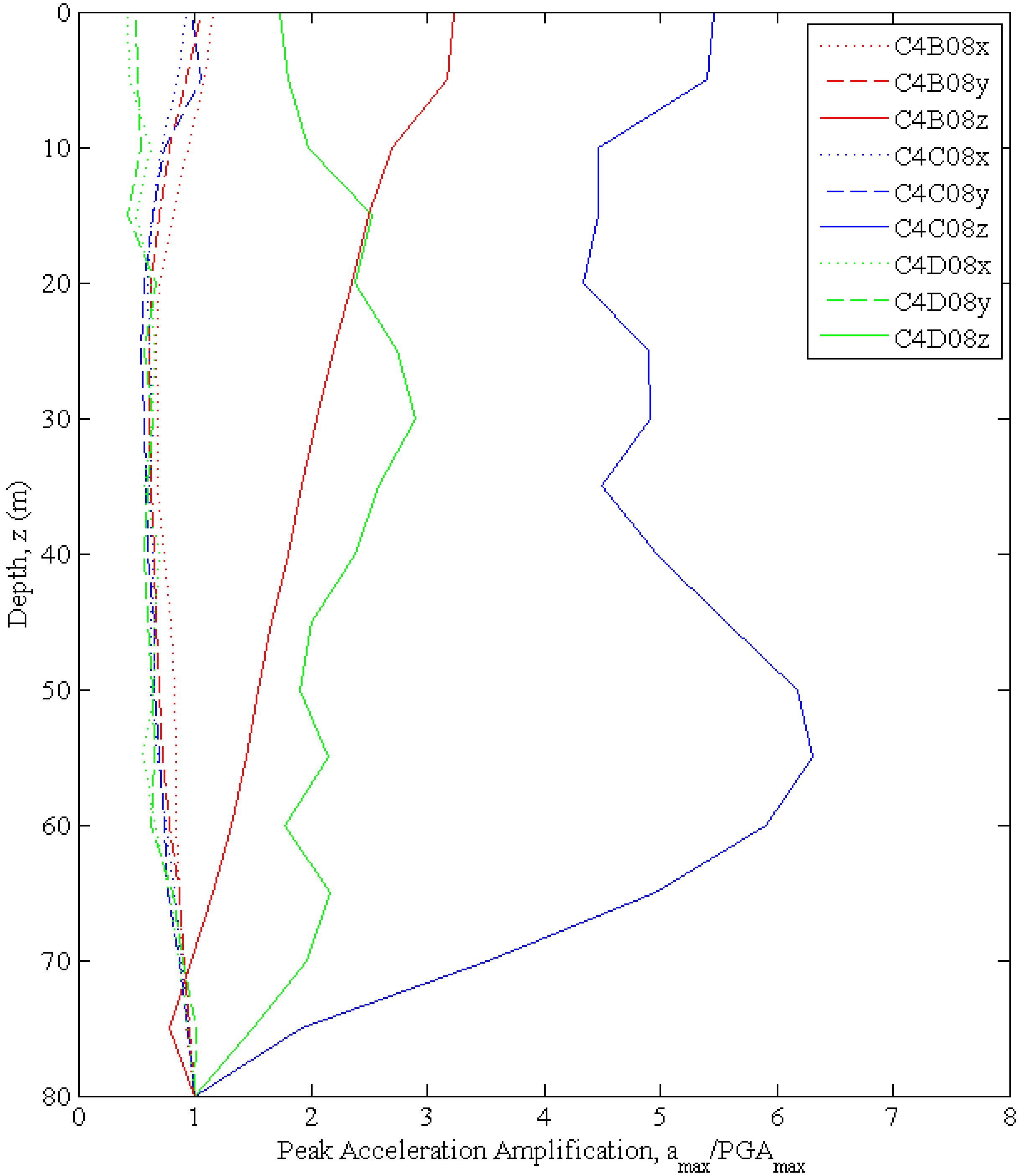

Figure C.7: Peak soil column acceleration data from the simulations with the cylindrical superstructure and simplified LR bearings subjected to ground motion 08

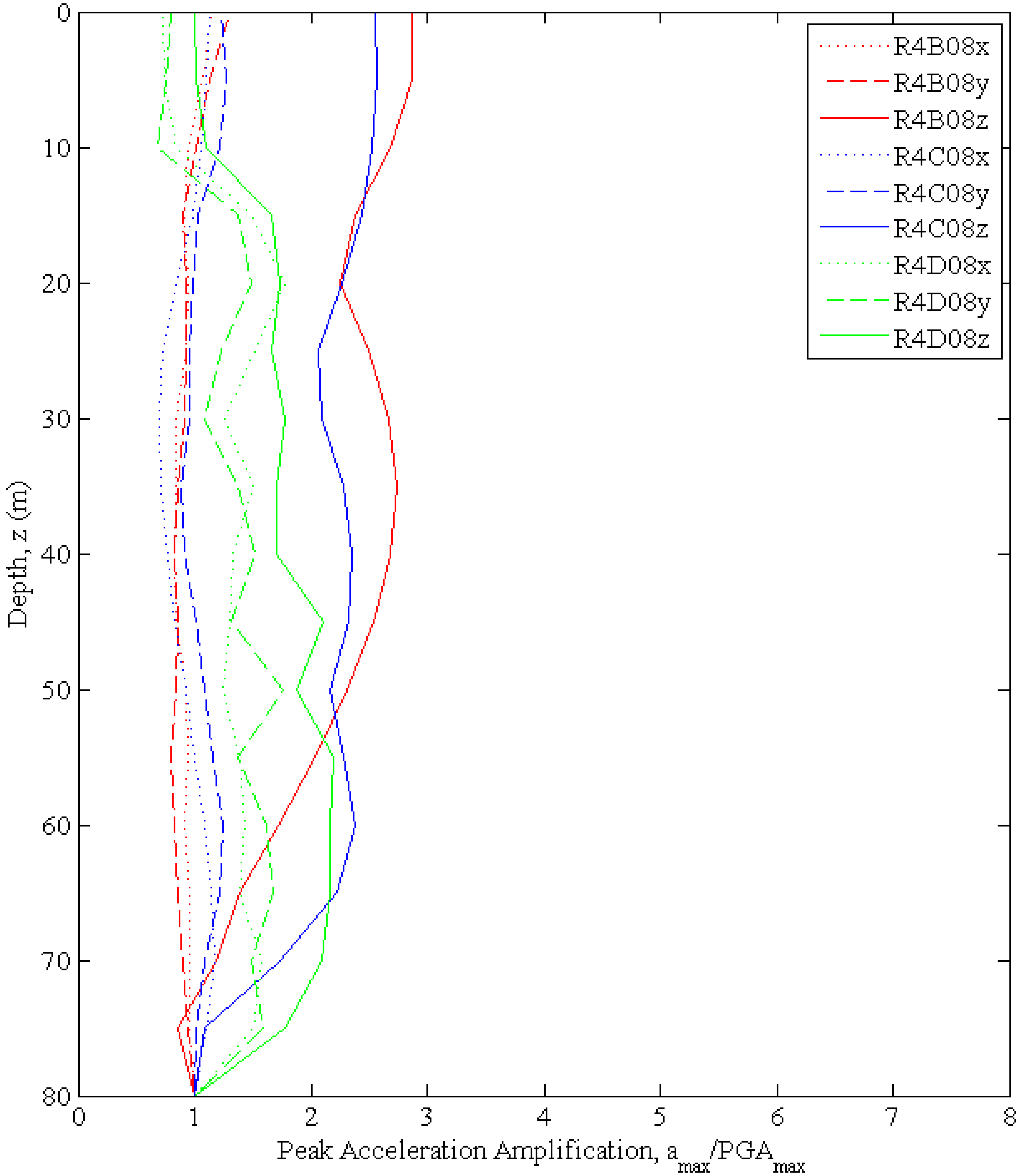

Figure C.8: Peak soil column acceleration data from the simulations with the rectangular superstructure and simplified LR bearings subjected to ground motion 08

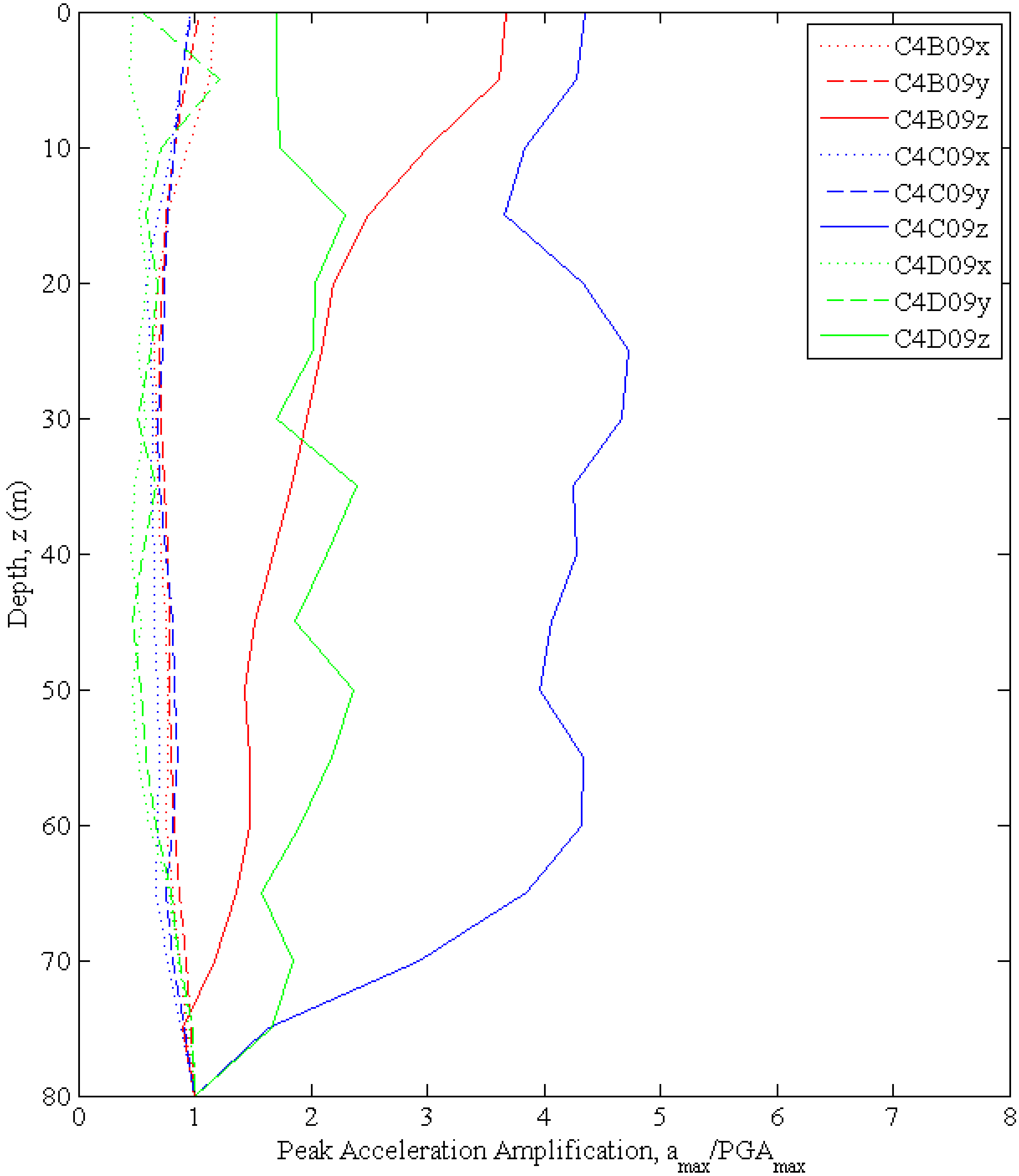

Figure C.9: Peak soil column acceleration data from the simulations with the cylindrical superstructure and simplified LR bearings subjected to ground motion 09

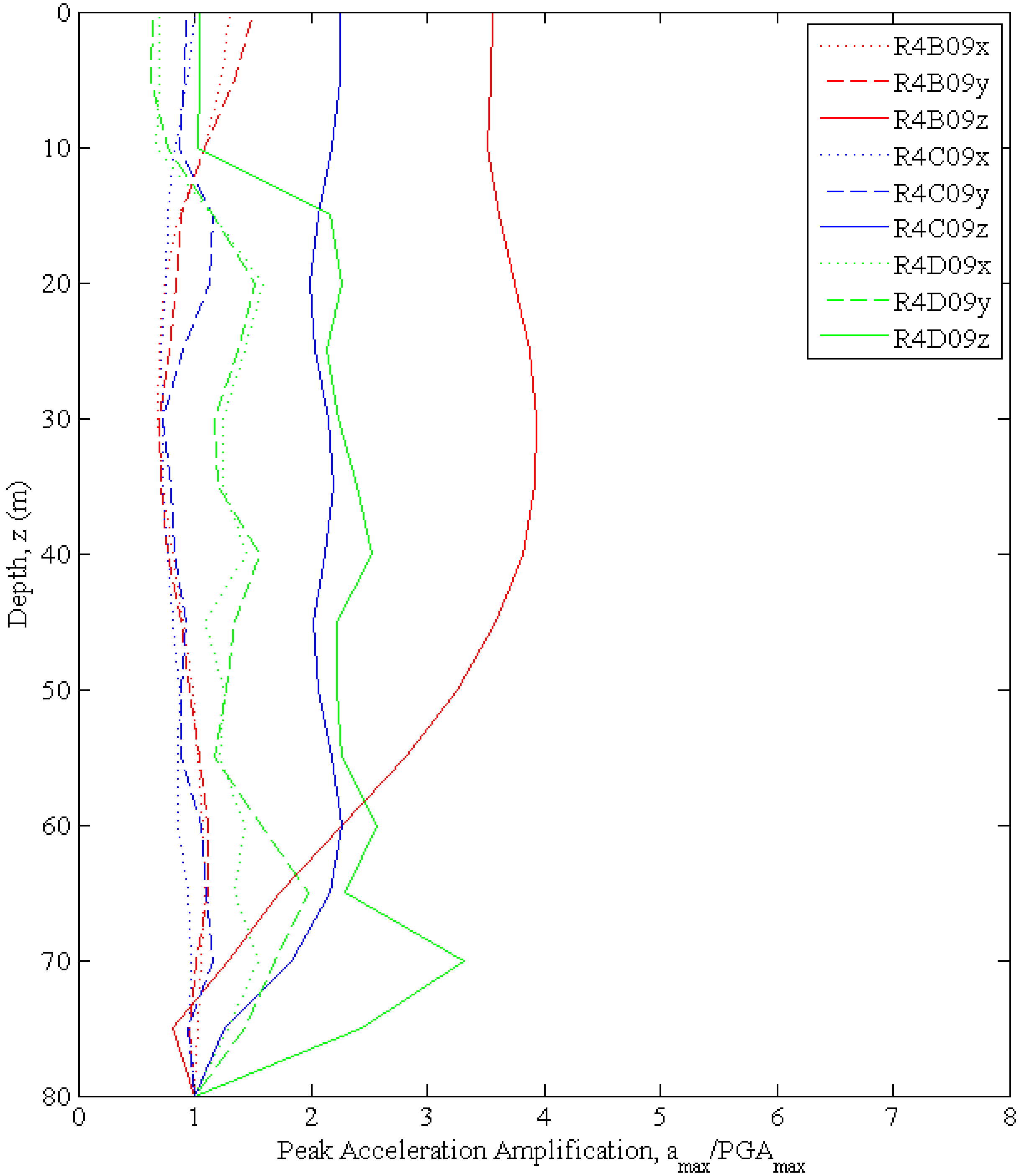

Figure C.10: Peak soil column acceleration data from the simulations with the rectangular superstructure and simplified LR bearings subjected to ground motion 09

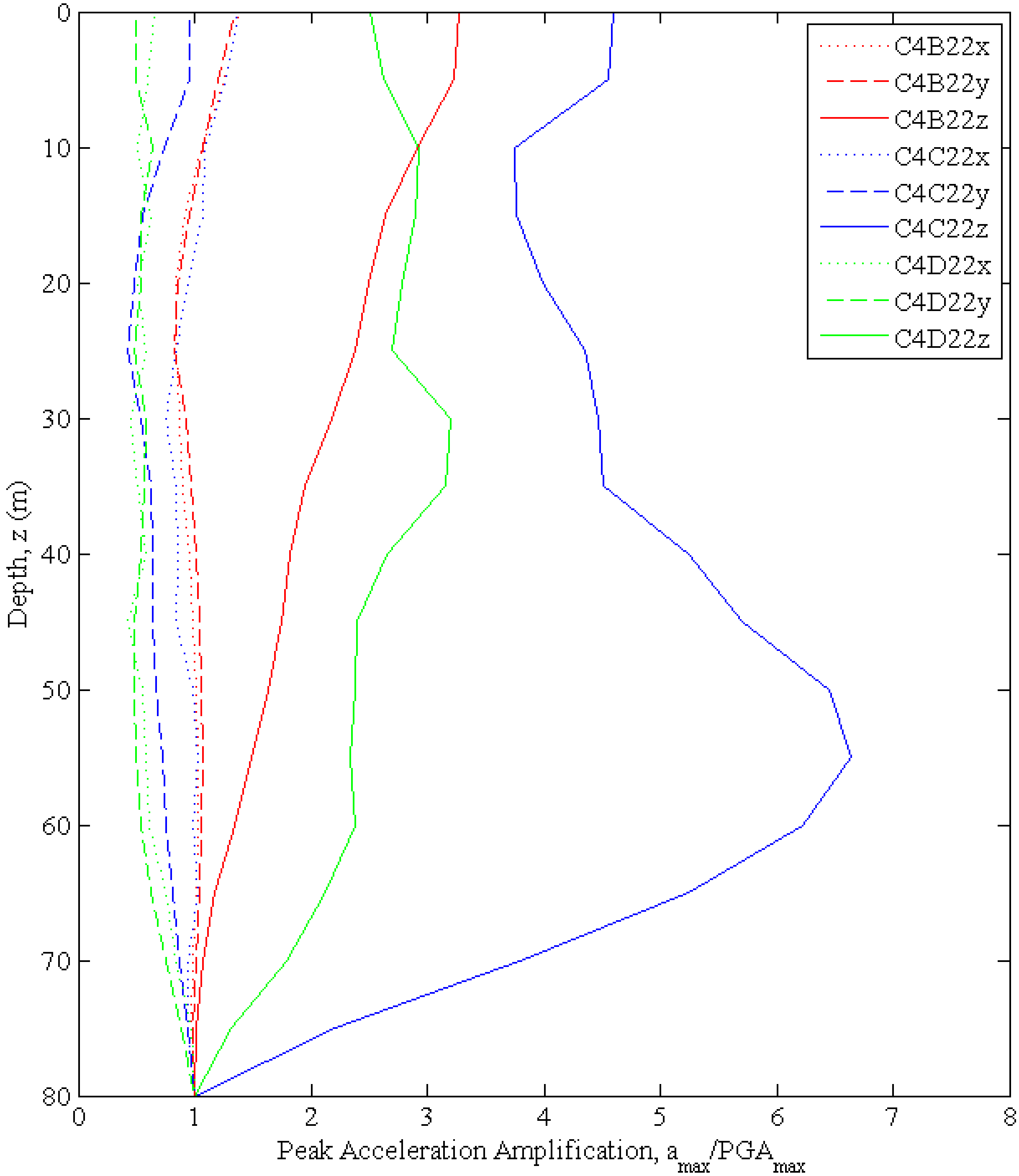

Figure C.11: Peak soil column acceleration data from the simulations with the cylindrical superstructure and simplified LR bearings subjected to ground motion 22

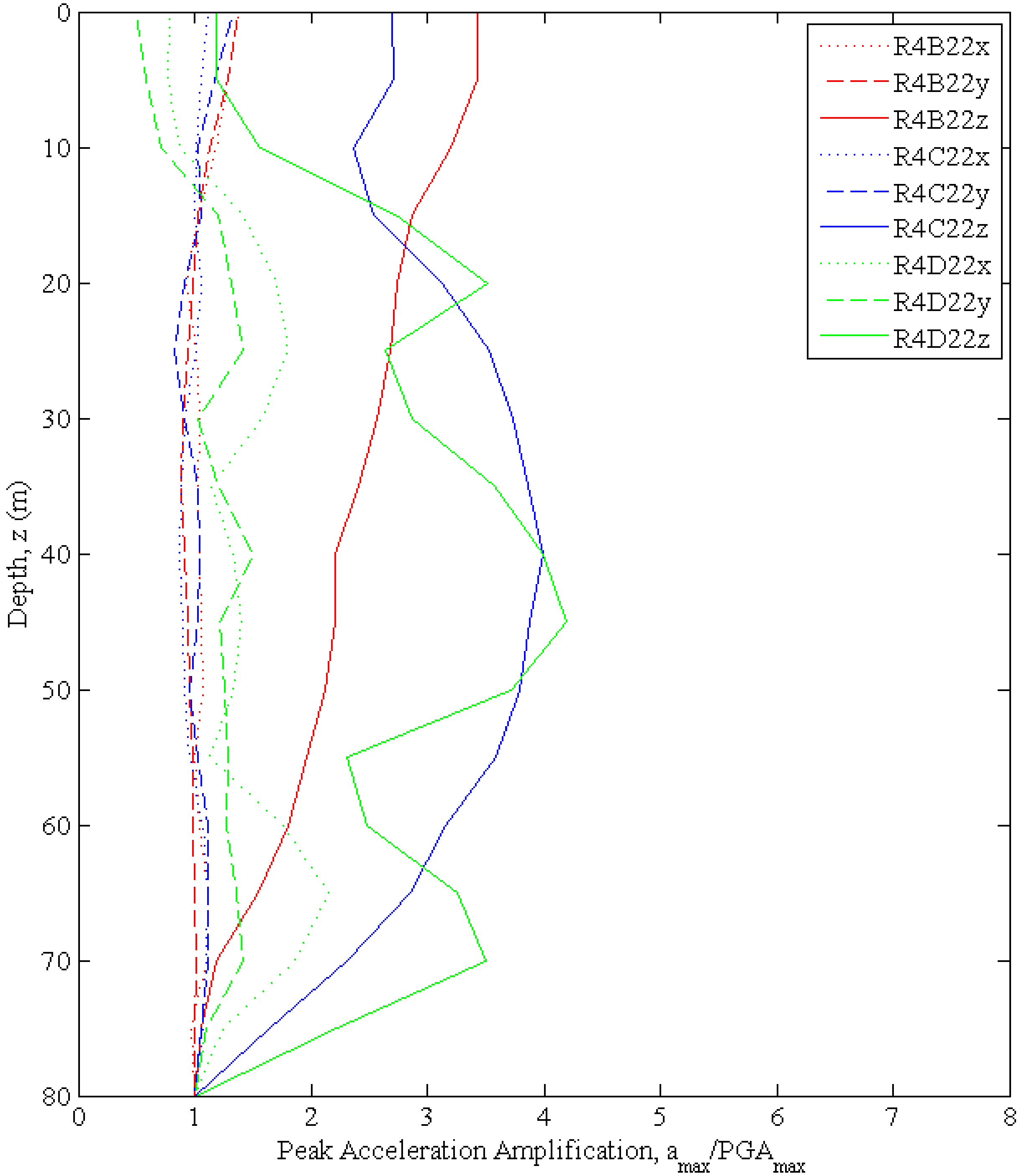

Figure C.12: Peak soil column acceleration data from the simulations with the rectangular superstructure and simplified LR bearings subjected to ground motion 22

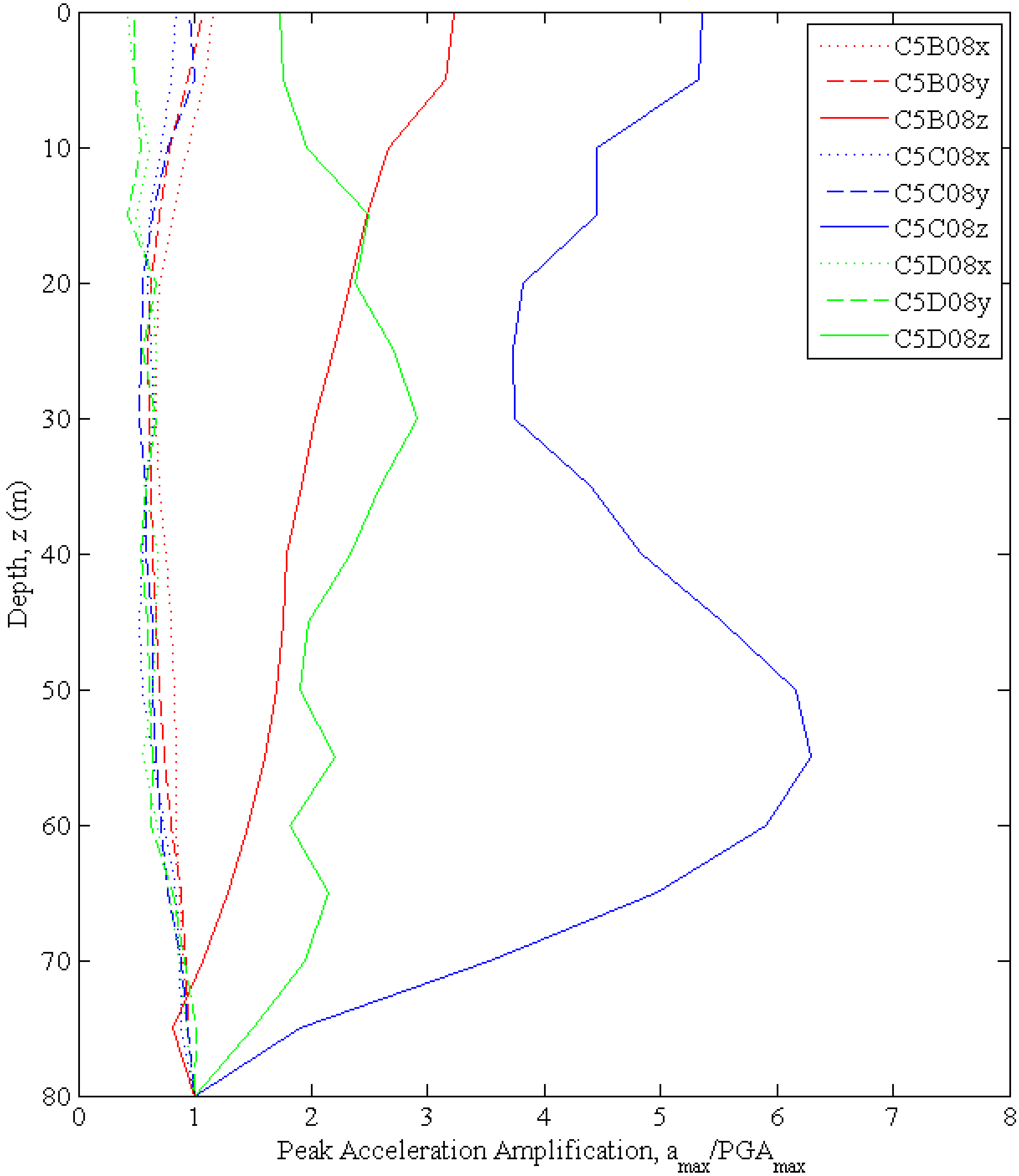

Figure C.13: Peak soil column acceleration data from the simulations with the cylindrical superstructure and robust LR bearings subjected to ground motion 08

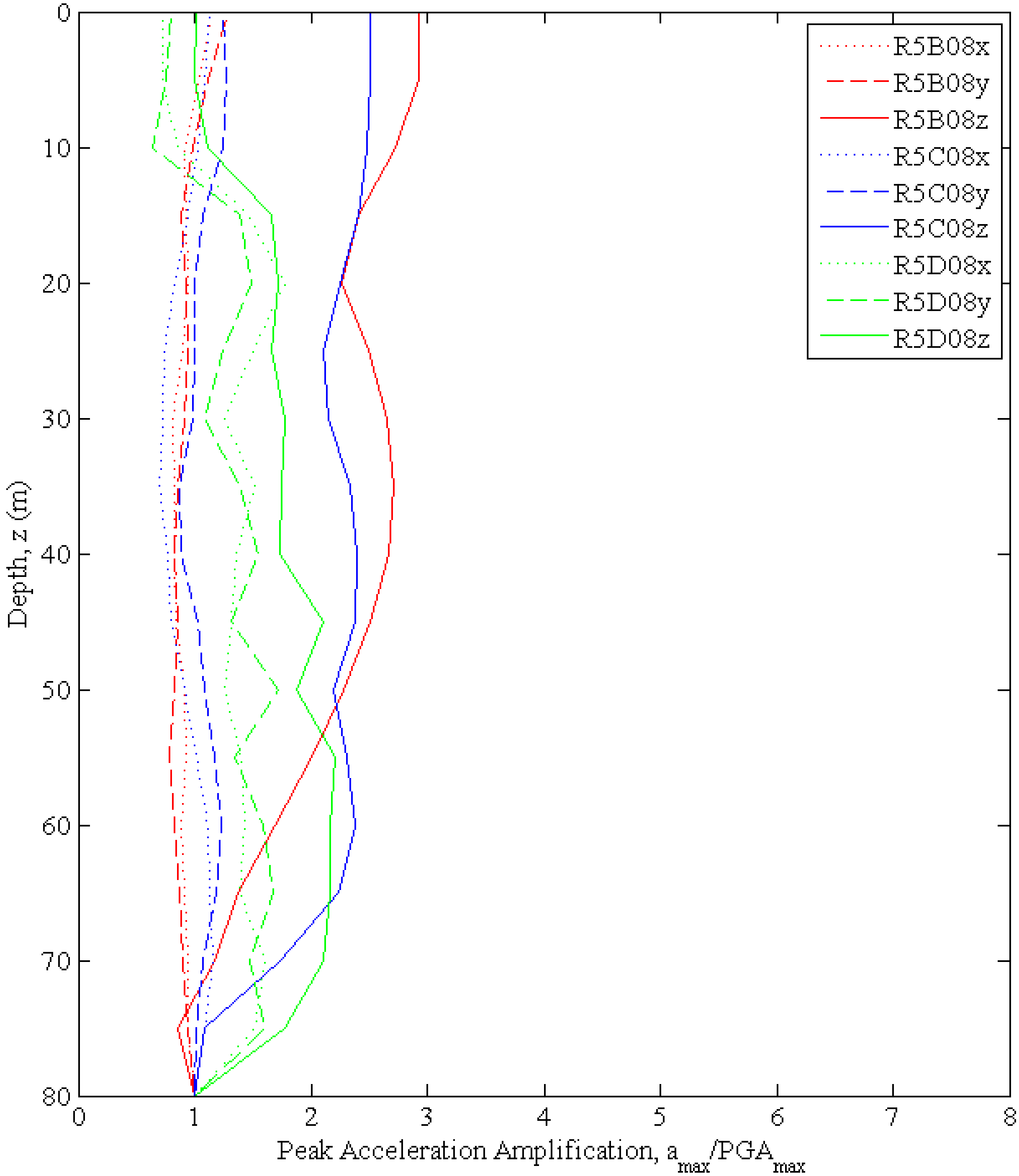

Figure C.14: Peak soil column acceleration data from the simulations with the rectangular superstructure and robust LR bearings subjected to ground motion 08

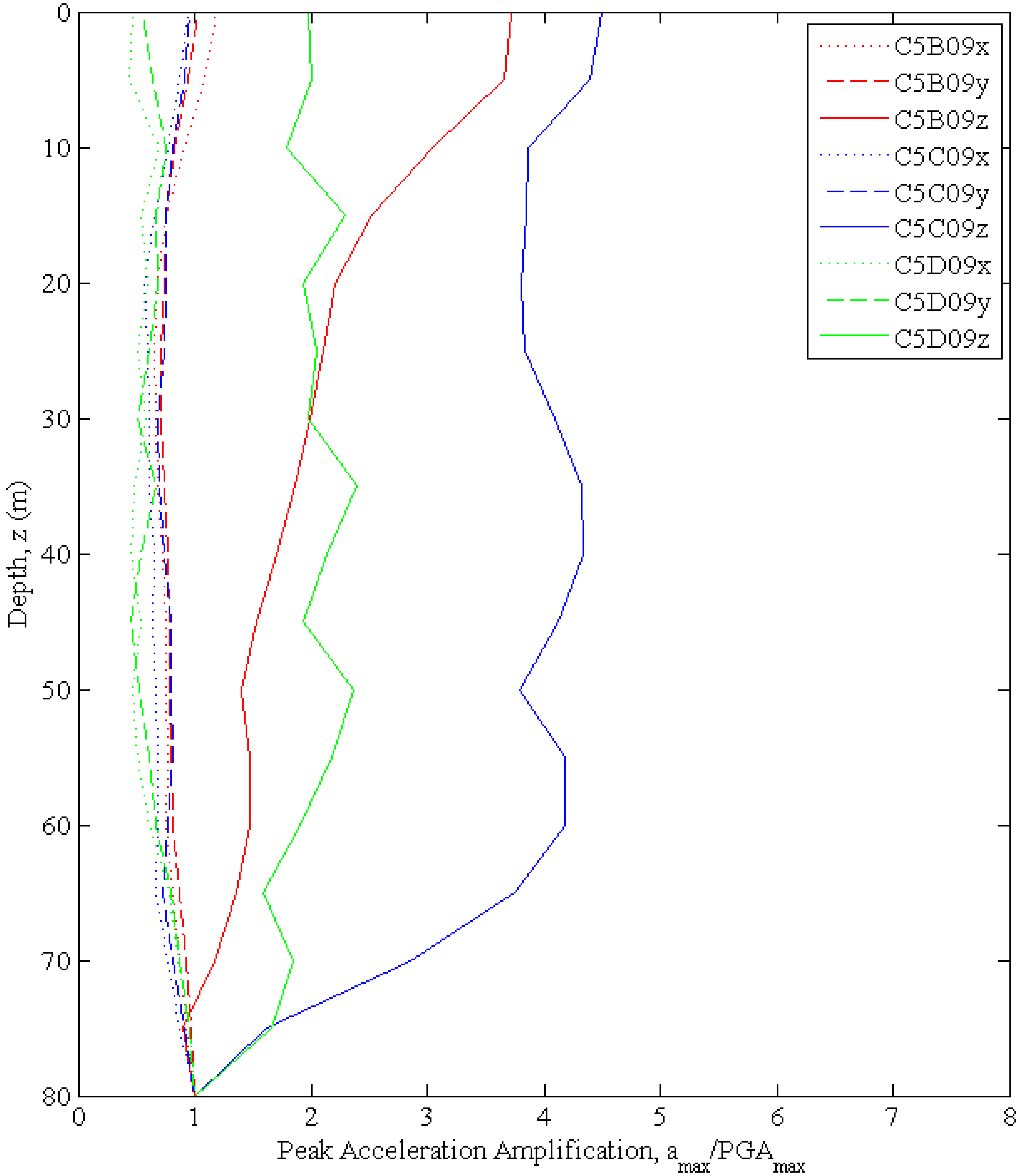

Figure C.15: Peak soil column acceleration data from the simulations with the cylindrical superstructure and robust LR bearings subjected to ground motion 09

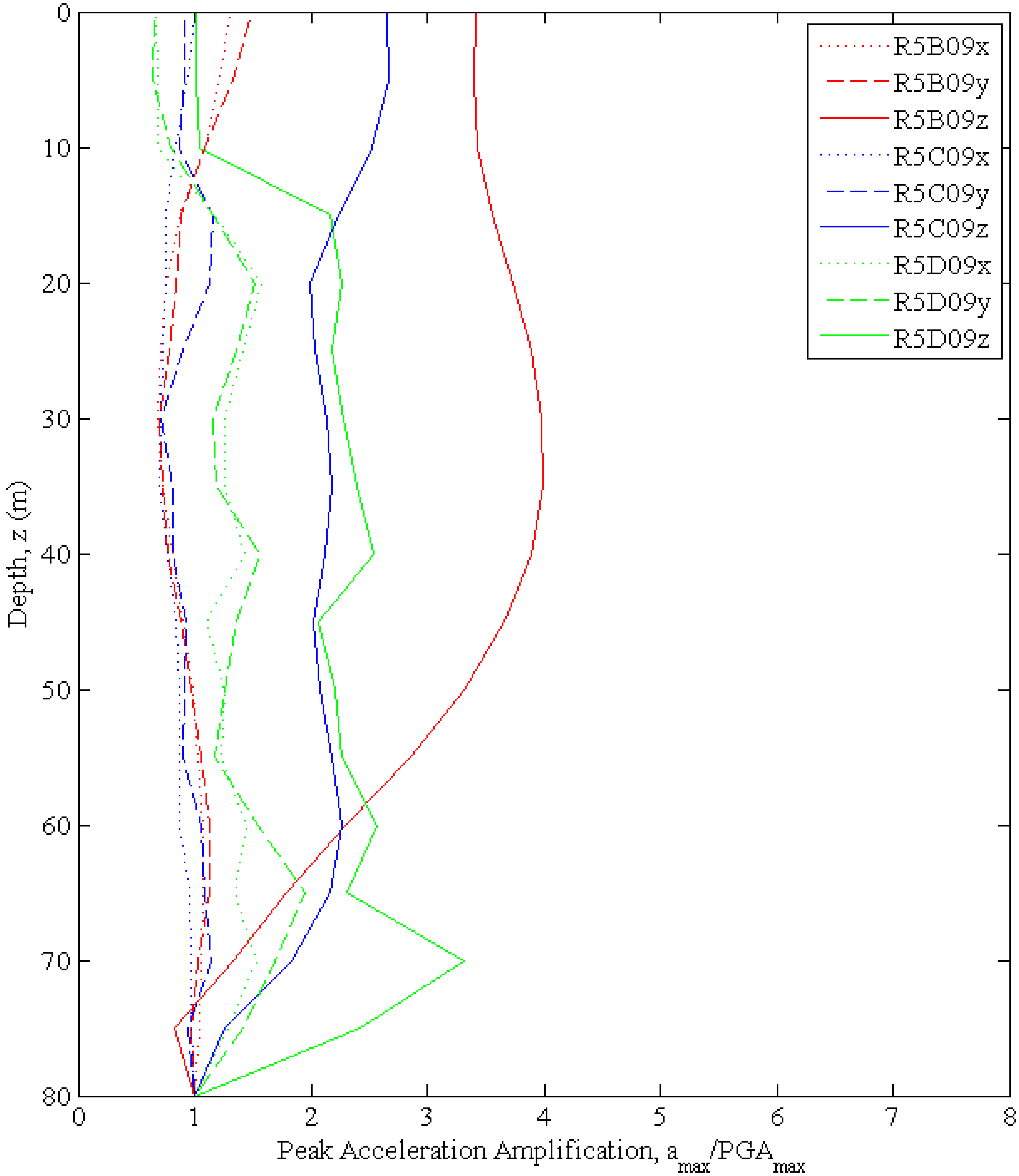

Figure C.16: Peak soil column acceleration data from the simulations with the rectangular superstructure and robust LR bearings subjected to ground motion 09

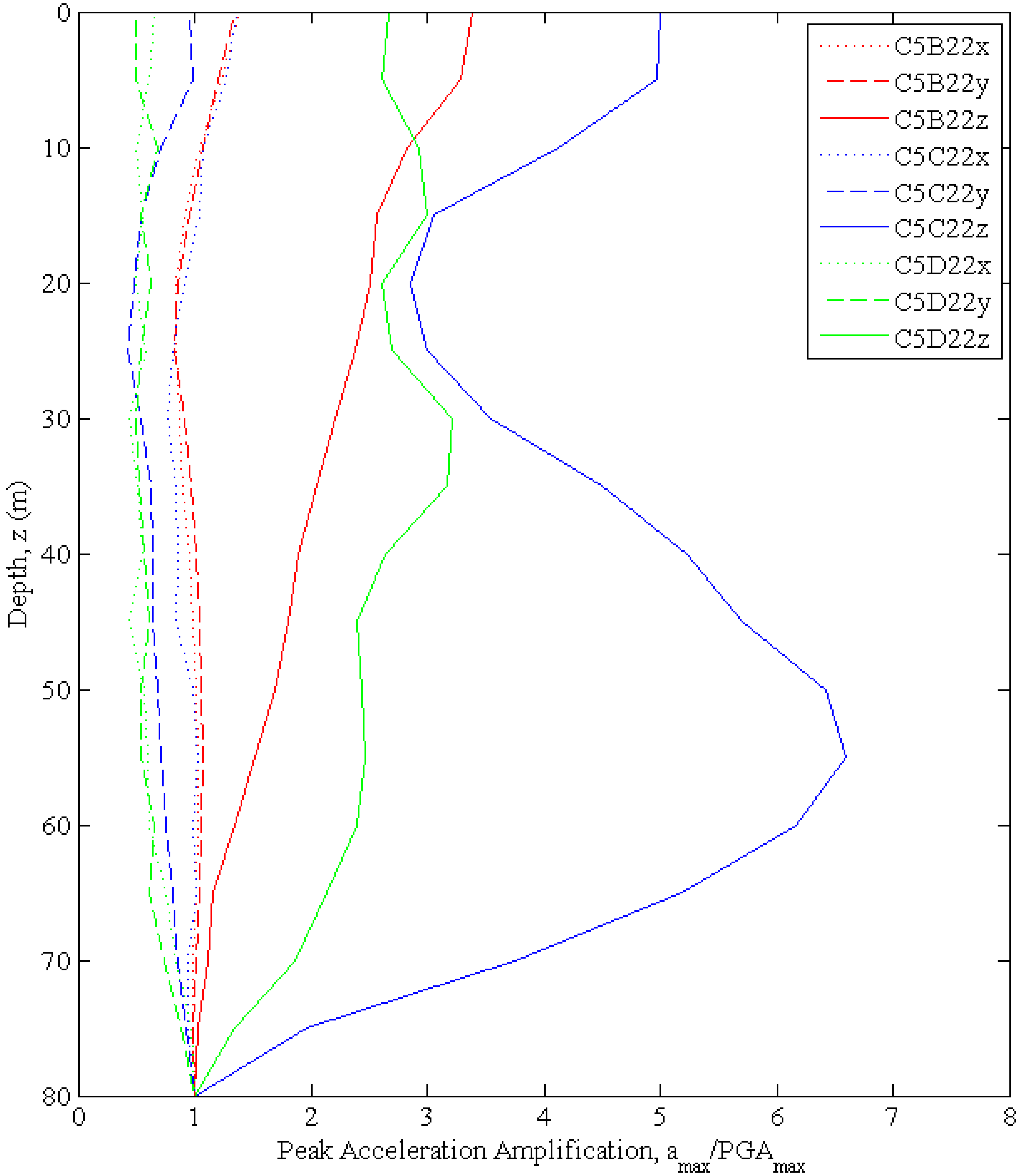

Figure C.17: Peak soil column acceleration data from the simulations with the cylindrical superstructure and robust LR bearings subjected to ground motion 22

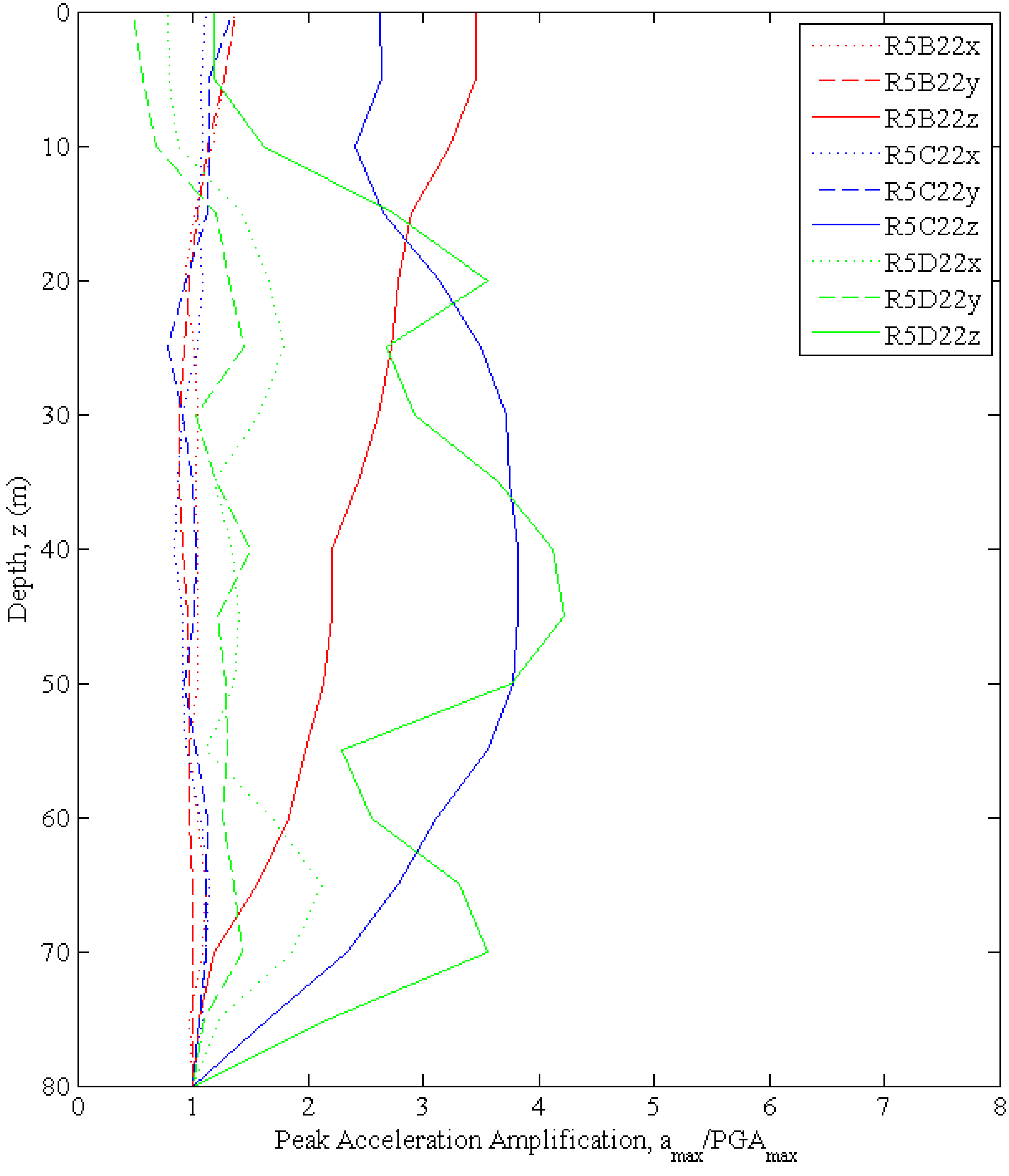

Figure C.18: Peak soil column acceleration data from the simulations with the rectangular superstructure and robust LR bearings subjected to ground motion 22

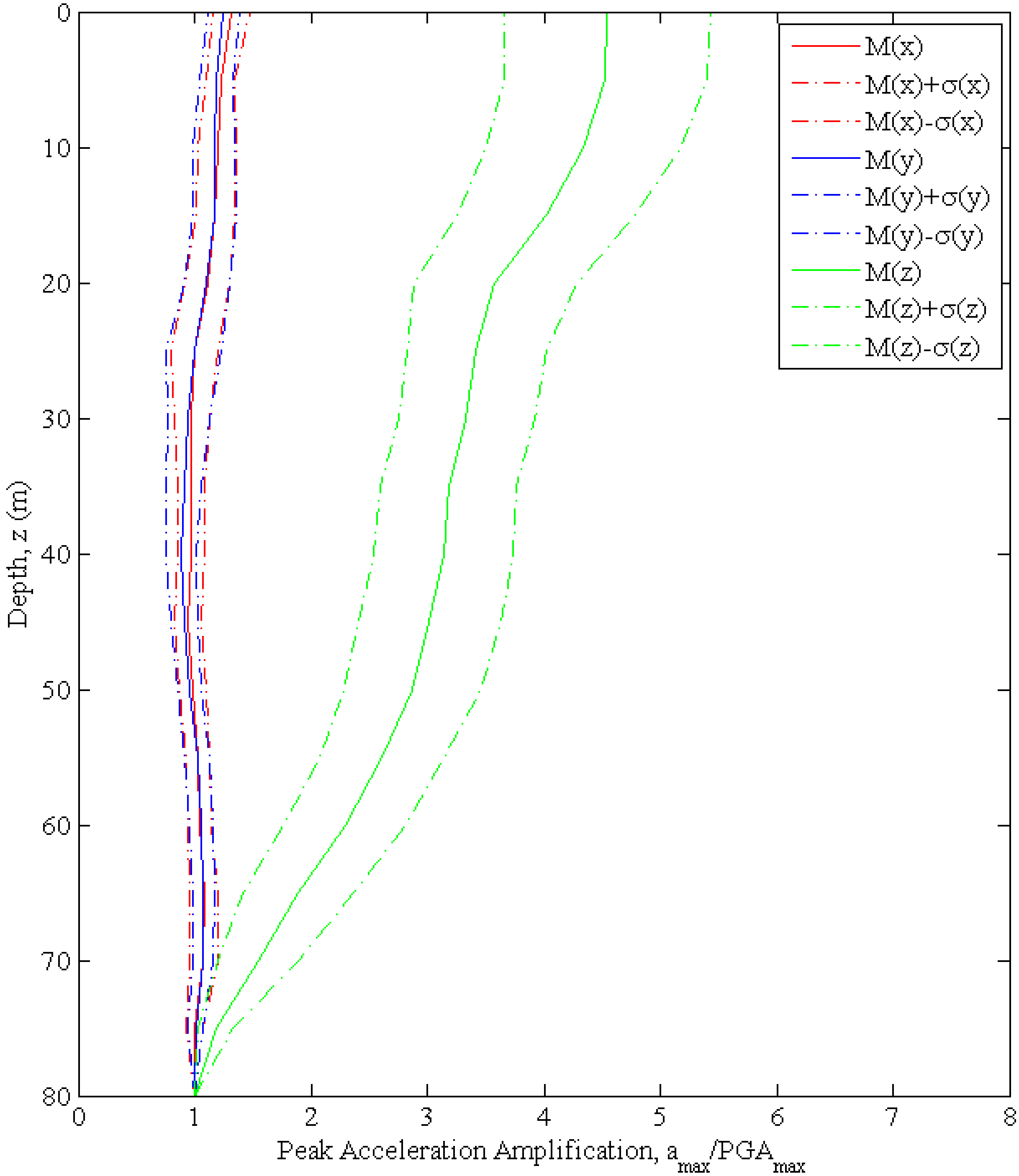

Figure C.19: Median and standard deviation soil data from the simulations with the rectangular superstructure and FP bearings subjected to all ground motions

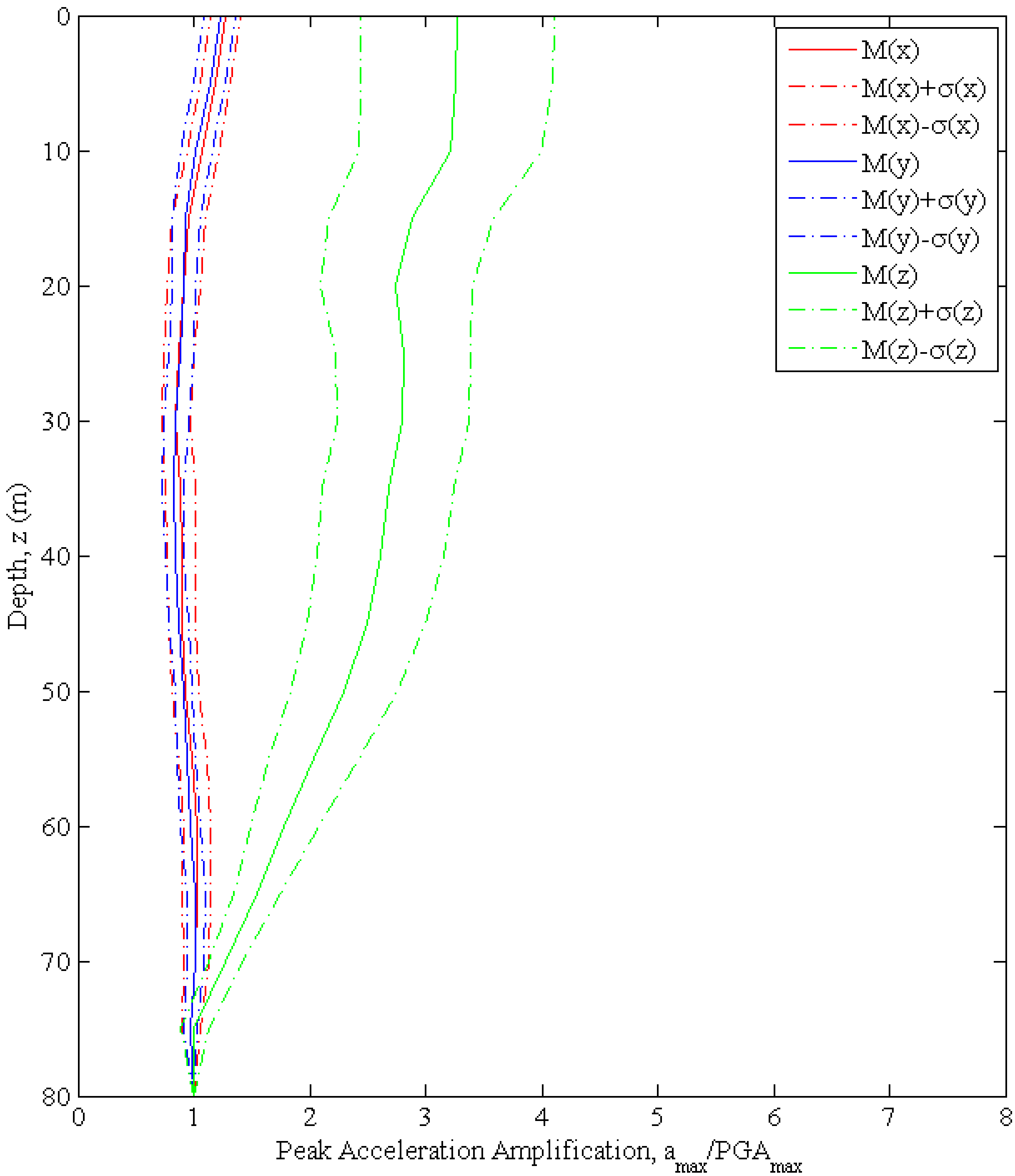

Figure C.20: Median and standard deviation soil data from the simulations with the rectangular superstructure and simplified LR bearings subjected to all ground motions

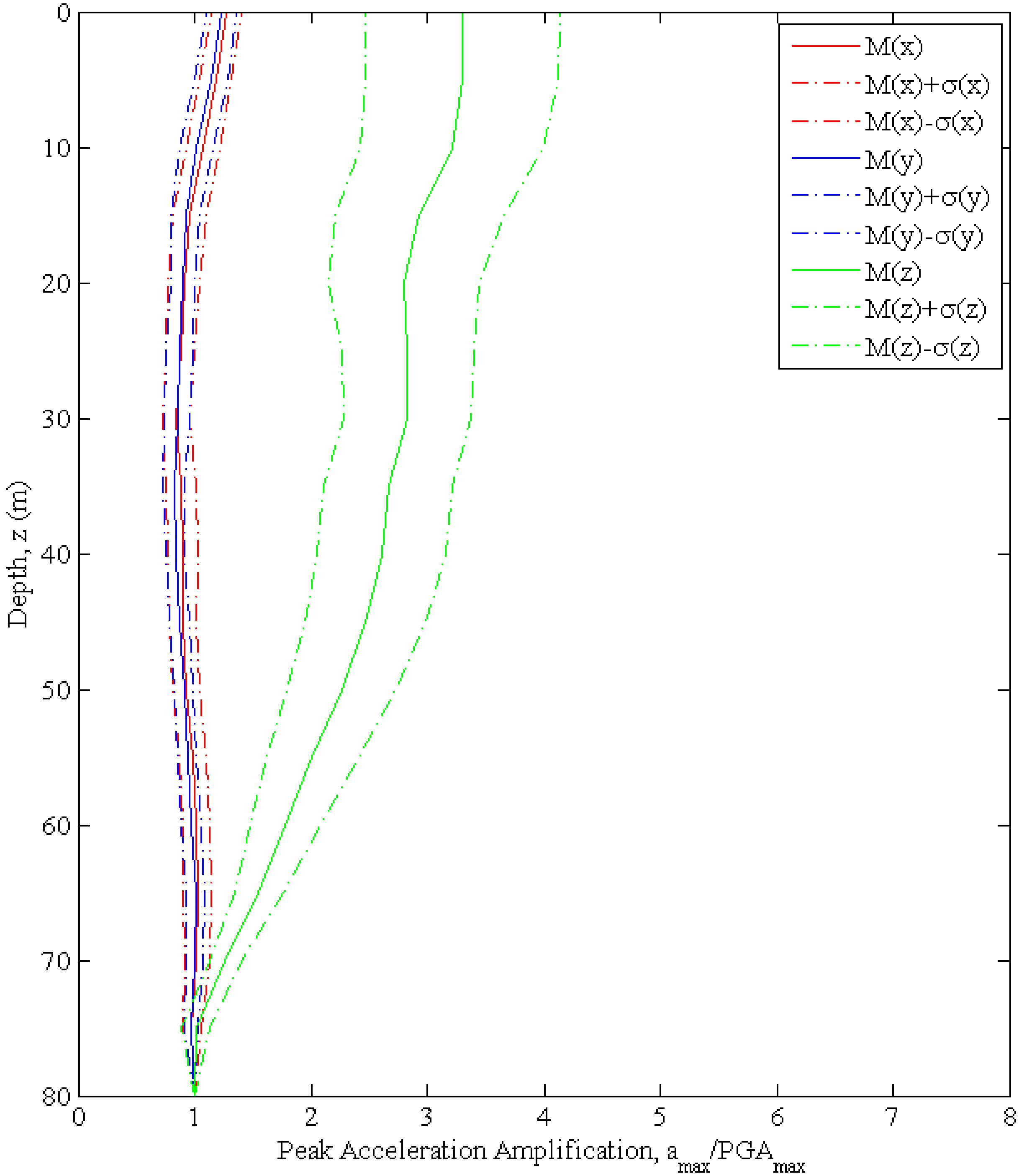

Figure C.21: Median and standard deviation soil data from the simulations with the rectangular superstructure and robust LR bearings subjected to all ground motions

Appendix D

Isolator Data

This appendix inventories isolator deformation data measured at four outer bearings for each superstructure. Tables D.1 through D.5 list the peak deformation response parameters over the four bearings for the many analysis cases. The specific response paramters of interest include the peak vertical compression deformation, dz^c_{max}, the peak vertical tension deformation or uplift, dz^t_{max}, and the peak lateral deformation, $\Delta_{max} = [\sqrt{dx^2 + dy^2}]_{max}$. For reference, the static compression deformation for the outer sliding and elastomeric bearings was found to be 0.031 cm and 0.37 cm respectively. Δ_{max} is compared to the lateral displacement limit, Δ_{lim}, which is the displacement causing contact with the restraint for friction brearings (1.23 m), or 400% shear strain in elastomeric bearings (1.24 m). This metric is used to determine if the chosen bearing designs "fail" for a given ground motion. Figures D.1 through D.6 show bar graphs presenting this peak data for the comparative tests subjected to the basic ground motions. Figures D.7 through D.9 show the peak values for all 30 motions as well as the median, M, and standard deviation, σ, of the data sets.

Case	dz^c_{max} (cm)	dz^t_{max} (cm)	Δ_{max} (cm)	$\Delta_{max}/\Delta_{lim}$	Failure?
C2N08	0.071	0.35	24.4	20%	No
C2N09	0.071	0.52	97.5	80%	No
C2N22	0.071	0.32	47.8	39%	No
C4N08	0.92	0.44	28.6	23%	No
C4N09	0.83	0.36	99.8	80%	No
C4N22	0.89	0.42	49.1	40%	No
C5N08	0.98	0.47	26.4	21%	No
C5N09	1.17	0.36	95.6	77%	No
C5N22	1.07	0.49	46.8	38%	No
R2N08	0.13	0.59	24.4	20%	No
R2N09	0.13	0.63	99.1	81%	No
R2N22	0.14	0.52	48.5	40%	No
R4N08	1.82	0.88	28.1	23%	No
R4N09	1.63	0.69	95.5	77%	No
R4N22	1.62	0.77	48.8	39%	No
R5N08	1.96	0.97	26.1	21%	No
R5N09	2.21	0.65	93.7	76%	No
R5N22	1.73	0.77	46.0	37%	No
C2B08	0.25	8.64	38.2	31%	No
C2B09	0.28	10.5	106.1	87%	No
C2B22	0.30	18.2	61.6	50%	No
C4B08	2.15	0.80	27.0	22%	No
C4B09	2.43	0.67	93.9	76%	No
C4B22	1.44	0.74	64.2	52%	No
C5B08	2.28	0.83	26.0	21%	No
C5B09	2.54	0.76	91.4	74%	No
C5B22	1.73	0.80	61.0	49%	No
R2B08	0.21	8.18	28.9	24%	No
R2B09	0.26	4.90	98.7	81%	No
R2B22	0.24	6.65	55.8	46%	No
R4B08	2.42	1.04	25.2	20%	No
R4B09	2.04	0.76	90.1	73%	No
R4B22	2.02	0.81	49.7	40%	No
R5B08	2.65	1.09	22.7	18%	No
R5B09	3.10	0.82	85.1	69%	No
R5B22	2.31	0.90	45.2	36%	No

Table D.1: Isolator data for the soil N and B cases in response to the basic motions

Case	dz^c_{max} (cm)	dz^t_{max} (cm)	Δ_{max} (cm)	$\Delta_{max}/\Delta_{lim}$	Failure?
C2C08	0.25	13.6	49.2	40%	No
C2C09	0.26	34.2	126.5	103%	Yes
C2C22	0.23	16.9	81.7	67%	No
C4C08	1.97	0.89	46.3	37%	No
C4C09	1.90	0.76	116.3	94%	No
C4C22	1.91	0.86	76.0	61%	No
C5C08	2.31	0.95	45.4	37%	No
C5C09	3.59	1.36	114.9	93%	No
C5C22	2.43	1.02	74.1	60%	No
R2C08	0.37	13.8	25.2	21%	No
R2C09	0.25	9.03	96.8	79%	No
R2C22	0.31	11.1	50.9	42%	No
R4C08	2.60	1.03	26.3	21%	No
R4C09	2.62	0.92	96.4	78%	No
R4C22	3.12	1.09	51.7	42%	No
R5C08	2.94	1.10	24.2	20%	No
R5C09	3.78	1.24	92.1	74%	No
R5C22	3.44	1.22	49.2	40%	No
C2D08	0.084	3.29	62.3	51%	No
C2D09	0.31	53.0	195.9	160%	Yes
C2D22	0.23	16.3	135.3	111%	Yes
C4D08	0.81	0.42	54.5	44%	No
C4D09	1.92	0.66	266.8	215%	Yes
C4D22	1.46	0.52	123.6	100%	Yes
C5D08	0.97	0.52	55.2	45%	No
C5D09	6.71	3.13	259.5	209%	Yes
C5D22	2.67	1.20	120.2	97%	No
R2D08	0.31	9.93	49.6	40%	No
R2D09	0.29	25.0	124.4	102%	Yes
R2D22	0.34	23.0	60.9	50%	No
R4D08	3.25	0.99	43.9	35%	No
R4D09	2.72	1.14	114.0	92%	No
R4D22	2.85	1.23	61.0	49%	No
R5D08	3.66	1.04	44.1	36%	No
R5D09	4.99	1.88	112.4	91%	No
R5D22	3.11	1.58	58.5	47%	No

Table D.2: Isolator data for the soil C and D cases in response to the basc motions

Case	dz^c_{max} (cm)	dz^t_{max} (cm)	Δ_{max} (cm)	$\Delta_{max}/\Delta_{lim}$	Failure?
R2B01	0.30	6.10	30.1	25%	No
R2B02	0.23	9.62	22.1	18%	No
R2B03	0.32	8.96	21.7	18%	No
R2B04	0.40	7.01	31.6	26%	No
R2B05	0.23	11.1	36.6	30%	No
R2B06	0.24	6.36	33.5	27%	No
R2B07	0.21	5.27	35.0	29%	No
R2B08	0.21	8.18	28.9	24%	No
R2B09	0.26	4.90	98.7	81%	No
R2B10	0.28	4.15	25.3	21%	No
R2B11	0.22	6.08	28.5	23%	No
R2B12	0.25	8.04	49.2	40%	No
R2B13	0.27	5.24	89.8	73%	No
R2B14	0.28	12.1	74.4	61%	No
R2B15	0.23	7.20	77.8	64%	No
R2B16	0.30	8.50	52.6	43%	No
R2B17	0.23	6.88	43.4	35%	No
R2B18	0.22	5.16	99.2	81%	No
R2B19	0.25	7.22	37.9	31%	No
R2B20	0.24	6.98	30.8	25%	No
R2B21	0.23	4.65	94.9	77%	No
R2B22	0.24	6.65	55.8	46%	No
R2B23	0.33	8.41	61.5	50%	No
R2B24	0.28	5.52	90.7	74%	No
R2B25	0.31	7.75	36.4	30%	No
R2B26	0.24	5.55	47.1	38%	No
R2B27	0.20	5.98	45.1	37%	No
R2B28	0.22	6.64	31.6	26%	No
R2B29	0.25	4.34	40.0	33%	No
R2B30	0.27	5.68	52.1	43%	No
M	0.24	6.64	41.7	34%	No
σ	0.044	1.89	24.4	20%	N/A

Table D.3: Isolator data for the soil B cases with a rectangular superstructure and isolator model 2 in response to all motions

Case	dz^c_{max} (cm)	dz^t_{max} (cm)	Δ_{max} (cm)	$\Delta_{max}/\Delta_{lim}$	Failure?
R4B01	1.99	1.09	24.6	20%	No
R4B02	1.89	1.51	18.6	15%	No
R4B03	2.33	1.12	26.2	21%	No
R4B04	3.46	1.42	32.1	26%	No
R4B05	2.02	1.14	31.9	26%	No
R4B06	2.40	0.93	34.5	28%	No
R4B07	2.00	0.97	34.4	28%	No
R4B08	2.42	1.04	25.2	20%	No
R4B09	2.04	0.76	90.1	73%	No
R4B10	2.47	0.85	28.5	23%	No
R4B11	2.26	0.87	28.6	23%	No
R4B12	1.87	0.94	42.3	34%	No
R4B13	2.37	0.91	87.2	70%	No
R4B14	2.29	0.95	65.6	53%	No
R4B15	2.62	1.19	65.4	53%	No
R4B16	2.12	1.29	43.6	35%	No
R4B17	1.97	0.81	37.8	30%	No
R4B18	2.79	1.17	61.2	49%	No
R4B19	2.39	1.20	41.4	33%	No
R4B20	2.27	1.04	25.5	21%	No
R4B21	2.41	1.06	65.4	53%	No
R4B22	2.02	0.81	49.7	40%	No
R4B23	2.38	0.92	55.7	45%	No
R4B24	2.08	0.89	85.7	69%	No
R4B25	3.19	1.01	39.0	31%	No
R4B26	2.40	1.26	41.1	33%	No
R4B27	2.18	0.99	43.4	35%	No
R4B28	2.32	1.08	30.4	25%	No
R4B29	2.03	0.80	38.7	31%	No
R4B30	2.40	1.00	46.8	38%	No
M	2.30	1.01	40.1	32%	No
σ	0.35	0.18	19.3	16%	N/A

Table D.4: Isolator data for the soil B cases with a rectangular superstructure and isolator model 4 in response to all motions

Case	dz^c_{max} (cm)	dz^t_{max} (cm)	Δ_{max} (cm)	$\Delta_{max}/\Delta_{lim}$	Failure?
R5B01	2.04	1.08	24.4	20%	No
R5B02	1.98	1.54	17.8	14%	No
R5B03	2.35	1.16	25.7	21%	No
R5B04	3.87	1.63	31.3	25%	No
R5B05	2.00	1.15	30.3	24%	No
R5B06	2.48	0.94	31.3	25%	No
R5B07	2.06	0.96	30.2	24%	No
R5B08	2.65	1.09	22.7	18%	No
R5B09	3.10	0.82	85.1	69%	No
R5B10	2.47	0.85	28.5	23%	No
R5B11	2.26	0.87	28.6	23%	No
R5B12	2.09	0.95	38.1	31%	No
R5B13	2.32	0.91	100.4	81%	No
R5B14	2.59	0.89	87.8	71%	No
R5B15	2.61	1.17	60.4	49%	No
R5B16	2.48	1.32	42.9	35%	No
R5B17	2.14	0.91	43.2	35%	No
R5B18	2.84	1.17	78.2	63%	No
R5B19	2.53	1.22	56.6	46%	No
R5B20	2.29	1.09	29.7	24%	No
R5B21	2.44	1.15	61.5	50%	No
R5B22	2.31	0.90	45.2	36%	No
R5B23	2.36	0.89	68.1	55%	No
R5B24	2.26	0.98	112.2	90%	No
R5B25	3.22	1.01	39.3	32%	No
R5B26	2.33	1.28	39.3	32%	No
R5B27	2.42	1.03	41.3	33%	No
R5B28	2.30	1.12	30.6	25%	No
R5B29	2.19	0.87	37.8	30%	No
R5B30	2.71	1.04	42.9	35%	No
M	2.35	1.03	39.3	32%	No
σ	0.40	0.19	24.4	20%	N/A

Table D.5: Isolator data for the soil B cases with a rectangular superstructure and isolator model 5 in response to all motions

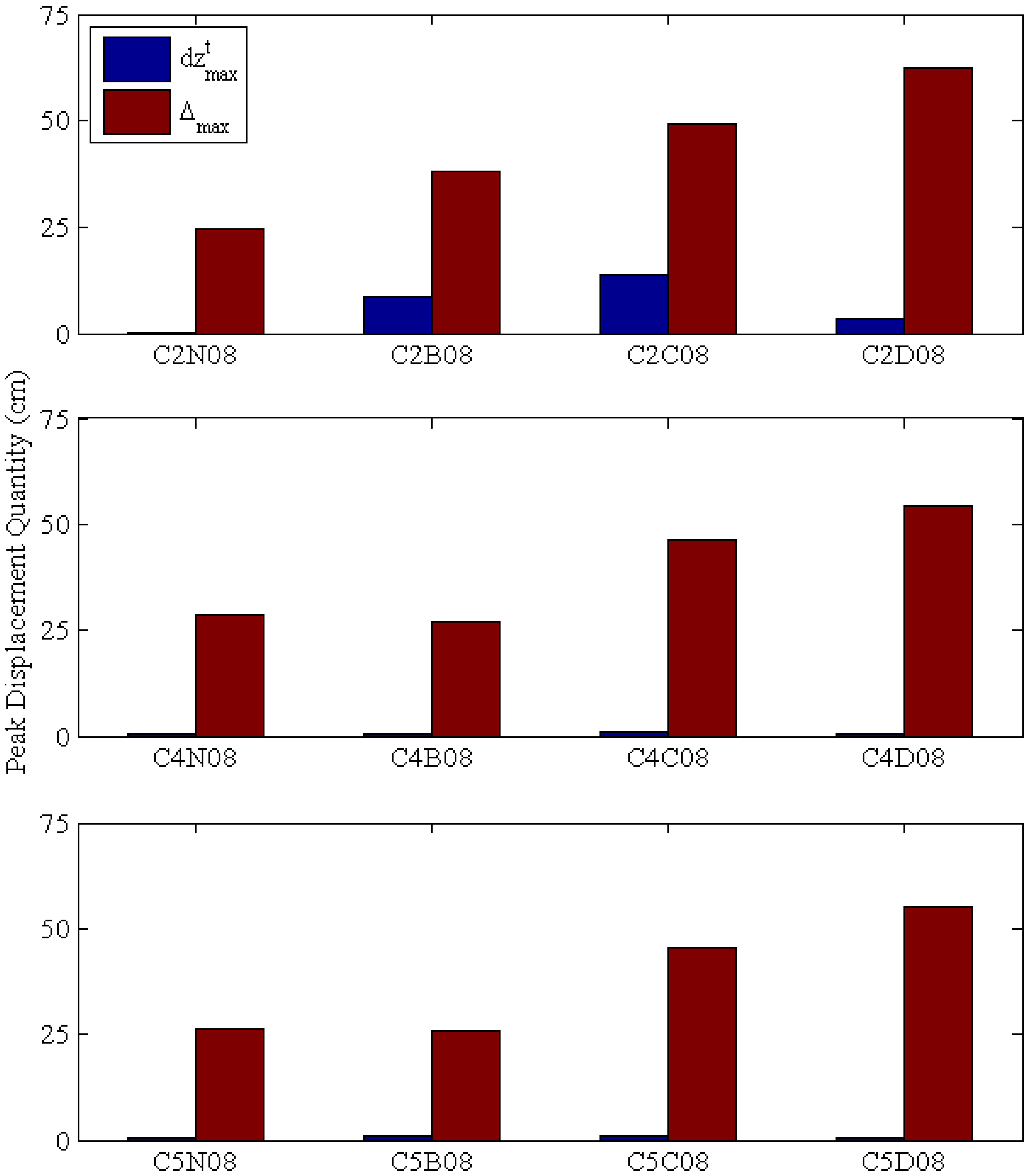

Figure D.1: Peak isolator data from the simulations with the cylindrical superstructure subjected to ground motion 08

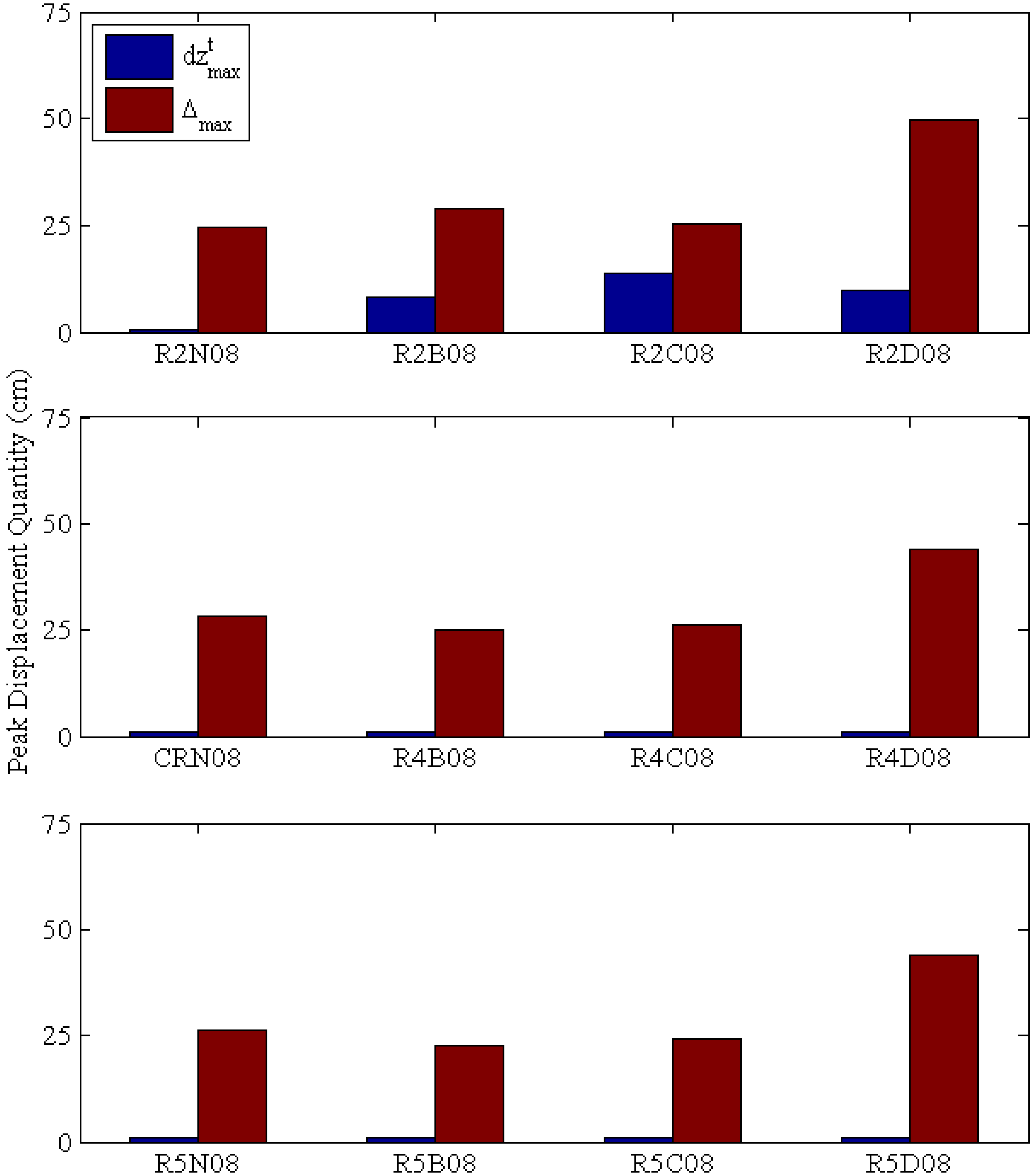

Figure D.2: Peak isolator data from the simulations with the rectangular superstructure subjected to ground motion 08

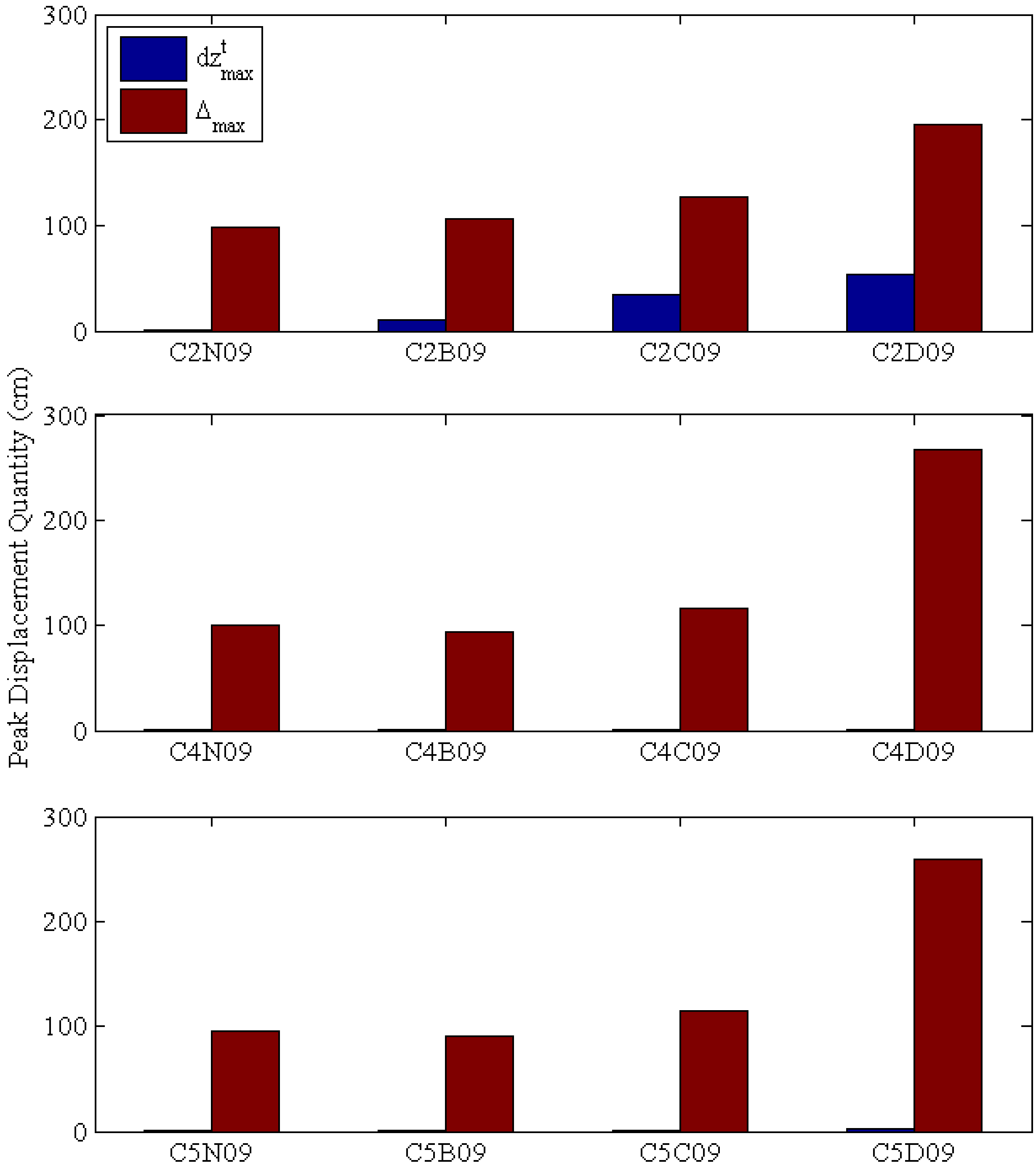

Figure D.3: Peak isolator data from the simulations with the cylindrical superstructure subjected to ground motion 09

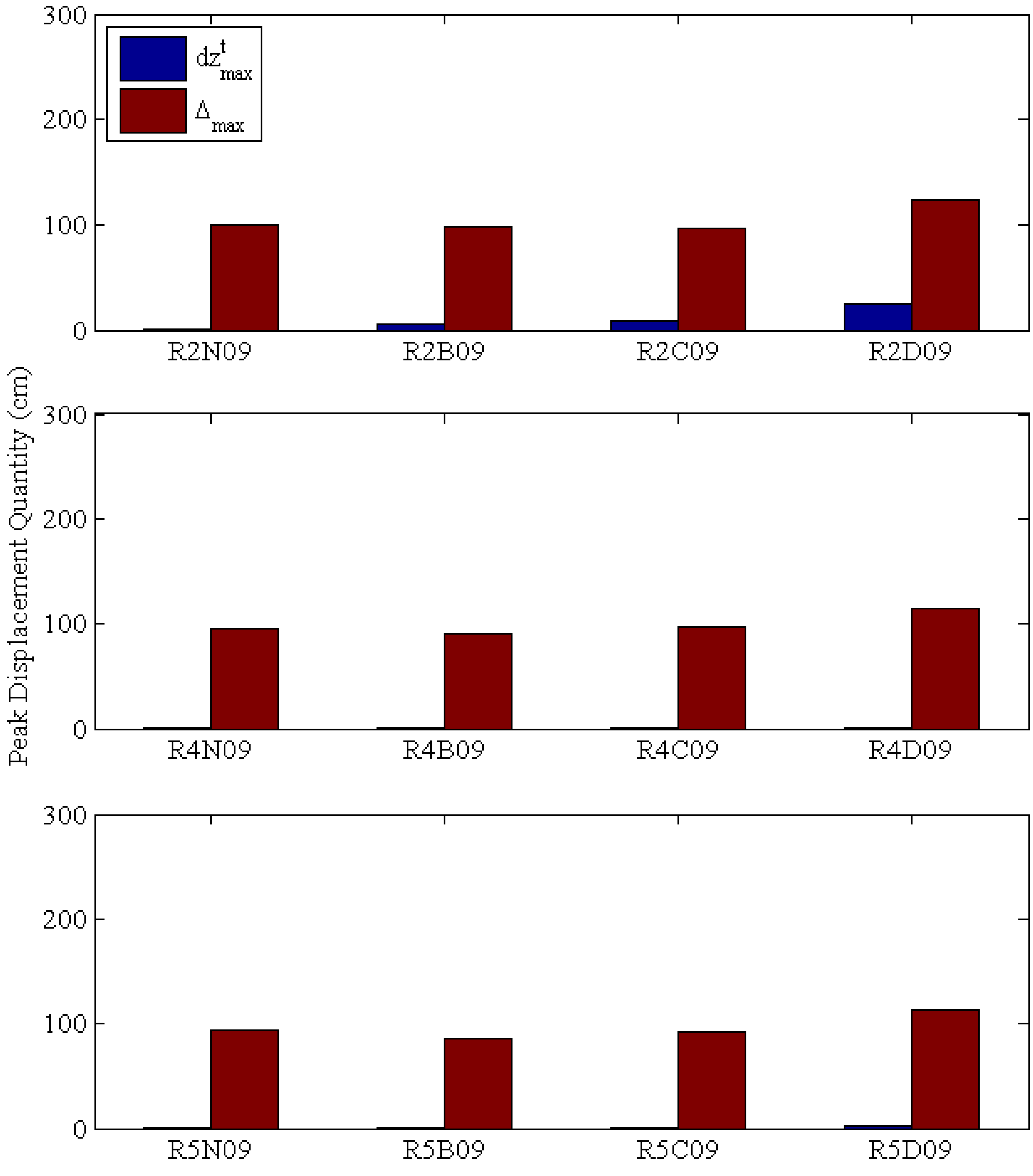

Figure D.4: Peak isolator data from the simulations with the rectangular superstructure subjected to ground motion 09

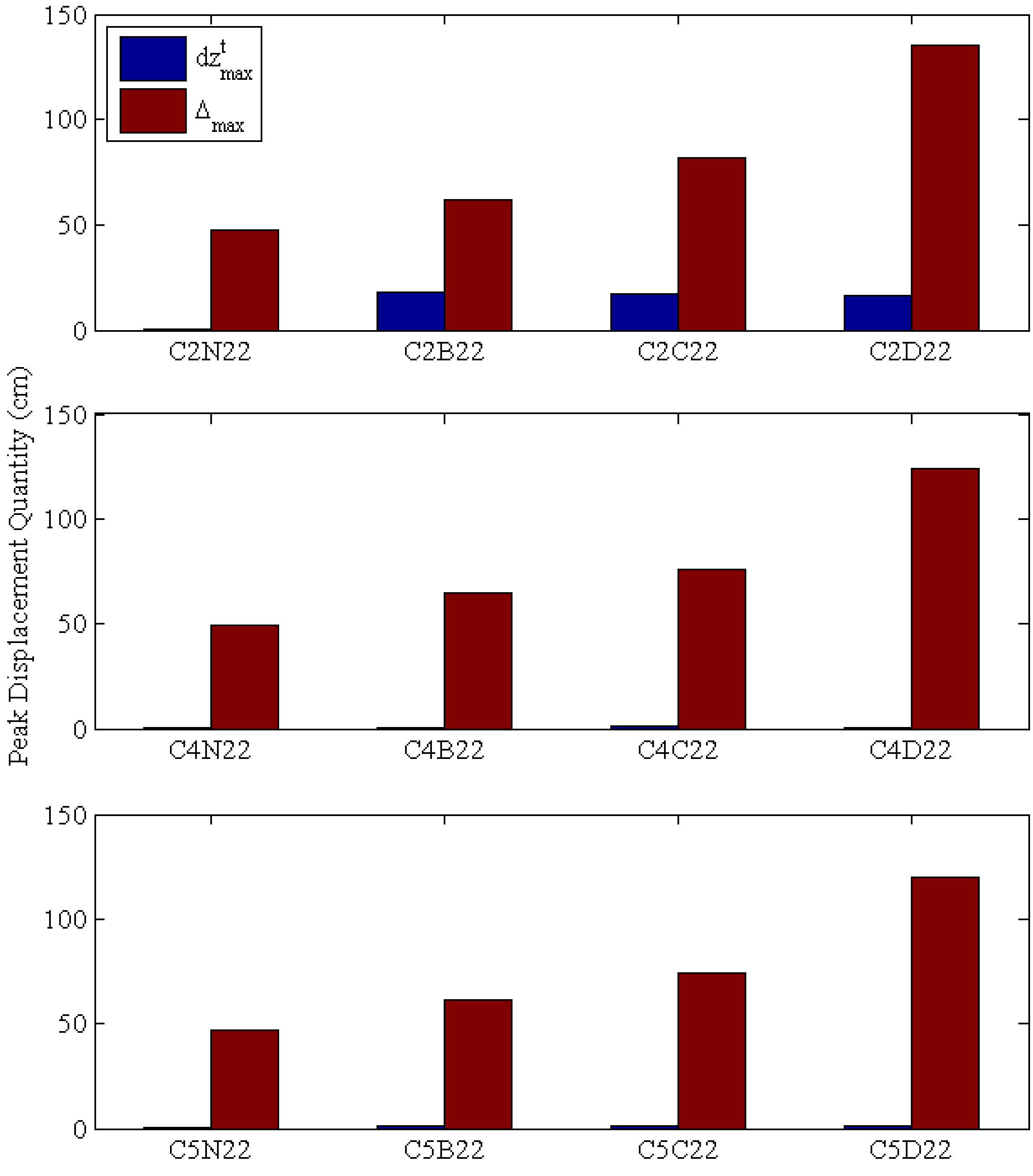

Figure D.5: Peak isolator data from the simulations with the cylindrical superstructure subjected to ground motion 22

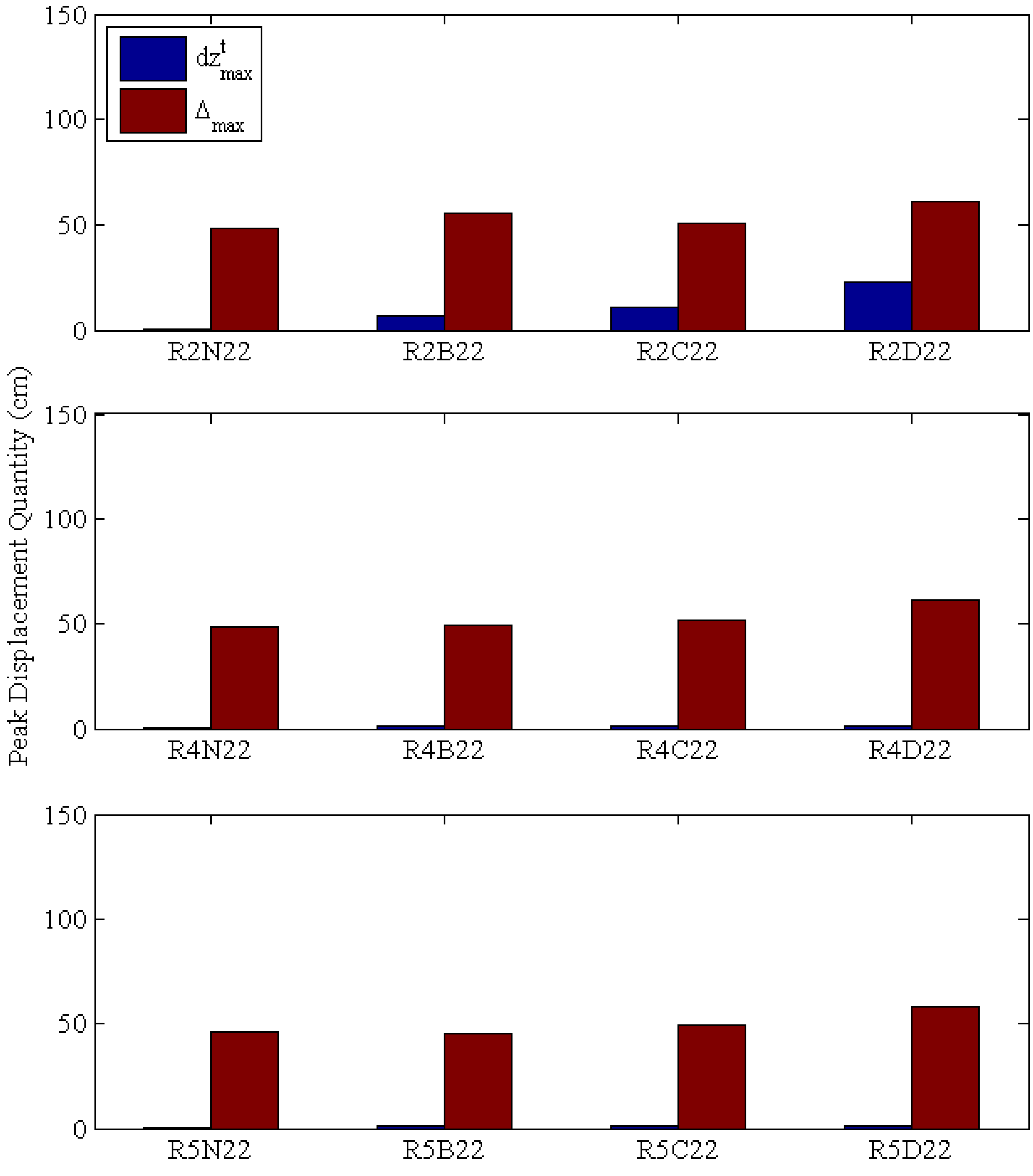

Figure D.6: Peak isolator data from the simulations with the rectangular superstructure subjected to ground motion 22

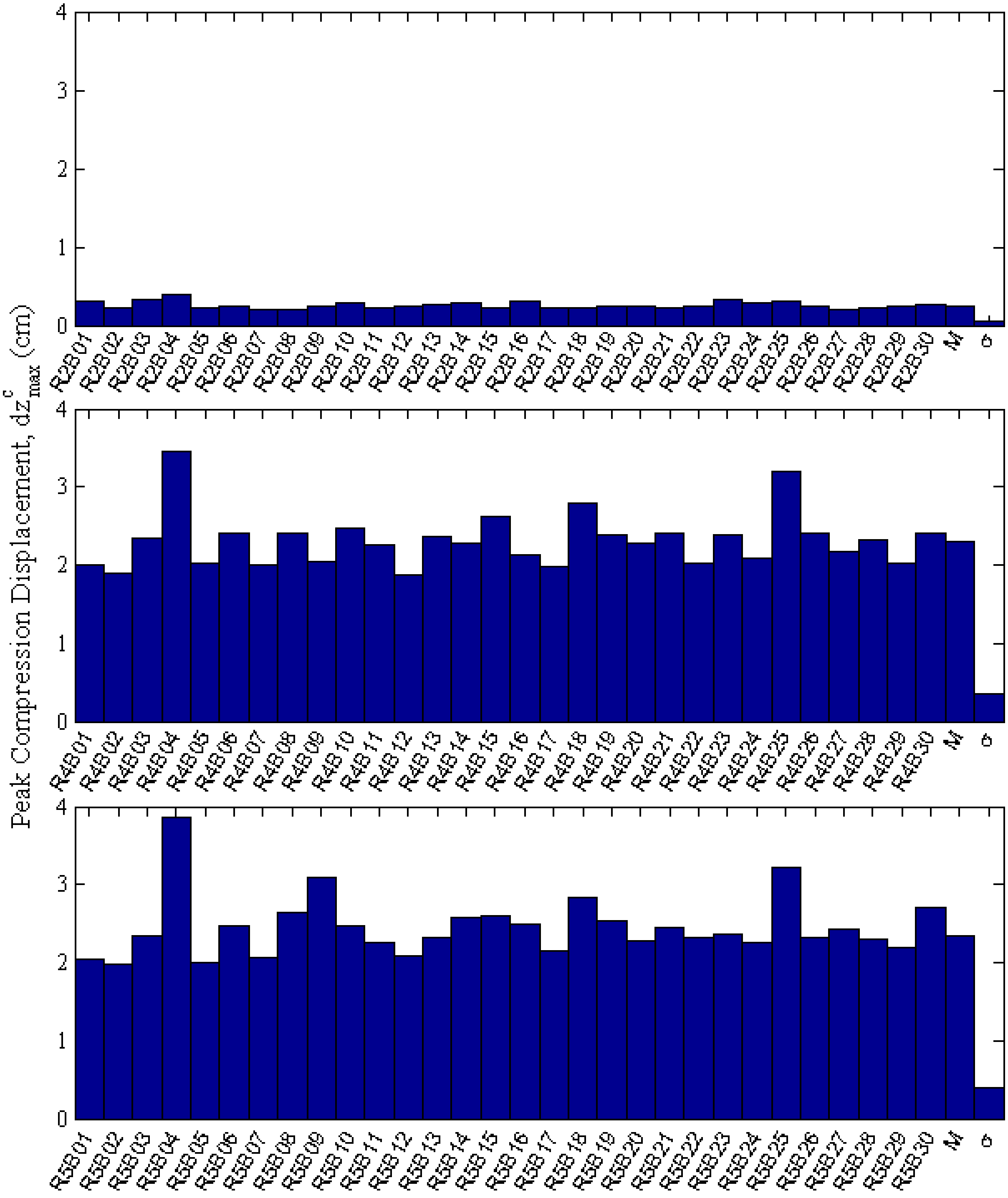

Figure D.7: Peak isolator compression displacement data from the simulations with the rectangular superstructure subjected to all ground motions

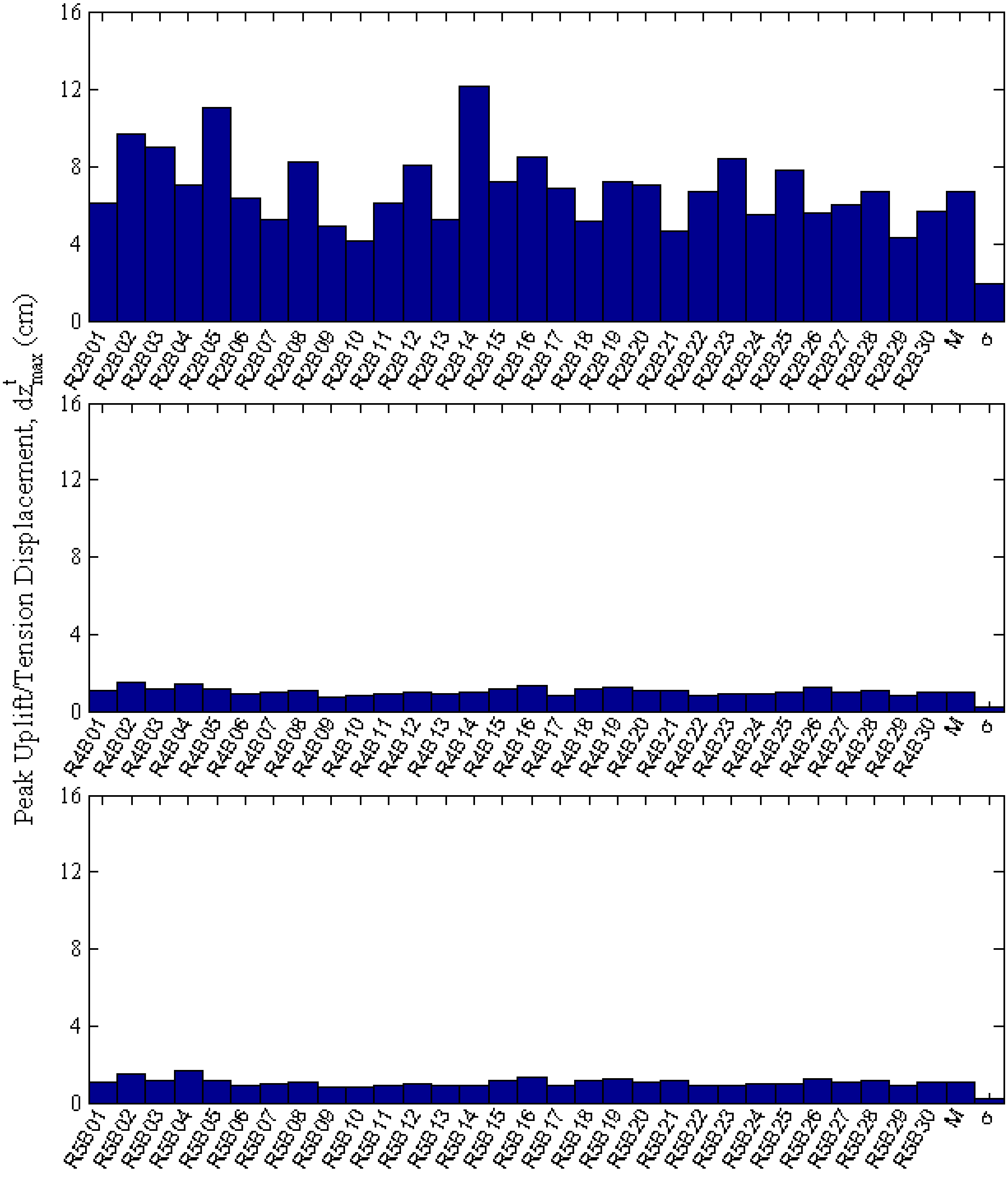

Figure D.8: Peak isolator uplift/tension displacement data from the simulations with the rectangular superstructure subjected to all ground motions

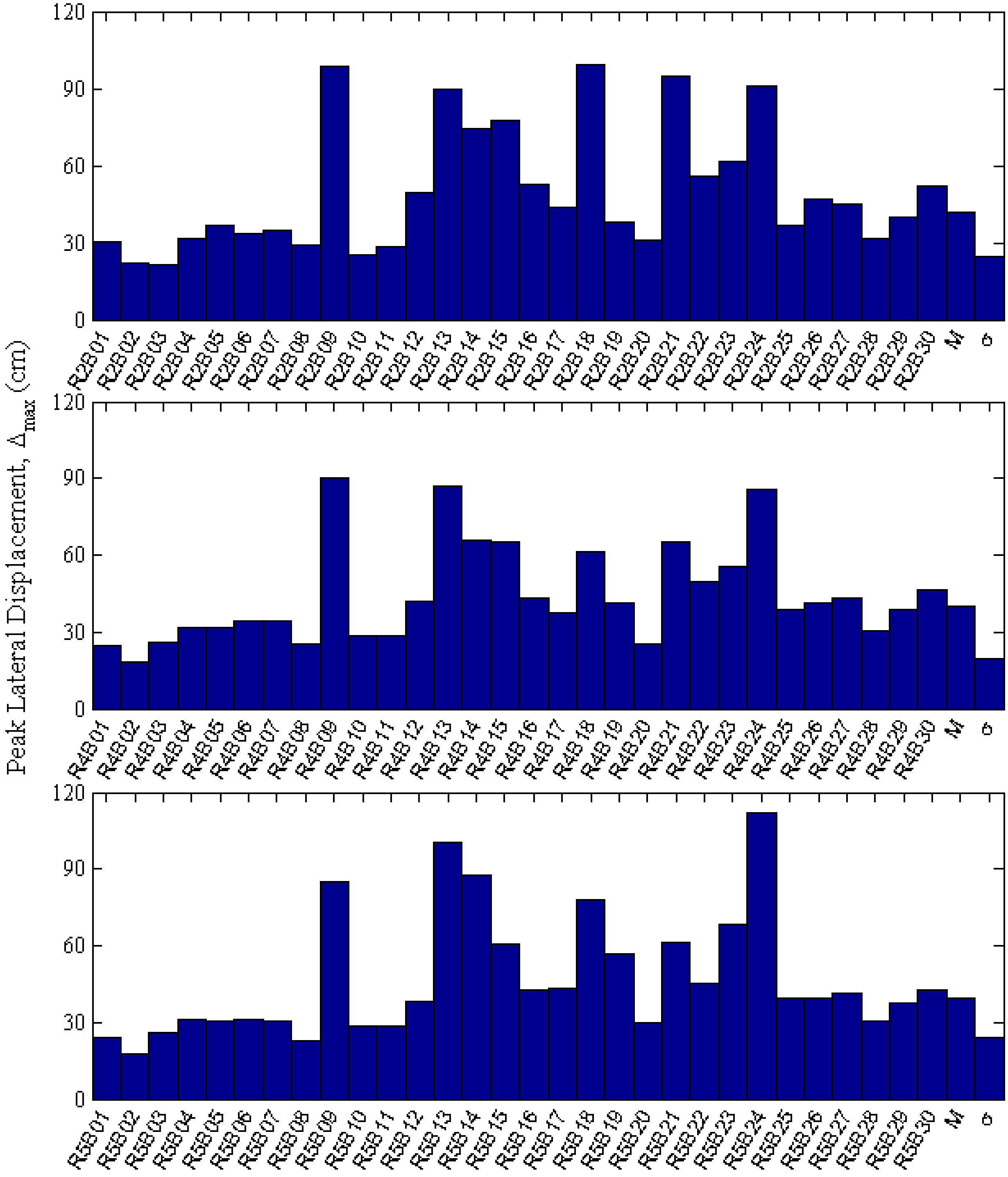

Figure D.9: Peak isolator lateral displacement data from the simulations with the rectangular superstructure subjected to all ground motions

Appendix E

Global Torsion and Overturning Data

This appendix details peak displacement and rotation data for the foundations and superstructures analyzed. Specifically, the peak x, y, and z displacements, $u_{x,max}$, $u_{y,max}$, and $u_{z,max}$ respectively, as well as peak torsion rotation, θ_{max}, overturning rotation about the x-axis (East-West), $\phi_{x,max}$, and overturning rotation about the y-axis (North-South), $\phi_{y,max}$, are solved for at the foundation level (f), isolated-slab level (i), and roof level (r). The rotations are solved for by taking the inverse sine of the peak differential-displacement between opposite tracers on the horizontal surface of interest divided by the distance between them. It should be noted that unlike the foundation and isolated-slab levels, the roof is not approximately-rigid, and therefore the values presented only represent the average rotations of the roof. Tables E.1 through E.10 present the peak diaplacement and rotation data for each of the three surfaces for the analysis cases considered. Figures E.1 through E.36 show bar plots of the peak data for the comparative cases subjected to teh basic ground motions. Figures E.37 through E.54 present all data peaks for the cases subjected to all 30 ground motions, as well as the median, M, and standard deviation, σ, of the data sets.

Case	$u^f_{x,max}$ (cm)	$u^f_{y,max}$ (cm)	$u^f_{z,max}$ (cm)	$u^i_{x,max}$ (cm)	$u^i_{y,max}$ (cm)	$u^i_{z,max}$ (cm)	$u^r_{x,max}$ (cm)	$u^r_{y,max}$ (cm)	$u^r_{z,max}$ (cm)
C2N08	9.00	19.0	9.10	10.0	17.1	9.13	10.3	17.3	9.33
C2N09	36.0	38.0	6.10	80.3	69.9	6.08	82.4	70.8	5.94
C2N22	21.0	26.0	20.0	25.3	37.2	19.7	25.6	37.9	19.5
C4N08	9.00	19.0	9.10	12.4	20.3	9.48	12.9	22.0	9.75
C4N09	36.0	38.0	6.10	80.2	72.3	5.91	82.5	74.1	5.78
C4N22	21.0	26.0	20.0	25.9	38.5	19.6	26.8	39.9	19.7
C5N08	9.00	19.0	9.10	12.3	20.6	9.49	12.7	21.7	9.75
C5N09	36.0	38.0	6.10	77.2	70.7	5.84	80.5	73.2	5.92
C5N22	21.0	26.0	20.0	26.3	37.4	19.6	27.5	39.0	19.7
R2N08	9.00	19.0	9.10	10.3	17.0	9.22	10.8	18.0	9.79
R2N09	36.0	38.0	6.10	81.7	70.0	6.03	83.9	71.5	5.83
R2N22	21.0	26.0	20.0	25.7	37.7	19.6	26.2	38.5	19.8
R4N08	9.00	19.0	9.10	12.3	19.5	9.78	12.9	20.6	10.3
R4N09	36.0	38.0	6.10	78.3	67.5	6.20	81.0	69.0	7.01
R4N22	21.0	26.0	20.0	24.5	36.9	19.9	25.0	39.1	20.2
R5N08	9.00	19.0	9.10	12.0	19.2	9.82	12.4	20.5	10.3
R5N09	36.0	38.0	6.10	76.4	68.3	6.07	79.5	71.1	6.63
R5N22	21.0	26.0	20.0	24.9	36.0	19.9	25.9	38.6	20.3
C2B08	10.7	20.7	10.7	11.8	19.5	11.4	15.8	31.8	11.9
C2B09	36.6	40.6	7.16	70.5	60.7	7.75	83.4	79.3	7.93
C2B22	23.9	26.0	20.9	31.9	41.1	21.4	37.3	51.8	21.6
C4B08	10.7	20.8	10.9	11.8	16.6	12.4	18.9	29.6	13.0
C4B09	36.4	40.6	7.26	79.9	51.7	8.26	94.3	71.8	8.86
C4B22	24.0	26.0	20.9	28.5	27.1	21.8	36.1	46.5	22.0
C5B08	10.7	20.8	10.9	11.7	15.6	12.4	19.2	30.9	13.0
C5B09	36.4	40.6	7.21	81.6	51.8	8.06	95.6	74.1	8.89
C5B22	24.0	25.9	20.9	29.4	28.3	21.8	35.9	45.7	22.0
R2B08	9.28	19.6	11.1	9.94	18.4	12.4	13.8	26.1	13.4
R2B09	36.8	38.4	7.58	80.7	70.3	8.60	85.3	78.2	9.14
R2B22	21.2	26.4	20.9	30.1	41.7	21.9	33.0	47.9	22.2
R4B08	9.25	19.5	11.1	9.81	18.9	13.0	13.5	22.5	13.8
R4B09	36.9	38.4	7.49	73.2	57.3	9.43	82.8	65.9	10.1
R4B22	21.2	26.5	20.9	23.1	32.9	22.2	27.9	45.7	22.8
R5B08	9.24	19.5	11.1	9.68	19.6	13.1	13.1	22.8	13.9
R5B09	37.0	38.4	7.52	71.9	55.6	9.92	81.2	64.3	10.7
R5B22	21.2	26.5	20.9	23.6	32.3	22.2	27.4	45.7	22.8

Table E.1: Displacement data for the soil N and B cases in response to the basic motions

Case	$u^f_{x,max}$ (cm)	$u^f_{y,max}$ (cm)	$u^f_{z,max}$ (cm)	$u^i_{x,max}$ (cm)	$u^i_{y,max}$ (cm)	$u^i_{z,max}$ (cm)	$u^r_{x,max}$ (cm)	$u^r_{y,max}$ (cm)	$u^r_{z,max}$ (cm)
C2C08	11.6	22.9	14.2	12.7	25.2	14.0	28.3	37.0	14.4
C2C09	37.8	42.7	11.4	82.8	66.6	12.3	112.9	121.7	12.8
C2C22	24.8	27.6	23.4	39.1	32.6	24.4	44.7	44.6	24.6
C4C08	11.7	23.0	14.3	14.4	22.3	16.2	22.6	33.8	16.9
C4C09	37.1	42.8	11.7	91.6	64.2	13.1	105.5	86.6	13.9
C4C22	25.1	27.5	24.8	38.8	28.0	25.2	47.0	56.0	25.5
C5C08	11.8	23.0	14.3	13.6	22.2	16.2	19.1	35.8	16.8
C5C09	37.0	42.8	11.7	98.0	63.9	13.5	110.4	89.4	14.2
C5C22	25.1	27.5	24.8	37.6	29.5	25.2	47.5	54.1	25.4
R2C08	9.29	20.1	13.3	8.57	23.2	14.5	14.1	38.8	15.3
R2C09	37.0	38.2	9.87	78.1	66.3	12.0	87.7	82.6	12.5
R2C22	21.4	27.0	23.5	30.1	38.0	25.0	31.9	54.4	25.5
R4C08	9.24	19.9	13.3	10.3	16.8	15.7	14.9	25.1	16.7
R4C09	36.9	38.3	9.92	76.2	58.7	12.9	87.1	75.5	13.9
R4C22	21.2	26.8	23.5	27.7	35.5	25.6	30.9	54.5	26.3
R5C08	9.26	19.9	13.3	10.2	17.7	15.7	14.6	25.4	16.7
R5C09	37.0	38.4	10.0	75.8	58.3	13.1	88.2	76.1	14.2
R5C22	21.2	26.8	23.5	28.9	35.9	25.6	31.8	57.2	26.3
C2D08	12.2	19.5	44.5	22.8	42.9	47.7	24.3	40.3	48.0
C2D09	52.1	45.6	38.5	124.3	148.3	41.0	197.5	195.8	41.3
C2D22	27.4	36.6	55.7	67.3	103.8	60.2	92.4	124.8	60.7
C4D08	11.4	19.5	44.3	22.3	37.9	48.0	24.3	36.7	48.3
C4D09	50.6	45.5	42.6	198.1	171.7	47.0	238.4	208.8	47.3
C4D22	28.4	33.6	60.5	61.6	91.9	66.4	70.7	107.2	66.8
C5D08	11.4	19.5	44.2	22.2	38.4	48.0	22.0	40.8	48.3
C5D09	50.9	45.5	42.7	197.5	170.2	49.1	257.1	212.0	49.2
C5D22	28.5	33.9	60.3	62.5	104.6	66.2	75.7	122.5	66.6
R2D08	8.75	17.4	39.8	12.5	27.6	46.9	19.3	46.9	47.2
R2D09	33.2	36.0	33.5	77.2	76.7	39.8	91.5	93.0	39.7
R2D22	18.0	27.0	45.8	26.5	37.6	50.6	43.5	56.7	50.7
R4D08	8.38	17.1	40.7	14.6	29.5	48.7	21.3	44.7	49.1
R4D09	34.9	36.6	34.7	78.7	69.7	41.7	100.8	88.6	42.4
R4D22	18.1	25.6	45.7	30.5	39.1	51.0	44.1	57.8	51.3
R5D08	8.91	16.9	40.7	13.9	29.5	48.8	20.2	46.6	49.2
R5D09	34.8	36.7	34.5	84.2	69.8	42.1	103.7	92.3	42.9
R5D22	18.0	25.4	45.7	29.9	40.3	51.0	44.5	58.7	51.3

Table E.2: Displacement data for the soil C and D cases in response to the basic motions

Case	$u^f_{x,max}$ (cm)	$u^f_{y,max}$ (cm)	$u^f_{z,max}$ (cm)	$u^i_{x,max}$ (cm)	$u^i_{y,max}$ (cm)	$u^i_{z,max}$ (cm)	$u^r_{x,max}$ (cm)	$u^r_{y,max}$ (cm)	$u^r_{z,max}$ (cm)
R2B01	11.0	16.1	4.98	10.3	13.6	6.06	12.3	19.9	6.50
R2B02	8.97	13.3	7.50	6.90	13.1	8.70	11.0	17.6	9.24
R2B03	13.5	16.5	21.2	15.9	14.5	22.4	18.1	16.0	23.0
R2B04	16.5	11.2	7.41	17.4	11.0	8.87	23.7	14.5	9.65
R2B05	15.3	24.3	23.5	11.3	30.7	25.1	14.9	35.4	25.8
R2B06	26.8	15.2	7.53	27.5	12.1	9.00	33.1	15.6	9.85
R2B07	14.6	23.9	12.8	18.0	28.7	13.9	19.1	35.5	14.7
R2B08	9.28	19.6	11.1	9.94	18.4	12.4	13.8	26.1	13.4
R2B09	36.8	38.4	7.58	80.7	70.3	8.60	85.3	78.2	9.14
R2B10	22.6	10.6	4.48	21.2	8.43	5.42	23.9	13.2	6.01
R2B11	17.9	14.4	10.8	12.1	18.5	12.6	18.5	23.8	13.7
R2B12	18.9	25.2	5.22	24.9	32.3	6.16	29.8	37.6	6.69
R2B13	29.0	36.1	34.6	40.4	87.6	36.2	44.5	97.3	36.3
R2B14	33.1	26.0	70.9	80.6	37.7	71.8	84.8	40.2	72.2
R2B15	37.1	29.1	29.4	53.1	37.8	31.1	57.4	55.2	32.0
R2B16	17.8	18.9	30.2	23.1	24.7	31.4	27.7	31.6	32.0
R2B17	17.2	19.4	24.7	19.6	21.6	26.3	23.4	30.3	27.0
R2B18	26.1	43.8	12.6	28.7	105.8	13.6	32.6	114.8	14.0
R2B19	21.4	22.0	8.62	31.3	29.5	10.0	36.6	34.0	11.0
R2B20	18.0	16.5	11.6	21.8	17.7	13.2	29.4	20.3	14.1
R2B21	34.0	39.3	12.7	43.4	98.5	13.8	47.7	104.9	14.7
R2B22	21.2	26.4	20.9	30.1	41.7	21.8	33.0	47.9	22.2
R2B23	28.2	29.8	10.8	44.6	44.8	11.7	48.9	48.6	12.2
R2B24	37.3	35.0	3.73	62.9	80.6	4.62	67.5	86.2	5.50
R2B25	17.8	18.1	10.4	23.2	18.5	11.4	25.0	20.8	11.7
R2B26	18.8	14.9	5.53	22.6	15.4	7.07	27.8	19.9	7.94
R2B27	20.7	24.2	9.70	27.3	35.7	11.0	32.4	44.4	11.8
R2B28	23.4	16.0	5.40	31.2	13.9	6.36	33.6	17.2	6.82
R2B29	23.0	14.0	15.2	30.3	19.7	16.2	32.7	22.6	17.0
R2B30	30.4	18.7	14.1	45.1	22.5	14.9	48.0	27.6	15.3
M	21.0	19.5	11.0	26.1	23.6	12.5	31.1	30.9	13.5
σ	8.12	8.89	13.4	18.9	27.0	13.4	19.1	28.4	13.3

Table E.3: Displacement data for the soil B cases with a rectangular superstructure and FP bearings in response to all motions

Case	$u^f_{x,max}$ (cm)	$u^f_{y,max}$ (cm)	$u^f_{z,max}$ (cm)	$u^i_{x,max}$ (cm)	$u^i_{y,max}$ (cm)	$u^i_{z,max}$ (cm)	$u^r_{x,max}$ (cm)	$u^r_{y,max}$ (cm)	$u^r_{z,max}$ (cm)
R4B01	10.9	16.1	5.06	10.1	10.2	6.43	12.7	20.1	7.40
R4B02	8.95	13.3	7.33	4.71	10.3	9.08	9.38	30.5	10.1
R4B03	13.5	16.5	21.0	18.7	12.1	22.7	20.9	17.0	23.4
R4B04	16.4	11.2	7.33	18.4	8.08	9.30	23.6	12.3	10.1
R4B05	15.3	24.2	23.5	14.9	28.4	26.1	19.7	32.5	27.1
R4B06	26.7	15.2	7.18	29.4	12.9	9.27	36.0	18.0	9.99
R4B07	14.6	23.9	12.8	18.4	31.3	15.2	19.8	45.5	16.4
R4B08	9.25	19.5	11.1	9.81	18.9	13.0	13.5	22.5	13.8
R4B09	36.9	38.4	7.49	73.2	57.3	9.43	82.8	65.9	10.1
R4B10	22.5	10.6	4.45	24.3	10.7	5.95	27.9	17.9	7.00
R4B11	17.8	14.6	11.3	14.2	16.9	13.5	19.3	23.1	14.3
R4B12	18.9	25.1	5.60	21.9	22.8	6.99	26.8	33.7	7.80
R4B13	28.9	36.1	34.5	40.0	83.1	34.4	44.0	94.8	35.5
R4B14	33.2	26.0	70.9	72.7	31.8	72.5	80.3	46.0	73.3
R4B15	37.1	29.2	29.4	48.3	35.2	31.5	62.5	58.3	32.7
R4B16	17.7	18.9	30.1	20.6	22.3	31.8	26.0	36.7	32.6
R4B17	17.2	19.5	24.6	22.9	24.7	26.9	29.4	37.0	27.9
R4B18	26.1	43.7	12.6	28.4	65.0	14.3	32.9	76.9	15.3
R4B19	21.4	22.0	8.83	34.0	31.9	10.9	40.5	39.3	11.6
R4B20	17.9	16.4	11.4	22.3	17.5	13.7	25.6	25.8	14.8
R4B21	34.0	39.3	12.6	44.9	72.6	14.9	51.9	86.7	15.9
R4B22	21.2	26.5	20.9	23.1	32.9	22.2	27.9	45.7	22.8
R4B23	28.2	29.8	10.9	42.8	40.3	12.2	47.8	47.9	12.9
R4B24	37.2	35.0	3.92	68.2	71.4	5.76	74.1	86.1	7.22
R4B25	17.9	17.9	10.3	24.3	21.3	12.2	25.2	24.1	14.7
R4B26	18.7	14.9	5.66	17.5	15.7	7.61	25.8	22.5	8.63
R4B27	20.7	24.2	9.81	27.6	34.4	11.7	34.4	44.5	12.5
R4B28	23.4	16.1	5.34	29.3	14.0	7.15	32.7	22.9	8.15
R4B29	23.0	14.0	15.3	30.9	20.7	16.6	33.7	30.9	17.3
R4B30	30.3	18.7	14.6	46.2	17.6	16.0	50.8	23.2	17.8
M	21.0	19.5	11.2	24.3	22.5	13.2	28.7	33.1	14.5
σ	8.14	8.89	13.4	17.7	20.4	13.2	19.2	22.5	13.2

Table E.4: Displacement data for the soil B cases with a rectangular superstructure and simplified LR bearings in response to all motions

Case	$u^f_{x,max}$ (cm)	$u^f_{y,max}$ (cm)	$u^f_{z,max}$ (cm)	$u^i_{x,max}$ (cm)	$u^i_{y,max}$ (cm)	$u^i_{z,max}$ (cm)	$u^r_{x,max}$ (cm)	$u^r_{y,max}$ (cm)	$u^r_{z,max}$ (cm)
R5B01	10.9	16.1	5.05	9.78	11.4	6.46	11.3	20.6	7.50
R5B02	8.95	13.3	7.31	4.21	11.0	9.08	9.34	30.9	10.2
R5B03	13.5	16.5	21.0	17.8	12.6	22.8	19.0	17.9	23.4
R5B04	16.4	11.2	7.32	17.7	9.54	9.32	24.8	13.7	10.1
R5B05	15.3	24.2	23.5	14.7	27.3	26.2	19.7	32.3	27.2
R5B06	26.7	15.2	7.13	28.7	12.6	9.21	33.8	16.6	9.87
R5B07	14.6	23.9	12.8	17.5	30.7	15.3	19.7	46.0	16.4
R5B08	9.24	19.5	11.1	9.66	19.6	13.1	13.1	22.8	13.9
R5B09	37.0	38.4	7.52	71.9	55.6	9.92	81.2	64.3	10.7
R5B10	22.5	10.6	4.45	24.3	10.7	5.95	27.9	17.9	7.00
R5B11	17.8	14.6	11.3	14.2	16.9	13.5	19.3	23.1	14.3
R5B12	18.9	25.1	5.59	21.2	19.5	7.10	25.5	30.4	7.90
R5B13	28.9	36.1	34.5	46.2	93.0	34.4	50.8	116.7	35.6
R5B14	33.2	26.0	70.9	95.1	33.8	72.7	104.8	48.3	73.6
R5B15	37.1	29.2	29.4	44.8	34.3	31.5	61.4	58.9	32.7
R5B16	17.7	18.9	30.1	20.4	23.1	31.8	25.9	36.7	32.5
R5B17	17.2	19.5	24.5	21.7	32.7	26.9	28.5	40.0	27.9
R5B18	26.1	43.7	12.6	42.8	78.9	14.5	46.4	104.1	15.4
R5B19	21.4	22.0	8.84	38.3	35.6	10.9	47.6	40.0	11.7
R5B20	18.0	16.5	11.4	20.1	18.6	13.8	26.0	26.3	14.9
R5B21	34.0	39.3	12.6	43.2	67.3	15.2	51.4	82.6	16.1
R5B22	21.2	26.5	20.9	23.6	32.3	22.2	27.4	45.7	22.8
R5B23	28.2	29.8	10.8	66.1	43.6	12.4	71.1	57.6	13.2
R5B24	38.5	34.9	4.19	95.0	82.1	5.82	102.0	108.4	7.2
R5B25	17.9	18.0	10.3	24.8	21.5	12.3	26.7	24.0	14.8
R5B26	18.7	14.9	5.67	16.6	16.3	7.66	25.8	23.4	8.68
R5B27	20.7	24.2	9.85	28.5	34.7	11.8	35.3	43.8	12.6
R5B28	23.4	16.1	5.36	29.6	15.1	7.18	33.0	23.0	8.13
R5B29	23.1	13.9	15.4	30.2	19.8	16.7	35.0	27.6	17.4
R5B30	30.4	18.7	14.6	42.7	17.3	16.2	46.0	22.6	18.0
M	21.0	19.5	11.2	24.5	22.3	13.3	28.2	31.6	14.5
σ	8.23	8.88	13.4	23.0	22.6	13.3	24.5	27.9	13.3

Table E.5: Displacement data for the soil B cases with a rectangular superstructure and robust LR bearings in response to all motions

Case	θ^f_{max} (°)	$\phi^f_{x,max}$ (°)	$\phi^f_{y,max}$ (°)	θ^i_{max} (°)	$\phi^i_{x,max}$ (°)	$\phi^i_{y,max}$ (°)	θ^r_{max} (°)	$\phi^r_{x,max}$ (°)	$\phi^r_{y,max}$ (°)
C2N08	0.0000	0.0000	0.0000	0.014	0.0082	0.0049	0.015	0.011	0.012
C2N09	0.0000	0.0000	0.0000	0.034	0.0084	0.020	0.036	0.013	0.034
C2N22	0.0000	0.0000	0.0000	0.023	0.0065	0.0090	0.023	0.011	0.017
C4N08	0.0000	0.0000	0.0000	0.035	0.016	0.010	0.036	0.022	0.020
C4N09	0.0000	0.0000	0.0000	0.22	0.018	0.021	0.22	0.025	0.034
C4N22	0.0000	0.0000	0.0000	0.063	0.016	0.017	0.065	0.021	0.022
C5N08	0.0000	0.0000	0.0000	0.029	0.020	0.011	0.029	0.026	0.022
C5N09	0.0000	0.0000	0.0000	0.24	0.029	0.031	0.24	0.035	0.041
C5N22	0.0000	0.0000	0.0000	0.059	0.017	0.020	0.062	0.022	0.025
R2N08	0.0000	0.0000	0.0000	0.0051	0.0048	0.0042	0.0054	0.012	0.0082
R2N09	0.0000	0.0000	0.0000	0.010	0.0038	0.0044	0.011	0.010	0.012
R2N22	0.0000	0.0000	0.0000	0.0061	0.0034	0.0044	0.0064	0.0097	0.0073
R4N08	0.0000	0.0000	0.0000	0.0015	0.0043	0.0033	0.0029	0.0097	0.0064
R4N09	0.0000	0.0000	0.0000	0.0091	0.0086	0.0055	0.017	0.020	0.011
R4N22	0.0000	0.0000	0.0000	0.0020	0.0053	0.0036	0.0036	0.012	0.0087
R5N08	0.0000	0.0000	0.0000	0.0020	0.0049	0.0048	0.0025	0.0091	0.0082
R5N09	0.0000	0.0000	0.0000	0.0099	0.011	0.0090	0.017	0.019	0.015
R5N22	0.0000	0.0000	0.0000	0.0038	0.0066	0.0042	0.0042	0.013	0.010
C2B08	0.0008	0.19	0.13	0.34	0.29	0.22	0.41	0.32	0.22
C2B09	0.0023	0.23	0.26	1.09	0.29	0.41	1.16	0.32	0.40
C2B22	0.0020	0.26	0.22	0.47	0.38	0.37	0.57	0.41	0.41
C4B08	0.0003	0.19	0.13	0.076	0.21	0.18	0.065	0.24	0.25
C4B09	0.0005	0.23	0.26	0.15	0.24	0.30	0.11	0.25	0.48
C4B22	0.0006	0.26	0.22	0.057	0.32	0.26	0.057	0.34	0.32
C5B08	0.0003	0.19	0.13	0.071	0.21	0.19	0.069	0.25	0.26
C5B09	0.0005	0.23	0.26	0.18	0.25	0.31	0.18	0.26	0.47
C5B22	0.0006	0.26	0.22	0.062	0.32	0.26	0.054	0.35	0.33
R2B08	0.0006	0.038	0.024	0.029	0.054	0.058	0.030	0.066	0.066
R2B09	0.0009	0.041	0.046	0.054	0.057	0.070	0.070	0.065	0.080
R2B22	0.0006	0.047	0.039	0.047	0.056	0.046	0.051	0.071	0.049
R4B08	0.0001	0.036	0.027	0.018	0.044	0.030	0.013	0.055	0.038
R4B09	0.0002	0.042	0.046	0.020	0.053	0.060	0.058	0.058	0.066
R4B22	0 .0001	0.047	0.038	0.018	0.056	0.049	0.019	0.062	0.053
R5B08	0.0001	0.036	0.027	0.020	0.046	0.030	0.015	0.056	0.037
R5B09	0.0002	0.042	0.047	0.017	0.056	0.061	0.041	0.065	0.068
R5B22	0.0001	0.047	0.038	0.018	0.056	0.050	0.018	0.069	0.055

Table E.6: Rotation data for the soil N and B cases in response to the basic motions

Case	θ^f_{max} (°)	$\phi^f_{x,max}$ (°)	$\phi^f_{y,max}$ (°)	θ^i_{max} (°)	$\phi^i_{x,max}$ (°)	$\phi^i_{y,max}$ (°)	θ^r_{max} (°)	$\phi^r_{x,max}$ (°)	$\phi^r_{y,max}$ (°)
C2C08	0.0020	0.26	0.18	0.44	0.38	0.36	0.43	0.41	0.40
C2C09	0.0084	0.39	0.41	2.32	0.69	0.80	2.78	0.71	0.80
C2C22	0.0040	0.34	0.35	1.15	0.43	0.48	1.41	0.45	0.53
C4C08	0.0010	0.26	0.17	0.070	0.32	0.23	0.052	0.33	0.31
C4C09	0.0019	0.39	0.41	0.16	0.42	0.47	0.25	0.44	0.53
C4C22	0.0015	0.35	0.34	0.12	0.41	0.38	0.073	0.43	0.42
C5C08	0.0010	0.26	0.17	0.068	0.32	0.23	0.054	0.34	0.32
C5C09	0.0018	0.39	0.41	0.18	0.44	0.47	0.25	0.46	0.54
C5C22	0.0015	0.35	0.34	0.13	0.41	0.38	0.078	0.43	0.42
R2C08	0.0015	0.069	0.048	0.069	0.14	0.057	0.079	0.15	0.063
R2C09	0.0046	0.080	0.079	0.12	0.12	0.11	0.12	0.13	0.12
R2C22	0.0018	0.086	0.066	0.063	0.13	0.074	0.081	0.14	0.081
R4C08	0.0005	0.063	0.044	0.046	0.086	0.048	0.047	0.098	0.055
R4C09	0.0002	0.075	0.077	0.039	0.099	0.096	0.054	0.11	0.11
R4C22	0.0004	0.083	0.064	0.048	0.097	0.077	0.031	0.12	0.084
R5C08	0.0004	0.063	0.044	0.040	0.086	0.049	0.041	0.098	0.056
R5C09	0.0003	0.074	0.077	0.037	0.10	0.096	0.048	0.11	0.11
R5C22	0.0004	0.083	0.064	0.038	0.099	0.079	0.027	0.12	0.087
C2D08	0.0061	0.39	0.23	0.46	0.40	0.24	0.46	0.41	0.25
C2D09	0.031	0.75	0.79	1.93	1.24	1.32	1.92	1.24	1.37
C2D22	0.018	0.53	0.49	1.47	0.85	0.67	1.48	0.88	0.72
C4D08	0.0021	0.38	0.21	0.060	0.39	0.24	0.061	0.40	0.25
C4D09	0.014	0.72	0.77	0.84	0.73	0.79	1.04	0.74	0.78
C4D22	0.0055	0.54	0.49	0.25	0.57	0.54	0.25	0.58	0.55
C5D08	0.0023	0.39	0.20	0.065	0.41	0.22	0.065	0.41	0.23
C5D09	0.017	0.72	0.78	0.87	0.75	0.82	1.07	0.75	0.82
C5D22	0.0052	0.54	0.50	0.44	0.58	0.55	0.44	0.59	0.57
R2D08	0.0069	0.19	0.14	0.16	0.25	0.17	0.16	0.26	0.17
R2D09	0.023	0.27	0.28	0.45	0.32	0.34	0.45	0.34	0.35
R2D22	0.014	0.20	0.19	0.29	0.29	0.24	0.29	0.30	0.24
R4D08	0.0005	0.19	0.14	0.0062	0.26	0.18	0.013	0.27	0.20
R4D09	0.0042	0.28	0.26	0.042	0.34	0.32	0.098	0.34	0.33
R4D22	0.0009	0.19	0.19	0.0097	0.26	0.22	0.013	0.28	0.23
R5D08	0 .0005	0.19	0.14	0.0052	0.26	0.18	0.011	0.27	0.20
R5D09	0.0047	0.28	0.26	0.064	0.33	0.32	0.13	0.34	0.33
R5D22	0.0007	0.18	0.19	0.010	0.25	0.22	0.013	0.28	0.23

Table E.7: Rotation data for the soil C and D cases in response to the basic motions

Case	θ^f_{max} (°)	$\phi^f_{x,max}$ (°)	$\phi^f_{y,max}$ (°)	θ^i_{max} (°)	$\phi^i_{x,max}$ (°)	$\phi^i_{y,max}$ (°)	θ^r_{max} (°)	$\phi^r_{x,max}$ (°)	$\phi^r_{y,max}$ (°)
R2B01	0.0004	0.041	0.030	0.058	0.052	0.036	0.059	0.057	0.050
R2B02	0.0004	0.032	0.023	0.031	0.062	0.039	0.029	0.066	0.047
R2B03	0.0003	0.031	0.024	0.030	0.047	0.054	0.033	0.051	0.062
R2B04	0.0009	0.028	0.050	0.065	0.054	0.068	0.080	0.065	0.078
R2B05	0.0005	0.031	0.035	0.092	0.051	0.10	0.093	0.053	0.11
R2B06	0.0004	0.035	0.034	0.030	0.044	0.053	0.029	0.049	0.072
R2B07	0.0004	0.033	0.025	0.039	0.044	0.063	0.040	0.051	0.075
R2B08	0.0006	0.038	0.024	0.029	0.054	0.058	0.030	0.066	0.066
R2B09	0.0009	0.041	0.046	0.054	0.057	0.070	0.070	0.065	0.080
R2B10	0.0005	0.035	0.037	0.057	0.048	0.049	0.056	0.063	0.059
R2B11	0.0005	0.033	0.033	0.069	0.058	0.056	0.070	0.060	0.064
R2B12	0.0012	0.047	0.035	0.047	0.084	0.056	0.052	0.081	0.058
R2B13	0.0005	0.044	0.034	0.033	0.048	0.041	0.035	0.068	0.051
R2B14	0.0007	0.033	0.044	0.047	0.097	0.11	0.049	0.11	0.11
R2B15	0.0005	0.051	0.050	0.041	0.12	0.085	0.051	0.13	0.087
R2B16	0.0004	0.038	0.037	0.060	0.054	0.063	0.074	0.068	0.078
R2B17	0.0005	0.038	0.036	0.018	0.050	0.059	0.023	0.066	0.065
R2B18	0.0006	0.041	0.042	0.030	0.064	0.051	0.037	0.073	0.060
R2B19	0.0005	0.042	0.036	0.041	0.052	0.075	0.045	0.063	0.091
R2B20	0.0005	0.029	0.046	0.040	0.037	0.084	0.043	0.053	0.092
R2B21	0.0012	0.053	0.035	0.036	0.070	0.054	0.037	0.083	0.055
R2B22	0.0006	0.047	0.039	0.047	0.056	0.046	0.051	0.071	0.049
R2B23	0.0004	0.036	0.033	0.042	0.062	0.093	0.036	0.062	0.099
R2B24	0.0006	0.028	0.037	0.070	0.046	0.065	0.071	0.060	0.068
R2B25	0.0008	0.039	0.037	0.11	0.054	0.049	0.11	0.064	0.055
R2B26	0.0004	0.039	0.032	0.038	0.042	0.054	0.043	0.041	0.063
R2B27	0.0005	0.052	0.049	0.075	0.062	0.054	0.076	0.072	0.065
R2B28	0.0004	0.030	0.044	0.045	0.051	0.062	0.045	0.060	0.070
R2B29	0.0005	0.034	0.046	0.046	0.043	0.050	0.047	0.049	0.058
R2B30	0.0007	0.043	0.036	0.047	0.065	0.044	0.048	0.073	0.053
M	0.0005	0.038	0.036	0.045	0.054	0.056	0.048	0.064	0.065
σ	0.0002	0.0070	0.0075	0.019	0.017	0.018	0.020	0.018	0.018

Table E.8: Rotation data for the soil B cases with a rectangular superstructure and FP bearings in response to all motions

Case	θ^f_{max} (°)	$\phi^f_{x,max}$ (°)	$\phi^f_{y,max}$ (°)	θ^i_{max} (°)	$\phi^i_{x,max}$ (°)	$\phi^i_{y,max}$ (°)	θ^r_{max} (°)	$\phi^r_{x,max}$ (°)	$\phi^r_{y,max}$ (°)
R4B01	0.0001	0.038	0.028	0.015	0.047	0.032	0.015	0.056	0.044
R4B02	0.0001	0.032	0.023	0.027	0.037	0.031	0.038	0.053	0.038
R4B03	0.0001	0.030	0.024	0.013	0.042	0.033	0.011	0.054	0.042
R4B04	0.0001	0.028	0.049	0.026	0.031	0.066	0.030	0.046	0.078
R4B05	0.0001	0.031	0.034	0.021	0.040	0.042	0.018	0.050	0.054
R4B06	0.0001	0.033	0.034	0.018	0.041	0.046	0.017	0.042	0.054
R4B07	0.0001	0.034	0.024	0.012	0.040	0.032	0.015	0.050	0.035
R4B08	0.0001	0.036	0.027	0.018	0.044	0.030	0.013	0.055	0.038
R4B09	0.0002	0.042	0.046	0.020	0.053	0.060	0.058	0.058	0.066
R4B10	0.0001	0.031	0.037	0.018	0.037	0.048	0.016	0.040	0.058
R4B11	0.0001	0.033	0.034	0.014	0.037	0.048	0.025	0.045	0.058
R4B12	0.0002	0.042	0.032	0.040	0.049	0.041	0.047	0.056	0.044
R4B13	0.0002	0.040	0.033	0.027	0.048	0.042	0.024	0.062	0.054
R4B14	0.0001	0.032	0.042	0.011	0.035	0.049	0.021	0.056	0.070
R4B15	0.0002	0.052	0.051	0.028	0.057	0.061	0.027	0.068	0.074
R4B16	0.0001	0.037	0.035	0.021	0.045	0.042	0.015	0.057	0.055
R4B17	0.0001	0.037	0.038	0.020	0.046	0.039	0.020	0.069	0.047
R4B18	0.0001	0.039	0.041	0.022	0.052	0.049	0.031	0.065	0.055
R4B19	0.0001	0.041	0.034	0.021	0.049	0.047	0.017	0.065	0.066
R4B20	0.0001	0.029	0.043	0.014	0.035	0.050	0.021	0.051	0.057
R4B21	0.0002	0.052	0.035	0.050	0.062	0.041	0.058	0.075	0.049
R4B22	0.0001	0.047	0.038	0.018	0.056	0.049	0.019	0.062	0.053
R4B23	0.0001	0.034	0.033	0.030	0.043	0.040	0.038	0.055	0.051
R4B24	0.0001	0.028	0.037	0.023	0.040	0.048	0.033	0.051	0.064
R4B25	0.0000	0.038	0.036	0.011	0.049	0.047	0.0096	0.054	0.054
R4B26	0.0001	0.038	0.033	0.026	0.047	0.038	0.037	0.053	0.050
R4B27	0.0002	0.051	0.049	0.030	0.065	0.054	0.034	0.070	0.060
R4B28	0.0001	0.029	0.043	0.034	0.034	0.047	0.026	0.038	0.049
R4B29	0.0001	0.032	0.045	0.020	0.041	0.050	0.012	0.046	0.058
R4B30	0.0001	0.038	0.035	0.023	0.044	0.041	0.027	0.052	0.055
M	0.0001	0.037	0.035	0.021	0.044	0.046	0.023	0.054	0.054
σ	0.0000	0.0069	0.0074	0.0086	0.0082	0.0087	0.013	0.0090	0.010

Table E.9: Rotation data for the soil B cases with a rectangular superstructure and simplified LR bearings in response to all motions

Case	θ^f_{max} (°)	$\phi^f_{x,max}$ (°)	$\phi^f_{y,max}$ (°)	θ^i_{max} (°)	$\phi^i_{x,max}$ (°)	$\phi^i_{y,max}$ (°)	θ^r_{max} (°)	$\phi^r_{x,max}$ (°)	$\phi^r_{y,max}$ (°)
R5B01	0.0001	0.038	0.027	0.019	0.048	0.030	0.019	0.058	0.041
R5B02	0.0002	0.032	0.023	0.037	0.035	0.031	0.048	0.054	0.040
R5B03	0.0001	0.030	0.024	0.014	0.042	0.033	0.017	0.053	0.043
R5B04	0.0001	0.028	0.049	0.029	0.031	0.068	0.033	0.048	0.080
R5B05	0.0001	0.031	0.034	0.018	0.040	0.042	0.014	0.050	0.055
R5B06	0.0001	0.033	0.034	0.017	0.043	0.046	0.027	0.045	0.055
R5B07	0.0001	0.034	0.024	0.013	0.040	0.033	0.015	0.051	0.036
R5B08	0.0001	0.036	0.027	0.020	0.046	0.030	0.015	0.056	0.037
R5B09	0.0002	0.042	0.047	0.017	0.056	0.061	0.041	0.065	0.068
R5B10	0.0001	0.031	0.037	0.018	0.037	0.048	0.016	0.040	0.058
R5B11	0.0001	0.033	0.034	0.014	0.037	0.048	0.025	0.045	0.058
R5B12	0.0002	0.043	0.032	0.036	0.049	0.043	0.041	0.057	0.046
R5B13	0.0002	0.040	0.033	0.037	0.052	0.045	0.039	0.064	0.056
R5B14	0.0001	0.032	0.042	0.014	0.035	0.050	0.024	0.058	0.070
R5B15	0.0002	0.052	0.051	0.023	0.058	0.063	0.028	0.067	0.077
R5B16	0.0001	0.037	0.035	0.021	0.046	0.042	0.015	0.058	0.055
R5B17	0.0001	0.037	0.038	0.023	0.046	0.039	0.021	0.065	0.047
R5B18	0.0001	0.039	0.041	0.021	0.061	0.050	0.041	0.062	0.056
R5B19	0.0001	0.042	0.034	0.024	0.050	0.046	0.015	0.063	0.066
R5B20	0.0001	0.028	0.044	0.015	0.035	0.050	0.023	0.053	0.059
R5B21	0.0001	0.051	0.035	0.048	0.062	0.042	0.057	0.077	0.051
R5B22	0.0001	0.047	0.038	0.018	0.056	0.050	0.018	0.069	0.055
R5B23	0.0001	0.034	0.033	0.022	0.044	0.040	0.031	0.056	0.055
R5B24	0.0001	0.028	0.037	0.027	0.051	0.048	0.037	0.061	0.065
R5B25	0.0001	0.038	0.036	0.0096	0.050	0.047	0.011	0.057	0.054
R5B26	0.0001	0.038	0.033	0.031	0.047	0.039	0.047	0.056	0.051
R5B27	0.0002	0.051	0.049	0.021	0.067	0.056	0.025	0.073	0.063
R5B28	0.0002	0.030	0.042	0.032	0.035	0.048	0.026	0.038	0.051
R5B29	0.0001	0.032	0.045	0.014	0.041	0.051	0.011	0.045	0.058
R5B30	0.0001	0.039	0.035	0.025	0.046	0.043	0.023	0.053	0.058
M	0.0001	0.037	0.035	0.021	0.046	0.046	0.025	0.057	0.055
σ	0.0000	0.0068	0.0074	0.0087	0.0089	0.0092	0.012	0.0092	0.011

Table E.10: Rotation data for the soil B cases with a rectangular superstructure and robust LR bearings in response to all motions

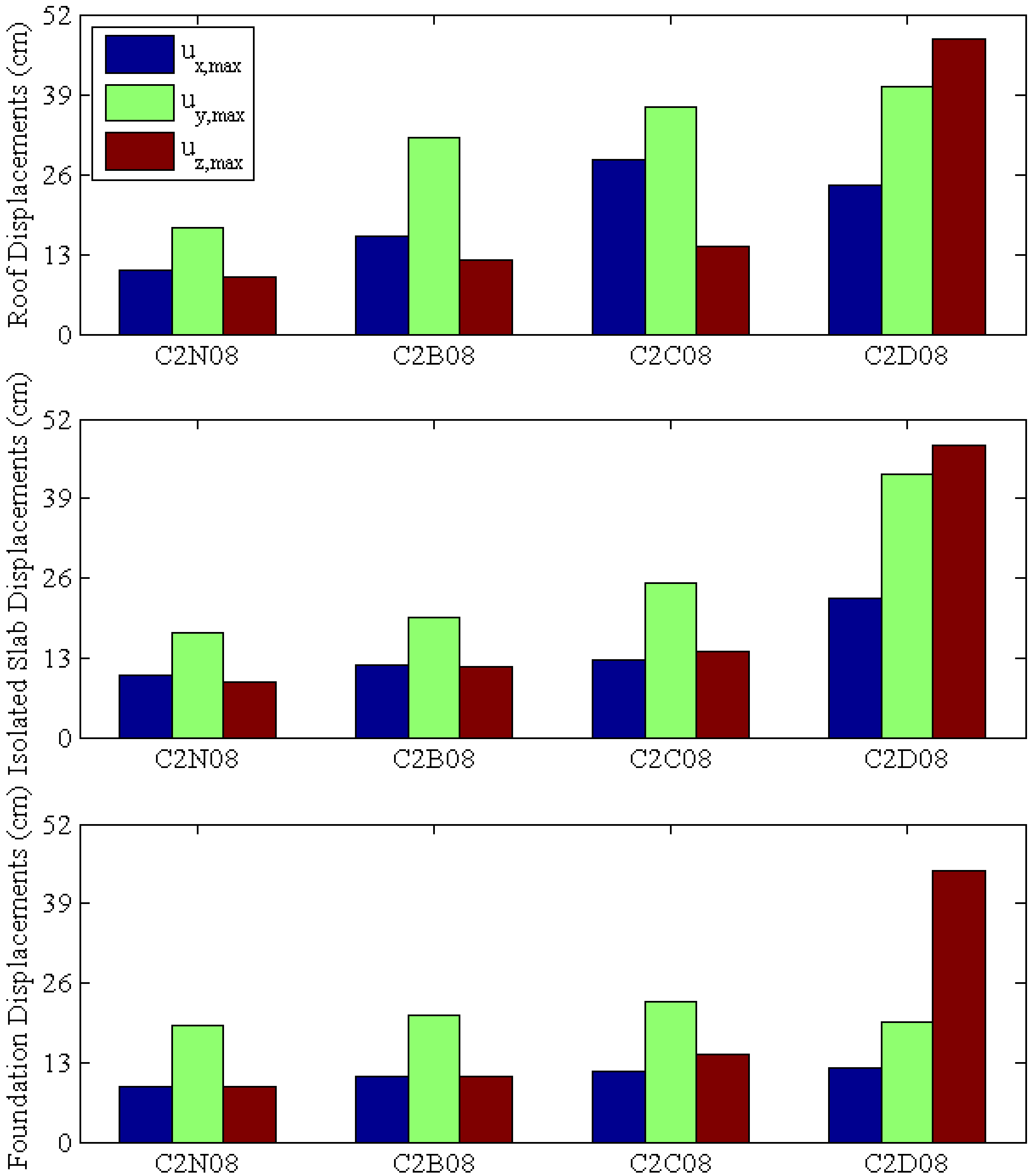

Figure E.1: Peak displacement data from the simulations with the cylindrical superstructure and FP isolators subjected to ground motion 08

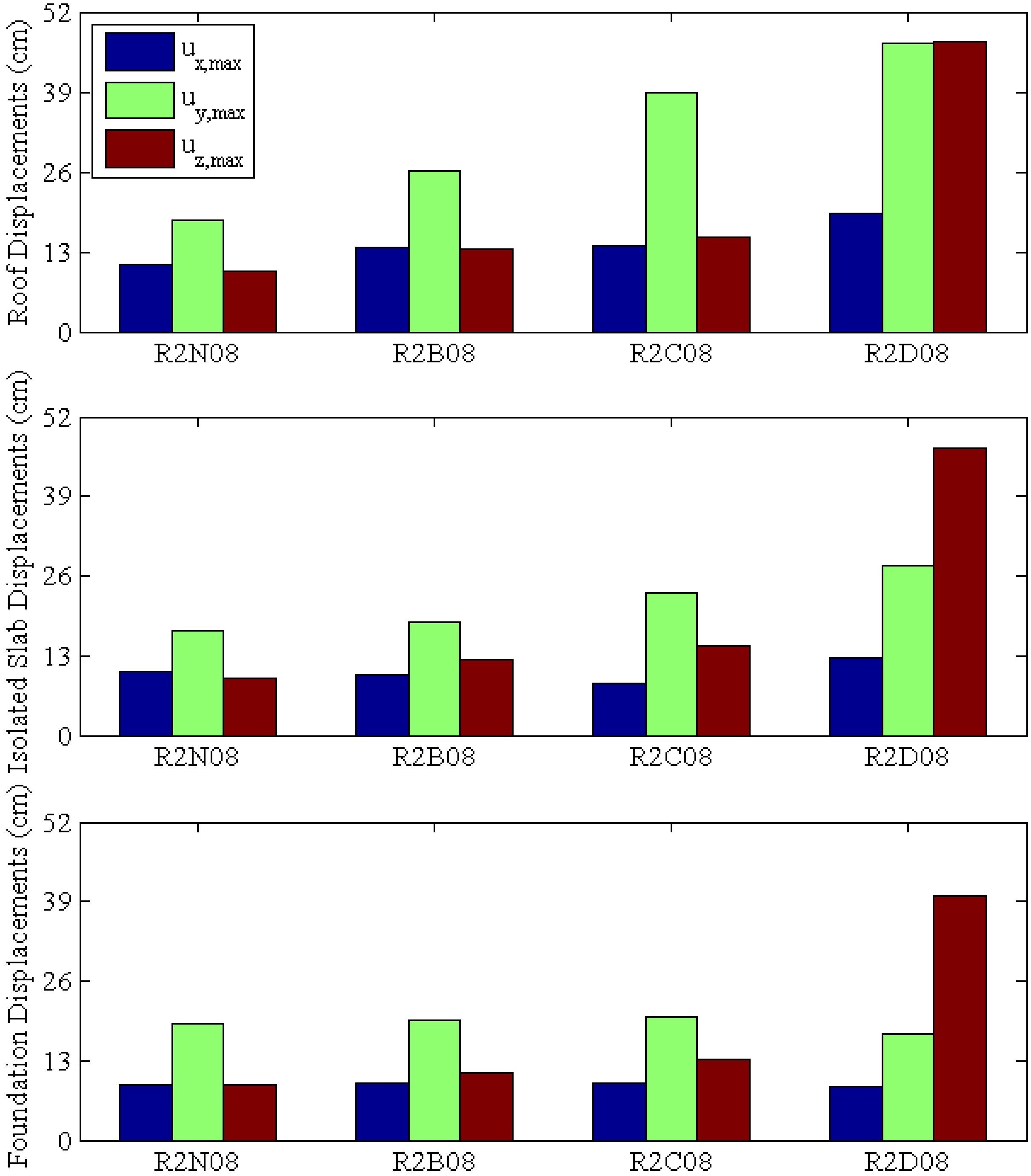

Figure E.2: Peak displacement data from the simulations with the rectangular superstructure and FP isolators subjected to ground motion 08

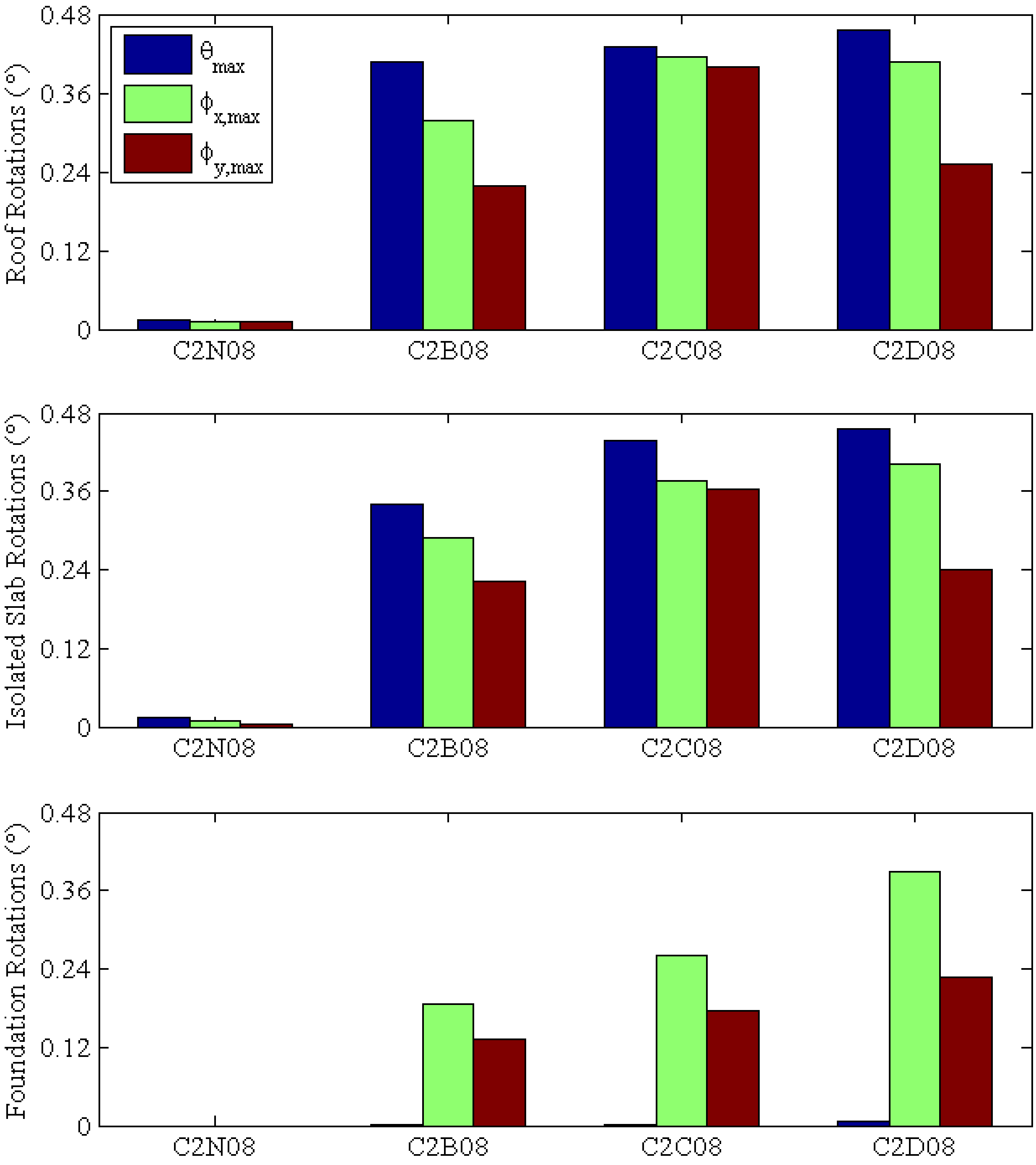

Figure E.3: Peak rotation data from the simulations with the cylindrical superstructure and FP isolators subjected to ground motion 08

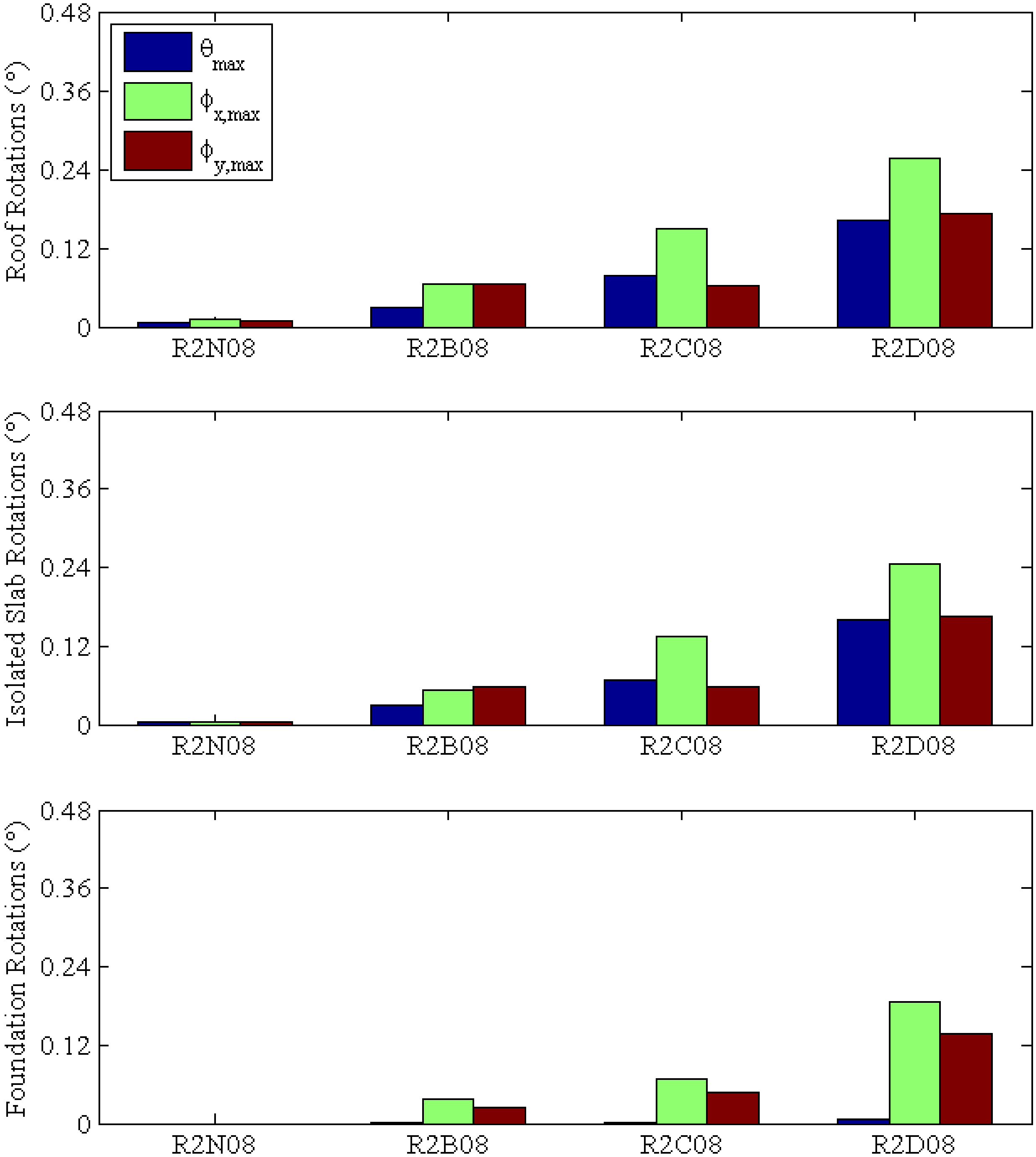

Figure E.4: Peak rotation data from the simulations with the rectangular superstructure and FP isolators subjected to ground motion 08

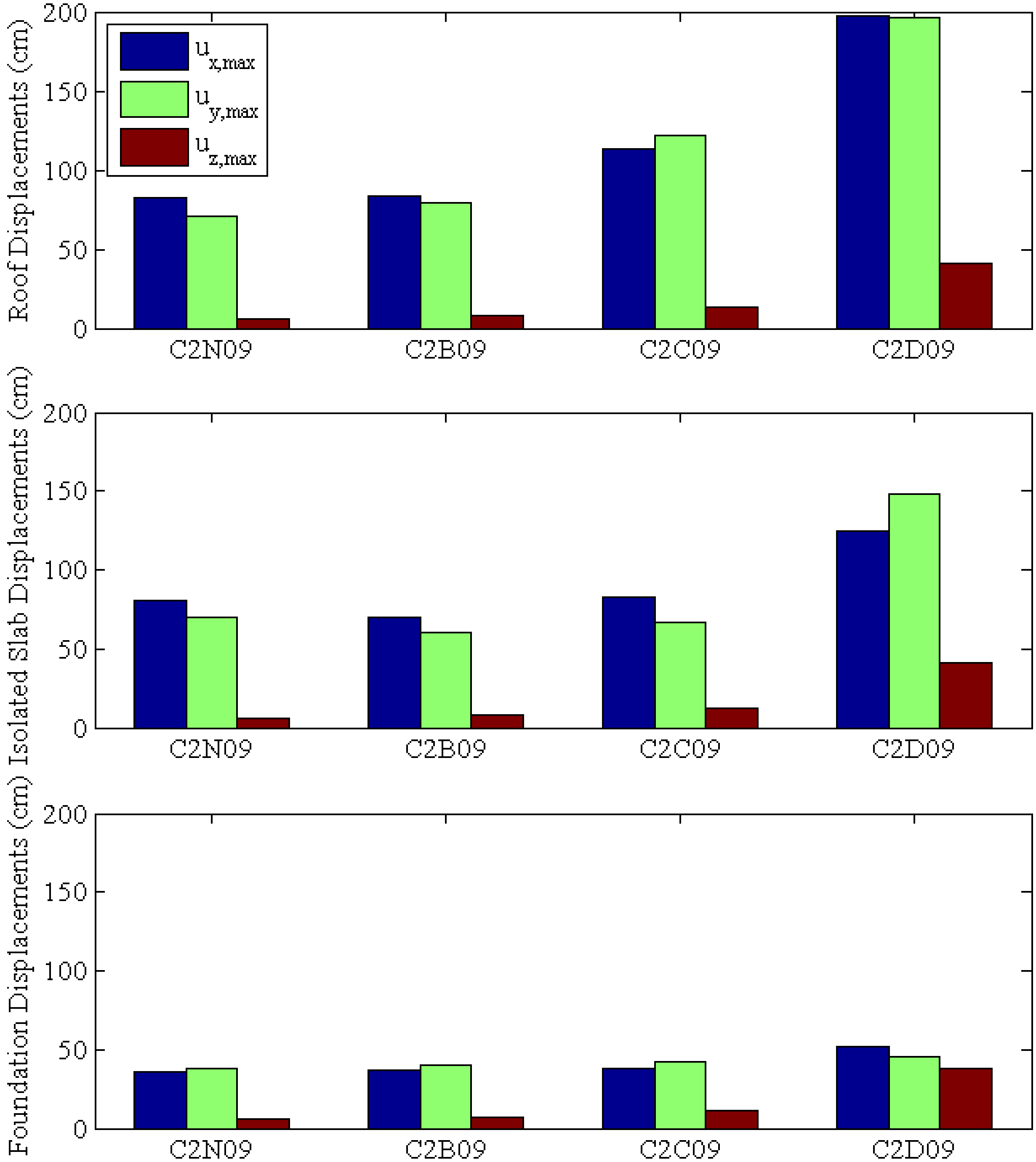

Figure E.5: Peak displacement data from the simulations with the cylindrical superstructure and FP isolators subjected to ground motion 09

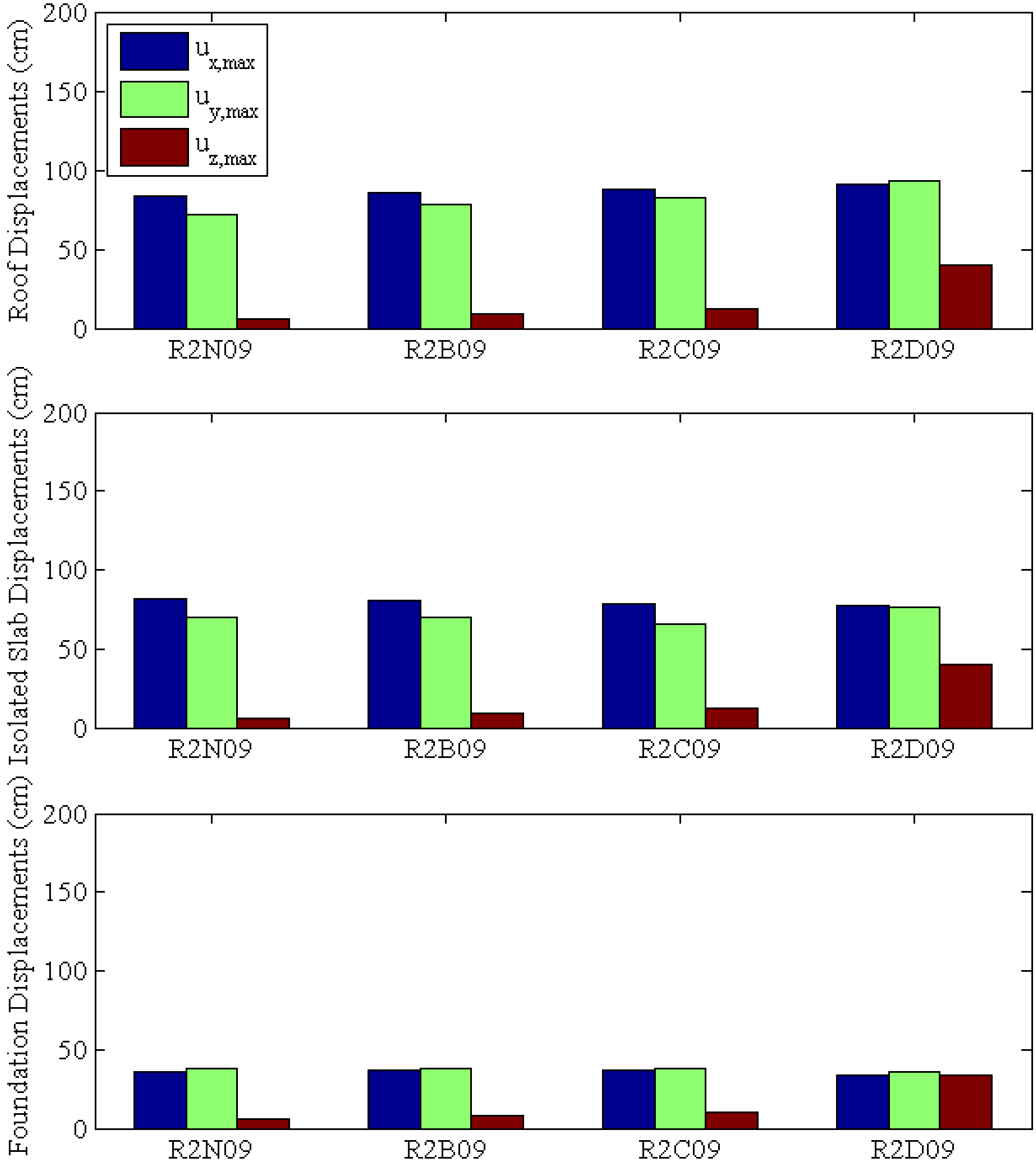

Figure E.6: Peak displacement data from the simulations with the rectangular superstructure and FP isolators subjected to ground motion 09

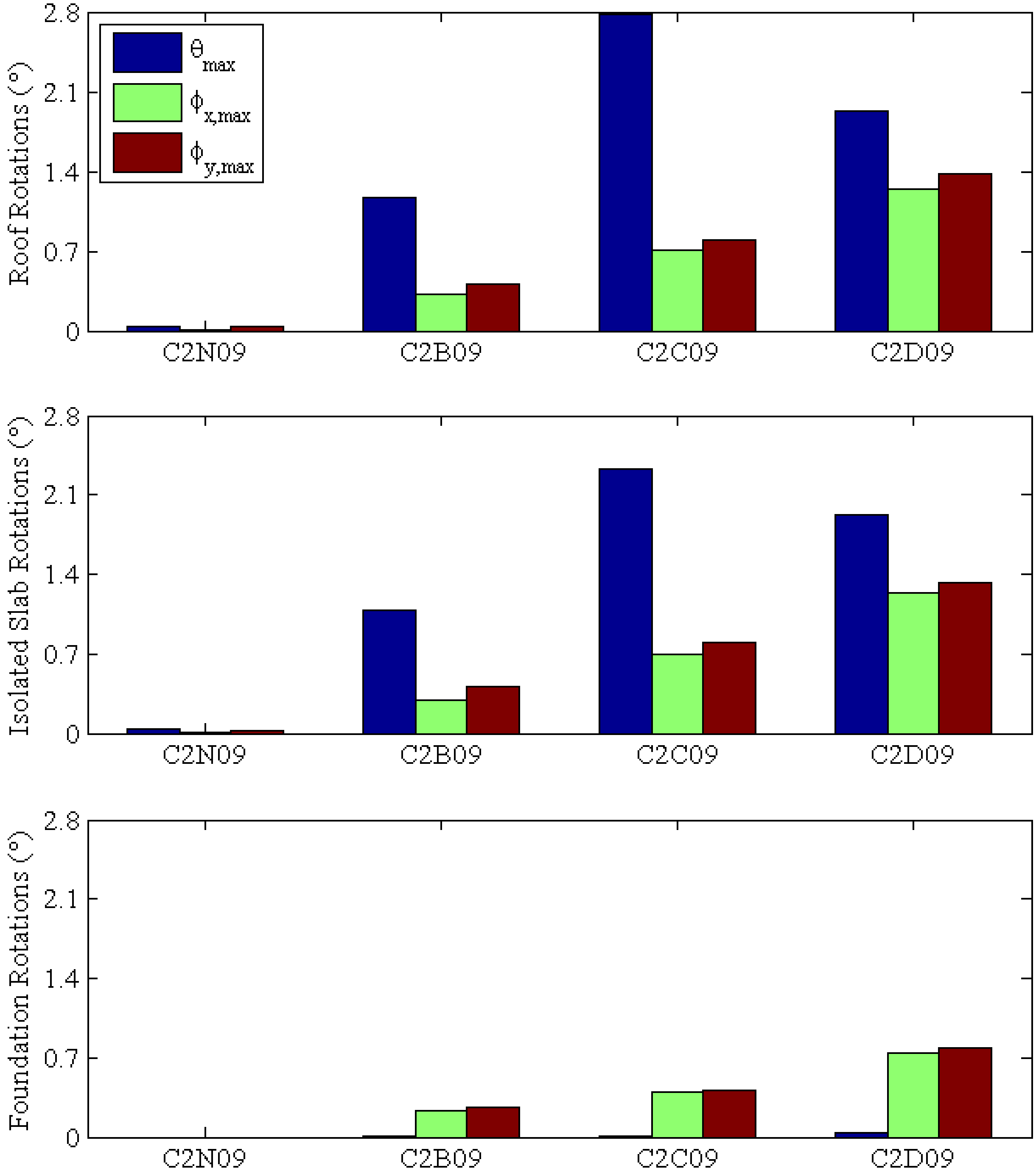

Figure E.7: Peak rotation data from the simulations with the cylindrical superstructure and FP isolators subjected to ground motion 09

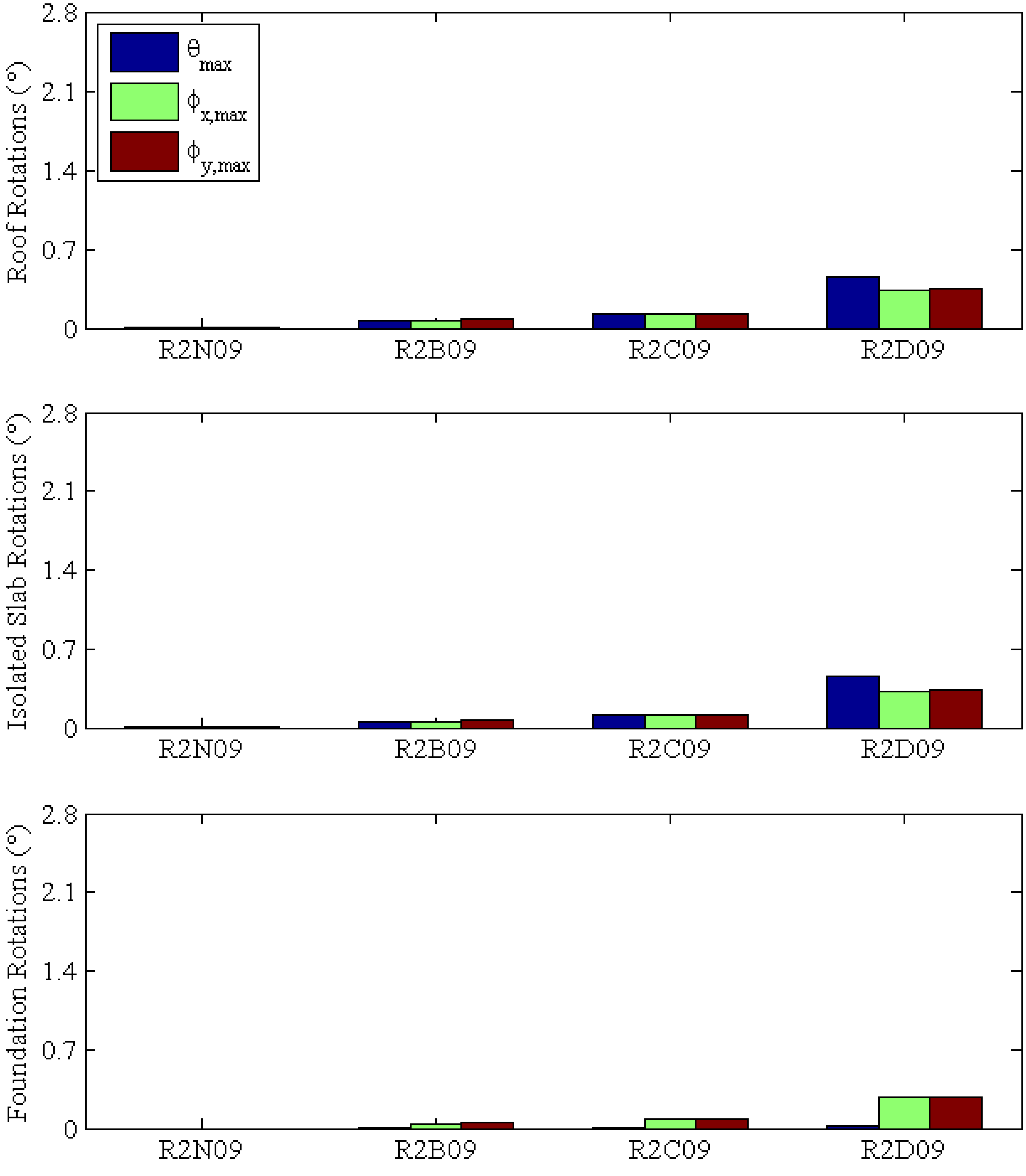

Figure E.8: Peak rotation data from the simulations with the rectangular superstructure and FP isolators subjected to ground motion 09

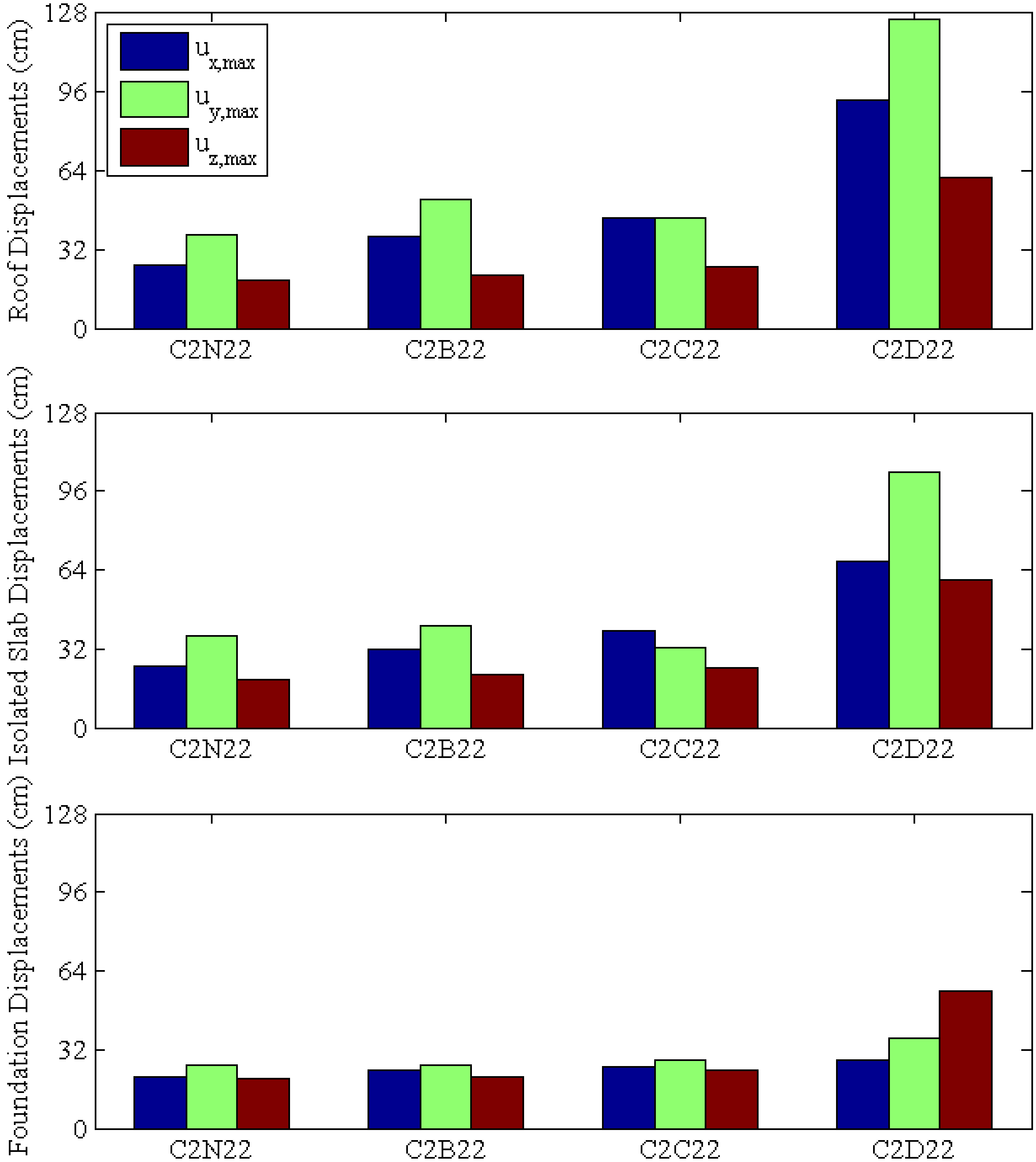

Figure E.9: Peak displacement data from the simulations with the cylindrical superstructure and FP isolators subjected to ground motion 22

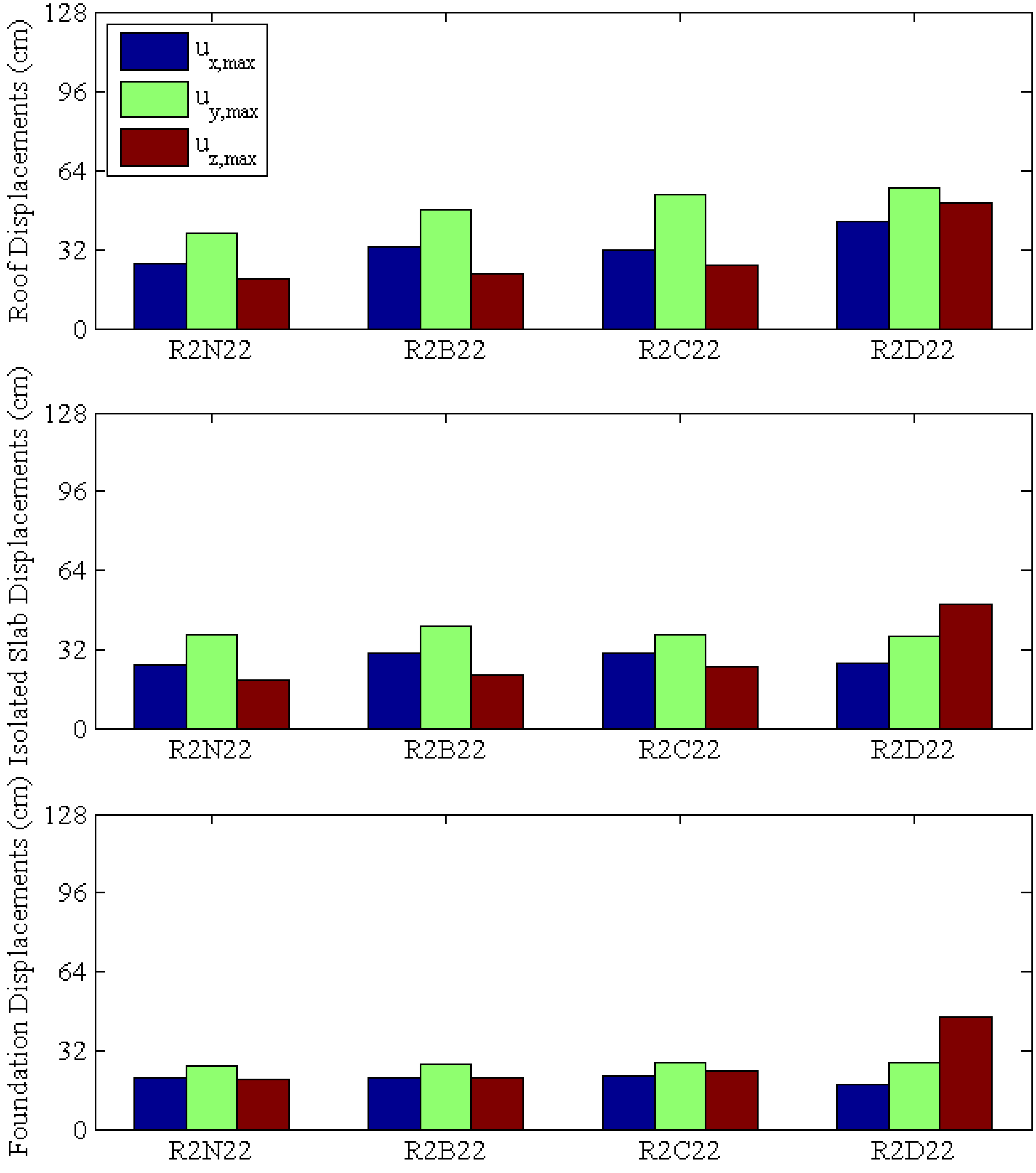

Figure E.10: Peak displacement data from the simulations with the rectangular superstructure and FP isolators subjected to ground motion 22

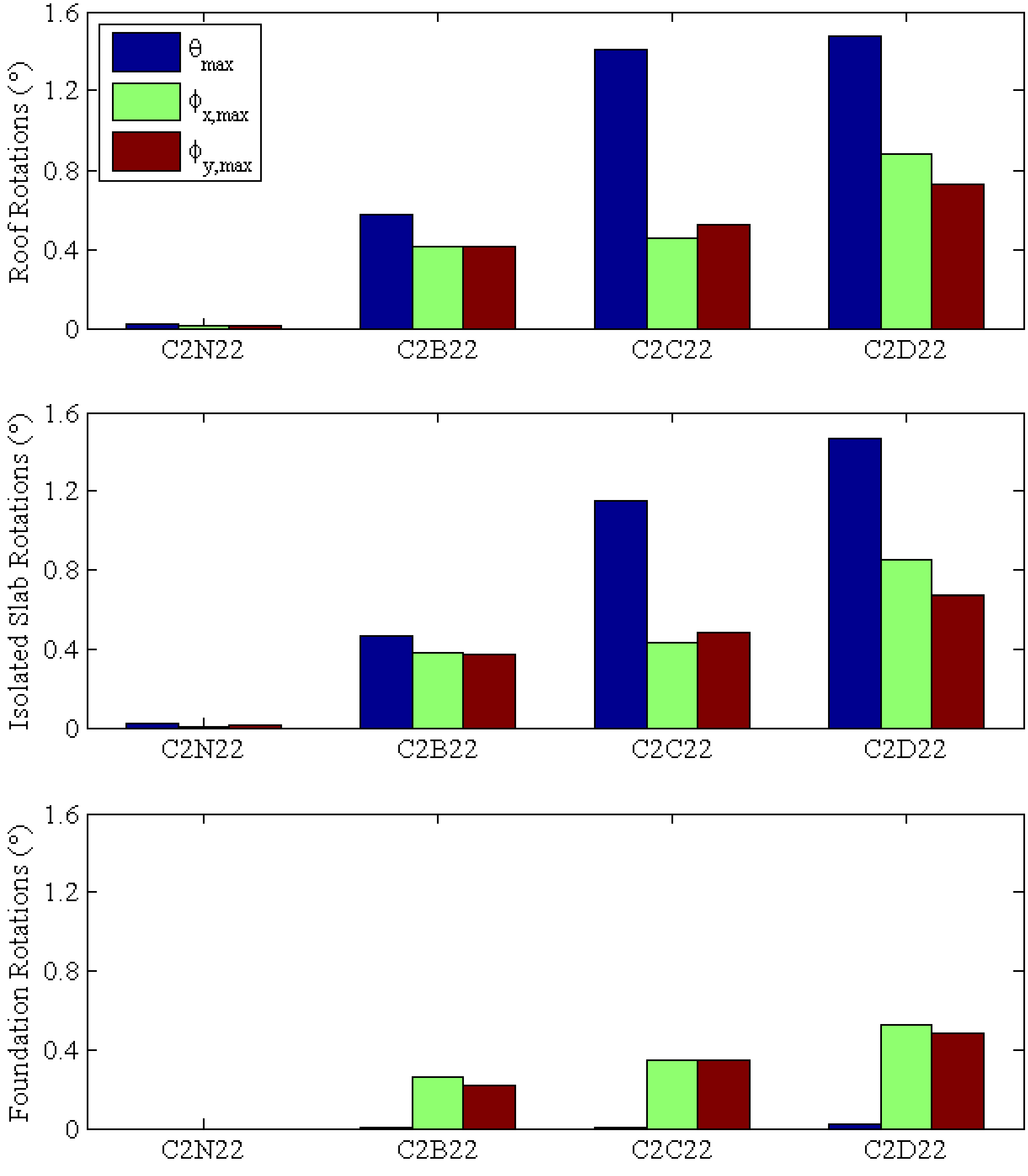

Figure E.11: Peak rotation data from the simulations with the cylindrical superstructure and FP isolators subjected to ground motion 22

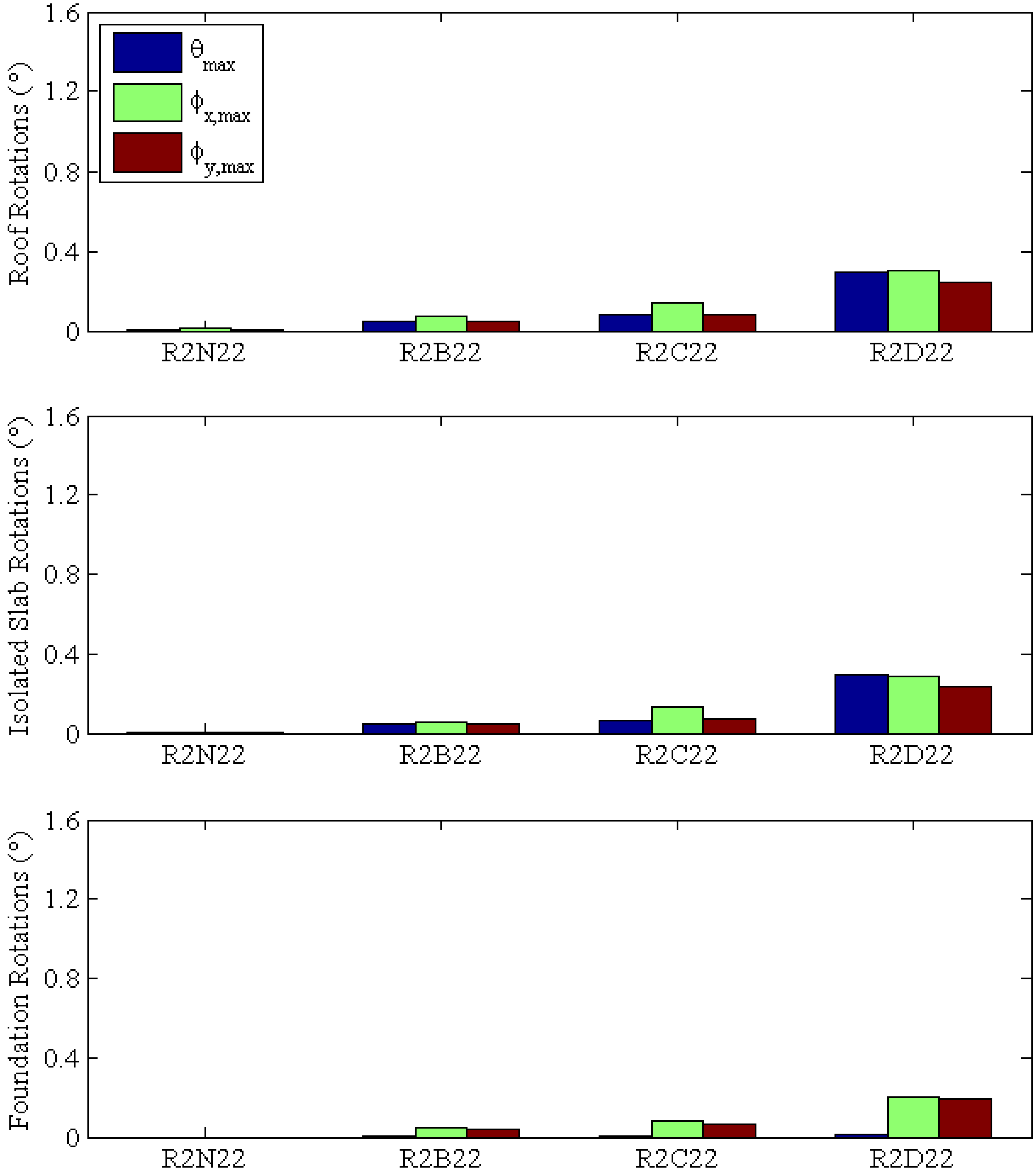

Figure E.12: Peak rotation data from the simulations with the rectangular superstructure and FP isolators subjected to ground motion 22

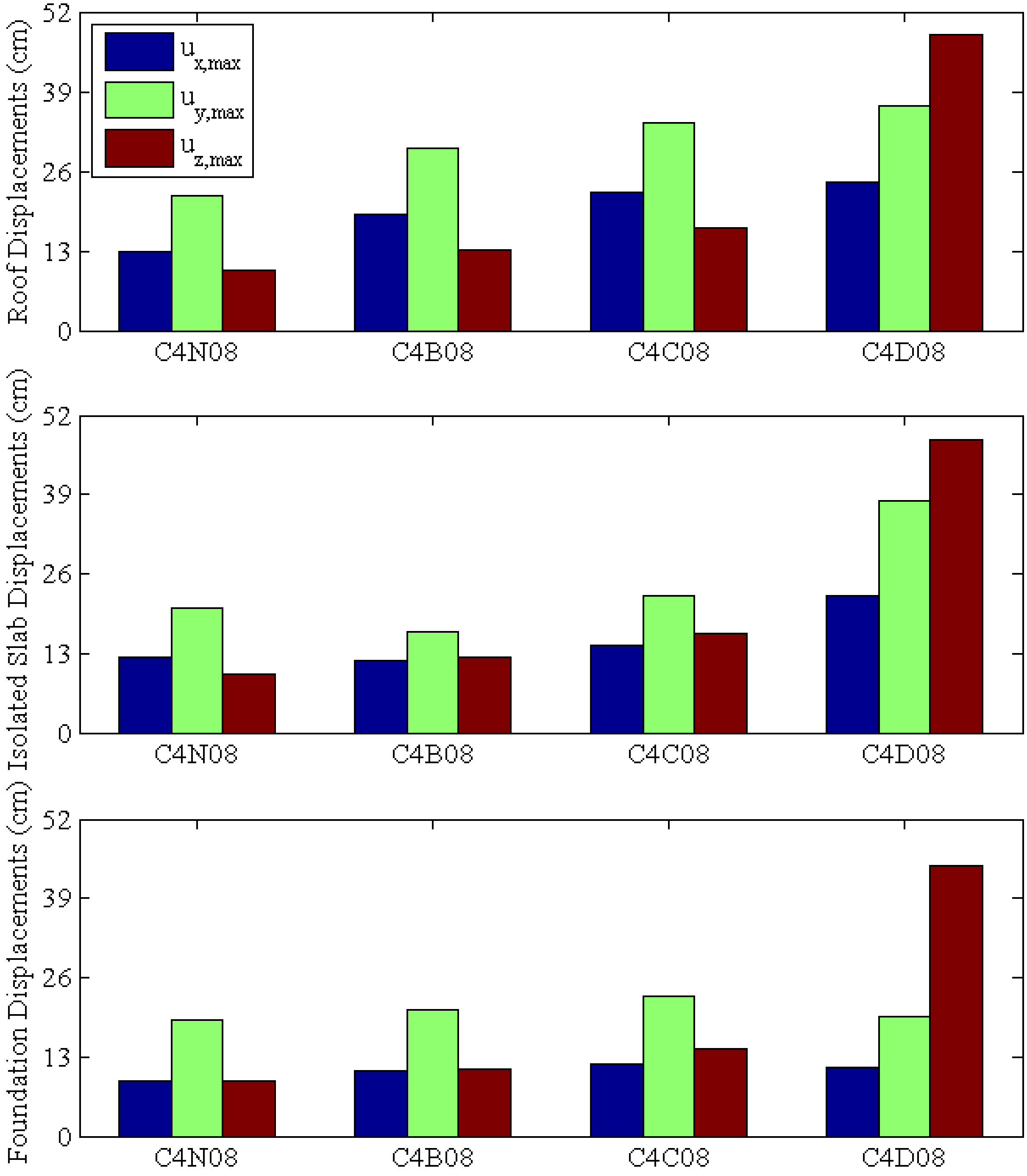

Figure E.13: Peak displacement data from the simulations with the cylindrical superstructure and simple LR isolators subjected to ground motion 08

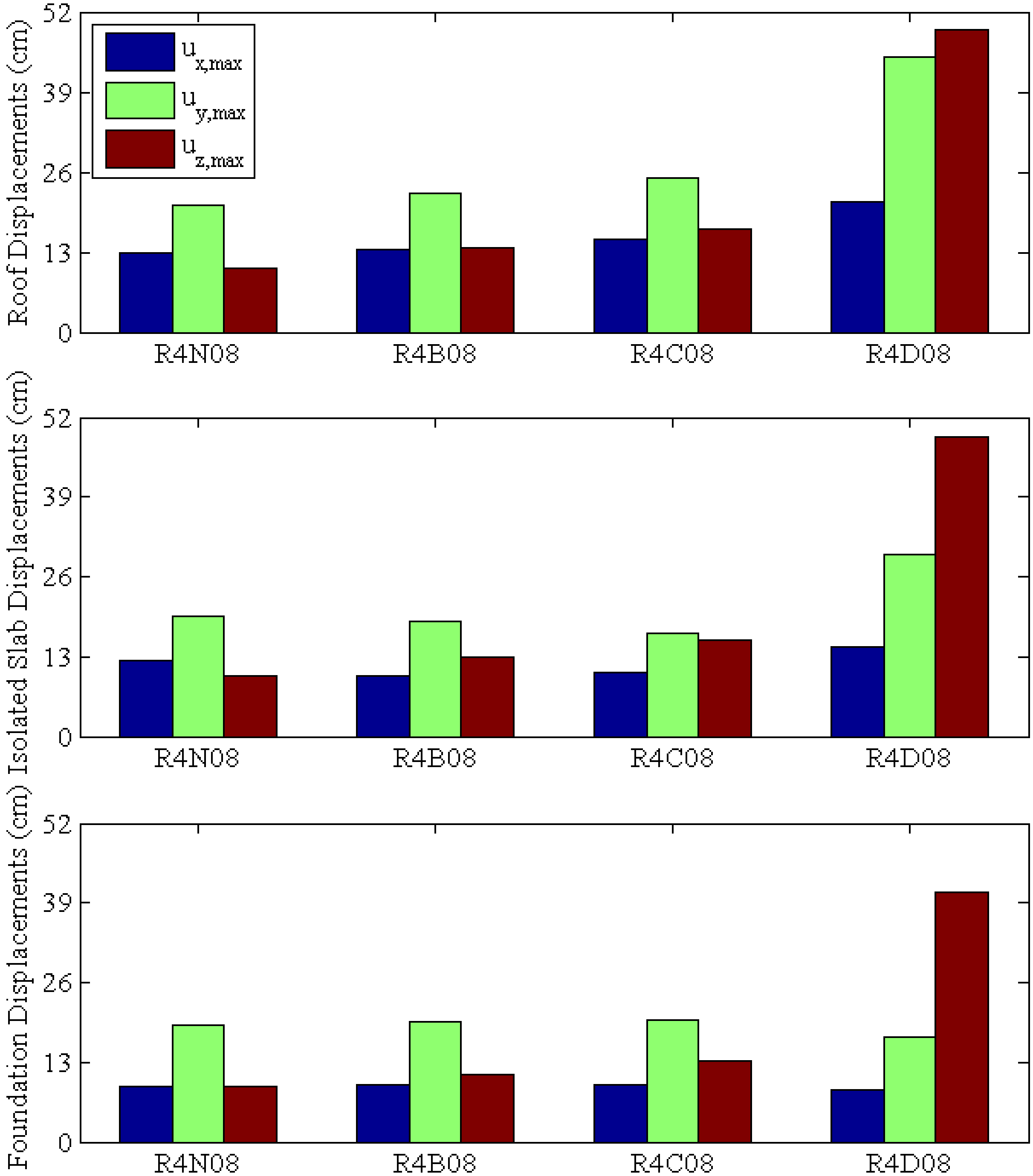

Figure E.14: Peak displacement data from the simulations with the rectangular superstructure and simple LR isolators subjected to ground motion 08

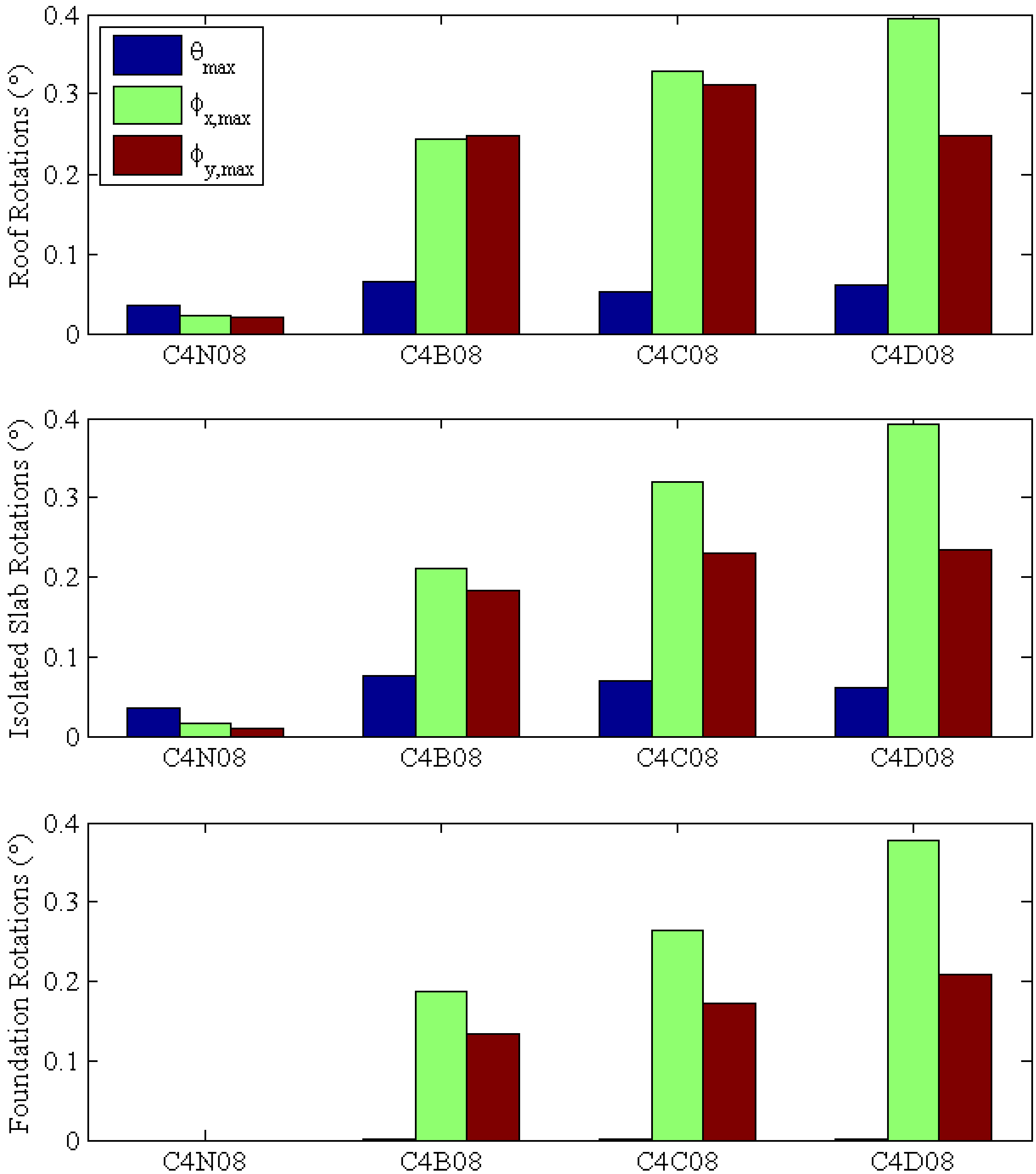

Figure E.15: Peak rotation data from the simulations with the cylindrical superstructure and simple LR isolators subjected to ground motion 08

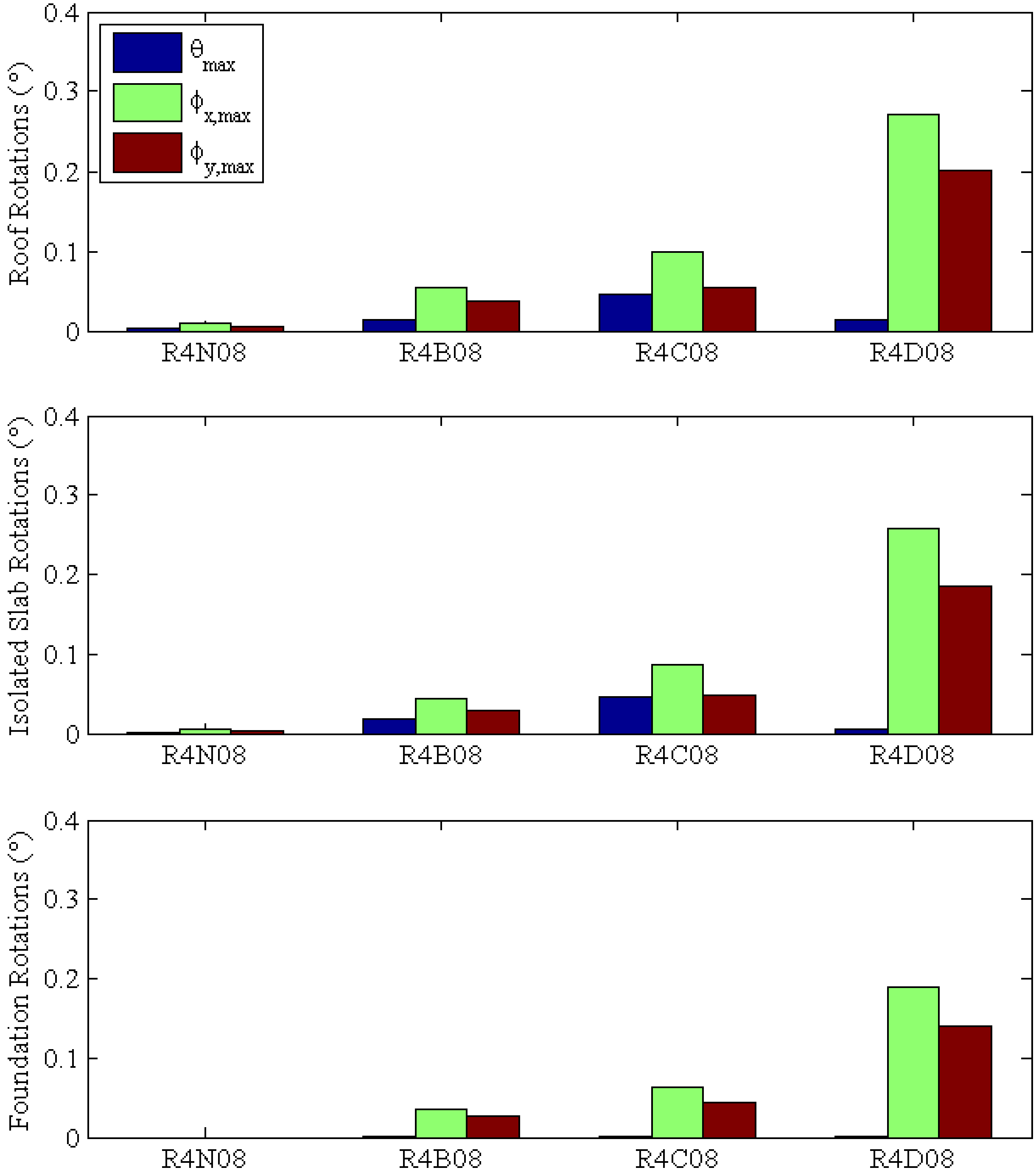

Figure E.16: Peak rotation data from the simulations with the rectangular superstructure and simple LR isolators subjected to ground motion 08

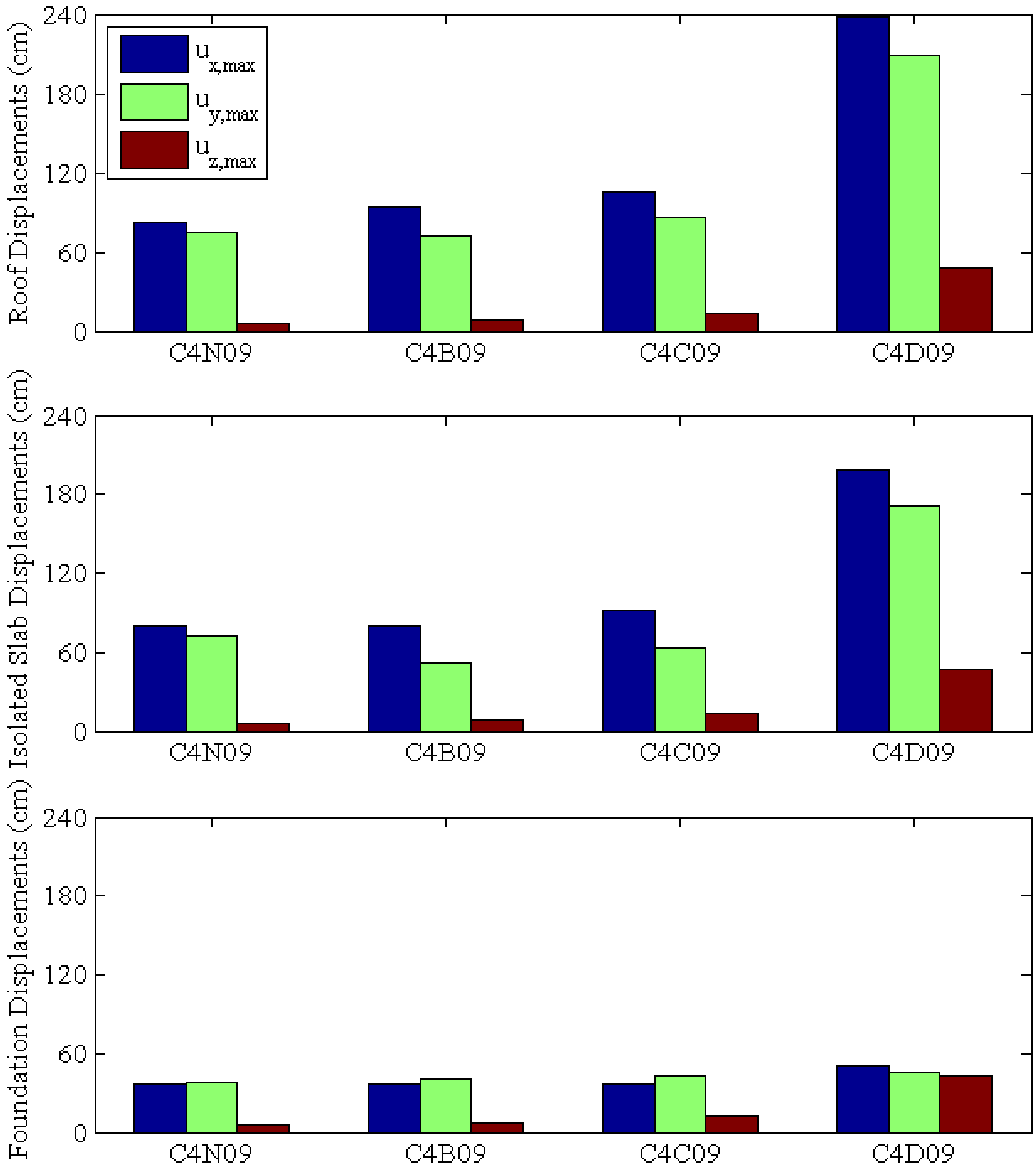

Figure E.17: Peak displacement data from the simulations with the cylindrical superstructure and simple LR isolators subjected to ground motion 09

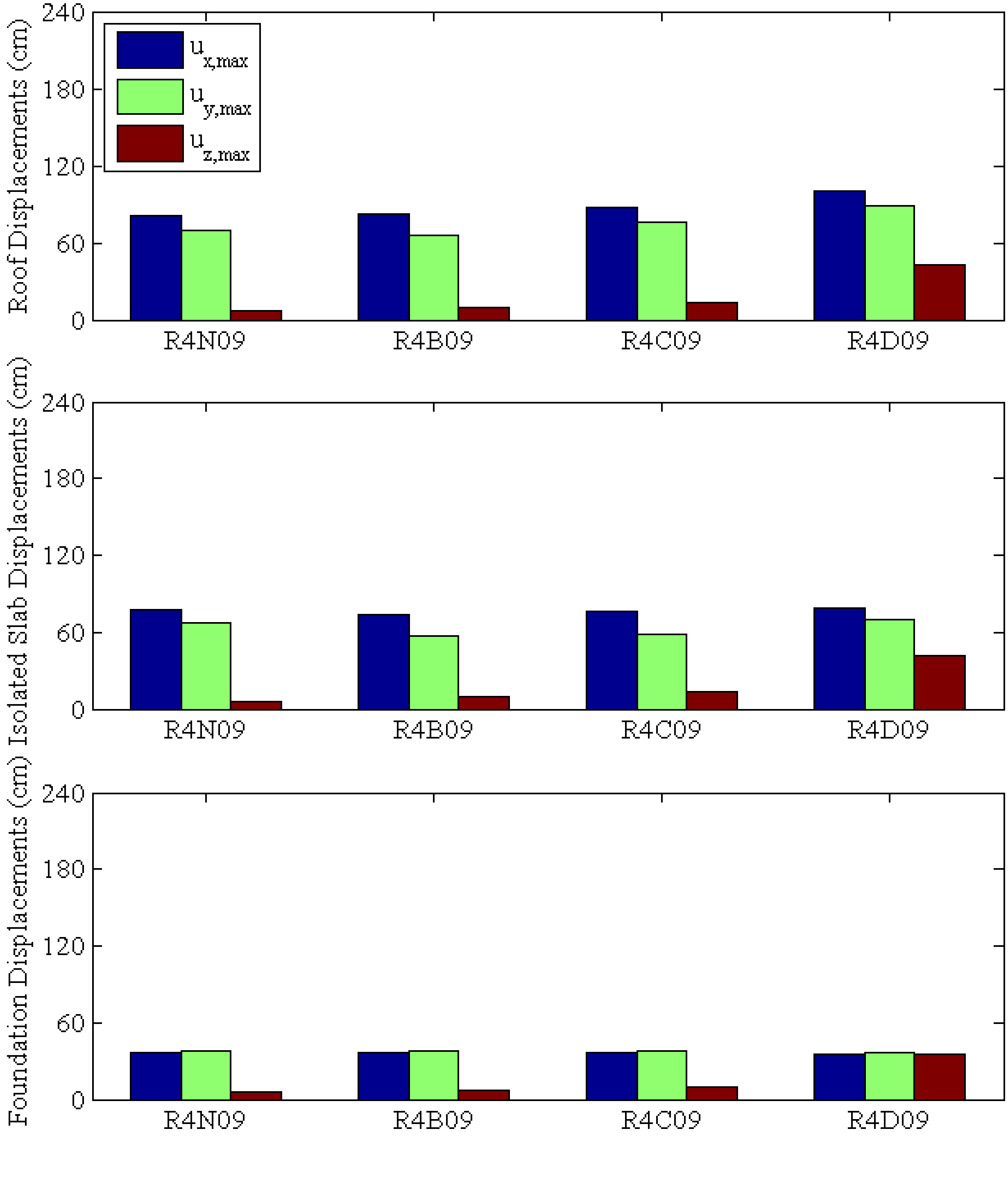

Figure E.18: Peak displacement data from the simulations with the rectangular superstructure and simple LR isolators subjected to ground motion 09

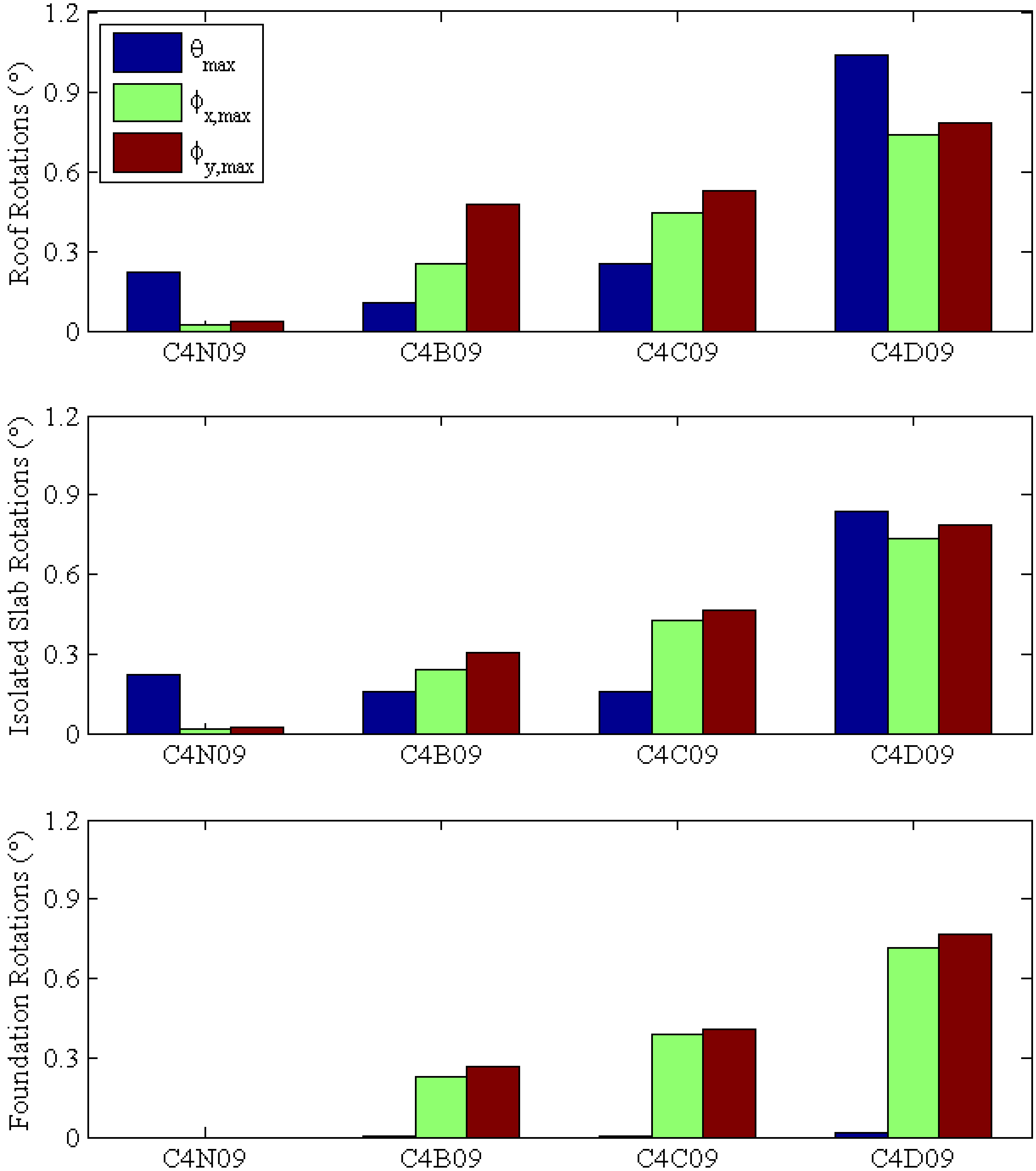

Figure E.19: Peak rotation data from the simulations with the cylindrical superstructure and simple LR isolators subjected to ground motion 09

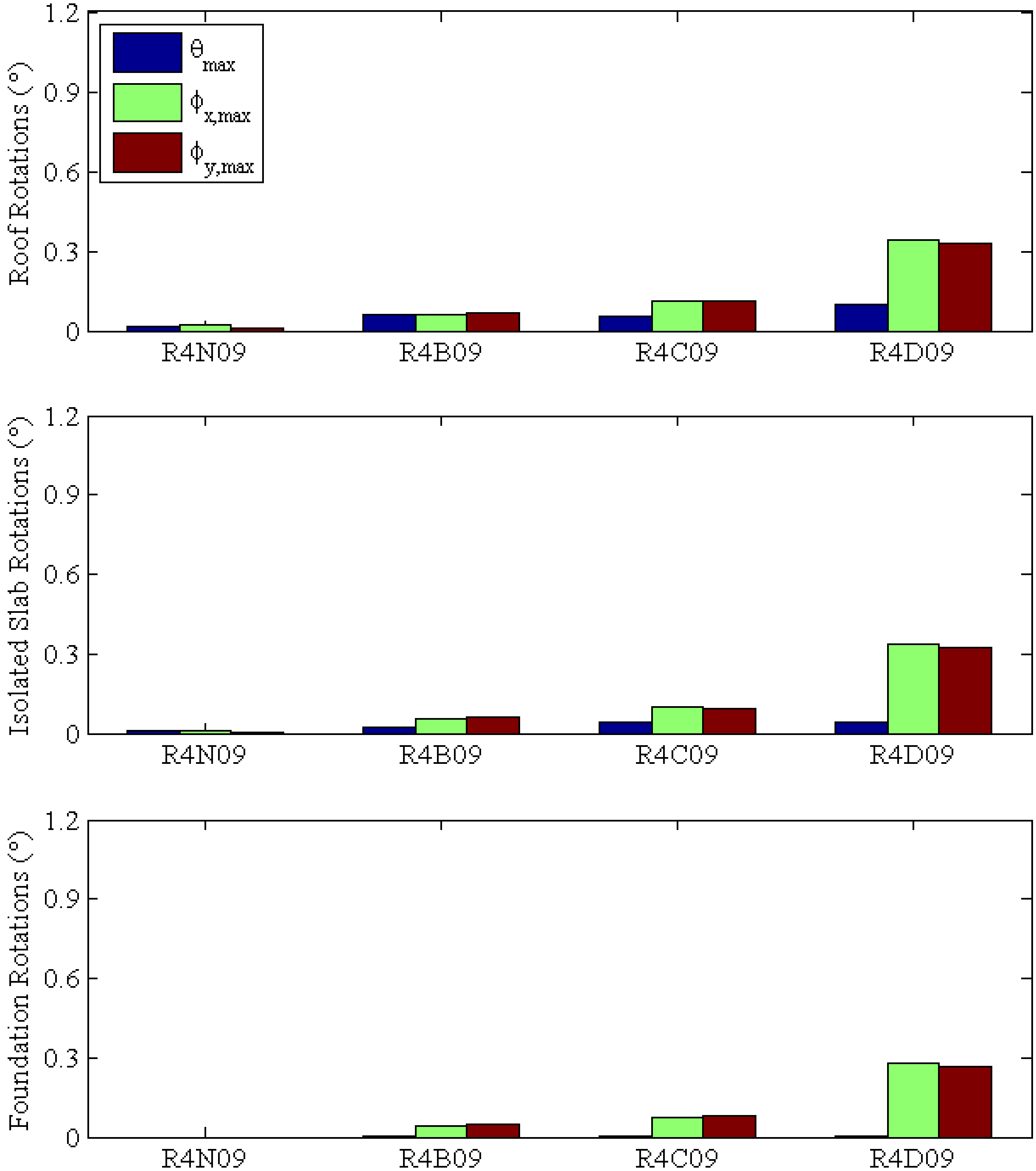

Figure E.20: Peak rotation data from the simulations with the rectangular superstructure and simple LR isolators subjected to ground motion 09

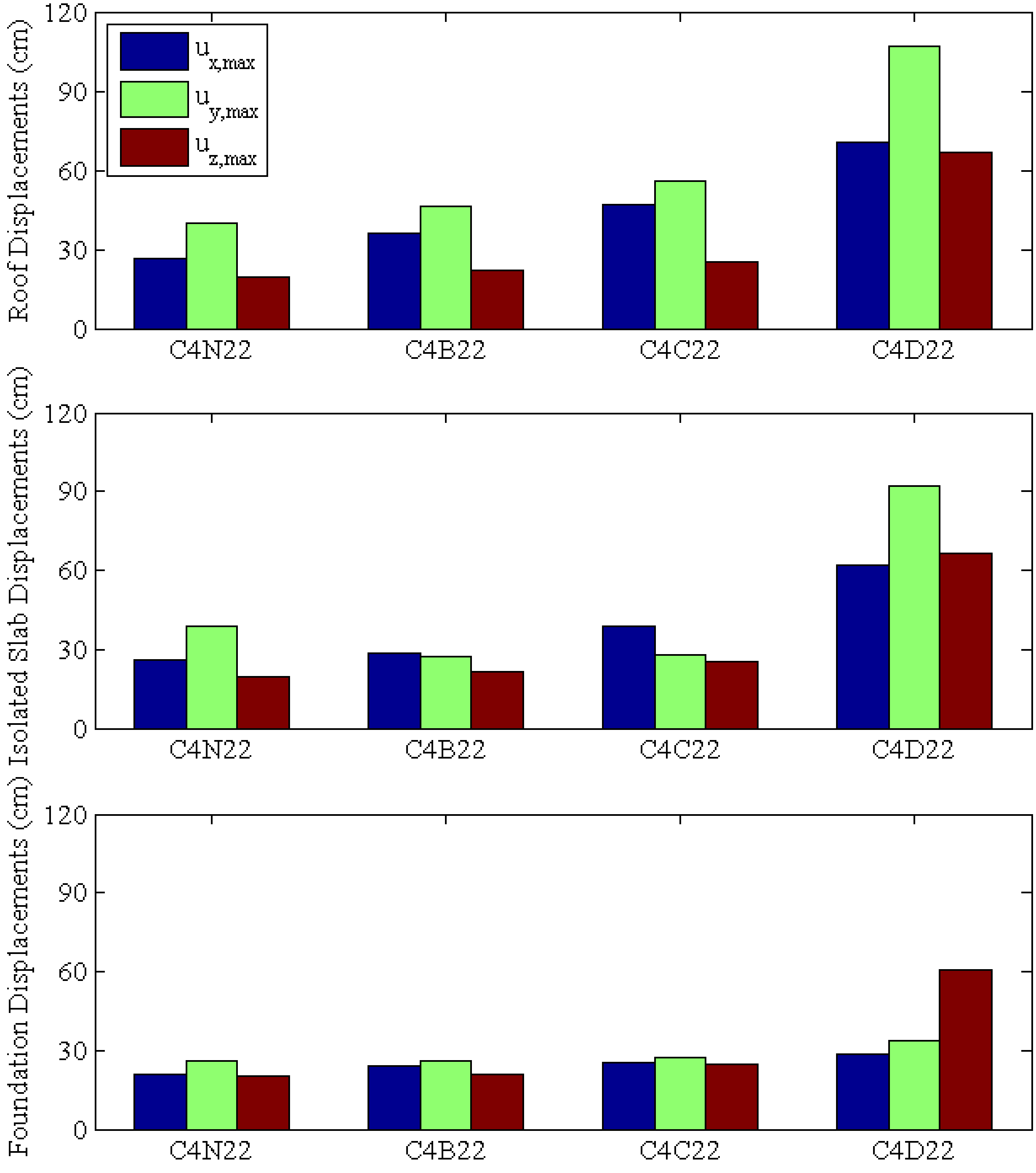

Figure E.21: Peak displacement data from the simulations with the cylindrical superstructure and simple LR isolators subjected to ground motion 22

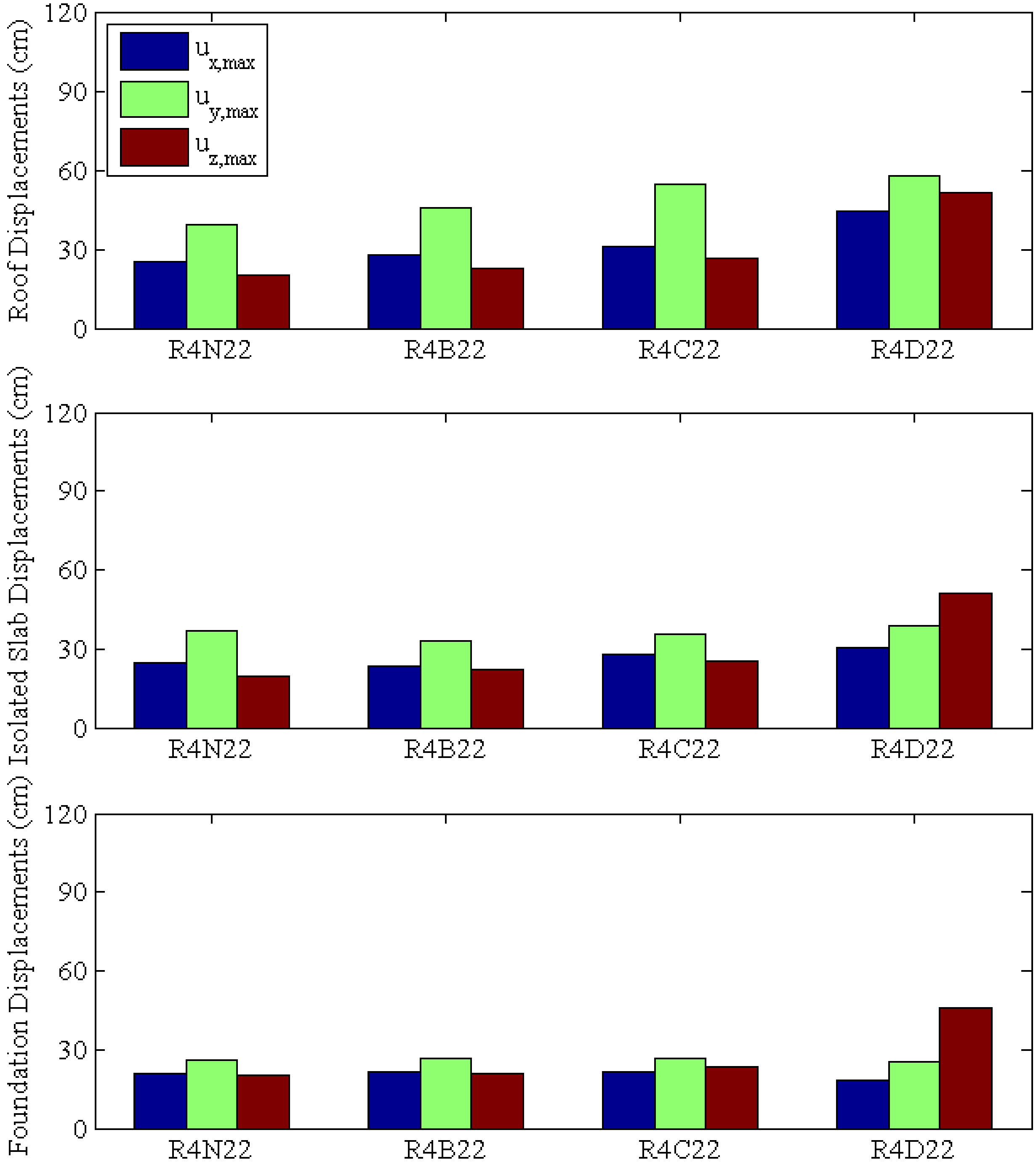

Figure E.22: Peak displacement data from the simulations with the rectangular superstructure and simple LR isolators subjected to ground motion 22

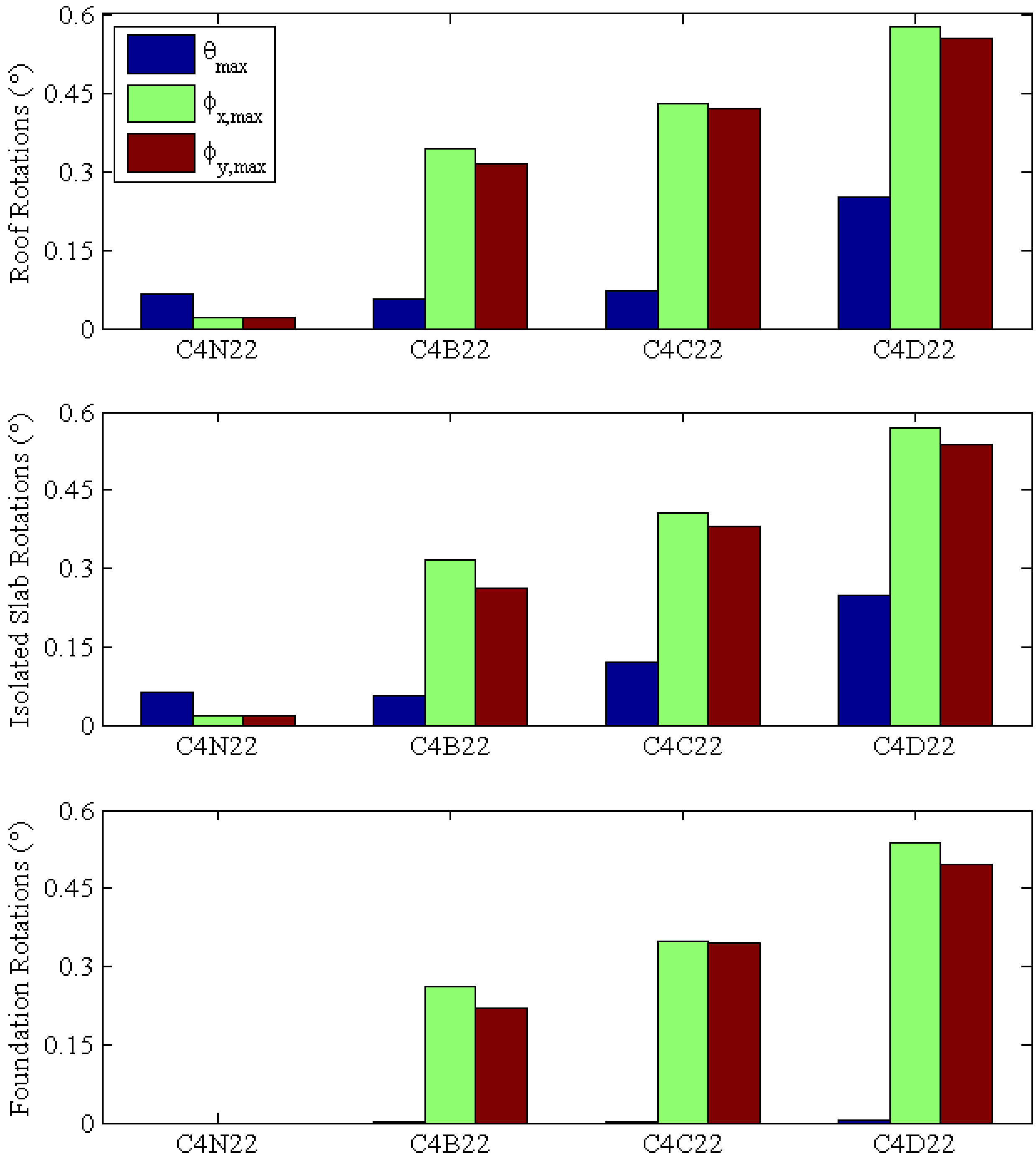

Figure E.23: Peak rotation data from the simulations with the cylindrical superstructure and simple LR isolators subjected to ground motion 22

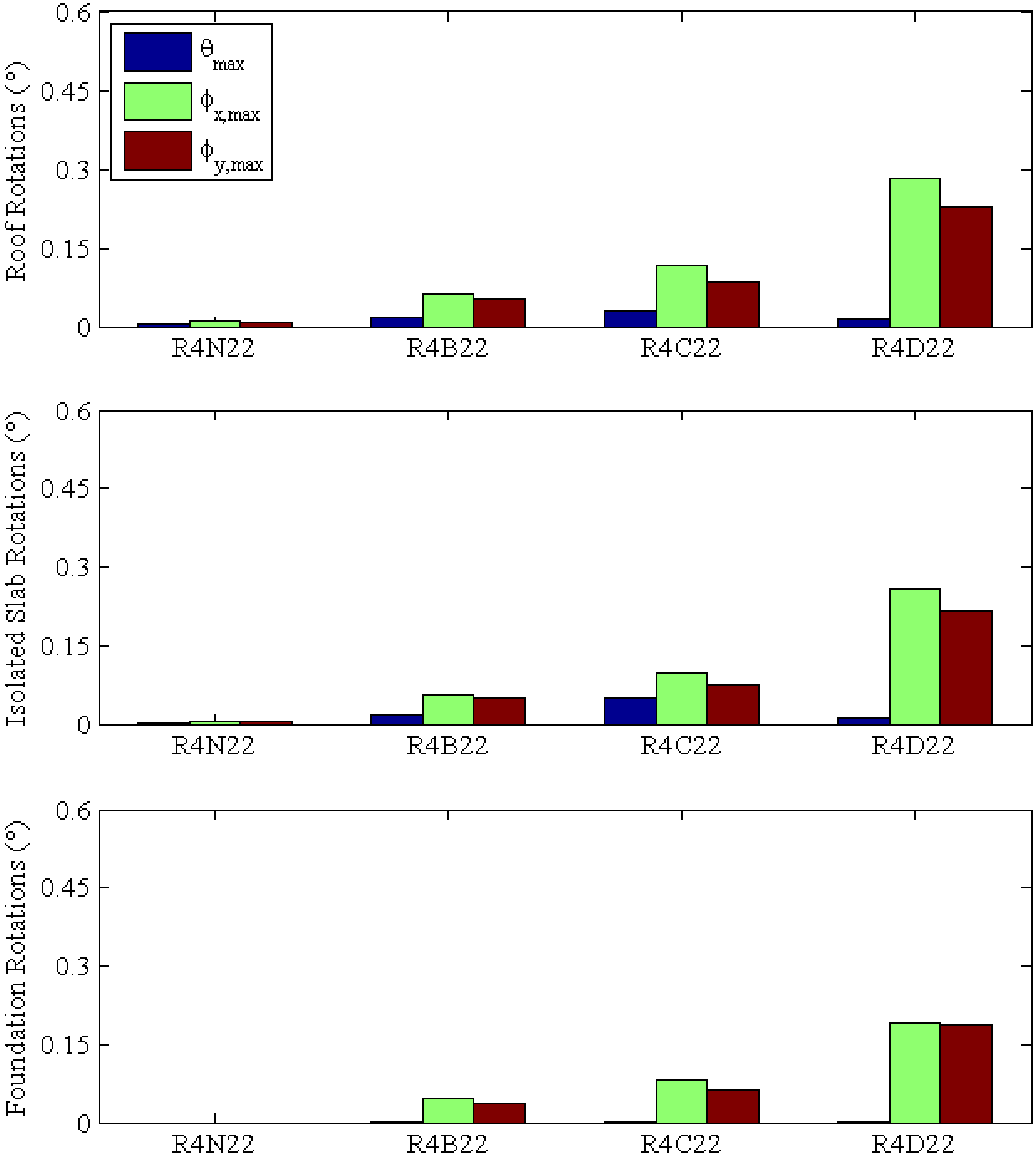

Figure E.24: Peak rotation data from the simulations with the rectangular superstructure and simple LR isolators subjected to ground motion 22

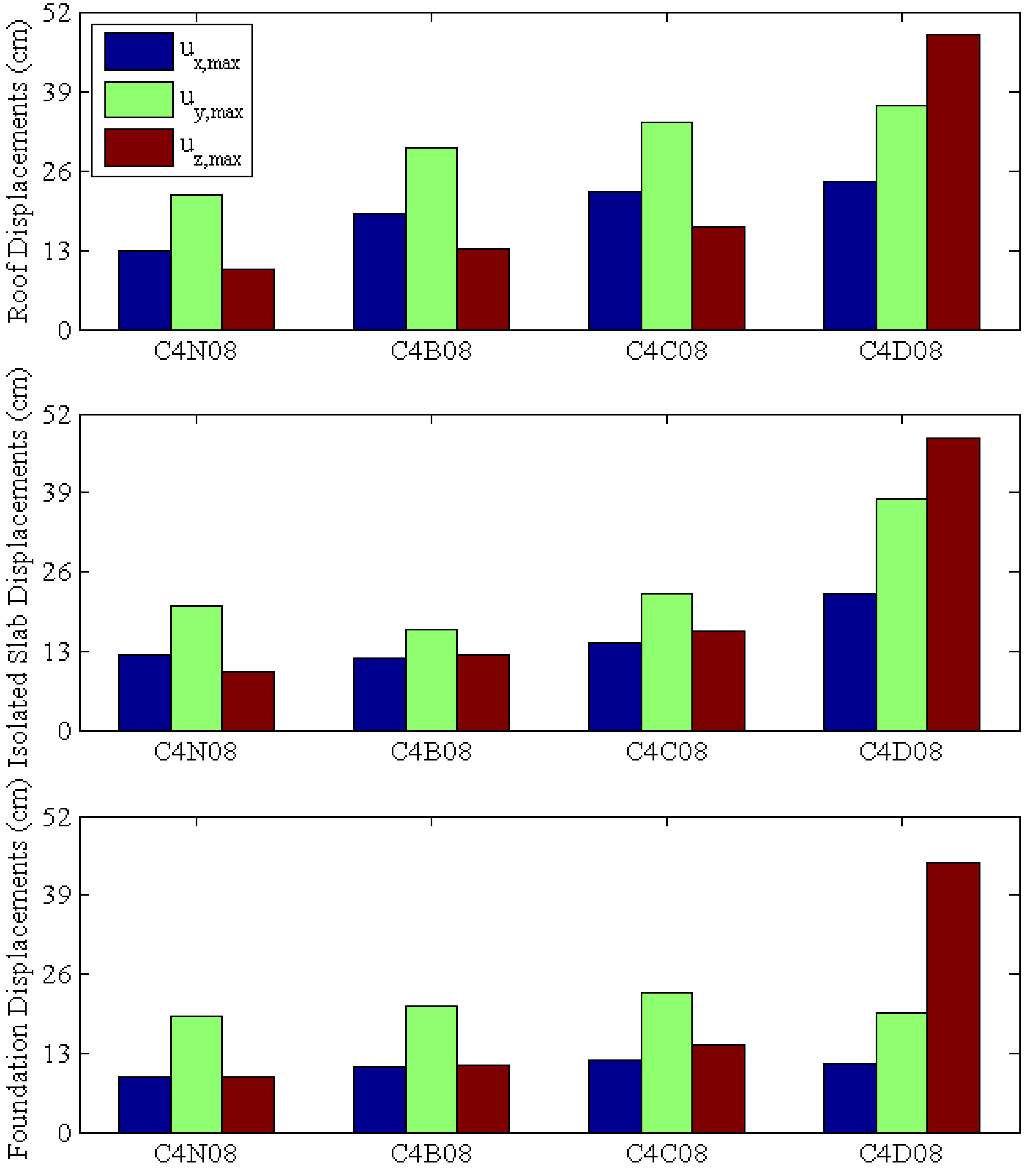

Figure E.25: Peak displacement data from the simulations with the cylindrical superstructure and robust LR isolators subjected to ground motion 08

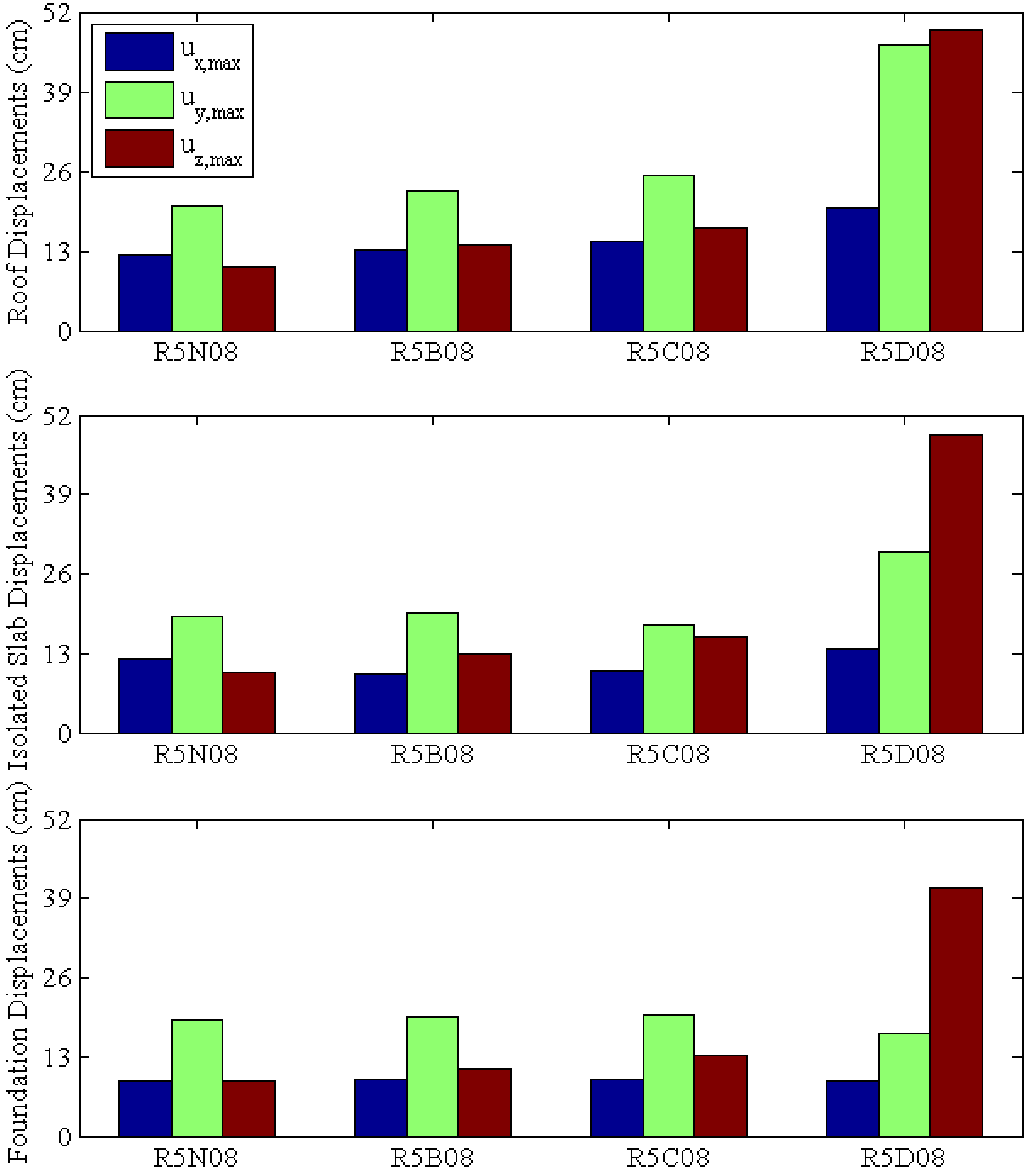

Figure E.26: Peak displacement data from the simulations with the rectangular superstructure and robust LR isolators subjected to ground motion 08

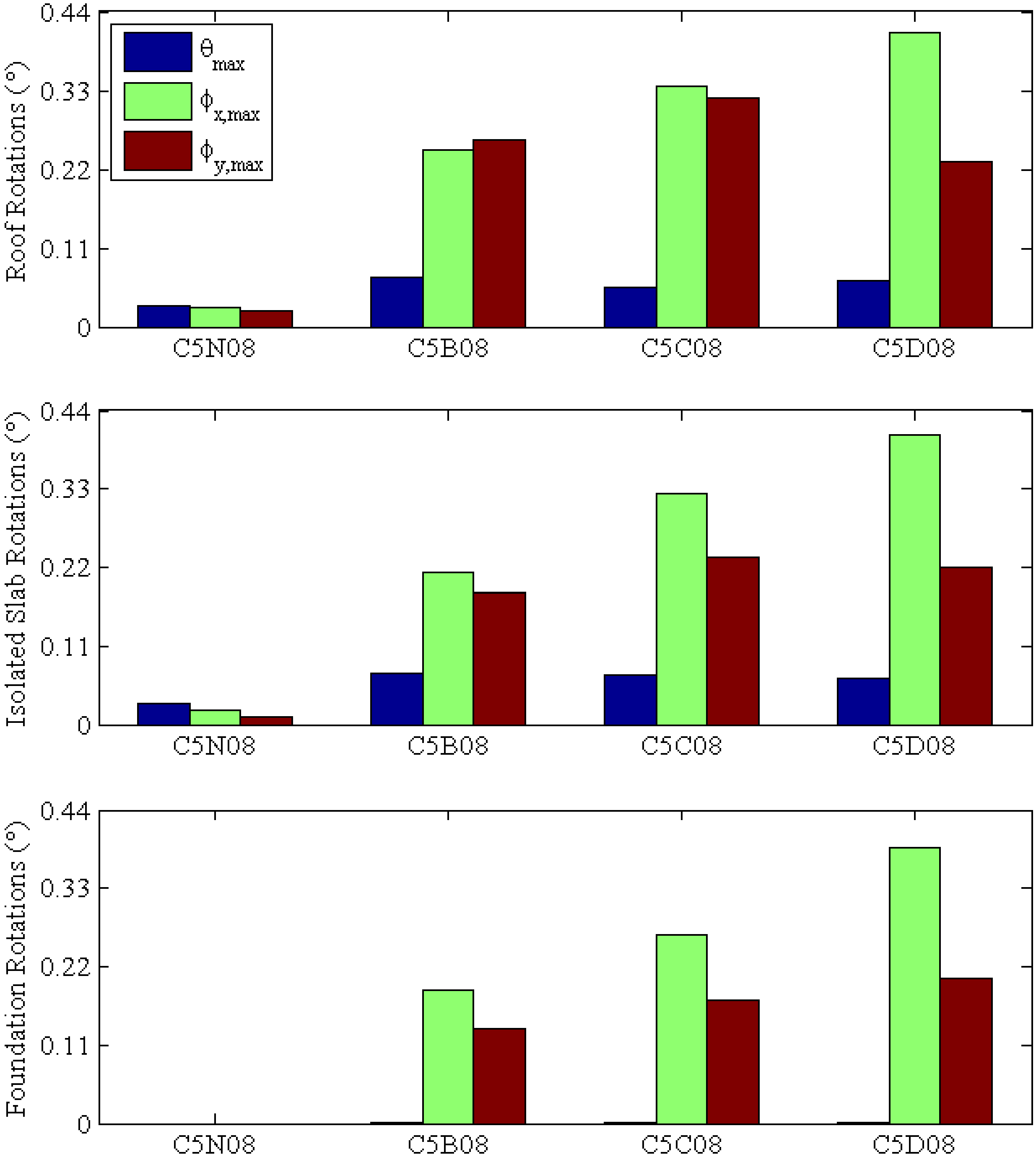

Figure E.27: Peak rotation data from the simulations with the cylindrical superstructure and robust LR isolators subjected to ground motion 08

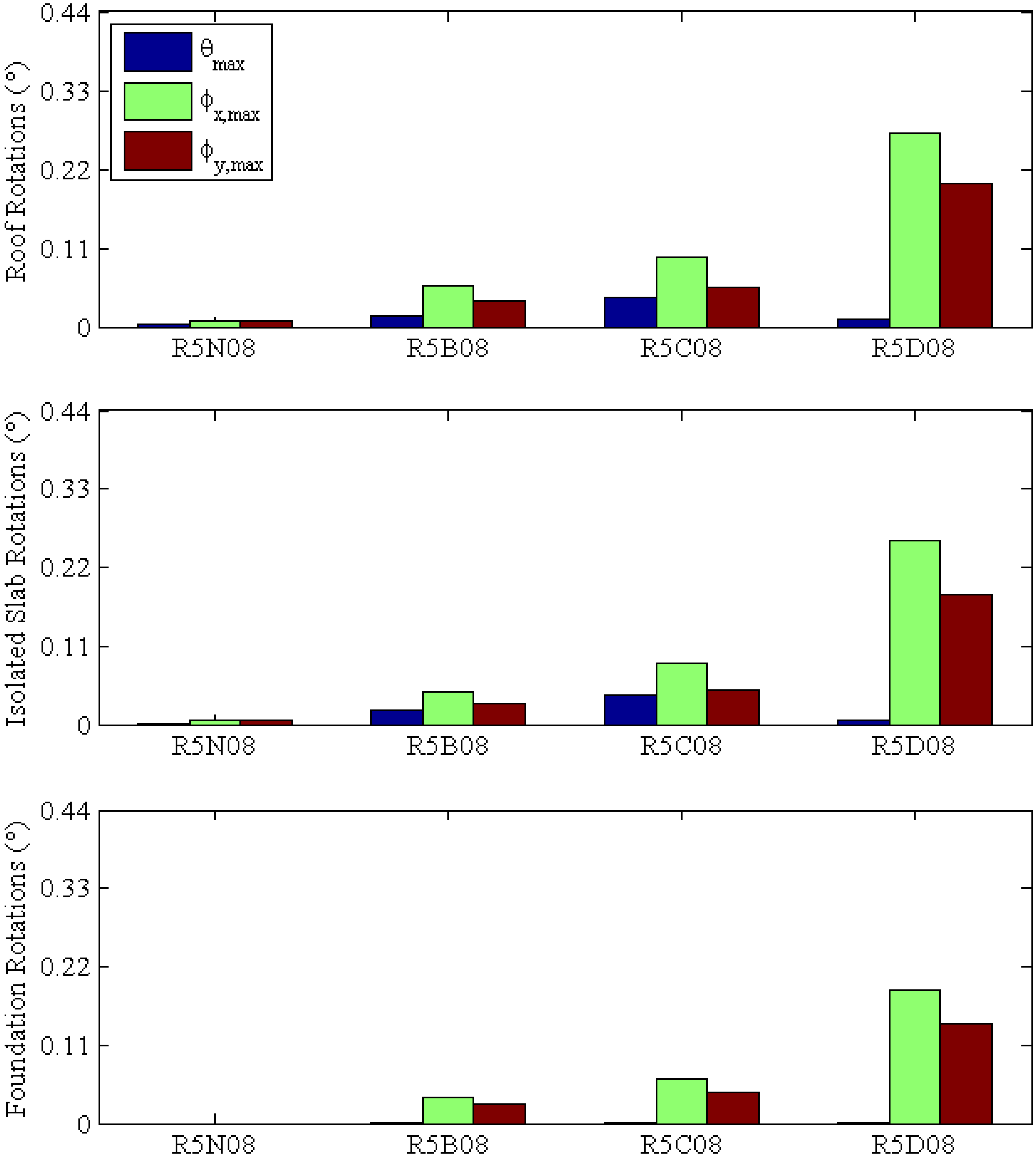

Figure E.28: Peak rotation data from the simulations with the rectangular superstructure and robust LR isolators subjected to ground motion 08

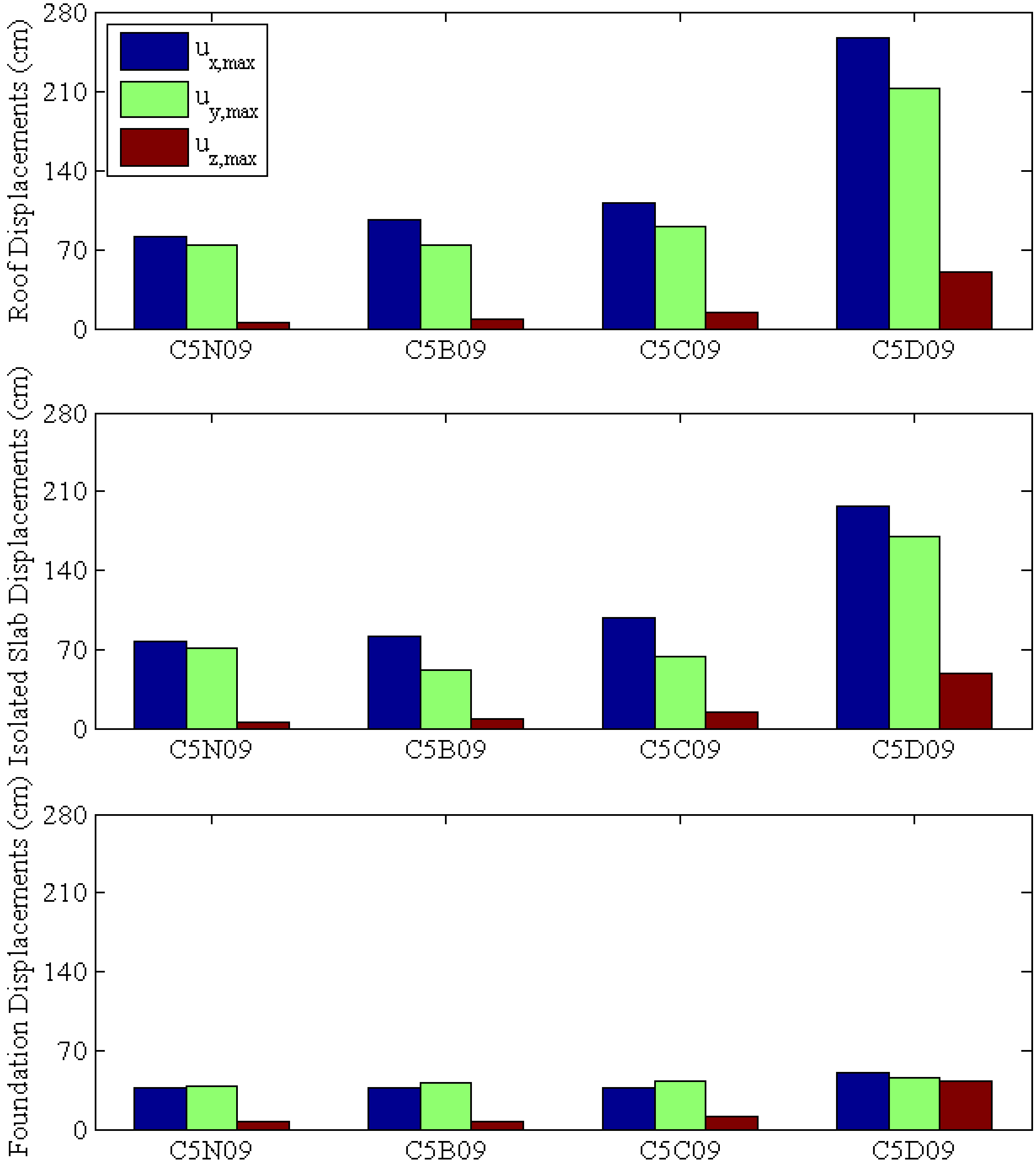

Figure E.29: Peak displacement data from the simulations with the cylindrical superstructure and robust LR isolators subjected to ground motion 09

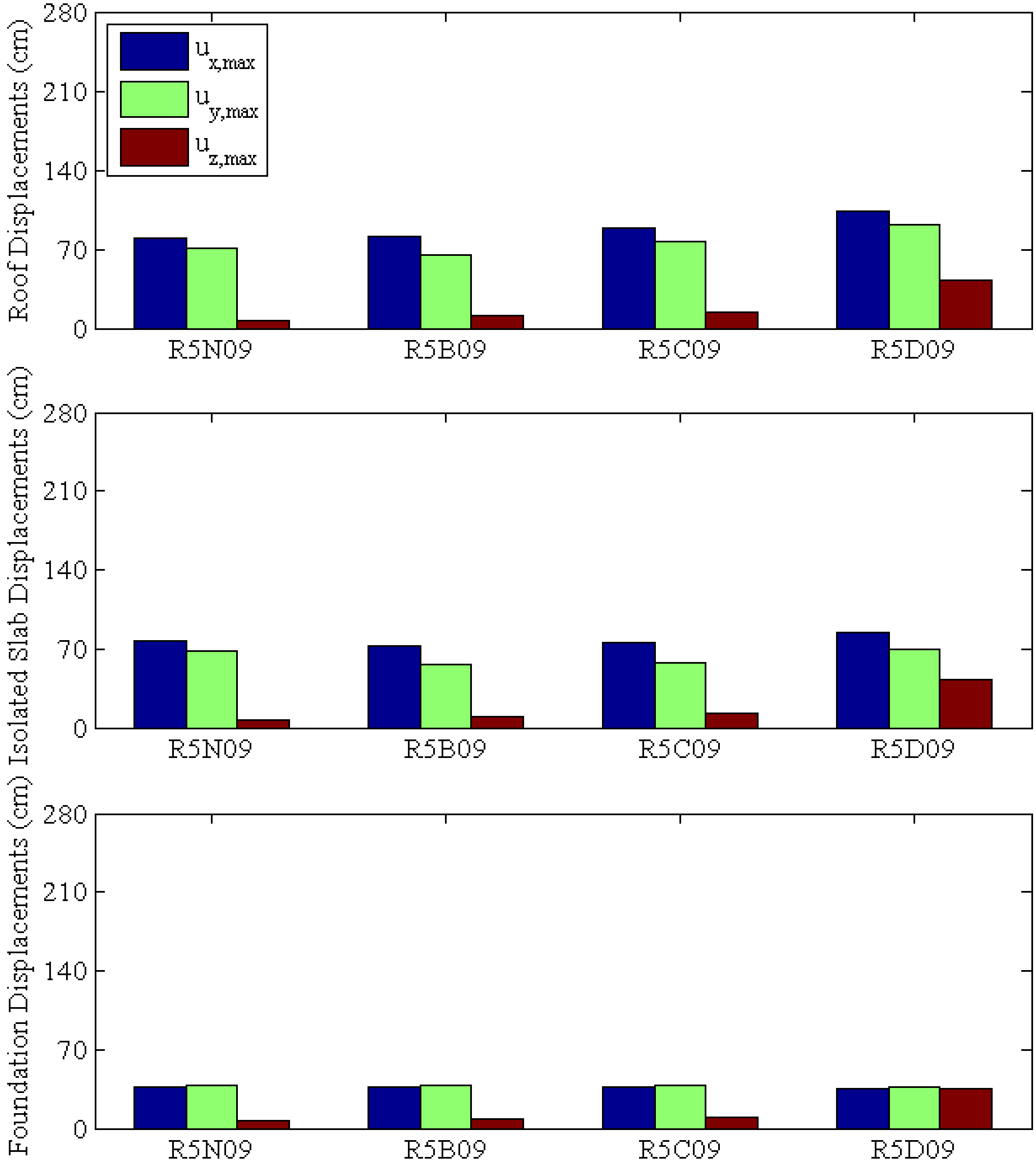

Figure E.30: Peak displacement data from the simulations with the rectangular superstructure and robust LR isolators subjected to ground motion 09

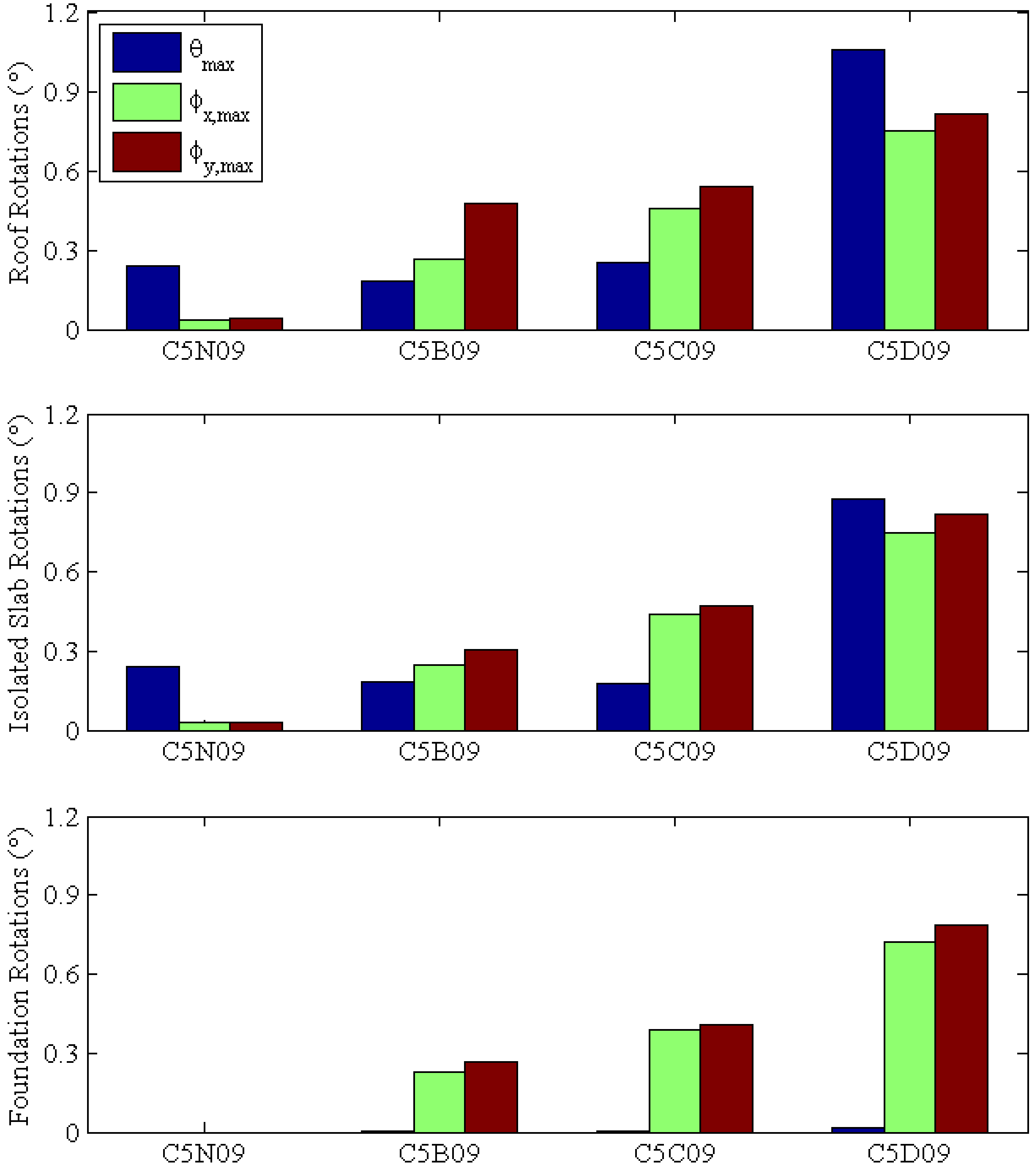

Figure E.31: Peak rotation data from the simulations with the cylindrical superstructure and robust LR isolators subjected to ground motion 09

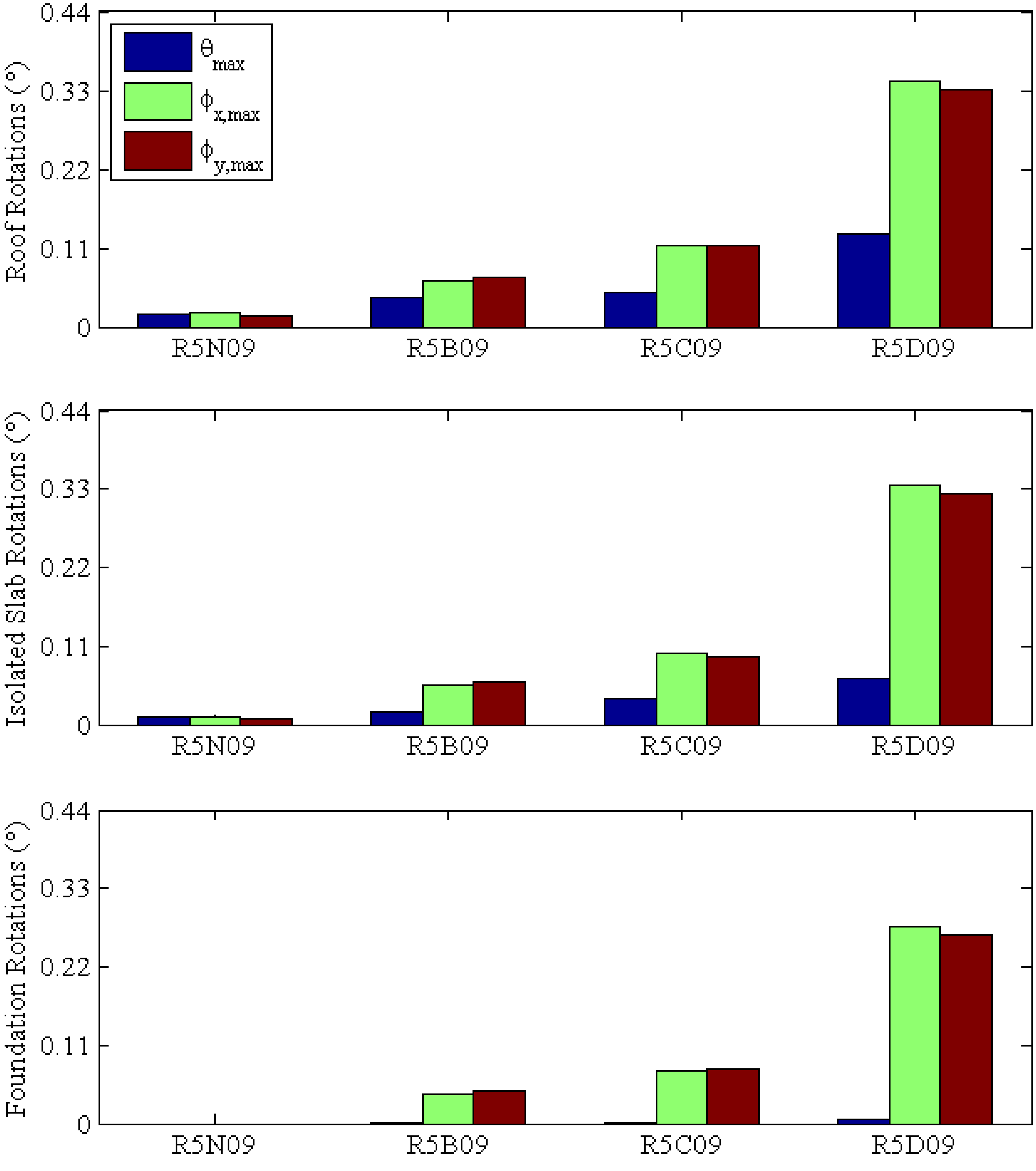

Figure E.32: Peak rotation data from the simulations with the rectangular superstructure and robust LR isolators subjected to ground motion 09

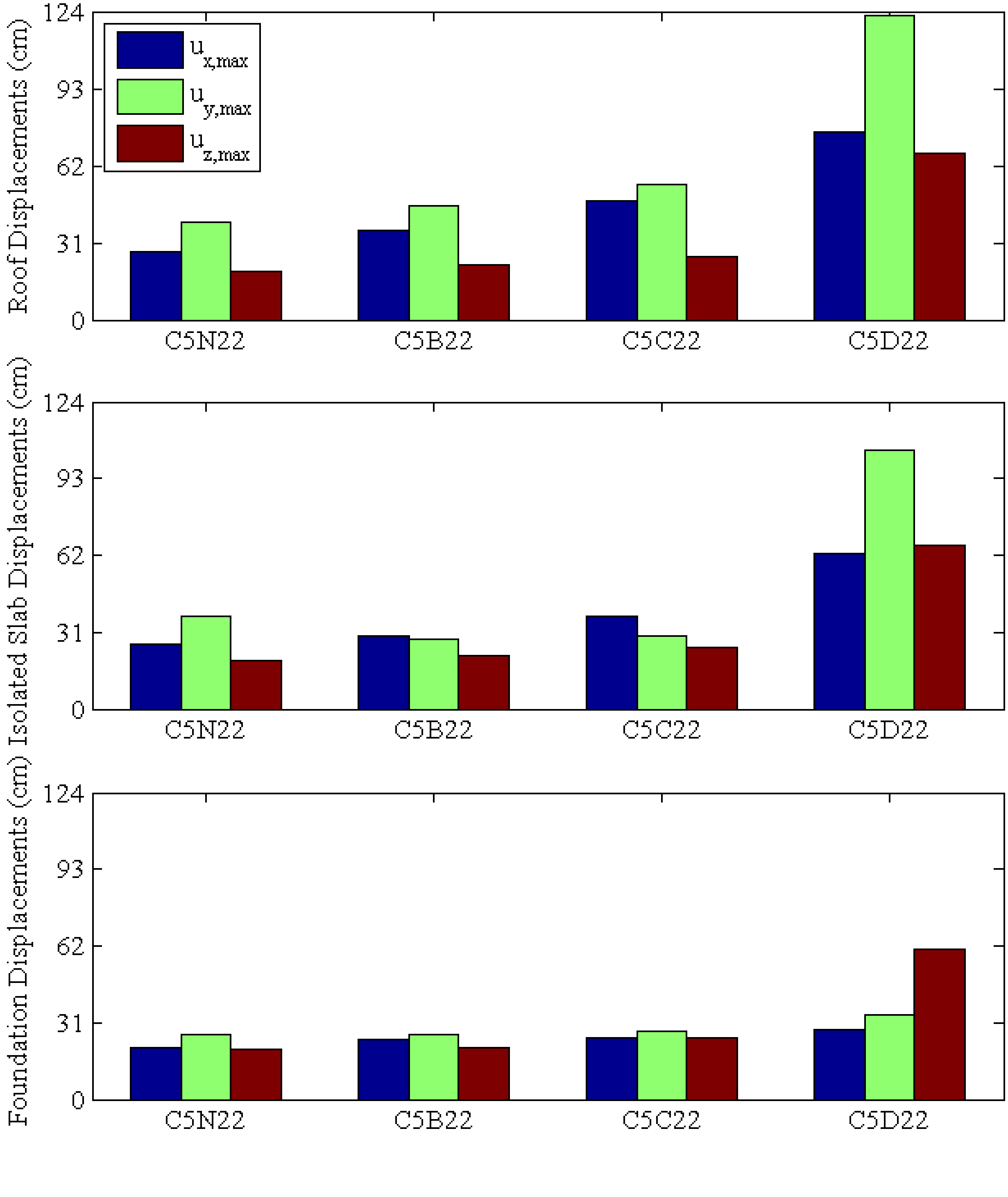

Figure E.33: Peak displacement data from the simulations with the cylindrical superstructure and robust LR isolators subjected to ground motion 22

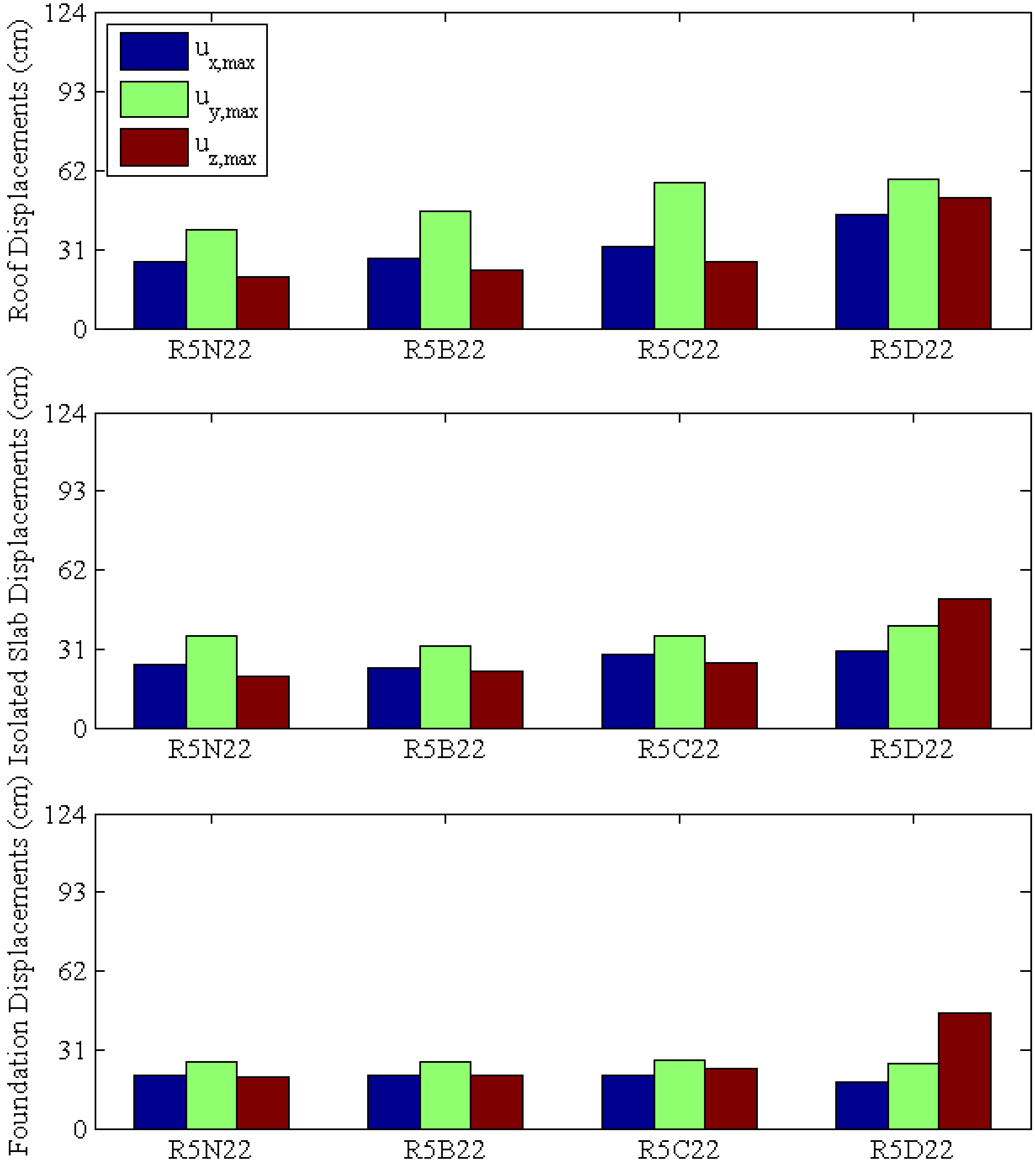

Figure E.34: Peak displacement data from the simulations with the rectangular superstructure and robust LR isolators subjected to ground motion 22

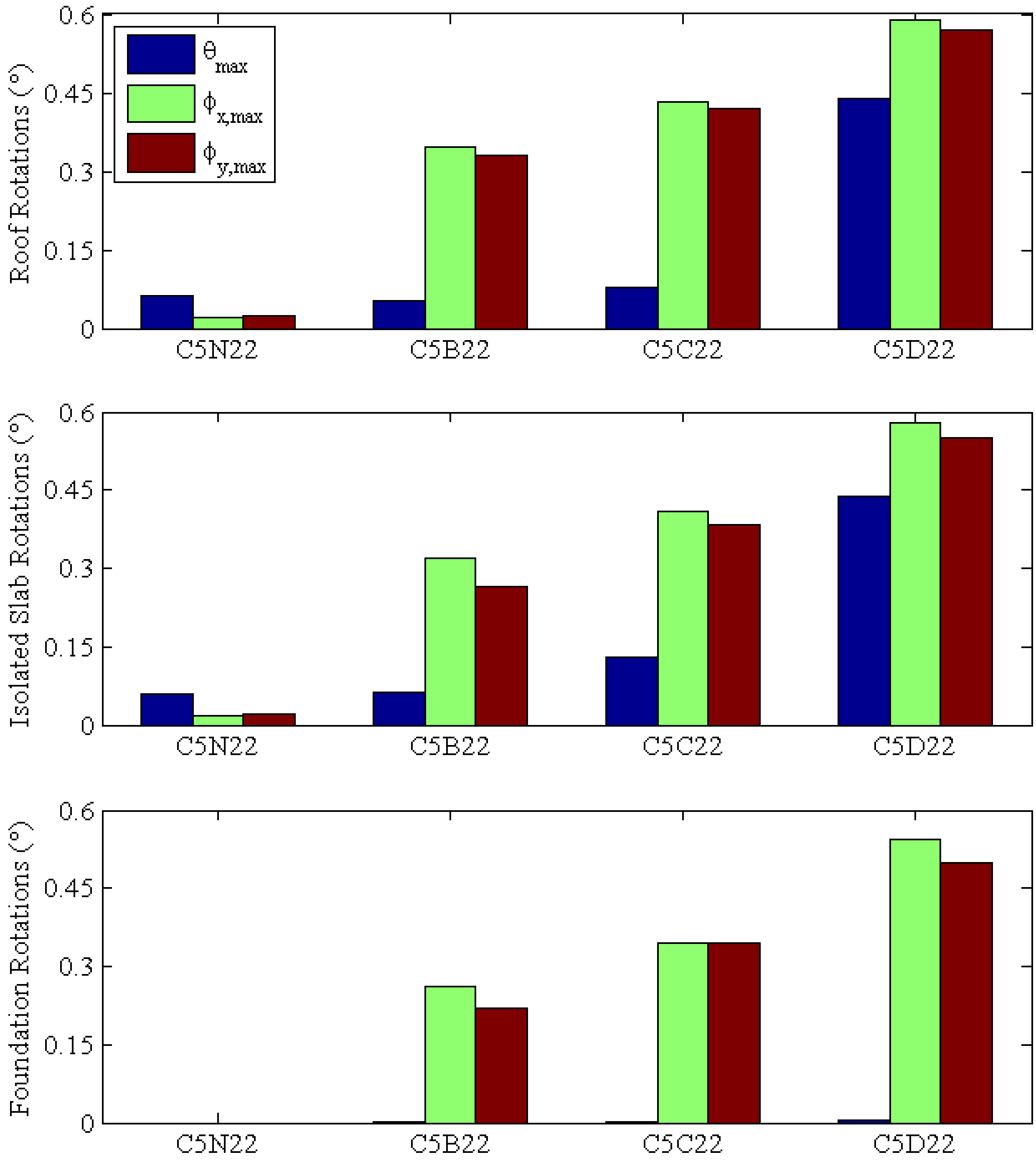

Figure E.35: Peak rotation data from the simulations with the cylindrical superstructure and robust LR isolators subjected to ground motion 22

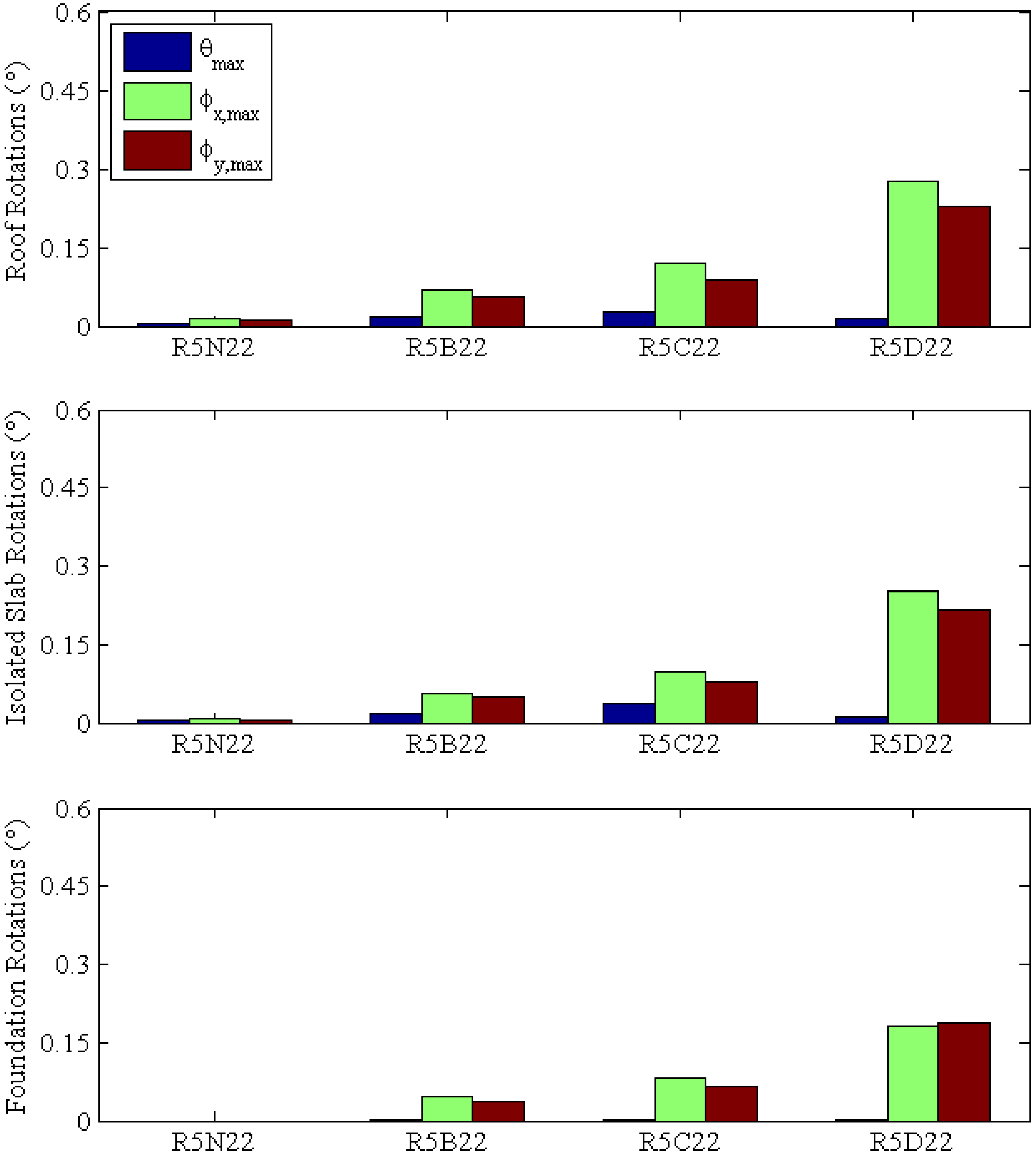

Figure E.36: Peak rotation data from the simulations with the rectangular superstructure and robust LR isolators subjected to ground motion 22

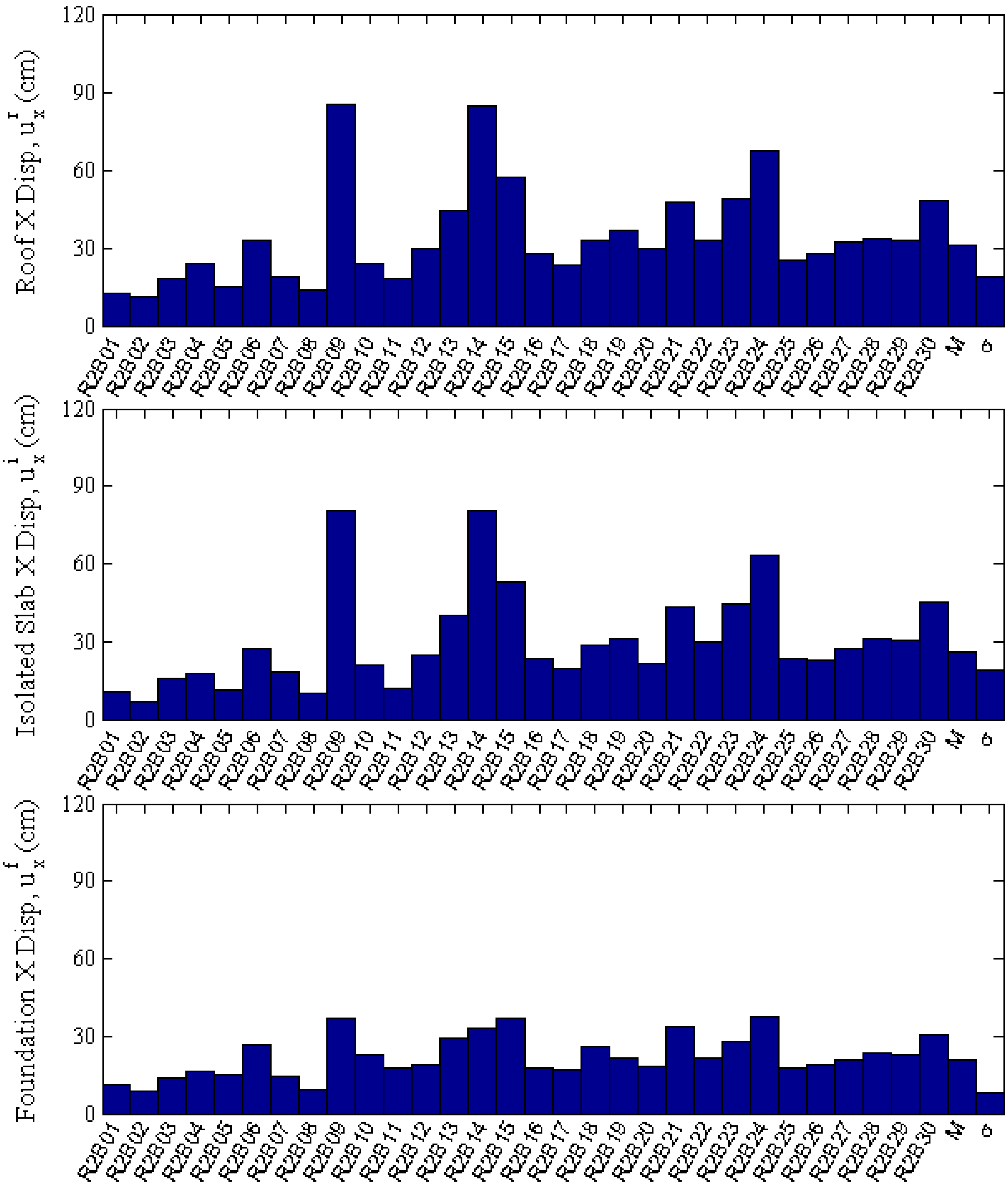

Figure E.37: Peak foundation, isolated slab, and roof x displacement data from the simulations with the rectangular superstructure and FP bearings subjected to all ground motions

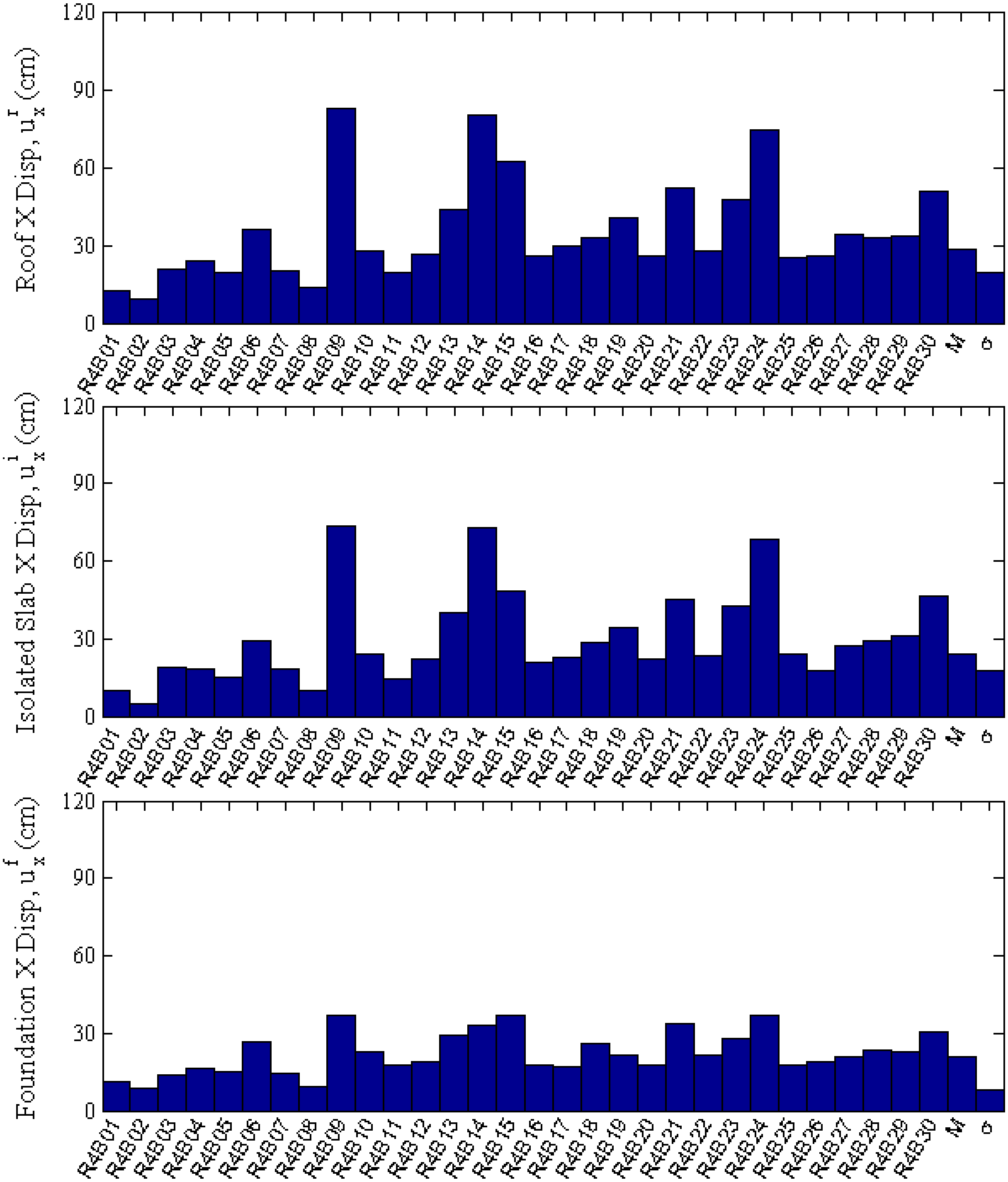

Figure E.38: Peak foundation, isolated slab, and roof x displacement data from the simulations with the rectangular superstructure and simplified LR bearings subjected to all ground motions

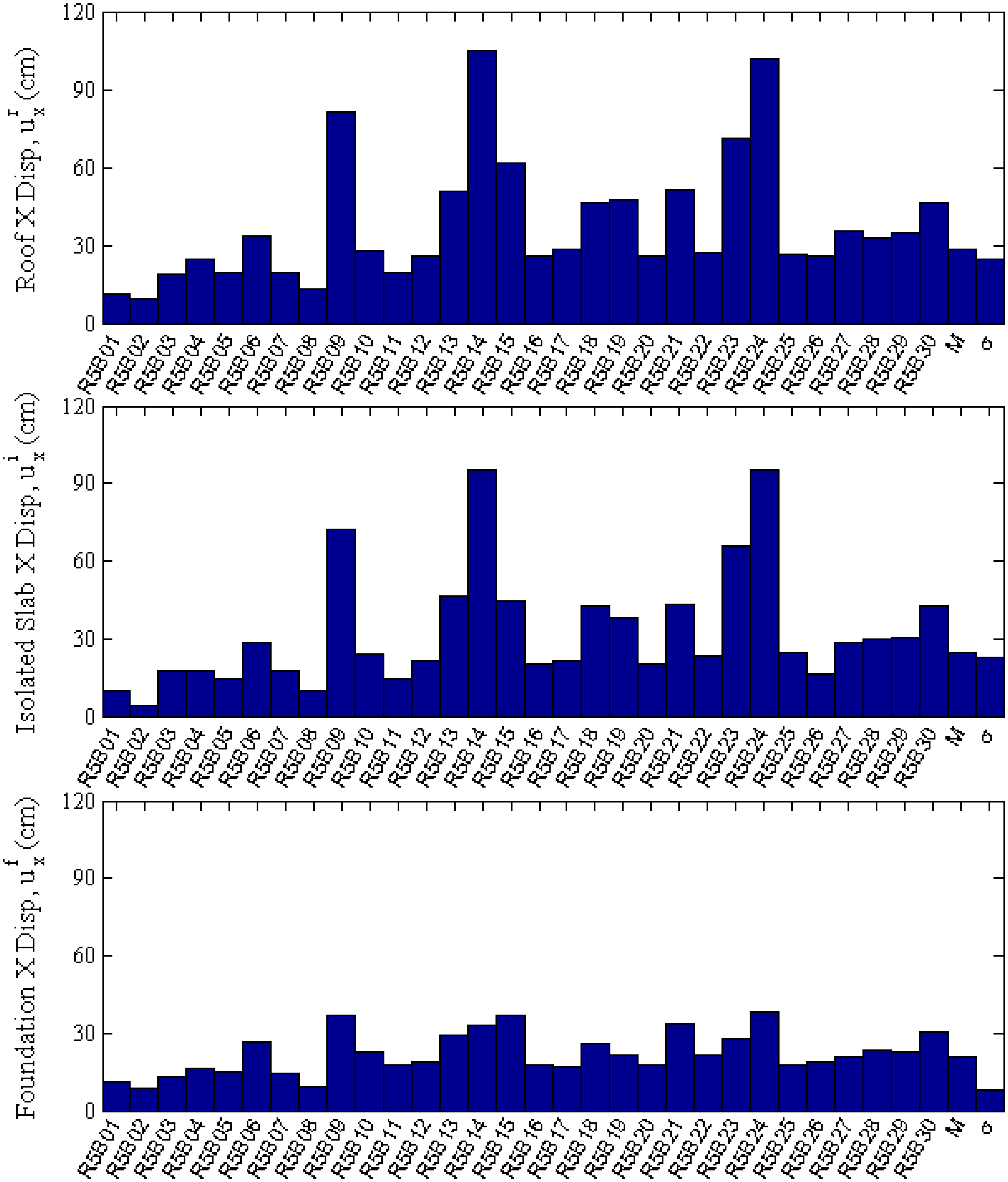

Figure E.39: Peak foundation, isolated slab, and roof x displacement data from the simulations with the rectangular superstructure and robust LR bearings subjected to all ground motions

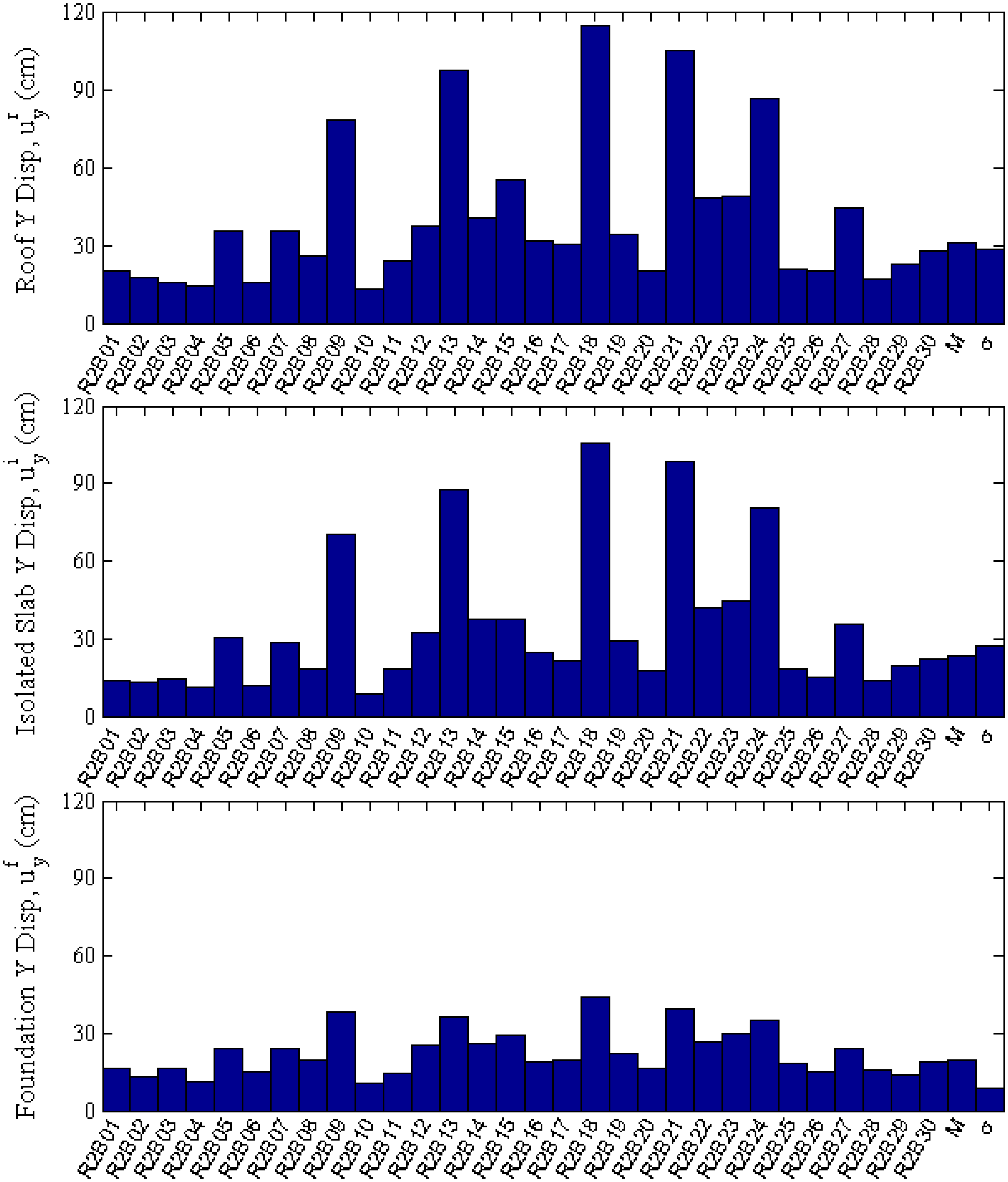

Figure E.40: Peak foundation, isolated slab, and roof y displacement data from the simulations with the rectangular superstructure and FP bearings subjected to all ground motions

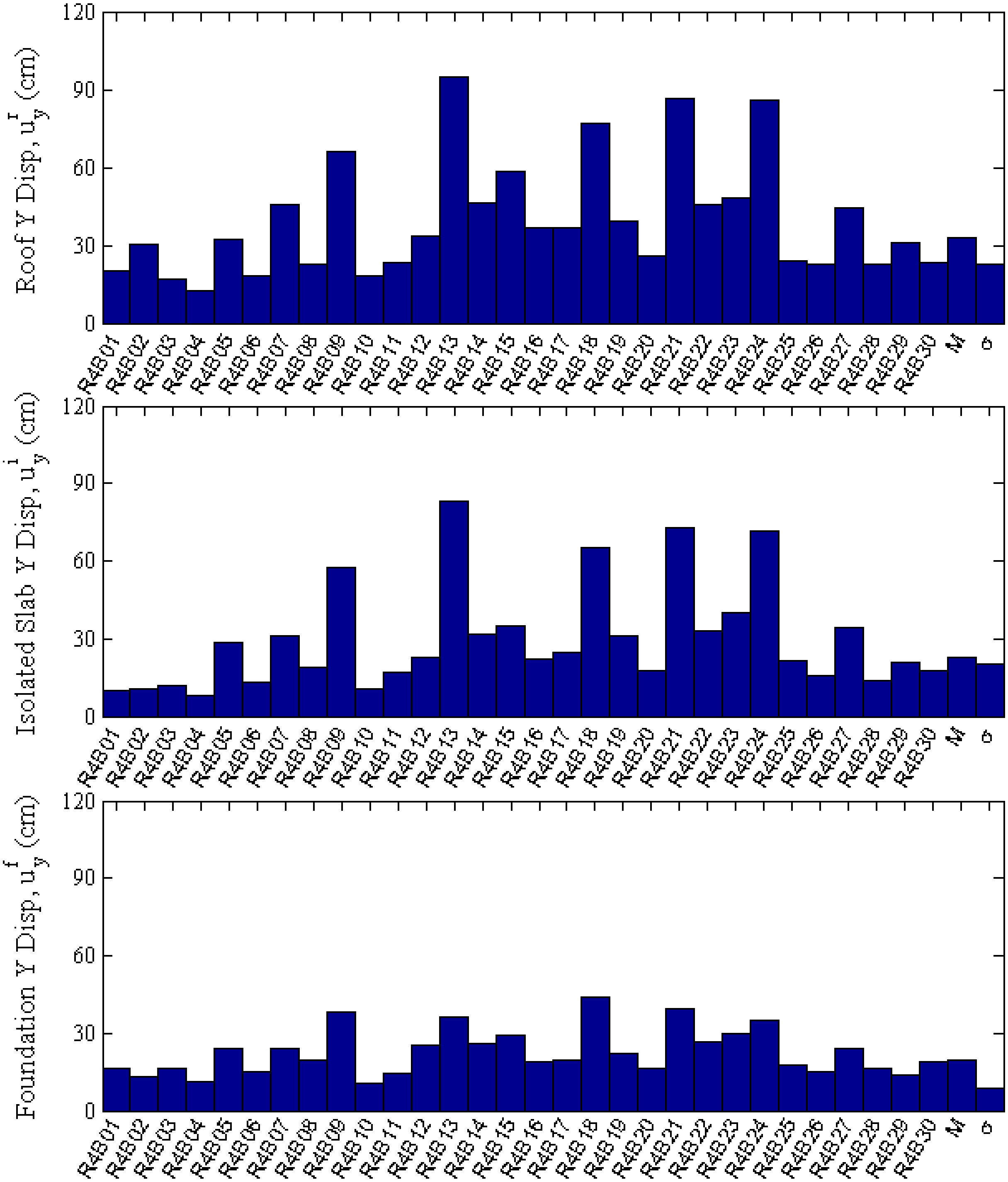

Figure E.41: Peak foundation, isolated slab, and roof y displacement data from the simulations with the rectangular superstructure and simplified LR bearings subjected to all ground motions

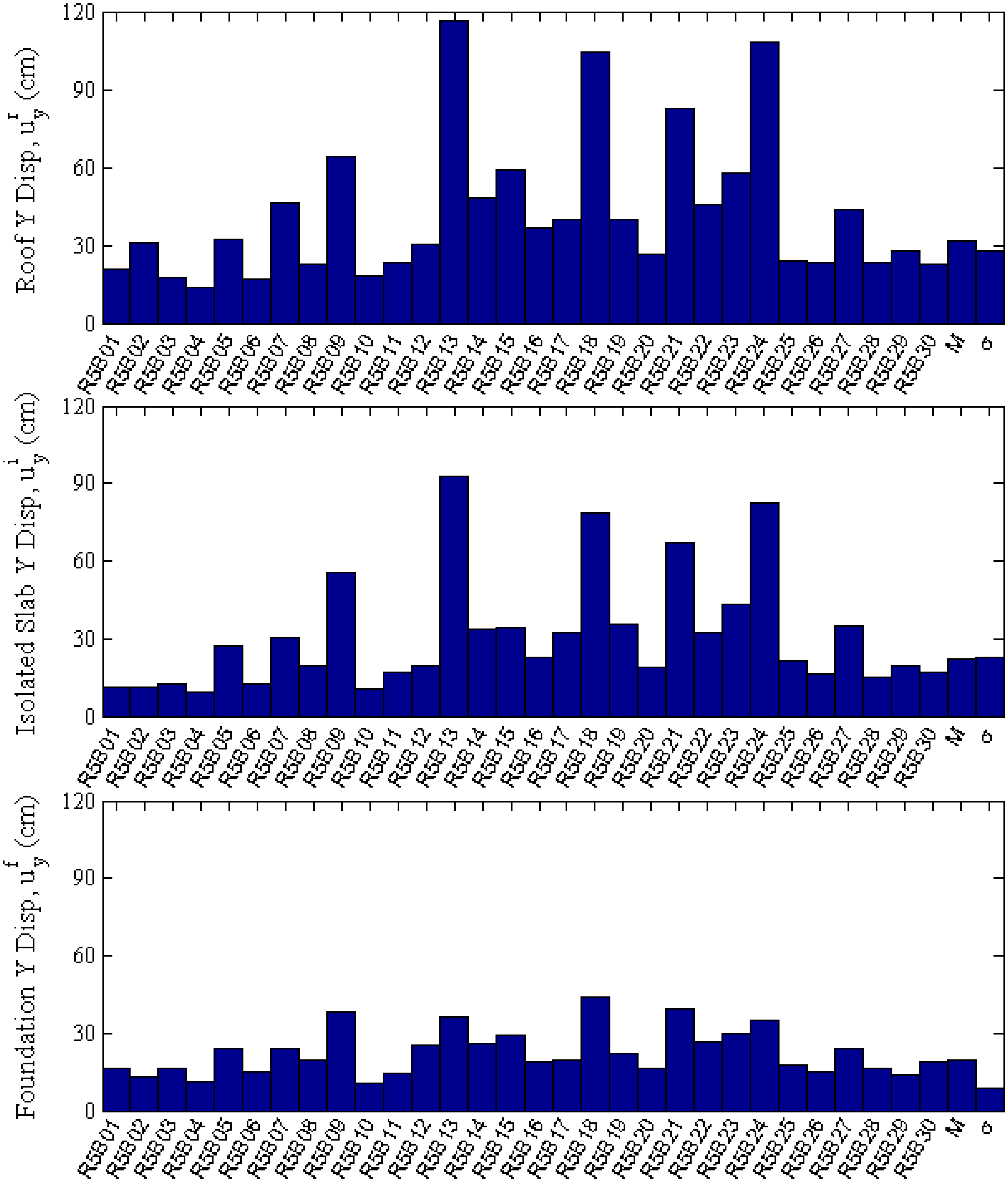

Figure E.42: Peak foundation, isolated slab, and roof y displacement data from the simulations with the rectangular superstructure and robust LR bearings subjected to all ground motions

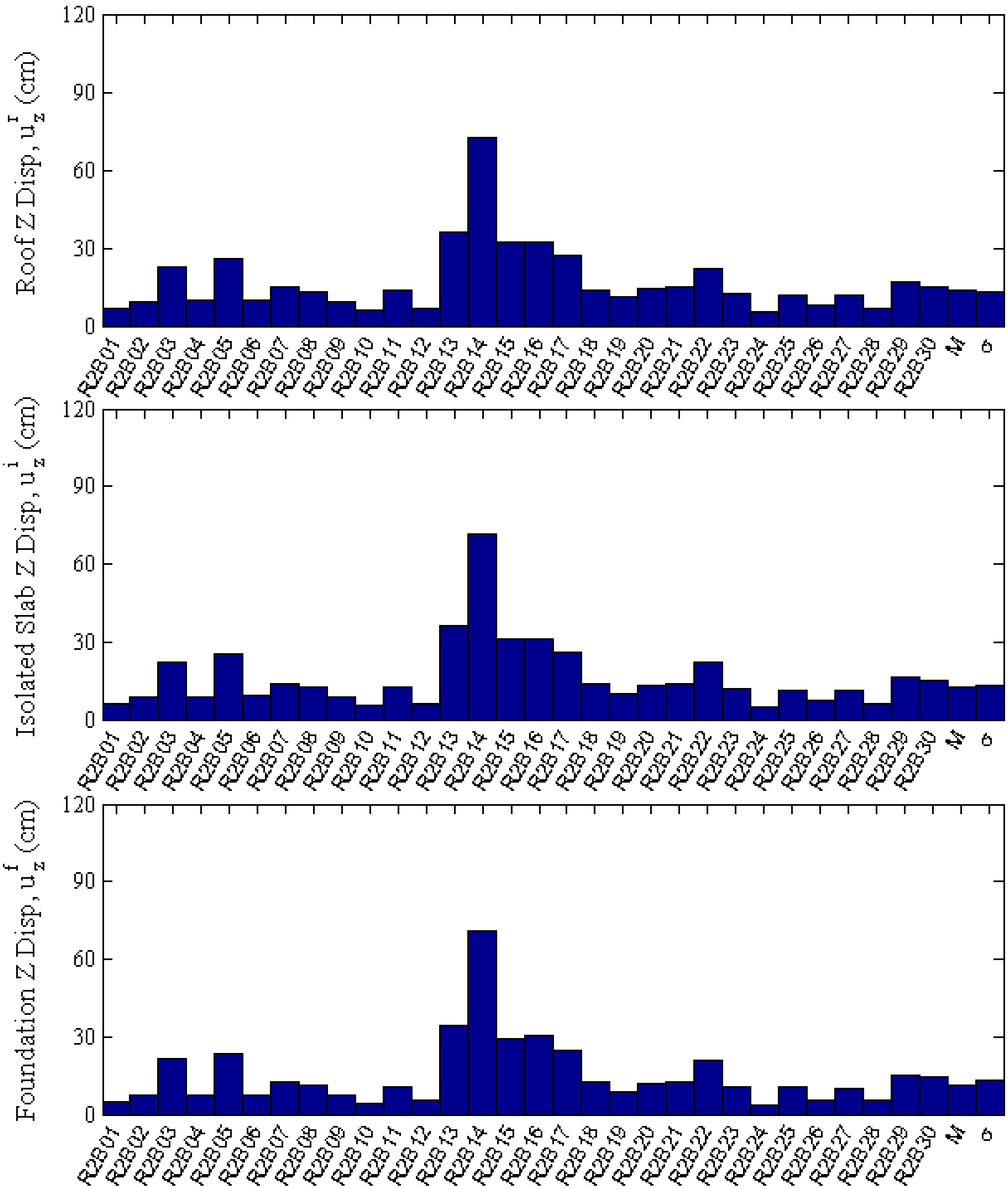

Figure E.43: Peak foundation, isolated slab, and roof z displacement data from the simulations with the rectangular superstructure and FP bearings subjected to all ground motions

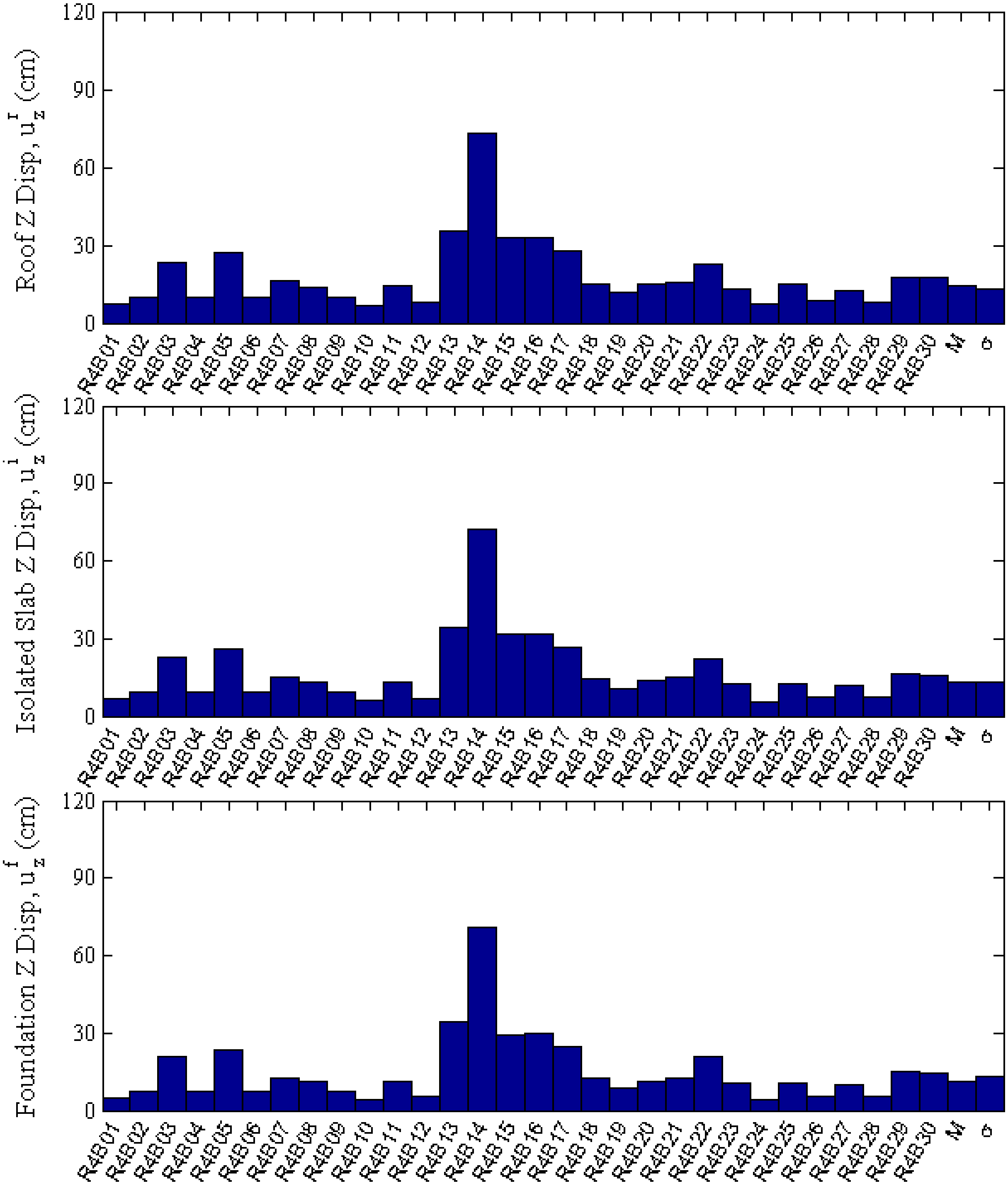

Figure E.44: Peak foundation, isolated slab, and roof z displacement data from the simulations with the rectangular superstructure and simplified LR bearings subjected to all ground motions

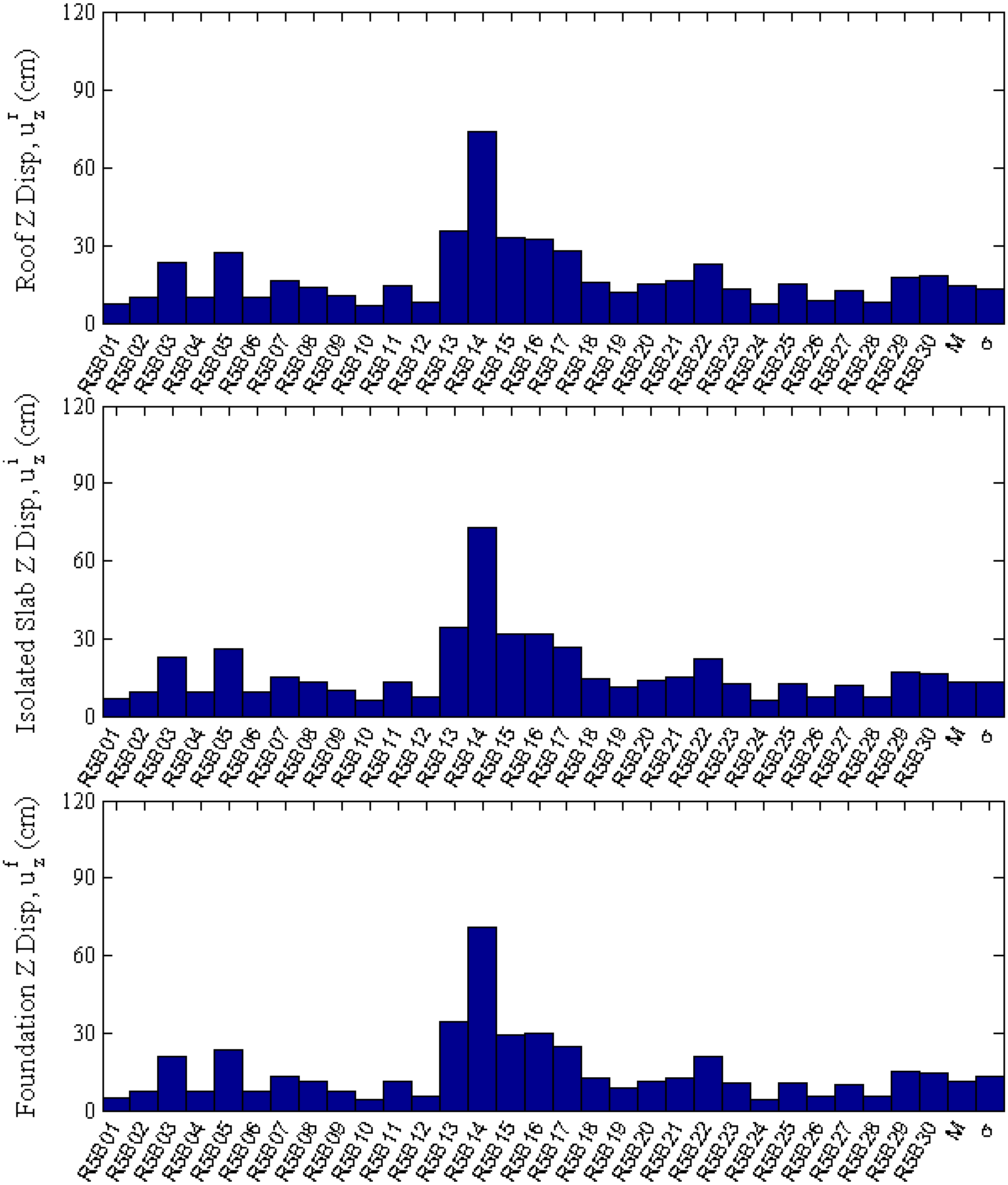

Figure E.45: Peak foundation, isolated slab, and roof z displacement data from the simulations with the rectangular superstructure and robust LR bearings subjected to all ground motions

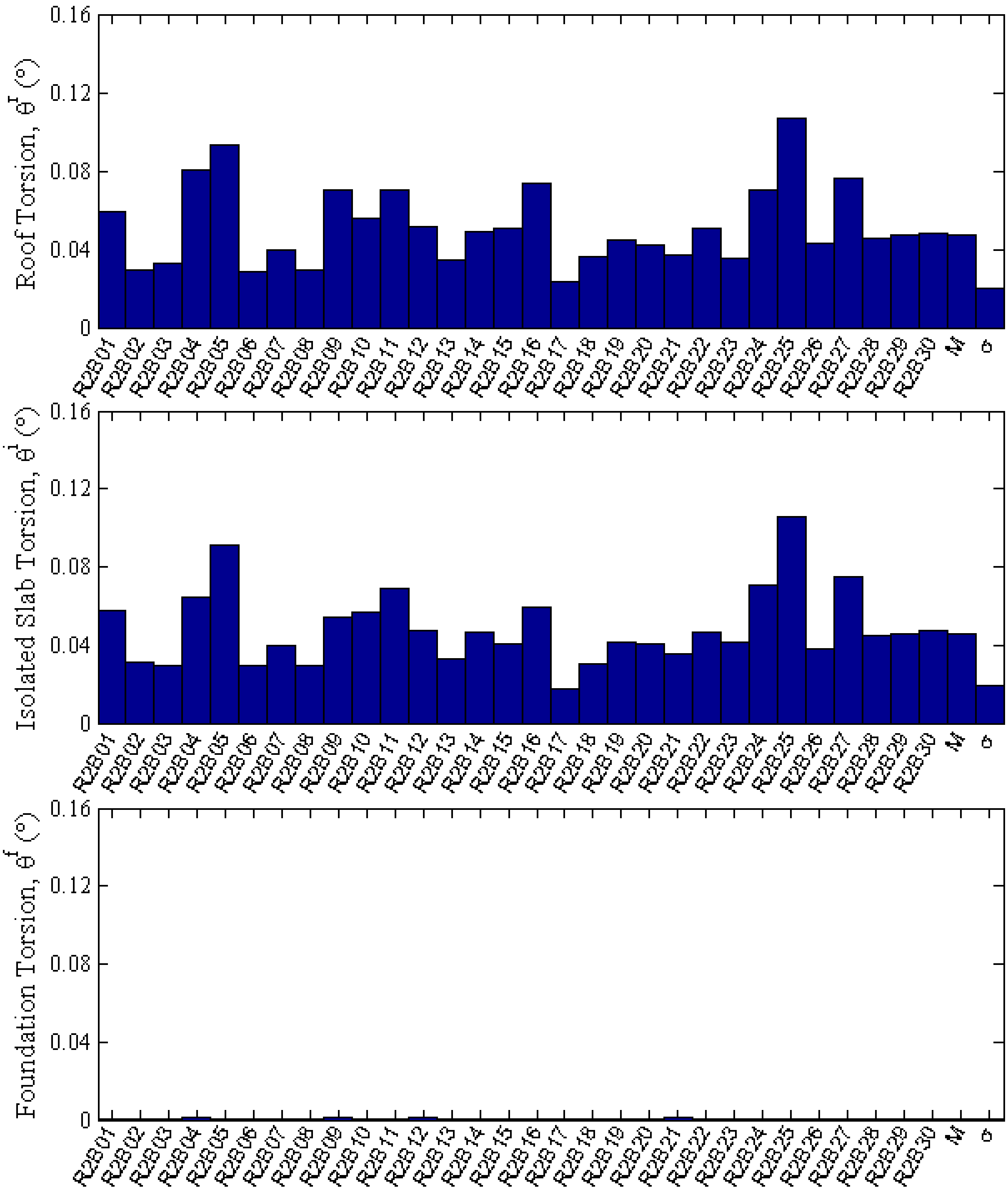

Figure E.46: Peak foundation, isolated slab, and roof torsion data from the simulations with the rectangular superstructure and FP bearings subjected to all ground motions

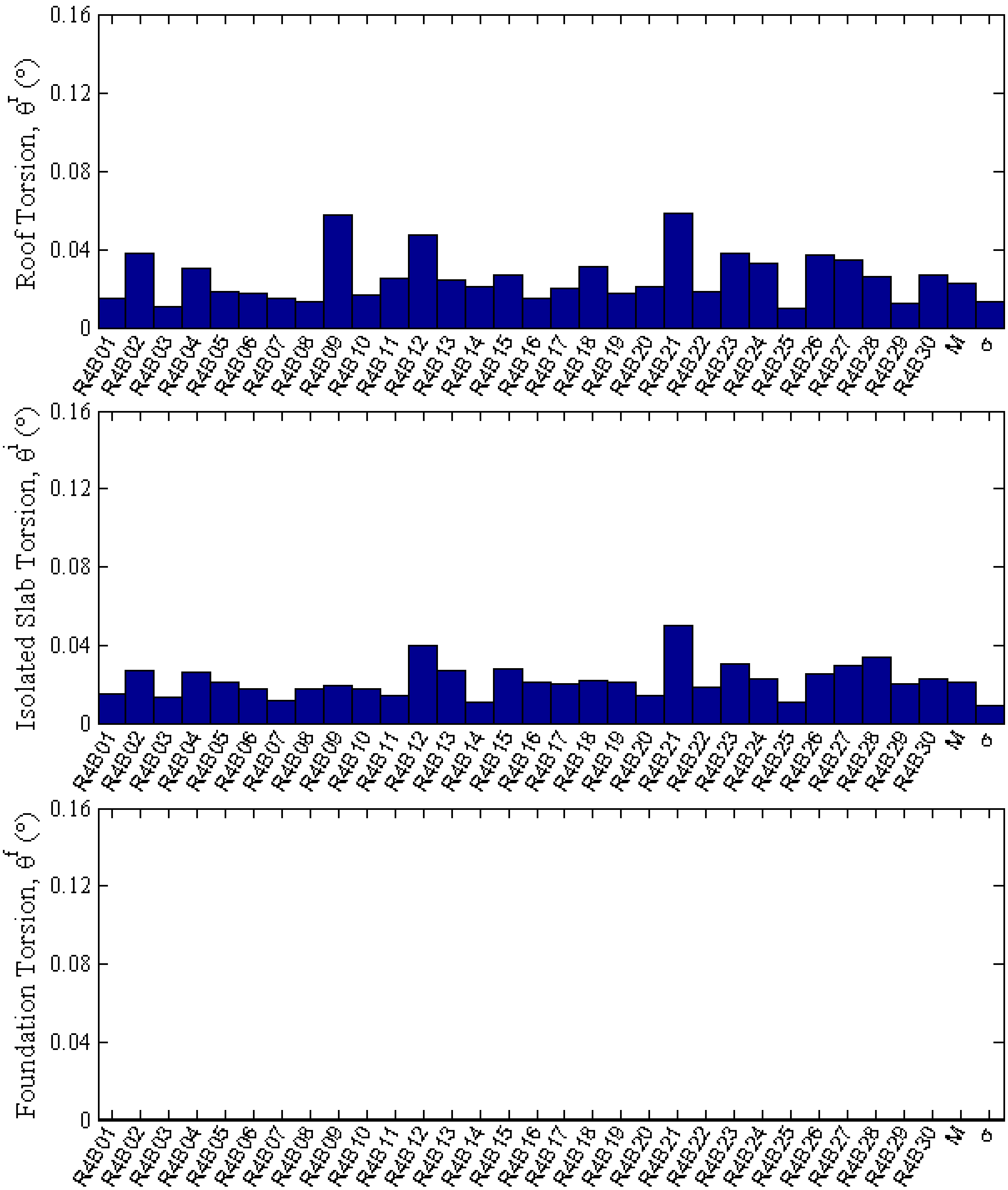

Figure E.47: Peak foundation, isolated slab, and roof torsion data from the simulations with the rectangular superstructure and simplified LR bearings subjected to all ground motions

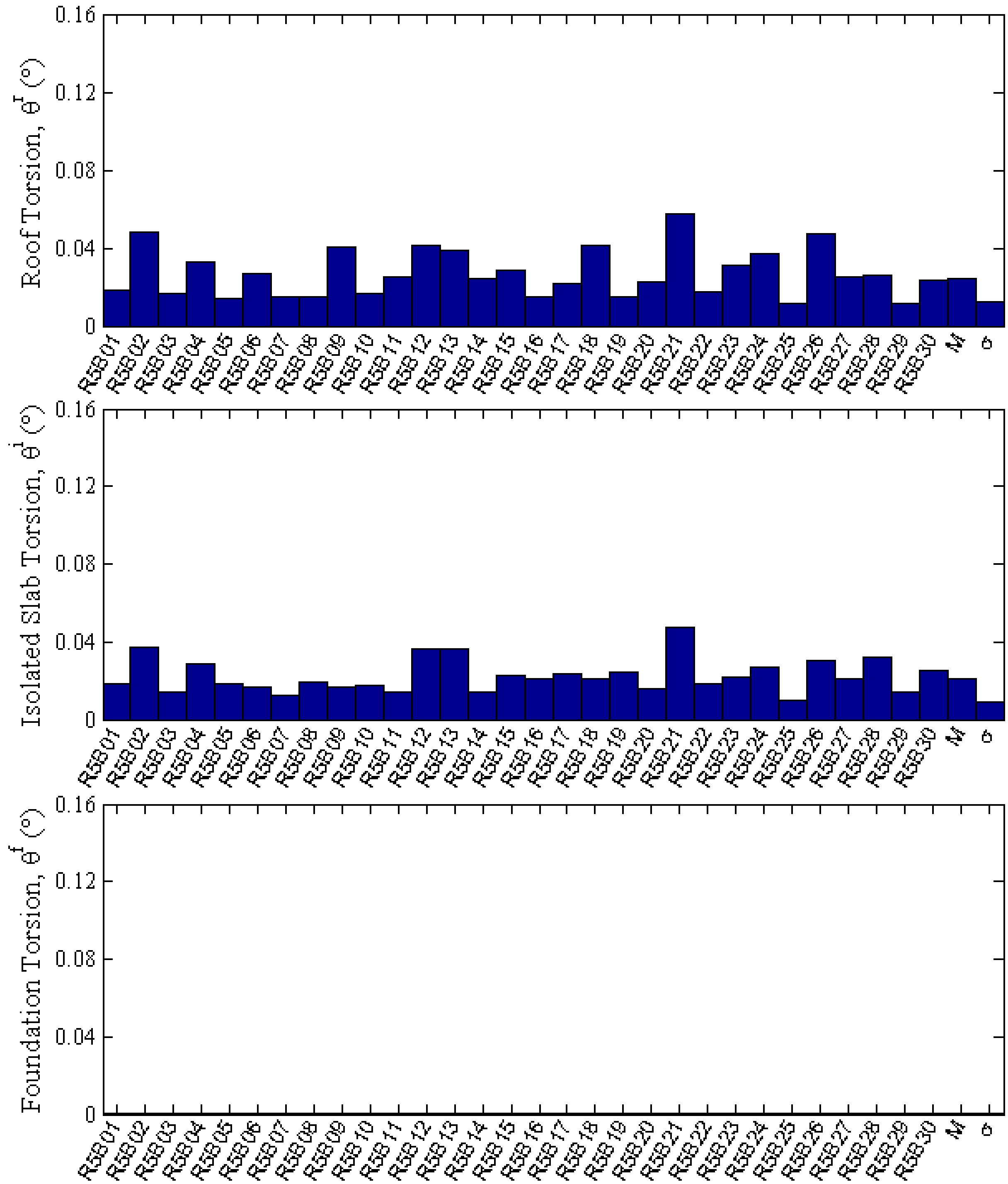

Figure E.48: Peak foundation, isolated slab, and roof torsion data from the simulations with the rectangular superstructure and robust LR bearings subjected to all ground motions

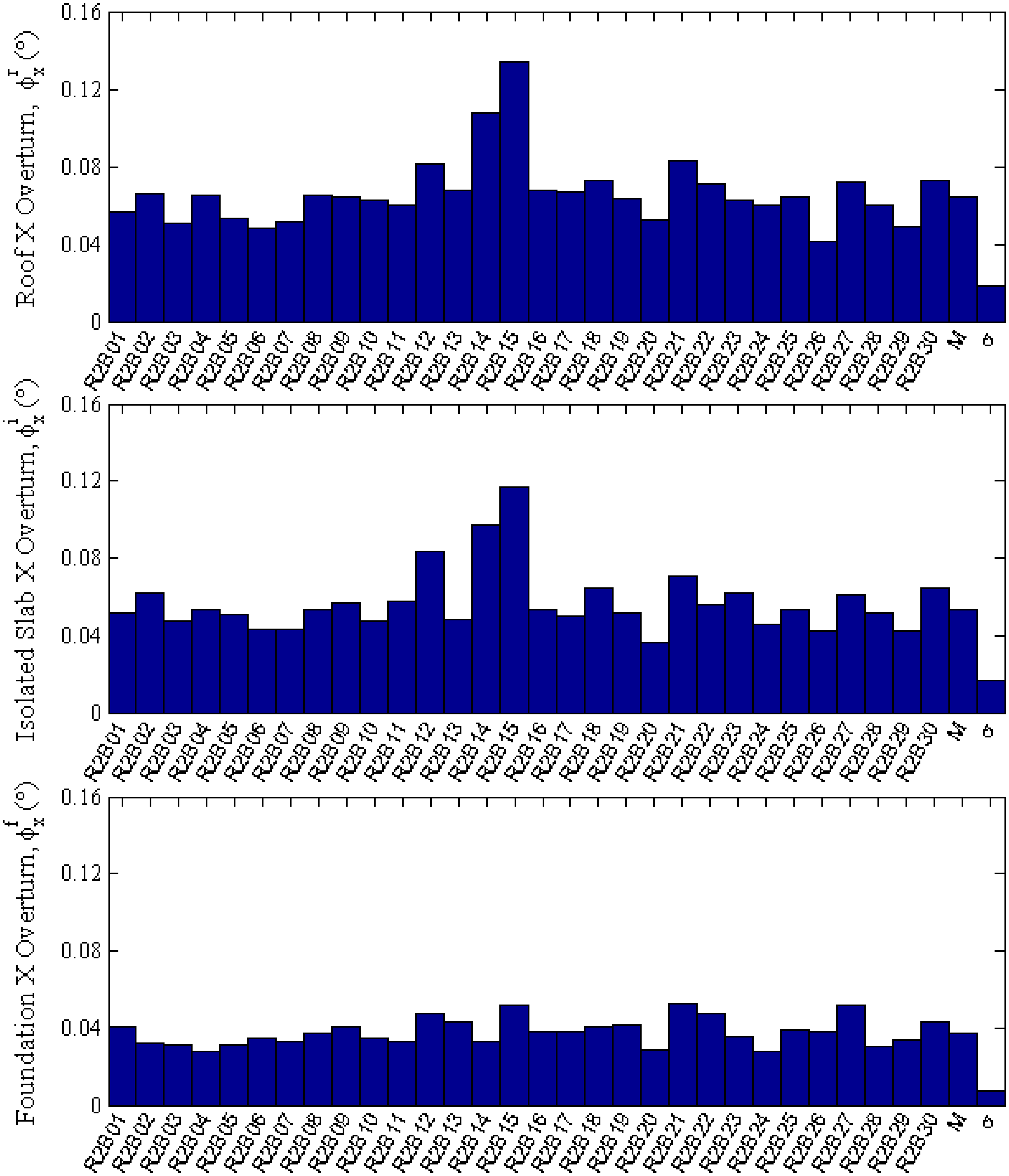

Figure E.49: Peak foundation, isolated slab, and roof x overturning rotation data from the simulations with the rectangular superstructure and FP bearings subjected to all ground motions

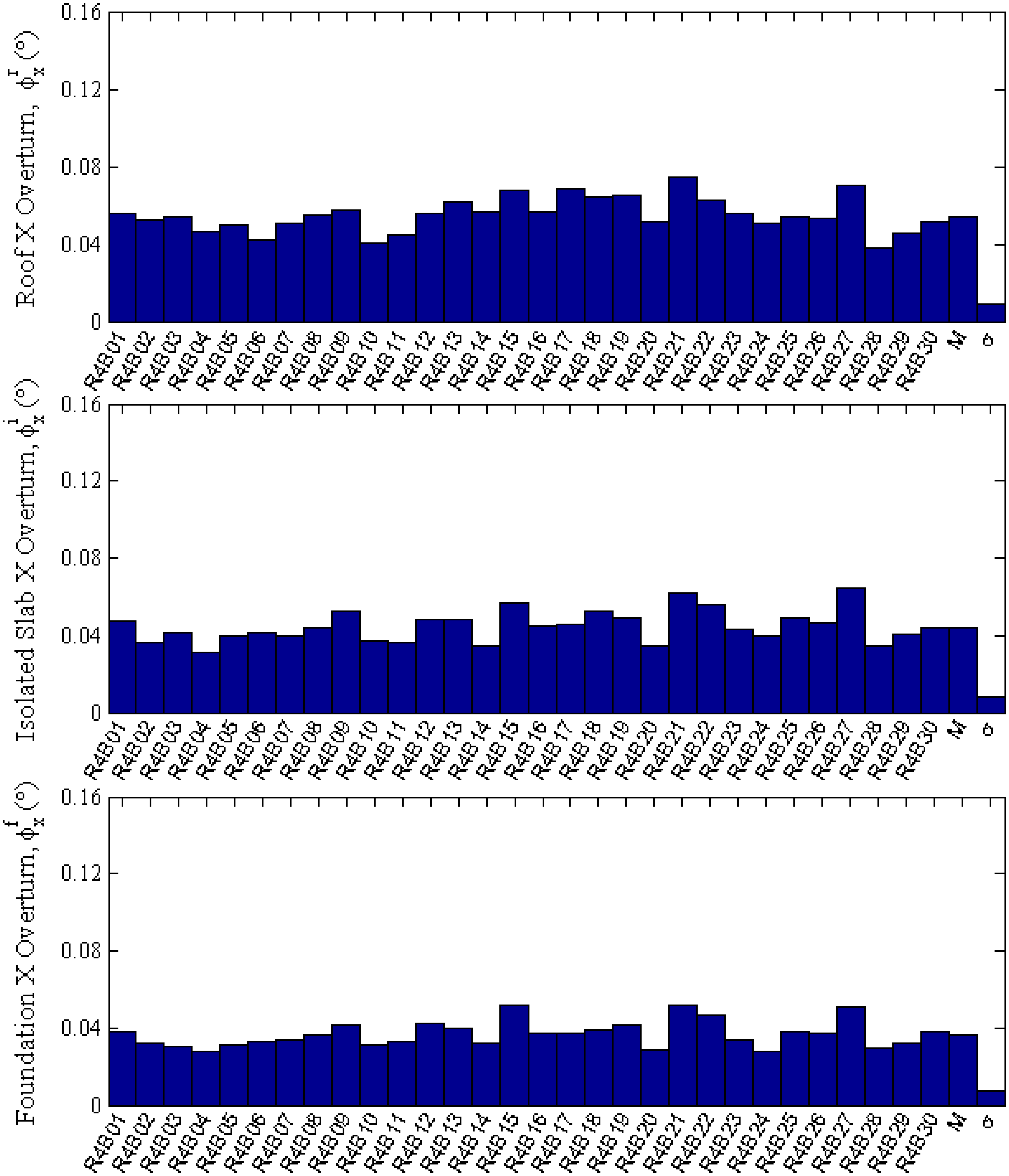

Figure E.50: Peak foundation, isolated slab, and roof x overturning rotation data from the simulations with the rectangular superstructure and simplified LR bearings subjected to all ground motions

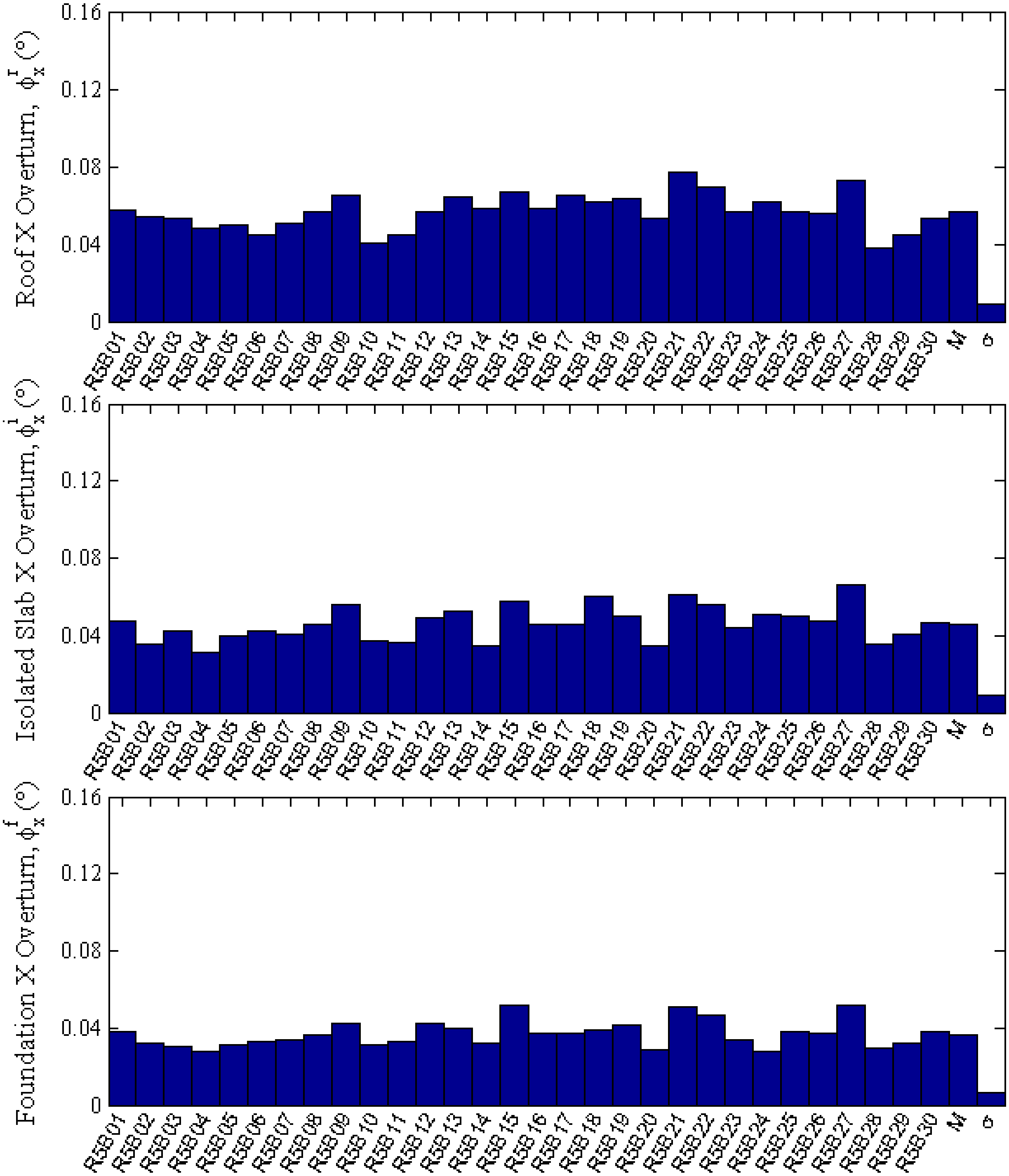

Figure E.51: Peak foundation, isolated slab, and roof x overturning rotation data from the simulations with the rectangular superstructure and robust LR bearings subjected to all ground motions

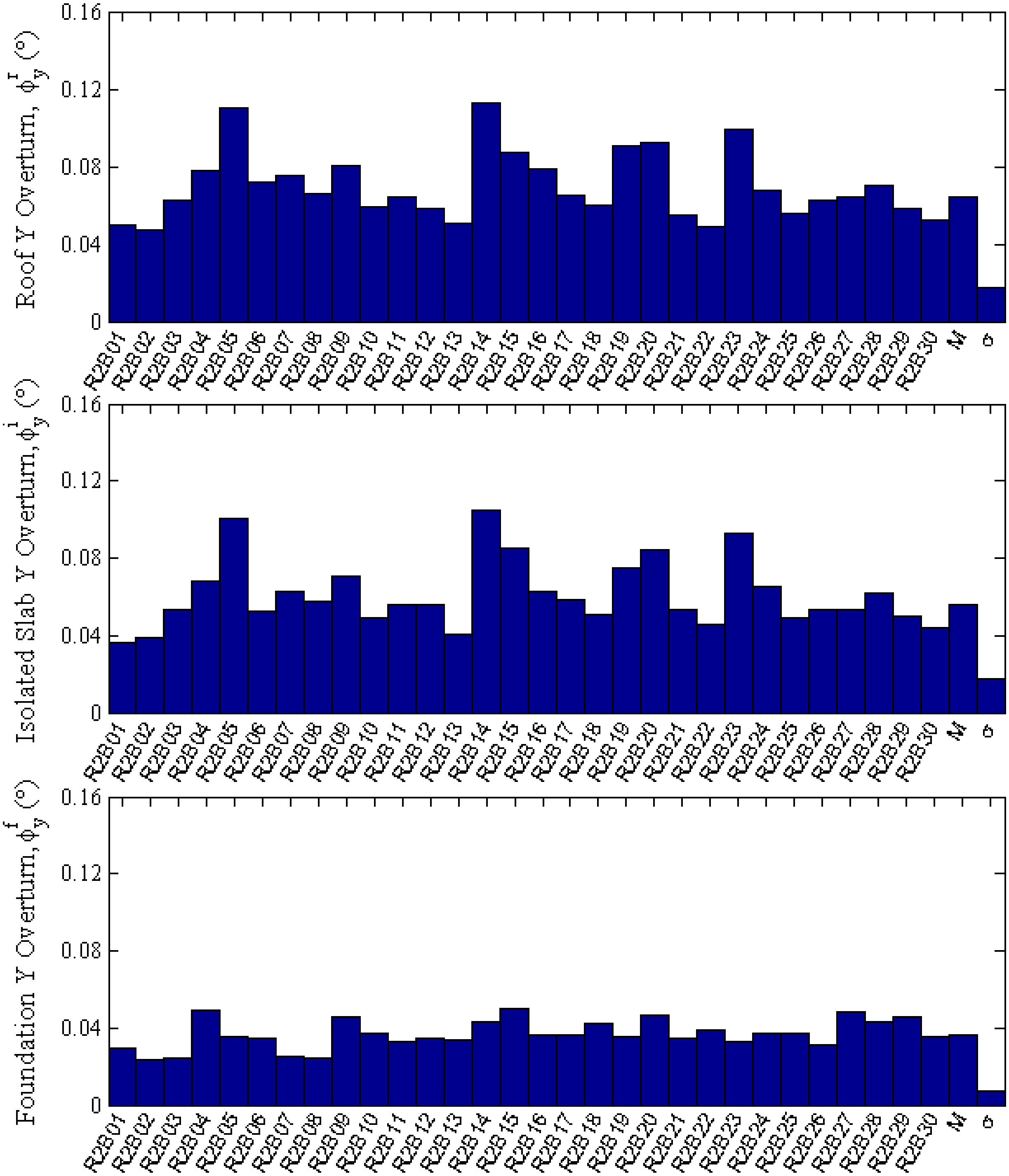

Figure E.52: Peak foundation, isolated slab, and roof y overturning rotation data from the simulations with the rectangular superstructure and FP bearings subjected to all ground motions

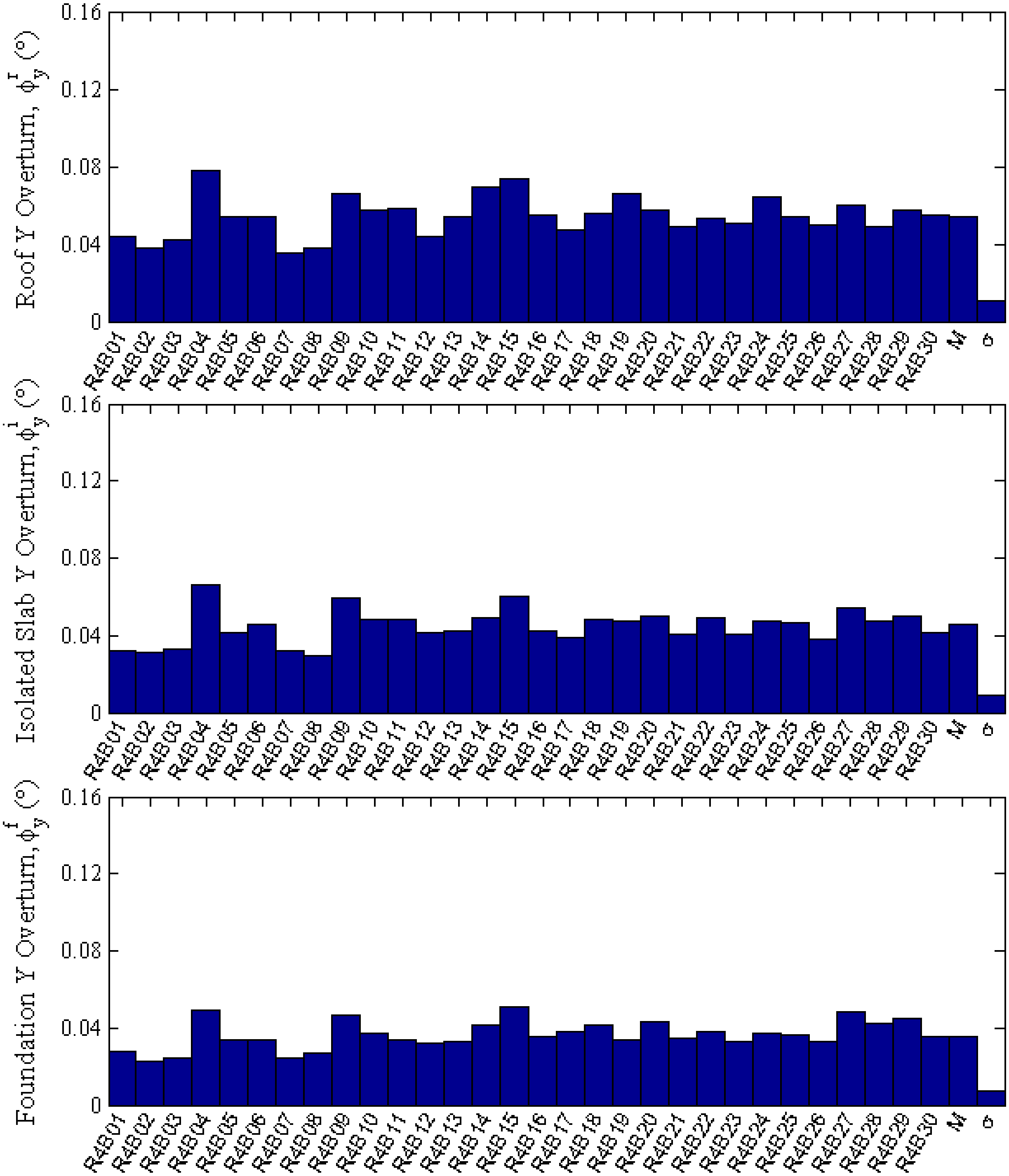

Figure E.53: Peak foundation, isolated slab, and roof y overturning rotation data from the simulations with the rectangular superstructure and simplified LR bearings subjected to all ground motions

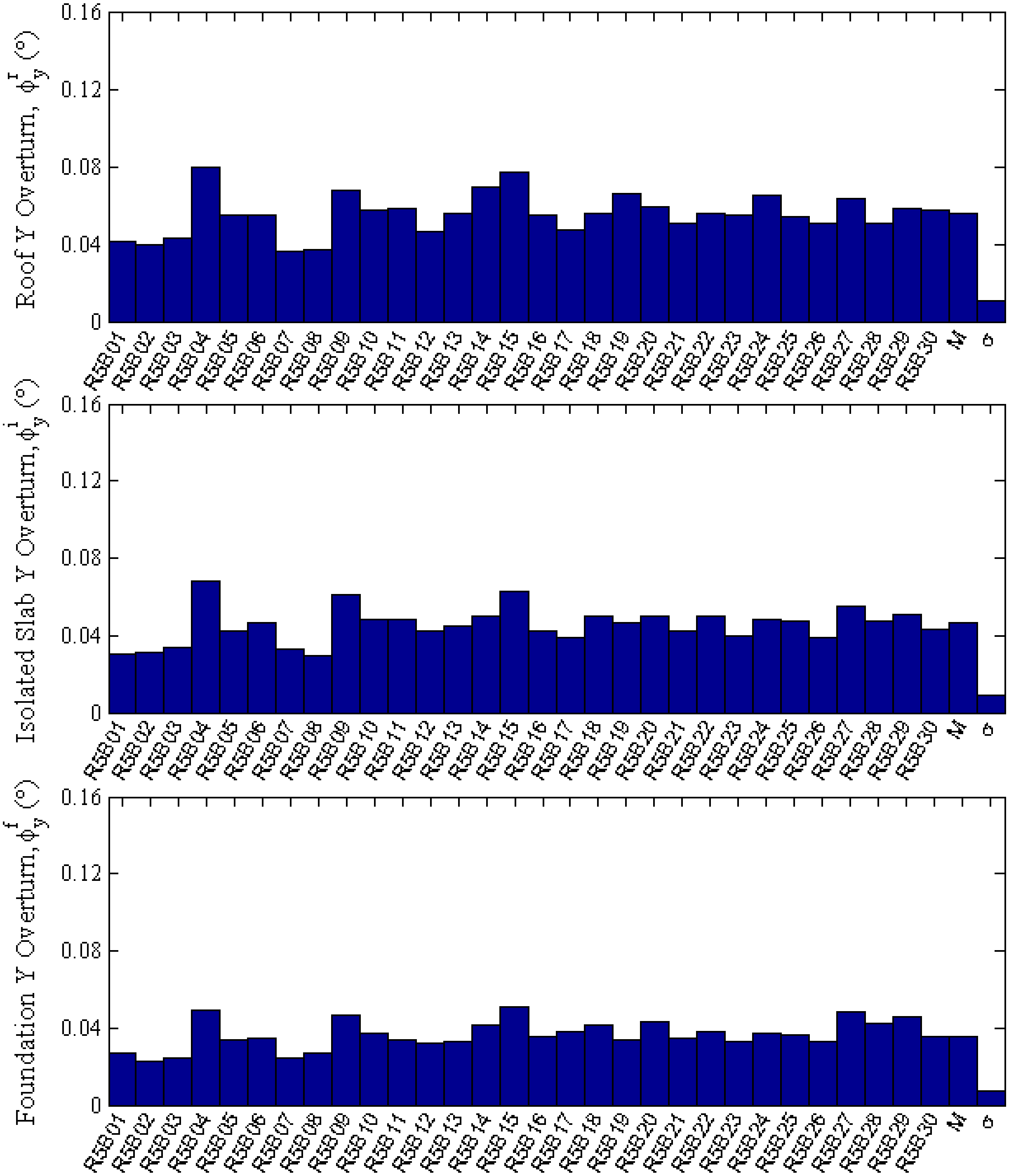

Figure E.54: Peak foundation, isolated slab, and roof y overturning rotation data from the simulations with the rectangular superstructure and robust LR bearings subjected to all ground motions

Appendix F

Superstructure Acceleration Data

This appendix presents peak directional acceleration amplification data, a_{max}/a^f_{max}, throughout the superstructres analyzed. For each simulation, the acceleration amplification ratios in the x, y, and z directions were measured along the height for the walls and vertical data was recorded along each floor and roof. Figures F.1 through F.24 show the average amplification peaks for all walls measured in each comparative simulation subjected to the basic motions, as well as the average isolated slab floor (dotted lines) and roof (solid lines) vertical amplification peaks. Figures F.25 through F.27 present the median data, along with standard deviations, for the simulations involving the rectangular superstructure atop soil column B subjected to all 30 ground motions.

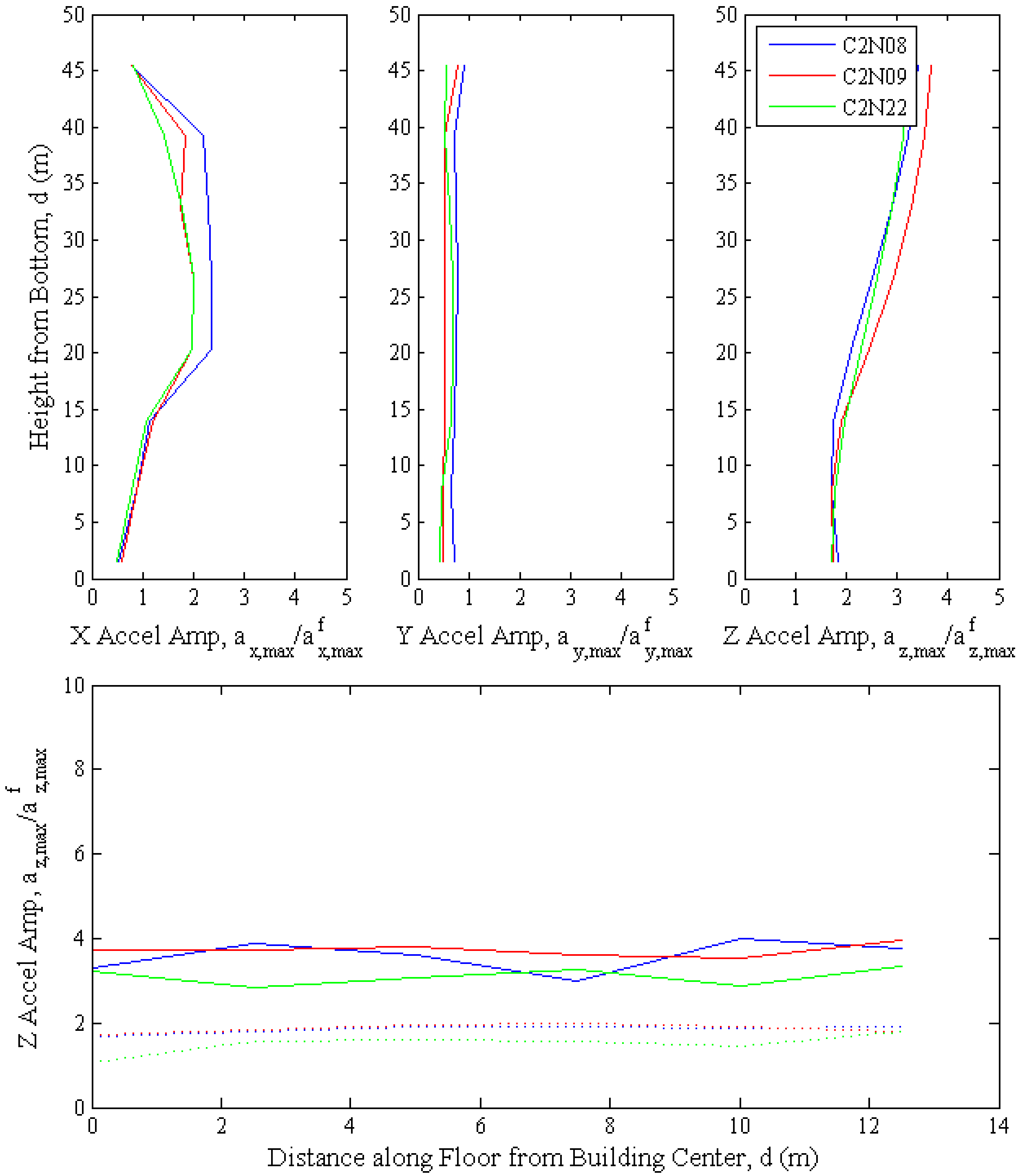

Figure F.1: Peak superstructure acceleration amplification data from the simulations with the cylindrical superstructure, no soil, and FP bearings subjected to the basic motions

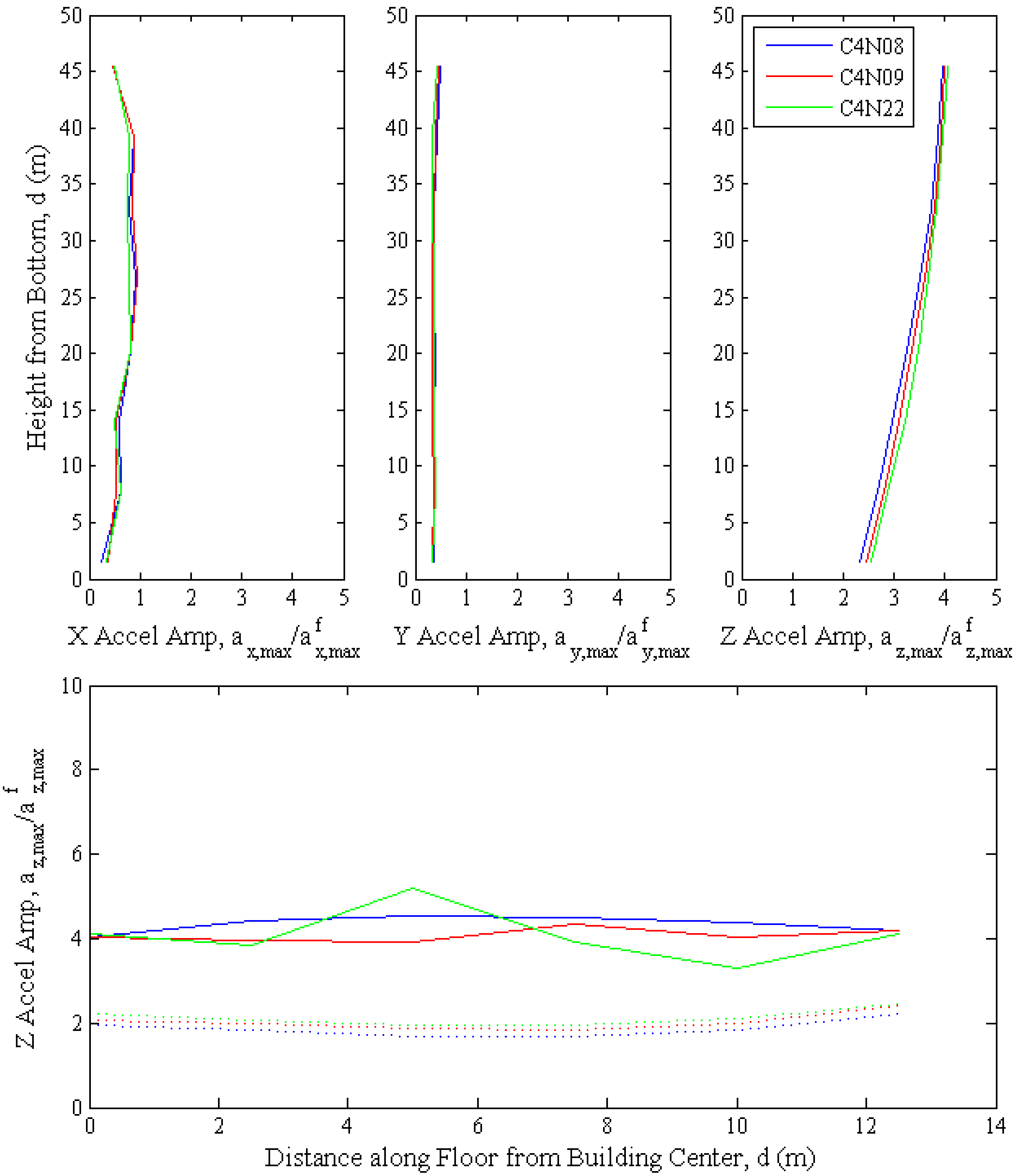

Figure F.2: Peak superstructure acceleration amplification data from the simulations with the cylindrical superstructure, no soil, and simplified LR bearings subjected to the basic motions

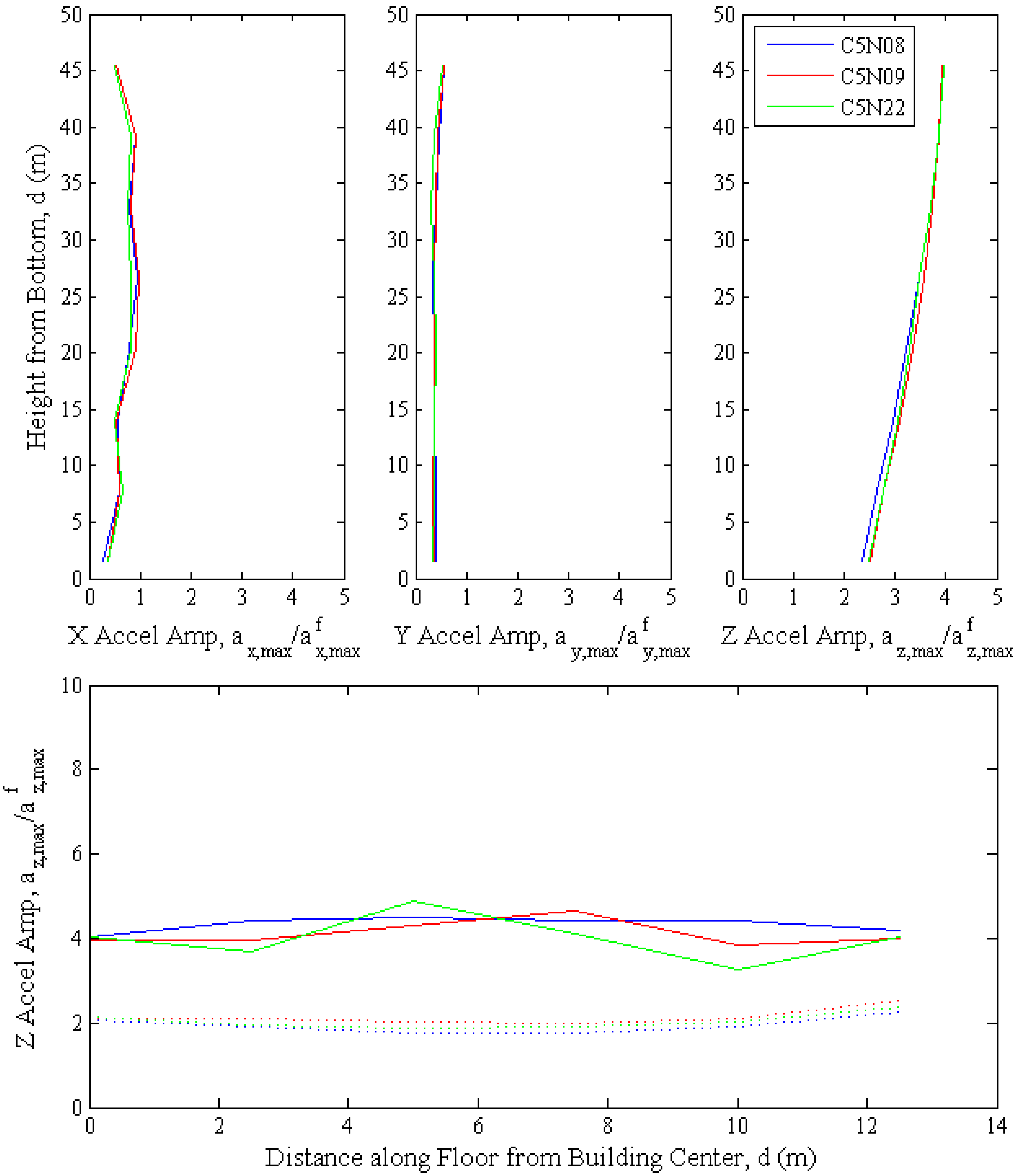

Figure F.3: Peak superstructure acceleration amplification data from the simulations with the cylindrical superstructure, no soil, and robust LR bearings subjected to the basic motions

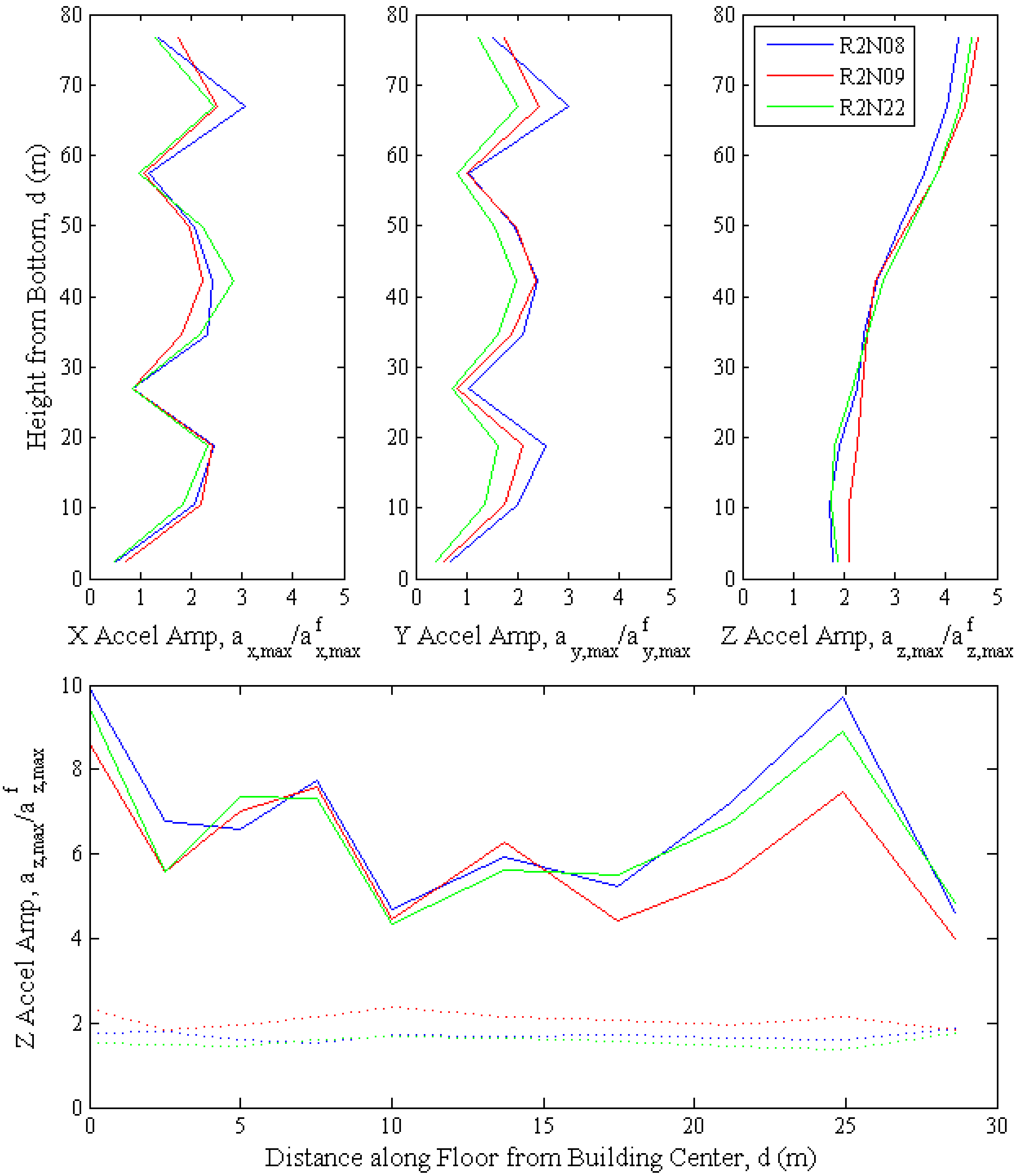

Figure F.4: Peak superstructure acceleration amplification data from the simulations with the rectangular superstructure, no soil, and FP bearings subjected to the basic motions

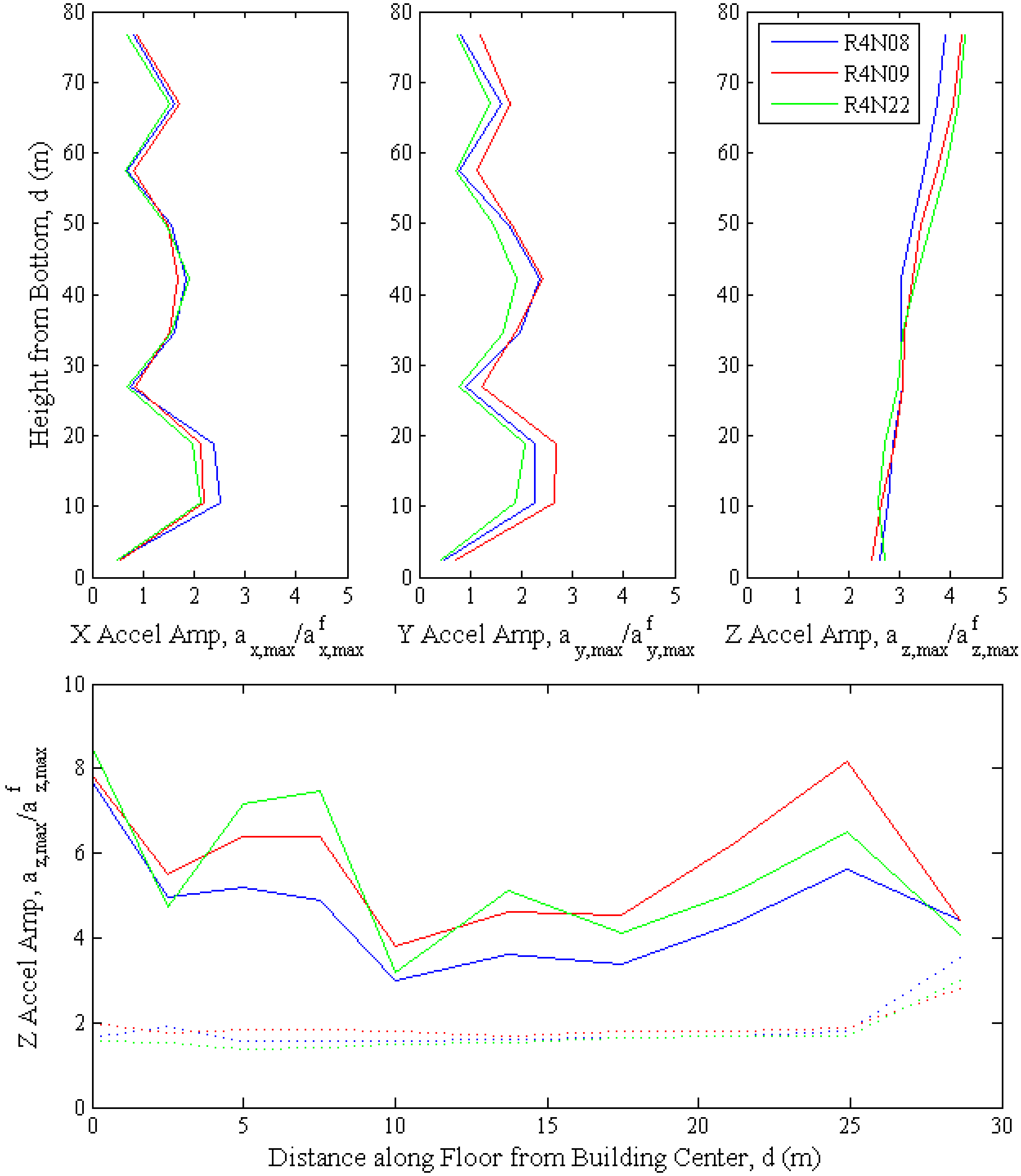

Figure F.5: Peak superstructure acceleration amplification data from the simulations with the rectangular superstructure, no soil, and simplified LR bearings subjected to the basic motions

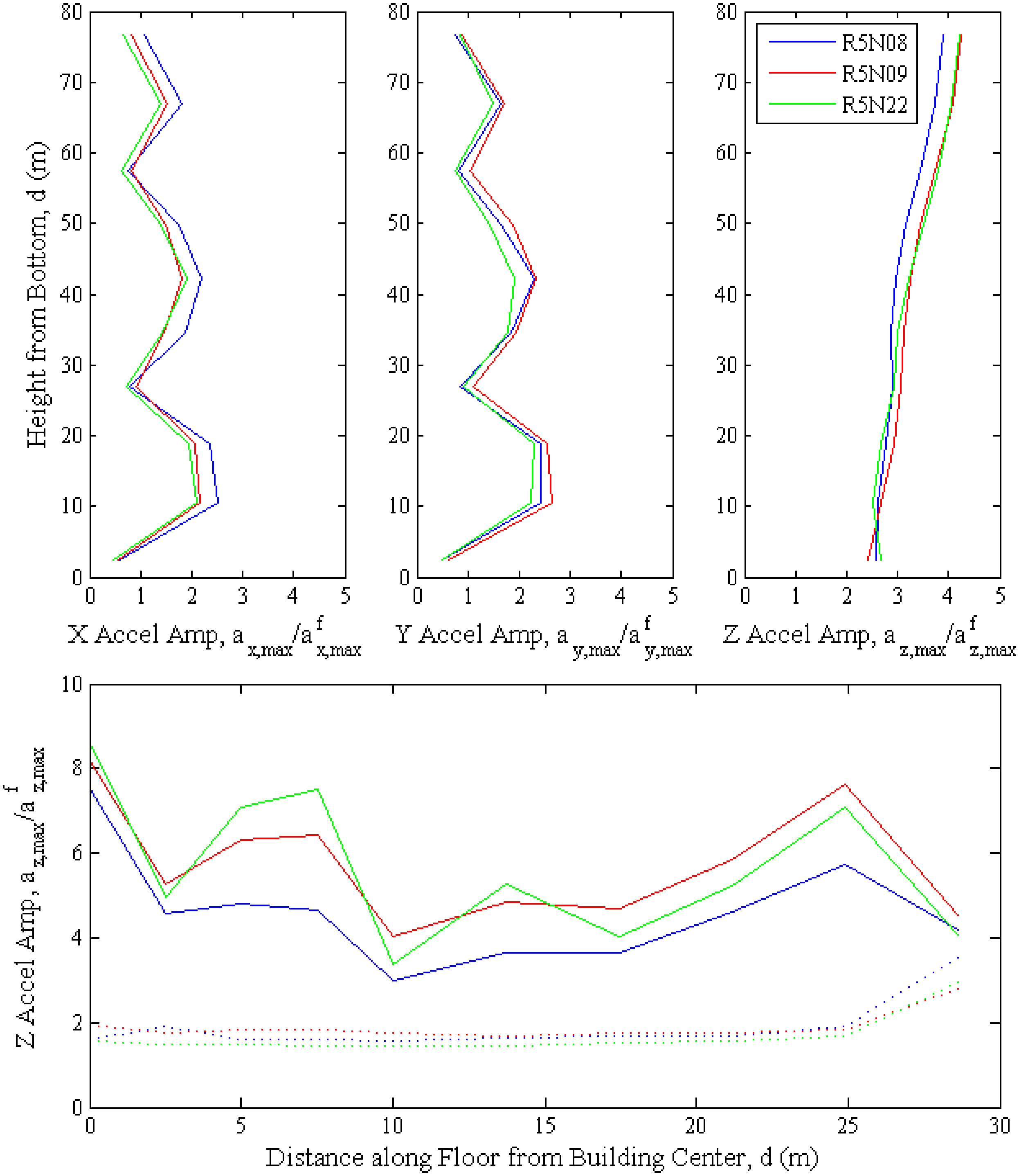

Figure F.6: Peak superstructure acceleration amplification data from the simulations with the rectangular superstructure, no soil, and robust LR bearings subjected to the basic motions

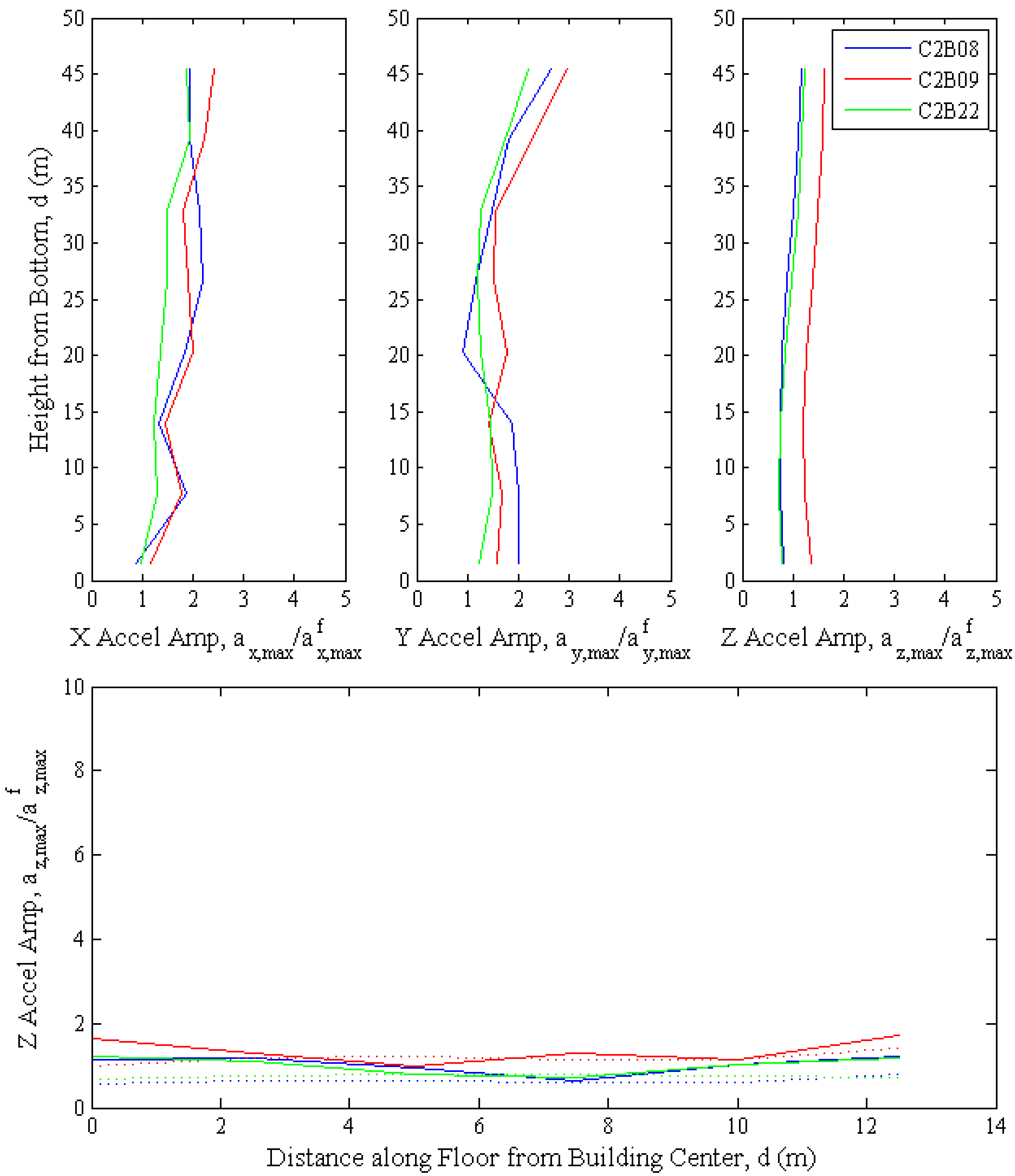

Figure F.7: Peak superstructure acceleration amplification data from the simulations with the cylindrical superstructure, soil column B, and FP bearings subjected to the basic motions

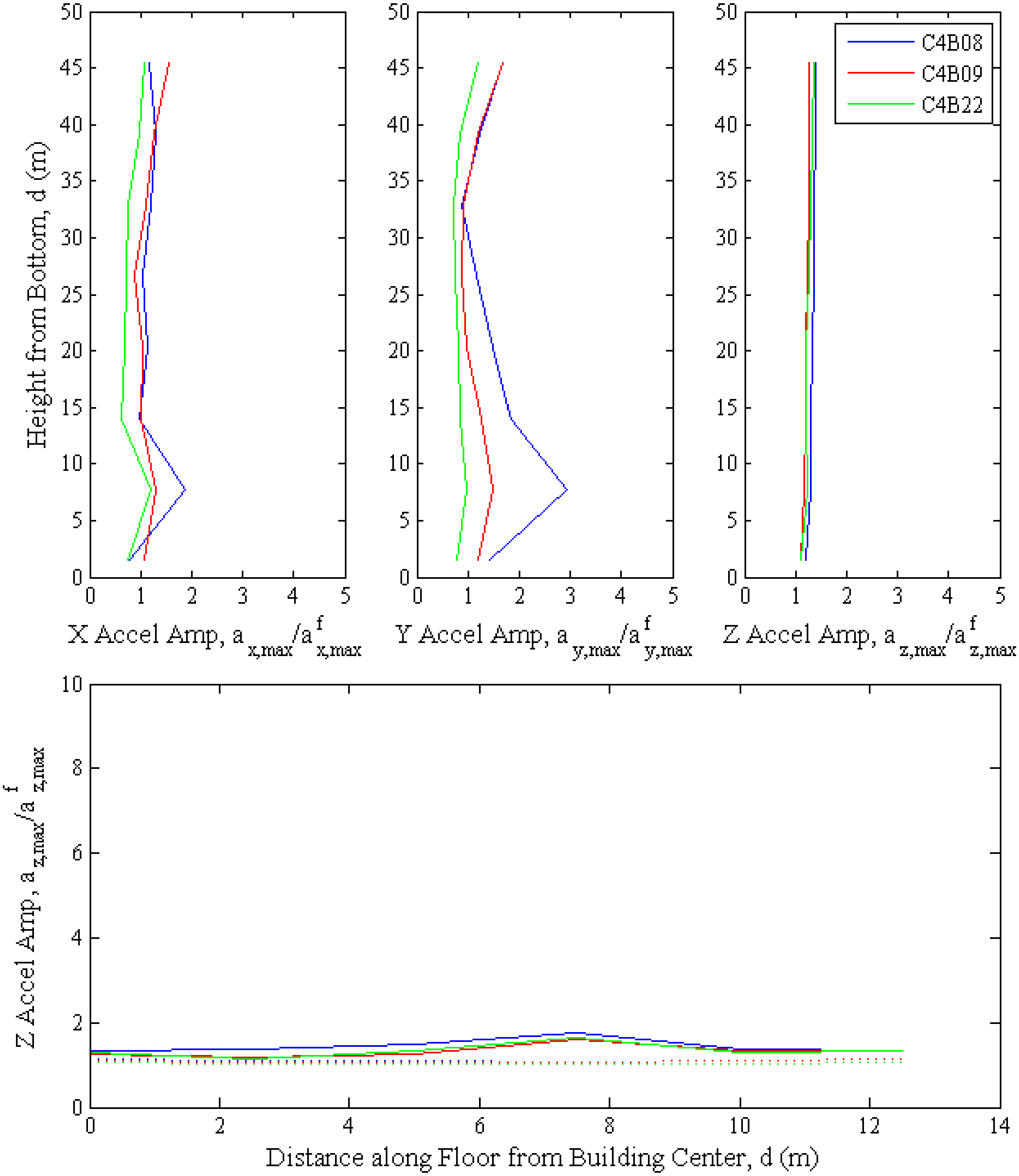

Figure F.8: Peak superstructure acceleration amplification data from the simulations with the cylindrical superstructure, soil column B, and simplified LR bearings subjected to the basic motions

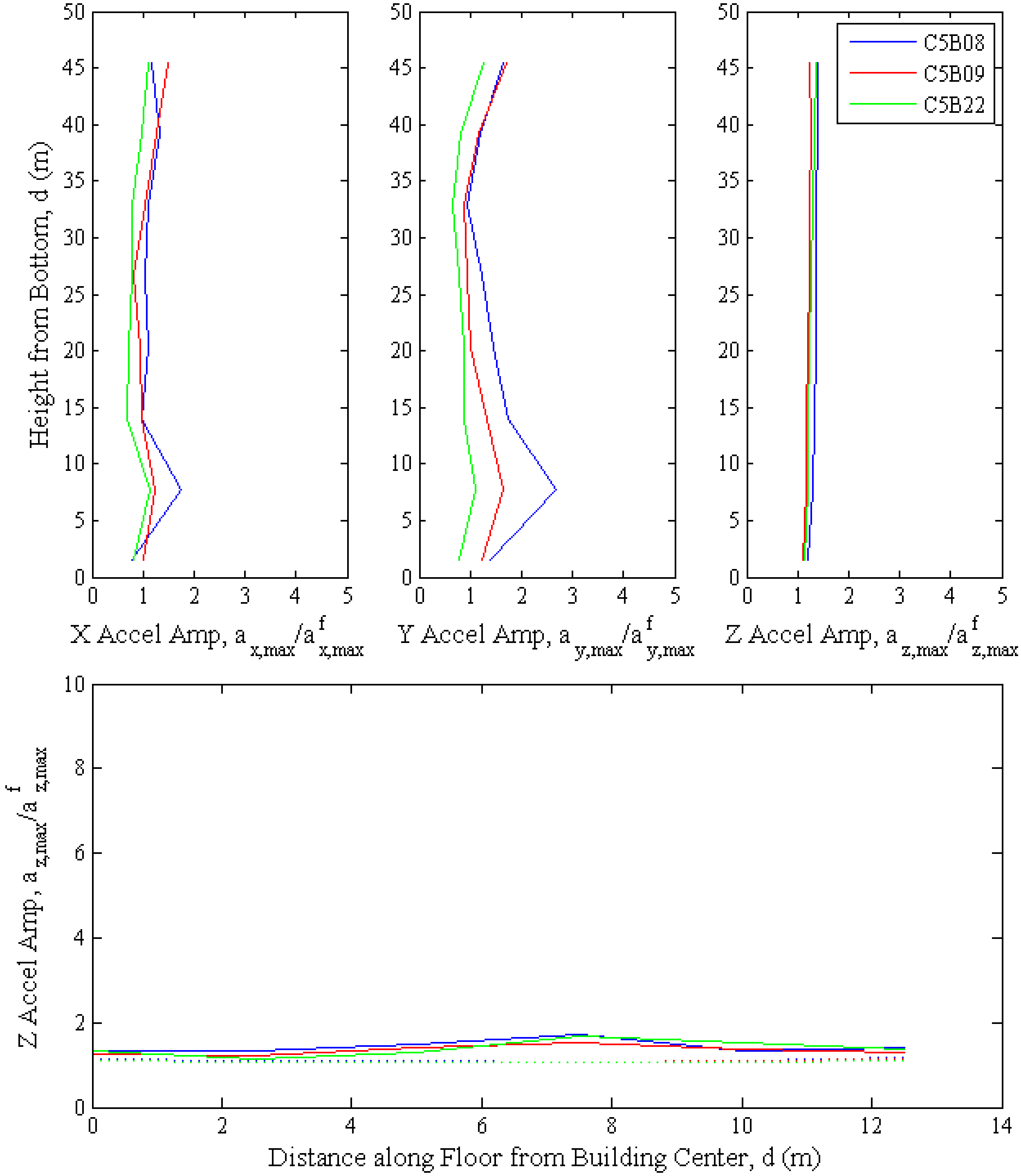

Figure F.9: Peak superstructure acceleration amplification data from the simulations with the cylindrical superstructure, soil column B, and robust LR bearings subjected to the basic motions

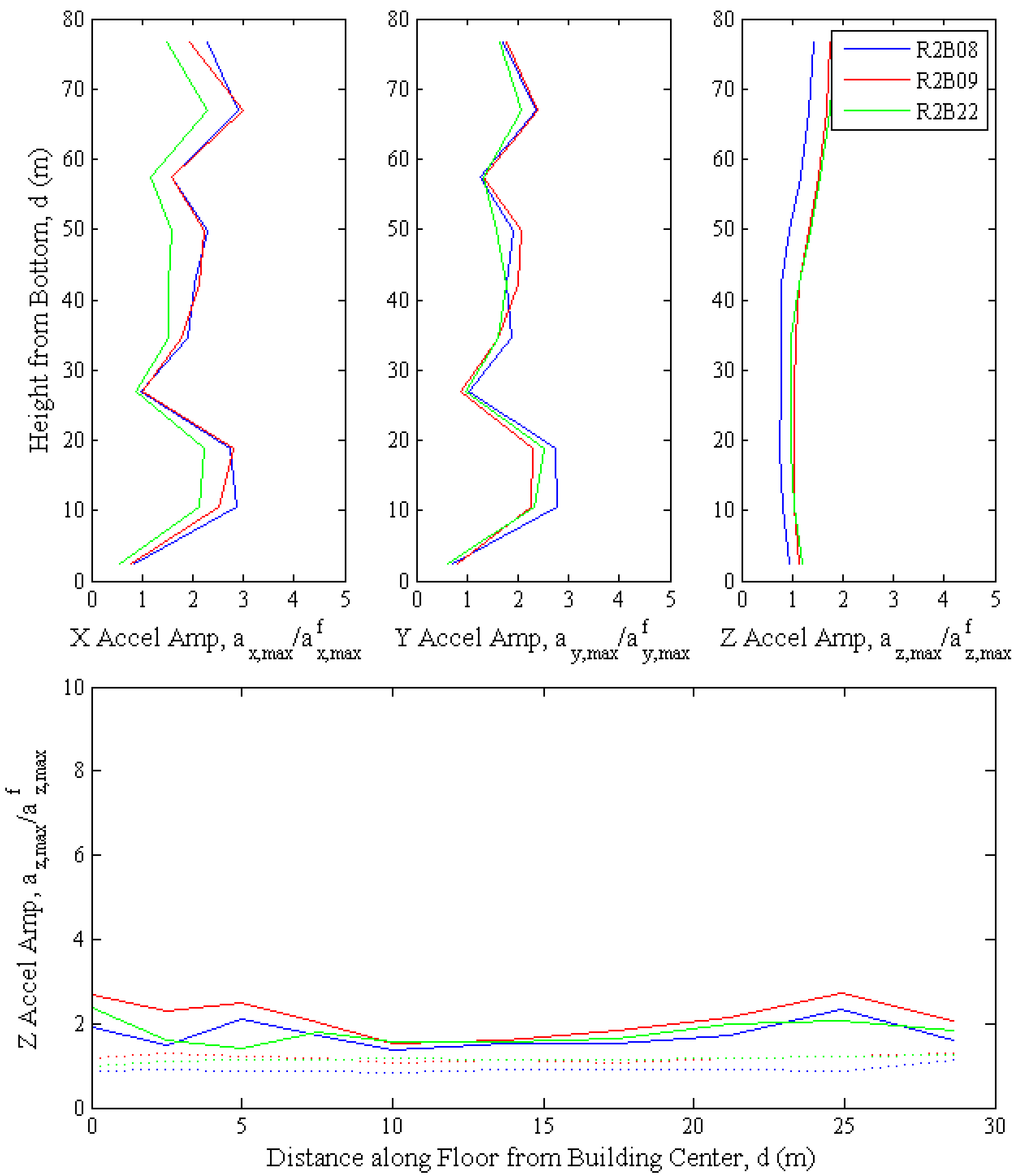

Figure F.10: Peak superstructure acceleration amplification data from the simulations with the rectangular superstructure, soil column B, and FP bearings subjected to the basic motions

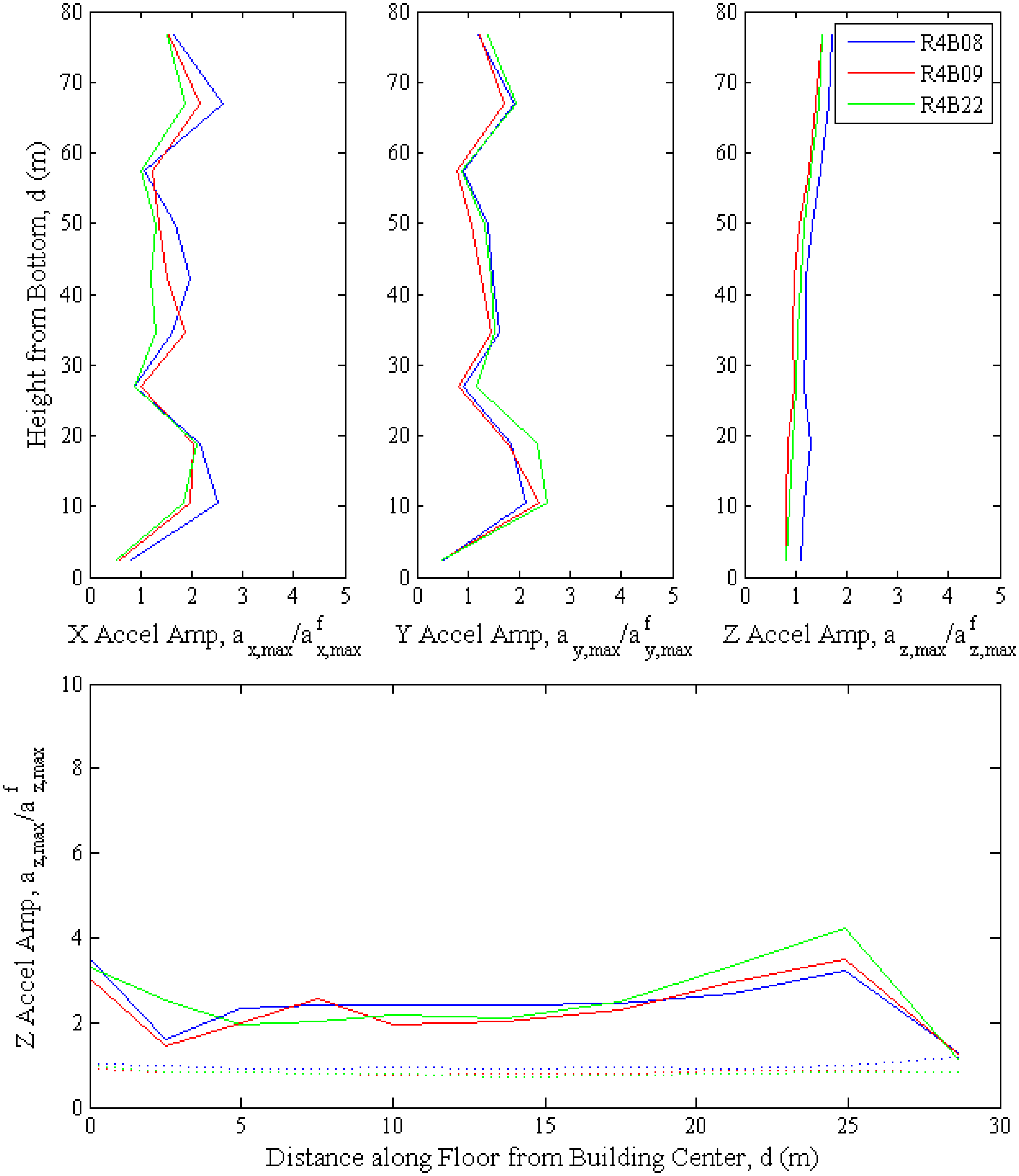

Figure F.11: Peak superstructure acceleration amplification data from the simulations with the rectangular superstructure, soil column B, and simplified LR bearings subjected to the basic motions

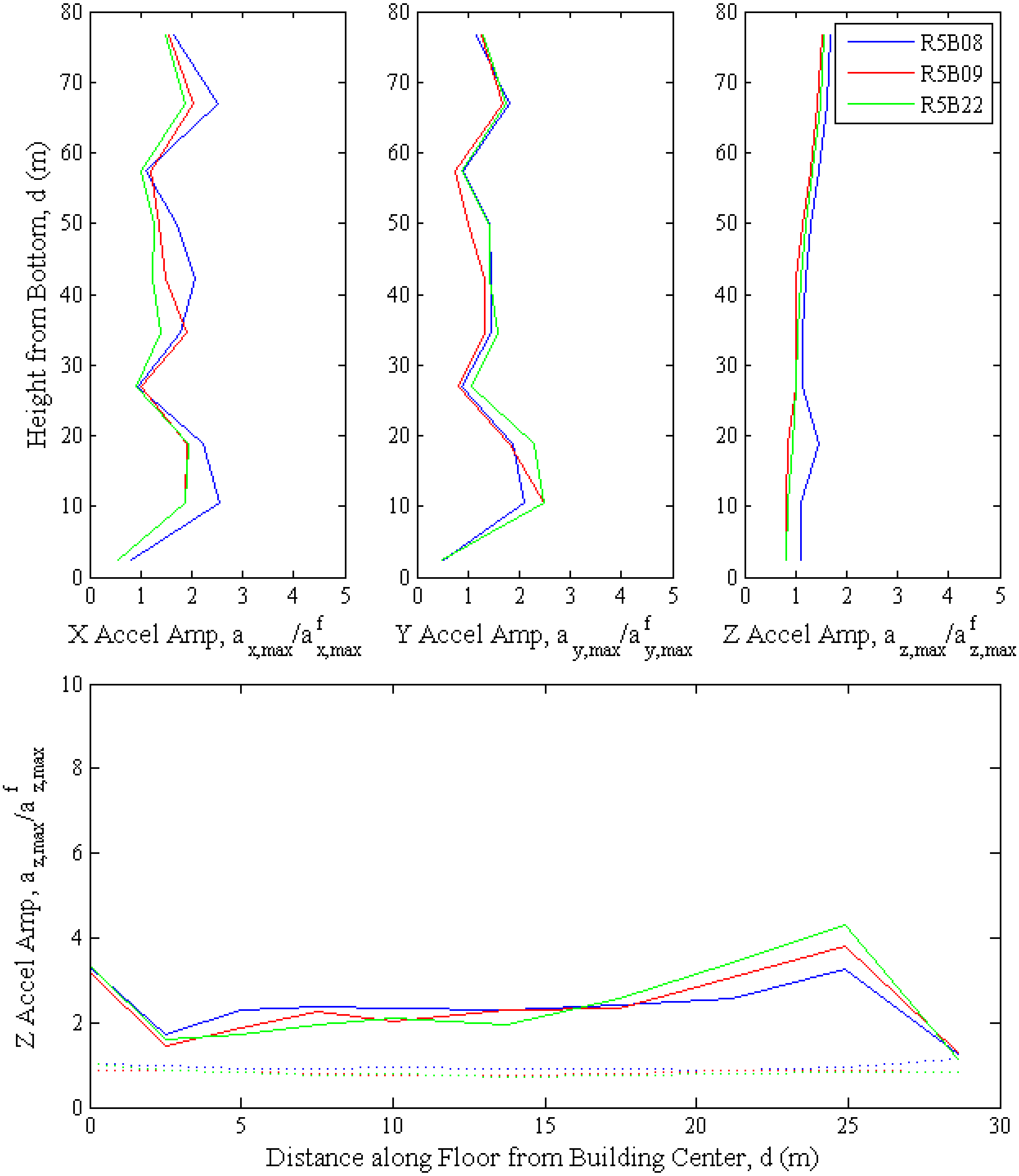

Figure F.12: Peak superstructure acceleration amplification data from the simulations with the rectangular superstructure, soil column B, and robust LR bearings subjected to the basic motions

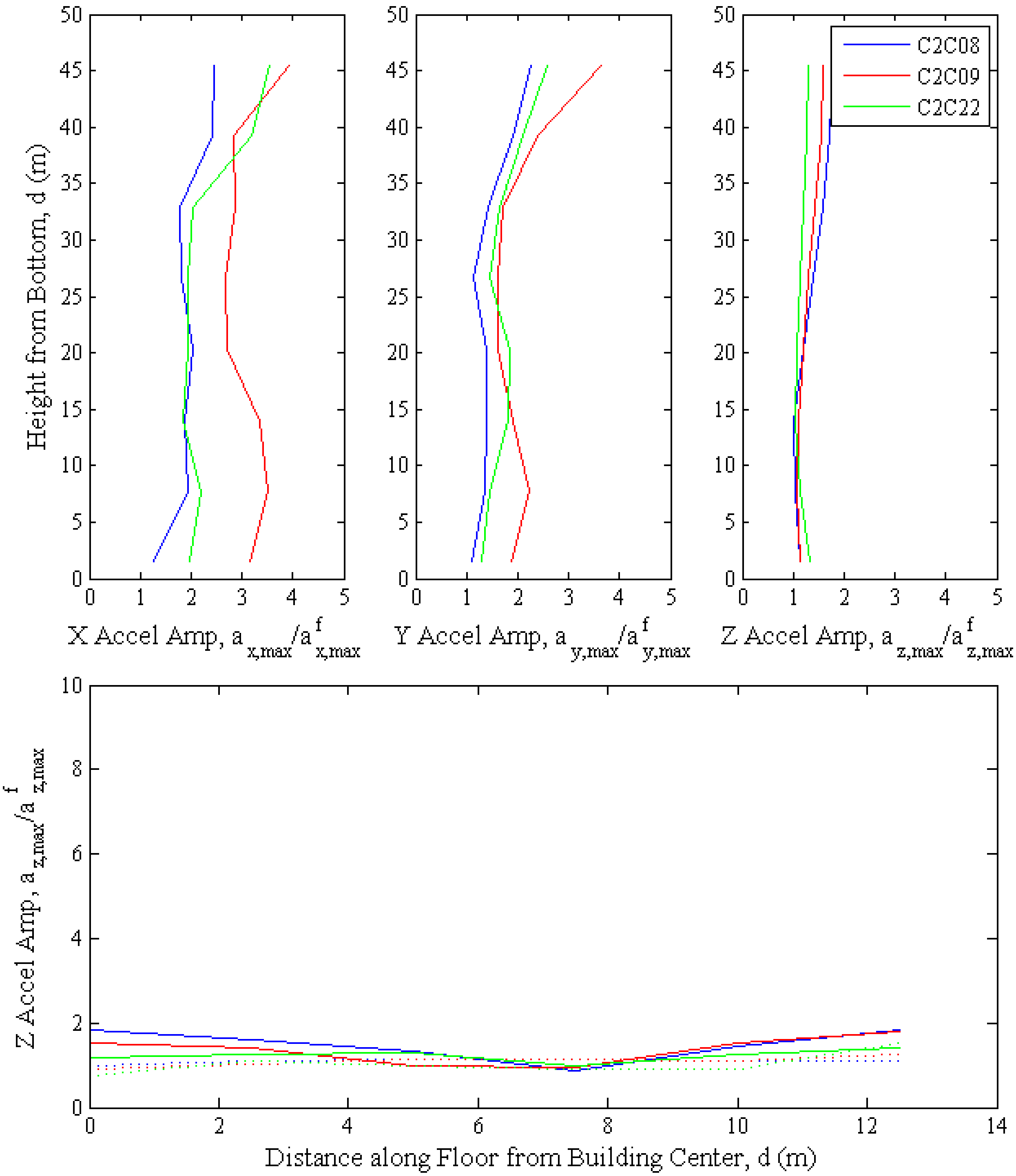

Figure F.13: Peak superstructure acceleration amplification data from the simulations with the cylindrical superstructure, soil column C, and FP bearings subjected to the basic motions

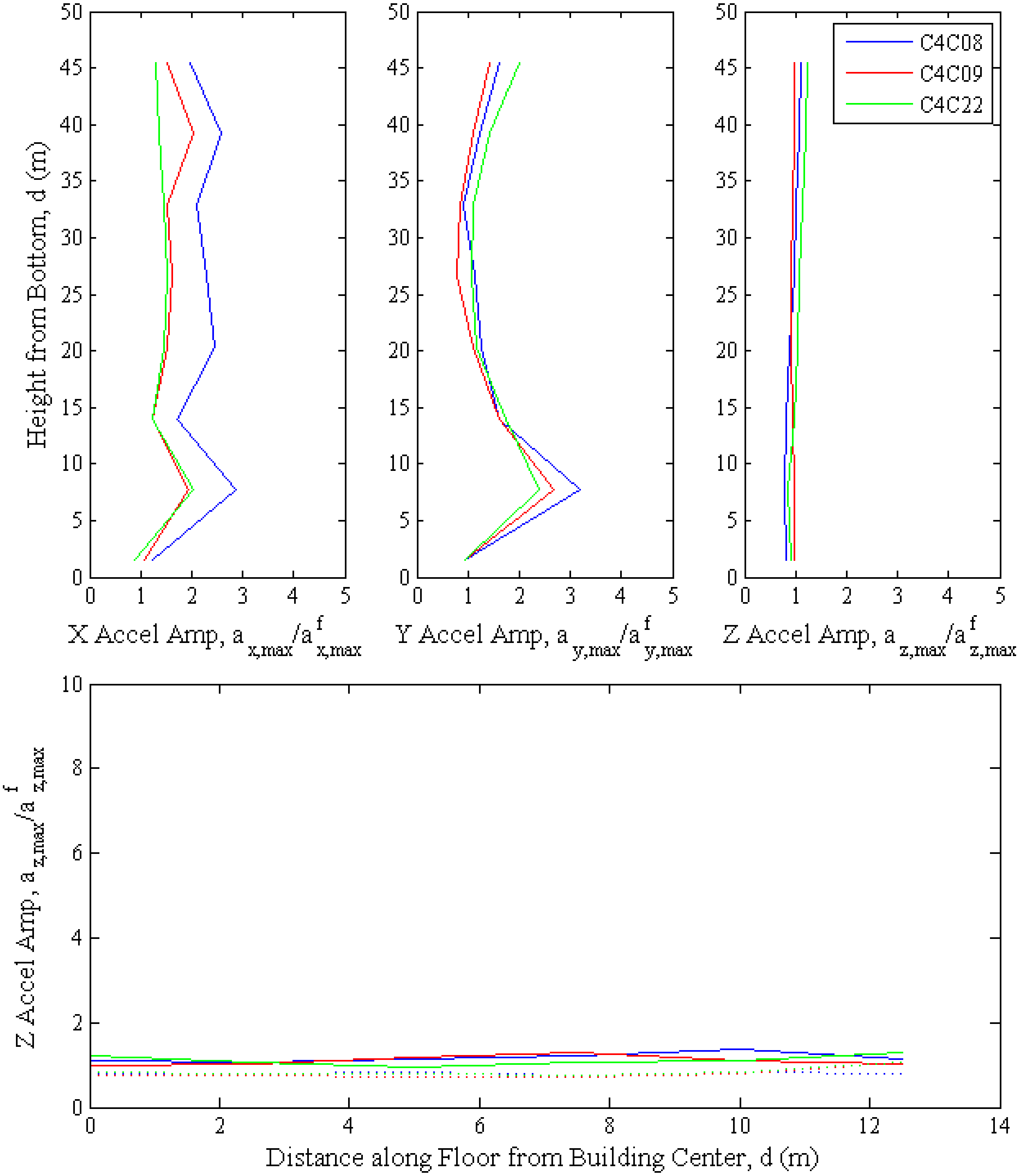

Figure F.14: Peak superstructure acceleration amplification data from the simulations with the cylindrical superstructure, soil column C, and simplified LR bearings subjected to the basic motions

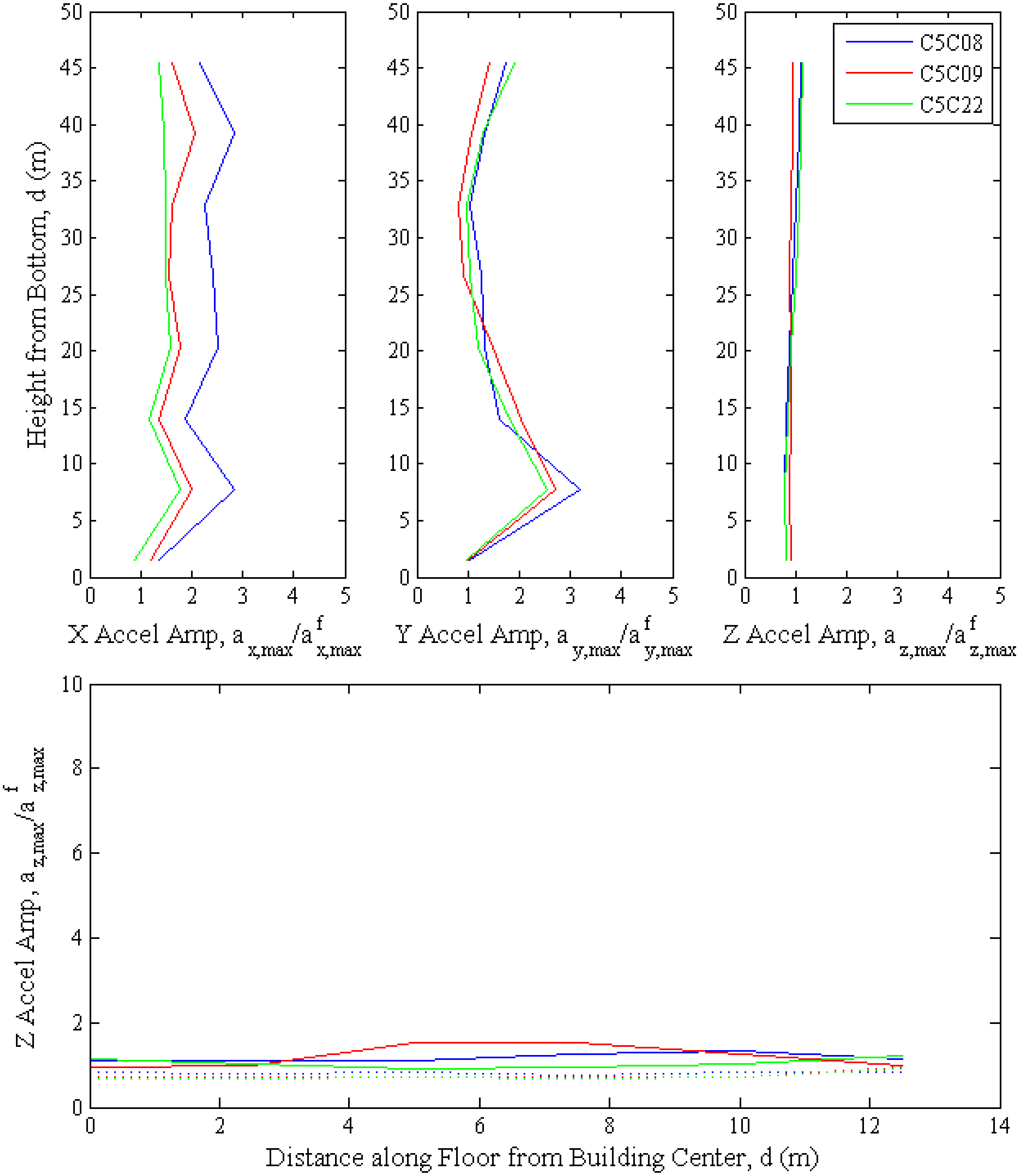

Figure F.15: Peak superstructure acceleration amplification data from the simulations with the cylindrical superstructure, soil column C, and robust LR bearings subjected to the basic motions

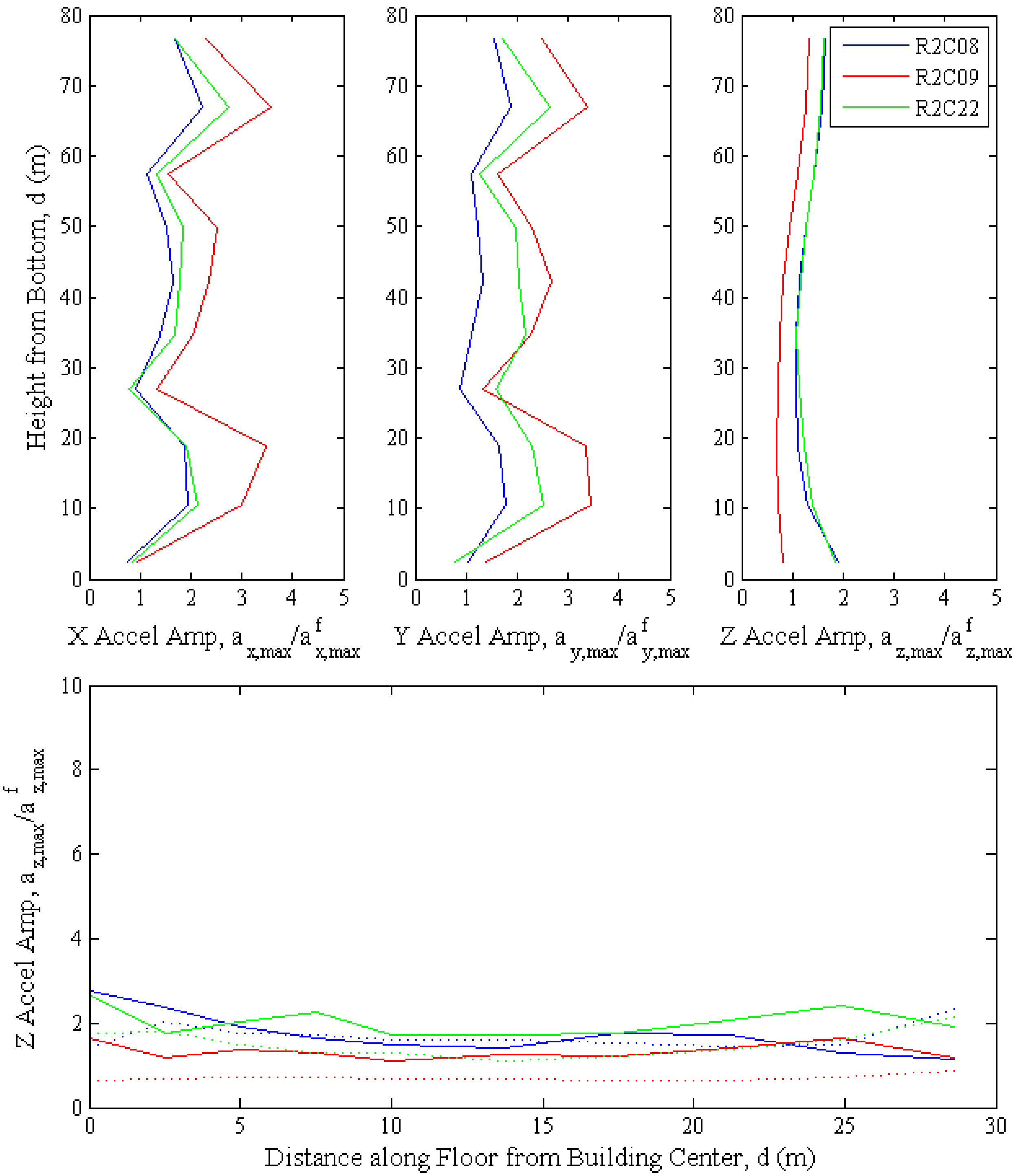

Figure F.16: Peak superstructure acceleration amplification data from the simulations with the rectangular superstructure, soil column C, and FP bearings subjected to the basic motions

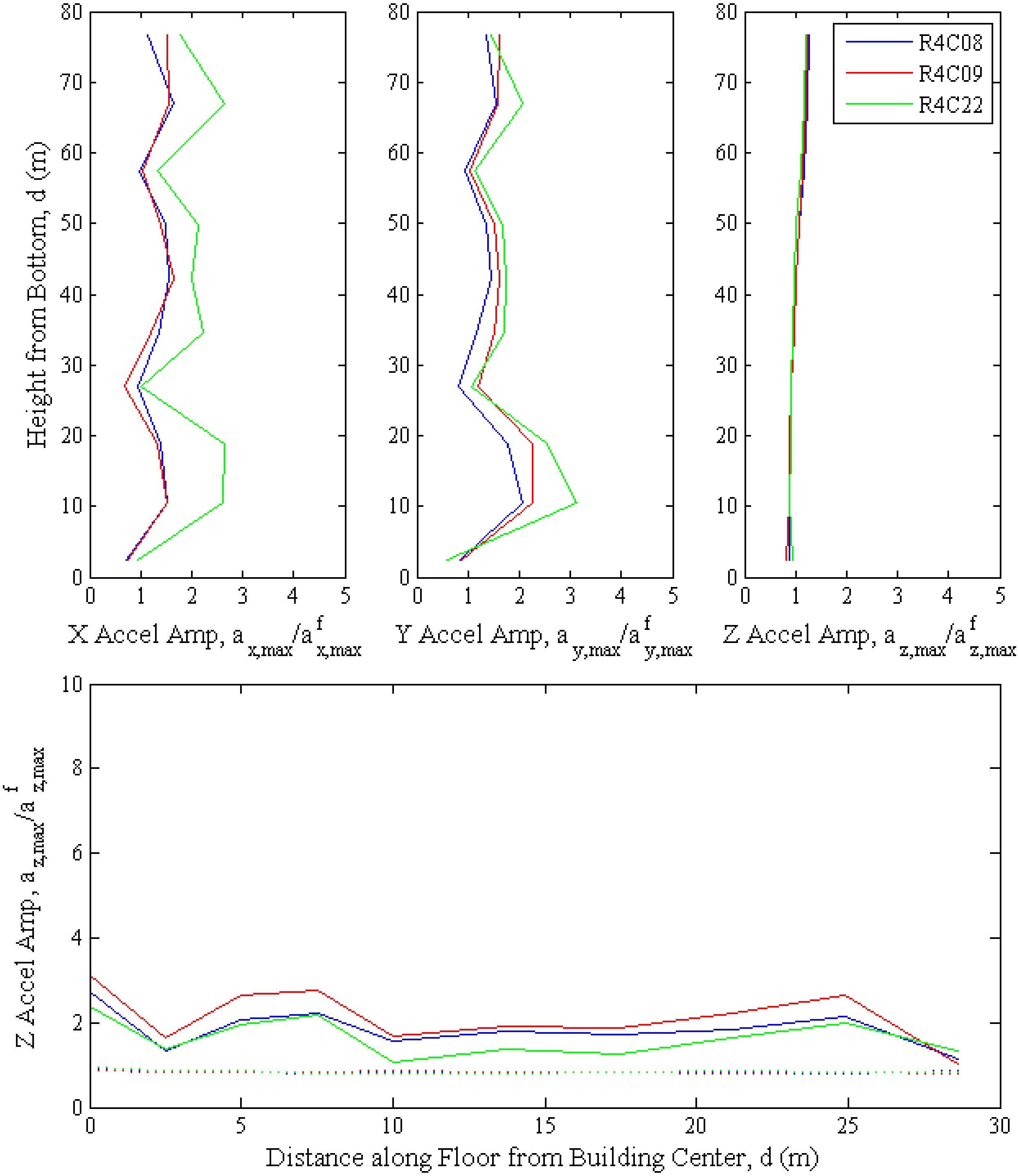

Figure F.17: Peak superstructure acceleration amplification data from the simulations with the rectangular superstructure, soil column C, and simplified LR bearings subjected to the basic motions

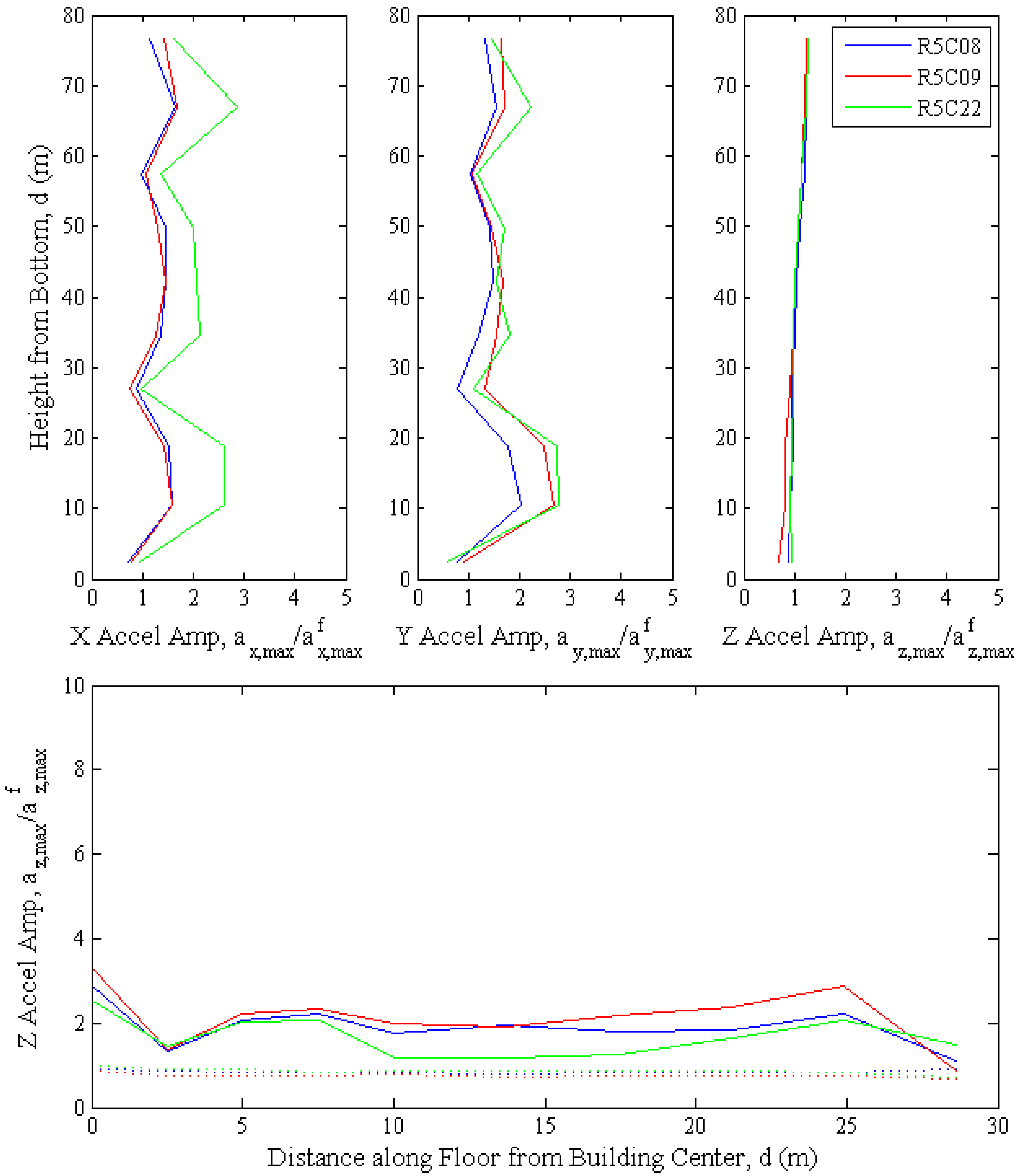

Figure F.18: Peak superstructure acceleration amplification data from the simulations with the rectangular superstructure, soil column C, and robust LR bearings subjected to the basic motions

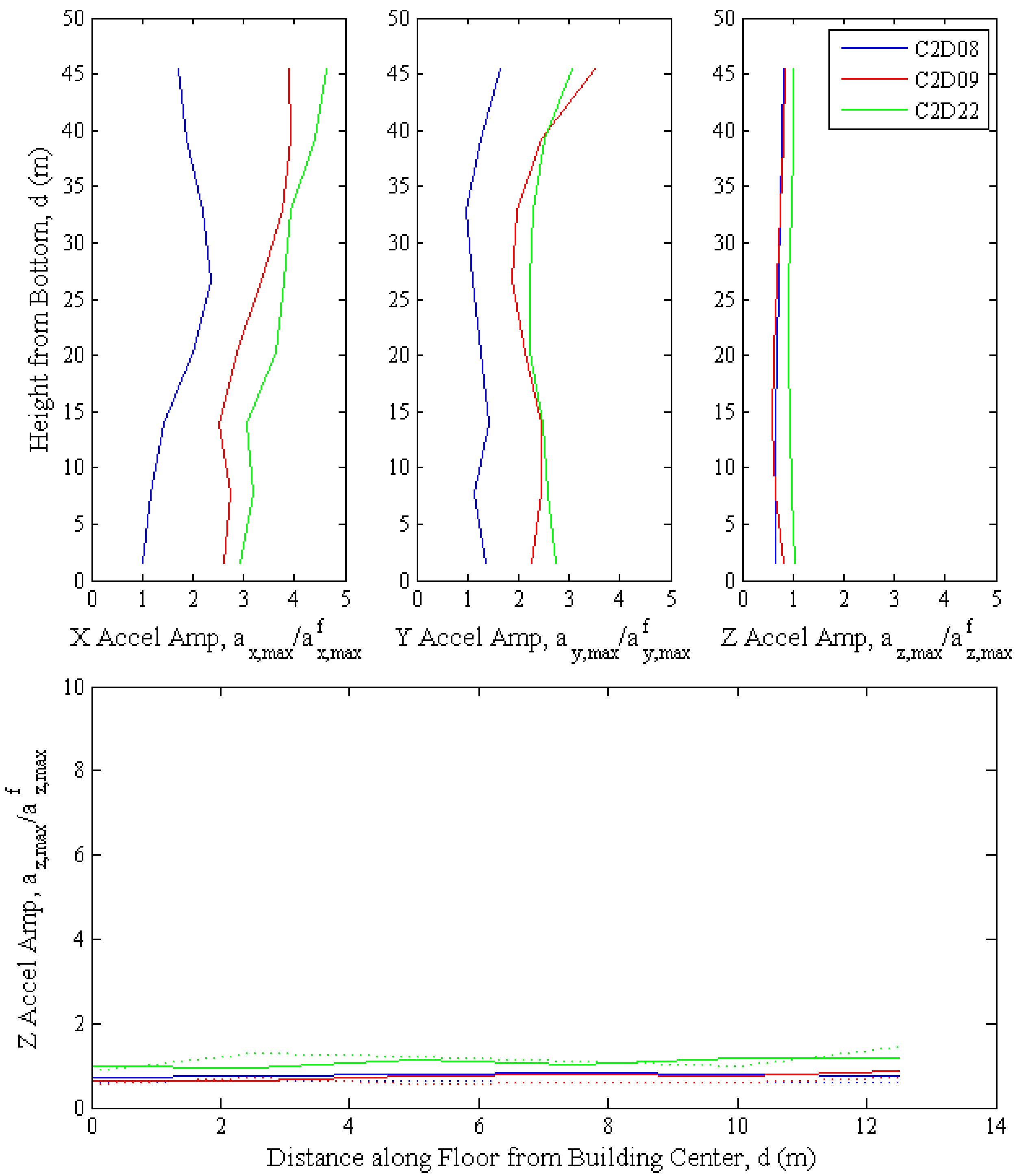

Figure F.19: Peak superstructure acceleration amplification data from the simulations with the cylindrical superstructure, soil column D, and FP bearings subjected to the basic motions

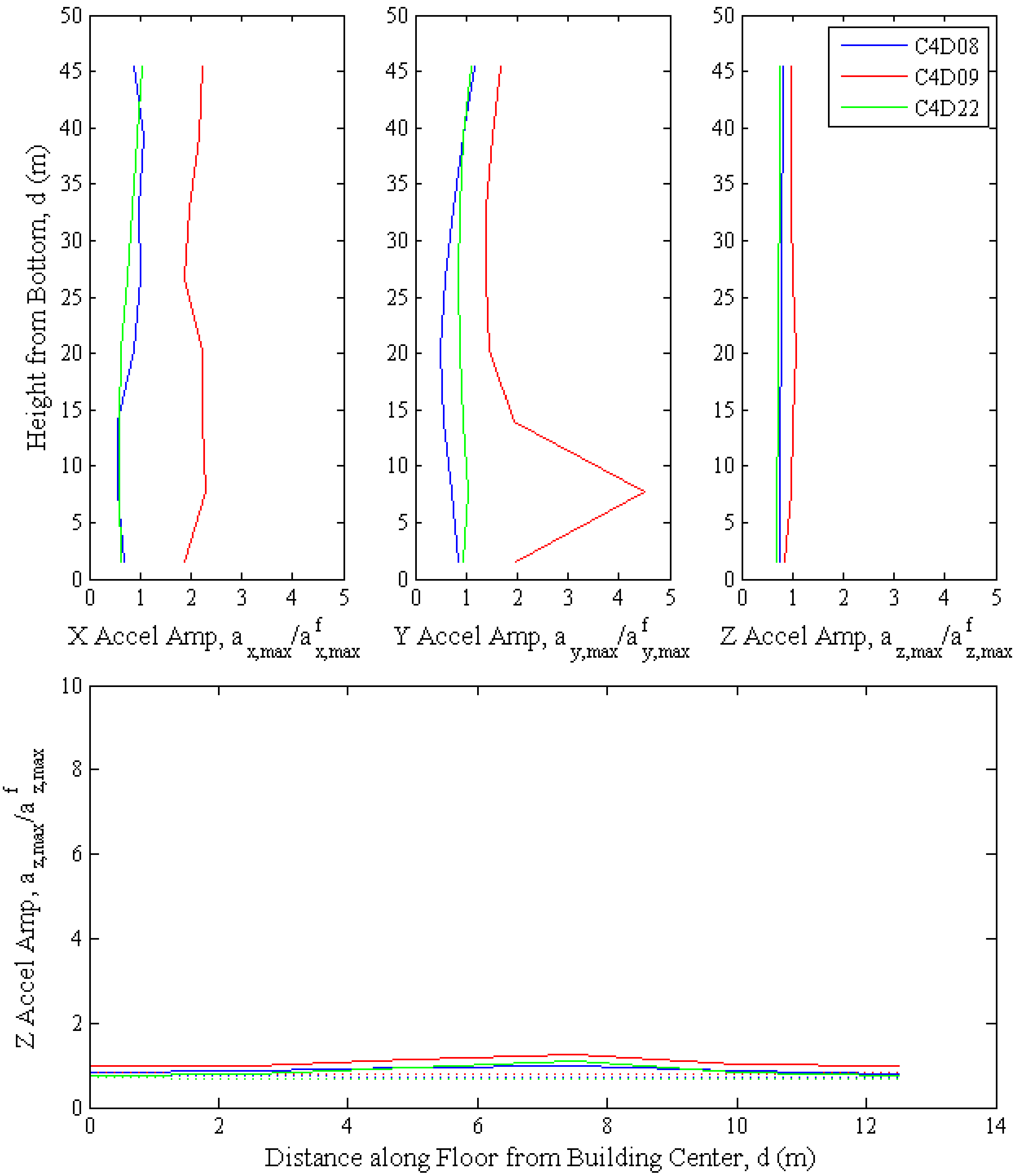

Figure F.20: Peak superstructure acceleration amplification data from the simulations with the cylindrical superstructure, soil column D, and simplified LR bearings subjected to the basic motions

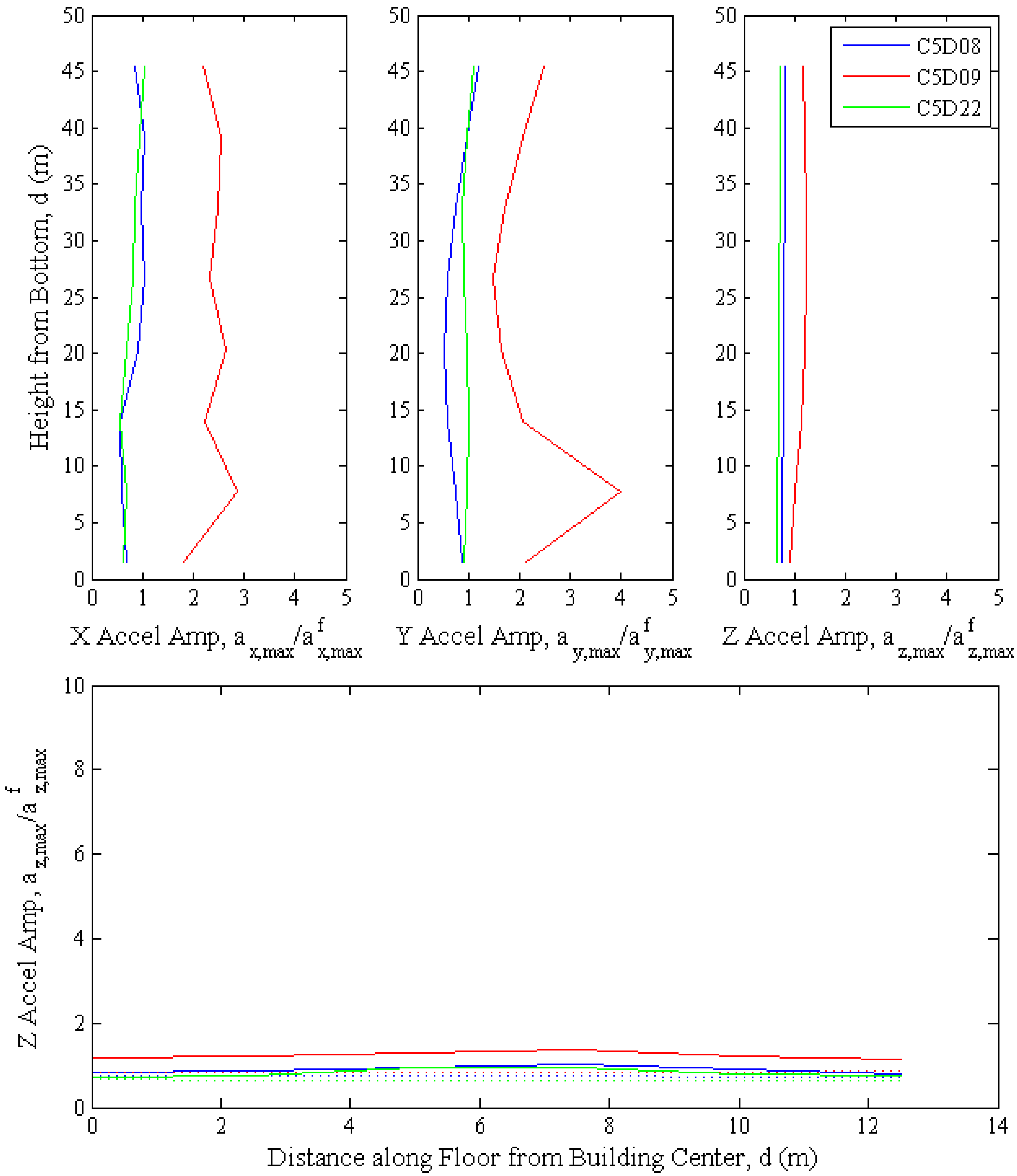

Figure F.21: Peak superstructure acceleration amplification data from the simulations with the cylindrical superstructure, soil column D, and robust LR bearings subjected to the basic motions

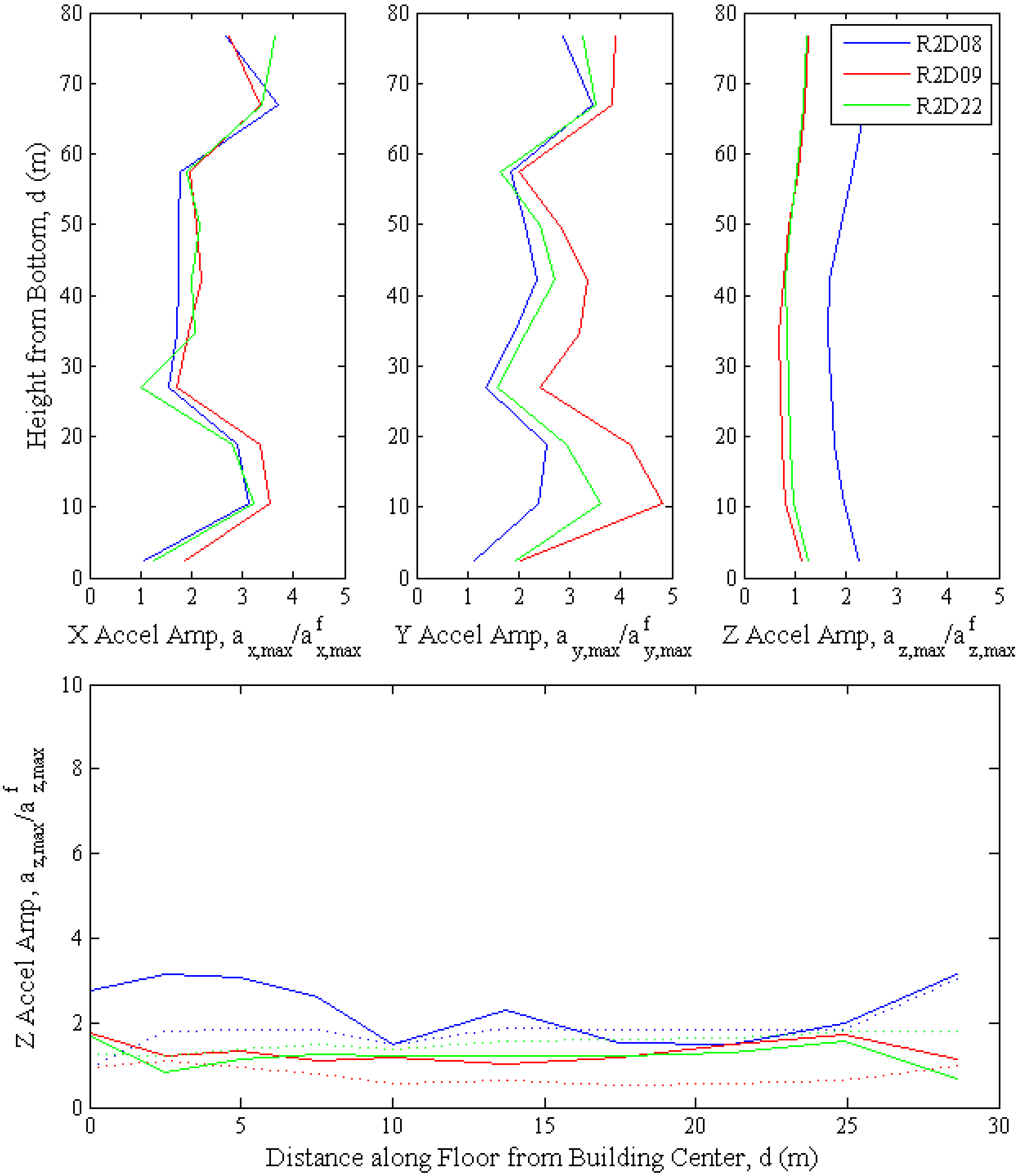

Figure F.22: Peak superstructure acceleration amplification data from the simulations with the rectangular superstructure, soil column D, and FP bearings subjected to the basic motions

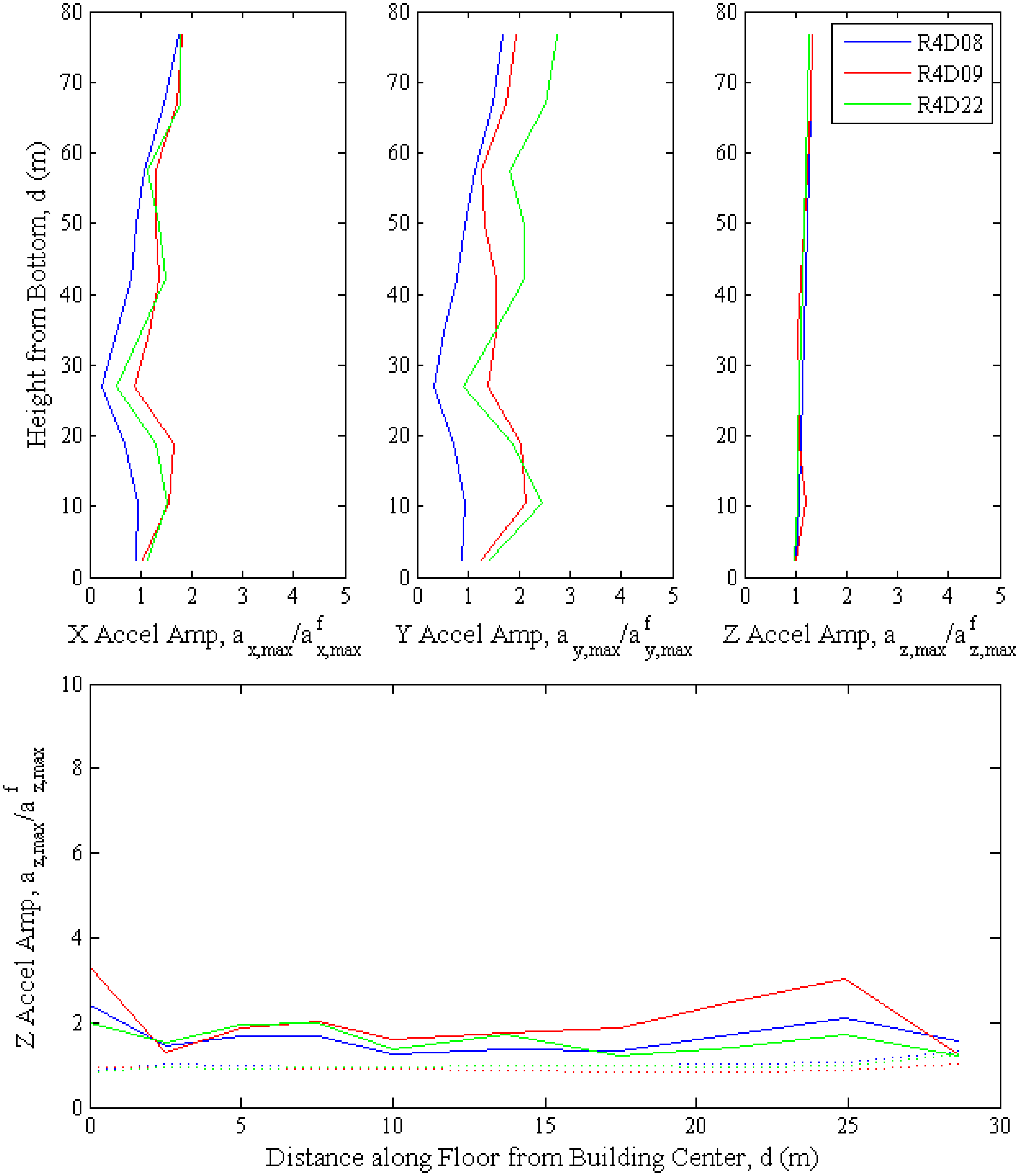

Figure F.23: Peak superstructure acceleration amplification data from the simulations with the rectangular superstructure, soil column D, and simplified LR bearings subjected to the basic motions

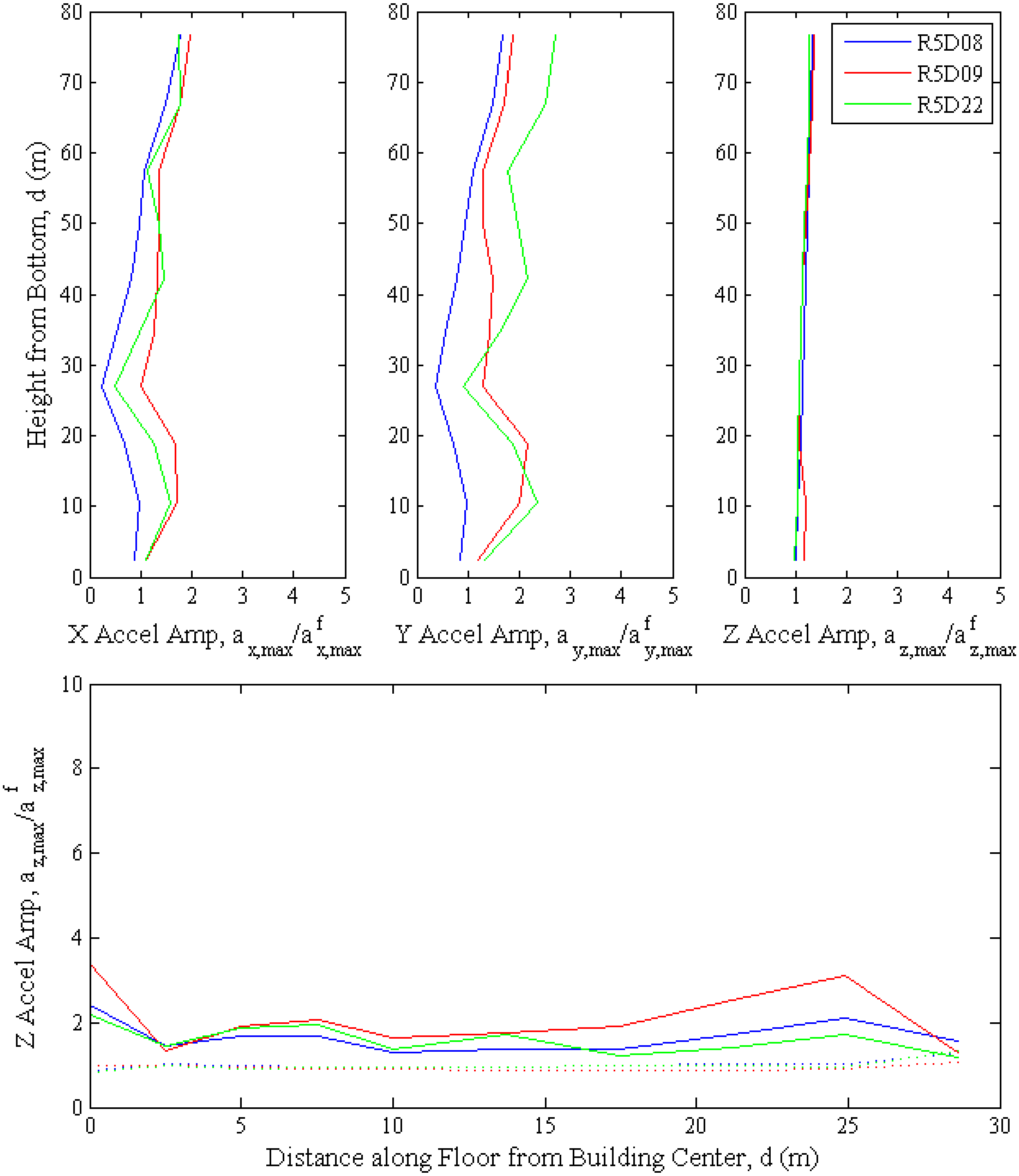

Figure F.24: Peak superstructure acceleration amplification data from the simulations with the rectangular superstructure, soil column D, and robust LR bearings subjected to the basic motions

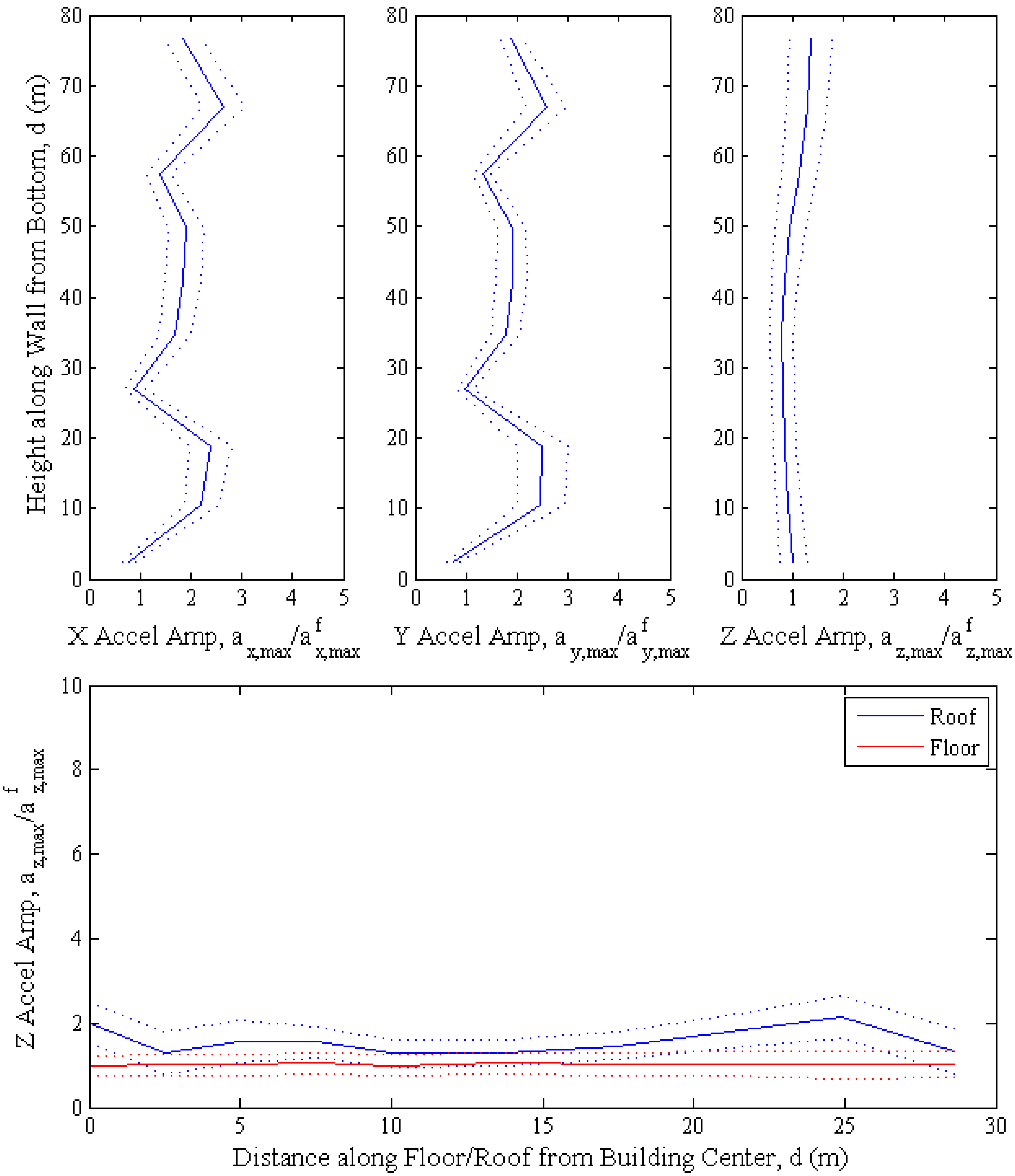

Figure F.25: Median superstructure acceleration amplification peaks from the simulations with the rectangular superstructure, soil column B, and FP bearings subjected to all ground motions

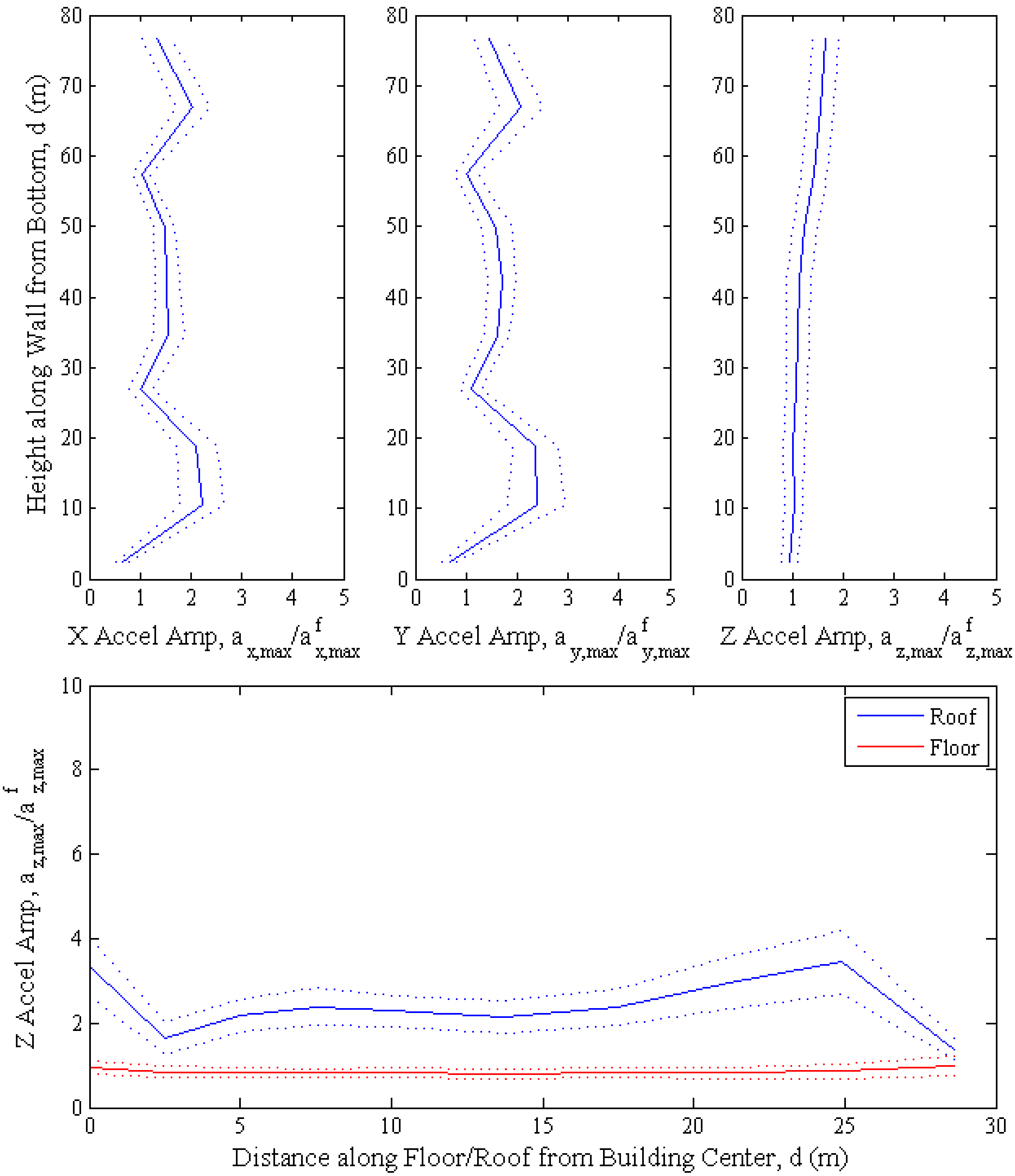

Figure F.26: Median superstructure acceleration amplification peaks from the simulations with the rectangular superstructure, soil column B, and simplified LR bearings subjected to all ground motions

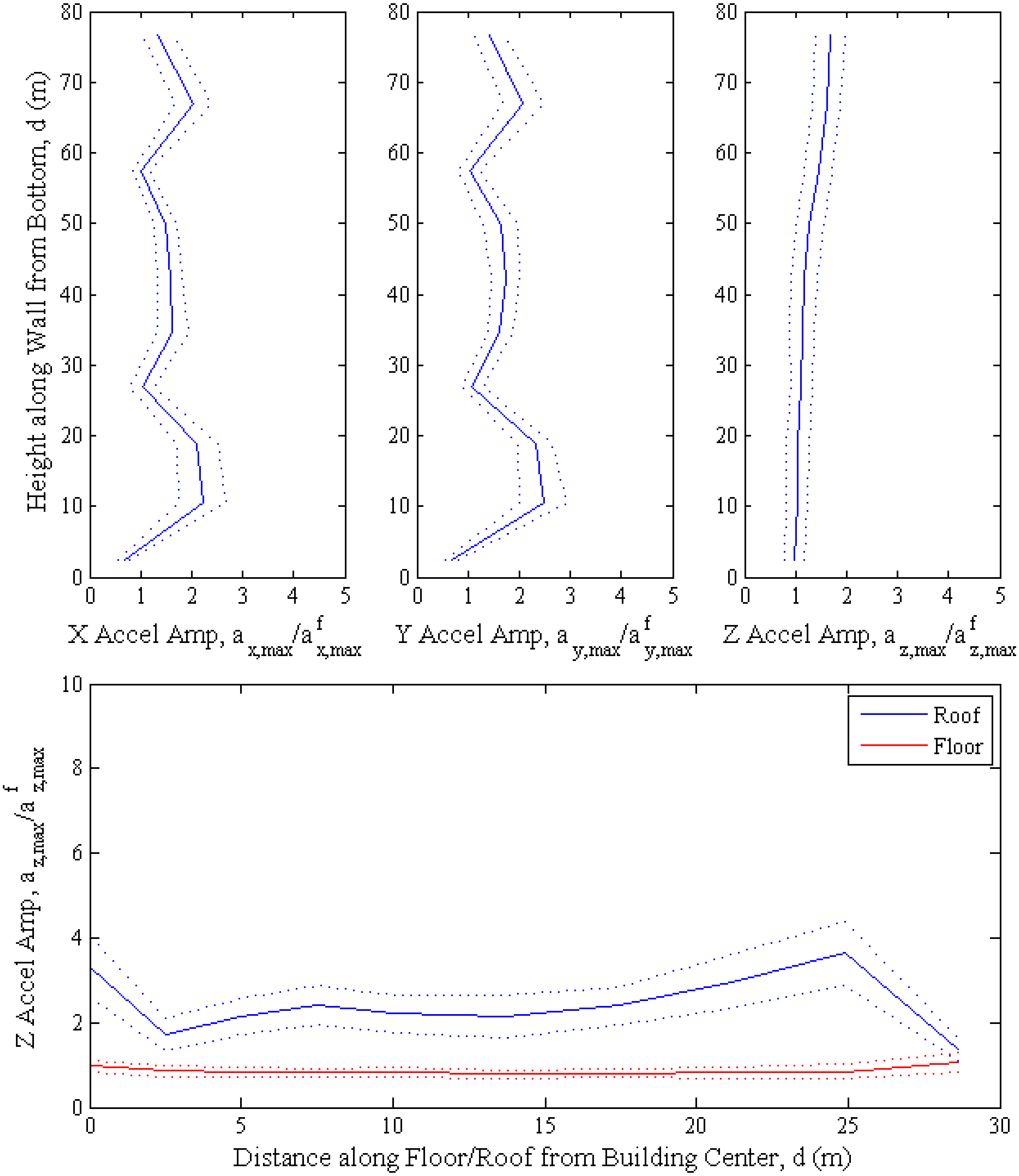

Figure F.27: Median superstructure acceleration amplification peaks from the simulations with the rectangular superstructure, soil column B, and robust LR bearings subjected to all ground motions